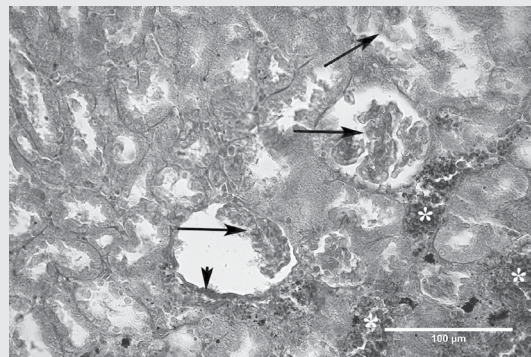


ISSN 0015-5659
eISSN 1644-3284
Impact Factor: 0.941

POLISH ANATOMICAL SOCIETY

FOLIA **MORPHOLOGICA**



Vol. 80 2021 No. 2


VIA MEDICA

https://journals.viamedica.pl/fovia_morphologica

FOLIA MORPHOLOGICA

An international multidisciplinary journal devoted to fundamental research in the morphological sciences
Official Journal of the Polish Anatomical Society
(a Constituent Member of European Federation for Experimental Morphology — EFEM)

EDITOR-IN-CHIEF

Janusz Moryś

Department of Anatomy and Neurobiology
Medical University of Gdańsk

https://journals.viamedica.pl/folia_morphologica

*See our website for information on manuscript status, aims and scope,
instructions for authors as well as editorial board.*

Folia Morphologica

Publishing, Subscription and Advertising Office:

VM Media sp. z o.o. VM Group sp.k., Grupa Via Medica

ul. Świętokrzyska 73, 80–180 Gdańsk, Poland

tel. (+48 58) 320 94 94, fax (+48 58) 320 94 60

Managing editor

Joanna Niezgoda

e-mail: joanna.niezgoda@viamedica.pl

Cover designer

Sylvia Scisłowska

The journal is published at: www.fm.viamedica.pl in one volume per year consisting of four numbers. **Subscription rates:** Paper subscription, 4 issues incl. package and postage institutional — 140 euro. The above prices are inclusive of regular postage costs. Payment should be made to: VM Media sp. z o.o. VM Group sp.k., Grupa Via Medica, Bank BGŻ Paribas SA account number: 15 1600 1303 0004 1007 1035 9021; SWIFT: PPABPLPK. Single issues, subscriptions orders and requests for sample copies should be send to e-mail: prenumerata@viamedica.pl. Electronic orders option available at: https://journals.viamedica.pl/folia_morphologica. The publisher must be notified of a cancellation of access to electronic version not later than two months before the end of a calendar year. After that date electronic access will be automatically prolonged for another year.

Advertising. For details on media opportunities within this electronic version of journal please contact the advertising sales department, ul. Świętokrzyska 73, 80–180 Gdańsk, Poland, tel: (+48 58) 320 94 94, e-mail: viamedica@viamedica.pl

The editors accept no responsibility for advertisement contents.

Folia Morphologica is the official journal of the Polish Anatomical Society. For information about the Society, please contact: Prof. Marek Grzybiak, Department of Clinical Anatomy, Medical University of Gdansk, ul. Dębinki 1, 80–211 Gdańsk, Poland, tel: +48 58 349 14 22, e-mail: grzybiak@gumed.edu.pl

All rights reserved, including translation into foreign languages. No part of this periodical, either text or illustration, may be used in any form whatsoever. It is particularly forbidden for any part of this material to be copied or translated into a mechanical or electronic language and also to be recorded in whatever form, stored in any kind of retrieval system or transmitted, whether in an electronic or mechanical form or with the aid of photocopying, microfilm, recording, scanning or in any other form, without the prior written permission of the publisher. The rights of the publisher are protected by national copyright laws and by international conventions, and their violation will be punishable by penal sanctions.

Editorial policies and author guidelines are published on journal website: https://journals.viamedica.pl/folia_morphologica

Legal note: https://journals.viamedica.pl/folia_morphologica/about/legalNote

Folia Morphologica is indexed by: BIOSIS Previews, CAS, CINAHL, CrossRef, Dental Abstracts, EBSCO, Elsevier BIOBASE, EMBIOLOGY, FMJ, Google Scholar, Index Copernicus (154.80), Index Medicus/MEDLINE, Index Scholar, Ministry of Science and Higher Education (70), NCBI/National Center for Biotechnology Information, Polish Medical Bibliography, Scopus, SJR, Thomson Reuters, Thomson Scientific Products — Biological Abstracts, Ulrich's Periodicals Directory, Veterinary Bulletin, WorldCat and Zoological Record. Position in Index Copernicus ranking systems is available at: www.indexcopernicus.com. Current Impact Factor of Folia Morphologica (2019) is 0.941.



FOLIA MORPHOLOGICA

Editor-in-Chief
JANUSZ MORYŚ

Department of Anatomy and Neurobiology, Medical University of Gdańsk
ul. Dębinki 1, 80–211 Gdańsk, Poland
tel. (+48 58) 349 1401, fax (+48 58) 349 1421, e-mail: jmorys@gumed.edu.pl

EDITORIAL ADVISORY BOARD

Rafael BOSCOLO-BERTO, *Department of Neuroscience, University of Padova, Italy*

Franciszek BURDAN, *Experimental Teratology Unit of the Human Anatomy Department, Medical University of Lublin, Poland*

Małgorzata BRUSKA, *Department of Anatomy, University Medical School, Poznań, Poland*

Mafalda CACCIOTTOLO, *USC Leonard Davis School of Gerontology, University of Southern California, Los Angeles, United States*

Stephen W. CARMICHAEL, *Department of Anatomy, Mayo Clinic, Rochester, United States*

Bogdan CISZEK, *Department of Human Anatomy, Medical University of Warsaw, Poland*

Om Prakash CHOUDHARY, *Department of Veterinary Anatomy and Histology, Central Agricultural University, Aizawl, India*

Carla D'AGOSTINO, *Neuromuscular Center, University of Southern California, Los Angeles, CA, United States*

Zygmund Antoni DOMAGAŁA, *Department of Anatomy, Medical University of Wrocław, Poland*

Rastislav DRUGA, *Department of Functional Anatomy, 2nd Medical Faculty Charles University, Prague, Czech Republic*

Jochen FANGHÄNEL, *Department of Anatomy, Ernst-Moritz-Arndt University, Greifswald, Germany*

Marek GRZYBIAK, *Elblag University of Humanities and Economics, Elblag, Poland*

Hans Jorgen GUNDERSEN, *Stereological Research Laboratory, University of Aarhus, Denmark*

Kazimierz JĘDRZEJEWSKI, *Department of Anatomy, Medical University of Łódź, Poland*

Leszek KACZMAREK, *Department of Molecular Cell Neurobiology, Nencki Institute, Warsaw, Poland*

Zbigniew KMIEĆ, *Department of Histology, Medical University of Gdańsk, Poland*

Henryk KOBRYŃ, *Department of Morphological Sciences, Warsaw, Agricultural University, Poland*

Przemysław KOWIAŃSKI, *Department of Human Anatomy and Physiology, Pomeranian University in Słupsk, Poland*

Dariusz KOZŁOWSKI, *2nd Department of Cardiology, Medical University of Gdańsk, Poland*

Marios LOUKAS, *Department of Anatomical Sciences, School of Medicine, St. George's University, Grenada, West Indies*

Mirosław ŁAKOMY, *Department of Animal Anatomy, Warmia and Masuria University, Olsztyn, Poland*

Andrzej ŁUKASZYK, *Department of Histology and Embryology, University Medical School, Poznań, Poland*

Alexander J. McDONALD, *Department of Cell Biology and Neuroscience, USC School of Medicine, Columbia, United States*

Stanisław MOSKALEWSKI, *Department of Histology and Embryology, Medical University of Warsaw, Poland*

Orlando PACIELLO, *Dipartimento di Patologia e Sanita animale, Univesita degli Studi di Napoli Federico II, Napoli, Italy*

Asla PITKÄNEN, *Department of Neurobiology, A.I. Virtanen Institute, University of Kuopio, Finland*

Michał POLGUJ, *Department of Angiology, Medical University of Łódź, Poland*

Michał K. STACHOWIAK, *Department of Molecular and Structural Neurobiology and Gene Therapy, State University of New York, Buffalo, United States*

Paweł SYSA, *Department of Histology and Embryology, Warsaw University of Life Sciences, Poland*

Michał SZPINDA, *Department of Anatomy, Nicolaus Copernicus University in Toruń, Collegium Medicum in Bydgoszcz, Poland*

Edyta SZUROWSKA, *2nd Department of Radiology, Medical University, Gdańsk, Poland*

Jean-Pierre TIMMERMANS, *Laboratory of Cell Biology and Histology/Central Core Facility for Microscopic Imaging, Department of Veterinary Sciences, University of Antwerp, Belgium*

Mirosław TOPOL, *Department of Angiology, Medical University of Łódź, Poland*

Mehmet Cudi TUNCER, *Department of Anatomy, University of Dicle, Medical School, Diyarbakır, Turkey*

Krzysztof TURLEJSKI, *Department of Biochemistry and Cell Biology, Cardinal Stefan Wyszyński University, Warsaw, Poland*

Jiro USUKURA, *Structural Biology Research Center, Nagoya, Japan*

Jerzy WALOCHA, *Department of Anatomy, Jagiellonian University, Collegium Medicum, Kraków, Poland*

Mark J. WEST, *Department of Neurobiology, Institute of Anatomy, Aarhus University, Denmark*

Maciej ZABEL, *Collegium Medicum University of Zielona Gora, Poland*

Marco ZEDDA, *Department of Veterinary Medicine, University of Sassari, Italy*

The distribution of ghrelin cells in the human and animal gastrointestinal tract: a review of the evidence

K.M. Mehdar

Najran University, East of Airport, Najran, Saudi Arabia

[Received: 2 April 2020; Accepted: 1 July 2020]

The growth hormone and appetite are regulated by a 28-peptide hormone called ghrelin, which is produced in the stomach, pituitary gland, and other body tissues. The physiological roles fulfilled by ghrelin include regulation of food intake, cardiac output, reproductive system, proliferation of cells, and formation of osteoblasts, as well as action against inflammation/fibrosis. The ghrelin present in the body can be distinguished as acylated ghrelin and deacylated ghrelin. Furthermore, both in humans and other animals, the entirety of the gastrointestinal tract comprises ghrelin cells, which are classified as open-type and closed-type cells. The present study reviews the evidence about how ghrelin cells are distributed in the human and the animal body. (Folia Morphol 2021; 80, 2: 225–236)

Key words: ghrelin, mucous membrane, stomach, gastrointestinal tract, gastric

OVERVIEW

The discovery of ghrelin as an endogenous ligand for the growth hormone secretagogue receptor (GHS-R) in the stomach was made in 1999. Since then, ghrelin has been found to be involved in growth hormone (GH) secretion, dietary intake, glucose metabolism, memory, and effects against depression [50, 79, 86].

Ghrelin is mainly produced in the upper part of the stomach, which is called the fundus. Ghrelin remains available in a proportion of 35–45% following a complete gastrectomy [4, 30, 73]. Its action on the body is related to its close association with the GH secretagogue subtype 1a (GHS-R1a), a G protein-coupled receptor [13]. A large number of tissues and organs, including the peripheral and central nervous systems, have high expression of both ghrelin and GHS-R1a. Thus, additional organs support ghrelin production, even though the stomach is the primary producer. Among the organs that have been found to have

ghrelin gene expression in both humans and rodents at various developmental stages are the intestine [32], brain [89], heart [57], lung [21], testis [27], immune cells [17], and pancreas [105].

Research has uncovered that ghrelin and GHS-R1a fulfil key bioactions in a wide range of physiological processes, including regulation and homeostasis of central food intake [66], modulation of the cardiovascular system [111], gastric acid production and circulation improvement [56], as well as regulation of cell proliferation and survival [74].

Ghrelin cells have maximum prevalence in the gastric body mucosa, but this prevalence decreases in the gastric antrum and in the small intestine, especially in rodents. In adult bodies, ghrelin is produced chiefly by the stomach, so other sources have not been closely investigated. For instance, studies on rodents have not considered other sources of ghrelin production, choosing to focus on the stomach fundus. However, it

Address for correspondence: Dr. K.M. Mehdar, Najran University, East of Airport, 1988 Najran, Saudi Arabia, e-mail: khlood.mehdar02@gmail.com

This article is available in open access under Creative Common Attribution-Non-Commercial-No Derivatives 4.0 International (CC BY-NC-ND 4.0) license, allowing to download articles and share them with others as long as they credit the authors and the publisher, but without permission to change them in any way or use them commercially.

has been reported that 20% of circulating ghrelin was still available in rodents following fundectomy [105].

GHRELIN HISTORY AND CHARACTERISTICS

The discovery of peptide derivatives mediating GH secretion from the anterior pituitary was made by Cyril Bowers and Frank Momany towards the end of the 1970s [8, 62]. The formation of the discovered growth hormone-released peptides (GHRPs) was found to be based on chemical alteration of met-enkephalin, including GHRP-6 and GHRP-2 [85]. In a 1996 study, GHS and GHRP were used as agonists by Roy Smith and Lex van der Ploeg to assess the GHS candidate MK0677 for the GHS-R1a clone [44]. This sparked methodical investigations with the purpose of categorising the endogenous GHS-R1 ligand. It was only with the discovery of the GHS-R1 cognate agonist in 1999 that the ligand became effective. The name "ghrelin" was given to the hormone consisting of 28 peptides that was isolated from rodent gastric extracts [49]. In 2000, it was found that ghrelin was responsible for regulation of weight and intake of fat and glucose by acting on the cerebral tissue [97].

Derived from the root "ghre" of proto-Indo-European origin, the term "ghrelin" reflects its function as a GH peptide. Interestingly, "ghre" and "lin" are widely accepted in hormone terminology [9, 65].

THE PROCESS OF GHRELIN DEVELOPMENT

To reach full development, ghrelin goes through a number of post-translational modifications. It undergoes translation as proghrelin, a precursor protein with 117 amino acids. This is followed by cleavage of the N-terminal signal co-translation to generate 94 amino acids and transfer to the endoplasmic reticulum lumen proghrelin comprising 23 amino acids and 66AA carboxyterminal peptide known as C-ghrelin (Fig. 1). By binding to fatty acyl group (o-ctanoyl), proghrelin undergoes octanoylation to serine residue (Ser3), which is the third amino acid related to the enzyme known as ghrelin O-acyltransferase (GOAT). A ghrelin acylation enzyme, GOAT, serves to highlight how important acyl modelling is for ghrelin physiology. Switch is of particular significance in octanoylation and, to a lesser extent, to the ghrelin effect on systemic metabolism. Clear evidence regarding the central function of GOAT in activating ghrelin has been brought forth [37, 109]. The formation of

mature ghrelin results from packaging proghrelin into secretory vesicles and alteration by protein convertase enzymes. Consisting of 28 amino acids, mature ghrelin is released into the circulation [34]. Conversely, if proghrelin is cleaved at the C-terminal (C-ghrelin), it can yield obestatin with 23 amino acids and opposite role to ghrelin [71].

The stomach-derived human ghrelin gene is present on the third chromosome (3p25-26) and consists of five exons and four introns. It secretes various bioactive molecules, including two types of ghrelin, namely, acylated ghrelin (AG) and deacylated ghrelin (DAG), as illustrated in Figure 1 [56]. In mammalian bodies, the stomach is the producer of AG [7].

In the human body, AG, DAG, and C-ghrelin are the forms of ghrelin found in the bloodstream [42, 70, 71]. GOAT undertakes acylation of the AG peptide, with expression restricted chiefly to the gut, stomach, and pancreas. Hydrolysis causes the loss of the N-acyl group from DAG [37]. Meanwhile, C-ghrelin comprises the entire obestatin coding area and may undergo cleavage for secretion of peptides, including obestatin [71].

In general, AG in the bloodstream is less than 10%, while DAG and C-ghrelin in the human bloodstream account for over 90% of the total ghrelin in the bloodstream [81].

When the gastric mucosa is surgically extracted, there is a reduction of around 80% in the synthesis of C-ghrelin in rats [20, 53] and in humans [4]. Understanding is yet to be achieved as to whether the same or similar secretory pathways release ghrelin and DAG into the circulation. In rats, gastric ghrelin is broken down via deacylation and N-terminal proteolysis [22], with deacylation being undertaken by lysophospholipase I [84]. In rats, receptor activity is not exhibited by DAG against GHS-R1a, GH release or other endocrine events. Another compound demonstrating bioaction is unesterified GHRL, the activity of which is underpinned by a GHS-R other than GHS-R1a [7, 82].

MORPHOLOGICAL CHARACTERISATION OF GHRELIN CELLS IN THE GASTROINTESTINAL TRACT

In earlier studies, gastric ghrelin was characterised as deriving from an ultra-structured, "hormonal-less" A-like cell present in rat pancreas and human P/D1 cells. In the rodent gastrointestinal tract (GIT), oxyntic mucosa has the greatest prevalence of ghrelin cells, followed by the gastric antrum and small intestine [18, 19, 75].

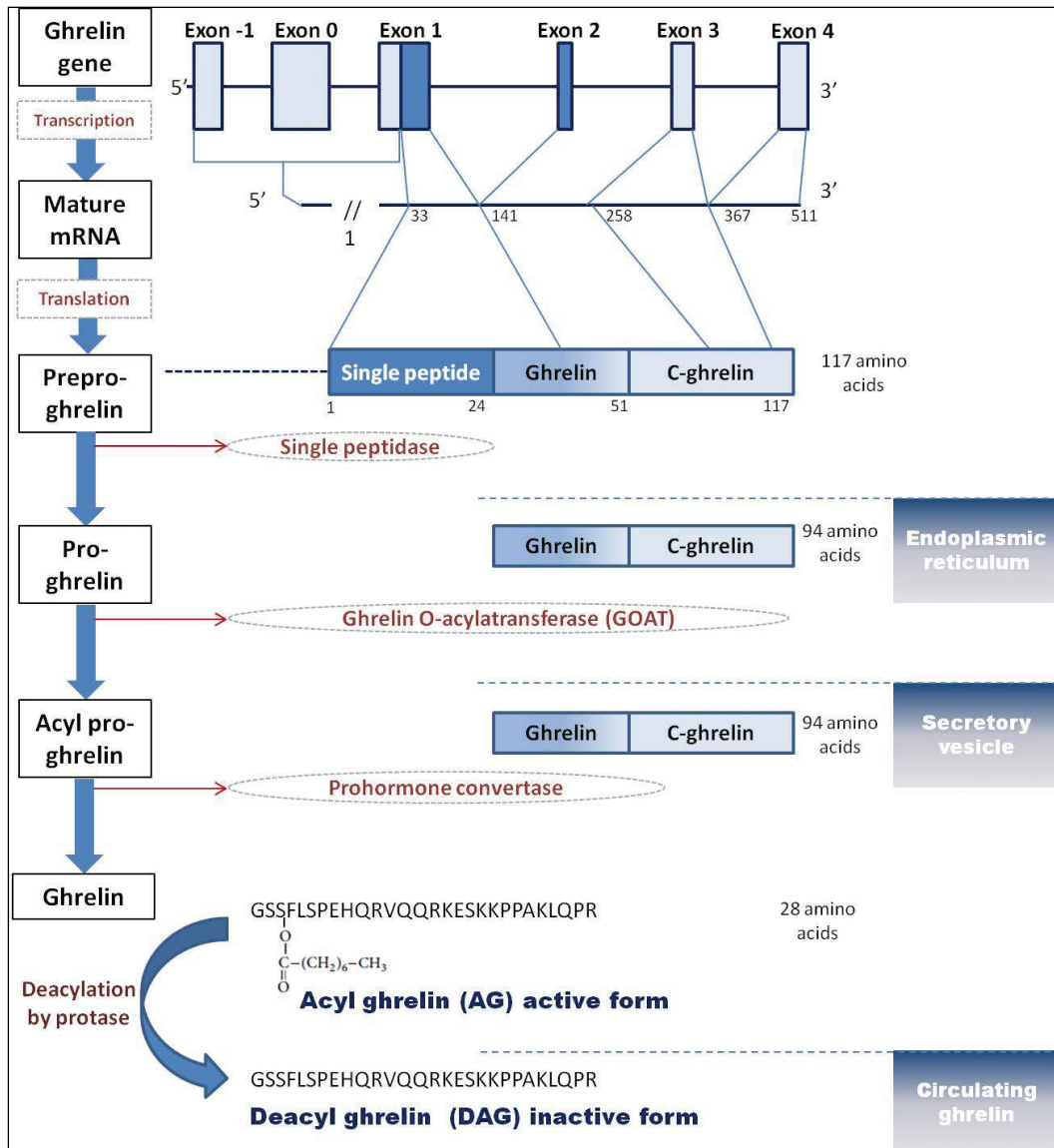


Figure 1. Schematic representation of the process of ghrelin maturation, starting with the structure of the human ghrelin gene to its active peptide.

In adult individuals, ghrelin is primarily produced by the stomach, so the other hormone sources have been studied to a lesser extent. The stomach fundus has been particularly extensively explored in studies on rodents. The ghrelin in the rodent bloodstream post-fundectomy has been reported to be at a level of 20% [19], reflecting the fact that there are other sources of the hormone besides the stomach, such as the pancreas and intestines [105]. The presence of ghrelin-containing X cells in rodent stomach has been indicated through immunohistochemistry, immunoelectron-based microscopy, and hybridisation [75, 78].

In rodents, ghrelin cells have been found throughout the GIT apart from the myenteric plexus, with the stomach body and upper part displaying the greatest

production of ghrelin cells. Meanwhile, in the large and small intestines, ghrelin cells are found in the epithelium of crypts and villi, but these cells are less dense in the large intestine [41, 45].

Most ghrelin entero-endocrine cells are classified as closed-type cells because they are not continuous to the gastrointestinal lumen. By contrast, ghrelin cells continuous to the gastrointestinal lumen are classified as open-type cells and are most prevalent in the stomach [94].

In terms of histology, there are clear differences between the ghrelin cells in the stomach and those in the intestinal tract. The stomach contains spherical cells of small size known as closed-type cells [19, 77, 112], while the small intestine and colon contain both

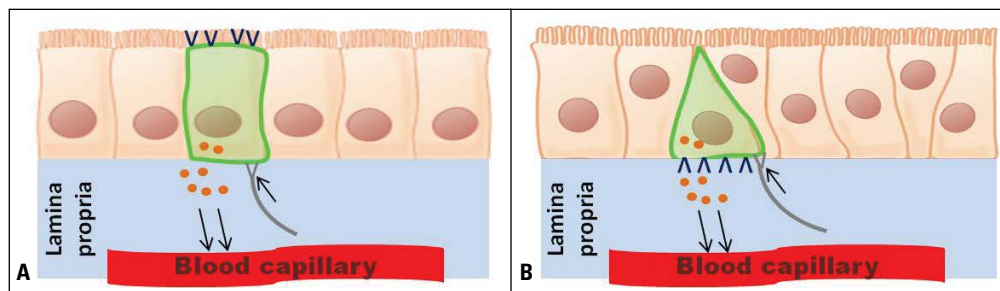


Figure 2. Schematic illustration of the two types of ghrelin cells; **A.** Closed-type ghrelin cells delineated in green colour; on the superior part, the cells are sealed by epithelial cells so there is no direct interaction with the lumen; when neurons are stimulated, ghrelin is released, as indicated by the grey colour, and the cell basal area gives rise to nutrient receptors, as indicated by the blue colour; **B.** Open-type ghrelin cells delineated in green colour; these cells communicate directly with the lumen on their superior part, while the inferior part gives rise to nutrient receptors, shown in blue colour. The small orange dots in both types of cells indicate the spread of ghrelin to lamina propria, from which it permeates the gastric capillaries and finally the systemic circulation.

Table 1. The distribution of ghrelin cells in humans and other animals, listed alphabetically

	Site of ghrelin cells	Morphology of the ghrelin cells	References
Amphibians and reptiles	Stomach (mucosal layer) not in myenteric plexuses and muscle layer	Closed cell type	[1, 11]
Canine	Stomach	Closed and open types	[75]
Chicken	First part of the stomach (middle layer of mucosal layer)	Closed cell type	[98]
Dog	Stomach	Closed and open types	[75]
Human	Stomach (all parts of the fundic gland)	Open and closed cell types	[26]
Mice	Gastric fundus	Closed and open types	[102]
Pigs	From stomach to cecum	Closed and open types	[100]
Rainbow trout	Stomach (mucosal layer)	Closed and open types	[79]
Rats	Stomach (from base to body of fundic gland)	Closed type only or both types	[79, 80]

closed-type cells with a pyramidal or expanded shape and open-type lumen cells that have more than one cytoplasmic process and are located in the apical cell membrane (Fig. 2).

The regulation of the open-type cells is mechanical, based on luminous signals (e.g. pH, nutrients), while the regulation of the closed-type cells is based either on mechanical effect or the effect of additional hormones released into the circulation from the GIT (e.g. leptin, somatostatin, glucagon) [38, 100]. One study on rainbow trout discovered that the distribution of ghrelin cells in the stomach mucosa encompassed both closed-type and open-type cells [76]. Furthermore, research employing electron microscopy has revealed that spherical and dense granules of gastric mucosal cells exhibited the ghrelin immunogold mark [75, 95, 110]. Ghrelin cells have somewhat small and round secretory granules, with varying electron density in their cores, from solid to rather electron-lucent. Consequently, the limiting membrane adheres closely to the dense core in the majority of granules.

In the foetus, there is no difficulty differentiating ghrelin cells from β cells based on the thick uneven structure of their granules [105]. Meanwhile, on a study on rodents, hamsters were shown to have significantly smaller ghrelin granule diameters (200.8 ± 8.8 nm) compared to mice (277.7 ± 11.1 nm) and rats (268.8 ± 13.0 nm) [55]. There were no major differences in ghrelin-immunoreactive cells between mice and humans (147 ± 30 nm); however, by comparison to rats and humans, dogs displayed considerably larger ghrelin cell granules (183 ± 37 nm vs. 273 ± 49 nm). Ultrastructure studies have characterised ghrelin cells as well-defined spherical, compact-to-thin, haloed secretory cells around 140 nm in width, located in the core of the oxyntic gland, and presenting X/A-like granules. In the stomach, ghrelin cells can be found in the proximity of cells that secrete histamine. In dogs, ghrelin cells are typically spherical and associated with a range of sizable, solid, electron-dense X-like granules of oval shape with significant marking for ghrelin antibodies [26].

Positive ghrelin cells are likely to be assimilated in the plasma instead of the intestinal tract because they are found close to capillaries and do not have contact with the oxyntic gland lumen [9]. Table 1 provides an overview of the GIT location of cells that secrete ghrelin.

GHRELIN CELL DISTRIBUTION IN HUMANS AND ANIMALS

Distribution of ghrelin cells in the human GIT

Gastrectomy is an intervention performed in cases of cancer or perforated ulcer, involving removal of the stomach, either partially or entirely. One study concluded that the stomach was the main source of ghrelin in the bloodstream since patients who had undergone complete gastrectomy exhibited a 65% reduction in plasma-like immune rates [4]. Similarly, a different study reported that the levels of immunoreactive ghrelin in plasma were almost halved in the aftermath of complete gastrectomy compared to pre-gastrectomy; however, there was a subsequent progressive rise in the plasma ghrelin levels, suggesting that other sources of ghrelin offset the ghrelin lost through stomach removal [87].

A sex-based difference in the distribution of ghrelin cells and levels of ghrelin in plasma has been discovered, with the plasma ghrelin levels being higher in females than in males [58].

It has also been proposed that, in humans, the levels of ghrelin in the bloodstream were regulated by sex hormones, since testosterone therapy was observed to enhance ghrelin levels in hypogonadal patients [52]. The regulatory effect of sex hormones was reinforced by the observation that there was a higher number of ghrelin cells with expression of the oestrogen α -receptor 3 days post-ovariectomy [36].

Anti-ghrelin antibody was employed by Tanaka-Shintani and Watanabe [93] to analyse how immunoreactive ghrelin cells were distributed in the gastric mucosa in humans, with results revealing that those cells were mainly located in the stomach fundus and there was a close correlation between their distribution and the distribution of parietal cells. The overall cell number for rich and mild types was 3.70 ± 3.31 and 1.18 ± 2.67 , respectively, for every area of the fundus. The area of the duodenum also contained immunoreactive ghrelin cells, although not in such a great abundance as the stomach [108].

Other studies reported that the intestine had the greatest concentration of immunoreactive ghrelin

cells, with lower concentrations in the duodenum, jejunum, and ileum, and absence in the colon. The majority of the ghrelin cells were present in the Lieberkühn crypts [61, 94].

Obese females have been observed to have a greater abundance of ghrelin cells than obese males ($p > 0.05$). The stomach body had the greatest concentration of ghrelin cells, followed by the fundus and antrum. By contrast, patients with *H. pylori* infection or gastritis were found to have a lower abundance of ghrelin cells [114].

A study that investigated how the levels of ghrelin in serum, the number of ghrelin cells, and weight were correlated in patients with Prader-Willi syndrome reported that the stomach fundus contained a number of ghrelin cells that was 2–3 times higher, while the levels of ghrelin in plasma were also abnormally high, even in younger patients [93].

In the context of embryonic development, ghrelin cells appear in the foetal stomach from day 18, proliferating in direct proportion with foetal growth. During the first week of embryonic development, positive-immunostained ghrelin cells emerged at the base of the gland, while in the third week, they emerged at the base and neck, achieving distribution from the base to the neck of the fundic gland during post-neonatal development [80]. In a different study, the number of immunoreactive ghrelin cells was low at day 21 of embryonic development, but grew progressively afterwards and then declined [43]. Furthermore, it has been suggested that the increase in the levels of gastric ghrelin mRNA by age was correlated with the rise in the number of ghrelin cells [69].

In humans, another organ associated with the presence of immunoreactive ghrelin cells is the pancreas. The cells secreting α glucagon and β insulin and the δ cells in pancreatic islets have endogenous expression of ghrelin, whilst the pancreatic α and β cells have preponderant expression of GSH-R1a [60, 99]. Furthermore, it has been discovered that, by comparison to the adult pancreas, the foetal and neonatal pancreas has a higher number of ghrelin cells.

Evidence has been produced regarding the consistent lack of hormone related to immunoreactive ghrelin cells in the common islet-type of cells, namely, α , β , δ , and pancreatic polypeptide cells (PP-cells) based on double or triple immunostaining for ghrelin and four major islet hormones (i.e. glucagon, insulin, somatostatin, and PP-cells) [40]. Ghrelin cells have also been found in foetal and neonatal rat pancreas

[25, 101] and in mouse pancreas [16]. Furthermore, from day 8 of mouse embryonic development, ghrelin cells start to participate in the formation of Langerhans islets. The pancreas secretes ghrelin on a constant basis during embryonic development, but the release rate decreases rapidly after birth. In humans, only a particular group of cells has ghrelin expression in islets; by contrast, in mice, a subset of ϵ -cells is chiefly responsible for the glucagon-based production of ghrelin in islets.

The insulin produced by the pancreatic β cells undertakes modulation of glucose homeostasis. The involvement of ghrelin in glucose homeostasis has been highlighted by a number of studies and it is presumed that, in humans, ghrelin has an effect on how this process is modulated [18].

Ghrelin and GHS-R1a may have a stimulating effect on the functions of the pancreas, as the receptor has been found to be present in islands. Furthermore, there is evidence that ghrelin and insulin have a reciprocal effect on the modulation of their production [18].

Distribution of ghrelin cells in rat GIT

In one study, anti-acylated rat ghrelin antiserum was employed to histologically characterise rat ghrelin cells and determine how they were distributed. It was observed that the distribution of ghrelin cells spanned the whole rat gastrointestinal mucosa, from the stomach to the colon. Moreover, both closed-type and open-type of cells were distinguished, as well as both types of ghrelin, with DAG being present mainly in the perinucleus region and AG occurring at the edges of the cytoplasm [77].

Morphometric analysis revealed that the greatest concentration of ghrelin cells was in the rat stomach, followed by the duodenum, with reduced concentration in the large and small intestines [68]. Sex-based differences ghrelin cell presence in rats have also been reported, with female rats displaying a higher number of ghrelin cells and from an earlier developmental stage [59].

In Teive et al. [94], Wistar rats were employed to determine whether it was possible to offset the ghrelin lost due to gastrectomy by increasing the presence of ghrelin cells in the duodenum. To that end, the rats were subjected to sleeve gastrectomy followed by reoperation 30–60 days later. The latter, involved dissection of a duodenal segment for the purposes of immunohistochemistry to determine the number of ghrelin cells. Results indicated a proliferation of immu-

nopositive ghrelin cells in the duodenum, which was considered to be unrelated to the sleeve gastrectomy.

In Sun et al. [90], a gradual rise in the levels of mRNA gastric ghrelin was observed during the second and third weeks post-partum. Similarly, in Sun et al. [92], the levels of gastric ghrelin increased constantly up to 3 months post-partum. Another study reported that the gastric and intestinal tract contained both open- and closed-type of ghrelin cells, with the stomach having the greatest concentration of ghrelin cells, while the number of open-type cells increased steadily from the stomach to the lower intestine. In addition, rats of both sexes exhibited positive ghrelin cells in the stomach immediately post-partum, with a steady rise in the level of expression of gastric ghrelin up to two months of age after birth [68].

In Wortley et al. [106], the use of immunohistochemistry and immunoelectron microscopy to investigate ghrelin cell distribution in the stomach of Wistar rats revealed that immunoreactive positive ghrelin cells spanned the area from the fundic gland neck region to the actual fundus glands. Furthermore, the granules of enteroendocrine type X cells were discovered via ultrastructural analysis to have positive-immunolabelled ghrelin cells.

Immunohistochemistry was also the approach adopted in McFarlane et al. [59] to identify ghrelin-positive mast cells and establish where they were found and how they were distributed. Results showed that ghrelin was produced by the mast cell granules, which were smaller than tryptase-positive mast cells. Thus, it was confirmed that mast cell granules present in rodent stomach wall contained ghrelin, implying that mast cells were an important ghrelin source.

Distribution of ghrelin cells in mouse GIT

The preferred animal model for developmental studies on gene modulation is the mouse. From the fact that appetite is stimulated by ghrelin in both rodents and humans, it has been deduced that the hormone represents an orexigenic antipode to anorexigenic leptin, anticipating that appetite suppression and weight loss could be achieved through pharmacologic ghrelin activation [91, 102]. However, this theory has not been supported by investigations of ghrelin on mouse models, which did not exhibit significant appetite suppression or weight loss [55, 109, 113, 115]. On the other hand, it has been observed that mice with ghrelin deficiency do not have an abnormal body weight or dietary intake, and actually,

it appears that, in mice, ghrelin serves primarily to regulate glucose in the blood. Several studies have reported that tolerance to glucose is enhanced by ghrelin ablation by stimulating elevated production of insulin [48, 107]. Similar to mice with ghrelin deficiency, mice with GHS-R deficiency do not gain weight when given a diet rich in fat. Some studies have argued that, to some extent, this might be due to the fact that such mice have a moderate pituitary and use fat selectively for energy purposes [39, 47]. In Churm et al. [12], it was found that mice with ghrelin deficiency and of different origins displayed reduced body weight and fat mass, which was tentatively attributed to intensified energy use and movement. Furthermore, studies on mouse models with ghrelin knockout concluded that dietary intake or development did not depend critically on the ghrelin peptide [113], and mice with ghrelin knockout did not eat less or were of smaller size, but they did differ from wild counterparts in terms of their behavioural phenotype related to dietary intake [102, 113].

Ghrelin cell distribution in non-mammalian vertebrates

A number of vertebrates have been identified to have ghrelin cells [29, 54], with evolutionary highly conserved ghrelin N-terminal areas. One study has been successful in isolating ghrelin from trout, revealing that octanoic or decanoic acid modified the third residue of ghrelin serine [23]. A different study has detected immunopositive ghrelin cells throughout the GIT, but with a gradual reduction in number from the stomach to the duodenum, ileum, cecum, and colon [114].

In Wortley et al. [106], hamsters were used to show that the ghrelin cells were the same as the X cells of proper gastric glands and those cells were fewer than in rats and mice. Meanwhile, in Steinert et al. [88], similarities were reported between ghrelin cells in mammals or birds and ghrelin cells in amphibians and reptiles; ghrelin cells were present on the stomach mucosal layer but absent on the mesenteric nerve plexus or stomach muscularis externa.

In birds, immunopositive ghrelin cells have been detected in the proventriculus mucous layer, which is the first area of the stomach fundic gland, where digestion enzymes act on the food intake alongside the gizzard. On the other hand, immunoreactive ghrelin cells have been found to be absent from the avian mesenteric plexus; compared to the mucosal

layer, a higher number of immunopositive cells has been identified in the middle layer and the majority of ghrelin cells were closed-type cells [72].

In Tschop et al. [96], the nutraceutical properties of a diet of *Spirulina* (*Arthrospira platensis*) were investigated by analysing the expression of oligopeptide transporter 1 (PepT1) and ghrelin in the GIT of zebrafish (*Danio rerio*). After 2 days of fasting, ghrelin began to be secreted and its levels increased after 5 days, initially in the stomach and then in the rest of the GIT. It was thus concluded that, in the context of fasting and feeding, the effect of ghrelin on zebrafish was opposite that of PepT1 [96].

THE ROLE OF GHRELIN AND RELATED RECEPTOR

A number of physiological processes unfold with the involvement of ghrelin. An overview of the key roles performed by ghrelin is provided in Figure 3.

Belonging to the superfamily of G-protein coupled receptors, the ghrelin receptor, GHS-R, has seven transmission domains across the helix. In humans, the GHS-R gene is made up of two exons and one intron and is located on chromosome 3 (3q26.2) [13]. GHS-R is differentiated into GHS-R1A, which is a 366 AA protein with seven transmembrane helix domains, and GHS-R1B, which is a 289 AA protein with five transmembrane helix domain [15].

In mammals, among the behaviours of greatest complexity is food intake, which is controlled by different homeostatic and external factors. A key hormone for food intake regulation is ghrelin [2, 10]. In rodents, ghrelin circulation intensifies during feeding before reverting to normal levels once fullness is achieved [2, 5]. Weight gain often accompanies chronic therapies owing to increase in adiposity [24]. In humans, food intake has been observed to increase when peripheral ghrelin was administered. There is also a regular increase and reduction in the levels of ghrelin in the human bloodstream, corresponding to the daily intervals of food consumptions [83].

Research using mouse models has reported that angiogenesis was consistently promoted when ghrelin was administered. According to a recently conducted study on rat model of cardiopulmonary bypass, cardiopulmonary bypass-related inflammatory response, apoptosis, and oxidative stress were reduced when ghrelin was administered, while the heart pumping function was maintained based on signalling GHS-R1a and Akt [14].

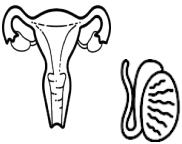







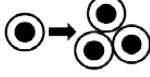

	Regulation of reproductive functions	<ul style="list-style-type: none"> ↑ GH secretion ↑ Food intake ↑ Appetite 	
	<ul style="list-style-type: none"> ↑ Gluconeogenesis ↑ Lipogenesis ↑ Inflammation 	<ul style="list-style-type: none"> ↑ Vasodilatation ↓ Blood pressure ↑ Cardiac output 	
	<ul style="list-style-type: none"> ↑ Gastric motility ↑ Acid secretion 	Regulation pancreatic secretion (exocrine and endocrine)	
	↓ Inflammation	<ul style="list-style-type: none"> ↑ Differentiation of osteoblast ↑ Mineral density 	
	Regulation of cell proliferation and apoptosis	<ul style="list-style-type: none"> ↑ Lipogenesis ↑ Lipid oxidation Inflammation 	

Figure 3. The key roles fulfilled by ghrelin in physiological processes; GH — growth hormone.

Studies on rats have also found that ghrelin and its receptor were associated with osteoblast development, with ghrelin being reported to help osteoblasts proliferate and differentiate both *in vitro* and *in vivo* [56]. The regulatory effect of ghrelin on bone development seems to be underpinned by ghrelin induction of the phosphorylation of adenosine monophosphate active protein kinase [46]. Despite promoting the growth of human osteoblasts, which show exclusive expression of GHS-R1b isoform inactive receptor, it appears that ghrelin has no effect on the differentiation of osteoclasts in rats [63]. Such results reflect the fact that the influence of ghrelin on bone turnover is not dependent on GHS-R1a. Furthermore, in more recent studies, ghrelin has been observed to regulate osteoclastogenesis and bone metabolism in an age-based manner by interacting with leptin [6, 33].

Mouse models of Parkinson’s disease and focal ischaemia/reperfusion have indicated that ghrelin-regulated GHS-R1a signals demonstrated protective effects. The neurological disorder of Parkinson’s disease manifests clinically as recurrent tremor, rigidity, and bradykinesia. A recent study on C57BL/6 mice found that GHS-R1a signalling dopaminergic neurons for triggering 1-methyl-4-phenyl-1,2,3,6-tetrahydropyridine (MPTP) neurotoxicity were controlled by ghrelin [31].

Ghrelin signals with GHS-R1a mediation could potentially participate in adult hippocampal neurogenesis as progenitor cells have been found to contain hippocampal GHS-R1a. The results of a recent study on adult mice pointed to the fact that hippocampal neuronal progenitor cells activated and differentiated in the sub-granular zone [64]. One study even proposed that GHS-R1a signalling could be the basis for a strategy for improving dysfunctional learning and memory, since it contributes significantly to the proliferation of adult hippocampal progenitor cells and the early differentiation of neurons, which in turn underpin the generation of agonists in ghrelin receptors [13].

Ghrelin and its receptor have been detected in both rat and human testes [35, 103, 104], as well as in the organs involved in the human female reproductive system, namely, the ovary, hilum, and corporal lutea [28]. Furthermore, by diminishing the differentiation of hypothalamic gonadotropin release hormone and increasing hormone luteinisation and production of follicle-stimulating hormones, ghrelin contributes significantly to the regulation of the hypothalamic-pituitary-gonadal axis [3].

Another key function attributed to ghrelin is the control of lipid storage by white adipose tissue. GH production is frequently stimulated by extensive ex-

posure to ghrelin, leading to an expansion in the fat mass. Ghrelin has additionally been observed to improve adipogenesis, enzyme action for fat storage, and the levels of triglycerides, whilst decreasing fat usage and lipolysis [10].

Soon after ghrelin was first identified, one study employed *in situ* hybridisation and immunocytochemistry to determine whether ghrelin could be expressed in the human pancreas [51]. Findings suggested that ghrelin had an effect on insulin production, being capable of suppressing this production in both humans and rodents, and β cells mediated the action of ghrelin [51].

The presence of immunoreactive ghrelin cells throughout the human pancreas has been confirmed via immunostaining. More specifically, the α , β , and δ cells in pancreatic islets have been found to have endogenous expression of ghrelin, whilst the α and β cells are the main types of pancreatic cells with GSH-R1a expression [60, 99]. Furthermore, the foetal and neonatal pancreas seems to have a considerably higher number of ghrelin cells than the adult pancreas. Moreover, evidence has been produced that immunoreactive ghrelin cells are never associated with hormone in the common α , β , δ , and PP-cells in pancreatic islets, as indicated by double or triple immunostaining for ghrelin and the four major islet hormones, namely, glucagon, insulin, somatostatin, and PP-cells [40]. Ghrelin cells have been confirmed to contribute to foetal and neonatal cellular development in rat pancreas [25, 67, 101], whilst also occurring in mouse pancreas [16].

Ghrelin immunoreactivity has also been reported in Langerhans cell islets, as well as in human β cells and human α cells [18].

Furthermore, from day 8 of mouse embryonic development, ghrelin cells start to participate in the formation of Langerhans islets. The pancreas secretes ghrelin on a constant basis during embryonic development, but the release rate decreases rapidly after birth. In humans, only a particular group of cells has ghrelin expression in islets; by contrast, in mice, a subset of ϵ -cells is chiefly responsible for the glucagon-based production of ghrelin in islets.

GHS-R has been reported to be extensively distributed within the lymphoid system, leading to the suggestion that ghrelin and GHS-R ligands could be potential signal modulators within the immune and endocrine systems, as well as between the central and peripheral nervous systems. Furthermore, human urogenital organs could possibly include nerve-im-

mune activity, as deduced from rat model research on ghrelin-positive mast cells in autonomic nerves [72].

CONCLUSIONS

The stomach is the main source of ghrelin. In terms of cellular types, the stomach and other areas of the GIT contain different forms of ghrelin cells, with both open-type and closed-type of ghrelin cells being present in the stomach and large and small intestines. The ghrelin cells in the stomach are considered to contribute the largest amount of ghrelin in the plasma, whereas the large and small intestines contribute a smaller amount. Further research is necessary in order to shed more light on the biological and histopathological properties of the ghrelin cells present in the large and small intestines.

REFERENCES

1. Akamizu T, Shinomiya T, Irako T, et al. Separate measurement of plasma levels of acylated and desacyl ghrelin in healthy subjects using a new direct ELISA assay. *J Clin Endocrinol Metab.* 2005; 90(1): 6–9, doi: [10.1210/jc.2004-1640](https://doi.org/10.1210/jc.2004-1640), indexed in Pubmed: [15483072](https://pubmed.ncbi.nlm.nih.gov/15483072/).
2. Akl A. Review Article. *SciFed J Immunol.* 2017; 1(1), doi: [10.23959/sfji-1000003](https://doi.org/10.23959/sfji-1000003).
3. Alkonyi B, Govindan RM, Chugani HT, et al. Focal white matter abnormalities related to neurocognitive dysfunction: an objective diffusion tensor imaging study of children with Sturge-Weber syndrome. *Pediatr Res.* 2011; 69(1): 74–79, doi: [10.1203/PDR.0b013e3181fcb285](https://doi.org/10.1203/PDR.0b013e3181fcb285), indexed in Pubmed: [20856167](https://pubmed.ncbi.nlm.nih.gov/20856167/).
4. Ariyasu H, Takaya K, Tagami T, et al. Stomach is a major source of circulating ghrelin, and feeding state determines plasma ghrelin-like immunoreactivity levels in humans. *J Clin Endocrinol Metab.* 2001; 86(10): 4753–4758, doi: [10.1210/jcem.86.10.7885](https://doi.org/10.1210/jcem.86.10.7885), indexed in Pubmed: [11600536](https://pubmed.ncbi.nlm.nih.gov/11600536/).
5. Barnett BP, Hwang Y, Taylor MS, et al. Glucose and weight control in mice with a designed ghrelin O-acyltransferase inhibitor. *Science.* 2010; 330(6011): 1689–1692, doi: [10.1126/science.1196154](https://doi.org/10.1126/science.1196154), indexed in Pubmed: [21097901](https://pubmed.ncbi.nlm.nih.gov/21097901/).
6. Barreiro ML, Gaytán F, Caminos JE, et al. Cellular location and hormonal regulation of ghrelin expression in rat testis. *Biol Reprod.* 2002; 67(6): 1768–1776, doi: [10.1095/biol-reprod.102.006965](https://doi.org/10.1095/biol-reprod.102.006965), indexed in Pubmed: [12444052](https://pubmed.ncbi.nlm.nih.gov/12444052/).
7. Bonior J, Ceranowicz P, Gajdosz R, et al. Molecular ghrelin system in the pancreatic acinar cells: the role of the polypeptide, caerulein and sensory nerves. *Int J Mol Sci.* 2017; 18(5), doi: [10.3390/ijms18050929](https://doi.org/10.3390/ijms18050929), indexed in Pubmed: [28468316](https://pubmed.ncbi.nlm.nih.gov/28468316/).
8. Bowers CY, Momany F, Reynolds GA, et al. Structure-activity relationships of a synthetic pentapeptide that specifically releases growth hormone in vitro. *Endocrinology.* 1980; 106(3): 663–667.
9. Caesar DD, Shakkarpude J, Shehar R, et al. Role of hunger hormone: ghrelin. *Int J Sci Nat.* 2016; 7(1): 6–15.
10. Cao Y, Tang J, Yang T, et al. Cardioprotective effect of ghrelin in cardiopulmonary bypass involves a reduction in inflammatory response. *PLoS One.* 2013; 8(1): e55021, doi: [10.1371/journal.pone.0055021](https://doi.org/10.1371/journal.pone.0055021), indexed in Pubmed: [23359315](https://pubmed.ncbi.nlm.nih.gov/23359315/).
11. Choe YH, Song SY, Paik KH, et al. Increased density of ghrelin-expressing cells in the gastric fundus and body in Prader-Willi syndrome. *J Clin Endocrinol Metab.* 2005; 90(9): 5441–5445, doi: [10.1210/jc.2004-1935](https://doi.org/10.1210/jc.2004-1935), indexed in Pubmed: [15956087](https://pubmed.ncbi.nlm.nih.gov/15956087/).
12. Churm R, Davies JS, Stephens JW, et al. Ghrelin function in human obesity and type 2 diabetes: a concise review. *Obes*

- Rev. 2017; 18(2): 140–148, doi: [10.1111/obr.12474](https://doi.org/10.1111/obr.12474), indexed in Pubmed: [27899023](https://pubmed.ncbi.nlm.nih.gov/27899023/).
13. Cong W, Golden E, Pantaleo N, et al. Ghrelin receptor signaling: a promising therapeutic target for metabolic syndrome and cognitive dysfunction. *CNS Neurol Disord Drug Targets*. 2010; 9(5): 557–563, doi: [10.2174/187152710793361513](https://doi.org/10.2174/187152710793361513), indexed in Pubmed: [20632971](https://pubmed.ncbi.nlm.nih.gov/20632971/).
 14. Costa JL, Naot D, Lin JM, et al. Ghrelin is an osteoblast mitogen and increases osteoclastic bone resorption in vitro. *Int J Pept*. 2011; 2011: 605193, doi: [10.1155/2011/605193](https://doi.org/10.1155/2011/605193), indexed in Pubmed: [21912562](https://pubmed.ncbi.nlm.nih.gov/21912562/).
 15. Cummings DE, Purnell JQ, Frayo RS, et al. A preprandial rise in plasma ghrelin levels suggests a role in meal initiation in humans. *Diabetes*. 2001; 50(8): 1714–1719, doi: [10.2337/diabetes.50.8.1714](https://doi.org/10.2337/diabetes.50.8.1714), indexed in Pubmed: [11473029](https://pubmed.ncbi.nlm.nih.gov/11473029/).
 16. Dantzer R. Cytokine-induced sickness behavior: mechanisms and implications. *Ann N Y Acad Sci*. 2001; 933: 222–234, doi: [10.1111/j.1749-6632.2001.tb05827.x](https://doi.org/10.1111/j.1749-6632.2001.tb05827.x), indexed in Pubmed: [12000023](https://pubmed.ncbi.nlm.nih.gov/12000023/).
 17. da Silva Pereira JA, da Silva FC, de Moraes-Vieira PM. The impact of ghrelin in metabolic diseases: an immune perspective. *J Diabetes Res*. 2017; 2017: 4527980, doi: [10.1155/2017/4527980](https://doi.org/10.1155/2017/4527980), indexed in Pubmed: [29082258](https://pubmed.ncbi.nlm.nih.gov/29082258/).
 18. Date Y, Nakazato M, Hashiguchi S, et al. Ghrelin is present in pancreatic: cells of humans and rats and stimulates insulin secretion. *Diabetes*. 2002; 51(1): 124–129, doi: [10.2337/diabetes.51.1.124](https://doi.org/10.2337/diabetes.51.1.124).
 19. de la Cour CD, Björkqvist M, Sandvik AK, et al. A-like cells in the rat stomach contain ghrelin and do not operate under gastrin control. *Regul Pept*. 2001; 99(2-3): 141–150, doi: [10.1016/S0167-0115\(01\)00243-9](https://doi.org/10.1016/S0167-0115(01)00243-9), indexed in Pubmed: [11384775](https://pubmed.ncbi.nlm.nih.gov/11384775/).
 20. de la Cour CD, Lindqvist A, Egecioglu E, et al. Ghrelin treatment reverses the reduction in weight gain and body fat in gastrectomised mice. *Gut*. 2005; 54(7): 907–913, doi: [10.1136/gut.2004.058578](https://doi.org/10.1136/gut.2004.058578), indexed in Pubmed: [15849166](https://pubmed.ncbi.nlm.nih.gov/15849166/).
 21. de Novaes Rocha N, de Oliveira MV, Braga C, et al. Ghrelin therapy improves lung and cardiovascular function in experimental emphysema. *Resp Res*. 2017; 18(1): 185, doi: [10.1186/s12931-017-0668-9](https://doi.org/10.1186/s12931-017-0668-9).
 22. de Vriese C, Gregoire F, Lema-Kisoka R, et al. Ghrelin degradation by serum and tissue homogenates: identification of the cleavage sites. *Endocrinology*. 2004; 145(11): 4997–5005, doi: [10.1210/en.2004-0569](https://doi.org/10.1210/en.2004-0569), indexed in Pubmed: [15256494](https://pubmed.ncbi.nlm.nih.gov/15256494/).
 23. Delporte C. Structure and physiological actions of ghrelin. *Scientifica (Cairo)*. 2013; 2013: 518909, doi: [10.1155/2013/518909](https://doi.org/10.1155/2013/518909), indexed in Pubmed: [24381790](https://pubmed.ncbi.nlm.nih.gov/24381790/).
 24. Dezaki K, Sone H, Yada T. Ghrelin is a physiological regulator of insulin release in pancreatic islets and glucose homeostasis. *Pharmacol Ther*. 2008; 118(2): 239–249, doi: [10.1016/j.pharmthera.2008.02.008](https://doi.org/10.1016/j.pharmthera.2008.02.008), indexed in Pubmed: [18433874](https://pubmed.ncbi.nlm.nih.gov/18433874/).
 25. Dixit V, Schaffer E, Pyle R, et al. Ghrelin inhibits leptin- and activation-induced proinflammatory cytokine expression by human monocytes and T cells. *J Clin Investigation*. 2004; 114(1): 57–66, doi: [10.1172/jci200421134](https://doi.org/10.1172/jci200421134).
 26. El-Salhy M, Gilja OH, Gundersen D, et al. Endocrine cells in the oxyntic mucosa of the stomach in patients with irritable bowel syndrome. *World J Gastrointest Endosc*. 2014; 6(5): 176–185, doi: [10.4253/wjge.v6.i5.176](https://doi.org/10.4253/wjge.v6.i5.176), indexed in Pubmed: [24891930](https://pubmed.ncbi.nlm.nih.gov/24891930/).
 27. Esener OBB, Gurel-Gurevin E, Isbilen-Basok B, et al. *Spirulina platensis* affects factors involved in spermatogenesis and increases ghrelin receptors in testis tissue of rats fed a high-fat diet. *Pol J Vet Sci*. 2017; 20(3): 467–475, doi: [10.1515/pjvs-2017-0056](https://doi.org/10.1515/pjvs-2017-0056), indexed in Pubmed: [29166288](https://pubmed.ncbi.nlm.nih.gov/29166288/).
 28. Fåk F, Friis-Hansen L, Weström B, et al. Gastric ghrelin cell development is hampered and plasma ghrelin is reduced by delayed weaning in rats. *J Endocrinol*. 2007; 192(2): 345–352, doi: [10.1677/joe.1.07077](https://doi.org/10.1677/joe.1.07077), indexed in Pubmed: [17283234](https://pubmed.ncbi.nlm.nih.gov/17283234/).
 29. Fujino K, Inui A, Asakawa A, et al. Ghrelin induces fasted motor activity of the gastrointestinal tract in conscious fed rats. *J Physiol*. 2003; 550(Pt 1): 227–240, doi: [10.1113/jphysiol.2003.040600](https://doi.org/10.1113/jphysiol.2003.040600), indexed in Pubmed: [12837928](https://pubmed.ncbi.nlm.nih.gov/12837928/).
 30. Garin MC, Burns CM, Kaul S, et al. Clinical review: the human experience with ghrelin administration. *J Clin Endocrinol Metab*. 2013; 98(5): 1826–1837, doi: [10.1210/jc.2012-4247](https://doi.org/10.1210/jc.2012-4247), indexed in Pubmed: [23533240](https://pubmed.ncbi.nlm.nih.gov/23533240/).
 31. Gaytan F, Barreiro ML, Caminos JE, et al. Expression of ghrelin and its functional receptor, the type 1a growth hormone secretagogue receptor, in normal human testis and testicular tumors. *J Clin Endocrinol Metab*. 2004; 89(1): 400–409, doi: [10.1210/jc.2003-031375](https://doi.org/10.1210/jc.2003-031375), indexed in Pubmed: [14715878](https://pubmed.ncbi.nlm.nih.gov/14715878/).
 32. Ge X, Yang H, Bednarek MA, et al. LEAP2 is an endogenous antagonist of the ghrelin receptor. *Cell Metab*. 2018; 27(2): 461–469.e6, doi: [10.1016/j.cmet.2017.10.016](https://doi.org/10.1016/j.cmet.2017.10.016), indexed in Pubmed: [29233536](https://pubmed.ncbi.nlm.nih.gov/29233536/).
 33. Gnanapavan S, Kola B, Bustin SA, et al. The tissue distribution of the mRNA of ghrelin and subtypes of its receptor, GHS-R, in humans. *J Clin Endocrinol Metab*. 2002; 87(6): 2988–2991, doi: [10.1210/jcem.87.6.8739](https://doi.org/10.1210/jcem.87.6.8739), indexed in Pubmed: [12050285](https://pubmed.ncbi.nlm.nih.gov/12050285/).
 34. Grönberg M, Tsolakis AV, Magnusson L, et al. Distribution of obestatin and ghrelin in human tissues: immunoreactive cells in the gastrointestinal tract, pancreas, and mammary glands. *J Histochem Cytochem*. 2008; 56(9): 793–801, doi: [10.1369/jhc.2008.951145](https://doi.org/10.1369/jhc.2008.951145), indexed in Pubmed: [18474938](https://pubmed.ncbi.nlm.nih.gov/18474938/).
 35. Gross L. Review Article. *Am J Int Law*. 1986; 80(1): 200–215.
 36. Gualillo O, Caminos JE, Kojima M, et al. Gender and gonadal influences on ghrelin mRNA levels in rat stomach. *Eur J Endocrinol*. 2001; 144(6): 687–690, doi: [10.1530/eje.0.1440687](https://doi.org/10.1530/eje.0.1440687), indexed in Pubmed: [11375804](https://pubmed.ncbi.nlm.nih.gov/11375804/).
 37. Gutierrez JA, Solenberg PJ, Perkins DR, et al. Ghrelin octanoylation mediated by an orphan lipid transferase. *Proc Natl Acad Sci U S A*. 2008; 105(17): 6320–6325, doi: [10.1073/pnas.0800708105](https://doi.org/10.1073/pnas.0800708105), indexed in Pubmed: [18443287](https://pubmed.ncbi.nlm.nih.gov/18443287/).
 38. Hass N, Schwarzenbacher K, Breer H. T1R3 is expressed in brush cells and ghrelin-producing cells of murine stomach. *Cell Tissue Res*. 2010; 339(3): 493–504, doi: [10.1007/s00441-009-0907-6](https://doi.org/10.1007/s00441-009-0907-6), indexed in Pubmed: [20063013](https://pubmed.ncbi.nlm.nih.gov/20063013/).
 39. Hayashida T, Murakami K, Mogi K, et al. Ghrelin in domestic animals: distribution in stomach and its possible role. *Domest Anim Endocrinol*. 2001; 21(1): 17–24, doi: [10.1016/S0739-7240\(01\)00104-7](https://doi.org/10.1016/S0739-7240(01)00104-7), indexed in Pubmed: [11524171](https://pubmed.ncbi.nlm.nih.gov/11524171/).
 40. Heller RS, Jenny M, Collombat P, et al. Genetic determinants of pancreatic epsilon-cell development. *Dev Biol*. 2005; 286(1): 217–224, doi: [10.1016/j.ydbio.2005.06.041](https://doi.org/10.1016/j.ydbio.2005.06.041), indexed in Pubmed: [16122727](https://pubmed.ncbi.nlm.nih.gov/16122727/).
 41. Hopkins AL, Nelson TAS, Guschina IA, et al. Unacylated ghrelin promotes adipogenesis in rodent bone marrow via ghrelin O-acyl transferase and GHS-R activity: evidence for target cell-induced acylation. *Sci Rep*. 2017; 7: 45541, doi: [10.1038/srep45541](https://doi.org/10.1038/srep45541), indexed in Pubmed: [28361877](https://pubmed.ncbi.nlm.nih.gov/28361877/).
 42. Hosoda H, Doi K, Nagaya N, et al. Optimum collection and storage conditions for ghrelin measurements: octanoyl modification of ghrelin is rapidly hydrolyzed to desacyl ghrelin in blood samples. *Clin Chem*. 2004; 50(6): 1077–1080, doi: [10.1373/clinchem.2003.025841](https://doi.org/10.1373/clinchem.2003.025841), indexed in Pubmed: [15161728](https://pubmed.ncbi.nlm.nih.gov/15161728/).
 43. Hosoda H, Kojima M, Mizushima T, et al. Structural divergence of human ghrelin. Identification of multiple ghrelin-derived molecules produced by post-translational processing. *J Biol Chem*. 2003; 278(1): 64–70, doi: [10.1074/jbc.M205366200](https://doi.org/10.1074/jbc.M205366200), indexed in Pubmed: [12414809](https://pubmed.ncbi.nlm.nih.gov/12414809/).
 44. Howard AD, Feighner SD, Cully DF, et al. A receptor in pituitary and hypothalamus that functions in growth hormone release. *Science*. 1996; 273(5277): 974–977, doi: [10.1126/science.273.5277.974](https://doi.org/10.1126/science.273.5277.974).
 45. Howick K, Griffin BT, Cryan JF, et al. From belly to brain: targeting the ghrelin receptor in appetite and food intake regulation. *Int J Mol Sci*. 2017; 18(2), doi: [10.3390/ijms18020273](https://doi.org/10.3390/ijms18020273), indexed in Pubmed: [28134808](https://pubmed.ncbi.nlm.nih.gov/28134808/).
 46. Jiang H, Li LJ, Wang J, et al. Ghrelin antagonizes MPTP-induced neurotoxicity to the dopaminergic neurons in mouse substantia nigra. *Exp Neurol*. 2008; 212(2): 532–537, doi: [10.1016/j.expneurol.2008.05.006](https://doi.org/10.1016/j.expneurol.2008.05.006), indexed in Pubmed: [18577498](https://pubmed.ncbi.nlm.nih.gov/18577498/).

47. Kaiya H, Kojima M, Hosoda H, et al. Peptide purification, complementary deoxyribonucleic acid (DNA) and genomic DNA cloning, and functional characterization of ghrelin in rainbow trout. *Endocrinology*. 2003; 144(12): 5215–5226, doi: [10.1210/en.2003-1085](https://doi.org/10.1210/en.2003-1085), indexed in Pubmed: [12970156](https://pubmed.ncbi.nlm.nih.gov/12970156/).
48. Kaiya H, Van der Geyten S, Kojima M, et al. Chicken ghrelin: purification, cDNA cloning, and biological activity. *Endocrinology*. 2002; 143(9): 3454–3463, doi: [10.1210/en.2002-220255](https://doi.org/10.1210/en.2002-220255), indexed in Pubmed: [12193558](https://pubmed.ncbi.nlm.nih.gov/12193558/).
49. Kojima M, Hosoda H, Date Y, et al. Ghrelin is a growth-hormone-releasing acylated peptide from stomach. *Nature*. 1999; 402(6762): 656–660, doi: [10.1038/45230](https://doi.org/10.1038/45230), indexed in Pubmed: [10604470](https://pubmed.ncbi.nlm.nih.gov/10604470/).
50. Kojima M, Kangawa K. Structure and function of ghrelin. *Results Probl Cell Differ*. 2008; 46: 89–115, doi: [10.1007/400_2007_049](https://doi.org/10.1007/400_2007_049), indexed in Pubmed: [18193177](https://pubmed.ncbi.nlm.nih.gov/18193177/).
51. Kreft H, Jetz W. Global patterns and determinants of vascular plant diversity. *Proc Natl Acad Sci USA*. 2007; 104(14): 5925–5930, doi: [10.1073/pnas.0608361104](https://doi.org/10.1073/pnas.0608361104), indexed in Pubmed: [17379667](https://pubmed.ncbi.nlm.nih.gov/17379667/).
52. Lee HM, Wang G, Englander EW. Ghrelin, a new gastrointestinal endocrine peptide that stimulates insulin secretion: enteric distribution, ontogeny, influence of endocrine, and dietary manipulations. *Endocrinology*. 2002; 143(1): 185–190.
53. Li B, Lin Q, Guo H, et al. Ghrelin regulates sepsis-induced rat acute gastric injury. *Mol Med Rep*. 2019; 19(6): 5424–5432, doi: [10.3892/mmr.2019.10208](https://doi.org/10.3892/mmr.2019.10208), indexed in Pubmed: [31059095](https://pubmed.ncbi.nlm.nih.gov/31059095/).
54. Lo Cascio P, Calabrò C, Bertuccio C, et al. Immunohistochemical characterization of Pept1 and ghrelin in gastrointestinal tract of zebrafish: effects of vegetarian diet on the neuroendocrine system cells after alimentary stress. *Front Physiol*. 2018; 9: 614, doi: [10.3389/fphys.2018.00614](https://doi.org/10.3389/fphys.2018.00614), indexed in Pubmed: [29881359](https://pubmed.ncbi.nlm.nih.gov/29881359/).
55. Longo KA, Charoenthongtrakul S, Giuliana DJ, et al. Improved insulin sensitivity and metabolic flexibility in ghrelin receptor knockout mice. *Regul Pept*. 2008; 150(1-3): 55–61, doi: [10.1016/j.regpep.2008.03.011](https://doi.org/10.1016/j.regpep.2008.03.011), indexed in Pubmed: [18453014](https://pubmed.ncbi.nlm.nih.gov/18453014/).
56. Lv Y, Liang T, Wang G, et al. Ghrelin, a gastrointestinal hormone, regulates energy balance and lipid metabolism. *Biosci Rep*. 2018; 38(5), doi: [10.1042/BSR20181061](https://doi.org/10.1042/BSR20181061), indexed in Pubmed: [30177523](https://pubmed.ncbi.nlm.nih.gov/30177523/).
57. Mani BK, Walker AK, Lopez Soto EJ, et al. Neuroanatomical characterization of a growth hormone secretagogue receptor-green fluorescent protein reporter mouse. *J Comp Neurol*. 2014; 522(16): 3644–3666, doi: [10.1002/cne.23627](https://doi.org/10.1002/cne.23627), indexed in Pubmed: [24825838](https://pubmed.ncbi.nlm.nih.gov/24825838/).
58. Matsubara M, Sakata I, Wada R. Estrogen modulates ghrelin expression in the female rat stomach. *Peptides*. 2004; 25(2): 289–297, doi: [10.1016/j.peptides.2003.12.020](https://doi.org/10.1016/j.peptides.2003.12.020), indexed in Pubmed: [15063011](https://pubmed.ncbi.nlm.nih.gov/15063011/).
59. McFarlane MR, Brown MS, Goldstein JL, et al. Induced ablation of ghrelin cells in adult mice does not decrease food intake, body weight, or response to high-fat diet. *Cell Metab*. 2014; 20(1): 54–60, doi: [10.1016/j.cmet.2014.04.007](https://doi.org/10.1016/j.cmet.2014.04.007), indexed in Pubmed: [24836560](https://pubmed.ncbi.nlm.nih.gov/24836560/).
60. McLarnon A. Metabolism: age-dependent balance of leptin and ghrelin regulates bone metabolism. *Nat Rev Endocrinol*. 2012; 8(9): 504, doi: [10.1038/nrendo.2012.116](https://doi.org/10.1038/nrendo.2012.116), indexed in Pubmed: [22751345](https://pubmed.ncbi.nlm.nih.gov/22751345/).
61. Mihalache L, Arhire LI, Giuscă SE, et al. Ghrelin-producing cells distribution in the stomach and the relation with *Helicobacter pylori* in obese patients. *Rom J Morphol Embryol*. 2019; 60(1): 219–225, indexed in Pubmed: [31263848](https://pubmed.ncbi.nlm.nih.gov/31263848/).
62. Momany FA, Bowers CY, Reynolds GA, et al. Design, synthesis, and biological activity of peptides which release growth hormone in vitro. *Endocrinology*. 1981; 108(1): 31–39, doi: [10.1210/endo-108-1-31](https://doi.org/10.1210/endo-108-1-31), indexed in Pubmed: [6109621](https://pubmed.ncbi.nlm.nih.gov/6109621/).
63. Moon M, Kim S, Hwang L, et al. Ghrelin regulates hippocampal neurogenesis in adult mice. *Endocr J*. 2009; 56(3): 525–531, doi: [10.1507/endocrj.k09e-089](https://doi.org/10.1507/endocrj.k09e-089), indexed in Pubmed: [19506321](https://pubmed.ncbi.nlm.nih.gov/19506321/).
64. Muccioli G, Lorenzi T, Lorenzi M, et al. Beyond the metabolic role of ghrelin: a new player in the regulation of reproductive function. *Peptides*. 2011; 32(12): 2514–2521, doi: [10.1016/j.peptides.2011.10.020](https://doi.org/10.1016/j.peptides.2011.10.020), indexed in Pubmed: [22074955](https://pubmed.ncbi.nlm.nih.gov/22074955/).
65. Müller TD, Nogueiras R, Andermann ML, et al. Ghrelin. *Mol Metab*. 2015; 4(6): 437–460, doi: [10.1016/j.molmet.2015.03.005](https://doi.org/10.1016/j.molmet.2015.03.005), indexed in Pubmed: [26042199](https://pubmed.ncbi.nlm.nih.gov/26042199/).
66. Nakazato M, Murakami N, Date Y, et al. A role for ghrelin in the central regulation of feeding. *Nature*. 2001; 409(6817): 194–198, doi: [10.1038/35051587](https://doi.org/10.1038/35051587), indexed in Pubmed: [11196643](https://pubmed.ncbi.nlm.nih.gov/11196643/).
67. Napolitano T, Silvano S, Vieira A, et al. Role of ghrelin in pancreatic development and function. *Diabetes Obes Metab*. 2018; 20 Suppl 2: 3–10, doi: [10.1111/dom.13385](https://doi.org/10.1111/dom.13385), indexed in Pubmed: [30230184](https://pubmed.ncbi.nlm.nih.gov/30230184/).
68. Nass R, Gaylinn BD, Thorner MO. The ghrelin axis in disease: potential therapeutic indications. *Mol Cell Endocrinol*. 2011; 340(1): 106–110, doi: [10.1016/j.mce.2011.02.010](https://doi.org/10.1016/j.mce.2011.02.010), indexed in Pubmed: [21356273](https://pubmed.ncbi.nlm.nih.gov/21356273/).
69. Pagotto U, Gambineri A, Pelusi C, et al. Testosterone replacement therapy restores normal ghrelin in hypogonadal men. *J Clin Endocrinol Metab*. 2003; 88(9): 4139–4143, doi: [10.1210/jc.2003-030554](https://doi.org/10.1210/jc.2003-030554), indexed in Pubmed: [12970277](https://pubmed.ncbi.nlm.nih.gov/12970277/).
70. Patterson M, Murphy KG, le Roux CW, et al. Characterization of ghrelin-like immunoreactivity in human plasma. *J Clin Endocrinol Metab*. 2005; 90(4): 2205–2211, doi: [10.1210/jc.2004-1641](https://doi.org/10.1210/jc.2004-1641), indexed in Pubmed: [15657369](https://pubmed.ncbi.nlm.nih.gov/15657369/).
71. Pemberton C, Wimalasena P, Yandle T, et al. C-terminal pro-ghrelin peptides are present in the human circulation. *Biochem Biophys Res Commun*. 2003; 310(2): 567–573, doi: [10.1016/j.bbrc.2003.09.045](https://doi.org/10.1016/j.bbrc.2003.09.045), indexed in Pubmed: [14521948](https://pubmed.ncbi.nlm.nih.gov/14521948/).
72. Perez-Tilve D, Heppner K, Kirchner H, et al. Ghrelin-induced adiposity is independent of orexigenic effects. *FASEB J*. 2011; 25(8): 2814–2822, doi: [10.1096/fj.11-183632](https://doi.org/10.1096/fj.11-183632), indexed in Pubmed: [21543764](https://pubmed.ncbi.nlm.nih.gov/21543764/).
73. Popovic V, Miljic D, Pekic S, et al. Low plasma ghrelin level in gastrectomized patients is accompanied by enhanced sensitivity to the ghrelin-induced growth hormone release. *J Clin Endocrinol Metab*. 2005; 90(4): 2187–2191, doi: [10.1210/jc.2004-1888](https://doi.org/10.1210/jc.2004-1888), indexed in Pubmed: [15644398](https://pubmed.ncbi.nlm.nih.gov/15644398/).
74. Pradhan G, Samson S, Sun Y. Ghrelin: much more than a hunger hormone. *Curr Opin Clin Nutr Metab Care*. 2013; 16(6): 619–624, doi: [10.1097/mco.0b013e328365b9be](https://doi.org/10.1097/mco.0b013e328365b9be).
75. Rindi G, Savio A, Torsello A, et al. Ghrelin expression in gut endocrine growths. *Histochem Cell Biol*. 2002; 117(6): 521–525, doi: [10.1007/s00418-002-0416-0](https://doi.org/10.1007/s00418-002-0416-0), indexed in Pubmed: [12107502](https://pubmed.ncbi.nlm.nih.gov/12107502/).
76. Sakata I, Mori T, Kaiya H, et al. Localization of ghrelin-producing cells in the stomach of the rainbow trout (*Oncorhynchus mykiss*). *Zoolog Sci*. 2004; 21(7): 757–762, doi: [10.2108/zsj.21.757](https://doi.org/10.2108/zsj.21.757), indexed in Pubmed: [15277719](https://pubmed.ncbi.nlm.nih.gov/15277719/).
77. Sakata I, Nakamura K, Yamazaki M, et al. Ghrelin-producing cells exist as two types of cells, closed- and opened-type cells, in the rat gastrointestinal tract. *Peptides*. 2002; 23(3): 531–536, doi: [10.1016/s0196-9781\(01\)00633-7](https://doi.org/10.1016/s0196-9781(01)00633-7), indexed in Pubmed: [11836003](https://pubmed.ncbi.nlm.nih.gov/11836003/).
78. Sakata I, Nakano Y, Osborne-Lawrence S, et al. Characterization of a novel ghrelin cell reporter mouse. *Regul Pept*. 2009; 155(1-3): 91–98, doi: [10.1016/j.regpep.2009.04.001](https://doi.org/10.1016/j.regpep.2009.04.001), indexed in Pubmed: [19361544](https://pubmed.ncbi.nlm.nih.gov/19361544/).
79. Sakata I, Sakai T. Ghrelin cells in the gastrointestinal tract. *Int J Pept*. 2010; 2010, doi: [10.1155/2010/945056](https://doi.org/10.1155/2010/945056), indexed in Pubmed: [20798855](https://pubmed.ncbi.nlm.nih.gov/20798855/).
80. Sakata I, Tanaka T, Matsubara M, et al. Postnatal changes in ghrelin mRNA expression and in ghrelin-producing cells in the rat stomach. *J Endocrinol*. 2002; 174(3): 463–471, doi: [10.1677/joe.0.1740463](https://doi.org/10.1677/joe.0.1740463), indexed in Pubmed: [12208667](https://pubmed.ncbi.nlm.nih.gov/12208667/).
81. Sangiao-Alvarellos S, Cordido F. Effect of ghrelin on glucose-insulin homeostasis: therapeutic implications. *Int J Pept*. 2010; 2010, doi: [10.1155/2010/234709](https://doi.org/10.1155/2010/234709), indexed in Pubmed: [20700401](https://pubmed.ncbi.nlm.nih.gov/20700401/).
82. Sato T, Nakamura Y, Shiimura Y, et al. Structure, regulation and function of ghrelin. *J Biochem*. 2012; 151(2): 119–128, doi: [10.1093/jb/mvr134](https://doi.org/10.1093/jb/mvr134), indexed in Pubmed: [22041973](https://pubmed.ncbi.nlm.nih.gov/22041973/).

83. Shah M, Kola B, Batavejic A, et al. AMP-activated protein kinase (AMPK) activation regulates in vitro bone formation and bone mass. *Bone*. 2010; 47(2): 309–319, doi: [10.1016/j.bone.2010.04.596](https://doi.org/10.1016/j.bone.2010.04.596), indexed in Pubmed: [20399918](https://pubmed.ncbi.nlm.nih.gov/20399918/).
84. Shanado Y, Kometani M, Uchiyama H, et al. Lysophospholipase I identified as a ghrelin deacylation enzyme in rat stomach. *Biochem Biophys Res Commun*. 2004; 325(4): 1487–1494, doi: [10.1016/j.bbrc.2004.10.193](https://doi.org/10.1016/j.bbrc.2004.10.193), indexed in Pubmed: [15555596](https://pubmed.ncbi.nlm.nih.gov/15555596/).
85. Smith RG, Van der Ploeg LH, Howard AD, et al. Peptidomimetic regulation of growth hormone secretion. *Endocr Rev*. 1997; 18(5): 621–645, doi: [10.1210/edrv.18.5.0316](https://doi.org/10.1210/edrv.18.5.0316), indexed in Pubmed: [9331545](https://pubmed.ncbi.nlm.nih.gov/9331545/).
86. Soleyman-Jahi S, Sadeghi F, Pastaki Khoshbin A, et al. Attribution of ghrelin to cancer; attempts to unravel an apparent controversy. *Front Oncol*. 2019; 9: 1014, doi: [10.3389/fonc.2019.01014](https://doi.org/10.3389/fonc.2019.01014), indexed in Pubmed: [31681567](https://pubmed.ncbi.nlm.nih.gov/31681567/).
87. Stefanov I, Ananiev J, Ivanova K, et al. Distribution of ghrelin-positive mast cells in rat stomach. *Biotechnol Biotechnol Equip*. 2017; 1–8, doi: [10.1080/13102818.2017.1326013](https://doi.org/10.1080/13102818.2017.1326013).
88. Steinert RE, Feinle-Bisset C, Asarian L, et al. Ghrelin, CCK, GLP-1, and PYY(3-36): secretory controls and physiological roles in eating and glycemia in health, obesity, and after RYGB. *Physiol Rev*. 2017; 97(1): 411–463, doi: [10.1152/physrev.00031.2014](https://doi.org/10.1152/physrev.00031.2014), indexed in Pubmed: [28003328](https://pubmed.ncbi.nlm.nih.gov/28003328/).
89. Suda Y, Kuzumaki N, Sone T, et al. Down-regulation of ghrelin receptors on dopaminergic neurons in the substantia nigra contributes to Parkinson's disease-like motor dysfunction. *Mol Brain*. 2018; 11(1): 6, doi: [10.1186/s13041-018-0349-8](https://doi.org/10.1186/s13041-018-0349-8), indexed in Pubmed: [29458391](https://pubmed.ncbi.nlm.nih.gov/29458391/).
90. Sun Y, Ahmed S, Smith RG. Deletion of ghrelin impairs neither growth nor appetite. *Mol Cell Biol*. 2003; 23(22): 7973–7981, doi: [10.1128/mcb.23.22.7973-7981.2003](https://doi.org/10.1128/mcb.23.22.7973-7981.2003), indexed in Pubmed: [14585959](https://pubmed.ncbi.nlm.nih.gov/14585959/).
91. Sun Y, Asnicar M, Saha PK, et al. Ablation of ghrelin improves the diabetic but not obese phenotype of ob/ob mice. *Cell Metab*. 2006; 3(5): 379–386, doi: [10.1016/j.cmet.2006.04.004](https://doi.org/10.1016/j.cmet.2006.04.004), indexed in Pubmed: [16679295](https://pubmed.ncbi.nlm.nih.gov/16679295/).
92. Sun Y, Wang P, Zheng H, et al. Ghrelin stimulation of growth hormone release and appetite is mediated through the growth hormone secretagogue receptor. *Proc Natl Acad Sci U S A*. 2004; 101(13): 4679–4684, doi: [10.1073/pnas.0305930101](https://doi.org/10.1073/pnas.0305930101), indexed in Pubmed: [15070777](https://pubmed.ncbi.nlm.nih.gov/15070777/).
93. Tanaka-Shintani M, Watanabe M. Distribution of ghrelin-immunoreactive cells in human gastric mucosa: comparison with that of parietal cells. *J Gastroenterol*. 2005; 40(4): 345–349, doi: [10.1007/s00535-004-1550-3](https://doi.org/10.1007/s00535-004-1550-3), indexed in Pubmed: [15870970](https://pubmed.ncbi.nlm.nih.gov/15870970/).
94. Teive MB, Russi RF, Vieira DS, et al. Quantitative immunohistochemical analysis of duodenal ghrelin cells after sleeve gastrectomy in Wistar rats. *Acta Cir Bras*. 2012; 27(9): 595–599, doi: [10.1590/s0102-86502012000900001](https://doi.org/10.1590/s0102-86502012000900001), indexed in Pubmed: [22936082](https://pubmed.ncbi.nlm.nih.gov/22936082/).
95. Tomasetto C, Karam SM, Ribieras S, et al. Identification and characterization of a novel gastric peptide hormone: the motilin-related peptide. *Gastroenterology*. 2000; 119(2): 395–405, doi: [10.1053/gast.2000.9371](https://doi.org/10.1053/gast.2000.9371), indexed in Pubmed: [10930375](https://pubmed.ncbi.nlm.nih.gov/10930375/).
96. Tschöp M, Flora DB, Mayer JP, et al. Hypophysectomy prevents ghrelin-induced adiposity and increases gastric ghrelin secretion in rats. *Obes Res*. 2002; 10(10): 991–999, doi: [10.1038/oby.2002.135](https://doi.org/10.1038/oby.2002.135), indexed in Pubmed: [12376579](https://pubmed.ncbi.nlm.nih.gov/12376579/).
97. Tschöp M, Smiley DL, Heiman ML. Ghrelin induces adiposity in rodents. *Nature*. 2000; 407(6806): 908–913, doi: [10.1038/35038090](https://doi.org/10.1038/35038090), indexed in Pubmed: [11057670](https://pubmed.ncbi.nlm.nih.gov/11057670/).
98. van der Lely AJ, Tschöp M, Heiman ML, et al. Biological, physiological, pathophysiological, and pharmacological aspects of ghrelin. *Endocr Rev*. 2004; 25(3): 426–457, doi: [10.1210/er.2002-0029](https://doi.org/10.1210/er.2002-0029), indexed in Pubmed: [15180951](https://pubmed.ncbi.nlm.nih.gov/15180951/).
99. Van Der Velde M, Van Der Eerden BCJ, Sun Y, et al. An age-dependent interaction with leptin unmasks ghrelin's bone-protective effects. *Endocrinology*. 2012; 153(8): 3593–3602, doi: [10.1210/en.2012-1277](https://doi.org/10.1210/en.2012-1277), indexed in Pubmed: [22700774](https://pubmed.ncbi.nlm.nih.gov/22700774/).
100. Vitari F, Di Giancamillo A, Deponti D, et al. Distribution of ghrelin-producing cells in the gastrointestinal tract of pigs at different ages. *Vet Res Commun*. 2012; 36(1): 71–80, doi: [10.1007/s11259-012-9517-y](https://doi.org/10.1007/s11259-012-9517-y), indexed in Pubmed: [22281862](https://pubmed.ncbi.nlm.nih.gov/22281862/).
101. Volante M, Allia E, Gugliotta P, et al. Expression of ghrelin and of the GH secretagogue receptor by pancreatic islet cells and related endocrine tumors. *J Clin Endocrinol Metab*. 2002; 87(3): 1300–1308, doi: [10.1210/jcem.87.3.8279](https://doi.org/10.1210/jcem.87.3.8279), indexed in Pubmed: [11889202](https://pubmed.ncbi.nlm.nih.gov/11889202/).
102. Walia P, Asadi A, Kieffer TJ, et al. Ontogeny of ghrelin, obestatin, preproghrelin, and prohormone convertases in rat pancreas and stomach. *Pediatr Res*. 2009; 65(1): 39–44, doi: [10.1203/PDR.0b013e31818bc134](https://doi.org/10.1203/PDR.0b013e31818bc134), indexed in Pubmed: [18784614](https://pubmed.ncbi.nlm.nih.gov/18784614/).
103. Wierup N, Sundler F. Human and murine pancreatic ghrelin cells. Developmental aspects and ultrastructure. *Regulatory Peptides*. 2004; 122(1): 48.
104. Wierup N, Sundler F. Neuropeptides: endocrine cells. *Encyclopedia of Neuroscience*. 2009: 891–897, doi: [10.1016/b978-008045046-9.01457-1](https://doi.org/10.1016/b978-008045046-9.01457-1).
105. Wierup N, Sundler F, Scott Heller R. The islet ghrelin cell. *J Mol Endocrinol*. 2014; 52(1): R35–R49, doi: [10.1530/jme-13-0122](https://doi.org/10.1530/jme-13-0122).
106. Wortley KE, Anderson KD, Garcia K, et al. Genetic deletion of ghrelin does not decrease food intake but influences metabolic fuel preference. *Proc Natl Acad Sci U S A*. 2004; 101(21): 8227–8232, doi: [10.1073/pnas.0402763101](https://doi.org/10.1073/pnas.0402763101), indexed in Pubmed: [15148384](https://pubmed.ncbi.nlm.nih.gov/15148384/).
107. Wortley KE, del Rincon JP, Murray JD, et al. Absence of ghrelin protects against early-onset obesity. *J Clin Invest*. 2005; 115(12): 3573–3578, doi: [10.1172/JCI26003](https://doi.org/10.1172/JCI26003), indexed in Pubmed: [16322795](https://pubmed.ncbi.nlm.nih.gov/16322795/).
108. Yabuki A, Ojima T, Kojima M, et al. Characterization and species differences in gastric ghrelin cells from mice, rats and hamsters. *J Anat*. 2004; 205(3): 239–246, doi: [10.1111/j.0021-8782.2004.00331.x](https://doi.org/10.1111/j.0021-8782.2004.00331.x), indexed in Pubmed: [15379929](https://pubmed.ncbi.nlm.nih.gov/15379929/).
109. Yang J, Brown MS, Liang G, et al. Goldstein, Identification of the acyltransferase that octanoylates ghrelin, an appetite-stimulating peptide hormone. *Cell*. 2008; 132(3): 387–396, doi: [10.1016/j.cell.2008.01.017](https://doi.org/10.1016/j.cell.2008.01.017), indexed in Pubmed: [18267071](https://pubmed.ncbi.nlm.nih.gov/18267071/).
110. Yoshihara F, Kojima M, Hosoda H, et al. Ghrelin: a novel peptide for growth hormone release and feeding regulation. *Curr Opin Clin Nutr Metab Care*. 2002; 5(4): 391–395, doi: [10.1097/00075197-200207000-00007](https://doi.org/10.1097/00075197-200207000-00007), indexed in Pubmed: [12107374](https://pubmed.ncbi.nlm.nih.gov/12107374/).
111. Zhang G, Yin X, Qi Y, et al. Ghrelin and cardiovascular diseases. *Curr Cardiol Rev*. 2010; 6(1): 62–70, doi: [10.2174/157340310790231662](https://doi.org/10.2174/157340310790231662), indexed in Pubmed: [21286280](https://pubmed.ncbi.nlm.nih.gov/21286280/).
112. Zhao CM, Furnes MW, Stenström B, et al. Characterization of obestatin- and ghrelin-producing cells in the gastrointestinal tract and pancreas of rats: an immunohistochemical and electron-microscopic study. *Cell Tissue Res*. 2008; 331(3): 575–587, doi: [10.1007/s00441-007-0514-3](https://doi.org/10.1007/s00441-007-0514-3), indexed in Pubmed: [18071756](https://pubmed.ncbi.nlm.nih.gov/18071756/).
113. Zhao TJ, Liang G, Li RL, et al. Ghrelin O-acyltransferase (GOAT) is essential for growth hormone-mediated survival of calorie-restricted mice. *Proc Natl Acad Sci*. 2010; 107(16): 7467–7472, doi: [10.1073/pnas.1002271107](https://doi.org/10.1073/pnas.1002271107).
114. Zhao Z, Sakai T. Characteristic features of ghrelin cells in the gastrointestinal tract and the regulation of stomach ghrelin expression and production. *World J Gastroenterol*. 2008; 14(41): 6306–6311, doi: [10.3748/wjg.14.6306](https://doi.org/10.3748/wjg.14.6306), indexed in Pubmed: [19009644](https://pubmed.ncbi.nlm.nih.gov/19009644/).
115. Zigman JM, Nakano Y, Coppari R, et al. Mice lacking ghrelin receptors resist the development of diet-induced obesity. *J Clin Invest*. 2005; 115(12): 3564–3572, doi: [10.1172/JCI26002](https://doi.org/10.1172/JCI26002), indexed in Pubmed: [16322794](https://pubmed.ncbi.nlm.nih.gov/16322794/).

The contribution of the middle cerebral artery and callosal artery to the vascularisation of the Facies convexa of the brain in horses with reference to the equine-specific cartographic pattern of the neopallium

L. Böing, F. Heun, H. Gasse

Institute of Anatomy, University of Veterinary Medicine Hannover, Germany

[Received: 7 April 2020; Accepted: 25 May 2020]

Background: *The extremely complex surface architecture of the equine brain does not allow a uniform transfer of anatomical data from other mammalian species, e.g., dog or cat. Rather, a special approach is required to elucidate the equine-specific patterns of cerebral vascular ramifications. Therefore, a novel cartographic system was applied. Prior attention was paid to the A. cerebri media (MCA) and to the A. corporis callosi (CA), as they spread over the widest part of the neopallium's Facies convexa (i.e. the lateral and dorsal surface), thus being of particular interest in terms of surgical treatment of trauma of the skull and brain.*

Materials and methods: *The brains of 17 adult warmblood horses were studied. The neopallium's Facies convexa was subdivided into 15 sectors clearly delineated by the primary sulci and by related auxiliary lines. The courses and destinations of main branches (= branches of 1st or 2nd order, with a minimum calibre of 0.75 mm) of MCA and CA were topographically analysed by means of superimposed graphical sketches.*

Results: *The MCA had six main branches (numbered in rostrocaudal direction); the CA had seven main branches. The main branches of the MCA spread over the widest part of the Facies convexa, but never reached the rostral pole and the caudal pole of the neopallium. Clearly, the main branches of CA proceeded from the hemisphere's medial side across the Margo dorsalis cerebri, thus supplying rostradorsal and dorsal sectors of the Facies convexa.*

Conclusions: *The topographical analysis of the vascular ramification patterns (regions of residence) in combination with the cartographic system of sectors of the neopallium respected the equine-specific surface architecture. It highlighted the distinct vascular supply areas and the particular multiple-supply situations especially in sectors presumably related to the equine area motorica. (Folia Morphol 2021; 80, 2: 237–247)*

Key words: horse, brain cartography, cerebrum, gyration, middle cerebral artery, callosal artery, ramification pattern

Address for correspondence: Dr. L. Böing, Institute of Anatomy, University of Veterinary Medicine Hannover, Bischofsholer Damm 15, D-30173 Hannover, Germany, tel: +49 511 856 7484, e-mail: lucien.boeing@tiho-hannover.de; hagen.gasse@tiho-hannover.de

This article is available in open access under Creative Common Attribution-Non-Commercial-No Derivatives 4.0 International (CC BY-NC-ND 4.0) license, allowing to download articles and share them with others as long as they credit the authors and the publisher, but without permission to change them in any way or use them commercially.

INTRODUCTION

The presence of several arterial branches supplying the brain hemispheres of horses was reported [1, 17, 24]. However, their further courses, positions and local distributions on the neopallium have not been described in detail. The same is true for the current sixth edition of the *Nomina Anatomica Veterinaria* [25] and the corresponding illustrated edition [5]: They list the cerebral stem arteries (e.g., *A. cerebri media* [MCA] on the brain's basolateral surface). However, they fail to display the individual branches originating from them and, for example, continuing along the neopallium's lateral and dorsal surface (i.e. *Facies convexa*).

Such a topographical description of a general vascularisation pattern of the equine cerebral hemispheres is challenged by the special surface architecture of the equine neopallium [2, 12]. In horses, the gyration pattern is complex [21, 23] due to the varying arrangements of the plentiful secondary sulci. A typical bow-like conformation of the gyri ("Bogenwindungen"), like in carnivores, does not exist in horses [1, 8, 20, 21]. Despite this, the significance of the primary sulci of the equine neopallium has been highlighted [21], as they occur regularly and can be used as the key features for a topographical orientation. However, the space between them is too wide (and the secondary sulci in between are too irregular) to allow an adequate topographical reference to certain sites of smaller dimensions. Consequently, a new cartographic system of orientation [3, 13] was introduced. It refers to the primary sulci [21] and to related auxiliary lines [3, 13], dividing the neopallium's surface into 21 sectors (15 of them on the lateral *Facies convexa*).

The aim of this study was to describe in appropriate detail the ramifications of the MCA and *A. corporis callosi* (CA). In particular, special attention was given to the neopallium's sectors to elucidate whether there was a basic ramification pattern and if specific vascular supply areas existed.

MATERIALS AND METHODS

The heads of 17 adult, warmblood horses were fixed by perfusion with 10% formalin (10 L on average) via the left *A. carotis communis* (the left and right *V. jugularis externa* were cut; however, the right *A. carotis communis* was clamped in order to prevent early reflux of the fixative). Five of the heads were subsequently injected with 60% latex milk via the same port. The cerebral hemispheres were macroscopically dissected *ex situ*.

The horses had been purchased from local animal trade companies to be used as specimens in the anatomical dissection classes of the University of Veterinary Medicine Hannover, Germany. They had been euthanased either prior to or immediately after their arrival, without being housed at the institute's facilities. All related procedures were carried out in accordance with the German Federal Law, that is the Protection of Animals Act (*Tierschutzgesetz* §4, §7, §7a) as well as the Directive of the European Parliament and of the Council for the Protection of Animals Used for Experimental and other Scientific Purposes (2010/63/EU). Accordingly (*Tierschutzgesetz* §7), no explicit permission to conduct this study was necessary because no medical procedures or experiments were carried out while the animals were alive, except intravenous injection for euthanasia. Euthanasia was carried out by qualified and authorized medical staff by means of an initial general anaesthesia by 2% isoflurane (*Isofluran* CP 1 mL/mL, CP-Pharma Handelsgesellschaft mbH, Burgdorf, Germany) and consecutively administering 60 mg/kg pentobarbital *i.v.* (*Euthadorm*® 400 mg/mL, CP-Pharma Handelsgesellschaft mbH, Burgdorf, Germany). This procedure was approved by the University's Animal Welfare Officer, confirmation TVO-2018-V-71.

The hemisphere's *Facies convexa* was subdivided in accordance with the previously described method [2, 12]. In this cartographic approach, firstly, the primary sulci [21] were the essential key landmarks (Fig. 1). Secondly, six points of orientation (PO-1 to PO-6) — all related to the aforementioned primary sulci — were marked on the *Facies convexa* of the neopallium (Fig. 1). Finally, auxiliary lines — oriented to these points of orientation — completed the division into 15 lateral and dorsal sectors (Fig. 1; red dotted lines).

Branches directly originating from the MCA or CA, i.e., branches of 1st order, were dissected together with those subsequently deriving from them, i.e., branches of 2nd order. Both categories of branches had a minimum width of 0.75 mm and were designated as the main branches. Further and smaller branches originating from these main branches were discriminated. The identified main branches were numbered in a rostrocaudal direction (i.e., main branch 1 was the most rostral one).

Standardised photographs (90° perspective, in lateral and medial view) were used to draw sketches of the individual arterial ramifications. These sketches were digitally superimposed in one graphical rep-

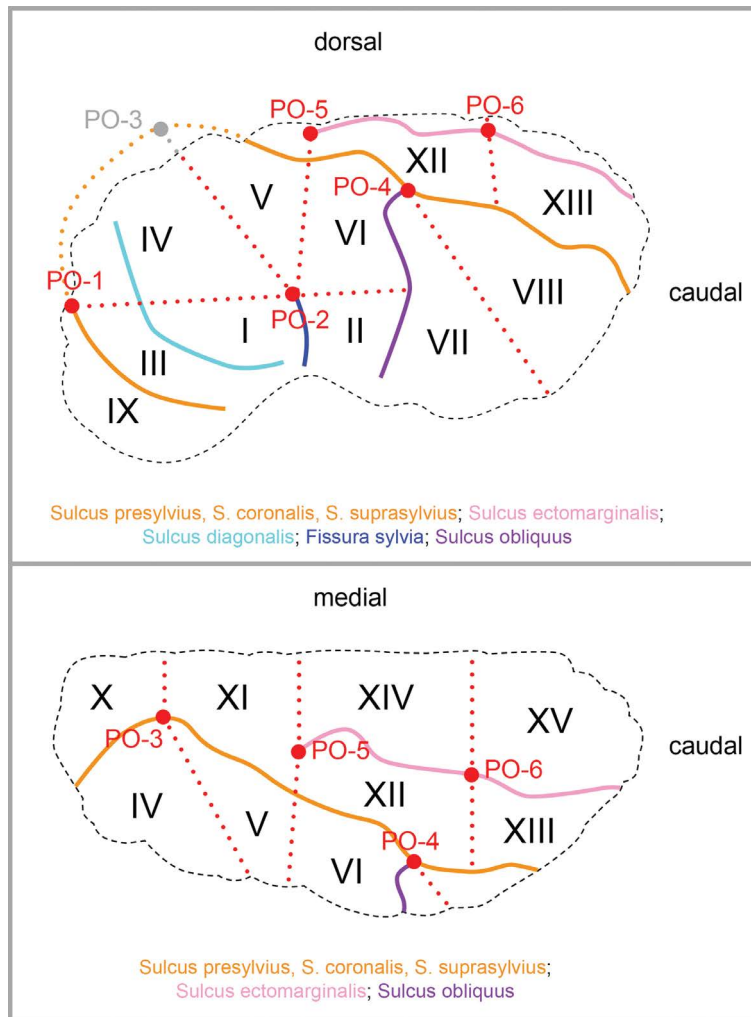


Figure 1. Graphical illustrations of the sectors I to XV located on the Facies convexa of the neopallium (top: lateral view; bottom: dorsal view). The coloured primary sulci [21] were topographically related to six points of orientation (PO-1 to PO-6) that were used to place auxiliary lines (red dotted). The latter divide the spaces between the primary sulci into the sectors. The numbering of the sectors always starts rostral (sector I) and caudal (sector II) to the Fissura sylvia, continuing thereafter in a concentric, bow-like manner. In the strictly lateral view (figure on top), parts of the sulcus coronalis (yellow dotted lines), and the PO-3 (grey) and sectors X, XI, XIV and XV are not visible. PO-1: Most rostral point on the continuation of sulcus presylvius, sulcus coronalis and sulcus suprasylvius; PO-2: Dorsal end of Fissura sylvia; PO-3: Most medial point on the continuation of sulcus presylvius, sulcus coronalis and sulcus suprasylvius; PO-4: Connection of sulcus obliquus with sulcus suprasylvius; PO-5: Rostral end of sulcus ectomarginalis; PO-6: Half way on sulcus ectomarginalis; the auxiliary line connected to PO-4 cuts the space between sulcus obliquus and sulcus suprasylvius into two parts of same size; the auxiliary line cutting PO-6 is connected orthogonally to the Margo dorsalis cerebri ("Mantelkante"); further auxiliary lines start at PO-1, PO-3 and PO-5, respectively, and are connected orthogonally to the Margo dorsalis cerebri.

resentation in order to highlight similarities in terms of a basic pattern of ramification. Furthermore, the sketches helped to display individual variations in the ramifications and courses of the respective blood vessels, i.e., their local distributions related to the neopallium's sectors.

The brain hemispheres slightly differed in size; this discrepancy was adjusted by proportional graphical scaling of the neopalliums' outlines. This procedure revealed that all of the brains had similar proportional dimensions because the contours of the superimposed,

individual sketches varied only slightly. Consequently, a mean contour was used in further illustrations.

RESULTS

Origin and ramification of MCA

The A. cerebri media originated (in 16 of 17 brains) from the A. cerebri rostralis (RCA) that represented the rostrolateral part of the circulus arteriosus cerebri (CAC). The MCA lay directly rostral to the lobus priformis; in some specimens, it took an initial, slightly curved, rostral course, in others, it ran almost verti-

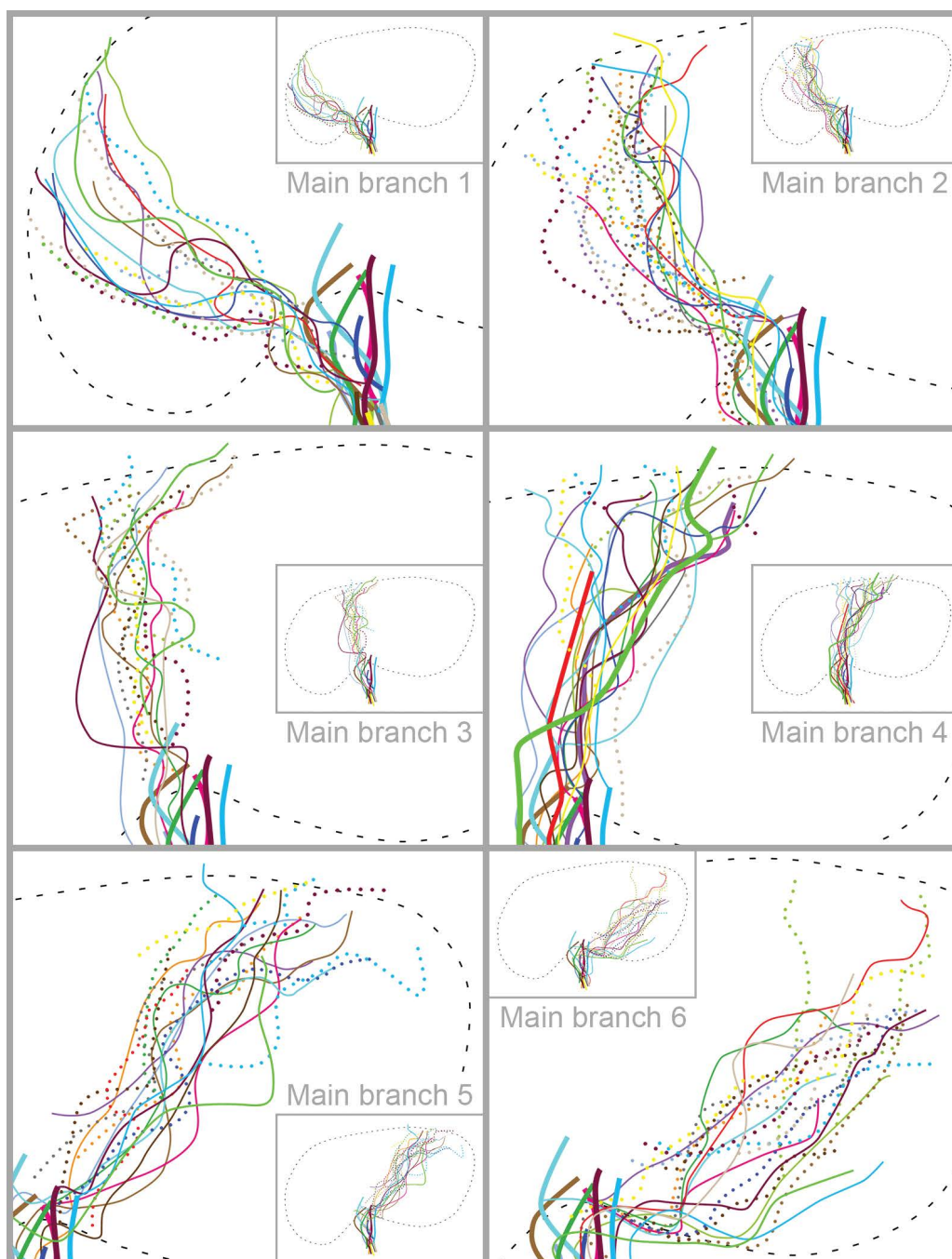


Figure 2. Graphical representations of the *A. cerebri media* (MCA; thick lines), and its six main branches. The comparative survey was facilitated by means of superimposition of the 17 sketches from the 17 equine brains (colour-coded). The main branches were of 1st order (thin lines) or of 2nd order (dotted lines). Lateral view (90° perspective); the neopallium is delineated by a mean contour (dashed line). Each of the main branches 1 to 6 spread over its typical region of residence (Note: When the MCA did not bifurcate, it ran far into the dorsal direction and was designated as the main branch 4).

cally in a dorsal direction. Finally, the MCA reached the neopallium in the region of the Fissura sylvia, i.e., between the ventral parts of sectors I and II. In one brain, there was no rostrolateral portion of a CAC due to the lack of a left RCA. In this single case, the left MCA represented the rostral branch of the left *A. carotis interna* (ICA).

Six main branches originated from the MCA (Fig. 2). Three of them were present in all brains (main branches 2, 4 and 6); the other main branches were found in 76–88% of the cases. Some of the main branches occurred double or three-fold in some brains; this applied to main branch 3 in 23% of the brains, and to main branches 2 and 4 in 41% of the brains.

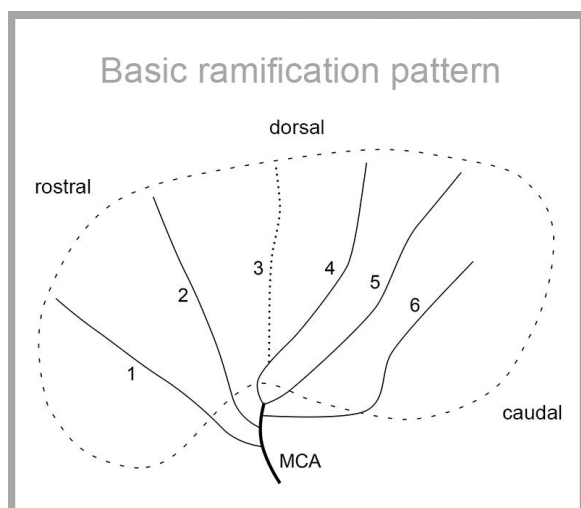


Figure 3. Sketch of a proposed basic pattern of ramification of the A. cerebri media (MCA) into six main branches; all of them were predominantly of 1st order, except main branch 3, which was mainly of 2nd order (dotted line). Note the bifurcation into main branches 4 and 5. Meandering courses are not displayed; approximate position on the neopallium according to Figure 2. Lateral view; dashed line — mean contour of the neopallium.

A bifurcation of the MCA was present in almost all of the brains (82%). Such a bifurcation was predominantly located slightly ventral to the sulcus rhinalis lateralis and rostral to the lobus piriformis (i.e., ventral to the region of the Fissura sylvia). The arms of this bifurcation (Fig. 3) were represented by main branch 4 (in 93% of the cases) and main branch 5 (in 58% of the cases). However, in a few brains (3 of the 17), no such bifurcation of the MCA was found at all. In those cases, the non-bifurcated MCA continued far, towards the neopallium's Margo dorsalis, and represented main branch 4 (Fig. 2).

The main branches originated directly from the MCA (except main branch 3) and, hence, were branches of 1st order (Figs. 2, 3). Only main branch 3 was an exception; it either ramified directly from the MCA as a branch of 1st order (in 40% of cases), or it represented a branch of 2nd order deriving from main branch 4 (in 40% of the cases), or it was a branch of 2nd order originating from main branch 2 (in 20% of the cases). The latter type of ramification, representing the majority of cases, was included in a graphical representation of a proposed basic pattern of ramification (Fig. 3).

The superimposed sketches of the six main branches (Fig. 2) showed that every main branch was encountered in a typical, limited space on the neopallium's surface (region of residence): main branches 1, 3 and 5 covered a region of residence that was

approximately the width of two fingers, whereas the positions of main branches 2, 4 and 6 varied within a region of up to the width of three fingers.

The averaged calibre of the MCA was 2.35 mm (2.00–2.75 mm). All main branches originating from it had an averaged calibre of 1.00–1.5 mm (1.16–1.42 mm); main branch 4 was the widest (1.42 mm).

Origin and ramification of CA

The left and right CA originated from an impaired, common trunk that resulted from the confluence of the left and right RCA in the median plane of the brain's ventral side. In one case only, the left RCA was absent so that the CAC was not closed rostrally. Hence, the aforementioned common trunk in the median plane was simply a continuation of the right RCA. The common trunk entered the space between the left and right cerebral hemisphere (fissura longitudinalis cerebri) and continued along the dorsal surface of the rostrum and genu corporis callosi.

Seven main branches originated from the CA (Figs. 4, 5). Main branch 5 was the only one found in all specimens; main branch 2 was present in 16 of 17 brains. Main branches 3 and 4 were the most variable, being present in only 10 of 17 brains.

The CA always terminated by forming a bifurcation; this was located vaguely at the transition of the genu corporis callosi into the truncus corporis callosi (or slightly caudal to that site). Main branch 5 (in 65% of the brains) and main branch 6 (in 58% of the brains) were the arms of this bifurcation (Fig. 5).

In the majority of specimens, main branches 2 to 6 were predominantly given off directly from the CA. The main branch 7, however, was a branch of 2nd order originating from main branch 6 in 55% of the brains.

Main branch 1 was extremely variable: it originated either from the CA (or from the CA's common trunk) or from the main branch 2 (in the latter case being a branch of 2nd order); in one case, it originated (as a branch of 2nd order) from main branch 3. Respecting this variability and the lack of a clearly dominating type of ramification, both types (1st order origin from CA and 2nd order origin from main branch 2) were integrated into the sketch of the basic ramification pattern (Fig. 5).

Main branch 3 was extremely variable too: plenty of alternative origins from either main branch 1, 2, 3 or 5 occurred — all of 2nd order (Fig. 4). However, in a slight majority of cases (40%), its 1st order origin — directly from the CA — was encountered.

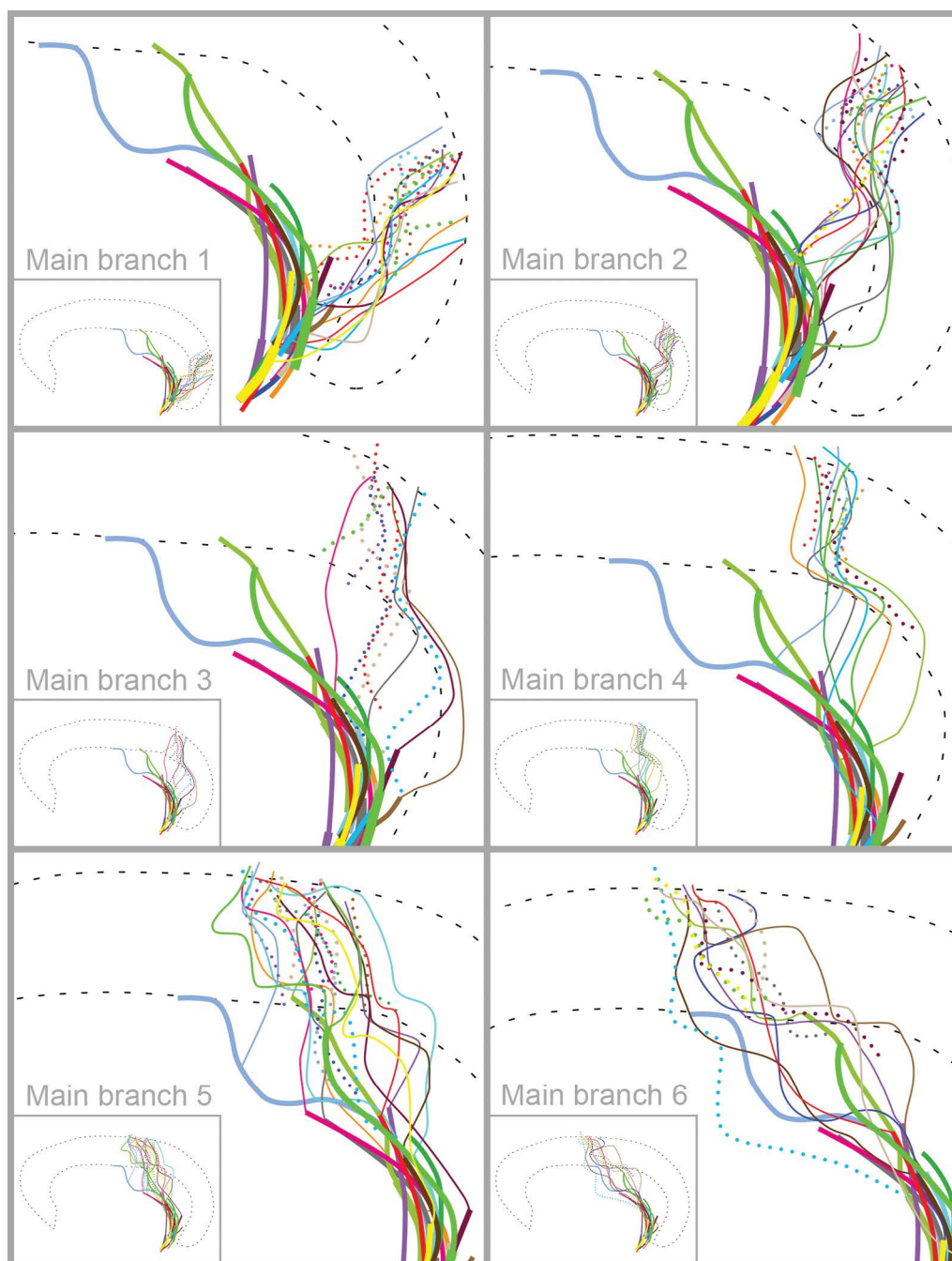


Figure 4. Graphical representations of the *A. corporis callosi* (CA; thick lines), and six of its seven main branches (for main branch 7 see Figure 5, left sketch). The comparative survey is facilitated by means of superimposition of the 17 sketches from the 17 equine brains (colour-coded). The main branches were of 1st order (thin lines) or of 2nd order (dotted lines). Medial view (90° perspective); the neopallium is delineated by a mean contour (dashed line). Each of the main branches spread over its typical region of residence.

Accordingly, this type of ramification was included in the sketch of a proposed basic pattern of ramification (Fig. 5) of the CA.

All main branches took a dorsal or caudodorsal course. Firstly, they entered the sulcus genualis, i.e., the long primary sulcus that continued into the sulcus cinguli and the sulcus splenialis in a caudal direction, which all delineated the medial border of the

neopallium. Then, the main branches, subsequently originating from the CA, ran almost vertically towards and across the neopallium's Margo rostralis and Margo dorsalis ("Mantelkante"). Accordingly, these main branches of the CA also reached regions on the lateral surface of the neopallium (Facies convexa), i.e., the rostradorsal sectors X, IV and V and the dorsal sectors XI and XIV.

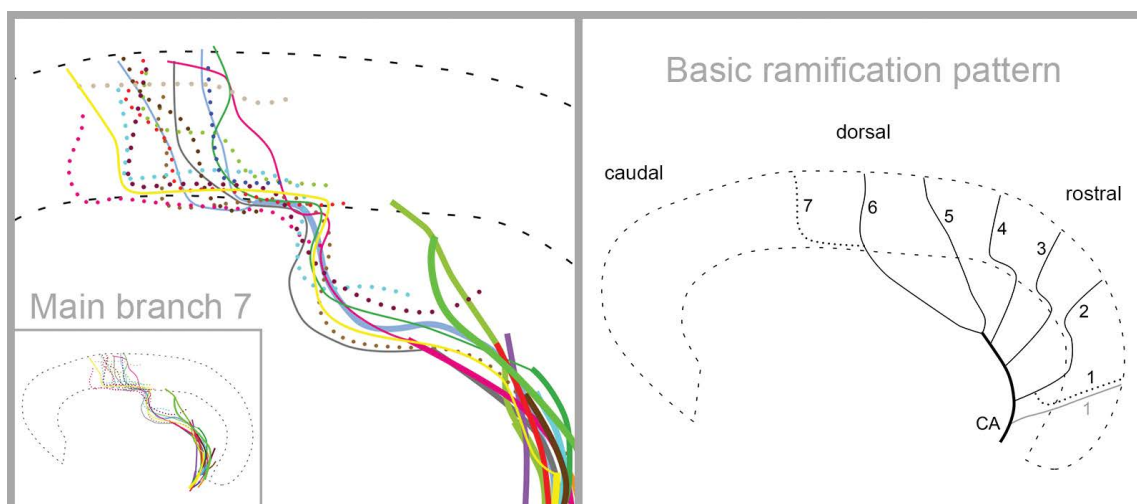


Figure 5. **Left side:** Graphical representation of the A. corporis callosi (CA; thick lines) and its main branch 7. Like in Figure 4, the 17 sketches from the 17 equine brains (colour-coded) were superimposed. The main branch 7 was either of 1st order (thin lines) or of 2nd order (dotted lines). Medial view (90° perspective); the neopallium is delineated by a mean contour (dashed line). **Right side:** Sketch of a proposed basic pattern of ramification of the CA into seven main branches, which were of 1st order (thin lines) or of 2nd order (dotted lines). As for main branch 1, no clear preference of either 1st or 2nd order type could be identified (both variations are displayed). Similarly, main branch 3 varied markedly too, but a slight majority of the 1st order type gave reason to prefer this type in this sketch (the other variations, as mentioned in the text, must be kept in mind). Note the bifurcation into main branches 5 and 6. Meandering courses are not displayed; approximate position on the neopallium according to Figure 4. Medial view; dashed line — mean contour of the neopallium.

The position of main branch 4 on the neopallium varied only slightly, meaning that its region of residence was relatively narrow (Fig. 4). In contrast, the regions of residence of the other main branches (Figs. 4, 5) were wider, i.e., up to the width of three fingers.

The averaged calibre of the CA was 1.93 mm (1.50–2.25 mm), while all main branches had an averaged calibre of approximately 1 mm (0.89–1.16 mm).

Supply areas of MCA

The main branches of the MCA spread over a region that represented the largest portion of the Facies convexa (i.e., sectors I to XV). However, they reached neither the rostral pole nor the caudal pole of the neopallium (Fig. 6). Every main branch was topographically related to more than one sector, and, in general, each of the 15 sectors was supplied by more than one main branch of MCA (except sector X; Table 1). Often, some main branches lay in certain sulci, but they never continued all the way exclusively inside them; instead, many main branches were seen to cross the gyri without following the course of a sulcus.

Main branch 1 often ran either in the sulcus suprasylvius or in the sulcus diagonalis. Accordingly, it was predominantly related to sector III and to the rostral third of sector I, as well as to a small ventral portion of sector IX (Fig. 6; Table 1). It also continued dorsally to reach sector IV.

Main branch 2 usually entered the sulcus diagonalis located between sectors I and III. In all brains, it reached sector IV (Fig. 6; Table 1). Sometimes, it took a slightly caudal course into the laterodorsal sector V.

Main branch 3 frequently ran along the Fissura sylvia and was primarily associated with sectors I, IV and V (Table 1; Fig. 6). Occasionally, it entered sector XI (in 62% of the cases) on the dorsal surface of the neopallium.

Main branch 4 was initially located in the Fissura sylvia (between sectors I and II). In its further course in a caudodorsal direction; however, it crossed sector VI and reached the dorsal sector XII that lay dorsal to the sulcus suprasylvius (Table 1; Fig. 6). Often, it even crossed the sulcus ectomarginalis and contributed to the vascular supply of sector XIV, too.

Main branch 5 was one of the dominant vascular branches in sector II (present here in 92% of the brains). On its way in a caudodorsal direction, it passed through sectors VII and VIII (Table 1; Fig. 6). It often followed the course of the sulcus obliquus towards its intersection with the sulcus suprasylvius.

Main branch 6 was finally encountered in sector VII, in the two rostral thirds of sector VIII and in a small rostral portion of sector XIII (Table 1; Fig. 6).

Supply areas of CA

Initially ramifying from the CA on the medial side of the brain's hemisphere, some of the main branches

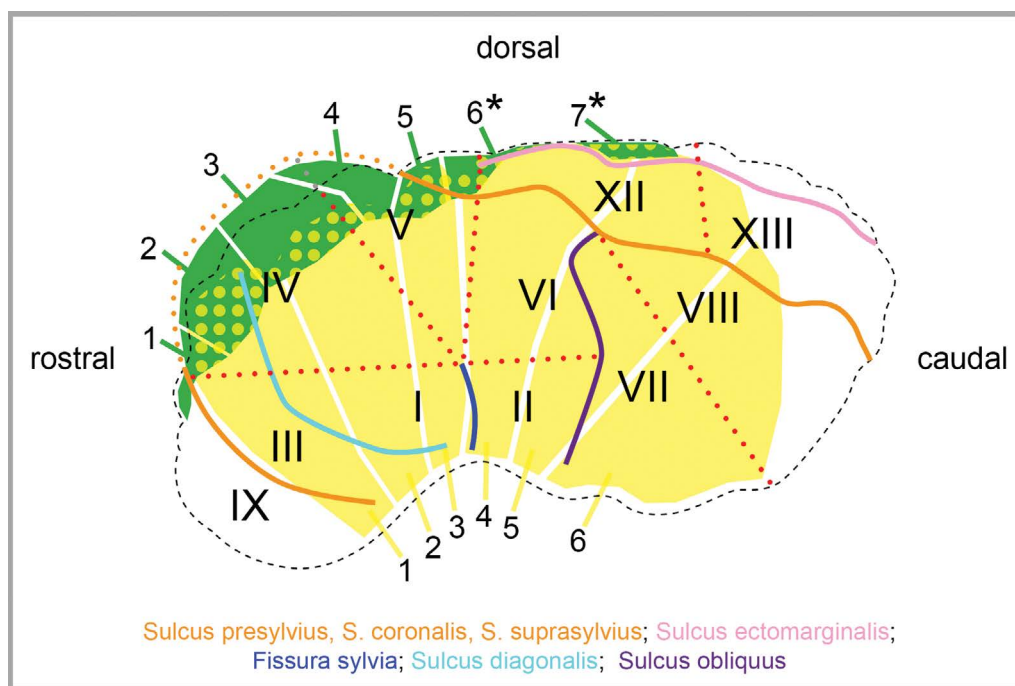


Figure 6. Graphical representation of the averaged supply areas of main branches 1 to 6 of the A. cerebri media (MCA; yellow) and main branches 1 to 7 of the A. corporis callosi (CA; green) on the Facies convexa of the equine brain. Lateral view (90° perspective). The colour-coded primary sulci [21] and the auxiliary lines (red dotted) mark the boundaries of the sectors (asterisks indicate dorsal sectors invisible in the lateral view; compare Figure 1). Note the multiple-supply situation (sectors shaded with two colours, i.e. yellow and green [e.g., sector IV]) facilitated by main branches from both MCA and CA.

Table 1. Survey on the presence of main branches 1–6 of the A. cerebri media (MCA) in the 15 sectors (I–XV) of the neopallium’s Facies convexa in 17 equine brains

Sector	Main branches of MCA					
	1 (n = 13)	2 (n = 17)	3 (n = 13)	4 (n = 17)	5 (n = 15)	6 (n = 17)
I	62%	88%	100%	71%	*	–
II	–	*	46%	88%	93%	65%
III	100%	88%	31%	*	–	–
IV	77%	100%	77%	*	*	–
V	–	53%	100%	53%	*	*
VI	–	–	*	88%	73%	*
VII	–	–	–	–	87%	100%
VIII	–	–	–	–	67%	88%
IX	69%	*	–	–	–	–
X	31%	–	–	–	–	–
XI	–	*	62%	59%	*	*
XII	–	–	*	88%	80%	*
XIII	–	–	–	*	67%	59%
XIV	–	–	*	88%	53%	*
XV	–	–	–	*	47%	*

100% — a main branch was encountered in the respective sector in all of the brains; *Values below 25% are not listed. Whenever a main branch ran along the boundary between two sectors (e.g., in a sulcus), it was supposed to supply each of the two neighbouring sectors and, therefore, was counted for both sectors individually. The number of samples (n) was smaller than 17 when the respective main branch was not found in the specimen

Table 2. Survey on the presence of main branches 1–7 of the A. corporis callosi (CA) in the 15 sectors (I–XV) of the neopallium's Facies convexa in 17 equine brains

Sector	Main branches of CA						
	1 (n = 14)	2 (n = 16)	3 (n = 10)	4 (n = 11)	5 (n = 17)	6 (n = 12)	7 (n = 13)
IV	29%	88%	80%	27%	–	–	–
V	–	*	30%	82%	59%	–	–
IX	86%	*	–	–	–	–	–
X	50%	100%	90%	73%	–	–	–
XI	–	–	30%	100%	100%	75%	*
XII	–	–	–	–	*	–	–
XIV	–	–	–	–	*	100%	77%
XV	–	–	–	–	–	–	*

100% — a main branch was encountered in the respective sector in all of the brains; *Values below 25% are not listed. Whenever a main branch ran along the boundary between two sectors (e.g., in a sulcus), it was supposed to supply each of the two neighbouring sectors and, therefore, was counted for both sectors individually. The number of samples (n) was smaller than 17 when the respective main branch was not found in the specimen

ran across the neopallium's Margo dorsalis ("Mantelkante") to continue on the lateral side, i.e., on the Facies convexa. In this way, they entered the rostro-dorsal and dorsal sectors X, XI and XIV and parts of sectors IV and V (Table 2; Fig. 6).

Consequently, each of these sectors was supplied by both cerebral stem arteries, i.e., MCA and CA (instead of only one of these) in terms of a so-called multiple-supply situation (Fig. 6; compare Tables 1 and 2).

DISCUSSION

Origin of MCA and CA

In 16 of the 17 specimens, the MCA originated from the RCA in accordance with the common pattern [1, 5, 25].

The CA always originated from a common, impaired trunk, as had been reported earlier [1, 11, 24]. Despite this anatomical evidence, the nomenclature is different in the related literature. Being formed by the confluence of the right and left RCA (rostro-lateral portion of the CAC), this common trunk was designated as the azygos anterior cerebral artery [11] or as the A. communicans rostralis [1]. Finally, other authors [5] described this trunk as being one of the three segments of the RCA, meaning that the right and left RCA formed the rostrolateral portion of the CAC (first segment); then the right and left RCA joined to form the A. communicans rostralis (second segment, representing the impaired trunk); and finally, the trunk rostrally bifurcated into a left and right artery (third segment); the latter continued

in a caudodorsal direction on the medial surface of each hemisphere without being given another name.

Hence, the term CA is not used at all in that context [5, 25]. In fact, it is not listed in the Nomina Anatomica Veterinaria [25] either. However, the term CA is used in current research articles [11, 18, 24] and textbooks [e.g. 1]. Considering the regular presence of these arteries in all 17 specimens in this study, and appreciating the descriptive value for topographical reasons, the present study gives substantial reason to add the terms A. cerebri rostralis impar (azygos anterior cerebral artery of [11]) and A. corporis callosi (or preferably, as in human anatomy, A. pericallosa instead of A. corporis callosi) to the Nomina Anatomica Veterinaria.

Ramification pattern of MCA

In human anatomy, the arterial branches of the MCA are named according to the sulci in which they usually occur, like for example, A. sulci centralis [7] that runs along the sulcus centralis. This concept appears to not be applicable to the horse: Firstly, the equine neopallium shows a very complex gyration pattern [21, 23] and, secondly, the arterial branches did not regularly run along the sulci, but often took a course across the gyri [2].

Supply areas of MCA and CA

The topographical analysis clearly revealed that the rostral pole and the caudal pole of the neopallium were always void of main branches from MCA and CA. The applied cartographic system of sectors was

a valuable tool to delineate these sites in appropriate detail (i.e., sector IX at the rostral pole, and the caudal parts of sectors VIII, XIII and XV at the caudal pole). Instead, these sectors were supplied via branches from the A. ethmoidalis externa (rostral pole, sector IX) and by branches of the A. cerebri caudalis (caudal pole, sectors VIII, XIII and XV), respectively, as previously described [2].

The widest part of the *Facies convexa*, however, was vascularised by the six main branches of MCA, each of them attributed to its special region of residence represented by the respective sectors of the cartographic system. It must be emphasized that every sector was always reached by more than one main branch, except sector X. Clearly, the rostr dorsal and dorsal portion of the *Facies convexa*, represented by sectors IV, V, X, XI and XIV, received an additional supply from the hemisphere's medial side, as main branches from the CA extended across the *Margo rostralis* and *Margo dorsalis* and — together with main branches from the MCA — contributed to a so-called multiple-supply situation. Furthermore, it must be pointed out that in sector X, branches from the CA compensated for the little supply contributed by branches from the MCA. In functional terms, considering early electrophysiological experiments [4] and histological data [6, 15], some of these special sectors (IV, V, X, XI) were particularly discussed [2, 12] with regard to the suggested position of the area *motorica* of the equine brain.

Additionally, the present study elucidates that it was the CA, which mainly contributed to supplying the larger parts of the respective sectors (IV, V, X, XI) within this motor area. Its branches were protected in the deep gap between the hemispheres as they proceeded from the interhemispheric *fissura longitudinalis cerebri*. Clinically, this feature may be regarded as some sort of a safety mechanism in cases of lateral cranial and brain trauma. Traumatic head injuries are common in horses [9, 10, 14, 16, 22]. In general, such traumatic insults may require surgical procedures [19]; knowledge of the special regions of residence where the typical main branches of the cerebral stem arteries were located may be helpful in terms of treatment and prognosis of the injury.

CONCLUSIONS

Transferring the vascular ramification patterns and regions of residence into the cartographic system of the neocortical sectors facilitated the detailed

description of characteristic vascular supply areas on the *Facies convexa* of the equine neopallium. This combination of two topographical procedures offered substantial advantages; firstly, to adequately observe the horse's complex and apparently complicated gyration pattern, and, secondly, to overcome immanent orientation problems by implementing a procedure that is reproducibly standardised.

Acknowledgements

We most gratefully acknowledge the expert contribution of our native speaker, Ms. Frances Sherwood-Brock, who meticulously revised the English manuscript.

REFERENCES

1. Böhme G. (ed.). Nickel R, Schummer A, Seiferle E. *Lehrbuch der Anatomie der Haustiere*, Bd. IV: Nervensystem, Sinnesorgane, Endokrine Drüsen (4th ed.). Parey, Stuttgart, Germany 2004.
2. Böing L. *Die arterielle Vaskularisation der Gehirnoberfläche beim adulten Warmblutpferd: Anatomische Untersuchung unter Berücksichtigung des tierartspezifischen Furchungsmusters des Neopalliums* (doctoral dissertation, submitted). University of Veterinary Medicine, Hannover 2020.
3. Böing L, Heun F, Gasse H. The arterial ramification pattern of the horse's brain with regard to topographical sectors of the neopallium (Poster 79). 114th Annual Meeting, Anatomische Gesellschaft, Würzburg 2019.
4. Breazile JE, Swafford BC, Biles DR. Motor cortex of the horse. *Am J Vet Res.* 1966; 27(121): 1605–1609, indexed in Pubmed: [5971615](#).
5. Constantinescu GM. *Illustrated Veterinary Anatomical Nomenclature* (4th ed.). Thieme, Stuttgart, Germany 2018.
6. Cozzi B, De Giorgio A, Peruffo A, et al. The laminar organization of the motor cortex in monodactylous mammals: a comparative assessment based on horse, chimpanzee, and macaque. *Brain Struct Funct.* 2017; 222(6): 2743–2757, doi: [10.1007/s00429-017-1369-3](#), indexed in Pubmed: [28210850](#).
7. Deller T. Hirngefäße. In: Waschke J, Böckers TM, Paulsen F. *Anatomie. Das Lehrbuch. Sobotta* (ISBN 978-3-437-44080-9). Urban-Fischer (in Elsevier), München, Germany 2015: 623–644.
8. Dexler H. Beiträge zur Kenntnis des feineren Baues des Zentralnervensystems der Ungulaten. *Gegenbaurs Morphologisches Jahrbuch.* 1904; 32: 288–389.
9. Feary DJ. Review of the management of traumatic brain injury in horses. *AAEP Proceedings.* 2007; 53: 519–524.
10. Fürst A, Jackson M, Kümmerle J, et al. Summary of current therapeutic measurements in head fractures of horses. *Pferdeheilkunde Equine Medicine.* 2010; 26(4): 503–514, doi: [10.21836/pem20100403](#).
11. Gillan LA. Blood supply to brains of ungulates with and without a rete mirabile caroticum. *J Comp Neurol.* 1974; 153(3): 275–290, doi: [10.1002/cne.901530305](#), indexed in Pubmed: [4817350](#).

12. Heun F. Morphometrische Untersuchung der topographischen Beziehungen zwischen externen Landmarks am Kopf und kartographischen Mustern des Neopalliums bei adulten Warmblutpferden (doctoral dissertation, submitted). University of Veterinary Medicine, Hannover 2020.
13. Heun F, Böing L, Gasse H. A stereotactic approach for a topographical mapping of the neopallium in the horse (Poster 80). 114th Annual Meeting, Anatomische Gesellschaft, Würzburg 2019.
14. Hug S. Epidemiologische Untersuchungen der Frakturpatienten der Pferdeambulanz - Bedeutung der Schlagverletzung als Ursache von Frakturen (doctoral dissertation). University of Zurich, Vetsuisse Faculty 2009.
15. Hummel G. Die Feinstruktur der motorischen Großhirnrinde des Pferdes. *J Vet Med C*. 1976; 5: 35–53, doi: [10.1111/j.1439-0264.1976.tb00655.x](https://doi.org/10.1111/j.1439-0264.1976.tb00655.x).
16. Hurcombe S. Traumatic head injury in horses. *Proceedings of the NAVC Conference*. 2010; 24: 146–149.
17. Jenke W. Die Gehirnarterien des Pferdes, Hundes, Rindes und Schweines verglichen mit denen des Menschen (doctoral dissertation). University of Veterinary Medicine, Dresden 1919.
18. Jerbi H, Vazquez N, Pérez W. Morphological configuration and topography of the brain arterial supply of the one-humped camel (*Camelus dromedarius*, Linnaeus 1758). *Int J Morphol*. 2019; 37(3): 1095–1100, doi: [10.4067/s0717-95022019000301095](https://doi.org/10.4067/s0717-95022019000301095).
19. Kramer J, Coates JR, Hoffman AG, et al. Preliminary anatomic investigation of three approaches to the equine cranium and brain for limited craniectomy procedures. *Vet Surg*. 2007; 36(5): 500–508, doi: [10.1111/j.1532-950X.2007.00297.x](https://doi.org/10.1111/j.1532-950X.2007.00297.x), indexed in Pubmed: [17614932](https://pubmed.ncbi.nlm.nih.gov/17614932/).
20. Lang A, Sherwood-Brock F, Gasse H. Hermann Dexler's "Beiträge zur Kenntnis des feineren Baues des Zentralnervensystems der Ungulaten." An Annotated English Translation of the Original German Article; Part V: Telencephalon – Adult Stages. University of Veterinary Medicine Hannover. 2018, doi: [10.15487/TiHo.4_2018.1/5](https://doi.org/10.15487/TiHo.4_2018.1/5).
21. Lang A, Wirth G, Gasse H. Review of the surface architecture of the equine neopallium: Principle elements of a cartographic pattern of sulci revisited and further elaborated. *Anat Histol Embryol*. 2018; 47(4): 280–297, doi: [10.1111/ahc.12355](https://doi.org/10.1111/ahc.12355), indexed in Pubmed: [29542168](https://pubmed.ncbi.nlm.nih.gov/29542168/).
22. Müller JM, Hellige M, Hoffmann MV, et al. Parietal cerebral defect after skull fracture as a cause of posttraumatic epilepsy in an Icelandic horse. *Pferdeheilkunde Equine Medicine*. 2011; 27(3): 306–310, doi: [10.21836/pem20110317](https://doi.org/10.21836/pem20110317).
23. Pillay P, Manger PR. Order-specific quantitative patterns of cortical gyrification. *Eur J Neurosci*. 2007; 25(9): 2705–2712, doi: [10.1111/j.1460-9568.2007.05524.x](https://doi.org/10.1111/j.1460-9568.2007.05524.x), indexed in Pubmed: [17459107](https://pubmed.ncbi.nlm.nih.gov/17459107/).
24. Rösslein C. Angioarchitektonische Untersuchungen an den Arterien des Encephalon und der Meninges beim Pferd (doctoral dissertation). Veterinary Faculty of Ludwig-Maximilians-Universität, München 1987.
25. World Association of Veterinary Anatomists. *Nomina Anatomica Veterinaria*, N.A.V. (6th ed.), 2017. <http://www.wava-amav.org>.

The anatomical landmarks effective in the localisation of the median nerve during orthopaedic procedures

E. Mizia¹, P.A. Pekala^{1,2}, B. Skinningsrud^{1,2}, B. Rutowicz¹, P. Piekos^{1,2}, A. Baginski¹, K.A. Tomaszewski^{2,3}

¹Department of Anatomy, Jagiellonian University Medical College, Krakow, Poland

²International Evidence-Based Anatomy Working Group, Krakow, Poland

³Faculty of Medicine and Health Sciences, Andrzej Frycz Modrzewski Krakow University, Krakow, Poland

[Received: 10 March 2020; Accepted: 30 March 2020]

Background: The aim of this study was to create a safe zone for surgeons who perform procedures in the wrist to avoid iatrogenic damage to the median nerve (MN) by identifying anatomical landmarks using ultrasound (USG).

Materials and methods: We measured the distances between the MN and two easily identifiable anatomical landmarks at the level of the proximal border of carpal ligament using USG.

Results: A total of 57 volunteers ($n = 114$ upper limbs) were included in this study. Our main findings revealed that the distance from the flexor carpi radialis tendon to MN (FCR-MN) was 7.87 mm (95% confidence interval 7.37–8.37) and the distance from flexor carpi ulnaris tendon to MN (FCU-MN) was 19.09 mm (95% confidence interval 18.51–19.67).

Conclusions: The tendons of FCR and FCU are easily identifiable landmarks that can be distinguished using simple palpation. Based on our USG findings, the area around FCR should be carefully navigated to avoid iatrogenic injury to the MN during surgical procedures around the carpal tunnel. (Folia Morphol 2021; 80, 2: 248–254)

Key words: median nerve, flexor carpi radialis, flexor carpi ulnaris, iatrogenic injury, carpal tunnel release, anatomical landmarks

INTRODUCTION

Carpal tunnel syndrome (CTS) is one of the most common nerve compression syndromes affecting the general population [19]. This condition may cause numbness, paraesthesias, burning sensations and pain in both the hand and arm. These effects begin to appear when the median nerve (MN), which passes through a narrow passageway in the wrist called the carpal tunnel (Fig. 1), is compressed by the flexor

tendons, carpal ligament, and surrounding carpal bones. It is believed that a constellation of risk factors contributes to the development of entrapping the MN. Some risk factors may include anatomical variations of the wrist, female sex, obesity, and daily repetitive hand motion to name a few [17]. Carpal tunnel syndrome is diagnosed clinically, often being confirmed by an electromyogram, while ultrasonography (USG) criteria have become increasingly useful

Address for correspondence: E. Mizia, MD, PhD, Department of Anatomy, Jagiellonian University Medical College, ul. Kopernika 12, 31–034 Kraków, Poland, tel: +48 12 422 95 11, e-mail: ewa.mizia@gazeta.pl

This article is available in open access under Creative Common Attribution-Non-Commercial-No Derivatives 4.0 International (CC BY-NC-ND 4.0) license, allowing to download articles and share them with others as long as they credit the authors and the publisher, but without permission to change them in any way or use them commercially.

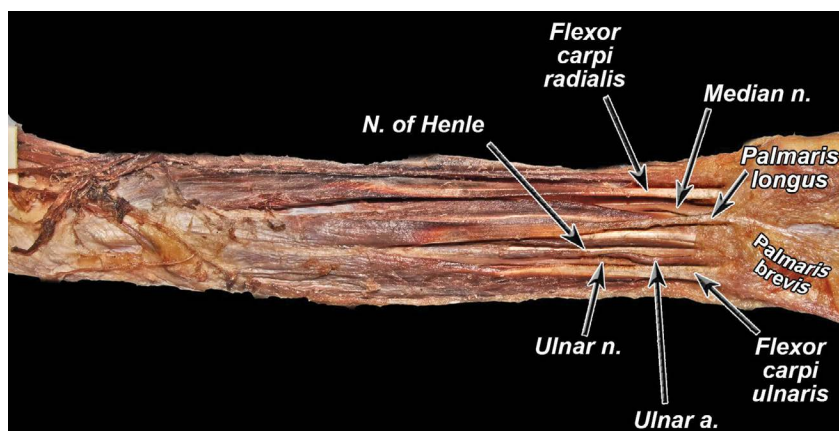


Figure 1. Cadaveric image of the wrist.

for the diagnosis. Ultrasonography is better tolerated, less expensive, yet just as effective as other diagnostic methods [1, 8]. It provides a good indication of the severity of the condition and it allows anatomical variants to be discerned [19].

If there is an early diagnosis of CTS, wrist splinting, non-steroidal anti-inflammatory drugs, and corticosteroids are typically initiated as treatment along with other physical rehabilitation techniques [24]. Although this type of conservative treatment may be the first-line choice when treating CTS, there is little evidence to suggest it has any practical long-term success at removing symptoms. That is why surgery is the only definite option in treatment in more severe cases of CTS [9].

Surgery entails cutting through the carpal tunnel ligament thereby releasing pressure on the MN to hopefully eradicate any associated symptoms. This can be achieved through either an open or an endoscopic procedure, which are the two available surgical techniques [2]. Both open and endoscopic release of the flexor retinaculum in CTS has yielded satisfactory results [3]. Risks involved in this surgery include infections, improper pressure release, scar formation and most importantly possible damage to the MN.

Although carpal tunnel surgery is considered to be one of the safest procedures performed by surgeons, there is still a minute risk that the MN may be lacerated or completely cut during the operation [13]. This is one of the most serious complications. An injured MN results in permanent damage that can result in variable symptoms such as decreased strength, sensation, and hand function in the median nerve innervated region. Moreover, severe nerve pain may emerge with any applied pressure to the site due to the development of a painful neuroma [22].

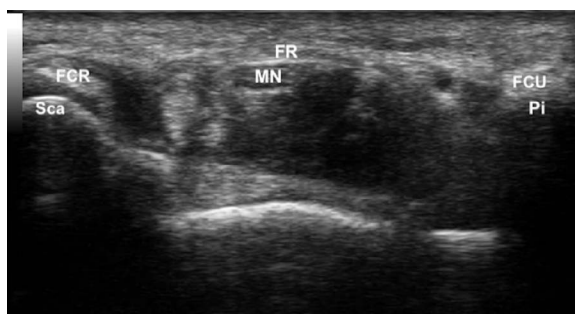


Figure 2. Cross section sonogram of carpal tunnel anatomy; FR — flexor retinaculum; Pi — pisiform bone; Sca — scaphoid bone; MN — median nerve; FCU — flexor carpi ulnaris; FCR — flexor carpi radialis.

The aim of this study was to identify a safe zone for surgeons who perform CTS release and other procedures in the wrist by analysing the anatomical variations in the course of the MN and its easily identifiable adjacent landmarks through the utilisation of USG.

MATERIALS AND METHODS

Patients

The local ethics committee has approved the protocol. Written and informed consent was obtained from every patient. Inclusion criteria were as follows: informed consent, no current or history of trauma in upper limbs. Exclusion criteria included: current or history of trauma of upper limbs, radiotherapy or surgery of upper limbs, rheumatoid diseases, or deformities of upper limbs.

Measurements

The following anatomical landmarks were visualised using the MyLab25 USG scanner with an 18 MHz transducer (Fig. 2):

- the lateral margin of the flexor carpi ulnaris (FCU) and/or its attachment to the pisiform bone (level 0 = proximal edge of the flexor retinaculum)
- the medial margin of the tendon of flexor carpi radialis (FCR).

A line was drawn along the medial edge of the FCR tendon on the palmar surface skin of the subject. The lateral edge of the USG transducer was adjacent to this line. The following parameters were assessed distally using the transverse position of the transducer (perpendicular to the long axis of the limb) at 0 cm, 1 cm, and 2 cm levels.

Level 0 (proximal edge of the flexor retinaculum):

- distance between the lateral margin of the FCU tendon and the medial margin of the MN;
- distance between the medial edge of the FCR tendon and the lateral margin of MN;
- transverse dimension of the MN (lateral);
- the anterior-posterior (AP) dimension of the MN.

Level 1 (1 cm distal from level 0):

- transverse dimension of the MN (lateral);
- the AP dimension of the MN.

Level 2 (2 cm distal from level 0):

- transverse dimension of the MN (lateral).
- the AP dimension of the MN.

Statistical analysis

To perform statistical analyses of the data obtained, elements of descriptive statistics such as mean values with standard deviations (SD) were calculated. Normal distribution was assessed using the Shapiro-Wilk test. In the case of a normal distribution, data was compared using Student's t-test. If the distribution was not normal, the Mann-Whitney U test was used. Authors compared the following groups: males vs. females, left side vs. right side, dominant hand vs. non-dominant hand. A p-value of < 0.05 was considered statistically significant. Calculations were performed using SPSS software.

Ethics

The research protocol was approved by the Jagiellonian University Medical College Ethics Committee. The study was performed in accordance with the ethical standards established in the 1964 Declaration of Helsinki and its later amendments. Informed consent was obtained. The study was conducted in 2018 in the local Department of Anatomy.

RESULTS

Patients

A total of 57 patients (n = 114 upper limbs, 55 patients with right dominant hand, 2 patients with left dominant hand, 27 females, 30 males) were included in this study.

Median nerve dimensions on the right and left side

On the right side, MN measured 2.06 mm (SD ± 0.46), 2.02 mm (SD ± 0.37), and 1.57 mm (SD ± 0.36) in the AP dimension and 5.77 mm (SD ± 0.89), 5.52 mm (SD ± 0.96), and 6.21 mm (SD ± 1.13) in the transverse (lateral-medial) dimension at 0, 1, and 2 cm distal to the proximal border of the flexor retinaculum, respectively (Table 1).

On the left side, MN measured 1.99 mm (SD ± 0.45), 1.96 mm (SD ± 0.42), and 1.74 mm (SD ± 0.57) in the AP dimension and 5.78 mm (SD ± 1.10), 5.88 mm (SD ± 1.09), and 6.21 mm (SD ± 1.14) in the lateral-medial dimension at 0, 1, and 2 cm distal to the proximal border of the flexor retinaculum, respectively. There were no statistically significant differences between sexes (Table 1).

Median nerve dimensions on the dominant and non-dominant hand

On the dominant hand, MN measured 2.05 mm (SD ± 0.46), 2.02 mm (SD ± 0.37), and 1.58 mm (SD ± 0.37) in the AP dimension and 5.75 mm (SD ± 0.87), 5.54 mm (SD ± 0.96), and 6.17 mm (SD ± 1.13) in the lateral-medial dimension at 0, 1, and 2 cm distal to the proximal border of the flexor retinaculum, respectively (Table 2).

On the non-dominant hand, MN measured 1.99 mm (SD ± 0.45), 1.97 mm (SD ± 0.41), and 1.73 mm (SD ± 0.57) in the AP dimension and 5.86 mm (SD ± 1.07), 5.91 mm (SD ± 1.06), and 6.28 mm (SD ± 1.12) in the lateral-medial dimension at 0, 1, and 2 cm distal to the proximal border of the flexor retinaculum, respectively (Table 2).

Anatomical landmarks measured at the level of the proximal border of the flexor retinaculum

The distance from FCR to MN (FCR-MN) was 7.87 mm (95% confidence interval [CI] 7.37–8.37), and the distance from FCU to MN (FCU-MN) was 19.09 mm (95% CI 18.51–19.67). In regard to sex, FCR-MN was 8.76 mm (95% CI 8.05–9.47) in males and 6.89 mm (95% CI 6.29–7.49) in females, and FCU-MN

Table 1. Median nerve dimensions measured at different levels distally from the proximal border of the carpal ligament in the right and left wrist with respect to sex

Level	Sex	Right (mm ± SD)		Left (mm ± SD)	
		Anteroposterior dimension	Lateral-medial dimension	Anteroposterior dimension	Lateral-medial dimension
0 cm	Overall	2.06 ± 0.46	5.77 ± 0.89	1.99 ± 0.45	5.78 ± 1.10
	Male	2.03 ± 0.39	6.01 ± 0.73*	2.02 ± 0.42	5.93 ± 1.09
	Female	2.08 ± 0.53	5.51 ± 0.99*	1.95 ± 0.48	5.62 ± 1.10
1 cm	Overall	2.02 ± 0.37	5.52 ± 0.96	1.96 ± 0.42	5.88 ± 1.09
	Male	2.10 ± 0.37	5.81 ± 0.85*	1.99 ± 0.32	6.20 ± 1.12*
	Female	1.93 ± 0.37	5.20 ± 0.99*	1.93 ± 0.51	5.53 ± 0.96*
2 cm	Overall	1.57 ± 0.36	6.21 ± 1.13	1.74 ± 0.57	6.21 ± 1.14
	Male	1.63 ± 0.38	6.43 ± 1.09*	1.74 ± 0.33	6.44 ± 0.95*
	Female	1.50 ± 0.34	5.97 ± 1.14*	1.74 ± 0.76	5.96 ± 1.28*

*Statistically significant differences between males and females; SD — standard deviation

Table 2. Median nerve dimensions measured at different levels distally from the proximal border of the carpal ligament in the dominant and non-dominant hand

Level	Dominant (mm ± SD)		Non-dominant (mm ± SD)	
	Anteroposterior dimension	Lateral-medial dimension	Anteroposterior dimension	Lateral-medial dimension
0 cm	2.05 ± 0.46	5.75 ± 0.87	1.99 ± 0.45	5.86 ± 1.07
1 cm	2.02 ± 0.37	5.54 ± 0.96	1.97 ± 0.41	5.91 ± 1.06
2 cm	1.58 ± 0.37	6.17 ± 1.13	1.73 ± 0.57	6.28 ± 1.12

*No statistically significant differences between dominant and non-dominant upper limbs; SD — standard deviation

Table 3. Anatomical landmarks measured at the level of proximal border of carpal ligament

Sex	Right (mm ± 95% CI)		Left (mm ± 95% CI)		Overall (mm ± 95% CI)	
	FCR-MN	FCU-MN	FCR-MN	FCU-MN	FCR-MN	FCU-MN
Overall	8.24* (7.49–8.99)	19.00 (18.22–19.78)	7.50* (6.85–8.15)	19.18 (18.33–20.03)	7.87 (7.37–8.37)	19.09 (18.51–19.67)
Male	9.20* (8.13–10.27)	20.08 (19.12–21.04)	8.31* (7.38–9.24)	20.11 (18.99–21.23)	8.76 (8.05–9.47)	20.09 (19.36–20.82)
Female	7.19* (6.29–8.10)	17.80* (16.69–18.91)	6.60* (5.82–7.38)	18.16* (16.96–19.36)	6.89 (6.29–7.49)	17.98 (17.17–18.79)

*Significant differences between right and left upper limbs; CI — confidence interval; FCR-MN — flexor carpi radialis tendon-median nerve; FCU-MN — flexor carpi ulnaris tendon-median nerve

was 20.09 mm (95% CI 19.36–20.82) in males and 17.98 mm (95% CI 17.17–18.79) in females (Table 3).

With respect to side, on the right, FCR-MN was 8.24 mm (95% CI 7.49–8.99) and FCU-MN was 19.00 mm (95% CI 18.22–19.78). In males, FCR-MN was 9.20 mm (95% CI 8.13–10.27) and FCU-MN was 20.08 mm (95% CI 19.12–21.04). In females, FCR-MN was 7.19 mm (95% CI 6.29–8.10) and FCU-MN was 20.08 mm (95% CI 19.12–21.04) (Table 3).

On the left side, FCR-MN was 7.50 mm (95% CI 6.85–8.15) and FCU-MN was 19.18 mm (95% CI 18.33–20.03). In males, FCR-MN was 8.31 mm (95% CI 7.38–9.24) and FCU-MN was 20.11 mm (95% CI 18.99–21.23). In females, FCR-MN was 6.60 mm (95%

CI 5.82–7.38) and FCU-MN was 18.16 mm (95% CI 16.96–19.36) (Table 3).

DISCUSSION

This study aimed to show how one can assess the position of MN using simple and well distinguished anatomical landmarks without the use of radiological techniques. This was achieved by analysing the anatomical variations in the course of the MN, the FCU with its attachment to the pisiform, and the FCR through the utilisation of USG. These anatomical structures can be clearly seen through the skin of the wrist, after surgical opening, and after trauma involving a laceration that exposes this area of the wrist.

We found that FCR-MN was 7.87 mm (95% CI 7.37–8.37) and FCU-MN was 19.09 mm (95% CI 18.51–19.67). The tendons of FCR and FCU are easily identifiable landmarks that can be distinguished in every patient through the skin using simple palpation. The safe zone from FCR is 7.37 mm — 95% of MNs are located within this distance — and going further medially would be a risk to injuring the MN iatrogenically. Laterally from the FCU, the safe zone is 18.51 mm — 95% of MNs are located in this area. There were also statistically significant differences between right and left upper limbs and males and females (Table 3). Knowledge of these anatomical landmarks can help prevent iatrogenic damage to the MN during carpal tunnel release and other surgical procedures in the wrist.

Carpal tunnel syndrome release is the most frequently performed surgical procedure in the wrist as CTS is the most common musculoskeletal disorder in both Europe and North America [4, 5, 7, 19]. The annual incidence of its diagnosis in the general population is thought to be around 3.8/1000 [19]. The incidence of CTS peaks between the ages of 40 to 60 years and it affects from 1 to 2/1000 men and 4 to 5/1000 women [4].

When there is a severe case or medical treatment for CTS fails, surgical intervention becomes the only alternative. Surgical treatment has many benefits to patients at this stage of CTS treatment as it may halt the development of motor deficits and resolve all symptoms. Since the 1990s, carpal tunnel release frequency has increased and according to the French Agency for Hospital Information (ATIH), they have increased from 9537 cases in 1995 to 142,405 in 2005 [5]. In the United States, 576,924 carpal tunnel releases were performed in 2006 as comparison [7].

The muscles of both the anterior forearm and of the thenar eminence, which control hand movement, are supplied by the MN. All forearm flexors, excluding the FCU and the portion of the flexor digitorum profundus which controls the fourth and fifth digits, are innervated by the MN. Additionally, the MN innervates the first and second lumbrical muscles and the muscles of the thenar eminence through the recurrent thenar branch. Innervation to the skin on the palmar side of the index finger, thumb, middle finger, half the ring finger thumb, and respective nail beds are also supplied by the MN.

Deficits in motor and sensory functions in areas supplied by the MN depend on the type of injury and

at which level the MN has sustained it. In CTS, motor and sensory deficits occur due to compression of the MN within the wrist. Motor deficits include weakness in flexion of the radial half of the digits and of the thumb and weakness in abduction and opposition of the thumb. Furthermore, the presence of an ape hand deformity may be present when attempting to form a fist also known as the benediction sign [23]. Sensory deficits include numbness and tingling in lateral 3.5 digits and their respective nail beds but not in the thenar eminence. Unlike in wrist laceration, sensation still persists in the central palm in CTS. This is due to the fact that the palmar cutaneous branch runs above the flexor retinaculum and is not affected in CTS.

A large retrospective review of 1332 CTS releases performed by two fellowship-trained hand surgeons at university hospitals from July 1993 to August 2006 concluded that the Indiana Tome technique can be used by experienced hand surgeons, offers early resumption of preoperative activities (2 days and 3 weeks), and has a low complication rate [11]. Eleven (0.83%) complications were noted out of 1332 cases by the 2 surgeons. Numbness and hypersensitivity in the third digital nerve distribution was the most common complication. Two of these 8 patients had normal 2-point discrimination and the other 6 had persistently 2-point discrimination greater than 10 mm despite resolution of preoperative paraesthesia symptoms [11].

Other commonly performed surgeries in the wrist include tendon repair [25], ganglion removal [10], MCP joint replacement [6], and trapeziectomy [16]. There are reports that the MN has been mistakenly harvested instead of the palmaris longus tendon which is commonly used as a tendon graft [12, 20]. Knowledge of relevant anatomy is, therefore, crucial to avoid inadvertent harvesting of the MN. The palmaris longus tendon is superficial to the antebrachial fascia at the wrist crease, and if it is absent, the MN will be the next most obvious midline structure [15]. In all the above-mentioned procedures, the MN may be in danger of iatrogenic injury and surgeons must be conscientious of its course and presence.

Recently, studies have proven that USG may serve as an irreplaceable and effective tool for surgeons who look to identify small nerves and calculating their risk of iatrogenic injury before procedures [21]. Identifying areas of risk allows for the creation of a safe zone for surgeons when performing various techniques involved in CTS surgery [18]. This safe zone, which can

be located through landmarks easily seen through the skin, stresses the importance of long-term memory of clinical anatomy, surgical awareness, and the training of surgical technique. Visualisation of the MN preoperatively or during an injection can be done with USG, but in case the operator lacks the appropriate skills or an USG scanner is unavailable, landmarks should be known. Ultimately, proper anatomical knowledge provided by the safe zone may help surgeons avoid iatrogenic injury to the MN while decompressing the carpal tunnel [18]. Other examples of safe zones established with USG includes the posterolateral approach to the sural nerve [14] and the infrapatellar branch of the saphenous nerve during tendon graft harvesting for knee ligament reconstruction [21].

Ultrasound has limited resolution even though it is now considered to be the best diagnostic tool to visualise nerves in real-time. This limited resolution may cause those who use USG examination to miss nerve terminal branches. The authors in this study, however, successfully tracked the MN within the borders of examined areas in all cases. Additionally, another limitation found in this study is the fact that the MN is in constant motion and changes positions as it runs between other anatomical structures. The authors minimised this limitation by examining all the limbs in the identical position the limb would be placed during a CTS release procedure. Observation bias was also held to a minimum by having two experienced surgeons present during the entirety of all examinations and having a third physician aid in unclear cases.

To the best of the knowledge of the authors, this is the first study to generate a topographic anatomical model created based on reliable clinical simulations to identify areas at high risk for iatrogenic MN injury. By revealing the course and position of the MN and its adjacent anatomical landmarks, we hope to provide crucial information to surgeons on the optimal technique to avoid iatrogenic MN injury while operating on the wrist.

CONCLUSIONS

The results obtained in this study are an anatomical overview of the anatomy and topography of the MN region. Using simple palpation, the tendons of the FCR and the FCU can be used as landmarks to help improve anatomical awareness of the MN, to effectively plan surgery, and to provide a surgical tool for physicians to ultimately avoid iatrogenic MN

injury. The safe zone medially from FCR is 7.37 mm and the safe zone laterally from the FCU is 18.51 mm.

REFERENCES

1. Aggarwal A, Srivastava DN, Jana M, et al. Comparison of different sequences of magnetic resonance imaging and ultrasonography with nerve conduction studies in peripheral neuropathies. *World Neurosurg.* 2017; 108: 185–200, doi: [10.1016/j.wneu.2017.08.054](https://doi.org/10.1016/j.wneu.2017.08.054), indexed in Pubmed: [28842238](https://pubmed.ncbi.nlm.nih.gov/28842238/).
2. Atroshi I, Hofer M, Larsson GU, et al. Extended follow-up of a randomized clinical trial of open vs endoscopic release surgery for carpal tunnel syndrome. *JAMA.* 2015; 314(13): 1399–1401, doi: [10.1001/jama.2015.12208](https://doi.org/10.1001/jama.2015.12208), indexed in Pubmed: [26441187](https://pubmed.ncbi.nlm.nih.gov/26441187/).
3. Beris AE, Lykissas MG, Kontogeorgakos VA, et al. Anatomic variations of the median nerve in carpal tunnel release. *Clin Anat.* 2008; 21(6): 514–518, doi: [10.1002/ca.20650](https://doi.org/10.1002/ca.20650), indexed in Pubmed: [18567020](https://pubmed.ncbi.nlm.nih.gov/18567020/).
4. Ghasemi-Rad M, Nosair E, Vegh A, et al. A handy review of carpal tunnel syndrome: from anatomy to diagnosis and treatment. *World J Radiol.* 2014; 6(6): 284–300, doi: [10.4329/wjr.v6.i6.284](https://doi.org/10.4329/wjr.v6.i6.284), indexed in Pubmed: [24976931](https://pubmed.ncbi.nlm.nih.gov/24976931/).
5. Haute Autorité De Santé (HAS). Rapport HAS — Chirurgie du syndrome du canal carpien: approche multidimensionnelle pour une décision pertinente 2012.
6. Houdek MT, Wagner ER, Rizzo M, et al. Metacarpophalangeal joint arthroplasty in the setting of trauma. *J Hand Surg Am.* 2015; 40(12): 2416–2420, doi: [10.1016/j.jhsa.2015.09.012](https://doi.org/10.1016/j.jhsa.2015.09.012), indexed in Pubmed: [26527597](https://pubmed.ncbi.nlm.nih.gov/26527597/).
7. Jain NB, Higgins LD, Losina E, et al. Epidemiology of musculoskeletal upper extremity ambulatory surgery in the United States. *BMC Musculoskelet Disord.* 2014; 15: 4, doi: [10.1186/1471-2474-15-4](https://doi.org/10.1186/1471-2474-15-4), indexed in Pubmed: [24397703](https://pubmed.ncbi.nlm.nih.gov/24397703/).
8. Kanafi Vahed L, Arianpur A, Gharedaghi M, et al. Ultrasound as a diagnostic tool in the investigation of patients with carpal tunnel syndrome. *Eur J Transl Myol.* 2018; 28(2): 7380, doi: [10.4081/ejtm.2018.7406](https://doi.org/10.4081/ejtm.2018.7406), indexed in Pubmed: [29991986](https://pubmed.ncbi.nlm.nih.gov/29991986/).
9. Kim PT, Lee HJ, Kim TG, et al. Current approaches for carpal tunnel syndrome. *Clin Orthop Surg.* 2014; 6(3): 253–257, doi: [10.4055/cios.2014.6.3.253](https://doi.org/10.4055/cios.2014.6.3.253), indexed in Pubmed: [25177448](https://pubmed.ncbi.nlm.nih.gov/25177448/).
10. Kuliński S, Gutkowska O, Urban M, et al. Dorsal and volar wrist ganglions: the results of surgical treatment. *Adv Clin Exp Med.* 2019; 28(1): 95–102, doi: [10.17219/acem/81202](https://doi.org/10.17219/acem/81202), indexed in Pubmed: [30070079](https://pubmed.ncbi.nlm.nih.gov/30070079/).
11. Lee WP, Schipper BM, Goitz RJ. 13-year experience of carpal tunnel release using the Indiana Tome technique. *J Hand Surg Am.* 2008; 33(7): 1052–1056, doi: [10.1016/j.jhsa.2008.03.013](https://doi.org/10.1016/j.jhsa.2008.03.013), indexed in Pubmed: [18762096](https://pubmed.ncbi.nlm.nih.gov/18762096/).
12. Leslie BM, Osterman AL, Wolfe SW. Inadvertent harvest of the median nerve instead of the palmaris longus tendon. *J Bone Joint Surg Am.* 2017; 99(14): 1173–1182, doi: [10.2106/JBJS.16.01218](https://doi.org/10.2106/JBJS.16.01218), indexed in Pubmed: [28719556](https://pubmed.ncbi.nlm.nih.gov/28719556/).
13. Mathen SJ, Nosrati NN, Merrell GA. Decreased rate of complications in carpal tunnel release with hand fellowship training. *J Hand Microsurg.* 2018; 10(1): 26–28, doi: [10.1055/s-0037-1618913](https://doi.org/10.1055/s-0037-1618913), indexed in Pubmed: [29706733](https://pubmed.ncbi.nlm.nih.gov/29706733/).
14. Mizia E, Pełkala PA, Chomiczki-Bindas P, et al. Risk of injury to the sural nerve during posterolateral approach to the

- distal tibia: An ultrasound simulation study. *Clin Anat.* 2018; 31(6): 870–877, doi: [10.1002/ca.23205](https://doi.org/10.1002/ca.23205), indexed in Pubmed: [29737558](https://pubmed.ncbi.nlm.nih.gov/29737558/).
15. Murphy RX, Jennings JF, Wukich DK. Major neurovascular complications of endoscopic carpal tunnel release. *J Hand Surg Am.* 1994; 19(1): 114–118, doi: [10.1016/0363-5023\(94\)90233-X](https://doi.org/10.1016/0363-5023(94)90233-X), indexed in Pubmed: [8169354](https://pubmed.ncbi.nlm.nih.gov/8169354/).
 16. Naram A, Lyons K, Rothkopf DM, et al. Increased complications in trapeziectomy with ligament reconstruction and tendon interposition compared with trapeziectomy alone. *Hand (N Y).* 2016; 11(1): 78–82, doi: [10.1177/1558944715617215](https://doi.org/10.1177/1558944715617215), indexed in Pubmed: [27418894](https://pubmed.ncbi.nlm.nih.gov/27418894/).
 17. Ozcakir S, Sigirli D, Avsaroglu H. High wrist ratio is a risk factor for carpal tunnel syndrome. *Clin Anat.* 2018; 31(5): 698–701, doi: [10.1002/ca.23198](https://doi.org/10.1002/ca.23198), indexed in Pubmed: [29722064](https://pubmed.ncbi.nlm.nih.gov/29722064/).
 18. Ozcanli H, Coskun NK, Cengiz M, et al. Definition of a safe-zone in open carpal tunnel surgery: a cadaver study. *Surg Radiol Anat.* 2010; 32(3): 203–206, doi: [10.1007/s00276-009-0498-7](https://doi.org/10.1007/s00276-009-0498-7), indexed in Pubmed: [19337677](https://pubmed.ncbi.nlm.nih.gov/19337677/).
 19. Petrover D, Richette P. Treatment of carpal tunnel syndrome: from ultrasonography to ultrasound guided carpal tunnel release. *Joint Bone Spine.* 2018; 85(5): 545–552, doi: [10.1016/j.jbspin.2017.11.003](https://doi.org/10.1016/j.jbspin.2017.11.003), indexed in Pubmed: [29154980](https://pubmed.ncbi.nlm.nih.gov/29154980/).
 20. Pełkala PA, Henry BM, Pełkala JR, et al. Congenital absence of the palmaris longus muscle: A meta-analysis comparing cadaveric and functional studies. *J Plast Reconstr Aesthet Surg.* 2017; 70(12): 1715–1724, doi: [10.1016/j.bjps.2017.08.002](https://doi.org/10.1016/j.bjps.2017.08.002), indexed in Pubmed: [28917934](https://pubmed.ncbi.nlm.nih.gov/28917934/).
 21. Pełkala PA, Miza E, Henry BM, et al. Injury to the infrapatellar branch of the saphenous nerve during tendon graft harvesting for knee ligament reconstruction: An ultrasound simulation study. *Clin Anat.* 2017; 30(7): 868–872, doi: [10.1002/ca.22904](https://doi.org/10.1002/ca.22904), indexed in Pubmed: [28514510](https://pubmed.ncbi.nlm.nih.gov/28514510/).
 22. Rasulić L, Savić A, Vitošević F, et al. Iatrogenic peripheral nerve injuries-surgical treatment and outcome: 10 years' experience. *World Neurosurg.* 2017; 103: 841–851.e6, doi: [10.1016/j.wneu.2017.04.099](https://doi.org/10.1016/j.wneu.2017.04.099), indexed in Pubmed: [28450236](https://pubmed.ncbi.nlm.nih.gov/28450236/).
 23. Seiler JG, Daruwalla JH, Payne SH, et al. Normal palmar anatomy and variations that impact median nerve decompression. *J Am Acad Orthop Surg.* 2017; 25(9): e194–e203, doi: [10.5435/JAAOS-D-16-00038](https://doi.org/10.5435/JAAOS-D-16-00038), indexed in Pubmed: [28837460](https://pubmed.ncbi.nlm.nih.gov/28837460/).
 24. Shi Q, Bobos P, Lalone EA, et al. Comparison of the short-term and long-term effects of surgery and non-surgical intervention in treating carpal tunnel syndrome: a systematic review and meta-analysis. *Hand (N Y).* 2020; 15(1): 13–22, doi: [10.1177/1558944718787892](https://doi.org/10.1177/1558944718787892), indexed in Pubmed: [30015499](https://pubmed.ncbi.nlm.nih.gov/30015499/).
 25. Tang JB. Recent evolutions in flexor tendon repairs and rehabilitation. *J Hand Surg Eur Vol.* 2018; 43(5): 469–473, doi: [10.1177/1753193418773008](https://doi.org/10.1177/1753193418773008), indexed in Pubmed: [29690810](https://pubmed.ncbi.nlm.nih.gov/29690810/).

An anatomical investigation of rare upper limb neuropathies due to the Struthers' ligament or arcade: a meta-analysis

E. Mizia¹, M.P. Zarzecki^{1,2}, J.R. Pekala^{1,2}, A. Baginski¹, L.N. Kaythampillai¹, M. Golebiowska¹, P.A. Pekala^{1,2}, J.A. Walocha^{1,2}, K.A. Tomaszewski^{1,2}

¹Department of Anatomy, Jagiellonian University Medical College, Krakow, Poland

²International Evidence-Based Anatomy Working Group, Krakow, Poland

[Received: 4 March 2020; Accepted: 30 March 2020]

Background: The Struthers' ligament (SL) is a fibrous band that originates from the supracondylar humeral process and inserts into the medial humeral epicondyle, potentially compressing both the median nerve and brachial artery. The controversial Struthers' arcade (SA) is a musculotendinous band found in the distal end of the arm that might compress the ulnar nerve. This study aimed to evaluate the pooled prevalence estimate of the SL and SA, and their anatomical features.

Materials and methods: A meticulous search of major electronic medical databases was carried out regarding both structures. Applicable articles (and all relevant references) were analysed. Data from the eligible articles was extracted and evaluated. The quality and the potential risk of bias in the included studies were assessed using the AQUA tool.

Results: The arcade was reported in 13 studies (510 arms), whereas the ligament in 6 studies (513 arms). The overall pooled prevalence estimate of the ligament was 1.8%, and 52.6% for the arcade. Most frequently, the ulnar nerve was covered by a tendinous arcade (42.2%). In all cases, the ligament inserted into the medial humeral epicondyle, but had various origins. Only 1 study reported compression of the median nerve by the ligament, whilst another contradicted this view.

Conclusions: Although the SL is rare, and the SA is a valid anatomical entity (though with a variable presentation), clinically meaningful neurovascular entrapments caused by these structures are infrequent. Nonetheless, a better understanding of each may be beneficial for the best patient outcomes. (Folia Morphol 2021; 80, 2: 255–266)

Key words: Struthers' arcade, Struthers' ligament, meta-analysis

INTRODUCTION

Neurovascular compressions of the upper limb may have highly variable clinical manifestations including pain, numbness, weakness and muscular atrophy [1]. Fortunately, the entrapment site is often easily localised with careful physical examination and/or radio-

graphic imaging [1]. Rare instances of such syndromes have been attributed to two anatomical structures: the Struthers' ligament (SL) and the Struthers' arcade (SA). These two structures are frequently confused, and some contention exists pertaining to their prevalence. Sir John Struthers described 9 arcades (a series of mus-

Address for correspondence: E. Mizia, MD, PhD, Department of Anatomy, Jagiellonian University Medical College, ul. Kopernika 12, 31–034 Kraków, Poland, tel/fax: +48 12 422 95 11, e-mail: ewa.mizia@gazeta.pl

This article is available in open access under Creative Common Attribution-Non-Commercial-No Derivatives 4.0 International (CC BY-NC-ND 4.0) license, allowing to download articles and share them with others as long as they credit the authors and the publisher, but without permission to change them in any way or use them commercially.

culotendinous and fibrous arches) in the arm — eight associated with the median nerve, and one with the ulnar nerve [2]. The eighth of this series was a fibrous structure known as the SL, and attached to a bony spur on the humerus. The ninth, known nowadays as the SA, was a fibrous band at the brachial fascia, and not anchored to any bony elements [2].

The SL typically begins at a bony projection approximately two inches above the medial epicondyle on the anteromedial aspect of the humerus, labelled the supracondylar process (or spur), which can usually be identified on X-ray imaging [33]. The ligament itself extends from this process, and attaches to the medial humeral epicondyle. The brachial artery, the median nerve, or both can run beneath this fibrous band. Initial descriptions suggested a prevalence of 1% in the human population [3]. Although it is an uncommon feature, its existence is undisputed. However, it has been implicated in causing a rare compression of the neurovascular entities, causing paraesthesia and numbness associated with forearm claudication or median nerve dysfunction [5]. A surgical procedure involving release of the entrapped element, in combination with excision of the SL and its bony spur, effectively eliminates all the clinical symptoms permanently [1].

The SA is a more disputed anatomical structure, with highly variable descriptions and classifications [12]. Kane et al. [24] were the first to apply Struthers' work and define the fibrous canal (definition as applied herein) with a roof formed by a deep fascial thickening, an anterior border at the medial intermuscular septum, and a lateral border at the humerus and the muscular fibre covering of the triceps brachii. Several subsequent reports have supported the existence of this structure to various degrees; however, the discrepancies in findings may be attributable to the differences in definition [15, 20, 34]. Alternatively, other authors [7, 32, 40] debate its existence altogether, suggesting that the previous findings are only anatomical variations of the intermuscular septum and the forearm fascia. As such, it is important not only to assess the prevalence of this structure, but also the clinical presentation, and its possible variations [37]. The disagreements regarding the SA extend to its role as a possible site for entrapment. Although it is unlikely as a primary site for entrapment, most tend to agree that it is a factor in recurrent ulnar neuropathy after an anterior transposition of the nerve at the elbow [14, 25, 31].

This study seeks to evaluate the differences from an anatomical perspective, establish the pooled prevalence estimate (PPE) of both the SL and the SA, assess their involvement in the median/ulnar nerve entrapments, respectively, and provide the answer as to whether the disputed SA is a valid anatomical structure. Becoming acquainted with the said variants is of immense importance to physicians encountering unusual upper limb neural entrapments that cannot be explained by more commonly existing pathologies.

MATERIALS AND METHODS

This study is a systematic review and meta-analysis, level of evidence: II.

Search strategy

An extensive search on the SA and the SL, as well as their anatomy, was conducted on PubMed, Embase, ScienceDirect and Web of Knowledge databases. The following search terms applied: "Struthers' ligament" OR "Ligament of Struthers" OR "supracondylar canal" OR "supracondylar spur" OR "supracondylar process" OR "supratrochlear spur" OR "avian spur" OR "Arcade of Struthers" OR "Struthers' Arcade." No restrictions were set to date or language of the original publication. Additionally, all references in the included articles were assessed to identify any other potentially eligible studies.

Study selection criteria

Eligibility for inclusion was governed by the following criteria: cadaveric or imaging studies containing information about the SL or the SA — both anatomically and clinically. Case reports, conference abstracts, letters to editors, reviews, or studies containing irrelevant or incomplete data about the SL or the SA were not considered.

Eligibility assessment

The authors (E.M., M.P.Z., J.R.P., L.N.K., M.G.) completed an independent review of all the included studies. Any disagreements were settled by consensus, where necessary also involving a consultation with the authors of the original study. Any studies published in a language not fluently spoken by the reviewing authors were translated by medical professionals fluent in both the original language of the manuscript and English.

Data extraction

The extraction of data from the included studies was performed separately by independent reviewers.

The following data was extracted: country of study origin, method, total number of patients/specimens with the SL/SA, as well as characteristics of modality. Elements of interest included laterality, typical vs. atypical presentation and type, morphology, relation to associated nerve, extent of compression, and insertion (the SL).

Quality assessment

The quality assessment was completed by independent reviewers by utilising the Anatomical Quality Assurance tool (the AQUA Tool), a versatile instrument capable of appraising anatomical studies [23]. This method employed a "risk of bias" table assessing the five domains: (1) Aim and subject characteristics; (2) Study design; (3) Characterisation of methods; (4) Descriptive anatomy; and (5) Results reporting. Each criterion level of bias was deemed "High", "Low," or "Unclear" in accordance to "Yes" or "No" answers to specific determining questions. Conditions where "Yes" was selected identified a "Low" risk of bias, whereas a "No" answer suggested a "High" risk. Any disagreements were resolved with discussions, or by involving an additional reviewer.

Statistical analysis

All the extracted data was processed using MetaXL version 5.3 (EpiGear International, Australia) as a meta-analysis with random-effects model. The PPE of the SL and the SA, respectively, was the primary measure of this study, with subsequent analysis by subgroups.

Heterogeneity was tested for using the χ^2 and Higgins I^2 tests. A significant heterogeneity was identified from a p-value of < 0.10 in the χ^2 test [22]. Heterogeneity was determined from the I^2 test according to the following scheme: 0% to 40% may not be present; 30% to 60% possible indications of moderate heterogeneity; 50% to 90% likely meaningful heterogeneity; and 75% to 100% suggests considerable heterogeneity [22].

In order to investigate possible sources of heterogeneity, subgroup analyses were completed to consider the effect of geographical distribution and modality. Confidence intervals were utilised to illustrate any determined statistical differences between two or more subgroups. Conclusions regarding statistical insignificance could be drawn if any such intervals overlapped [22].

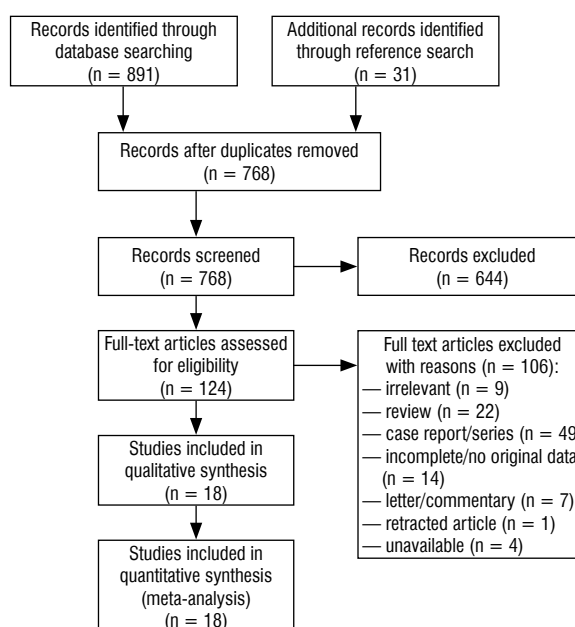


Figure 1. The Preferred Reporting Items for Systematic Reviews and Meta-Analyses (PRISMA) flow chart.

RESULTS

Study identification

The study selection process is illustrated in Figure 1. Initially, 891 articles were identified according to the specified parameters across all major electronic databases. Additional 31 articles were included when the cited articles of the previous group were checked. Of all the articles, 124 were identified as potentially meeting the inclusion criteria, from which 108 were deemed ineligible, for reasons such as being case reports/series, containing irrelevant/incomplete/no original data or were letters/commentaries to the editor. Therefore, 18 studies were utilised for this meta-analysis (5 pertaining to the SL, 12 to the SA and 1 study to both the SA and the SL).

Characteristics of the included studies

The tables outline the characteristics of the included studies in this meta-analysis. The 6 studies pertaining to the SL ($n = 513$ upper limbs) were conducted from 1983 to 2017. The 13 studies reporting on the SA ($n = 510$ upper extremities) were published from 1991 to 2016. The prevalence rates of the relevant structures are reported in (Tables 1, 2).

Prevalence of the SL

A complete assessment of the SL was completed according to a subgroup analysis by geography,

Table 1. The characteristics of the included studies for the Struthers ligament (SL)

Study	Country	Type of study	Number of limbs	Prevalence (%)
Bilecenoglu et al., 2005 [8]	Turkey	Cadaveric	30	3.3
Caetano et al., 2017 [11]	Brazil	Cadaveric	60	0.1
Dellon, 1987 [17]	USA	Cadaveric	43	0.0
Gessini et al., 1983 [19]	Italy	Surgery	238	0.4
Gunther et al., 1993 [21]	USA	Cadaveric	38	2.6
Dellon, 1986 [16]	USA	Cadaveric	104	0.0

Table 2. The characteristics of the included studies for the Struthers arcade

Study	Country	Type of study	Number of limbs	Prevalence (%)
Al-Qattan and Murray, 1991 [2]	Canada	Cadaveric	25	68.0
Bartels et al., 2003 [7]	Netherlands	Cadaveric	10	0.0
Caetano et al. 2017 [12]	Brazil	Cadaveric	40	100.0
Gonzalez et al., 2001 [20]	USA	Cadaveric	39	66.7
Mirza et al., 2014 [27]	USA	Cadaveric	26	7.7
Poujade et al., 2014 [30]	France	Cadaveric	18	33.3
Siqueira and Martins, 2005 [32]	Brazil	Cadaveric	60	18.3
Tubbs et al., 2011 [38]	USA	Cadaveric	30	86.7
Tiyaworanan et al., 2010 [37]	Thailand	Cadaveric	62	85.5
Von Schroeder and Schecker, 2003 [39]	Canada	Cadaveric	14	100.0
Yoshida et al., 2014 [41]	Japan	Surgery	82	1.2
Zhong et al., 2016 [42]	China	Cadaveric	64	57.8
Zhong et al., 2016 [42]*	China	Medical imaging	40	50.0

*One study was conducted as a cadaveric and a medical imaging investigation on two separate populations

Table 3. The modality and geographical distribution of the Struthers ligament (SL) studies

Subgroup	Number of studies (no. of subjects)	Pooled prevalence of SL; % (95% CI)	I ² ; % (95% CI)	Cochran's Q, p-value
Overall	6 (513)	1.8 (0.1–5.2)	70.7 (31.7–87.4)	17.1, p = 0.004
Cadaveric	5 (275)	2.3 (0.0–7.4)	71.7 (28.6–88.8)	14.1, p = 0.007
North America	3 (185)	0.8 (0.0–2.6)	17.1 (0.0–91.4)	2.4, p = 0.299

CI — confidence interval

Table 4. Prevalence of the Struthers ligament (SL) in respect to side

Number of studies (no. of subjects with SL)	Right side SL; % (95% CI)	Left side SL; % (95% CI)	I ² ; % (95% CI)	Cochran's Q, p-value
4 (9)	55.8 (24.7–84.8)	44.2 (15.2–75.3)	0.0 (0.0–82.7)	2.7, p = 0.449

CI — confidence interval

laterality, reported median nerve compression, and insertion, the results of which can be found, respectively. The geographical analysis differentiated all the studies (PPE 1.8%; 95% confidence interval [CI] 0.1–5.2%) from cadaveric studies (PPE 2.3%; 95% CI 0.0–7.4%), as well as those reporting from North America (PPE 0.8%; 95% CI 0.0–2.6%) (Table 3).

Four studies (Table 4) included which side the SL was present on. The SL appears slightly more often on the right side (55.8%; 95% CI 24.7–84.8) than the left (44.2%; 95% CI 15.2–75.3).

Gessini's surgical study [19] from Italy supported the SL as a contributor to median nerve compression, whereas Gunther's cadaveric study [21]

Table 5. The median nerve compression by the Struthers ligament (SL)

Study	Country	Type of study	Number of limbs with SL	Prevalence of median nerve compression (%)
Gessini et al., 1983 [19]	Italy	Surgery	1	100.0
Gunther et al., 1993 [21]	USA	Cadaveric	1	0.0

Table 6. The insertion points of the Struthers ligament (SL)

Study	Country	Type of study	Number of limbs with SL	Prevalence of medial epicondyle insertion (%)
Bilecenoglu et al., 2005 [8]	Turkey	Cadaveric	1	100.0
Gessini et al., 1983 [19]	Italy	Surgery	1	100.0
Gunther et al., 1993 [21]	USA	Cadaveric	1	100.0

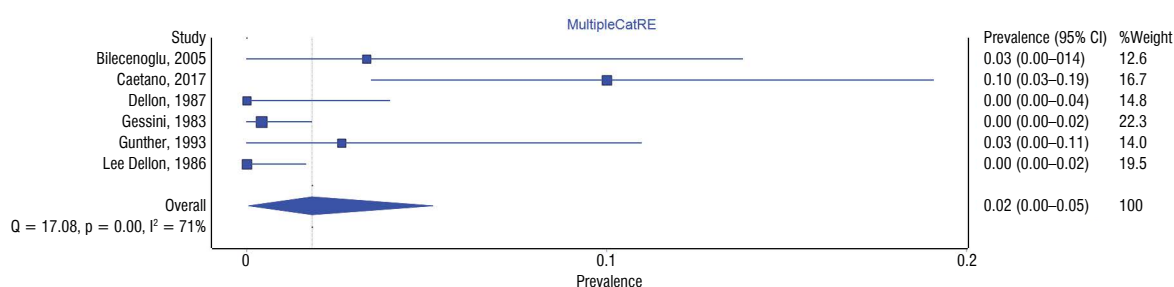


Figure 2. Prevalence of the Struthers ligament forest plot; CI — confidence interval.

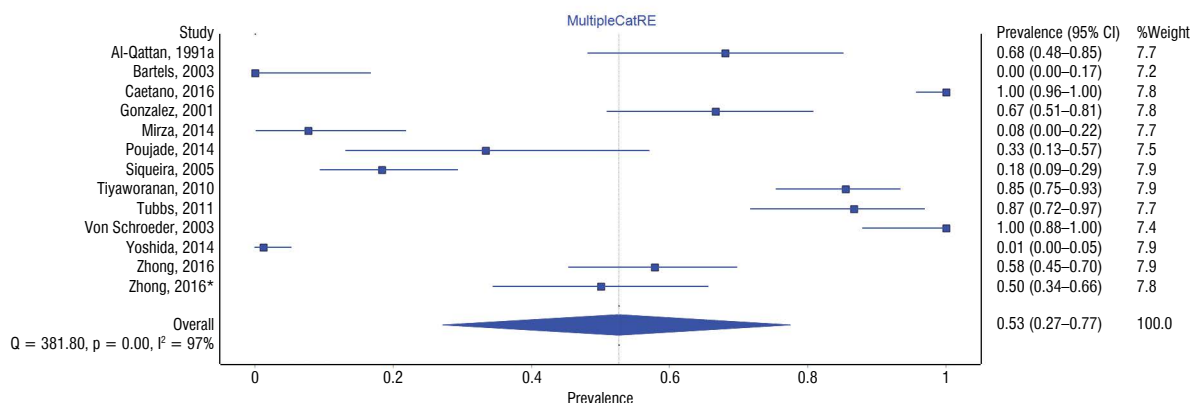


Figure 3. Prevalence of the Struthers arcade forest plot; *one study was conducted as a cadaveric and a medical imaging investigation on two separate populations; CI — confidence interval.

from the United States did not support this finding (Table 5).

Lastly, 3 studies (Table 6) outlined the distal insertion point of the SL. In all cases, the SL was found to terminate at the medial humeral epicondyle. Notwithstanding, the origin of the SL varied in all those three instances, as in 1 case it was attached to the supracondylar humeral process, in another into the anteromedial surface of the humerus (with no bony

spur present) and into the brachialis muscle in the last case (Fig. 2).

Prevalence of the SA

Similarly to the analysis of the SL, assessment of the SA was divided by subgroups — geographical prevalence, atypical prevalence, atypical type, morphology, relation to the ulnar nerve, and ulnar nerve compression.

Table 7. The modality and geographical distribution of the Struthers arcade (SA) studies

Subgroup	Number of studies (no. of subjects)	Pooled prevalence of SA; % (95% CI)	I ² ; % (95% CI)	Cochran's Q, p-value
Overall	13 (510)	52.6 (27.1–77.5)	96.9 (95.8–97.7)	381.8, p < 0.001
Cadaveric	11 (388)	59.6 (35.0–82.1)	95.4 (93.4–96.8)	218.4, p < 0.001
North America	5 (134)	69.4 (32.3–97.1)	93.7 (88.3–96.7)	64.0, p < 0.001
Asia	4 (248)	45.2 (0.0–94.2)	98.2 (97.1–98.9)	169.7, p < 0.001
South America	2 (100)	68.0 (0.0–100.0)	99.1 (98.1–99.5)	105.6, p < 0.001
Europe	2 (28)	15.1 (0.0–59.1)	83.2 (30.0–96.0)	6.0, p = 0.015

CI — confidence interval

Table 8. The definitions of the Struthers arcade applied in this meta-analysis.

Author	Year	Definition
Kane et al. [24]	1973	Fibrous canal with roof formed by a deep fascial thickening, an anterior border at the medial intermuscular septum, and a lateral border at the humerus and the muscular fibre covering of the triceps brachii. (Considered as the “classical” in this study.)
Al-Qattan and Murray [2]	1991	“Classical” definition provided by Kane et al. OR Multiple ligaments of the thickened deep fascia and medial intermuscular septum passing superficial and deep to the ulnar nerve OR Roof formed by the triceps muscular fibres alone. (Both considered as the “atypical” in this study.)
Tubbs et al. [38]	2011	Thickening of the brachial fascia OR Thickening of the internal brachial ligament OR Thickening of the medial intermuscular septum. (All three considered as the “atypical” in this study.)

Table 9. Prevalence of the classical and atypical Struthers arcade

Type	Number of studies (no. of subjects)	Pooled prevalence; % (95% CI)	I ² ; % (95% CI)	Cochran's Q, p-value
Classical	8 (142)	72.8 (30.0–100.0)	95.8 (93.5–97.2)	165.6, p < 0.001
Atypical	8 (142)	27.2 (0.0–70.0)	95.8 (93.5–97.2)	165.6, p < 0.001

CI — confidence interval

The geographical analysis separated all the studies (PPE 52.6%; 95% CI 27.1–77.5%) from cadaveric studies (PPE 59.6%; 95% CI 35.0–82.1%), as well as those reporting from North America (PPE 69.4%; 95% CI 32.3–97.1%), Asia (PPE 45.2%; 95% CI 0.0–94.2%), South America (PPE 68.0%; 95% CI 0.0–100.0%), and Europe (PPE 15.1%; 95% CI 0.0–59.1%) (Fig. 3, Table 7).

The formal description of the SA by Kane et al. [24] (a fibrous canal with a roof formed by a deep fascial thickening, an anterior border at the medial intermuscular septum, and a lateral border at the humerus and the muscular fibre covering of the triceps brachii) did not always apply to the findings of certain included studies due to its variability in presentation [2, 27, 32, 38]. The variant definitions of the SA

can be found in Table 8. Since most of the authors described their SA in accordance with the definition stated by Kane et al. [24], we applied this term as the classical type in opposition to the atypical SAs, found and described less commonly. All the typical and unusual SAs encountered in analysed studies fit into one of the definitions from Table 8. Table 9 presents the PPE of the typical and atypical SAs, and Table 10 reports the types of the atypical SAs (when reported in the respective studies). The most common of the atypical types is a thickening of the brachial fascia, found in 39.3% (95% CI 0.0–89.0%) of the reported 38 structures.

The morphology of the SA was found to be mostly musculotendinous (PPE 54.2; 95% CI 12.6–89.1%), or

Table 10. Types of the atypical Struthers arcade

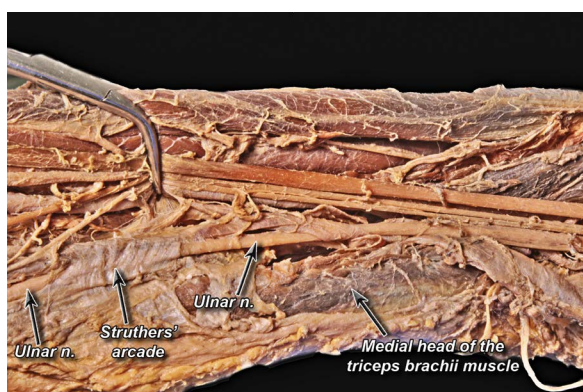
Type	Number of studies (no. of subjects)	Pooled prevalence; % (95% CI)	I ² ; % (95% CI)	Cochran's Q, p-value
Multiple ligaments of thickened deep fascia and medial intermuscular septum	4 (38)	16.6 (0.0–62.2)	83.5 (58.3–93.5)	18.2, p < 0.001
Roof formed by the triceps muscular fibres alone	4 (38)	24.1 (0.0–72.8)	83.5 (58.3–93.5)	18.2, p < 0.001
Thickening of the brachial fascia	4(38)	39.3 (0.0–89.0)	83.5 (58.3–93.5)	18.2, p < 0.001
Thickening of the internal brachial ligament	4 (38)	9.6 (0.0–49.9)	83.5 (58.3–93.5)	18.2, p < 0.001
Thickening of the medial intermuscular septum	4 (38)	10.4 (0.0–51.6)	83.5 (58.3–93.5)	18.2, p < 0.001

CI — confidence interval

Table 11. Morphological types of the Struthers arcade

Type	Number of studies (no. of subjects)	Pooled prevalence; % (95% CI)	I ² ; % (95% CI)	Cochran's Q, p-value
Musculotendinous	10 (193)	54.2 (12.6–89.1)	96.0 (94.3–97.3)	227.2, p < 0.001
Tendinous	10 (193)	38.5 (3.5–77.3)	96.0 (94.3–97.3)	227.2, p < 0.001
Muscular	10 (193)	7.2 (0.0–33.5)	96.0 (94.3–97.3)	227.2, p < 0.001

CI — confidence interval

**Figure 4.** A tendinous Struthers arcade found during a routine cadaveric dissection.

otherwise tendinous (PPE 38.5; 95% CI 3.5–77.3%), or muscular (PPE 7.2; 95% CI 0.0–33.5%) (Table 11). Examples of the SAs found during our own routine cadaveric examinations are presented on Figure 4 (a tendinous arcade) and Figure 5 (a musculotendinous arcade).

The various relations of the SA to the ulnar nerve are shown in Table 12, where it most typically presented as a tendinous arcade passing over the ulnar nerve (PPE 42.2; 95% CI 2.5–77.9%). Table 13 presents the findings of the 3 studies concerning the prevalence of ulnar nerve compression. Forty limbs from 1 study [12] were reported to show no compression, whereas all the SAs of Mirza et al. [27] and

**Figure 5.** A musculotendinous Struthers arcade found during a routine cadaveric dissection.

Yoshida et al. [41] were associated with the ulnar nerve compression.

Risk of bias analysis

The complete appraisal of the included studies in terms of the risk of bias they pose is presented in Table 14. All in all, the vast majority of the studies were assessed as having a “High” risk of bias in Domains 1 and 3, due to the lack of complete information about the patients' baseline characteristics and demographics, as well as the specialty and experience of the scientists in charge of a particular part of the study. Domains 2 and 5 were evaluated as being at “Low” risk of bias for all the included studies. Nonetheless,

Table 12. Relation of the Struthers arcade to the ulnar nerve

Type	Number of studies (no. of subjects)	Pooled prevalence; % (95% CI)	I ² ; % (95% CI)	Cochran's Q, p-value
Musculotendinous arcade covers the nerve	9 (193)	34.2 (0.0–71.6)	96.5 (94.9–97.6)	227.2, p < 0.001
Tendinous arcade passing over the ulnar nerve	9 (193)	42.2 (2.5–77.9)	96.5 (94.9–97.6)	227.2, p < 0.001
Triceps muscle covers the nerve	9 (193)	13.8 (0.0–43.9)	96.5 (94.9–97.6)	227.2, p < 0.001
The ulnar nerve passing anteriorly to the arcade	9 (193)	2.5 (0.0–21.9)	96.5 (94.9–97.6)	227.2, p < 0.001
Triceps aponeurosis covers the nerve	9 (193)	3.6 (0.0–24.9)	96.5 (94.9–97.6)	227.2, p < 0.001
Multiple ligaments of thickened deep fascia and medial inter-muscular septum pass superficially and deeply to the nerve	9 (193)	3.7 (0.0–25.2)	96.5 (94.9–97.6)	227.2, p < 0.001

CI — confidence interval

Table 13. The ulnar nerve compression by the Struthers arcade (SA)

Study	Country	Type of study	Number of limbs with SA	Prevalence of ulnar nerve compression (%)
Caetano et al. 2017 [12]	Brazil	Cadaveric	40	0.0
Mirza et al., 2014 [27]	USA	Cadaveric	2	100.0
Yoshida et al., 2014 [41]	Japan	Surgery	1	100.0

Table 14. The risk of bias analysis

Study	Risk of bias				
	Objective(s) and study characteristics	Study design	Methodology characterisation	Descriptive anatomy	Reporting of results
Al-Qattan and Murray, 1991 [2]	High	Low	High	Low	Low
Bartels et al., 2003 [7]	High	Low	High	Low	Low
Bilecenoglu et al., 2005 [8]	High	Low	High	Low	Low
Caetano et al., 2017 [11]	High	Low	High	Low	Low
Caetano et al., 2017 [12]	High	Low	High	Low	Low
Dellon et al, 1987 [17]	High	Low	High	Low	Low
Gessini et al., 1983 [19]	High	Low	High	Low	Low
Gonzalez et al., 2001 [20]	High	Low	High	Low	Low
Gunther et al., 1993 [21]	High	Low	High	Low	Low
Dellon 1986 [16]	High	Low	High	Low	Low
Mirza et al., 2014 [27]	High	Low	High	Low	Low
Poujade et al., 2014 [30]	High	Low	High	Low	Low
Siqueira and Martins, 2005 [32]	Low	Low	High	Low	Low
Tiyaworanan et al., 2010 [37]	High	Low	High	High	Low
Tubbs et al., 2011 [38]	High	Low	High	Low	Low
Von Schroeder and Schecker, 2003 [39]	High	Low	High	Low	Low
Yoshida et al., 2014 [41]	High	Low	High	High	Low
Zhong et al., 2016 [42]	High	Low	High	Low	Low

Domain 4 had two studies at “High” risk of bias due to them not specifying their definition of the SA (Table 14).

DISCUSSION

This study aims to clarify the differences between the SL and the SA, and investigate their respective

properties in a clinically relevant manner. Disagreements in prior publications exist, promoting a poor understanding of these structures and their implications in the treatment of upper limb neuropathies [11]. In order to improve patient outcomes during the associated procedures, this meta-analysis attempted to evaluate the SL and the SA in terms of their PPE, anatomical features (such as e.g. morphology), and relation to the median and ulnar nerves, respectively.

Clinicians must consider the possible involvement of these two structures in their practice — especially in surgeries. The SL is rare, and is typically associated with the brachial artery and/or the median nerve. Due to its low prevalence, it is infrequently being considered in the differential diagnosis as a cause of entrapment [21]. Also, even if present (when identified by radiographs) it may not necessarily be the origin of the symptoms [21]. The SA is a valid structure, most typically presenting as a musculotendinous band associated with the ulnar nerve, but has extensive variability. Primary entrapment has not been described, but it has been largely implicated in failed cubital tunnel surgery, or otherwise during the anterior transposition of the ulnar nerve, which may be the result of unsuccessful decompression or formation of a new site of compression [15, 18, 32]. Since both structures have been suggested to be involved in neuropathies, it is of immense importance for medical professionals to get acquainted with their variants and consider them in the differential diagnoses. This recommendation is especially valid in cases which cannot be explained by more commonly prevalent conditions, e.g. cubital tunnel syndrome in case of the ulnar nerve entrapment.

Henceforth, patients presenting with unusual cases (such as with the SL or the SA involvement) may be treated more accurately by medical professionals acquainted with their infrequent causes, possibly mitigating the risk of permanent nerve injuries. Compressions to the median, radial, or ulnar nerve, which occur especially when such bands of fibrous or muscular tissue traverse them, may lead to upper limb entrapment peripheral neuropathies [8]. Ulnar nerve neuropathies at the elbow are important in particular, as they are the second most common entrapment neuropathy in adults [10].

The SL is a consistently reported structure, and our PPE findings (1.8%) are in line with that of previous descriptions [3, 5, 29, 35]. These results support that this structure is vestigial, and is likely analogous to the

latissimocondyloideus muscle found in climbing animals [3, 9], which serves to protect the neurovascular bundle and provides attachment for the pronator teres muscle by forming an end-epitrochlear foramen [3].

Although we report that it may be slightly more prevalent on the right side, this result is only based on 9 cases, so the statistical power is not significant. Only 2 reports were included in this analysis concerning the prevalence of median nerve compression as a result of the SL, with one supporting and one opposing this view [19, 21]. Therefore no appropriate conclusions can be drawn. However, a series of cases have been described where radiological examination of a patient complaining of paraesthesia and numbness have identified the characteristic spur, and subsequent release surgery has yielded reduced or eliminated clinical symptoms following recovery [1, 4, 5]. Ay et al. [6] describe success using Barnard and McCoy classical approach to remove the periosteum of the spur, the binding fibres of the pronator teres muscle, and the fibrous extension.

Although entrapment syndromes are typically evaluated using magnetic resonance imaging and electromyography, their application in the SL-related conditions is poorly described [4, 13]. Palpation of the bony process may or may not be possible, so it cannot be used as an indication for investigative imaging [9]. In addition, rare instances have been reported where the SL was found associated with only a minimal protrusion, or none whatsoever [35]. Gunther et al. [21] report that the supracondylar spur is most typically an incidental finding on radiography, and that no surgical corrections should be made without any clinical complaints present. Furthermore, a clinician should not automatically assume that the SL (if present) is responsible for any neuropathies prior to investigation. However, the surgeon should be conscious of these structures during surgical exploration. Also, it may be beneficial to recognize that the SL likely inserts into the medial humeral epicondyle (possibly lending aid to the identification of this rare anatomical variant) as per all the reports evaluated herein [8, 19, 21].

Since the overall PPE of the SL is very low, it will ultimately be a rare cause of entrapment. Importantly, Laha et al. [26] define a simple differentiation of the median nerve entrapment by the SL and its bony ligament from the more common pronator syndrome because of pronator teres weakness found in the latter.

Lastly, Taylor et al. [36] discuss the possibility of using the SL (associated with the coracobrachialis

muscle) during restoration of normal facial expression procedures in the longstanding facial paralysis, as it might be used to replace the orbicularis oris muscle and eliminate the deviation of the lips towards the unaffected side whilst smiling. Nonetheless, additional research is required on this matter to ensure the development of safe and effective treatments.

Many previous reports have had opposing views on whether or not the SA is a true structure, or just a product of a specific method of dissection, and further still, if its presence could be related to entrapment [7, 12, 16, 39]. The results of the study herein suggest that the SA can be found in most individuals, but that its presentation is highly variable, described in Tables 8–11. Al-Qattan and Murray [2], Mirza et al. [27], Siqueira and Martins [32] and Tubbs et al. [38], all describe at least some occurrence of an atypical SA, differing by the source of the thickened fascia or musculotendinous band. Even more inconsistency lies in the morphology of the SA, where most tended to be musculotendinous, but a large proportion was still found to be solely tendinous or muscular. Another factor may be, as Bartels et al. [7] suggest, where any dissection can be conducted to replicate a fibrous structure depending on the stepwise technique. However, earlier reports on the arcade clearly differentiate the absence or presence with images and descriptions of their division [34].

The course of the SA was described in 9 studies, and it most frequently presents as either a musculotendinous or tendinous arcade covering or passing over the ulnar nerve. Only 3 included studies specifically outlined the prevalence of the ulnar nerve compression from the SA, the results of which either suggested a 100% association with compression or 0%. Therefore, an extensively variable presentation of this structure may be likely, suggesting a difficulty in differentiating the possible interactions of the SA.

Firstly, inaccurate reporting may be the result of confusion between the SL and the SA [11] as the two similarly named structures appear in the same region. This clarification is imperative for future consistency.

Al-Qattan and Murray [2] report that when performing a procedure to release an entrapped nerve, an atypical SA with a roof of multiple ligaments may have resulted in further entrapment, and that ligaments passing deep to the ulnar nerve should also be released at their insertions. Bartels et al. [7] and Dellon [16] claim to have never observed any such tendinous arches during their nerve entrapment

release surgeries, and suggest that any observed bands are likely the result of improper release of the brachial fascial sheath during the previously undertaken anterior transposition of the ulnar nerve that now became the fibrotic point of compression of the nerve. Bartels et al. [7] also suggest that the edge of the sheath that was cut might become more fibrotic and hence resemble the structure known as the SA. Dellon [16] continues to suggest that an appropriate incision for the cubital tunnel release should be into the brachium, but end more proximally to the medial humeral epicondyle. Attempts to further study the causes of secondary entrapments have not been successful [28, 29, 38].

The disparity in the frequencies of surgeons finding the SA may be in part due to the differences in dissection methodologies; Bartels et al. [7] suggest that in order to standardise the procedure, a step by step dissection focusing on the fascial coverings should be demonstrated. Otherwise, Bartels et al. [7] report that the findings may be in part by the cut edge becoming more fibrotic, and therefore appearing as a tendinous band, however this secondary observation was not the case for most of the included cases.

Overall, the findings of this analysis suggest that the SA is a common structure, albeit with great variability in terms of morphology, relation to the ulnar nerve, or otherwise atypical. It is not likely to be the primary site for nerve entrapment, but it is largely implicated in post transposition syndrome [14]. To reduce the likeliness of a secondary compression, the ulnar nerve must be adequately mobilized from the SA or otherwise any soft tissue attachments that may cause compression [37].

Although a thorough risk of bias assessment was completed, and the quality of the analysed data was evaluated, this study is still subject to the limitations of the availability of the previously published studies. Since the SL is not frequently found, large scale studies cannot be realistically executed, thus potentially reducing the effects of bias altogether. Fortunately, the statistical power of this meta-analysis enabled appropriate conclusions to be drawn. The disagreements regarding the SA (such as its involvement in entrapment, or its existence altogether) added to the difficulty in the investigation, as the findings tended to be bimodal — either largely present, or completely absent. However, with a comprehensive study, and efforts to explicate the discrepancies, statistically significant values could be obtained.

CONCLUSIONS

Since some of the upper limb entrapment peripheral neuropathies have been reported in association with the presence of the SL or the SA, a clinical picture of these two structures must be established in practice. Although the presence of the SL is infrequent, and the manifestation of the SA is highly variable, they are still important considerations in treatment of the aforementioned condition. The SL had a PPE of 1.8% overall, and may be found minimally more likely on the right side (55.8%) than the left (44.2%), but seems to always insert into the medial humeral epicondyle. It was associated with median nerve compression in one of the two studies on the matter. The SA is a valid anatomical structure, and has an overall PPE of 52.6%. Although most typically presenting as a musculotendinous band, it has extensive variability, and may be problematic in procedures involving the anterior transposition of the ulnar nerve. In view of the foregoing, a better understanding of each may be beneficial for the best patient outcomes.

Acknowledgements

The study was supported by "The Best of the Best! 3.0 (Najlepszy z Najlepszych! 3.0)" grant from the Polish Ministry of Science and Higher Education.

Krzysztof A. Tomaszewski was supported by the Polish Ministry of Science and Higher Education grant for young scientists.

We would like to express our gratitude to Mr Jacency Urbaniak for taking the anatomical pictures presented in this work.

REFERENCES

- Al-Naib I. Humeral supracondylar spur and Struthers' ligament. A rare cause of neurovascular entrapment in the upper limb. *Int Orthop*. 1994; 18(6): 393–394, doi: [10.1007/BF00187089](https://doi.org/10.1007/BF00187089), indexed in Pubmed: [7698874](https://pubmed.ncbi.nlm.nih.gov/7698874/).
- Al-Qattan MM, Murray KA. The Arcade of Struthers: An Anatomical Study. *J Hand Surg*. 1991; 16(3): 311–314, doi: [10.1016/0266-7681\(91\)90059-w](https://doi.org/10.1016/0266-7681(91)90059-w).
- Al-Qattan MM, Husband JB. Median nerve compression by the supracondylar process: a case report. *J Hand Surg Br*. 1991; 16(1): 101–103, doi: [10.1016/0266-7681\(91\)90142-b](https://doi.org/10.1016/0266-7681(91)90142-b), indexed in Pubmed: [2007799](https://pubmed.ncbi.nlm.nih.gov/2007799/).
- Andreisek G, Crook DW, Burg D, et al. Peripheral neuropathies of the median, radial, and ulnar nerves: MR imaging features. *Radiographics*. 2006; 26(5): 1267–1287, doi: [10.1148/rg.265055712](https://doi.org/10.1148/rg.265055712), indexed in Pubmed: [16973765](https://pubmed.ncbi.nlm.nih.gov/16973765/).
- Aydinlioglu A, Cirak B, Akpinar F, et al. Bilateral median nerve compression at the level of Struthers' ligament. Case report. *J Neurosurg*. 2000; 92(4): 693–696, doi: [10.3171/jns.2000.92.4.0693](https://doi.org/10.3171/jns.2000.92.4.0693), indexed in Pubmed: [10761661](https://pubmed.ncbi.nlm.nih.gov/10761661/).
- Ay S, Bektas U, Yilmaz C, et al. An unusual supracondylar process syndrome. *J Hand Surg Am*. 2002; 27(5): 913–915, doi: [10.1053/jhsu.2002.34309](https://doi.org/10.1053/jhsu.2002.34309), indexed in Pubmed: [12239685](https://pubmed.ncbi.nlm.nih.gov/12239685/).
- Bartels RH, Grotenhuis JA, Kauer JMG. The arcade of Struthers: an anatomical study. *Acta Neurochir (Wien)*. 2003; 145(4): 295–300, doi: [10.1007/s00701-003-0006-5](https://doi.org/10.1007/s00701-003-0006-5), indexed in Pubmed: [12748890](https://pubmed.ncbi.nlm.nih.gov/12748890/).
- Bilecenoglu B, Uz A, Karalezli N. Possible anatomic structures causing entrapment neuropathies of the median nerve: an anatomic study. *Acta Orthop Belg*. 2005; 71(2): 169–176, indexed in Pubmed: [16152850](https://pubmed.ncbi.nlm.nih.gov/16152850/).
- Blakeborough A, Chennells PM, Cape J. Case report: cellist's elbow? — vascular entrapment in association with the ligament of Struthers. *Clin Radiol*. 1994; 49(12): 902–904, doi: [10.1016/s0009-9260\(05\)82891-0](https://doi.org/10.1016/s0009-9260(05)82891-0), indexed in Pubmed: [7828404](https://pubmed.ncbi.nlm.nih.gov/7828404/).
- Bradshaw DY, Shefner JM. Ulnar neuropathy at the elbow. *Neurol Clin*. 1999; 17(3): 447–461, doi: [10.1016/s0733-8619\(05\)70147-x](https://doi.org/10.1016/s0733-8619(05)70147-x), indexed in Pubmed: [10393748](https://pubmed.ncbi.nlm.nih.gov/10393748/).
- Caetano EB, Sabongi JJ, Vieira LA, et al. Struthers' ligament and supracondylar humeral process: an anatomical study and clinical implications. *Acta Ortop Bras*. 2017; 25(4): 137–142, doi: [10.1590/1413-785220172504168330](https://doi.org/10.1590/1413-785220172504168330), indexed in Pubmed: [28955169](https://pubmed.ncbi.nlm.nih.gov/28955169/).
- Caetano EB, Sabongi Neto JJ, Vieira LA, et al. The arcade of Struthers: an anatomical study and clinical implications. *Rev Bras Ortop*. 2017; 52(3): 331–336, doi: [10.1016/j.rboe.2016.07.006](https://doi.org/10.1016/j.rboe.2016.07.006), indexed in Pubmed: [28702393](https://pubmed.ncbi.nlm.nih.gov/28702393/).
- Camerlinck M, Vanhoenacker FM, Kiekens G. Ultrasound demonstration of Struthers' ligament. *J Clin Ultrasound*. 2010; 38(9): 499–502, doi: [10.1002/jcu.20700](https://doi.org/10.1002/jcu.20700), indexed in Pubmed: [20931650](https://pubmed.ncbi.nlm.nih.gov/20931650/).
- Campbell WW, Landau ME. Controversial entrapment neuropathies. *Neurosurg Clin N Am*. 2008; 19(4): 597–608, vi, doi: [10.1016/j.nec.2008.07.001](https://doi.org/10.1016/j.nec.2008.07.001), indexed in Pubmed: [19010284](https://pubmed.ncbi.nlm.nih.gov/19010284/).
- Caputo AE, Watson HK. Subcutaneous anterior transposition of the ulnar nerve for failed decompression of cubital tunnel syndrome. *J Hand Surg Am*. 2000; 25(3): 544–551, doi: [10.1053/jhsu.2000.6005](https://doi.org/10.1053/jhsu.2000.6005), indexed in Pubmed: [10811760](https://pubmed.ncbi.nlm.nih.gov/10811760/).
- Dellon A. Musculotendinous variations about the medial humeral epicondyle. *J Br Soc Surg Hand*. 1986; 11(2): 175–181, doi: [10.1016/0266-7681\(86\)90254-8](https://doi.org/10.1016/0266-7681(86)90254-8).
- Dellon A, Mackinnon S. Musculoaponeurotic variations along the course of the median nerve in the proximal forearm. *J Hand Surg*. 1987; 12(3): 359–363, doi: [10.1016/0266-7681\(87\)90189-6](https://doi.org/10.1016/0266-7681(87)90189-6).
- Eversman W. Entrapment and compression neuropathies. In: Green D, editor. *Operative hand surgery*, Vol. 2. Churchill Livingstone, New York 1993: 1341–1385.
- Gessini L, Jandolo B, Pietrangeli A. Entrapment neuropathies of the median nerve at and above the elbow. *Surg Neurol*. 1983; 19(2): 112–116, doi: [10.1016/0090-3019\(83\)90405-6](https://doi.org/10.1016/0090-3019(83)90405-6), indexed in Pubmed: [6845137](https://pubmed.ncbi.nlm.nih.gov/6845137/).
- Gonzalez MH, Lotfi P, Bendre A, et al. The ulnar nerve at the elbow and its local branching: an anatomic study. *J Hand Surg Br*. 2001; 26(2): 142–144, doi: [10.1054/jhsb.2000.0532](https://doi.org/10.1054/jhsb.2000.0532), indexed in Pubmed: [11281666](https://pubmed.ncbi.nlm.nih.gov/11281666/).

21. Gunther SF, DiPasquale D, Martin R. Struthers' ligament and associated median nerve variations in a cadaveric specimen. *Yale J Biol Med.* 1993; 66(3): 203–208.
22. Henry BM, Tomaszewski KA, Walocha JA. Methods of Evidence-Based Anatomy: a guide to conducting systematic reviews and meta-analysis of anatomical studies. *Ann Anat.* 2016; 205: 16–21, doi: [10.1016/j.aanat.2015.12.002](https://doi.org/10.1016/j.aanat.2015.12.002), indexed in Pubmed: [26844627](https://pubmed.ncbi.nlm.nih.gov/26844627/).
23. Henry BM, Tomaszewski KA, Ramakrishnan PK, et al. Development of the anatomical quality assessment (AQUA) tool for the quality assessment of anatomical studies included in meta-analyses and systematic reviews. *Clin Anat.* 2017; 30(1): 6–13, doi: [10.1002/ca.22799](https://doi.org/10.1002/ca.22799), indexed in Pubmed: [27718281](https://pubmed.ncbi.nlm.nih.gov/27718281/).
24. Kane E, Kaplan EB, Spinner M. [Observations of the course of the ulnar nerve in the arm]. *Ann Chir.* 1973; 27(5): 487–496, indexed in Pubmed: [4712764](https://pubmed.ncbi.nlm.nih.gov/4712764/).
25. Kleinman WB. Revision ulnar neuroplasty. *Hand Clin.* 1994; 10(3): 461–477, indexed in Pubmed: [7962151](https://pubmed.ncbi.nlm.nih.gov/7962151/).
26. Laha RK, Dujovny M, DeCastro SC. Entrapment of median nerve by supracondylar process of the humerus. Case report. *J Neurosurg.* 1977; 46(2): 252–255, doi: [10.3171/jns.1977.46.2.0252](https://doi.org/10.3171/jns.1977.46.2.0252), indexed in Pubmed: [833644](https://pubmed.ncbi.nlm.nih.gov/833644/).
27. Mirza A, Mirza JB, Lee BK, et al. An anatomical basis for endoscopic cubital tunnel release and associated clinical outcomes. *J Hand Surg Am.* 2014; 39(7): 1363–1369, doi: [10.1016/j.jhsa.2014.04.030](https://doi.org/10.1016/j.jhsa.2014.04.030), indexed in Pubmed: [24881897](https://pubmed.ncbi.nlm.nih.gov/24881897/).
28. Ochiai N, Hayashi T, Ninomiya S. High ulnar nerve palsy caused by the arcade of struthers. *J Hand Surg.* 2016; 17(6): 629–631, doi: [10.1016/0266-7681\(92\)90188-8](https://doi.org/10.1016/0266-7681(92)90188-8).
29. Popinchalk SP, Schaffer AA. Physical examination of upper extremity compressive neuropathies. *Orthop Clin North Am.* 2012; 43(4): 417–430, doi: [10.1016/j.ocl.2012.07.011](https://doi.org/10.1016/j.ocl.2012.07.011), indexed in Pubmed: [23026457](https://pubmed.ncbi.nlm.nih.gov/23026457/).
30. Pujjade T, Hanouz N, Lecoq B, et al. Ultrasound-guided surgical treatment for ulnar nerve entrapment: a cadaver study. *Chir Main.* 2014; 33(4): 256–262, doi: [10.1016/j.main.2014.05.006](https://doi.org/10.1016/j.main.2014.05.006), indexed in Pubmed: [24981578](https://pubmed.ncbi.nlm.nih.gov/24981578/).
31. Rogers MR, Bergfield TG, Aulicino PL. The failed ulnar nerve transposition. Etiology and treatment. *Clin Orthop Relat Res.* 1991(269): 193–200, indexed in Pubmed: [1864038](https://pubmed.ncbi.nlm.nih.gov/1864038/).
32. Siqueira MG, Martins RS. The controversial arcade of Struthers. *Surg Neurol.* 2005; 64 (Suppl 1): S17–S20, doi: [10.1016/j.surneu.2005.04.017](https://doi.org/10.1016/j.surneu.2005.04.017), indexed in Pubmed: [15967222](https://pubmed.ncbi.nlm.nih.gov/15967222/).
33. Smith RV, Fisher RG. Struthers ligament: a source of median nerve compression above the elbow. Case report. *J Neurosurg.* 1973; 38(6): 778–779, doi: [10.3171/jns.1973.38.6.0778](https://doi.org/10.3171/jns.1973.38.6.0778), indexed in Pubmed: [4710659](https://pubmed.ncbi.nlm.nih.gov/4710659/).
34. Spinner M, Kaplan EB. The relationship of the ulnar nerve to the medial intermuscular septum in the arm and its clinical significance. *Hand.* 1976; 8(3): 239–242, doi: [10.1016/0072-968x\(76\)90008-5](https://doi.org/10.1016/0072-968x(76)90008-5), indexed in Pubmed: [976822](https://pubmed.ncbi.nlm.nih.gov/976822/).
35. Suranyi L. Median nerve compression by Struthers ligament. *J Neurol Neurosurg Psychiatry.* 1983; 46(11): 1047–1049, doi: [10.1136/jnnp.46.11.1047](https://doi.org/10.1136/jnnp.46.11.1047), indexed in Pubmed: [6655479](https://pubmed.ncbi.nlm.nih.gov/6655479/).
36. Taylor GI, Cichowitz A, Ang SG, et al. Comparative anatomical study of the gracilis and coracobrachialis muscles: implications for facial reanimation. *Plast Reconstr Surg.* 2003; 112(1): 20–30, doi: [10.1097/01.PRS.0000065909.86735.F7](https://doi.org/10.1097/01.PRS.0000065909.86735.F7), indexed in Pubmed: [12832872](https://pubmed.ncbi.nlm.nih.gov/12832872/).
37. Tiyaworanan P, Jianmongkol S, Thammaroj T. Anatomical study of arcade of Struthers. *Hand Surg.* 2010; 15(3): 157–159, doi: [10.1142/S0218810410004941](https://doi.org/10.1142/S0218810410004941), indexed in Pubmed: [21089187](https://pubmed.ncbi.nlm.nih.gov/21089187/).
38. Tubbs RS, Deep A, Shoja MM, et al. The arcade of Struthers: An anatomical study with potential neurosurgical significance. *Surg Neurol Int.* 2011; 2: 184, doi: [10.4103/2152-7806.91139](https://doi.org/10.4103/2152-7806.91139), indexed in Pubmed: [22276238](https://pubmed.ncbi.nlm.nih.gov/22276238/).
39. von Schroeder HP, Schecker LR. Redefining the “Arcade of Struthers”. *J Hand Surg Am.* 2003; 28(6): 1018–1021, doi: [10.1016/s0363-5023\(03\)00421-0](https://doi.org/10.1016/s0363-5023(03)00421-0), indexed in Pubmed: [14642520](https://pubmed.ncbi.nlm.nih.gov/14642520/).
40. Wehrli L, Oberlin C. The internal brachial ligament versus the arcade of Struthers: an anatomical study. *Plast Reconstr Surg.* 2005; 115(2): 471–477, doi: [10.1097/01.prs.0000150144.73603.24](https://doi.org/10.1097/01.prs.0000150144.73603.24), indexed in Pubmed: [15692352](https://pubmed.ncbi.nlm.nih.gov/15692352/).
41. Yoshida A, Okutsu I, Hamanaka I. Minimally invasive endoscopic ulnar nerve assessment and surgery for cubital tunnel syndrome patients — relation between endoscopic nerve findings and clinical symptoms. *Asia-Pacific J Sport Med Arthrosc Rehabil Technol.* 2014; 1(3): 96–101, doi: [10.1016/j.asmart.2014.01.003](https://doi.org/10.1016/j.asmart.2014.01.003).
42. Zhong S, Zhong Z, Yu Yu, et al. Ultrasonic observation and clinical application of arcade of struthers in the Mid-Arm. *World Neurosurg.* 2016; 91: 560–566.e1, doi: [10.1016/j.wneu.2016.03.061](https://doi.org/10.1016/j.wneu.2016.03.061), indexed in Pubmed: [27032522](https://pubmed.ncbi.nlm.nih.gov/27032522/).

Ultrasound-guided topographic anatomy of the medial calcaneal branches of the tibial nerve

Ł. Warchoł¹, J.A. Walocha¹, E. Mizia¹, M. Bonczar², H. Liszka¹, M. Koziej¹

¹Department of Anatomy, Jagiellonian University Medical College, Krakow, Poland

²Intermed Medical Clinic, Zabierzow, Poland

[Received: 4 April 2020; Accepted: 26 May 2020]

Background: The purpose of this study was to evaluate the topographic anatomy of the tibial nerve and its medial calcaneal branches in relation to the tip of the medial malleolus and to the posterior superior tip of the calcaneal tuberosity using the ultrasound examination and to verify its preoperative usefulness in surgical treatment.

Materials and methods: Bilateral ultrasound examination was performed on 30 volunteers and the location of the tibial nerve bifurcation and medial calcaneal branches origin were measured. Medial calcaneal branches were analysed in reference to the amount and their respective nerves of origin.

Results: In 77% of cases, tibial nerve bifurcation occurred below the tip of the medial malleolus with the average distance of 5.9 mm and in 48% of cases above the posterior superior tip of the calcaneal tuberosity with the average distance of 2.7 mm. In 73% of cases medial calcaneal branches occurred as a single branch originating from the tibial nerve (60%). The average distance of the first, second and third medial calcaneal branch was accordingly 9.3 mm above, 9.5 mm below and 11.6 mm below the tip of the medial malleolus and 17.7 mm above, 1.6 mm below and 4 mm below the posterior superior tip of the calcaneal tuberosity.

Conclusions: As the tibial nerve and its branches present a huge variability in the medial ankle area, in order to prevent the iatrogenic injuries, the preoperative or intraoperative ultrasound assessment (sonosurgery) of its localisation should be introduced into the clinic. (Folia Morphol 2021; 80, 2: 267–274)

Key words: medial calcaneal nerve, ultrasound-guided nerve examination, tarsal tunnel syndrome, medial plantar nerve, lateral plantar nerve, sonosurgery

INTRODUCTION

The tibial nerve arises as a branch of the sciatic nerve bifurcation in the popliteal fossa. It runs distally on the tibialis posterior muscle together with the posterior tibial vessels. Usually at the level of flexor retinaculum it terminally divides into lateral

and medial plantar nerve. During distal course, the tibial nerve emits medial calcaneal branches which are variable in number and origin. The tibial nerve and its branches provide innervation to the posterior lower leg, foot and sole muscles and the skin of medial foot and sole [28].

Address for correspondence: Dr. Ł. Warchoł, Department of Anatomy, Jagiellonian University Medical College, ul. Kopernika 12, 31–034 Kraków, Poland, tel: +48 601 865 239, e-mail: l.warchol@uj.edu.pl

This article is available in open access under Creative Common Attribution-Non-Commercial-No Derivatives 4.0 International (CC BY-NC-ND 4.0) license, allowing to download articles and share them with others as long as they credit the authors and the publisher, but without permission to change them in any way or use them commercially.

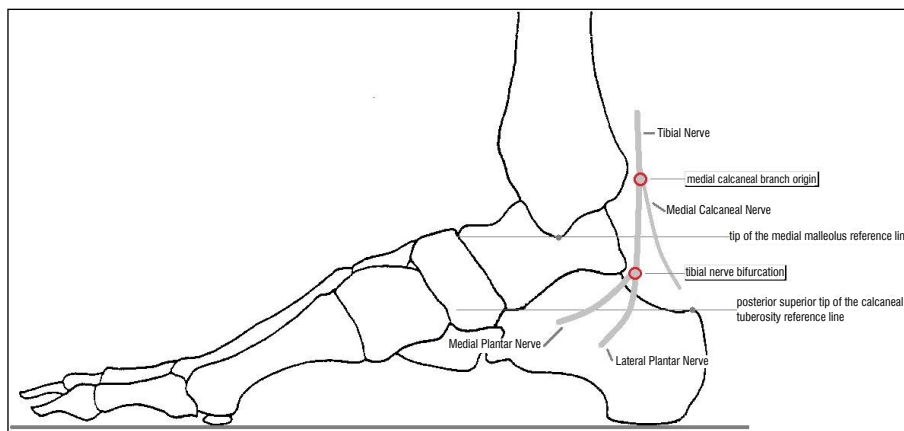


Figure 1. Foot scheme with the measured points and the reference lines.

The knowledge of topographic anatomy of peripheral neurovascular bundles is important in surgical procedures, especially in the medial ankle surgery. It helps to understand the pathophysiology of the tarsal tunnel syndrome and its symptoms such as heel and sole burning pain, paraesthesia and numbness radiating to the toes and proximally on the medial side of the calf with often nocturnal presentation [2, 5, 22, 24, 25, 39]. The tibial nerve and its branches may be entrapped in the tarsal tunnel by various internal and external mechanisms [8]. Additionally other medical conditions with body fluid retention and chronic inflammatory processes may lead to nerve compression [13]. Rising prevalence of diabetes mellitus contributes to a large number of compression syndromes [36]. Currently, popular outdoor activities (e.g. jogging) also bring new cases of foot pain [23].

One of the utmost treatment options for the foot pain syndromes is a surgery [1, 20]. It must be performed with the highest awareness of tibial nerve anatomy without inflicting iatrogenic damage. According to anatomy books, atlases and cadaveric dissection studies, the tibial nerve presents a various pattern of its bifurcation as well as origin and number of medial calcaneal branches [6, 7, 9–11, 14–17, 21, 27, 30, 31, 33]. In relation to the anatomical landmarks we tried to establish the most common topographic localisation of the tibial nerve and its final branches and to encourage to the preoperative ultrasound examination prior to medial ankle surgeries.

MATERIALS AND METHODS

Patients. The study was conducted on the 30 volunteers (n = 60 lower limbs). There were 16 females and 14 males. The average age of the volunteers was 25.7 years (range 19–50 years). The inclusion criteria were as follows: age 18 years or older, written

informed consent for the examination. The exclusion criteria were: any lower limb trauma, surgical or radiotherapeutic procedures of the lower limb, deformation of the lower limb, and chronic disease of the lower limb.

The ultrasound examination was performed on the Mylab Gold 25 ultrasound scanner with an 18 MHz linear probe (penetration depth 3.0 cm) in the Department of Anatomy between December 2016 and April 2017. The examination and measurements were performed by an orthopaedic surgeon with more than 20 years of experience in ultrasound examination.

The ultrasound examination was performed with the volunteer lying prone with the foot in neutral position (ankle fixed in the foot stabilising device and adjusted to the right angle). Each procedure was initiated 40 cm proximally to the tip of the medial malleolus, continuing distally along the tibial nerve course up to its bifurcation and further looking for medial malleolus branches. Following points were marked on the skin with the fine tip skin marker: the tibial nerve bifurcation point, medial calcaneal branches origin, the tip of the medial malleolus and the posterior superior tip of the calcaneal tuberosity (attachment point of the Achilles tendon to the calcaneal tuberosity). Lines crossing the marked points were drawn parallel to the foot plane (Fig. 1). Distances from the reference lines (the tip of the medial malleolus line and the posterior superior tip of the calcaneal tuberosity) to the tibial nerve bifurcation line and to the medial calcaneal branches origin lines were measured with the calliper. If the measured point was below the reference line the value is in negative numbers, if above the reference line the value is in positive number. Medial calcaneal branches were analysed with regards to the number of branches, nerve of origin and relation to the ref-

Table 1. Tibial nerve bifurcation location according to the reference line

Location	Tip of the medial malleolus	Posterior superior tip of the calcaneal tuberosity
Above the reference line	14 (23.3%)	23 (38.3%)
At the level of the reference line	0 (0.0%)	8 (13.3%)
Below the reference line	46 (76.7%)	29 (48.3%)

Table 2. Results of measurements [mm] and statistics

Reference line	Measured point	N	Mean ± standard deviation	Median	Maximum	Minimum	Lower quartile (Q1)	Upper quartile (Q3)	Sex differences	
Tip of the medial malleolus	Tibial nerve bifurcation	60	-5.93 ± 19.59	-8.00	60	-33	-19.50	-1.50	P = 0.6929	
	Medial calcaneal branch origin	1 st branch	60	9.27 ± 61.73	-1.00	337	-27	-7.00	6.50	P = 0.9409
		2 nd branch	16	-9.50 ± 10.09	-8.50	2	-35	-14.00	-0.50	
	3 rd branch	4	-11.75 ± 9.03	-11.00	-4	-21	-19.50	-4.00		
Posterior superior tip of the calcaneal tuberosity	Tibial nerve bifurcation	60	2.67 ± 19.79	0.00	72	-26	-10.00	7.50	P = 0.6776	
	Medial calcaneal branch origin	1 st branch	60	17.67 ± 61.18	7.00	343	-17	3.00	13.50	P = 0.8939
		2 nd branch	16	-1.63 ± 11.28	-1.00	12	-29	-6.50	8.00	
	3 rd branch	4	-4.00 ± 8.45	-2.50	3	-14	-11.00	3.00		

reference lines. The results were transformed into rates and tabulated.

Statistical analysis

Obtained data was statistically processed using descriptive statistics such as percentage, mean, standard deviation. A p-value of < 0.05 was considered as statistically significant. Two groups were compared using the Mann-Whitney test or t-test depending normal distribution. All analyses were performed using MedCalc version 16.8.

The research protocol was approved by the local Ethics Committee (registry no. 122.6120.315.2016). The study was performed in accordance with the ethical standards established in the 1964 Declaration of Helsinki and its later amendments. The volunteers were informed about the study protocol and gave both informed and written consent to participate in the study.

RESULTS

There were 30 volunteers (n = 60 lower limbs) with an average age of 25.7 ± 7 amongst which 32 (53.3%) were female and 28 (46.7%) male feet.

The bifurcation of the tibial nerve into the medial and lateral plantar nerve most frequently occurred below the tip of the medial malleolus (76.7%) with the mean distance of 5.93 ± 19.59 mm and above the posterior superior tip of the calcaneal tuberosity (48.3%) with the mean distance of 2.67 ± 19.79 mm (Tables 1, 2). There was no significant difference be-

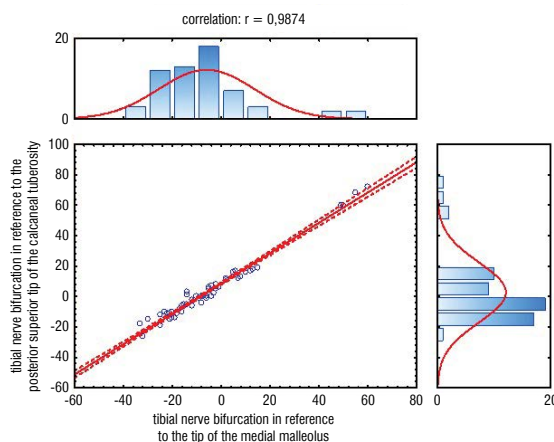


Figure 2. Correlation of the reference lines according to the tibial nerve bifurcation.

tween the sexes (p > 0.05). The correlation between the reference lines of the tip of the medial malleolus and the posterior superior tip of the calcaneal tuberosity has been proven to be statistically significant (r = 0.9874, p < 0.05) (Fig. 2).

The medial calcaneal branches were identified in the range from one to three ramifications. A total of 80 medial calcaneal branches were visualised. In 44 (73.3%) patients, only one medial calcaneal branch was identified with no significant differences between the sexes (p > 0.05). Two medial calcaneal branches were presented in 12 patients, and three branches in 4 patients (Table 3). Most commonly medial calcaneal

Table 3. Division of the medial calcaneal nerve according to the number of branches

Number of branches	Male feet (n = 28)	Female feet (n = 32)	Pooled sexes feet (n = 60)	Percentage
One	16 (57.1%)	28 (87.5%)	44	73.3%
Two	10 (35.7%)	2 (6.3%)	12	20%
Three	2 (7.1%)	2 (6.3%)	4	6.7%

Table 4. Pattern of the medial calcaneal branches presentation according to the nerve of origin

Nerve of origin	Male feet (n = 28)	Female feet (n = 32)	Pooled sexes feet (n = 60)	Percentage
Single branch of TN	14 (50.0%)	22 (68.8%)	36	60%
Single branch of LPN	2 (7.1%)	5 (15.6%)	7	11.7%
One branch of TN and one of LPN	6 (21.4%)	0 (0.0%)	6	10%
Two branches of TN	3 (10.7%)	1 (3.1%)	4	6.7%
Two branches of TN and one of MPN	0 (0.0%)	2 (6.3%)	2	3.3%
Two branches of TN and one of LPN	2 (7.1%)	0 (0.0%)	2	3.3%
One branch of TN and one of MPN	1 (3.6%)	1 (3.1%)	2	3.3%
Single branch of MPN	0 (0.0%)	1 (3.1%)	1	1.7%

TN — tibial nerve; LPN — lateral plantar nerve; MPN — medial plantar nerve

Table 5. Location of all medial calcaneal branches according to the reference lines [mm]

Reference line	Location	N = 78	Percentage	Mean	Median	Maximum	Minimum
Tip of the medial malleolus	Above the reference line	25	31.25%				
	At the level of the reference line	7	8.75%	-3.97	-3	23	-35
	Below the reference line	48	60.0%				
Posterior superior tip of the calcaneal tuberosity	Above the reference line	56	70.0%				
	At the level of the reference line	2	2.5%	4.36	5	34	-29
	Below the reference line	22	27.5%				

Two maximum distal locations were excluded from the statistics (330/335 mm, 337/343 mm)

branch originated from the tibial nerve as a single branch (60%). If there were two medial calcaneal branches, they emerged from the tibial and lateral plantar nerve most frequently (Table 4). Most of the medial calcaneal branches were located below the tip of the medial malleolus with the mean distance of 3.97 mm and above the posterior superior tip of the calcaneal tuberosity with the mean distance of 4.36 mm (Table 5). It may be assumed that majority of branches were located between the tip of the medial malleolus and the posterior superior tip of the calcaneal tuberosity.

First medial calcaneal branch (n = 60) originated 9.27 ± 61.73 mm above the tip of the medial malleolus and 17.67 ± 61.18 mm above the posterior superior tip of the calcaneal tuberosity with no statistically significant differences between the sexes ($p > 0.05$) (Table 6). Second medial calcaneal branch

(n = 16) originated 9.50 ± 10.09 mm below the tip of the medial malleolus and 1.63 ± 11.28 mm below the posterior superior tip of the calcaneal tuberosity. Third medial calcaneal branch (n = 4) originated 11.75 ± 9.03 mm below the tip of the medial malleolus and 4.00 ± 8.45 mm below the posterior superior tip of the calcaneal tuberosity (Table 2, Figs. 3, 4). In 1 volunteer (n = 2 feet) an exceptionally long distance of the first medial calcaneal branch was measured: 330 mm on the left lower limb and 337 mm on the right lower limb above the tip of the medial malleolus and respectively 335 mm and 343 mm above the posterior superior tip of the calcaneal tuberosity.

DISCUSSION

Up to 15% of adult population suffers from the plantar heel pain [3]. According to Oztuna et al. [32], nerve entrapment is one of the reasons for this

Table 6. First medial calcaneal branch location in relation to reference according to the sex

Reference line	Sex	N	Mean ± standard deviation	Median	Maximum	Minimum	Lower quartile (Q1)	Upper quartile (Q3)	P-value	Correlation
Tip of the medial malleolus	Female	32	-0.91 ± 11.51	-0.5	23.0	-22	-8.5	6.0	0.9409	0.9463
	Male	28	20.89 ± 88.95	-1.5	337.0	-27	-6.5	6.5		
Posterior superior tip of the calcaneal tuberosity	Female	32	7.56 ± 12.03	6.5	34.0	-16	3.5	14.5	0.8939	
	Male	28	29.21 ± 88.05	7.0	343.0	-17	2.0	13.0		

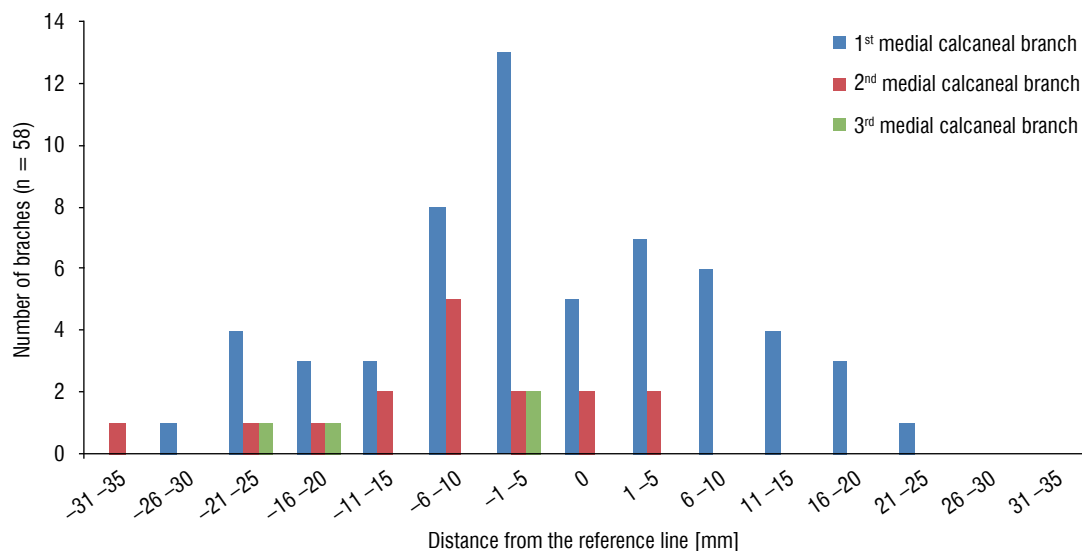


Figure 3. Medial calcaneal branches location in relation to the medial malleolus; two maximum distal locations were not included in the table (330 mm, 337 mm).

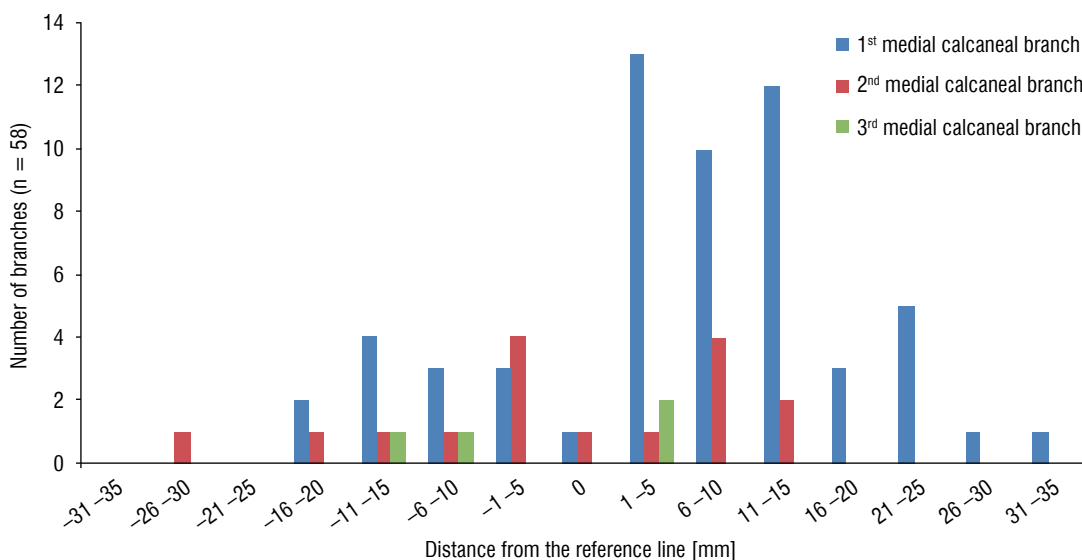


Figure 4. Medial calcaneal branches location in relation to the posterior superior tip of the calcaneal tuberosity; two maximum distal locations were not included in the table (335 mm, 343 mm).

condition. As operative decompression of the tarsal tunnel is one of the most effective treatment options it is essential to perform the surgery in concordance with the anatomical structures in order to avoid its iatrogenic injury [12].

The first description of the tibial nerve and its branches variable anatomy was published by Horwitz [17] in 1938. Dissecting 100 lower extremities author states that the tibial nerve bifurcation occurs 1.3 cm above the tip of the medial malleolus. As for the medial calcaneal branch(es), he underlines its difference in number, location and origin. Dellon et al. [10] in 1984 examined 31 cadaver feet. For the first time the malleolar-calcaneal axis (MCA) was proposed as the reference line for the measurements. In 90% of the cases the tibial nerve bifurcation occurred within 1 cm of the MCA. Medial calcaneal branch originates above the flexor retinaculum in 65% of cases. The author emphasizes variability of left and right feet bifurcation locations as well as the number and location of the medial calcaneal branches. For the first time a substantial differences between mentioned studies are pointed out. Only 15% of Dellon et al. [10] cases presented the tibial nerve bifurcation at the level of Horwitz [17] results.

Comparing data obtained in the other published studies, the tibial nerve bifurcation was located inside the tarsal tunnel in 99.9% (Joshi et al. [21]), 93% (Havel et al. [15]), 88% (Torres et al. [37]) and 73% (Louisa et al. [27]) of cases. Heimkes et al. [16] defined the tarsal tunnel as the oval osteofibrous canal between talus, calcaneus and flexor retinaculum which stretches from the medial malleolus to the calcaneus. These data correspond with the results of the present study in which 76.7% of cases presented the bifurcation below the tip of the medial malleolus with the mean distance of 5.93 ± 19.59 mm. According to the tarsal tunnel definition it may be assumed that majority of the nerves (tibial nerve, lateral and medial plantar nerve) localised by the authors run and divide in the tarsal tunnel where it may be compressed.

Location of the tibial nerve bifurcation was the subject of many cadaveric studies [37]. Most of them were conducted according to the MCA reference line which was fixed between the centre of the medial malleolus and the medial calcaneal tuberosity [21, 27]. Some authors suggest the tip of the lateral malleolus as the reference point which is localised

below the tip of the medial malleolus [26, 38]. Nevertheless, in the present study the authors introduced different, parallel to the foot plane reference lines: a line crossing the tip of the medial malleolus and a line crossing the posterior superior tip of the calcaneal tuberosity. Measurement according to those two reference lines proved to have a high correlation ($r = 0.9874$). The authors believe that those bony, easy palpable through skin orientation points may appear of better use in the clinic environment.

Many authors published various results in relation to the number, location and origin of the medial calcaneal branches. Havel et al. [15], Louisa et al. [27] reported the occurrence of the range of one to two branches of the medial calcaneal nerves. Other published studies states the occurrence of the range of one to three (Torres et al. [37]) and even four (Joshi et al. [21]) branches of the medial calcaneal nerves. Single medial calcaneal branch is the most often finding in reports from Havel et al. [15] and Torres et al. [37] whilst two branches are most commonly registered by Louisa et al. [27] and Dellon et al. [10]. Joshi et al. [21] found single medial calcaneal branch in the same number of dissected lower limbs as for two branches. In the present study the authors visualised a range of one to three medial calcaneal branches with the most common single branch (73.3% of the lower limbs) which is similar to reports by Torres et al. [37] and Havel et al. [15].

In the range of differences, the authors of all other publications indicated the tibial nerve as the most frequent nerve of origin for the medial calcaneal branch(es) [15, 21, 27, 37]. The present study states that despite there is a single, double or triple branching pattern the tibial nerve is the most often nerve of origin (87% of cases). As for other ramification models, the lateral plantar nerve gives off medial calcaneal branch(es) in 25% of cases followed by medial plantar nerve present in 8% of cases. Some authors finds medial calcaneal branch(es) originating only from the tibial nerve [35], others claim it goes off only from the tibial or lateral plantar nerve [14, 17, 21, 23], yet another reports it originates only from the tibial or medial plantar nerve [4].

Medial calcaneal branch(es) location also appears to be a matter of variance among published studies. Some authors observes majority of the medial calcaneal ramifications proximally to the tarsal tunnel [7, 27, 37], others locate it distally [9, 14]. In the

present study the authors registered 60% of medial calcaneal branches located below the tip of the medial malleolus at the same time 70% of them is located above posterior superior tip of the calcaneal tuberosity. It allows assuming that most of the ramifications are located between the two reference lines.

As a single case of an exceptionally distant location of the medial calcaneal branch of 330 mm and 337 mm above the tip of the medial malleolus may appear odd or suggest examiners mistake. It finds confirmation with Torres et al. [37] study where the authors also report a maximal ramification occurring 346.6 mm above the MCA.

Iborra et al. [18, 19] and Mullick et al. [29] confirm that the use of ultrasound in the tarsal tunnel syndrome operative treatment leads to respectively 90.12% and 93% excellent and good results. In the cadaveric study the authors proved that a high-resolution ultrasonography can visualize the entire course of the tibial nerve as well as its tiny branches which may be applied in the decompression surgeries [18, 19, 29]. Also a sonosurgery, which is a “minimally invasive surgical technique performed with the continuous ultrasound imagining and the use of endoscopic tools” seems promising in improving the surgical result by reducing the risk of iatrogenic injuries [34].

Limitations of the study

The fact that tibial nerve and its branches run together with vessels between muscles and other anatomical structures may mean that its localisation changes during the lower limb movement. Therefore for the sake of this study a standardised positioning set up was arranged with all patients lying prone with the foot in neutral position (ankle fixed in the foot stabilising device and adjusted to the right angle). Second limitation is the localisation of the posterior superior tip of the calcaneal tuberosity, which depends on the foot arch. The angle between calcaneal inclination line and the horizontal line (heel pitch angle) varies in cavus, neutral and flat foot. Therefore in cavus foot the measured distance may be longer whilst shorter in the flat foot. Another restriction is a limited ultrasound resolution. Although authors were able to track the tibial nerve till its final bifurcation the high frequency ultrasound might miss some tiny terminal nerves, such as medial calcaneal branches. To reduce this factor ultrasound examination was conducted by an experienced orthopaedic surgeon.

CONCLUSIONS


To conclude, the authors of the present study together with the other analysed publications proved that the anatomy of the tibial nerve and its distal branches observed in the medial ankle area is different between left and right limbs, gender and amongst individuals. As is the origin, location and division pattern on the medial calcaneal branch(es). Because of these anatomical variations, it is difficult to suggest any safe zone area for the medial ankle surgical treatment, as so the preoperative or intraoperative ultrasound examination is highly recommended.

REFERENCES

1. Ahmad M, Tsang K, Mackenney PJ, et al. Tarsal tunnel syndrome: a literature review. *Foot Ankle Surg.* 2012; 18(3): 149–152, doi: [10.1016/j.fas.2011.10.007](https://doi.org/10.1016/j.fas.2011.10.007), indexed in Pubmed: [22857954](https://pubmed.ncbi.nlm.nih.gov/22857954/).
2. Aldridge T. Diagnosing heel pain in adults. *Am Fam Physician.* 2004; 70(2): 332–338, indexed in Pubmed: [15291091](https://pubmed.ncbi.nlm.nih.gov/15291091/).
3. Alshami AM, Souvlis T, Coppieters MW. A review of plantar heel pain of neural origin: differential diagnosis and management. *Man Ther.* 2008; 13(2): 103–111, doi: [10.1016/j.math.2007.01.014](https://doi.org/10.1016/j.math.2007.01.014), indexed in Pubmed: [17400020](https://pubmed.ncbi.nlm.nih.gov/17400020/).
4. Andreasen Struijk LNS, Birn H, Teglbjaerg PS, et al. Size and separability of the calcaneal and the medial and lateral plantar nerves in the distal tibial nerve. *Anat Sci Int.* 2010; 85(1): 13–22, doi: [10.1007/s12565-009-0045-y](https://doi.org/10.1007/s12565-009-0045-y), indexed in Pubmed: [19449089](https://pubmed.ncbi.nlm.nih.gov/19449089/).
5. Bailie DS, Kelikian AS. Tarsal tunnel syndrome: diagnosis, surgical technique, and functional outcome. *Foot Ankle Int.* 1998; 19(2): 65–72, doi: [10.1177/107110079801900203](https://doi.org/10.1177/107110079801900203), indexed in Pubmed: [9498577](https://pubmed.ncbi.nlm.nih.gov/9498577/).
6. Bilge O, Ozer MA, Govsa F. Neurovascular branching in the tarsal tunnel. *Neuroanatomy.* 2003; 2: 39–41.
7. Davis TJ, Schon LC. Branches of the tibial nerve: anatomic variations. *Foot Ankle Int.* 1995; 16(1): 21–29, doi: [10.1177/107110079501600105](https://doi.org/10.1177/107110079501600105), indexed in Pubmed: [7697149](https://pubmed.ncbi.nlm.nih.gov/7697149/).
8. De Maeseneer M, Madani H, Lenchik L, et al. Normal anatomy and compression areas of nerves of the foot and ankle: US and MR imaging with anatomic correlation. *Radiographics.* 2015; 35(5): 1469–1482, doi: [10.1148/rg.2015150028](https://doi.org/10.1148/rg.2015150028), indexed in Pubmed: [26284303](https://pubmed.ncbi.nlm.nih.gov/26284303/).
9. Dellon AL, Kim J, Spaulding CM. Variations in the origin of the medial calcaneal nerve. *J Am Podiatr Med Assoc.* 2002; 92(2): 97–101, doi: [10.7547/87507315-92-2-97](https://doi.org/10.7547/87507315-92-2-97), indexed in Pubmed: [11847261](https://pubmed.ncbi.nlm.nih.gov/11847261/).
10. Dellon AL, Mackinnon SE. Tibial nerve branching in the tarsal tunnel. *Arch Neurol.* 1984; 41(6): 645–646, doi: [10.1001/archneur.1984.04210080053013](https://doi.org/10.1001/archneur.1984.04210080053013), indexed in Pubmed: [6721738](https://pubmed.ncbi.nlm.nih.gov/6721738/).
11. Didia BC, Horsefall AU. Medial calcaneal nerve. An anatomical study. *J Am Podiatr Med Assoc.* 1990; 80(3): 115–119, doi: [10.7547/87507315-80-3-115](https://doi.org/10.7547/87507315-80-3-115), indexed in Pubmed: [2332828](https://pubmed.ncbi.nlm.nih.gov/2332828/).
12. Doneddu PE, Coraci D, Loreti C, et al. Tarsal tunnel syndrome: still more opinions than evidence. *Status*

- of the art. *Neurol Sci.* 2017; 38(10): 1735–1739, doi: [10.1007/s10072-017-3039-x](https://doi.org/10.1007/s10072-017-3039-x), indexed in Pubmed: [28664501](https://pubmed.ncbi.nlm.nih.gov/28664501/).
13. Flanigan RM, DiGiovanni BF. Peripheral nerve entrapments of the lower leg, ankle, and foot. *Foot Ankle Clin.* 2011; 16(2): 255–274, doi: [10.1016/j.fcl.2011.01.006](https://doi.org/10.1016/j.fcl.2011.01.006), indexed in Pubmed: [21600446](https://pubmed.ncbi.nlm.nih.gov/21600446/).
 14. Govsa F, Bilge O, Ozer MA. Variations in the origin of the medial and inferior calcaneal nerves. *Arch Orthop Trauma Surg.* 2006; 126(1): 6–14, doi: [10.1007/s00402-005-0088-z](https://doi.org/10.1007/s00402-005-0088-z), indexed in Pubmed: [16333630](https://pubmed.ncbi.nlm.nih.gov/16333630/).
 15. Havel PE, Ebraheim NA, Clark SE, et al. Tibial nerve branching in the tarsal tunnel. *Foot Ankle.* 1988; 9(3): 117–119, doi: [10.1177/107110078800900304](https://doi.org/10.1177/107110078800900304), indexed in Pubmed: [2852629](https://pubmed.ncbi.nlm.nih.gov/2852629/).
 16. Heimkes B, Posel P, Stotz S, et al. The proximal and distal tarsal tunnel syndromes. An anatomical study. *Int Orthop.* 1987; 11(3): 193–196, doi: [10.1007/BF00271447](https://doi.org/10.1007/BF00271447), indexed in Pubmed: [3623755](https://pubmed.ncbi.nlm.nih.gov/3623755/).
 17. Horwitz MT. Normal anatomy and variations of the peripheral nerves of the leg and foot application in operations for vascular diseases: study of one hundred specimens. *Arch Surg.* 1938; 36(4): 626–636, doi: [10.1001/arch-surg.1938.01190220068005](https://doi.org/10.1001/arch-surg.1938.01190220068005).
 18. Iborra A, Villanueva M, Sanz-Ruiz P. Results of ultrasound-guided release of tarsal tunnel syndrome: a review of 81 cases with a minimum follow-up of 18 months. *J Orthop Surg Res.* 2020; 15(1): 30, doi: [10.1186/s13018-020-1559-1](https://doi.org/10.1186/s13018-020-1559-1), indexed in Pubmed: [31992296](https://pubmed.ncbi.nlm.nih.gov/31992296/).
 19. Iborra A, Villanueva M, Barrett SL, et al. Anatomic delineation of tarsal tunnel innervation via ultrasonography. *J Ultrasound Med.* 2018; 37(6): 1325–1334, doi: [10.1002/jum.14499](https://doi.org/10.1002/jum.14499), indexed in Pubmed: [29205431](https://pubmed.ncbi.nlm.nih.gov/29205431/).
 20. Iborra Á, Villanueva-Martínez M, Barrett SL, et al. Ultrasound-Guided release of the tibial nerve and its distal branches: a cadaveric study. *J Ultrasound Med.* 2019; 38(8): 2067–2079, doi: [10.1002/jum.14897](https://doi.org/10.1002/jum.14897), indexed in Pubmed: [30589453](https://pubmed.ncbi.nlm.nih.gov/30589453/).
 21. Joshi SS, Joshi SD, Athavale AS. Anatomy of tarsal tunnel and its applied Significance. *J Anat Soc india.* 2006; 55(1): 52–56.
 22. Keck C. The tarsal-tunnel syndrome. *J Bone Joint Surg.* 1962; 44(1): 180–182, doi: [10.2106/00004623-196244010-00015](https://doi.org/10.2106/00004623-196244010-00015).
 23. Kim DI, Kim YS, Han SH. Topography of human ankle joint: focused on posterior tibial artery and tibial nerve. *Anat Cell Biol.* 2015; 48(2): 130–137, doi: [10.5115/acb.2015.48.2.130](https://doi.org/10.5115/acb.2015.48.2.130), indexed in Pubmed: [26140224](https://pubmed.ncbi.nlm.nih.gov/26140224/).
 24. Kopell HP, Thompson WA. [Peripheral entrapment neuropathies of the lower extremity]. *N Engl J Med.* 1960; 262: 56–60, doi: [10.1056/NEJM196001142620202](https://doi.org/10.1056/NEJM196001142620202), indexed in Pubmed: [13848498](https://pubmed.ncbi.nlm.nih.gov/13848498/).
 25. Lam SJ. A tarsal-tunnel syndrome. *Lancet.* 1962; 2(7270): 1354–1355, doi: [10.1016/s0140-6736\(62\)91024-3](https://doi.org/10.1016/s0140-6736(62)91024-3), indexed in Pubmed: [13928212](https://pubmed.ncbi.nlm.nih.gov/13928212/).
 26. Lijoi F, Lughi M, Baccarani G. Posterior arthroscopic approach to the ankle: an anatomic study. *Arthroscopy.* 2003; 19(1): 62–67, doi: [10.1053/jars.2003.50003](https://doi.org/10.1053/jars.2003.50003), indexed in Pubmed: [12522404](https://pubmed.ncbi.nlm.nih.gov/12522404/).
 27. Louisiana S, Masquelet AC. The medial and inferior calcaneal nerves: an anatomic study. *Surg Radiol Anat.* 1999; 21(3): 169–173, doi: [10.1007/BF01630895](https://doi.org/10.1007/BF01630895), indexed in Pubmed: [10431329](https://pubmed.ncbi.nlm.nih.gov/10431329/).
 28. Moore KL. *Clinically oriented anatomy.* 8th Ed, LWW 2017.
 29. Mullick T, Dellon AL. Results of decompression of four medial ankle tunnels in the treatment of tarsal tunnels syndrome. *J Reconstr Microsurg.* 2008; 24(2): 119–126, doi: [10.1055/s-2008-1076089](https://doi.org/10.1055/s-2008-1076089), indexed in Pubmed: [18459088](https://pubmed.ncbi.nlm.nih.gov/18459088/).
 30. Ndiaye A, Dia A, Konate I, et al. [Topographic anatomy of the tibial nerve in the medial malleolus: application to the effect of nerve block anesthesia]. *Morphologie.* 2003; 87(277): 25–27, indexed in Pubmed: [14717067](https://pubmed.ncbi.nlm.nih.gov/14717067/).
 31. Netter FH. *Atlas of human anatomy.* 7th Ed, Elsevier 2018.
 32. Oztuna V, Ozge A, Eskandari MM, et al. Nerve entrapment in painful heel syndrome. *Foot Ankle Int.* 2002; 23(3): 208–211, doi: [10.1177/107110070202300304](https://doi.org/10.1177/107110070202300304), indexed in Pubmed: [11934062](https://pubmed.ncbi.nlm.nih.gov/11934062/).
 33. Paulsen F, Waschke J. *Sobotta atlas of human anatomy.* 15th Ed, Urban & Fischer 2012.
 34. Pilecki Z, Pilecki G, Bubnov R. Introduction to sonosurgery. *EPMA J.* 2014; 5(S1), doi: [10.1186/1878-5085-5-s1-a66](https://doi.org/10.1186/1878-5085-5-s1-a66).
 35. Rondhuis JJ, Huson A. The first branch of the lateral plantar nerve and heel pain. *Acta Morphol Neerl Scand.* 1986; 24(4): 269–279, indexed in Pubmed: [3425404](https://pubmed.ncbi.nlm.nih.gov/3425404/).
 36. Rowley WR, Bezold C, Arikan Y, et al. *Diabetes 2030: Insights from Yesterday, Today, and Future Trends.* *Popul Health Manag.* 2017; 20(1): 6–12, doi: [10.1089/pop.2015.0181](https://doi.org/10.1089/pop.2015.0181), indexed in Pubmed: [27124621](https://pubmed.ncbi.nlm.nih.gov/27124621/).
 37. Torres ALG, Marcus Castro Ferreira MC. Study of the anatomy of the tibial nerve and its branches in the distal medial leg. *Acta Ortop Bras.* 2012; 20(3): 157–164.
 38. Warchoł Ł, Mróz I, Mizia E, et al. Vascular density of inferior tibiofibular joint: cadaveric experimental study. *Folia Med Cracov.* 2017; 57(1): 47–54, indexed in Pubmed: [28608862](https://pubmed.ncbi.nlm.nih.gov/28608862/).
 39. Yates B. *Merriman's Assessment of the Lower Limb.* 3rd Ed. Churchill Livingstone, New York 2008.

The dimensions of the sphenoid sinuses: evaluation before the functional endoscopic sinus surgery

J. Jaworek-Troć^{1, 2}, M. Zarzecki¹, I. Zamojska¹, J. Iwanaga³, W. Przybycień¹, M. Mazur¹, R. Chrzan², J.A. Walocha¹ 

¹Department of Anatomy, Jagiellonian University Medical College, Krakow, Poland

²Department of Radiology, Jagiellonian University Medical College, Krakow, Poland

³Department of Neurosurgery, Tulane University, New Orleans, United States

[Received: 4 March 2020; Accepted: 18 May 2020]

Background: The following study aimed to evaluate the dimensions (anteroposterior, transverse and vertical) of the sphenoid sinuses in the adult population.

Materials and methods: The study was conducted as a retrospective analysis of the computed tomography (CT) scans of the paranasal sinuses of 296 patients (147 females and 149 males), who did not present any pathology in the sphenoid sinuses. The CT scans of the paranasal sinuses were done with the spiral CT scanner, without using any contrast medium. After obtaining transverse planes, frontal and sagittal planes were created using secondary reconstruction tool.

Results: The anteroposterior dimension was found to be 2.65 cm on average, in the range of 0.5–4.3 cm. The transverse dimension was on average 1.98 cm, ranging from 0.5 cm to 4.9 cm. The average vertical dimension was found to be 2.1 cm, in the range of 0.7–3.7 cm.

Conclusions: Due to the high incidence of the anatomical variants of the paranasal sinuses, a CT scan is recommended in all patients before a planned surgery in order to avoid the potential iatrogenic complications. Dimensions of the sphenoid sinuses might point towards more at risk variants, but there is still a substantial amount of research that needs to be done in that aspect. (Folia Morphol 2021; 80, 2: 275–282)

Key words: sphenoid sinus, anatomy, dimensions, functional endoscopic sinus surgery

INTRODUCTION

Sphenoid sinuses are located in the diaphysis of the sphenoid bone. They are air-filled spaces that are lined up with mucous membrane. There is a high incidence of variance in their size, shape, the number of the septa present and the extent of their filling with air [9, 10, 12].

A surgeon, before carrying out an invasive procedure in the paranasal sinuses, has to take into account

the adjoining structures (nervous and vascular) that are next to the walls of the sphenoid sinuses. It is crucial to evaluate the anatomical parameters of the sinuses ahead of the planned surgery (including endoscopy), as to minimise the surgical risk and avoid complications that might arise during the procedure [1, 6, 8, 11, 13, 14, 17–20, 22].

Address for correspondence: Prof. J.A. Walocha, MD, PhD, Department of Anatomy, Jagiellonian University Medical College, ul. Kopernika 12, 31–034 Kraków, Poland, tel: +48 12 422 95 11, e-mail: j.walocha@uj.edu.pl

This article is available in open access under Creative Common Attribution-Non-Commercial-No Derivatives 4.0 International (CC BY-NC-ND 4.0) license, allowing to download articles and share them with others as long as they credit the authors and the publisher, but without permission to change them in any way or use them commercially.

A clear-cut image of the osseous structures of the paranasal sinuses can be obtained by the computed tomography (CT), which is regarded as one of the most accurate methods of imaging of the sinuses (it allows for a distinction between the anatomical variants of the sinuses).

Recently it has been possible to notice the advancement of the functional endoscopic sinus surgery (FESS) [3, 4]. The minor number of the classical extensive surgeries of the paranasal sinuses still carried out was obtained thanks to the minimally invasive endoscopic procedures.

In the surgical treatment of the chronic paranasal sinusitis, the FESS is commonly regarded as a method of choice. In comparison to classical surgeries, endoscopic techniques allow for a better insight into the otherwise difficult to assess places, cause less collateral damage during the operation and facilitate a shorter recovery period for the patients [6, 15].

MATERIALS AND METHODS

Two hundred ninety-six patients ($n = 296$; 147 females, 149 males) were referred to the Department of Medical Imaging of the University Hospital in Krakow, Poland. People over 18 years of age, without any visible/confirmed pathology in the sphenoid sinuses, were included in this retrospective analysis of the paranasal sinuses CT scans. The patients who suffered from a head injury or underwent a surgical procedure involving nasal, orbital, or cranial basis regions were excluded from the study.

Standard procedure in the option Siemens CARE Dose 4D applied while obtaining the CT scans of the paranasal sinuses, using spiral CT scanner (Siemens Somatom Sensation 16). No contrast medium was given to the patients. Sagittal and frontal planes were obtained by using the multiplanar reconstruction (MPR) tool, after the images of transverse planes were taken. Siemens Volume Wizard diagnostic station was used in order to evaluate the data.

The analysis of the obtained images involved the three dimensions of each of the sphenoid sinuses studied: anteroposterior (in the longest part of the sinuses), transverse (in the widest part of the sinuses) and vertical dimensions (in the highest part of the sinuses).

RESULTS

The anteroposterior dimension was on average 2.65 cm (2.6 cm in females, 2.7 cm in males), in the

range of 0.5–4.3 cm (0.5–4.2 cm in females, 0.6–4.3 cm in males). The smallest anteroposterior dimension of the right sphenoid sinuses noted was 0.6 cm (1 cm in females, 0.6 cm in males), and 0.5 cm of the left sphenoid sinuses (0.5 cm in females, 0.8 cm in males). On the other side, the biggest anteroposterior dimension of the right sphenoid sinuses was 4.1 cm (4 cm in females, 4.1 cm in males), and 4.3 cm of the left sphenoid sinuses (4.2 cm in females, 4.3 in males).

The median value of the anteroposterior dimension of the female sphenoid sinuses (2.55 cm; 2.25–2.9 cm) was significantly different from the median value of the same dimension in the males (2.8 cm; 2.4–3.1 cm; $p = 0.001$, Mann-Whitney's test). Moreover, there was a significant variation found between the median value of the anteroposterior dimension of the right sphenoid sinuses in females (2.7 cm; 2.05–3.0 cm) and males (2.8 cm; 2.2–3.2 cm; $p = 0.021$, Mann-Whitney's test). Similarly, the median value of the anteroposterior dimension of the left sphenoid sinuses in females (2.7 cm; 2.1–3.0 cm) was significantly different to the one in males (2.9 cm; 2.3–3.4 cm; $p = 0.005$, Mann-Whitney's test).

Rarely there were sphenoid sinuses found that would have the same anteroposterior dimension — they were noted only in 17 patients (12 females, 5 males).

No statistically significant differences were found between the prevalence of the different/equal anteroposterior dimension of the right and left sphenoid sinuses in females and males ($p = 0.075$, χ^2 test). In both males and females the different dimension of the right and left sphenoid sinuses comprised over 90% of the cases (Tables 1, 2, Fig. 1).

The transverse dimension was 1.98 cm on average (1.85 cm in females, 2.1 cm in males), in the range of 0.5–4.9 cm (0.7–3.7 cm in females, 0.5–4.9 cm in males). The smallest transverse dimension of the right sphenoid sinuses was 0.5 cm (0.7 cm in females, 0.5 cm in males), and 0.8 cm in the case of the left sinuses (0.9 cm in females, 0.8 cm in males). On the other side, the biggest transverse dimension of the right sphenoid sinuses was 4.9 cm (3.2 cm in females, 4.9 cm in males), and 4.6 cm of the left sinuses (3.7 cm in females, 4.6 cm in males).

The median value of the transverse dimension of the female sphenoid sinuses (1.75 cm; 1.6–2 cm) was significantly different to the one of males (2 cm; 1.75–2.4 cm; $p = 0.001$, Mann-Whitney's test). Moreover, there was a significant variation between

Table 1. The anteroposterior dimensions of the sphenoid sinuses in centimetre

The anteroposterior dimension	Females	Males	Total
Overall			
Mean \pm standard deviation	2.6 \pm 0.52	2.75 \pm 0.54	2.65 \pm 0.54
Median (Q ₁ –Q ₃)	2.55 (2.25–2.9)	2.8 (2.4–3.1)	2.7 (2.35–3)
Minimum–maximum	0.5–4.3	0.6–4.3	0.5–4.3
Right sphenoid sinus			
Mean \pm standard deviation	2.56 \pm 0.65	2.71 \pm 0.72	2.63 \pm 0.69
Median (Q ₁ –Q ₃)	2.7 (2.05–3.0)	2.8 (2.2–3.2)	2.7 (2.175–3.2)
Minimum–maximum	1–4	0.6–4.1	0.6–4.1
Left sphenoid sinus			
Mean \pm standard deviation	2.55 \pm 0.72	2.79 \pm 0.78	2.67 \pm 0.76
Median (Q ₁ –Q ₃)	2.7 (2.1–3.0)	2.9 (2.3–3.4)	2.8 (2.2–3.2)
Minimum–maximum	0.5–4.3	0.8–4.3	0.5–4.3

Table 2. The prevalence of the different/equal anteroposterior (AP) dimensions of the right and left sphenoid sinuses

	F	F%	M	M%	F + M	F + M%
AP RSS \neq LSS	135	91.84%	144	96.64%	279	94.26%
AP RSS=LSS	12	8.16%	5	3.36%	17	5.74%

RSS — right sphenoid sinus; LSS — left sphenoid sinus; RSS \neq LSS — different anteroposterior dimensions; RSS=LSS — equal anteroposterior dimensions; F — females, F% — the percentage of females, M — males; M% — the percentage of males

**Figure 1.** A computed tomography scan of the paranasal sinuses, transverse plane. The measurement method of the anteroposterior dimensions of the right and left sphenoid sinuses.

the median value of the transverse dimension of the right sphenoid sinuses in females (1.8 cm; 1.5–2.1 cm) and males (1.9 cm; 1.5–2.4 cm; $p = 0.031$, Mann-Whit-

ney's test). Similarly, the median value of the transverse dimension of the left sphenoid sinuses in females (1.7 cm; 1.5–2.3 cm) differed significantly from the one in males (2.1 cm; 1.7–2.7 cm; $p < 0.001$, Mann-Whitney's test).

Likewise in the case of this dimension there were not many sinuses with equal transverse dimensions found — such situation was noted only in 14 patients (7 females, 7 males).

No statistically significant relations were found between the prevalence of the different/equal transverse dimensions of the right and left sphenoid sinuses in females and males ($p = 0.979$, χ^2 test). In both female and male groups, the sinuses that had different transverse dimensions of the right and left sphenoid sinuses predominated (95%; Tables 3, 4, Fig. 2).

The vertical dimension was 2.1 cm on average (2 cm in females, 2.2 cm in males), in the range of 0.7–3.7 cm (0.7–3.7 cm in females, 1–3.4 cm in males). The smallest vertical dimension of the right sphenoid sinuses was 1 cm (1.1 cm in females, 1 cm in males), and 0.7 cm of the left sphenoid sinuses (0.7 cm in females, 1.1 cm in males), and the biggest vertical dimension of the right sphenoid sinuses was 3.7 cm

Table 3. The transverse dimensions of the sphenoid sinuses in centimetre

The transverse dimension	Females	Males	Total
Overall			
Mean \pm standard deviation	1.85 \pm 0.38	2.12 \pm 0.54	1.98 \pm 0.49
Median (Q ₁ –Q ₃)	1.75 (1.6–2)	2 (1.75–2.4)	1.85 (1.65–2.15)
Minimum–maximum	0.7–3.7	0.5–4.1	0.5–4.9
Right sphenoid sinus			
Mean \pm standard deviation	1.82 \pm 0.48	2.04 \pm 0.76	1.93 \pm 0.64
Median (Q ₁ –Q ₃)	1.8 (1.5–2.1)	1.9 (1.5–2.4)	1.8 (1.5–2.2)
Minimum–maximum	0.7–3.2	0.5–4.9	0.5–4.9
Left sphenoid sinus			
Mean \pm standard deviation	1.88 \pm 0.60	2.21 \pm 0.75	2.05 \pm 0.70
Median (Q ₁ –Q ₃)	1.7 (1.5–2.3)	2.1 (1.7–2.7)	1.9 (1.5–2.5)
Minimum–maximum	0.9–3.7	0.8–4.6	0.8–4.6

Table 4. The prevalence of the different/equal transverse dimensions (Transv.) of the right and left sphenoid sinuses

	F	F%	M	M%	F + M	F + M%
Transv. RSS \neq LSS	140	95.24%	142	95.3%	282	95.27%
Transv. RSS=LSS	7	4.76%	7	4.7%	14	4.73%

RSS — right sphenoid sinus; LSS — left sphenoid sinus; RSS \neq LSS — different transverse dimensions; RSS=LSS — equal transverse dimensions; F — females; F% — the percentage of females; M — males; M% — the percentage of males

**Figure 2.** A computed tomography scan of the paranasal sinuses, transverse plane. The measurement method of the transverse dimensions of the right and left sphenoid sinuses.

(3.7 cm in females, 3.4 cm in males), and 3.2 cm of the left sphenoid sinuses (3.1 cm in females, 3.2 cm in males).

The median value of the vertical dimension of the female sphenoid sinuses (2 cm; 1.85–2.2 cm) was significantly different from the ones of males (2.2 cm; 1.95–2.45 cm; $p = 0.001$, Mann-Whitney's test). Moreover, there was a significant difference between the median values of the vertical dimension of the right sphenoid sinuses in females (2.1 cm; 1.8–2.3 cm) and males (2.2 cm; 1.9–2.5 cm; $p = 0.002$, Mann-Whitney's test). Similarly, the median value of the vertical dimension of the left sphenoid sinuses in females (2 cm; 1.7–2.25 cm) differed significantly from the one of males (2.2 cm; 1.9–2.5 cm; $p < 0.001$, Mann-Whitney's test).

Likewise in the case of this dimension, there were not many sinuses with equal vertical dimensions — such situation was noted only in 24 patients (12 females, 12 males).

No statistically significant relations were found between the prevalence of the different/equal vertical dimensions of the right and left sphenoid sinuses in females and males ($p = 0.972$, χ^2 test). In both female and male groups the sphenoid sinuses with varied vertical dimensions predominated (92%; Tables 5, 6, Fig. 3).

Table 5. The vertical dimensions of the sphenoid sinuses in centimetre

The vertical dimension	Females	Males	Total
Overall			
Mean \pm standard deviation	2.02 \pm 0.31	2.21 \pm 0.31	2.12 \pm 0.35
Median (Q ₁ –Q ₃)	2 (1.85–2.2)	2.2 (1.95–2.45)	2.1 (1.9–2.3)
Minimum–maximum	0.7–3.7	1.0–3.4	0.7–3.7
Right sphenoid sinus			
Mean \pm standard deviation	2.05 \pm 0.39	2.2 \pm 0.49	2.125 \pm 0.44
Median (Q ₁ –Q ₃)	2.1 (1.8–2.3)	2.2 (1.9–2.5)	2.1 (1.8–2.4)
Minimum–maximum	1.1–3.7	1–3.4	1–3.7
Left sphenoid sinus			
Mean \pm standard deviation	1.99 \pm 0.40	2.23 \pm 0.42	2.11 \pm 0.43
Median (Q ₁ –Q ₃)	2 (1.7–2.25)	2.2 (1.9–2.5)	2.1 (1.8–2.4)
Minimum–maximum	0.7–3.1	1.1–3.2	0.7–3.2

Table 6. The prevalence of the different/equal vertical dimensions (Vert.) of the right and left sphenoid sinuses

	F	F%	M	M%	F + M	F + M%
Vert. RSS \neq LSS	135	91.84%	137	91.95%	272	91.89%
Vert. RSS=LSS	12	8.16%	12	8.05%	24	8.11%

RSS — right sphenoid sinus; LSS — left sphenoid sinus; RSS \neq LSS — different vertical dimensions; RSS=LSS — equal vertical dimensions; F — females; F% — the percentage of females; M — males; M% — the percentage of males



Figure 3. A computed tomography scan of the paranasal sinuses, frontal plane. The measurement method of the vertical dimensions of the right and left sphenoid sinuses.

DISCUSSION

The average dimensions of the sphenoid sinuses did not differ significantly amongst the genders.

The anteroposterior dimension was 2.65 cm on average, in the range of 0.5–4.3 cm. The different

anteroposterior dimension of the two sphenoid sinuses in one patient was the most prevalent variant — 94.26% of the patients.

Similar results were obtained by Mutlu et al. [18], who found the anteroposterior dimension to be 2.76 cm on average (ranging from 1.07 to 4.17 cm), and Sareen et al. [20], who determined it to be 2.5 cm on average (in the range of 1.3–3.4 cm).

Elwany et al. [5] provided the following data for the anteroposterior dimension of the sphenoid sinuses: the mean of 1.6 cm (the presellar type) and 3.1 cm (the postsellar type), the smallest 1.2 cm (the presellar type) and 2.6 cm (the postsellar type), as well as the biggest 1.8 cm (the presellar type) and 3.9 cm (the postsellar type). On the other hand, Stokovic et al. [21] evaluated the average anteroposterior dimension to be 1.66 cm (in the range of 0.65–3.45 cm) (Table 7).

The transverse dimension was 1.98 cm on average, in the range of 0.5–4.9 cm. The different anteroposterior dimensions of the two sphenoid sinuses in one patient was the most prevalent variant — 95.27% of the patients (95.24% of females, 95.3% of males).

Table 7. The reported anteroposterior dimensions of the sphenoid sinuses (cm)

Author (material and methods)	The mean	The smallest	The biggest	RSS=LSS	RSS≠LSS
Mutlu et al. (69 HRCT)	2.76	1.07	4.17	-	-
Sareen et al. (20 skulls, dissection study)	2.5	1.3	3.4	-	-
Elwany et al. 1983 (100 X-rays, 100 skulls X-rayed, 50 skulls — dissection study)	1.6/3.1	1.2/2.6	1.8/3.9	-	-
Stokovic et al. (51 skulls CBCT)	1.66	0.65	3.45	-	-
Jaworek-Troć et al. (296 CT scans)	2.65	0.5	4.3	5.74%	94.26%

CT — computed tomography; CBCT — cone-beam computed tomography; HRCT — high-resolution CT; RSS — right sphenoid sinus; LSS — left sphenoid sinus; RSS≠LSS — different anteroposterior dimensions; RSS=LSS — equal anteroposterior dimensions

Table 8. The reported transverse dimensions of the sphenoid sinuses (cm)

Author (material and methods)	The mean	The smallest	The biggest	RSS=LSS	RSS≠LSS
Mutlu et al. (69 HRCT)	3.18	2.13	5.54	-	-
Elwany et al. 1983 (100 X-rays, 100 skulls X-rayed, 50 skulls — dissection study)	1.2/1.9	0.7/1.4	1.4/2.4	-	-
Stokovic et al. (51 skulls CBCT)	1.43	0.55	3.5	-	-
Jaworek-Troć et al. (296 CT scans)	1.98	0.5	4.9	4.73%	95.27%

CT — computed tomography; CBCT — cone-beam computed tomography; HRCT — high-resolution CT; RSS — right sphenoid sinus; LSS — left sphenoid sinus; RSS≠LSS — different transverse dimensions; RSS=LSS — equal transverse dimensions

Table 9. The reported vertical dimensions of the sphenoid sinuses (cm)

Author (material and methods)	The mean	The smallest	The biggest	RSS=LSS	RSS≠LSS
Sareen et al. (20 skulls, dissection study)	2.2	1.4	3.6	-	-
Awadalla et al. (25 skulls, dissection study and 364 CT and/or MRI scans)	1.89	-	-	-	-
Elwany et al. 1983 (100 X-rays, 100 skulls X-rayed, 50 skulls — dissection study)	1.4/2.6	1.0/2.4	1.6/2.9	-	-
Stokovic et al. (51 skulls CBCT)	1.71	0.96	3.25	-	-
Jaworek-Troć et al. (296 CT scans)	2.1	0.7	3.7	8.11%	91.89%

CT — computed tomography; CBCT — cone-beam computed tomography; HRCT — high-resolution CT; MRI — magnetic resonance imaging; RSS — right sphenoid sinus; LSS — left sphenoid sinus; RSS≠LSS — different vertical dimensions; RSS=LSS — equal vertical dimensions

Mutlu et al. [18] obtained similar results, evaluating the mean transverse dimension of the right and left sphenoid sinuses as 3.18 cm (in the range of 2.13–5.54 cm). However, the aforementioned researchers provided the total dimension of the both sinuses (combining the measurement of the right and left sphenoid sinuses).

Elwany et al. [5] provided the following transverse dimensions of the sphenoid sinuses: the mean of 1.2 cm (the presellar type) and 1.9 cm (the postsellar type), the smallest 0.7 cm (the presellar type) and 1.4 cm (the postsellar type) and the biggest 1.4 cm (the presellar type) and 2.4 cm (the postsellar type). On the other hand, Stokovic et al. [21] estimated the average transverse dimension as 1.43 cm (ranging from 0.55 to 3.5 cm) (Table 8).

The vertical dimension was 2.1 cm on average, in the range of 0.7–3.7 cm. The different vertical dimensions in one patient was the most often variant — in 91.89% of the patients (91.84% females, 91.95% males).

Similar results were obtained by Sareen et al. [20], who assessed the mean vertical dimension of the sphenoid sinuses to be 2.2 cm (ranging from 1.4 to 3.6 cm).

Awadalla et al. [2] provided a different method of measuring the sphenoid sinuses by taking the length of the sinuses in their superior (the mean length was 13.9 mm) and inferior parts (the mean length was 25.9 mm), as well as the height in their anterior (the mean height was 18.9 mm) and posterior parts (the mean height was 12.1 mm). The mean height obtained by the aforementioned scientists in the

anterior part of the sinuses is akin to the average vertical dimension obtained in the present study. The discrepancies may be due to the method of measuring the dimensions of the sphenoid sinuses.

Elwany et al. [5] reported the following data for the vertical dimensions of the sphenoid sinuses: the mean of 1.4 cm (the presellar type) and 2.6 cm (the postsellar type), the smallest 1.0 cm (the presellar type) and 2.4 cm (the postsellar type), as well as the biggest 1.6 cm (the presellar type) and 2.9 cm (the postsellar type). On the other hand, Stokovic et al. [21] evaluated the average vertical dimension of the sphenoid sinuses to be 1.71 cm (ranging from 0.96 to 2.5 cm) (Table 9).

Lupascu et al. [16] evaluated the mean dimensions of the sphenoid sinuses as 24/20.5/18 mm (23.4/22.1/19.2 mm for the male group and 24.5/18.6/17.1 mm for the female group), but they did not provide the methods or the information to which dimension the obtained data applies.

The size of the sphenoid sinuses can be a predictor of the thickness of its walls, as suggested by Elwany et al. [5] who noted an inverse correlation between them, i.e. the bigger the sinus, the thinner its walls. That fact is of immense importance, as there is a higher risk of iatrogenic injuries done to the neighbouring critical neurovascular structures, namely the carotid artery or the optic nerve, when the walls of the sphenoid sinus are thinner [5]. The aforementioned authors have also found that the intercarotid distance was 4–9 mm shorter than the transverse dimension of the sinus, possibly allowing to pinpoint the location of the carotid arteries without any carotid dehiscence visible within the lumen of the sinus during the surgery [5].

Furthermore, there are studies that have found a correlation between the presence of the protrusion of the carotid canal or the optic nerve into the lumen of the sphenoid sinus and its type or dimensions [7, 21]. Stokovic et al. [21] noticed that in the case of the sellar type of the sinuses, chance of it being of “high risk” (defined as “pneumatization extensions to all parts of the sphenoid and protrusions of all neurovascular structures,” i.e. the maxillary nerve, pterygoid nerve, optic nerve and internal carotid artery) increased with its dimensions. The aforementioned authors have divided it further into three subcategories: a) the first one with high probabilities of pterygoid process pneumatization and optic and pterygoid nerve protrusions increased with sinus’ height; b) the second one with high probabilities of pterygoid process and greater wings pneumatization and maxillary nerve protrusions associated with width; c) and the third one with contra- and ipsi-lateral internal carotid protrusion with higher odds in the postsellar type and with greater sinus’ length [21]. Notwithstanding, the authors themselves state that more research should be carried out due to the limited sample they had (51 skulls).

sions increased with sinus’ height; b) the second one with high probabilities of pterygoid process and greater wings pneumatization and maxillary nerve protrusions associated with width; c) and the third one with contra- and ipsi-lateral internal carotid protrusion with higher odds in the postsellar type and with greater sinus’ length [21]. Notwithstanding, the authors themselves state that more research should be carried out due to the limited sample they had (51 skulls).

CONCLUSIONS




As pointed by our analysis, the anteroposterior dimension was on average 2.65 cm, the transverse dimension 1.98 cm, and the vertical dimension 2.1 cm. The great variance in the anatomy of the paranasal sinuses may complicate the surgical procedures undertaken in the aforementioned region. Knowledge of the dimensions of the sphenoid sinuses might point towards a higher chance of various neurovascular structures protrusion that might not be noted on standard imaging. Nonetheless, there is still a need of further research in this aspect that might hopefully prove useful in avoiding iatrogenic injuries to critical neurovascular structures surrounding the sphenoid sinuses. As such a study has not yet been conducted in the Polish population, we aimed to present the up-to-date representation of sphenoid sinuses’ dimensions combined with deductions of other, referenced here authors, in furtherance of diminishing the number of iatrogenic complications in the meantime.

REFERENCES

1. Abdullah BJ, Arasaratnam A, Kumar G, et al. The sphenoid sinuses: computed tomographic assessment of septation, relationship to the internal carotid arteries and sidewall thickness in the Malaysian population. *J HK Coll Radiol*. 2001; 4: 185–188.
2. Awadalla AM, Hussein Y, ElKammash TH. Anatomical and radiological parameters of the sphenoidal sinus among Egyptians and its impact on sellar region surgery. *Egyptian J Neurosurgery*. 2015; 30(1): 1–12.
3. Becker DG. The minimally invasive, endoscopic approach to sinus surgery. *J Long Term Eff Med Implants*. 2003; 13(3): 207–221, doi: [10.1615/jlongtermeffmedimplants.v13.i3.70](https://doi.org/10.1615/jlongtermeffmedimplants.v13.i3.70), indexed in Pubmed: [14516186](https://pubmed.ncbi.nlm.nih.gov/14516186/).
4. Bogusławska R. Badanie zatok przynosowych metodą tomografii komputerowej dla celów chirurgii endoskopowej. Warszawa, 1995.
5. Elwany S, Yacout YM, Talaat M, et al. Surgical anatomy of the sphenoid sinus. *J Laryngol Otol*. 1983; 97(3): 227–241, doi: [10.1017/s0022215100094056](https://doi.org/10.1017/s0022215100094056), indexed in Pubmed: [6833847](https://pubmed.ncbi.nlm.nih.gov/6833847/).

6. Eryilmaz A, Ozeri C, Bayiz U, et al. Functional endoscopic sinus surgery (FESS). *Turk J Med Res.* 1993; 11(5): 221–223.
7. Güldner C, Pistorius SM, Diogo I, et al. Analysis of pneumatization and neurovascular structures of the sphenoid sinus using cone-beam tomography (CBT). *Acta Radiol.* 2012; 53(2): 214–219, doi: [10.1258/ar.2011.110381](https://doi.org/10.1258/ar.2011.110381), indexed in Pubmed: [22383784](https://pubmed.ncbi.nlm.nih.gov/22383784/).
8. Haetinger RG, Navarro JAC, Liberti EA. Basilar expansion of the human sphenoidal sinus: an integrated anatomical and computerized tomography study. *Eur Radiol.* 2006; 16(9): 2092–2099, doi: [10.1007/s00330-006-0208-3](https://doi.org/10.1007/s00330-006-0208-3), indexed in Pubmed: [16642328](https://pubmed.ncbi.nlm.nih.gov/16642328/).
9. Jaworek-Troć J, Zarzecki M, Bonczar A, et al. Sphenoid bone and its sinus — anatomo-clinical review of the literature including application to FESS. *Folia Med Cracov.* 2019; 59(2): 45–59, doi: [10.24425/fmc.2019.128453](https://doi.org/10.24425/fmc.2019.128453).
10. Jaworek-Troć J, Zarzecki M, Mróz I, et al. The total number of septa and antra in the sphenoid sinuses — evaluation before the FESS. *Folia Med Cracov.* 2018; 58(3): 67–81, doi: [10.24425/fmc.2018.125073](https://doi.org/10.24425/fmc.2018.125073), indexed in Pubmed: [30521512](https://pubmed.ncbi.nlm.nih.gov/30521512/).
11. Kantarci M, Karasen RM, Alper F, et al. Remarkable anatomic variations in paranasal sinus region and their clinical importance. *Eur J Radiol.* 2004; 50(3): 296–302, doi: [10.1016/j.ejrad.2003.08.012](https://doi.org/10.1016/j.ejrad.2003.08.012), indexed in Pubmed: [15145491](https://pubmed.ncbi.nlm.nih.gov/15145491/).
12. Kapakin S. The paranasal sinuses: three-dimensional reconstruction, photo-realistic imaging, and virtual endoscopy. *Folia Morphol.* 2016; 75(3): 326–333, doi: [10.5603/FM.a2016.0006](https://doi.org/10.5603/FM.a2016.0006), indexed in Pubmed: [26916200](https://pubmed.ncbi.nlm.nih.gov/26916200/).
13. Kazkayasi M, Karadeniz Y, Arikan OK. Anatomic variations of the sphenoid sinus on computed tomography. *Rhinology.* 2005; 43(2): 109–114, indexed in Pubmed: [16008065](https://pubmed.ncbi.nlm.nih.gov/16008065/).
14. Keast A, Yelavich S, Dawes P, et al. Anatomical variations of the paranasal sinuses in Polynesian and New Zealand European computerized tomography scans. *Otolaryngol Head Neck Surg.* 2008; 139(2): 216–221, doi: [10.1016/j.otohns.2008.05.014](https://doi.org/10.1016/j.otohns.2008.05.014), indexed in Pubmed: [18656718](https://pubmed.ncbi.nlm.nih.gov/18656718/).
15. Krzeski A, Osuch-Wójcikiewicz E, Szwedowicz P, et al. Chirurgia endoskopowa w leczeniu guzów jam nosa i zatok przynosowych. *Mag ORL.* 2004; 3(3): 79–84.
16. Lupascu M, Comsa G, Zainea V. Anatomical variations of the sphenoid sinus: a study of 200 cases. *ARS Medica Tomitana.* 2014; 20(2): 57–62, doi: [10.2478/arsm-2014-0011](https://doi.org/10.2478/arsm-2014-0011).
17. Mafee MF, Chow JM, Meyers R. Functional endoscopic sinus surgery: anatomy, CT screening, indications, and complications. *Am J Roentgenol.* 1993; 160(4): 735–744, doi: [10.2214/ajr.160.4.8456654](https://doi.org/10.2214/ajr.160.4.8456654), indexed in Pubmed: [8456654](https://pubmed.ncbi.nlm.nih.gov/8456654/).
18. Mutlu C, Unlu HH, Goktan C, et al. Radiologic anatomy of the sphenoid sinus for intranasal surgery. *Rhinology.* 2001; 39(3): 128–132, indexed in Pubmed: [11721501](https://pubmed.ncbi.nlm.nih.gov/11721501/).
19. Pérez-Piñas I, Sabaté J, Carmona A, et al. Anatomical variations in the human paranasal sinus region studied by CT. *J Anat.* 2000; 197 (Pt 2): 221–227, doi: [10.1046/j.1469-7580.2000.19720221.x](https://doi.org/10.1046/j.1469-7580.2000.19720221.x), indexed in Pubmed: [11005714](https://pubmed.ncbi.nlm.nih.gov/11005714/).
20. Sareen D, Agarwal AK, Kaul JM, et al. Study of sphenoid sinus anatomy in relation to endoscopic surgery. *Int J Morphol.* 2005; 23(3), doi: [10.4067/s0717-95022005000300012](https://doi.org/10.4067/s0717-95022005000300012).
21. Štoković N, Trkulja V, Dumić-Čule I, et al. Sphenoid sinus types, dimensions and relationship with surrounding structures. *Ann Anat.* 2016; 203: 69–76, doi: [10.1016/j.aanat.2015.02.013](https://doi.org/10.1016/j.aanat.2015.02.013), indexed in Pubmed: [25843780](https://pubmed.ncbi.nlm.nih.gov/25843780/).
22. Terra ER, Guedes FR, Manzi FR, et al. Pneumatization of the sphenoid sinus. *Dentomaxillofac Radiol.* 2006; 35(1): 47–49, doi: [10.1259/dmfr/55048928](https://doi.org/10.1259/dmfr/55048928), indexed in Pubmed: [16421265](https://pubmed.ncbi.nlm.nih.gov/16421265/).

Unusual variations in the branching pattern of the coeliac trunk and their clinical significance

A. Juszcak¹, J. Czyżowski², A. Mazurek¹, J.A. Walocha¹, A. Pasternak¹

¹Department of Anatomy, Jagiellonian University Medical College, Krakow, Poland

²Institute of Diagnostic Imaging, J. Dietl Specialist Hospital, Krakow, Poland

[Received: 23 April 2020; Accepted: 7 June 2020]

Background: The anatomical variations of the coeliac trunk are due to developmental changes in the ventral segmental arteries. Multidetector computed tomography (MDCT) has been used to investigate vascular anatomy for scientific and diagnostic purposes. These studies allow for much larger sample sizes than traditional cadaveric studies. The aim of this research was to isolate rare anatomical variants of the coeliac trunk and emphasize their clinical significance.

Materials and methods: A descriptive, retrospective study was carried out on MDCT angiographies performed from January 2020 till March 2020 in Polish patients. Coeliac trunk was studied and normal and anatomical variations were identified.

Results: Out of total 350 patients, hepatogastrosplenic trunk was predominant. However, we observed: coeliaco-mesenteric and hepatogastric trunk type, hepatic artery variations and coeliac axis stenosis with collateral mesenteric circulation.

Conclusions: Rare variations of the coeliac trunk should always be anticipated before radiological and surgical interventions. Knowledge of unusual coeliac trunk anatomy is important in hepatopancreatobiliary surgery, transplantology, and interventional radiology. (Folia Morphol 2021; 80, 2: 283–289)

Key words: coeliac trunk, variations, multidetector computed tomography angiography

INTRODUCTION

The main mesenteric vessels, the coeliac trunk, the superior mesenteric artery (SMA), and the inferior mesenteric artery (IMA) develop from the primitive ventral segmental (splanchnic) branches, which are originally paired vessels. They become the unpaired after the fusion of two dorsal aortae and, next, nourish the gut tube (after yolk sac incorporation) [42]. There is regression of all segmental arteries as development proceeds, except for three of these primitive communications, with only precursors to the three major mesenteric vessels and longitudinal anastomotic

vessels remained. The 10th segmental artery gives rise to the coeliac trunk, the 13th segmental artery gives rise to the SMA, and the 21st or 22nd artery gives rise to the IMA. The longitudinal anastomotic vessels between the coeliac trunk and SMA, and between the SMA and IMA disappear [25, 36, 38, 47]. Persistence, incomplete regression, or disappearance of parts of these primitive ventral segmental arteries could give rise to numerous variations of SMA (Fig. 1) [33, 52]. Understanding the different anatomical variations of mesenteric circulation is mandatory in various diagnostic and surgical procedures in the upper abdomen.

Address for correspondence: A. Pasternak, MD, PhD, Department of Anatomy, Jagiellonian University Medical College, ul. Kopernika 12, 31–034 Kraków, Poland, tel: +48 12 422 95 11, fax: +48 12 422 95 11, e-mail: artur.pasternak@uj.edu.pl

This article is available in open access under Creative Common Attribution-Non-Commercial-No Derivatives 4.0 International (CC BY-NC-ND 4.0) license, allowing to download articles and share them with others as long as they credit the authors and the publisher, but without permission to change them in any way or use them commercially.

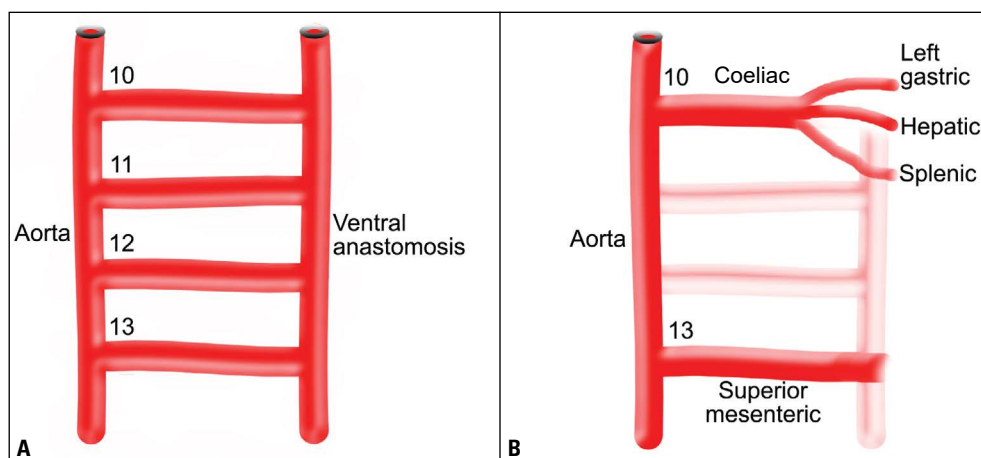


Figure 1. The embryologic origin of the visceral arteries; **A.** Primitive ventral segmental arteries; **B.** Normal anatomy demonstrating the coeliac trunk arising from the 10th and superior mesenteric artery from 13th segmental artery, respectively.

Nowadays, evaluation of arteries branching from the abdominal aorta is possible owing to a minimally invasive examination — the multidetector computed tomography angiography (MDCTA). The latest 64-row computed tomography (CT) scanners allow for a very high spatial resolution (up to 0.4 mm) and a temporal resolution of only a few seconds. These technical developments have made it possible to acquire detailed knowledge of the abdominal vasculature prior to surgery. This makes the technique indispensable for surgeons, for example, in planning liver transplantation surgery or, more commonly, in fashioning intestinal anastomoses, the success of which is dependent on adequate vascularity [10].

The purpose of this study is to determine arterial branches of the coeliac trunk by using noninvasive imaging technique, MDCTA of the abdominal aorta. Owing to the large number of the analysed examinations, it was possible to isolate rare anatomical variants of coeliac trunk and emphasize their clinical significance.

MATERIALS AND METHODS

A computer search was performed to identify all the patients who had undergone MDCTA of the abdominal aorta at the Institute of Diagnostic Imaging, J. Dietl Specialist Hospital in Krakow, Poland between January 2020 and March 2020. A total of 350 CT angiographies of abdominal aorta of patients was included in our study and retrospectively reviewed to evaluate the visibility of the coeliac trunk and its branches. All patients met the following inclusion criteria: performance of CT scan in the arterial and venous phase for a variety of clinical indications. Exclusion criteria were the presence of any condition likely to affect normal

vascular anatomy, such as prior gastric resection surgery; extended jejunoileal resections; colonic resections; anterior rectal resection; partial pancreaticoduodenectomy; bariatric surgery; liver, pancreas, bowel or multiorgan transplants; and major hepatic resections. Patients were also excluded if they had aneurysmal disease of the splanchnic arteries, severe aortic atherosclerosis, arteritis with possible involvement of the vessels being studied (Kawasaki's disease, polyarteritis nodosa, Takayasu's arteritis, Churg-Strauss syndrome). The study was reviewed and approved by the local Ethics Committee; number 1072.6120.78.2019. The requirement for informed patient consent was waived due to the retrospective nature of the study. CT images were obtained with a 64-channel MDCT scanner (Aquilion 64, Toshiba Medical Systems Corporation, Tokyo, Japan). The contrast medium used was iohexal (Omnipaque 350; GE Healthcare AS, Oslo, Norway), which was administered intravenously by injection pump at a rate of 3–4 mL/s. The dose of the contrast agent was 1 mL/kg body weight and the upper limit of dose was set at 100 mL for every patient.

Image analysis was done on a dedicated Toshiba console equipped with reconstruction software. We used multiplanar reconstructions (MPRs) in the three spatial planes and three-dimensional reconstructions using maximum intensity projection (MIP) and volume rendering (VR). The arterial phase was used to create vascular maps of the coeliac axis including the origin(s) of the hepatic artery and origin of the SMA. Images were interpreted by a radiologist with 15 years of experience in abdominal and vascular imaging. Statistical analysis was done with the Statistical Package for the Social Sciences (SPSS) version 21.

Table 1. Hepatic artery variations: Michels' classification

Description	Type
Normal anatomy	I
Replaced left hepatic artery arising from left gastric artery	II
Replaced right hepatic artery arising from superior mesenteric artery	III
Coexistence of type I and type II	IV
Accessory left hepatic artery arising from left gastric artery	V
Accessory right hepatic artery arising from superior mesenteric artery	VI
Coexistence of type V and type VI	VII
Replaced right hepatic artery and accessory left hepatic artery or replaced left hepatic artery and accessory right hepatic artery	VIII
Common hepatic artery arising from superior mesenteric artery	IX
Common hepatic artery arising from the left gastric artery	X

RESULTS

The study population comprised 198 women (56.6%) and 152 men (43.4%) aged between 46 and 88 years (mean age 62.7 ± 15.3). According to Adachi and Michels' classification different types of normal anatomy or anatomic variants were described (Table 1).

Hepato-gastro-splenic trunk

This is the classical trifurcation of the coeliac trunk, detected in a total of 340 (97.14%) patients of our series. The typical variant was defined as: the vascular trunk located approximately 1 cm above the SMA and splitting into 3 branches: left gastric artery (LGA), common hepatic artery (CHA) and splenic artery (SA).

Coeliaco-mesenteric trunk type

Common origin of the coeliac trunk and of the SMA — the coeliaco-mesenteric trunk (CMT) — was observed in 5 (1.4%) patients (Fig. 2).

Hepato-gastric trunk type

Common hepatic and left gastric arteries origin from a common trunk whereas the splenic artery originates from the aorta (1/0, 28%) (Fig. 3).

Hepatic artery variations

The following two hepatic arterial variants were observed: the gastro-splenic trunk with the common hepatic artery arising from the SMA (Michels' classification type IX) (Fig. 4) and the gastro-splenic trunk

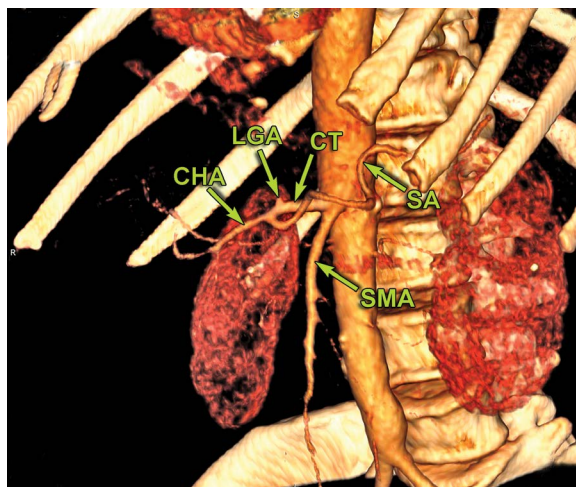


Figure 2. Coeliaco-mesenteric trunk type; CT — coeliac trunk; LGA — left gastric artery; CHA — common hepatic artery; SA — splenic artery; SMA — superior mesenteric artery.

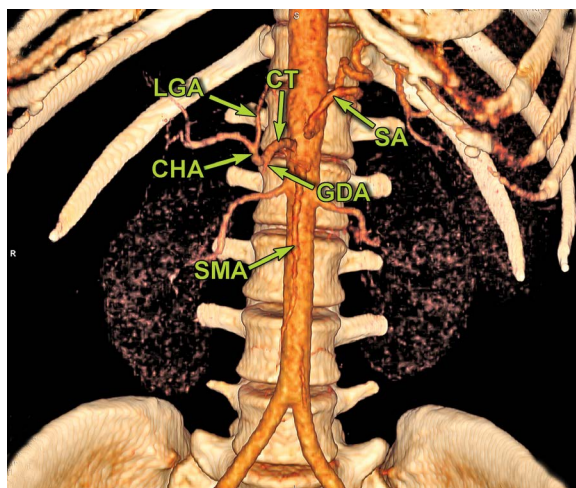


Figure 3. Hepato-gastric trunk type in association with the independent arising of splenic artery (SA); CT — coeliac trunk; CHA — common hepatic artery; LGA — left gastric artery; GDA — gastroduodenal artery; SMA — superior mesenteric artery.

with the CHA arising independently from aorta and accessory right hepatic artery originating from CHA (Fig. 5).

Coeliac artery stenosis

In 1 case there was coeliac artery stenosis resulting in the development of collateral mesenteric circulation, i.e. coeliac artery compression syndrome (CACS) (Fig. 6).

We also observed coeliac artery stenosis with extended collateral mesenteric circulation and SMA originating from aorta slightly above the coeliac trunk (Fig. 7).

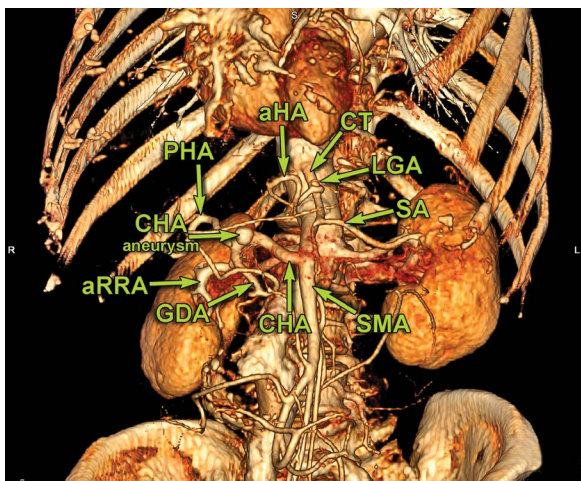


Figure 4. Gastro-splenic trunk type in association with the common hepatic artery (CHA) arising from the superior mesenteric artery; CT — coeliac trunk; LGA — left gastric artery; SA — splenic artery; PHA — proper hepatic artery; GDA — gastroduodenal artery; SMA — superior mesenteric artery; aRRA — accessory right renal artery; CHA aneurysm — common hepatic artery aneurysm; aHA — accessory hepatic artery.

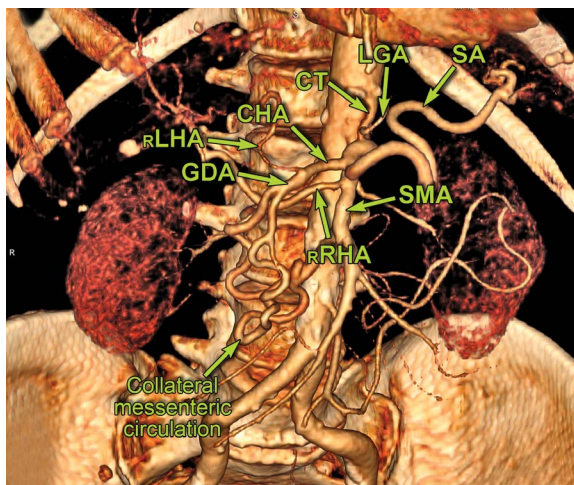


Figure 6. Coeliac artery stenosis resulting in the development of collateral mesenteric circulation; CT — coeliac trunk; LGA — left gastric artery; CHA — common hepatic artery; SA — splenic artery; SMA — superior mesenteric artery; rRHA — replaced right hepatic artery; GDA — gastroduodenal artery; rLHA — replaced left hepatic artery.

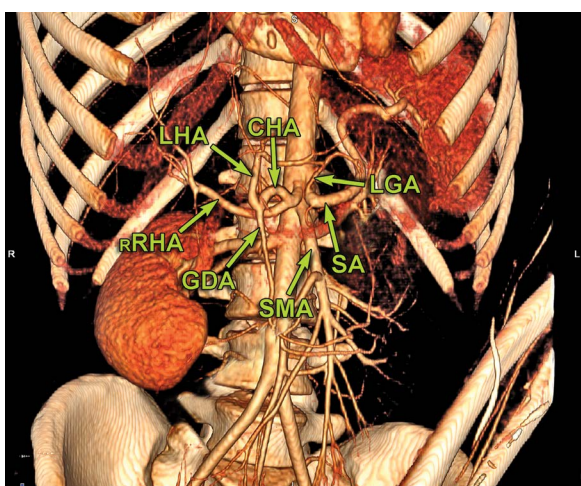


Figure 5. Gastro-splenic trunk in association with the common hepatic artery (CHA) arising independently from aorta and accessory right hepatic artery originating from CHA; LGA — left gastric artery; SA — splenic artery; SMA — superior mesenteric artery; GDA — gastroduodenal artery; rRHA — replaced right hepatic artery; LHA — left hepatic artery.

In either case the stenosed coeliac trunk corresponded with a hepato-gastro-splenic type in a false configuration.

DISCUSSION

Most of anatomical reports on the variation of CT are cadaver based studies [14, 22, 23, 29, 35, 39]. However, in recent years MDCT has been used to investigate vascular anatomy for scientific and

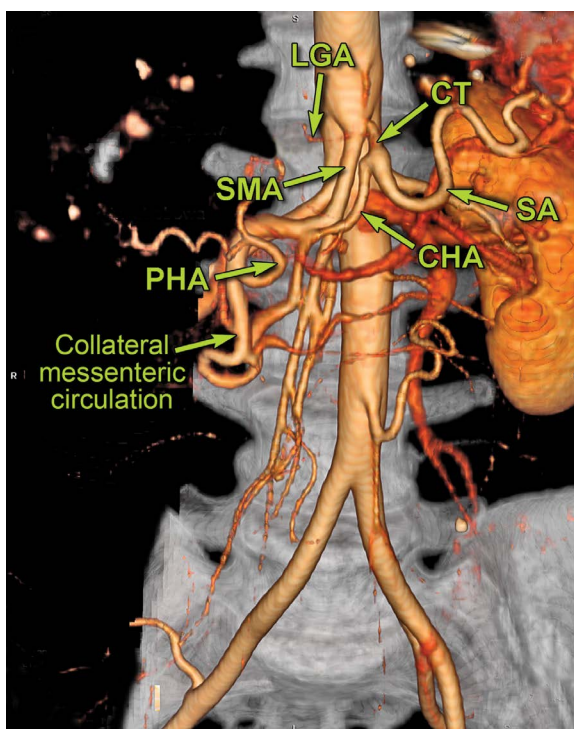


Figure 7. Coeliac artery stenosis with extended collateral mesenteric circulation and superior mesenteric artery (SMA) originating from aorta slightly above the coeliac trunk; CT — coeliac trunk; LGA — left gastric artery; SA — splenic artery; CHA — common hepatic artery; PHA — proper hepatic artery.

diagnostic purposes. These studies allow for much larger sample sizes than traditional cadaveric studies.

The anatomical variations of the CT, SMA and IMA are due to developmental changes in the ventral seg-

mental arteries [6]. Incomplete fusion or malfusion of the vitelline arteries during the developmental stage may be responsible for the variations of the coeliac trunk.

A CMT occurs when the 10th to 12th vitelline arteries regress and a large portion of the ventral anastomosis persists to connect the coeliac artery and branches to the SMA. The common trunk of the coeliac artery and the SMA is a rare variation and according to the earlier studies, it has been found in < 2% of patients [34, 42]. A patient with CMT is at risk of mesenteric ischaemia because there lack some of the protective benefits of dual-origin vessels with multiple mutually supporting anastomoses [2, 48, 49]. Anything that compromises the single common trunk arising from the abdominal aorta puts the entire vascular region of the major abdominal viscera at risk of ischaemia [43]. Furthermore, CMT variant could change the SMA angle from the aorta, thus increasing or decreasing the potential for compression of the third portion of the duodenum [43]. Pathologies involving CMT are very rare and include stenosis and aneurysms of the common trunk [9, 24]. A common CMT thus has a strong potential for development and progression of atherosclerosis along the trunk, which can have severe consequences as it results in ischaemia of the regions supplied by both the coeliac trunk and SMA. Review of the literature reveals several cases of coeliacomesenteric stenosis [1, 4, 24, 27, 30, 37, 44]. In these case reports, one patient had an open bypass graft, two had percutaneous angioplasty/stenting, one underwent open surgical endarterectomy with patch-graft angioplasty, one underwent open thrombectomy and one had extra-anatomic right iliac retrograde SMA bypass grafting. The CMT has been reported to be affected by aneurysms, atherosclerotic degeneration, thrombosis, and nutcracker syndrome [28].

The types of hepatic artery variation have been detailed described in Michels' classification [32] and other studies [8, 16, 41], as well as anatomical monographs [28]. According to Michels' classification [32], the most common variant observed was a replaced right hepatic artery originating from the SMA (Michels III), identified in 9.3% of patients. It is important to recognize a replaced right hepatic artery when performing pancreaticoduodenectomy and for porta hepatis dissection during hepatic resection. Therefore, if a head or uncinat process pancreatic cancer involves a replaced right hepatic, it precludes the patient from surgical resection. The second most common arterial variant identified was a replaced left hepatic artery (LHA) originating from the left gastric artery, seen in 5.9% of

patients (Michels II). It is important to detect this variant prior to performing left hepatectomy because this vessel must be identified and ligated; the knowledge of this variant facilitates portal dissection because the major arterial branch to the left liver does not need to be found in the porta hepatis. A replaced LHA arising from LGA, may provide a source for collaterals during obstruction of structures in porta hepatis. In addition, it may get damaged during oesophagogastrectomy. This may lead to increased mortality due to hepatic necrosis [15]. Only patients with chronic liver diseases and a reduction of liver reserve functions are most susceptible to ischaemia caused by the replaced LHA ligation; in effect, Huang et al. [17] suggested that the replaced LHA should be preserved in these cases. In order to reduce these ischaemic liver complications, some surgeons suggested a number of techniques for the preservation of the replaced LHA: preservation and peeling of the LGA along with the low tie of the LGA [7]. The LGA branches, directed towards the lesser curvature and the oesophagus, are ligated separately to preserve the LGA and replaced LHA. Next, the LGA is ligated distal to the origin of the replaced accessory LHA. The third most common arterial variant observed was the common hepatic artery arising from the SMA, seen in 3.6% of cases (Michels IX). We identified this variant in our study. Michels IX variant requires a twisting in anastomosis' order since the artery has to be sutured before the portal vein because of its deeper location posterior to the vein. An accessory LHA originating from the left gastric artery was found (Michels V). This accessory artery provides an additional source of arterial blood to the left hepatic lobe and may be sutured without compromising the arterial supply to the left hepatic lobe [18]. Knowledge of the variant hepatic arteries is of greatest importance in liver transplantation, since appropriate technical adjustments must be made both in organ procurement and in re-anastomosis in the recipient [12].

Patients with stenosis or occlusion of a single mesenteric artery seldom develop symptoms of chronic mesenteric ischaemia. It is commonly accepted that this is due to the extensive mesenteric arterial collateral circulation. However, mesenteric ischaemia may occur in these patients, for example, in patients with CACS (Dunbar syndrome). This is nonatherosclerotic, respiration-dependent anatomical compression of the coeliac artery by the median arcuate ligament and diaphragmatic crura, which leads to extensive mesenteric collateral circulation. This extrinsic compression

causes a constellation of symptoms including nausea, vomiting, weight loss, and postprandial epigastric pain [26]. Extensive collaterals are likely to have a compensating function preventing ischaemia in the coeliac artery outflow region [45].

Several studies have demonstrated successful treatment of CACS with coeliac artery release through release of the arcuate ligament [3, 5, 13, 19, 46].

Regarding gastrectomy with D2 lymphadenectomy for cancer, it is necessary during surgery to ligate at the root and cut off the left gastric artery, which may affect the hepatic tissue supplied by the replaced/ accessory LHA deriving from the LGA, thus influencing hepatic function, especially for the replaced right hepatic artery [11, 31, 40]. Therefore, accurate preoperative assessment of whether the abnormal LHA is replaced by the right hepatic artery or accessory right hepatic artery is especially important.

Preoperative knowledge of variant arterial anatomy may reduce extensive exploration during surgery and consequently decrease the risk of vascular damage [51]. According to our current and previous findings, we suggest to apply reconstruction method for evaluation of variations at least in patients who are candidate for mentioned surgical or interventional procedures [20, 21]. Preoperative MDCTA with three-dimensional reconstruction should be performed before any major surgery on the upper gastrointestinal organs to identify all vascular variations to allow optimal preoperative planning.

CONCLUSIONS



Rare variations of the coeliac trunk should always be anticipated before radiological and surgical interventions. Knowledge of unusual coeliac trunk anatomy is important in hepatopancreatobiliary surgery, transplantology, and interventional radiology.

REFERENCES

1. Ailawadi G, Cowles RA, Stanley JC, et al. Common celiomesenteric trunk: aneurysmal and occlusive disease. *J Vasc Surg.* 2004; 40(5): 1040–1043, doi: [10.1016/j.jvs.2004.08.028](https://doi.org/10.1016/j.jvs.2004.08.028), indexed in Pubmed: [15557926](https://pubmed.ncbi.nlm.nih.gov/15557926/).
2. Alakkam A, Hill RV, Saggio G. Superior mesenteric origin of the proper hepatic artery: embryological and clinical implications. *Surg Radiol Anat.* 2016; 38(6): 747–750, doi: [10.1007/s00276-015-1599-0](https://doi.org/10.1007/s00276-015-1599-0), indexed in Pubmed: [26650050](https://pubmed.ncbi.nlm.nih.gov/26650050/).
3. Aschenbach R, Basche S, Vogl TJ. Compression of the celiac trunk caused by median arcuate ligament in children and adolescent subjects: evaluation with contrast-enhanced MR angiography and comparison with Doppler US evaluation. *J Vasc Interv Radiol.* 2011; 22(4): 556–561, doi: [10.1016/j.jvir.2010.11.007](https://doi.org/10.1016/j.jvir.2010.11.007), indexed in Pubmed: [21316263](https://pubmed.ncbi.nlm.nih.gov/21316263/).
4. Ayers NP, Zacharias SJ, Abu-Fadel MS, et al. Successful use of blunt microdissection catheter in a chronic total occlusion of a celiomesenteric artery. *Catheter Cardiovasc Interv.* 2007; 69(4): 546–549, doi: [10.1002/ccd.20954](https://doi.org/10.1002/ccd.20954), indexed in Pubmed: [17192962](https://pubmed.ncbi.nlm.nih.gov/17192962/).
5. Berard X, Cau J, Déglise S, et al. Laparoscopic surgery for coeliac artery compression syndrome: current management and technical aspects. *Eur J Vasc Endovasc Surg.* 2012; 43(1): 38–42, doi: [10.1016/j.ejvs.2011.09.023](https://doi.org/10.1016/j.ejvs.2011.09.023), indexed in Pubmed: [22001148](https://pubmed.ncbi.nlm.nih.gov/22001148/).
6. Cavdar S, Sehirli U, Pekin B. Celiomesenteric trunk. *Clin Anat.* 1997; 10(4): 231–234, doi: [10.1002/\(SICI\)1098-2353\(1997\)10:4<231::AID-CA2>3.0.CO;2-V](https://doi.org/10.1002/(SICI)1098-2353(1997)10:4<231::AID-CA2>3.0.CO;2-V), indexed in Pubmed: [9213038](https://pubmed.ncbi.nlm.nih.gov/9213038/).
7. Cirocchi R, D'Andrea V, Amato B, et al. Aberrant left hepatic arteries arising from left gastric arteries and their clinical importance. *Surgeon.* 2020; 18(2): 100–112, doi: [10.1016/j.surge.2019.06.002](https://doi.org/10.1016/j.surge.2019.06.002), indexed in Pubmed: [31337536](https://pubmed.ncbi.nlm.nih.gov/31337536/).
8. Daly J. Long-term hepatic arterial infusion chemotherapy. *Arch Surg.* 1984; 119(8): 936, doi: [10.1001/archsurg.1984.01390200054013](https://doi.org/10.1001/archsurg.1984.01390200054013).
9. Detroux M, Anidjar S, Nottin R. Aneurysm of a common celiomesenteric trunk. *Ann Vasc Surg.* 1998; 12(1): 78–82, doi: [10.1007/s100169900120](https://doi.org/10.1007/s100169900120), indexed in Pubmed: [9452002](https://pubmed.ncbi.nlm.nih.gov/9452002/).
10. Ferrari R, De Cecco CN, Iafrate F, et al. Anatomical variations of the coeliac trunk and the mesenteric arteries evaluated with 64-row CT angiography. *Radiol Med.* 2007; 112(7): 988–998, doi: [10.1007/s11547-007-0200-2](https://doi.org/10.1007/s11547-007-0200-2), indexed in Pubmed: [17952680](https://pubmed.ncbi.nlm.nih.gov/17952680/).
11. Friesen SR. The significance of the anomalous origin of the left hepatic artery from the left gastric artery in operations upon the stomach and esophagus. *Am Surg.* 1957; 23(12): 1103–1108, indexed in Pubmed: [13488026](https://pubmed.ncbi.nlm.nih.gov/13488026/).
12. Gielecki J, Zurada A, Sonpal N, et al. The clinical relevance of coeliac trunk variations. *Folia Morphol.* 2005; 64(3): 123–129, indexed in Pubmed: [16228946](https://pubmed.ncbi.nlm.nih.gov/16228946/).
13. Grottemeyer D, Duran M, Iskandar F, et al. Median arcuate ligament syndrome: vascular surgical therapy and follow-up of 18 patients. *Langenbecks Arch Surg.* 2009; 394(6): 1085–1092, doi: [10.1007/s00423-009-0509-5](https://doi.org/10.1007/s00423-009-0509-5), indexed in Pubmed: [19506899](https://pubmed.ncbi.nlm.nih.gov/19506899/).
14. Gurgacz AM, Horbaczewska A, Klimek-Piotrowska W, et al. Variations in hepatic vascularisation: lack of a proper hepatic artery. Two case reports. *Folia Morphol.* 2011; 70(2): 130–134, indexed in Pubmed: [21630235](https://pubmed.ncbi.nlm.nih.gov/21630235/).
15. Hemming AW, Finley RJ, Evans KG, et al. Esophagogastrectomy and the variant left hepatic artery. *Ann Thorac Surg.* 1992; 54(1): 166–168, doi: [10.1016/0003-4975\(92\)91173-7](https://doi.org/10.1016/0003-4975(92)91173-7), indexed in Pubmed: [1610235](https://pubmed.ncbi.nlm.nih.gov/1610235/).
16. Hiatt JR, Gabbay J, Busuttill RW. Surgical anatomy of the hepatic arteries in 1000 cases. *Ann Surg.* 1994; 220(1): 50–52, doi: [10.1097/0000658-199407000-00008](https://doi.org/10.1097/0000658-199407000-00008), indexed in Pubmed: [8024358](https://pubmed.ncbi.nlm.nih.gov/8024358/).
17. Huang CM, Chen QY, Lin JX, et al. Short-term clinical implications of the accessory left hepatic artery in patients undergoing radical gastrectomy for gastric cancer. *PLoS One.* 2013; 8(5): e64300, doi: [10.1371/journal.pone.0064300](https://doi.org/10.1371/journal.pone.0064300), indexed in Pubmed: [23717589](https://pubmed.ncbi.nlm.nih.gov/23717589/).
18. Iezzi R, Cotroneo AR, Giancristofaro D, et al. Multidetector-row CT angiographic imaging of the celiac trunk: anatomy and normal variants. *Surg Radiol Anat.* 2008; 30(4): 303–310, doi: [10.1007/s00276-008-0324-7](https://doi.org/10.1007/s00276-008-0324-7), indexed in Pubmed: [18286222](https://pubmed.ncbi.nlm.nih.gov/18286222/).
19. Jimenez JC, Harlander-Locke M, Dutson EP. Open and laparoscopic treatment of median arcuate ligament syndrome. *J Vasc Surg.* 2012; 56(3): 869–873, doi: [10.1016/j.jvs.2012.04.057](https://doi.org/10.1016/j.jvs.2012.04.057), indexed in Pubmed: [22743019](https://pubmed.ncbi.nlm.nih.gov/22743019/).

20. Juszcak A, Czyżowski J, Mazurek A, et al. Anatomical variants of celiac trunk in Polish population using multidetector computed tomography angiography. *Folia Morphol.* 2020 [Epub ahead of print], doi: [10.5603/FM.a2020.0051](https://doi.org/10.5603/FM.a2020.0051), indexed in Pubmed: [32394417](https://pubmed.ncbi.nlm.nih.gov/32394417/).
21. Juszcak A, Mazurek A, Walocha JA, et al. Coeliac trunk and its anatomic variations: a cadaveric study. *Folia Morphol.* 2021; 80(1): 114–121, doi: [10.5603/FM.a2020.0042](https://doi.org/10.5603/FM.a2020.0042), indexed in Pubmed: [32301103](https://pubmed.ncbi.nlm.nih.gov/32301103/).
22. Juszcak A, Solewski B, Loukas M, et al. Unusual branching pattern of celiac trunk associated with supernumerary hepatic arteries and abnormal adrenal venous drainage – case study and review of the literature. *Folia Med Cracov.* 2017; 57(3): 29–36, indexed in Pubmed: [29263452](https://pubmed.ncbi.nlm.nih.gov/29263452/).
23. Kahn CI, MacNeil M, Fanola C, et al. Complex arterial patterning in an anatomical donor. *Trans Res Anat.* 2018(12): 11–19.
24. Kalra M, Panneton JM, Hofer JM, et al. Aneurysm and stenosis of the celiomesenteric trunk: a rare anomaly. *J Vasc Surg.* 2003; 37(3): 679–682, doi: [10.1067/mva.2003.37](https://doi.org/10.1067/mva.2003.37), indexed in Pubmed: [12618711](https://pubmed.ncbi.nlm.nih.gov/12618711/).
25. Katagiri H, Ichimura K, Sakai TA. case of celiacomesenteric trunk with some other arterial anomalies in a Japanese woman. *Anat Sci Int.* 2007; 82: 53–58.
26. Kim EN, Lamb K, Relles D, et al. Median arcuate ligament syndrome-review of this rare disease. *JAMA Surg.* 2016; 151(5): 471–477, doi: [10.1001/jamasurg.2016.0002](https://doi.org/10.1001/jamasurg.2016.0002), indexed in Pubmed: [26934394](https://pubmed.ncbi.nlm.nih.gov/26934394/).
27. Lagoutte N, Facy O, Guiu B, et al. Celiacomesenteric trunk: a variation that must be known before aortic surgery. *Clin Pract.* 2011; 1(3): e69, doi: [10.4081/cp.2011.e69](https://doi.org/10.4081/cp.2011.e69), indexed in Pubmed: [24765330](https://pubmed.ncbi.nlm.nih.gov/24765330/).
28. Lanz VT, Wachsmuth W. *Lanz/Wachsmuth Practical Anatomy.* Springer-Verlag, Berlin 2003.
29. Lee JK, Kang SR, Kim J, et al. A rare variation of the incomplete coeliac trunk. *Folia Morphol.* 2016; 75(1): 122–124, doi: [10.5603/FM.a2015.0074](https://doi.org/10.5603/FM.a2015.0074), indexed in Pubmed: [26365854](https://pubmed.ncbi.nlm.nih.gov/26365854/).
30. Lovisetto F, Finocchiaro De Lorenzi G, Stancampiano P, et al. Thrombosis of celiacomesenteric trunk: report of a case. *World J Gastroenterol.* 2012; 18(29): 3917–3920, doi: [10.3748/wjg.v18.i29.3917](https://doi.org/10.3748/wjg.v18.i29.3917), indexed in Pubmed: [22876046](https://pubmed.ncbi.nlm.nih.gov/22876046/).
31. Lurie AS. The significance of the variant left accessory hepatic artery in surgery for proximal gastric cancer. *Arch Surg.* 1987; 122: 725–728.
32. Michels NA. Newer anatomy of the liver and its variant blood supply and collateral circulation. *Am J Surg.* 1966; 112(3): 337–347, doi: [10.1016/0002-9610\(66\)90201-7](https://doi.org/10.1016/0002-9610(66)90201-7), indexed in Pubmed: [5917302](https://pubmed.ncbi.nlm.nih.gov/5917302/).
33. Nantiskarn C, Kiat A. Aberrant branches of the superior mesenteric artery detected by MDCT angiography of abdominal aorta. *Asian Biomedicine.* 2012; 6(2): 219–226.
34. Nebesar RA, Kornblith PL, Pollard JJ, Michels NA. *Celiac and superior mesenteric arteries: a correlation of angiograms with dissections.* Little, Brown, Boston 1969.
35. Olewnik Ł, Wysiadecki G, Polguy M, et al. Types of coeliac trunk branching including accessory hepatic arteries: a new point of view based on cadaveric study. *Folia Morphol.* 2017; 76(4): 660–667, doi: [10.5603/FM.a2017.0053](https://doi.org/10.5603/FM.a2017.0053), indexed in Pubmed: [28612916](https://pubmed.ncbi.nlm.nih.gov/28612916/).
36. Oran I, Yesildag A, Memis A. Aortic origin of right hepatic artery and superior mesenteric origin of splenic artery: two rare variations demonstrated angiographically. *Surg Radiol Anat.* 2001; 23(5): 349–352, doi: [10.1007/s00276-001-0349-7](https://doi.org/10.1007/s00276-001-0349-7), indexed in Pubmed: [11824137](https://pubmed.ncbi.nlm.nih.gov/11824137/).
37. Ratra A, Campbell S. Recurrent mesenteric ischemia from celiomesenteric trunk stenosis. *Cureus.* 2018; 10(6): e2751, doi: [10.7759/cureus.2751](https://doi.org/10.7759/cureus.2751), indexed in Pubmed: [30094108](https://pubmed.ncbi.nlm.nih.gov/30094108/).
38. Rosenblum JD, Boyle CM, Schwartz LB. The mesenteric circulation. *Anatomy and physiology.* *Surg Clin North Am.* 1997; 77(2): 289–306, doi: [10.1016/s0039-6109\(05\)70549-1](https://doi.org/10.1016/s0039-6109(05)70549-1), indexed in Pubmed: [9146713](https://pubmed.ncbi.nlm.nih.gov/9146713/).
39. Selvaraj L, Sundaramurthi I. Study of normal branching pattern of the coeliac trunk and its variations using CT angiography. *J Clin Diagn Res.* 2015; 9(9): AC01–AC04, doi: [10.7860/JCDR/2015/12593.6523](https://doi.org/10.7860/JCDR/2015/12593.6523), indexed in Pubmed: [26500893](https://pubmed.ncbi.nlm.nih.gov/26500893/).
40. Shinohara T, Ohyama S, Muto T, et al. The significance of the aberrant left hepatic artery arising from the left gastric artery at curative gastrectomy for gastric cancer. *Eur J Surg Oncol.* 2007; 33(8): 967–971, doi: [10.1016/j.ejso.2007.02.030](https://doi.org/10.1016/j.ejso.2007.02.030), indexed in Pubmed: [17418995](https://pubmed.ncbi.nlm.nih.gov/17418995/).
41. Suzuki T, Nakayasu A, Kawabe K, et al. Surgical significance of anatomic variations of the hepatic artery. *Am J Surg.* 1971; 122(4): 505–512, doi: [10.1016/0002-9610\(71\)90476-4](https://doi.org/10.1016/0002-9610(71)90476-4), indexed in Pubmed: [5098656](https://pubmed.ncbi.nlm.nih.gov/5098656/).
42. Tandler J. über die Varietäten der Arteria coeliaca und deren Entwicklung. Beiträge und Referate zur Anatomie und Entwicklungsgeschichte. *Anat Embryol.* 1904; 25(2): 473–500, doi: [10.1007/bf02300762](https://doi.org/10.1007/bf02300762).
43. Tang W, Shi J, Kuang LQ, et al. Celiomesenteric trunk: New classification based on multidetector computed tomography angiographic findings and probable embryological mechanisms. *World J Clin Cases.* 2019; 7(23): 3980–3989, doi: [10.12998/wjcc.v7.i23.3980](https://doi.org/10.12998/wjcc.v7.i23.3980), indexed in Pubmed: [31832400](https://pubmed.ncbi.nlm.nih.gov/31832400/).
44. Tasleem SH, Younas F, Syed FA, et al. Endovascular repair of common celiomesenteric trunk stenosis. *Vasa.* 2010; 39(4): 341–343, doi: [10.1024/0301-1526/a000059](https://doi.org/10.1024/0301-1526/a000059), indexed in Pubmed: [21104624](https://pubmed.ncbi.nlm.nih.gov/21104624/).
45. van Petersen AS, Kolkman JJ, Gerrits DG, et al. Dutch Mesenteric Ischemia Study Group. Clinical significance of mesenteric arterial collateral circulation in patients with celiac artery compression syndrome. *J Vasc Surg.* 2017; 65(5): 1366–1374, doi: [10.1016/j.jvs.2016.11.052](https://doi.org/10.1016/j.jvs.2016.11.052), indexed in Pubmed: [28259570](https://pubmed.ncbi.nlm.nih.gov/28259570/).
46. van Petersen AS, Vriens BH, Huisman ADB, et al. Retroperitoneal endoscopic release in the management of celiac artery compression syndrome. *J Vasc Surg.* 2009; 50(1): 140–147, doi: [10.1016/j.jvs.2008.12.077](https://doi.org/10.1016/j.jvs.2008.12.077), indexed in Pubmed: [19563962](https://pubmed.ncbi.nlm.nih.gov/19563962/).
47. Walker TG. Mesenteric vasculature and collateral pathways. *Semin Intervent Radiol.* 2009; 26(3): 167–174, doi: [10.1055/s-0029-1225663](https://doi.org/10.1055/s-0029-1225663), indexed in Pubmed: [21326561](https://pubmed.ncbi.nlm.nih.gov/21326561/).
48. Wang Yi, Chen P, Shen N, et al. Celiomesenteric trunk with concurrent aneurysm: report of a case. *Surg Today.* 2010; 40(5): 477–481, doi: [10.1007/s00595-009-4164-9](https://doi.org/10.1007/s00595-009-4164-9), indexed in Pubmed: [20425555](https://pubmed.ncbi.nlm.nih.gov/20425555/).
49. Wang Yi, Cheng C, Wang Lu, et al. Anatomical variations in the origins of the celiac axis and the superior mesenteric artery: MDCT angiographic findings and their probable embryological mechanisms. *Eur Radiol.* 2014; 24(8): 1777–1784, doi: [10.1007/s00330-014-3215-9](https://doi.org/10.1007/s00330-014-3215-9), indexed in Pubmed: [24859597](https://pubmed.ncbi.nlm.nih.gov/24859597/).
50. Whitley A, Oliverius M, Kocián P, et al. Variations of the celiac trunk investigated by multidetector computed tomography: Systematic review and meta-analysis with clinical correlations. *Clin Anat.* 2020; 33(8): 1249–1262, doi: [10.1002/ca.23576](https://doi.org/10.1002/ca.23576), indexed in Pubmed: [32012339](https://pubmed.ncbi.nlm.nih.gov/32012339/).
51. Winston CB, Lee NA, Jarnagin WR, et al. CT angiography for delineation of celiac and superior mesenteric artery variants in patients undergoing hepatobiliary and pancreatic surgery. *Am J Roentgenol.* 2007; 189(1): W13–W19, doi: [10.2214/AJR.04.1374](https://doi.org/10.2214/AJR.04.1374), indexed in Pubmed: [17579128](https://pubmed.ncbi.nlm.nih.gov/17579128/).
52. Yi SQ, Li J, Terayama H, et al. A rare case of inferior mesenteric artery arising from the superior mesenteric artery, with a review of the review of the literature. *Surg Radiol Anat.* 2008; 30(2): 159–165, doi: [10.1007/s00276-007-0298-x](https://doi.org/10.1007/s00276-007-0298-x), indexed in Pubmed: [18189117](https://pubmed.ncbi.nlm.nih.gov/18189117/).

Anatomical variants of coeliac trunk in Polish population using multidetector computed tomography angiography

A. Juszczak¹, J. Czyżowski², A. Mazurek¹, J.A. Walocha¹, A. Pasternak¹

¹Department of Anatomy, Jagiellonian University Medical College, Krakow, Poland

²Institute of Diagnostic Imaging, J. Dietl Specialist Hospital, Krakow, Poland

[Received: 19 March 2020; Accepted: 14 April 2020]

Background: Multidetector computed tomography angiography (MDCTA) has become a major part in evaluation of normal anatomy and its variants in patients undergoing operative or interventional procedures. The purpose of this study was to assess the frequency of anatomical variation of coeliac trunk in patients undergoing MDCTA of the abdominal aorta.

Materials and methods: A descriptive, retrospective study was carried out on MDCTAs performed from January 2014 till January 2020 in Polish patients. Coeliac trunk was studied and normal and anatomical variations were noted according to Adachi's classification. All patients with abnormalities affecting the vessels or a history of any vascular abnormality were excluded from the study.

Results: Out of total 1000 patients, hepatogastrosplenic trunk was found in 93.0%. True and false types of trifurcation were observed. Hepatosplenic trunk was found in 2.8%, coeliacomesenteric trunk in 1.1%, hepatomesenteric trunk in 1.7% gastrosplenic trunk was found in 1.4%. We have not observed hepatosplenomesenteric trunk.

Conclusions: The type and knowledge of anatomy is of prime importance for an optimum preoperative planning in surgical or radiological procedure. MDCTA allows minimally invasive assessment of arterial anatomy with high quality three-dimensional reconstruction images. (Folia Morphol 2021; 80, 2: 290–296)

Key words: celiac trunk, variations, multidetector computed tomography angiography

INTRODUCTION

The most common classical type of coeliac trunk branching pattern is referred to as trifurcation (Fig. 1A, B) and was first observed by von Haller [37], i.e. tripus Halleri. It has been considered to be the normal appearance of computed tomography (CT). According to Haller, coeliac trunk divides into common hepatic artery (CHA), splenic artery (SA) and left gastric artery

(LGA), which usually arises as a tributary elsewhere in this trunk, while the other divisions of coeliac trunk rarely occur in human populations. The anatomical variations of coeliac trunk were classified for the first time by Adachi in 1928 [1]. Investigations were performed on 252 people of Japanese origin and these formed the basis of Adachi's classification of the 6 types of division of coeliac trunk and superior mesen-

Address for correspondence: A. Pasternak, MD, PhD, Department of Anatomy, Jagiellonian University Medical College, ul. Kopernika 12, 31–034 Kraków, Poland, tel: +48 12 422 95 11, fax: +48 12 422 95 11, e-mail: artur.pasternak@uj.edu.pl

This article is available in open access under Creative Common Attribution-Non-Commercial-No Derivatives 4.0 International (CC BY-NC-ND 4.0) license, allowing to download articles and share them with others as long as they credit the authors and the publisher, but without permission to change them in any way or use them commercially.

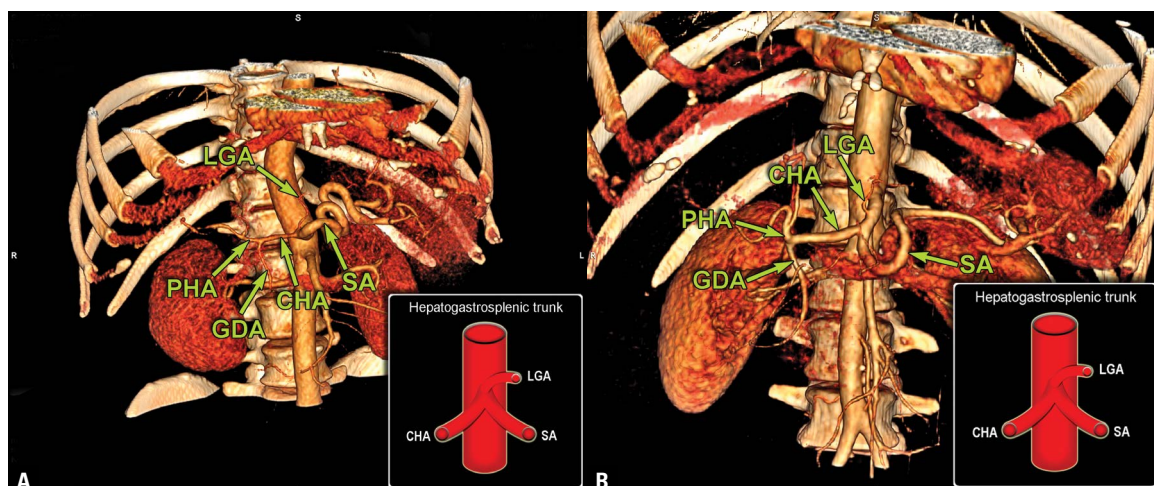


Figure 1. A. True tripod; B. False tripod; CHA — common hepatic artery; GDA — gastroduodenal artery; LGA — left gastric artery; PHA — proper hepatic artery; SA — splenic artery.

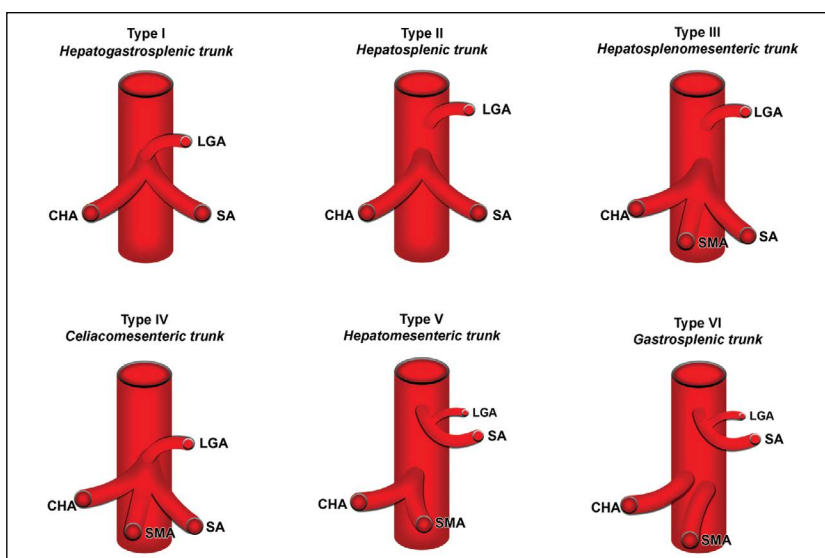


Figure 2. Coeliac trunk trifurcation types according to Adachi; CHA — common hepatic artery; LGA — left gastric artery; SA — splenic artery; SMA — superior mesenteric.

Table 1. Adachi’s classification of coeliac trunk variations

Trunk classification	Trunk classification number	Percentage
Hepatogastrosplenic	1	86%
Hepatosplenic	2	8%
Gastrosplenic	6	3%
Coeliacomesenteric	4	1.5%
Hepatosplenomesenteric	3	1%
Hepatomesenteric	5	0.5%

teric artery (SMA) (Fig. 2, Table 1). Knowledge of coeliac trunk branching pattern is mandatory in laparoscopic surgery, liver transplants, radiological abdominal in-

terventions and penetrating abdominal injuries [42]. Lack of familiarity with such variants can result in insufficient management and predispose patients to inadvertent injury during open surgical procedures or percutaneous interventions. In recent 20 years, with the widespread use of multidetector computed tomography and angiography (MDCTA), it is easy to collect a large sampling of data on the angiographic anatomy of the abdomen in daily radiological practice. Then, the variation patterns and radiological findings of coeliac trunk can be classified and evaluated in detail by MDCTA. The main purpose of this study was to evaluate the frequency of normal and anatomical variations of coeliac trunk in Polish patients undergoing MDCTA of

the abdominal aorta for various clinical indications. The use of MDCTA allowed for identification of its types and prevalence in a large study population. We also discussed their clinical implications and the probable embryological mechanisms by which the observed variations are achieved. It has become significant to be aware of the normal variations in the vascular supply of these organs, in order to prevent complications during and after surgery.

MATERIALS AND METHODS

This study was conducted at the Institute of Diagnostic Imaging, J. Dietl Specialist Hospital in Krakow, Poland. One thousand patients referred to CT angiogram of abdominal aorta for various reasons irrespective of age and gender were included in this study. All the patients underwent abdominal MDCTA in Aquilion 64, Toshiba Medical Systems Corporation, Tokyo, Japan. Local Institutional Ethical Committee approval was obtained. Being a retrospective study, informed consent was not obtained as the data was collected retrospectively from the electronic medical record database. Abdominal CT angiographic images from 01.2014 till 01.2020 were studied for coeliac trunk anatomical variation. The pattern of the aortic origin of branches of coeliac trunk and its branches was analysed.

Multiphase enhanced MDCT scan was performed after intravenous administration of contrast agent (Omnipaque 350; GE Healthcare AS, Oslo, Norway) at 350 mg of iodine per millilitre and 30 mL of sterile saline (0.9% NaCl) by using a power injector at a rate of 3–4 mL/s. The dose of the contrast agent was 1 mL/kg body weight and the upper limit of dose was set at 100 mL for every patient. Data obtained during the arterial phase were used to evaluate the anatomy of the coeliac trunk. The raw axial images obtained from MDCT were processed on the workstation to obtain three-dimensional (3D) reconstruction with maximum intensity projection (MIP) and volume rendering (VR). The analysis of the images was carried out by an experienced radiologist.

Identification of coeliac trunk and its branches was possible in all patients examined. Patients with distorted anatomy due to previous abdominal surgery, degenerative spine conditions or any abnormality that involved the vessels were excluded. The pattern of the aortic origin of the four major arteries: left gastric, the common hepatic, splenic and superior mesenteric arteries were analysed in the study. The instructional 3D models of the coeliac trunk and its

abnormalities were designed. Anatomical variations of the coeliac trunk were reported according to Adachi's classification (Table 1). Coeliac trunk was also assessed for its diameter, distance from the SMA, angle of departure from the abdominal aorta and projection on the spine.

Statistical analysis

Statistical package for social sciences (SPSS) version 21 was used for statistical analysis. Mean and standard deviation was calculated for age of the patients. Frequency and percentages was calculated for normal anatomy and anatomical variations of coeliac trunk. Comparison was done to see the relationship among coeliac artery variant. Chi-square test was applied. P-value was taken as < 0.05 .

RESULTS

Out of total 1000 patients, 510 (51%) were males and 490 (49%) were females. The mean age of the patients was 65.2 ± 19.75 years. According to Adachi's first classification, there are 6 branching types of the coeliac trunk: hepatogastrosplenic, hepatosplenic, hepatosplenomesenteric, hepatomesenteric, gastrosplenic, coeliacomesenteric. Hepatogastrosplenic trunk (type I according to Adachi's classification) dividing into 3 branches i.e. LGA, CHA and SA was found in 93.0% (930/1000). Two different types of this trifurcation were observed: (a) a true tripod when the coeliac trunk ended in a complete trifurcation ($\approx 35\%$, 325/930) and (b) a false tripod when the three arteries did not have a common origin ($\approx 65\%$, 605/930) (Fig. 1A, B). Type II (i.e. hepatosplenic trunk) was found in 2.8% (28/1000) (Fig. 3). Type IV (i.e. coeliacomesenteric trunk) was found in 1.1% (11/1000) (Fig. 4), type V (i.e. hepatomesenteric trunk) was found in 1.7% (17/1000) (Fig. 5), type VI (i.e. gastrosplenic trunk) was found in 1.4% (14/1000) (Fig. 6). We have not observed type III (i.e. hepatosplenomesenteric trunk). The level of coeliac trunk origin was found to be at the inter-vertebral disc between T12 and L1 in all of the cases. The angle of departure of the coeliac trunk from the abdominal aorta varied widely from 6.8° to 85.6° (Table 2).

On average, the coeliac trunk calibre was 11.7 mm, with the largest one of 18.1 mm and the smallest of 5.3 mm, and standard deviation of 0.13. The mean distance between the coeliac trunk and the SMA was 15 mm, the largest — 22 mm, and the shortest — 3 mm, with standard deviation of 0.4.

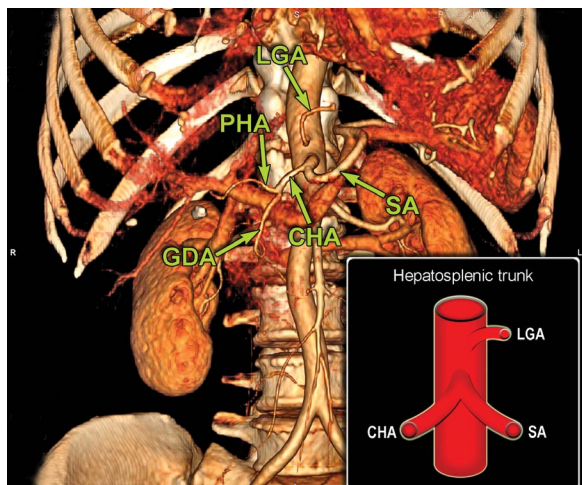


Figure 3. Hepatosplenic trunk; abbreviations — see Figure 1.

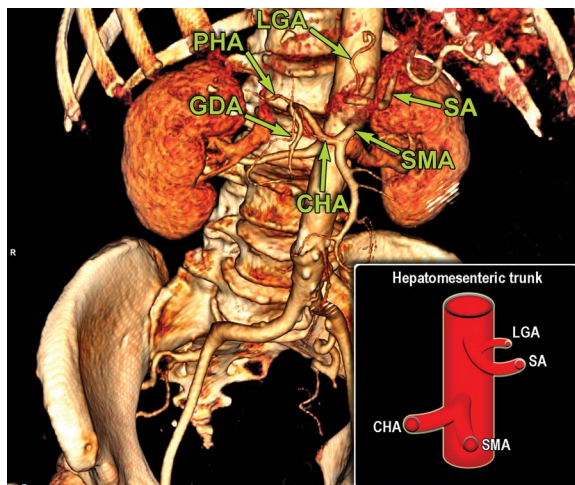


Figure 5. Hepatomesenteric trunk; abbreviations — see Figure 1.

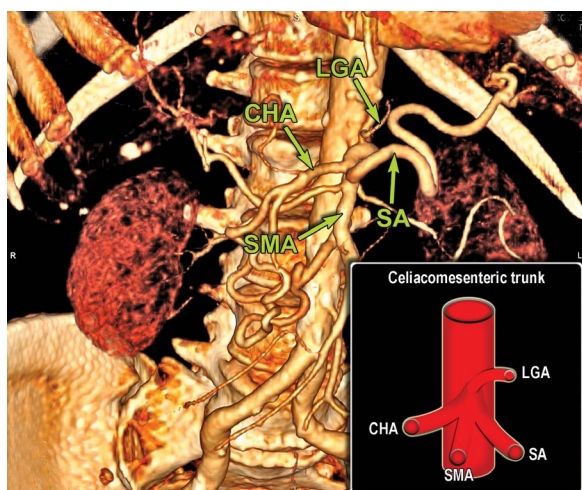


Figure 4. Coeliacomesenteric trunk; abbreviations — see Figure 1.

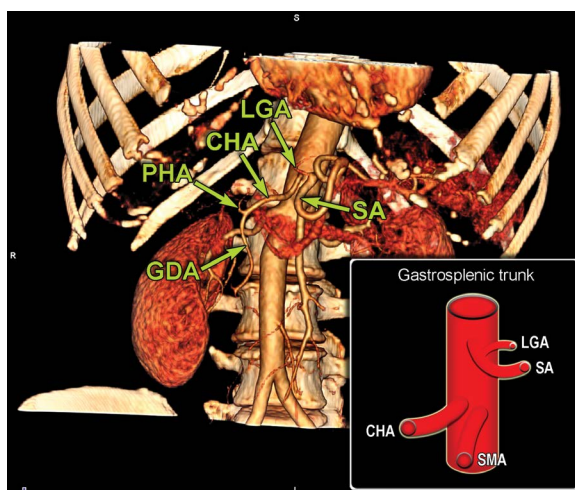


Figure 6. Gastrosplenic trunk; abbreviations — see Figure 1.

Table 2. Coeliac trunk variations according to Adachi's classification found in the study

Trunk classification	Trunk classification number	Percentage
Hepatogastrosplenic	1	93%
Hepatosplenic	2	2.8%
Gastrosplenic	6	1.4%
Coeliacomesenteric	4	1.1%
Hepatosplenomesenteric	3	0%
Hepatomesenteric	5	1.7%

DISCUSSION

Anatomic variations of the coeliac trunk and SMA occur due to anomalous embryogenesis of primitive ventral blood vessels originating from the abdominal

aorta [33]. In our study, there were 4 types of coeliac axis variation identified in 70 patients, with normal coeliac axis anatomy in 930 (93%) patients as compared with 89% in the dissection study conducted by Michels [25]; 91% in the study conducted by Sureka et al. [31]; 86% in the study conducted by Sankar et al. [29]; 85.1%, 89.5%, and 95.4%, respectively, in cadaver studies, imaging studies, and liver transplantation studies, as reported by Panagouli et al. [27]; 89.1% in the study conducted by Song et al. [30]; 89.8% in the study conducted by Chen et al. [8], who analysed a population defined as homogeneous in Japan; and 90% in the study conducted by Araujo-Neto et al. [2]. The hepatosplenic trunk (2.8%) was the most common coeliac artery variation with separate origin of LGA and SMA followed by coeliacomesenteric trunk (1.1%). Gastrosplenic trunk with separate origin of

SMA and CHA from aorta was not found in our study which was found in 0.22% and 0.83% in the studies of Song et al. [30] and Sureka et al. [31], respectively.

Multidetector computed tomography angiography has become a valuable tool for the visualisation of normal vascular anatomy and its variants. Furthermore, reformatted 3D MDCT images allow visualisation of vascular structures in angiography equivalent planes other than the axial, which is useful for evaluation of complex vascular anatomy [3, 14]. Rapid volumetric acquisition of thin-slice high resolution images of the abdominal arteries during the phase of maximal contrast enhancement with the help of MDCT allows 3D reconstructions to be created, providing the radiologist and the surgeon with a 3D model of the patient's arterial anatomy. MDCT angiography has a reported accuracy of 97–98% compared with conventional angiography for detecting arterial variants [41]. The disadvantages include potential for contrast reactions, nephrotoxicity, and exposure to ionizing radiation.

Knowledge about the spectrum of coeliac trunk variations is important for planning surgical or interventional procedures in the upper abdomen. Identification of coeliac trunk variations may avoid vascular complications during medical procedures, such as hepatobiliary surgery, pancreatic surgery, gastrectomy and others like transcatheter arterial chemoembolisation [10, 13, 24, 34, 40].

Many endovascular procedures require detailed acquaintance regarding specific features of the particular blood vessels. It is especially noticeable in planning embolisation both as intervention to control haemorrhage and as bariatric procedure. Haemorrhages can occur in the course of many vascular and non-vascular pathologies such as ruptured aneurysms, pseudocysts (due to pancreatitis which commonly lead to erosion of the splenic artery [4, 16]) or posttraumatic injuries (very often due to splenic injuries [9]) and inflammatory diseases. i.e. pancreatitis with related bleeding [19]. In most of the mentioned cases the procedure is done within splenic artery or its branches [9, 19] and it is crucial to be acquainted with variations of the course of this artery, especially when the surgeon is planning the proximal splenic artery embolisation which is faster instead of the distal, recommended to focal lesions in the spleen [9].

The embolisation is also used in bariatric treatment. Recent studies revealed that the procedure of embolisation the LGA could improve loss of weight, decreases the concentration of ghrelin and HbA1c

[21, 32, 39], but the veritable efficacy is still investigated [39]. It is important to take into account detailed features of the LGA (s-shape) and its variation of emerging from the coeliac axis and notice that the position of the coeliac trunk might be horizontal, parallel or inferior which could affect manipulation difficulties [21].

One should bear in mind various angles of departure of the coeliac axis from abdominal aorta. In our study angle varied widely from 6.8° do 85.6°. Besides a hepatectomy, systemic chemotherapy and arterial chemoinfusion therapy are used to treat primary and liver metastatic cancers. Catheter insertion is necessary for arterial infusion chemotherapy, and there are surgical and percutaneous catheter insertion methods. The catheter insertion route is selected depending on the branching angle (upward or downward) of the origin of the coeliac artery in some cases, and assessments of the branching angle before catheter insertion may increase the reliability of the technique. In recent studies Tokue et al. [35] measured the branching angle of the coeliac trunk in 1200 patients aged 19–91 years with hepatocellular carcinoma. Similarly to our results, the branching was downward in most of patients. Prior information of the branching angle before catheter insertion may increase the reliability of the insertion technique and the completion rate of the therapy.

Many recent studies about liver transplantation revealed that the knowledge about the anatomy of the hepatic and aberrant (accessory or replaced) hepatic arteries emerging directly from the coeliac trunk or its branches is significant to prevent complications both at the recipients and the living donors [6, 7, 15, 17, 22, 38]. The complications after donation which eventuate from imprecise analysis of hepatic arteries and the other vessels include: sepsis, acute hepatic failure, biliary leaks of stricture or vascular thrombosis [6]. Thus, there is a trend to preserve accessory and replaced hepatic arteries as well as it is possible if there is not insurance about the blood supply in the same area of liver. In some cases this preservation could not be equal at the recipient and the donor so that it is important to analyse meticulously distribution of arteries in both circumstances [6, 7, 38]. According to Michels' classification there are described cases of replaced left hepatic artery (10%) and accessory left hepatic artery (8%), both originating from LGA [25]. The appropriate retaining of arteries supplying the donor's left lobe is essential to provide adequate

regeneration of the rest of liver [6, 7]. During planning the surgery in some cases there could be difficulties to palpate the accessory hepatic artery branching of the LGA. This could be resolved by finding the LGA which sometimes could not pass from the coeliac axis (for example in the hepatosplenic trunk) [38]. The replaced right hepatic artery frequently originating from the proper hepatic artery (from CHA) but sometimes (11%) it arises from superior mesenteric artery [25] and it also should be considered in planning the transplant procedure.

The awareness of variations of the coeliac axis is also significant in treatment for patients with diagnosed hepatocellular carcinoma and the other primary hepatic cancers. Roma et al. [28] revealed that the right inferior phrenic artery — one of the branches of the abdominal aorta or the coeliac trunk (which is the second most common origin [5, 20]) is the part of the collateral circulation and supplies the liver cancer in the most cases. This fact has an impact on planning treatment of the peripheral lesions such as the chemoembolisation procedure [28]. Maki et al. [22] mentioned that this artery and the other ones (left inferior phrenic, gastric, internal mammary arteries and omental arteries) creating the collateral circulation of the liver should be preserved to avoid postoperative alanine aminotransferase elevation due to hepatic ischaemia.

Considering the other oncological issues: gastric, oesophageal and pancreatic cancer, the procedure of resection of the neoplasms very often includes lymphadenectomy of the lymph nodes surrounding the coeliac axis, LGA or the CHA and SA [6, 12, 26]. The variations of the coeliac trunk and its branches could restrict surgeon's manipulations during dissecting lymph nodes and lead to prolonged operative time and increased risk of iatrogenic complications [6, 26]. It is also crucial to analyse thoroughly the anatomy of the blood vessels which are considered to sacrifice during the procedure. Maki et al. [22] noted that ligation the LGA during gastrectomy could lead to liver ischaemia because of presence of the accessory or replaced left hepatic artery and Kim et al. [18] suggested preservation of the accessory left hepatic artery if the diameter of the LGA is equal or larger than 5 mm.

Our study provides an insight into the anatomical patterns found in Poland. According to our finding, the prevalence of variations was significant, so we suggest applying 3D reconstruction method for evaluation of variation at least in patients who are

candidate for mentioned surgical or interventional procedures. Further studies of this nature could lead to better technical planning of surgical procedures and avoiding inadvertent injuries that might compromise the results of medical procedures, leading to complications. Better knowledge of anatomical variations could ultimately contribute to reducing the rates of morbidity and mortality in endovascular procedures, abdominal surgeries, and transplantations, especially those of the liver and pancreas [11, 23, 36].

CONCLUSIONS


Our study identified the variations in coeliac trunk anatomy in a sample of Polish population using Adachi's classification. Our results correlated well with studies in other populations. Adequate knowledge of these variations would be of great help to the interventional radiologist and hepatobiliary surgeon.

REFERENCES

1. Adachi B. *Das Arteriensystem der Japaner*. Vol. 2. Verlag der Kaiserlich-Japanischen Universitat zu Kyoto 1928.
2. Araujo Neto SA, Franca HA, de Mello Júnior CF, et al. Anatomical variations of the celiac trunk and hepatic arterial system: an analysis using multidetector computed tomography angiography. *Radiol Bras*. 2015; 48(6): 358–362, doi: [10.1590/0100-3984.2014.0100](https://doi.org/10.1590/0100-3984.2014.0100), indexed in Pubmed: [26811552](https://pubmed.ncbi.nlm.nih.gov/26811552/).
3. Arifuzzaman M, Nasim Na, Adel H, et al. Anatomical variants of celiac trunk, hepatic and renal arteries in a population of developing country using multidetector computed tomography angiography. *J Ayub Med Coll Abbottabad*. 2017; 29(3): 450–454.
4. Brahmbhatt P, McKinney J, Litchfield J, et al. Mediastinal pancreatic pseudocyst with hemorrhage and left gastric artery pseudoaneurysm, managed with left gastric artery embolization and placement of percutaneous transhepatic pseudocyst drainage. *Gastroenterol Rep (Oxf)*. 2016; 4(3): 241–245, doi: [10.1093/gastro/gou084](https://doi.org/10.1093/gastro/gou084), indexed in Pubmed: [25502760](https://pubmed.ncbi.nlm.nih.gov/25502760/).
5. Brasil IR, de Araujo IF, Lima AA, et al. Computed tomography angiography study of variations of the celiac trunk and hepatic artery in 100 patients. *Radiol Bras*. 2018; 51(1): 32–36, doi: [10.1590/0100-3984.2016.0179](https://doi.org/10.1590/0100-3984.2016.0179), indexed in Pubmed: [29540943](https://pubmed.ncbi.nlm.nih.gov/29540943/).
6. Cai L, Yeh BM, Westphalen AC, et al. Adult living donor liver imaging. *Diagn Interv Radiol*. 2016; 22(3): 207–214, doi: [10.5152/dir.2016.15323](https://doi.org/10.5152/dir.2016.15323), indexed in Pubmed: [26912106](https://pubmed.ncbi.nlm.nih.gov/26912106/).
7. Catalano OA, Singh AH, Uppot RN, et al. Vascular and biliary variants in the liver: implications for liver surgery. *Radiographics*. 2008; 28(2): 359–378, doi: [10.1148/rg.282075099](https://doi.org/10.1148/rg.282075099), indexed in Pubmed: [18349445](https://pubmed.ncbi.nlm.nih.gov/18349445/).
8. Chen H, Yano R, Emura S, et al. Anatomic variation of the celiac trunk with special reference to hepatic artery patterns. *Ann Anat*. 2009; 191(4): 399–407, doi: [10.1016/j.aanat.2009.05.002](https://doi.org/10.1016/j.aanat.2009.05.002), indexed in Pubmed: [19540742](https://pubmed.ncbi.nlm.nih.gov/19540742/).
9. Cornelis van der Vlies H, van Delden OM, Punt BJ, et al. Literature review of the role of ultrasound, computed tomography, and transcatheter arterial embolization for the treatment of traumatic splenic injuries. *Cardiovasc Intervent Radiol*. 2010; 33(6): 1079–1087, doi: [10.1007/s00270-010-9943-6](https://doi.org/10.1007/s00270-010-9943-6), indexed in Pubmed: [20668852](https://pubmed.ncbi.nlm.nih.gov/20668852/).
10. Egorov VI, Yashina NI, Fedorov AV, et al. Celiac-mesenteric arterial aberrations in patients undergoing extended pancreatic resections: correlation of CT angiography with findings at surgery. *JOP*. 2010; 11(4): 348–357, indexed in Pubmed: [20601809](https://pubmed.ncbi.nlm.nih.gov/20601809/).

11. Ekingen A, Tuncer MC, Ertuğrul Ö. Investigation of proper hepatic artery and gastroduodenal artery variations by multidetector computed tomography angiography method. *Acta Chir Belg.* 2020; 120(2): 102–115, doi: [10.1080/00015458.2019.1570744](https://doi.org/10.1080/00015458.2019.1570744), indexed in Pubmed: [30714485](https://pubmed.ncbi.nlm.nih.gov/30714485/).
12. Fink DM, Steele MM, Hollingsworth MA. The lymphatic system and pancreatic cancer. *Cancer Lett.* 2016; 381(1): 217–236, doi: [10.1016/j.canlet.2015.11.048](https://doi.org/10.1016/j.canlet.2015.11.048), indexed in Pubmed: [26742462](https://pubmed.ncbi.nlm.nih.gov/26742462/).
13. Ganeshan A, Upponi S, Hon Lq, et al. Hepatic arterial infusion of chemotherapy: the role of diagnostic and interventional radiology. *Ann Oncol.* 2008; 19(5): 847–851, doi: [10.1093/annonc/mdm528](https://doi.org/10.1093/annonc/mdm528), indexed in Pubmed: [18029972](https://pubmed.ncbi.nlm.nih.gov/18029972/).
14. Iezzi R, Cotroneo AR, Giancristofaro D, et al. Multidetector-row CT angiographic imaging of the celiac trunk: anatomy and normal variants. *Surg Radiol Anat.* 2008; 30(4): 303–310, doi: [10.1007/s00276-008-0324-7](https://doi.org/10.1007/s00276-008-0324-7), indexed in Pubmed: [18286222](https://pubmed.ncbi.nlm.nih.gov/18286222/).
15. Ishigami K, Zhang Y, Rayhill S, et al. Does variant hepatic artery anatomy in a liver transplant recipient increase the risk of hepatic artery complications after transplantation? *Am J Roentgenol.* 2004; 183(6): 1577–1584, doi: [10.2214/ajr.183.6.01831577](https://doi.org/10.2214/ajr.183.6.01831577), indexed in Pubmed: [15547194](https://pubmed.ncbi.nlm.nih.gov/15547194/).
16. Jain SK, Rajendran V, Jain MK, et al. Hemorrhagic pseudocyst of pancreas treated with coil embolization of gastroduodenal artery: a case report and review of literature. *Case Rep Surg.* 2015; 2015: 480605, doi: [10.1155/2015/480605](https://doi.org/10.1155/2015/480605), indexed in Pubmed: [26819796](https://pubmed.ncbi.nlm.nih.gov/26819796/).
17. Juszczak A, Solewski B, Loukas M, et al. Unusual branching pattern of celiac trunk associated with supernumerary hepatic arteries and abnormal adrenal venous drainage - case study and review of the literature. *Folia Med Cracov.* 2017; 57(3): 29–36, indexed in Pubmed: [29263452](https://pubmed.ncbi.nlm.nih.gov/29263452/).
18. Kim J, Kim SuMi, Seo JE, et al. Should an aberrant left hepatic artery arising from the left gastric artery be preserved during laparoscopic gastrectomy for early gastric cancer treatment? *J Gastric Cancer.* 2016; 16(2): 72–77, doi: [10.5230/jgc.2016.16.2.72](https://doi.org/10.5230/jgc.2016.16.2.72), indexed in Pubmed: [27433391](https://pubmed.ncbi.nlm.nih.gov/27433391/).
19. Kim J, Shin JH, Yoon HKI, et al. Endovascular intervention for management of pancreatitis-related bleeding: a retrospective analysis of thirty-seven patients at a single institution. *Diagn Interv Radiol.* 2015; 21(2): 140–147, doi: [10.5152/dir.2014.14085](https://doi.org/10.5152/dir.2014.14085), indexed in Pubmed: [25616269](https://pubmed.ncbi.nlm.nih.gov/25616269/).
20. Kimura S, Okazaki M, Higashihara H, et al. Analysis of the origin of the right inferior phrenic artery in 178 patients with hepatocellular carcinoma treated by chemoembolization via the right inferior phrenic artery. *Acta Radiol.* 2007; 48(7): 728–733, doi: [10.1080/02841850701376334](https://doi.org/10.1080/02841850701376334), indexed in Pubmed: [17729002](https://pubmed.ncbi.nlm.nih.gov/17729002/).
21. Kordzadeh A, Lorenzi B, Hanif MA, et al. Left gastric artery embolisation for the treatment of obesity: a systematic review. *Obes Surg.* 2018; 28(6): 1797–1802, doi: [10.1007/s11695-018-3211-2](https://doi.org/10.1007/s11695-018-3211-2), indexed in Pubmed: [29616467](https://pubmed.ncbi.nlm.nih.gov/29616467/).
22. Maki H, Satodate H, Satou S, et al. Clinical evaluation of the aberrant left hepatic artery arising from the left gastric artery in esophagectomy. *Surg Radiol Anat.* 2018; 40(7): 749–756, doi: [10.1007/s00276-018-2022-4](https://doi.org/10.1007/s00276-018-2022-4), indexed in Pubmed: [29651566](https://pubmed.ncbi.nlm.nih.gov/29651566/).
23. Marco-Clement I, Martinez-Barco A, Ahumada N, et al. Anatomical variations of the celiac trunk: cadaveric and radiological study. *Surg Radiol Anat.* 2016; 38(4): 501–510, doi: [10.1007/s00276-015-1542-4](https://doi.org/10.1007/s00276-015-1542-4), indexed in Pubmed: [26267305](https://pubmed.ncbi.nlm.nih.gov/26267305/).
24. Matsuki M, Tanikake M, Kani H, et al. Dual-phase 3D CT angiography during a single breath-hold using 16-MDCT: assessment of vascular anatomy before laparoscopic gastrectomy. *Am J Roentgenol.* 2006; 186(4): 1079–1085, doi: [10.2214/AJR.04.0733](https://doi.org/10.2214/AJR.04.0733), indexed in Pubmed: [16554582](https://pubmed.ncbi.nlm.nih.gov/16554582/).
25. Michels NA. Newer anatomy of the liver and its variant blood supply and collateral circulation. *Am J Surg.* 1966; 112(3): 337–347, doi: [10.1016/0002-9610\(66\)90201-7](https://doi.org/10.1016/0002-9610(66)90201-7), indexed in Pubmed: [5917302](https://pubmed.ncbi.nlm.nih.gov/5917302/).
26. Mu GC, Huang Y, Liu ZM, et al. Clinical research in individual information of celiac artery CT imaging and gastric cancer surgery. *Clin Transl Oncol.* 2013; 15(10): 774–779, doi: [10.1007/s12094-013-1002-8](https://doi.org/10.1007/s12094-013-1002-8), indexed in Pubmed: [23359186](https://pubmed.ncbi.nlm.nih.gov/23359186/).
27. Panagouli E, Venieratos D, Lolis E, et al. Variations in the anatomy of the celiac trunk: A systematic review and clinical implications. *Ann Anat.* 2013; 195(6): 501–511, doi: [10.1016/j.aanat.2013.06.003](https://doi.org/10.1016/j.aanat.2013.06.003), indexed in Pubmed: [23972701](https://pubmed.ncbi.nlm.nih.gov/23972701/).
28. Roma S, D'Amato D, Ranalli T, et al. Vascular anomalies of the celiac trunk and implications in treatment of HCC with TACE. Description of a case and review of the literature. *Radiol Case Rep.* 2019; 14(10): 1221–1227, doi: [10.1016/j.radcr.2019.07.011](https://doi.org/10.1016/j.radcr.2019.07.011), indexed in Pubmed: [31428216](https://pubmed.ncbi.nlm.nih.gov/31428216/).
29. Sankar KD, Bhanu PS, Susan PJ. Variant Anatomy of the Celiac Trunk and its Branches. *Int J Morphol.* 2011; 29(2): 581–584, doi: [10.4067/s0717-95022011000200047](https://doi.org/10.4067/s0717-95022011000200047).
30. Song SY, Chung JW, Yin YHu, et al. Celiac axis and common hepatic artery variations in 5002 patients: systematic analysis with spiral CT and DSA. *Radiology.* 2010; 255(1): 278–288, doi: [10.1148/radiol.09090389](https://doi.org/10.1148/radiol.09090389), indexed in Pubmed: [20308464](https://pubmed.ncbi.nlm.nih.gov/20308464/).
31. Sureka B, Mittal MK, Mittal A, et al. Variations of celiac axis, common hepatic artery and its branches in 600 patients. *Indian J Radiol Imaging.* 2013; 23(3): 223–233, doi: [10.4103/0971-3026.120273](https://doi.org/10.4103/0971-3026.120273), indexed in Pubmed: [24347852](https://pubmed.ncbi.nlm.nih.gov/24347852/).
32. Takahashi EA, Takahashi N, Reisenauer CJ, et al. Body composition changes after left gastric artery embolization in overweight and obese individuals. *Abdom Radiol (NY).* 2019; 44(7): 2627–2631, doi: [10.1007/s00261-019-02002-6](https://doi.org/10.1007/s00261-019-02002-6), indexed in Pubmed: [30949784](https://pubmed.ncbi.nlm.nih.gov/30949784/).
33. Tandler J. über die Varietäten der Arteria coeliaca und deren Entwicklung. Beiträge und Referate zur Anatomie und Entwicklungsgeschichte. *Anathefte.* 1904; 25(2): 473–500, doi: [10.1007/bf02300762](https://doi.org/10.1007/bf02300762).
34. Tang W, Shi J, Kuang LQ, et al. Celiomesenteric trunk: New classification based on multidetector computed tomography angiographic findings and probable embryological mechanisms. *World J Clin Cases.* 2019; 7(23): 3980–3989, doi: [10.12998/wjcc.v7.i23.3980](https://doi.org/10.12998/wjcc.v7.i23.3980), indexed in Pubmed: [31832400](https://pubmed.ncbi.nlm.nih.gov/31832400/).
35. Tokue H, Tokue A, Tsushima Y. Multidetector-row computed tomography for evaluating the branching angle of the celiac artery: a descriptive study. *BMC Med Imaging.* 2012; 12: 36, doi: [10.1186/1471-2342-12-36](https://doi.org/10.1186/1471-2342-12-36), indexed in Pubmed: [23259976](https://pubmed.ncbi.nlm.nih.gov/23259976/).
36. Ülger BV, Hatipoğlu ES, Ertuğrul Ö, et al. Variations in the vascular and biliary structures of the liver: a comprehensive anatomical study. *Acta Chir Belg.* 2018; 118(6): 354–371, doi: [10.1080/00015458.2018.1438565](https://doi.org/10.1080/00015458.2018.1438565), indexed in Pubmed: [29433396](https://pubmed.ncbi.nlm.nih.gov/29433396/).
37. von Haller A. *Icones anatomicae in quibus aliquae partes corporis humani delineate proponuntur et arteriarum potissimum historia continetur.* Vandenhoeck, Gottingen 1765.
38. Watson CJE, Harper SJF. Anatomical variation and its management in transplantation. *Am J Transplant.* 2015; 15(6): 1459–1471, doi: [10.1111/ajt.13310](https://doi.org/10.1111/ajt.13310), indexed in Pubmed: [25981150](https://pubmed.ncbi.nlm.nih.gov/25981150/).
39. Weiss CR, Abiola GO, Fischman AM, et al. Bariatric embolization of arteries for the treatment of obesity (BEAT obesity) trial: results at 1 year. *Radiology.* 2019; 291(3): 792–800, doi: [10.1148/radiol.2019182354](https://doi.org/10.1148/radiol.2019182354), indexed in Pubmed: [30938624](https://pubmed.ncbi.nlm.nih.gov/30938624/).
40. Winston CB, Lee NA, Jarnagin WR, et al. CT angiography for delineation of celiac and superior mesenteric artery variants in patients undergoing hepatobiliary and pancreatic surgery. *Am J Roentgenol.* 2007; 189(1): W13–W19, doi: [10.2214/AJR.04.1374](https://doi.org/10.2214/AJR.04.1374), indexed in Pubmed: [17579128](https://pubmed.ncbi.nlm.nih.gov/17579128/).
41. Winter TC, Nghiem HV, Freeny PC, et al. Hepatic arterial anatomy: demonstration of normal supply and vascular variants with three-dimensional CT angiography. *Radiographics.* 1995; 15(4): 771–780, doi: [10.1148/radiographics.15.4.7569128](https://doi.org/10.1148/radiographics.15.4.7569128), indexed in Pubmed: [7569128](https://pubmed.ncbi.nlm.nih.gov/7569128/).
42. Zaki SM, Abdelmaksoud AHK, Khaled BEA, et al. Anatomical variations of hepatic artery using the multidetector computed tomography angiography. *Folia Morphol.* 2020; 79(2): 247–254, doi: [10.5603/FM.a2019.0090](https://doi.org/10.5603/FM.a2019.0090), indexed in Pubmed: [31436302](https://pubmed.ncbi.nlm.nih.gov/31436302/).

A macroscopic comparison study on main branches of arteria brachialis and arteria subscapularis in Southern Karaman and Hasak sheep breeds

H. Kara¹, Z. Özüdogru², H. Balkaya¹, D. Özdemir¹

¹Department of Anatomy, Faculty of Veterinary Medicine, Ataturk University, Erzurum, Turkey

²Department of Anatomy, Faculty of Veterinary Medicine, Aksaray University, Aksaray, Turkey

[Received: 24 January 2020; Accepted: 10 May 2020]

Background: The Southern Karaman sheep, which is very fertile in terms of meat and milk production and is often preferred in livestock raising, is known as a domestic sheep breed. The Hasak sheep is a breed formed by the triple crossbreeding of the German Black-headed, Hampshire and Akkaraman breeds. Arterial feeding of the forelimb is provided by arteria axillaris, a continuation of arteria subclavia. In this study, it was aimed to examine the forelimb arteries in Southern Karaman and Hasak sheep breeds.

Materials and methods: Totally, 8 Southern Karaman and 8 Hasak sheep were obtained from Konya Bahri Dagdas International Agricultural Institute. The sheep were anesthetised with xylazine and ketamine and extravasated by cutting the arteria carotis communis in the neck area of the sheep. The forelimbs of the sheep separated from the body were fixed in 10% formaldehyde solution and then dissections were made and the course and branching of the arteries were examined.

Results: It was determined that the arteria brachialis was divided into two main branches as distal arteria brachialis and proximal arteria subscapularis at the articulatio humeri level of the arteria axillary. Arteria mediana, which is a continuation of arteria brachialis, was also examined in different parts of antebrachium and ended by splitting into branches.

Conclusions: According to the findings of the Southern Karaman and Hasak sheep breeds, it was determined that the forelimb arteries had some anatomical differences but were similar in structure to many sheep breeds. (Folia Morphol 2021; 80, 2: 297–301)

Key words: arteria, axillaris, brachialis, subscapularis, fore limb, sheep

INTRODUCTION

The Southern Karaman sheep is described as a separate breed formed as a result of the crossbreeding of the Karagül male sheep with the Akkaraman and Dağlıç sheep brought by the Yörüks (Türkmens) who

migrated from Turkistan to the Mediterranean during the Ottoman period. The Southern Karaman sheep is very productive in terms of meat and milk and it is often preferred in livestock breeding [10, 13]. The Hasak sheep is a breed formed by the triple cross-

Address for correspondence: H. Kara, PhD, Department of Anatomy, Faculty of Veterinary Medicine, Ataturk University, Erzurum 25240, Turkey, tel: +904422317188, e-mail: h.goktas@atauni.edu.tr

This article is available in open access under Creative Common Attribution-Non-Commercial-No Derivatives 4.0 International (CC BY-NC-ND 4.0) license, allowing to download articles and share them with others as long as they credit the authors and the publisher, but without permission to change them in any way or use them commercially.

breeding of the German Black-headed, Hampshire and Akkaraman breeds at the Konya Bahri Dagdas International Agricultural Institute [13, 19, 21].

In ruminants, the arterial feeding of the forelimb is provided by the arteria axillaris, a continuation of the arteria subclavia, the branch of truncus brachiocephalicus that emerges from the arcus aorta [7, 15]. The arteria subclavia dexter et sinister originate from the chest cavity and after their passage to the forelimb, the section up to the musculus teres major beam is referred to as the arteria axillaris. Arteria axillaris is divided into two main branches, proximal and distal, at the level of articulatio humeri. On the musculus subscapularis of arteria axillaris, the thickest of the branches that travel proximal along the margo caudalis of the scapula and emerge from arteria axillaris are referred to as arteria subscapularis. The distal part of arteria axillaris from the chorda of musculus teres major to collum radii is called arteria brachialis [4, 6]. The distal part of arteria brachialis after collum radii is named to as arteria mediana [3, 11, 15]. The branches of arteria subscapularis are arteria thoracodorsalis, arteria circumflexa humeri caudalis and arteria circumflexa scapula. In addition to these branches, many rami muscularis are also among the branches separated. Arteria profunda brachii, arteria bicipitalis, arteria collateralis ulnaris, arteria brachialis superficialis, arteria transversa cubiti, arteria interossea communis, arteria ulnaris branches originate from arteria brachialis [4, 6].

The aim of this study was to examine the morphological structure of the forelimb arteries in the Southern Karaman and Hasak sheep.

MATERIALS AND METHODS

Totally, 8 Southern Karaman and 8 Hasak sheep used in this study were obtained from Konya Bahri Dagdas International Agriculture Institute. The sheep were anesthetised with xylazine HCl (0.2 mg/kg/IV) and ketamine HCl (2.2 mg/kg/IV) [18] and extravasated by cutting the arteria carotis communis in the neck area of the sheep. Then, the body cavity along the median line was opened and the internal organs were removed. Latex, which is described as the raw material of rubber mixed with red dye, was given into arteria axillaris with injectors of various sizes depending on vessel diameter and then left in 10% formaldehyde solution for fixation for 72 hours after applying latex injection method [1, 2, 8, 9, 22]. Then the forelimb arteries were examined individually

and their anatomical structures, routes and branches were examined and each photographed separately. Nomina Anatomica Veterinaria [23] was based on the naming of the vessels.

RESULTS

In both breeds studied, arteria axillaris was identified at the level of articulatio humeri to divide into two main branches, namely arteria brachialis, which ran along the limb distally in the triangular area between musculus subscapularis and musculus teres major, and arteria subscapularis, which ran towards the scapula in the caudodorsal direction. The branches of arteria subscapularis which ran along the margo caudalis of the scapula were arteria circumflexa humeri caudalis, arteria thoracodorsalis, ramus tricipitis and arteria circumflexa scapula (Fig. 1A, B). The first branch of the arteria subscapularis, which continued in proximal, was identified as arteria circumflexa humeri caudalis, which gave it towards the front of the limb. It was determined that arteria circumflexa humeri caudalis navigated between musculus brachialis and musculus triceps brachii immediately after its origin. The second branch of arteria subscapularis was arteria thoracodorsalis. This branch originated from the same place as arteria circumflexa humeri caudalis, moving in different directions and within 1 cm proximal of the beginning of arteria brachialis and in the caudal direction. It was determined to continue between musculus latissimus dorsi and musculus teres major. Later, the arteria subscapularis was found to give thin muscular branches in the cranial direction, with 3 in the Southern Karaman sheep and 2 in the Hasak sheep. After giving the second of these branches in the Southern Karaman sheep and the first in the Hasak sheep, it was determined that the ramus tricipitis originated to feed musculus triceps brachii and run caudal, i.e. in the caudal direction as arteria thoracodorsalis. In its further course, arteria subscapularis gave arteria circumflexa scapula, which run laterally, along the scapula's margo cranialis, to feed musculus supraspinatus and musculus subscapularis (Fig. 1A, B).

Arteria circumflexa humeri cranialis, arteria profunda brachii, arteria collateralis ulnaris, arteria bicipitalis, arteria transversa cubiti, arteria interossea communis branches were found to originate from arteria brachialis and continue distally as arteria mediana. It was observed that the first branch separated from the arteria brachialis was the arteria circumflexa

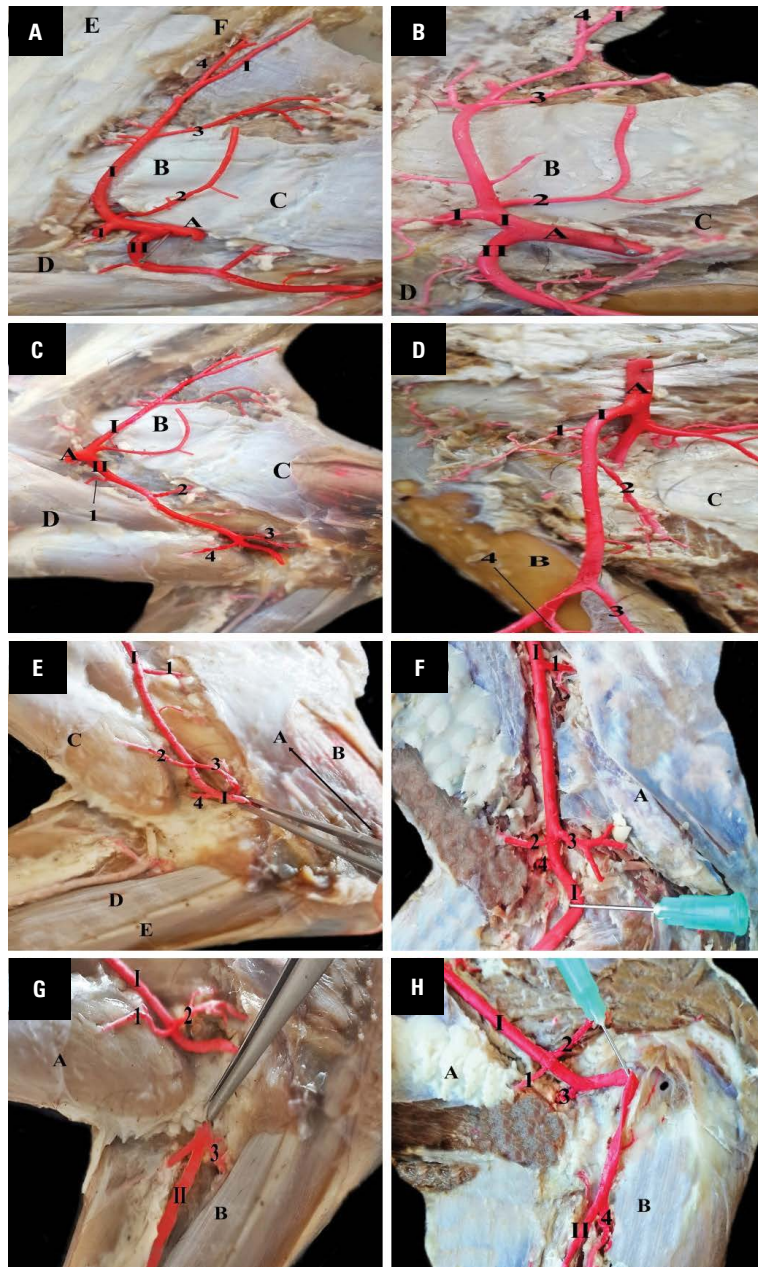


Figure 1. The branches of arteria brachialis and arteria subscapularis in Southern Karaman and Hasak sheep; **A.** Arteria subscapularis and its branches in Southern Karaman sheep, A — arteria axillaris, B — musculus teres major, C — musculus triceps brachii, D — musculus biceps brachii, E — musculus supraspinatus, F — musculus subscapularis, I — arteria subscapularis, II — arteria brachialis, 1 — arteria circumflexa humeri caudalis, 2 — arteria thoracodorsalis, 3 — ramus tricipitis, 4 — arteria circumflexa scapula; **B.** Arteria subscapularis and its branches in Hasak sheep, A — arteria axillaris, B — musculus teres major, C — musculus triceps brachii, D — musculus biceps brachii, I — arteria subscapularis, II — arteria brachialis, 1 — arteria circumflexa humeri caudalis, 2 — arteria thoracodorsalis, 3 — ramus tricipitis, 4 — arteria circumflexa scapula; **C.** Arteria brachialis and its branches in Southern Karaman sheep, A — arteria axillaris, B — musculus teres major, C — musculus triceps brachii, D — musculus biceps brachii, I — arteria subscapularis, II — arteria brachialis, 1 — arteria circumflexa humeri cranialis, 2 — arteria profunda brachii, 3 — arteria collateralis ulnaris, 4 — arteria bicipitalis; **D.** Arteria brachialis and its branches in Hasak sheep, A — arteria axillaris, B — os femur, C — musculus triceps brachii, I — arteria brachialis, 1 — arteria circumflexa humeri cranialis, 2 — arteria profunda brachii, 3 — arteria collateralis ulnaris, 4 — arteria bicipitalis; **E.** Arteria transversa cubiti in Southern Karaman sheep, A — articulatio cubiti, B — musculus triceps brachii, C — musculus biceps brachii, D — musculus flexor carpi radialis, I — arteria brachialis, 1 — arteria profunda brachii, 2 — arteria bicipitalis, 3 — arteria collateralis ulnaris, 4 — arteria transversa cubiti; **F.** Arteria transversa cubiti in Hasak sheep, A — musculus triceps brachii, I — arteria brachialis, 1 — arteria profunda brachii, 2 — arteria bicipitalis, 3 — arteria collateralis ulnaris, 4 — arteria transversa cubiti; **G.** Arteria interossea communis in Southern Karaman sheep, A — musculus biceps brachii, B — musculus flexor carpi radialis, I — arteria brachialis, II — arteria mediana, 1 — arteria bicipitalis, 2 — arteria collateralis ulnaris, 3 — arteria interossea communis; **H.** Arteria interossea communis in Hasak sheep, A — musculus biceps brachii, B — musculus flexor carpi radialis, I — arteria brachialis, II — arteria mediana, 1 — arteria bicipitalis, 2 — arteria collateralis ulnaris, 3 — arteria transversa cubiti, 4 — arteria interossea communis.

humeri cranialis in order to feed the musculus biceps brachii. It was determined that this branch run towards the cranio-lateral aspect of the limb. It was determined that arteria brachialis gave arteria profunda brachii on the distal part of tuberositas teres major (Fig. 1C–H). It was seen that after giving this branch, arteria brachialis gave thin muscular branches which continued in the same direction as it. Later, it was observed that two branches originating from the arteria brachialis that they continued in different directions. The branch that continued in the cranial direction was arteria bicipitalis and the branch that continued in the caudal direction was arteria collateralis ulnaris. Arteria collateralis ulnaris followed along the distal edge of musculus triceps brachii. It was determined that arteria bicipitalis was dispersed in musculus biceps brachii to feed it. Arteria brachialis was observed to give arteria transversa cubiti at the level of articulatio cubiti. Arteria brachialis gave its last branch, arteria interossea communis, at the level of the spatium interosseum antebrachii proximalis, then continued as the arteria mediana, cruising along the distal of the limb (Fig. 1E–H).

DISCUSSION

In mammals [6], it was reported that arteria axillaris was a continuation of the arteria subclavian and that arterial vascularisation of the forearm was provided by this vessel [17]. Arteria axillaris was found at the level of articulatio humeri [4]. Similar to us, previous report found that it continued towards the scapula with the name arteria subscapularis and arteria brachialis, which ran along the distal part of the limb [4].

Arteria circumflexa humeri caudalis have been reported to originate from arteria subscapularis [15, 16] and originate from the same place as arteria thoracodorsalis in ruminant [20]. Our results were similar to those of the literature.

Similar to our findings, previous studies [6, 14–17] reported that arteria thoracodorsalis originated from arteria subscapularis with the origin of arteria circumflexa humeri caudalis. However, unlike our findings, other previous study was reported that arteria thoracodorsalis originated from the dorsal wall of arteria axillaris [5].

The arteria subscapularis in the Southern Karaman and Hasak sheep continued its path as arteria circumflexa scapula after giving off arteria thoracodorsalis; it was also determined by Dursun [4] and Nickel [14].

Previous studies suggested that arteria brachialis continues as arteria mediana along the leg after giving the branch of arteria Interosseous communis [5, 11, 17]. Nur and Ari [17] reported that the arteria interosseous cranialis branch arises instead of the arteria interosseous communis branch, one of the branches separated from the arteria brachialis. It has been determined our findings differed from those of Nur and Ari [17], and showed similarities with other literature [5, 11].

Arteria circumflexa humeri cranialis at the proximal level of the humerus was reported to originate from the axial arteries of the medial face [6]. In addition, Nickel [14] reported that arteria circumflexa humeri cranialis originated from arteria brachialis. Our study findings were in line with the findings of Nickel [14], while they differ from those of Dursun [6].

According to Nur et al. [16] and Getty [11], arteria profunda brachii originated from arteria brachialis and according to Dursun [6] it was the first branch of arteria brachialis. Our study findings were similar to those in the literature, but differently, it was not the first branch of the arteria brachialis, but the second branch from the arteria brachialis that emerged after the arterial circumflexa humeri cranialis.

Similar to our study findings, it was reported that arteria collateralis ulnaris was a branch emerging from arteria brachialis and that it was distributed to musculus triceps brachii and arteria bicipitalis was distributed to musculus biceps brachii [4, 5, 17].

Ghoshal and Getty [12] determined that the palmar branch of the cranial interosseous artery passes through the distal interosseous space of the forearm and divides into a superficial and deep branch in goats [12]. Nickel noticed arterial communication between a branch of Ramus volaris profundus and a branch of arteria medianoradialis in three cases [14]. Also, Dursun [4] reported that arteria interosseous communis originated from arteria brachialis at the level of spatium interosseum antebrachii proximalis. In our study, arteria interosseous communis branches were found to originate from arteria brachialis and continue distally as arteria mediana.

CONCLUSIONS


In conclusion, the forelimb arteries in Southern Karaman and Hasak sheep breeds were found similar in regards of structure and morphology to the sheep breeds and some mammals. In addition to the ana-

tomical findings, this also will contribute to scientific studies on the forelimb arteries in the sheep breeds.

REFERENCES

1. Aycan K, Bilge A. Plastik enjeksiyon ve korozyon metodu ile vasküler system anatomisinin araştırılması. *ErciyesÜniv Tıp FakDerg.* 1984; 614: 545–552.
2. Buggei JA. standardisedplastik injection technique for anatomical purposes. *Acta Anat.* 1963; 51: 177–192.
3. Doğuer S. Evcil hayvanların komparatif sistematik anatomisi: dolaşım sistemi-angiologia. *Anakara Univ Vet Fak Yay, Anakara Univ Basımevi, Ankara* 1970.
4. Dursun N. Veteriner Komparatif Anatomi Dolasım Sistemi (Angiologia). *A.Ü. Vet. Fak. Yayınları, Ankara* 1981.
5. Dursun N, Tıpırdamaz S, Gezici M. Köpeklerde ön ekstremitenin arterial vaskularizasyonu, *S Ü Vet Fak Derg.* 1989; 5(1): 175–189.
6. Dursun N. Veteriner Anatomi II. *Medisan Yayın, Ankara* 1994.
7. Dyce KM, Sack WO, Wensing CJG. Text book of veterinary anatomy. *WB Saunders Company, Philadelphia* 1987.
8. Ekim O, Tunalı S. Hazıroğlu Merih R. Evcil memeli hayvanlarda böbreklerin soğuk ortam tekniği ile silikon plastinasyonu. *Vet Hekim Der Derg.* 2014; 85(2): 1–11.
9. Erençin Z, Hassa O, Sağlam M, et al. Enjeksiyon yoluyla damar ve kanal sistemleri için plastic demonstrasyon metodlarının geliştirilmesi. *Ankara Üniv Vet Fak Derg.* 1967; 14(3): 444–452.
10. Ertuğrul M, Dellal G, Soysal I, et al. Türkiye Yerli Koyun Irklarının Korunması, *Bursa Uludağ Üniversitesi Ziraat Fakültesi Dergisi.* 2009; 23(2): 97–119.
11. Getty R. Sisson and Grossman's the anatomy of the domestic animals. 5th ed. *WB Saunders Co, London* 1975.
12. Ghoshal NG, Getty R. The arterial supply to appendages of the goat (*Capra hircus*). *Iowa State University Veterinarian,* 1967; 29(3):123-144.
13. Kaymakçı M, Taşkın T. Türkiye Koyuncululuğunda Melezleme Çalışmaları. *Hayvansal Üretim.* 2008; 49(2): 43–51.
14. Nickel W. Arterien und Venen der Vordergliedmasse der Ziege. *Dissertation, Hannover, Germany, Tierärztliche Hochschule.* 1962.
15. Nickel R, Schummer A, Seiferle E. The anatomy of the domestic animals. *Verlag Paul Parey, Berlin* 1981.
16. Nur İH, Karadağ H, Arı HH, et al. Yenizellenda tavşanlarında Arteria Axillaris ve Dalları Üzerinde Makroanatomik Bir Çalışma. *F Ü Sağlık Bil Derg.* 1995; 9(2): 189–195.
17. Nur İH, Arı HH. Van kedilerinde ön kolun arterial donanımı üzerinde makroanatomik ve subgros bir çalışma. *YYÜ Vet Fak Derg.* 2000; 11: 93–103.
18. Özüdoğru Z, Aksoy G. Tuj koyununun ön bacak venaları üzerine makroanatomik bir çalışma. *Kafkas Univ Vet Fak Derg.* 2009; 15(5): 771–778.
19. Teke BE, Özüdoğru Z, Özdemir D, et al. Hasak Koyunlarında Kalp Kas Köprüleri ve Koroner Arterler. *J Bahri Dagdas Animal Res.* 2017; 6(1): 1–12.
20. Popesko P. Atlas of the topographical anatomy of the domestic animals 1975.
21. Sönmez R, Kaymakçı M, Eliçin A, et al. Türkiye Koyun Islahı Çalışmaları. *Bursa Uludağ Üniversitesi Ziraat Fakültesi Dergisi.* 2009; 23(2): 43–65.
22. Tekdemir I, Uz A, Tüccar E, et al. Vasküler Anatomi Çalışmalarında Renklendirilmiş Lateks Uygulaması. *AU Tıp Fakültesi Derg.* 1999; 52(1): 23–26.
23. World Association of Veterinary Anatomists. International Committee on Veterinary Gross Anatomical Nomenclature. *Nomina anatomica veterinaria.* Hannover; Columbia [Mo.]; Ghent; Sapporo: The Editorial Committee, 2005.

Case series and a systematic review concerning the level of the aortic bifurcation

E. Panagouli¹ , I. Antonopoulos¹, G. Tsoucalas², D. Chrysikos¹, A. Samolis¹, V. Protogerou¹, D. Venieratos¹, T. Troupis¹

¹Department of Anatomy, Medical School, National and Kapodistrian University of Athens, Greece

²Department of Anatomy, Medical School, Democritus University of Thrace, Alexandroupolis, Greece

[Received: 8 May 2020; Accepted: 26 May 2020]

Background: The aim of this study is to present the level of aortic bifurcation in a sample of Greek origin (case series) and to perform an up-to-date systematic review in the existing literature.

Materials and methods: Seventy-six formalin-fixed adult cadavers were dissected and studied in order to research the level of aortic bifurcation. Additionally, PubMed and Google Scholar databases were searched for eligible articles concerning the level of aortic bifurcation for the period up to February 2020.

Results: The mean level of aortic bifurcation according to our case series was the lower third of the L4 vertebral body (21/76, 27.6%). The level of aortic bifurcation ranged between the lower third of the L3 vertebral body and the lower third of the L5 body. No statistically significant correlation was found between the two sexes. The systematic review of the literature revealed 31 articles which were considered eligible and a total number of 3537 specimens were retracted. According to the recorded findings the most common mean level of aortic bifurcation was the body of L4 vertebra (1495/3537 cases, 42.2%), while the range of aortic bifurcation was described to occur from upper third of L3 vertebrae to the upper third of the S1 vertebrae in the 52.8% of the cases (1866/3537).

Conclusions: The mean level of AA corresponds to the body of L4 and presents a great range (from L3U to S1U). Knowledge of the mean level of aortic bifurcation and its probable ranges is of great significance for interventional radiologists and especially vascular surgeons that deal with aneurism proximal to the aortic bifurcation. (Folia Morphol 2021; 80, 2: 302–309)

Key words: aorta, intervertebral discs, lumbar vertebra, bifurcation, anatomy

INTRODUCTION

The aorta (or arteria magna) commences at the upper part of the left ventricle of the heart and after following a short ascending course, it forms the arcus aortae over the left lung's root and then follows a descending trajectory within the thorax as thoracic

aorta. After passing through the aortic opening of the diaphragm, at the level of the 12th thoracic vertebra, it is considered as the abdominal aorta (AA) [22, 31, 32].

Inside the abdominal cavity the AA terminates its course usually at the left side of the lower border of the 4th lumbar vertebra (L4), where it bifurcates into

Address for correspondence: Dr. E. Panagouli, Department of Anatomy, Medical School, University of Athens, Mikras Asias str. 75, 116 27 Athens, Greece, tel: 30 2107462394, fax: 30 2107462398, e-mail: eleni72000@yahoo.gr

This article is available in open access under Creative Common Attribution-Non-Commercial-No Derivatives 4.0 International (CC BY-NC-ND 4.0) license, allowing to download articles and share them with others as long as they credit the authors and the publisher, but without permission to change them in any way or use them commercially.

the right and left common iliac arteries. The width of the aorta just after passing through the diaphragm is considerably larger than the corresponding one at the level of its bifurcation [39].

According to the available literature, most commonly, aortic bifurcation occurs at the lower level of the L4 [6, 22], with a range which varies from the level of the L2 to the level of the upper third of the first sacral vertebra (S1) [6, 22]. However, AA tends to bifurcate lower than higher [6]. Additionally, it seems that in older persons, osteoporosis and intervertebral disc degeneration lead to a caudal shift of the aortic bifurcation [21, 32].

The purpose of the present study is twofold: (1) To present the level of aortic bifurcation in a sample of Caucasian origin (case series); (2) To perform an up-to-date systematic review concerning the level of aortic bifurcation in the available literature.

MATERIALS AND METHODS

Design of the case series

Seventy-six formalin-fixed adult human cadavers of Caucasian (Greek) origin, of which 39 were males and 37 females, were dissected for educational and research purposes at the Anatomy Department of the Medical School of Athens. All the cadavers derived from body donation with informed consent [27], written and signed with signature authentication by the donator himself. The authors retained approval for the present research's protocol from the ethics committee of our institution. The age of the cadavers ranged between 39 and 98 years (average age 75.4 years, standard deviation [SD] \pm 11.23, standard error [SE] = 1.288). In every one cadaver dissected, we identified and revealed the AA and its branches according to the Clemente's Anatomy Dissector [10].

The level of the AA bifurcation was measured in relation to the bodies of the lumbar vertebrae and the intervertebral discs. The bodies of the vertebrae were divided into upper, middle and lower thirds.

Statistical analysis

All the measurements were recorded in the form of tables and then subjected to statistical analysis in order to calculate the average, maximum and minimum value. For comparing continuous variables, the t-test was applied and for nominal variables the χ^2 test. All the statistical analysis was performed by SPSS 15.0.

Design of the systematic review

Study design. The present study was developed according to PRISMA guidelines, following current guidelines on conducting systematic reviews and meta-analysis of anatomical studies [17]. For the purpose of the systematic review, PubMed and Google Scholar electronic databases were searched for eligible articles for the period up to February 2020. No publication year restrictions were imposed. The following search terms were used: level of aortic bifurcation OR level of abdominal aorta bifurcation OR aortic bifurcation with lumbar vertebrae. The references of all the articles which were considered eligible were also thoroughly checked.

Inclusion criteria. Only original research articles examining the level of aortic bifurcation in relation to the bodies of the lumbar vertebrae in a human population sample (cadaveric or clinical study) and written in English or French were selected to be included to this systematic review. Single case reports and studies with overlapping populations were excluded. No limitations concerning race, age, sex or journal were imposed. Any type of unpublished material was excluded.

Eligibility assessment. Three independent reviewers (E.P., G.T. and V.P.) checked the studies which were retrieved for eligibility. Papers which did not meet eligibility criteria, duplicated studies or studies containing incomplete or irrelevant data were excluded. Eligible studies retrieved from reference lists checking were also added. Assessment of bias was performed with anatomical quality assessment tool (AQUA) [16, 17].

Data extraction. The studies considered eligible were screened by two independent reviewers (E.P. and G.T.) who extracted all the relevant data. For each study considered eligible the following parameters were collected: year of publication, type of the study (cadaveric, clinical, imaging), number of specimens, age, range and mean vertebral level of aortic bifurcation. After the evaluation of data, the results were recorded in the form of Tables 1 and 2. The range, the mean level of bifurcation, as well as the frequency and percentage of each category were calculated.

RESULTS

Case series

The bifurcation of AA was observed on each cadaver dissected without identifying any anatomical variation.

Table 1. Eligible studies

Authors, year	Type of studies	N	Age
George, 1935	Cadaveric study	105	> 17 years
Anson and McVay, 1936	Cadaveric study	100	–
Cauldwell and Anson, 1943	Cadaveric study	294	18 to 78 years
Lerona and Tewfik, 1975	Pelvic arteriograms	100	15 to 82 years
Watt and Park, 1978	Angiographic study	9	2 to 13 years
Kawahara et al., 1996	Cadaveric study	21	75 years
Kornreich et al., 1997	CT study	180	–
Chithrki et al., 2002	MRI study	441	15 to 95 years
Lee et al., 2004	MRI study	210	67.3 ± 0.8 years
Inamasu et al., 2005	MRI study	100	–
Pennington and Soames, 2005	Cadaveric study	15	67 to 95 years
Pirro et al., 2005	Cadaveric study	42	81 ± 8 years
Datta et al., 2007	CTA study	76	
Lakchayapakorn and Siriprakarn, 2008	Cadaveric study	65	73 ± 10 years
Khamanarong et al., 2009	Cadaveric study	187	67.3 ± 0.8 years
Prakash et al., 2011	Cadaveric study	54	16 to 74 years
Mirjalili et al., 2012	CT study	108	60 ± 17 years (18–97 years)
Vaccaro et al., 2012	MRI study	30	41 years (19–89 years)
Barrey et al., 2013	MRI study	146	46 ± 12 years
Butoi et al., 2013	Cadaveric study	148	–
Sharma et al., 2013	Cadaveric study	35	–
Deswal et al., 2014	Cadaveric study	25	–
Ashwini et al., 2014	Cadaveric study	40	–
Ogeng'o et al., 2014	Cadaveric study	106	27 to 81 years
Marchi et al., 2015	MRI study	108	–
Keskinoz et al., 2016	MDCT study	200	50 to 84 years
Molinares et al., 2016	MRI study	100	57.4 years (22–88 years).
Myung-Sang, 2017	CT study	48	30 to 90 years
Gregory et al., 2019	CTA study	232	Neonate to 19 years
Bečulić et al., 2019	MRI study	40	53.7 years (26–69 years)
Goyal et al., 2019	CT study	100	43.78 ± 13.1 years (19–70 years)

CT — computed tomography; CTA — computed tomography angiography; MDCT — multidetector computed tomography; MRI — magnetic resonance imaging

The mean level of AA bifurcation (21/76, 27.6%) was the lower third of the L4 vertebral body (L4L). In relation to the vertebral bodies, the level of AA bifurcation ranged between the lower third of the L3 vertebral body (L3L) and the lower third of the L5 body (L5L) (Fig. 1).

Both in females (32.4%, 12/37) and males (23.1%, 9/39) the mean level of bifurcation corresponded also to the lower third of the L4 body (L4L). In females the level of bifurcation ranged between the lower third of the L3 body (L3L) and the middle third of the L5 vertebral body (L5M) and in males between the

L3–L4 intervertebral disk and the L5L. However, no statistically significant correlation was found between the two sexes ($p = 0.521$, $p > 0.05$).

The AA division levels in relation to the lumbar vertebral bodies and the relevant intervertebral discs in the total of the cadaveric specimens are depicted in Figure 2 and between the sexes in Figure 3.

Systematic review

All details regarding the selection of eligible studies are presented in Figure 4 (PRISMA flow diagram). Eventually 31 articles were found eligible and were

Table 2. Mean level and range of aorta bifurcation related to vertebral bodies

Authors, year	N	Level	Range
George, 1935	105	L4L (25/105)	L3L to L5L
Anson and McVay, 1936	100	L4M (32/100)	L3M to L5M
Cauldwell and Anson, 1943	294	L4–L5 (83/294)	L3M to L5L
Lerona and Tewfik, 1975	100	L4L (35/100)	L4U to L5L
Watt and Park, 1978	9	L4 (5/9)	L4 to L5–S1
Kawahara et al., 1996	21	L4–L5 (9/21)	L3 to L5
Kornreich et al., 1997	180	L4U (62/180)	L3U to S1U
Chithrki et al., 2002	441	L4 (295/441)	L3U to L5M
Lee et al., 2004	210	L4U (94/210)	L3L to L5U
Inamasu et al., 2005	100	L4 (55/100)	L3 to L5
Pennington and Soames, 2005	15	L4L (6/15)	L4U to S1U
Pirro et al., 2005	42	L5 (21/42)	L3 to S1
Datta et al., 2007	76	L4 (39/76)	L3 to S1
Lakchayapakorn and Siriprakarn, 2008	65	L4M (41/65)	L3 to L5
Khamanarong et al., 2009	187	L4 (131/187)	L4 to L5
Prakash et al., 2011	50	L4 (27/50)	L3 to L5
Mirjalili et al., 2012	108	L4 (65/108)	L3L to L5L
Vaccaro et al., 2012	30	L4 (22/30)	L3 to L5
Barrey et al., 2013	146	L4 (93/146)	L3-L4 to L4–L5
Butoi et al., 2013	148	L4–L5 (40/148)	L3M to L5–S1
Sharma et al., 2013	35	L4 (19/35)	L3 to L5
Deswal et al., 2014	25	L4 (16/25)	L3 to L5
Ashwini et al., 2014	40	L4 (22/40)	L3 to L5–S1
Ogeng'o et al., 2014	106	L4L (41/106)	L3-L4 to L5
Marchi et al., 2015	108	L4 (56/108)	L3 to L5
Keskinoz et al., 2016	200	L4M (53/200)	L3M to L5U
Molinares et al., 2016	100	L4M (33/100)	L3L to L5L
Myung-Sang, 2017	48	L3-L4 (23/48)	L3 to L5
Gregory et al., 2019	232	L4 (155/232)	L3 to L5
Bečulić et al., 2019	40	L4L (14/40)	L3M to L5–S1
Goyal et al., 2019	100	L4U(38/100)	L3U to L5U
Present series	76	L4L (21/76)	L3L to L5L
Total	3537	L4 (1495/3537)	L3U to S1U

included (Table 1). Due to overlapping population, a previous study of the authors was not included [23]. Among them, 14 were cadaveric studies [1, 2, 7, 8, 12, 13, 19, 21, 23, 31, 33–36], 8 were magnetic resonance imaging (MRI) studies [4, 5, 9, 18, 24, 26, 29, 37], 4 were computed tomography (CT) studies [14, 22, 28, 30], 2 were computed tomography angiography (CTA) studies [11, 15], 1 multidetector computed tomography (MDCT) study [20], 1 was angiographic study [38] and 1 was based on pelvic arteriograms [25]. Mean age or age range where included when

available. Low risk of bias was detected. However, the lack of clearly defined demographic characteristics might represent a factor compromising the quality of studies.

The mean level of bifurcation and the range of the bifurcation level of the AA in relation to the bodies of the lumbar vertebrae and the intervertebral discs for each study are recorded in Table 2. In cases where the vertebral bodies were not subdivided into upper, middle and lower thirds, as in our study, only the corresponding vertebra is mentioned.

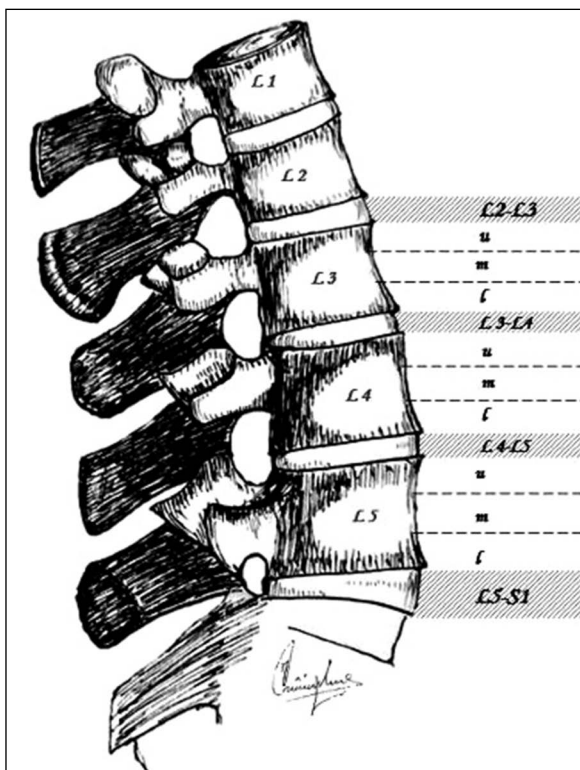


Figure 1. Ranges of the level of abdominal aorta (AA) bifurcation; U — upper; m — middle; l — lower.

A total number of 3537 specimens resulted from the eligible studies. According to the recorded findings the most common mean level of AA bifurcation was the body of L4 vertebra (1495/3537 cases, 42.2%). In the studies were the body of the vertebra was divided in three thirds, the bifurcation most frequently occurred at upper third of L4. Considerably less frequently the mean level corresponded to L4–L5

intervertebral disc (132/3537 cases 3.7%), while the L3–L4 intervertebral disc and the body of L5 were observed as mean level of bifurcation in only a few studies (23/3537, 0.65% and 21/3537, 0.59%). Concerning the range of AA bifurcation, a great variability was observed, as the bifurcation was described to occur from upper third of L3 vertebrae to the upper third of the S1 vertebrae in the 52.8% of the cases (1866/3537). The results are represented in Table 3.

DISCUSSION

Topographic anatomy of AA bifurcation is fairly important for many medical procedures as gynaecology, abdominal surgery or radiology, in order to avoid complications or misdiagnosis [31]. Clinically, the umbilicus is considered to be a reliable surface landmark for the level of AA bifurcation [3]. More accurate, the level of AA bifurcation is evaluated in relation to the vertebral bodies and especially the lower lumbar ones and rarely in relation to the sacrum. Several studies have been performed and may be found in the available literature covering this field, [1, 2, 4, 5, 7–9, 11–15, 18–26, 28–31, 33–38] either in cadaveric material or by the use of CT, MRI and CTA. According to the results of the present study, the bifurcation of the AA corresponds in most of the cases to the body of L4 vertebra — upper, medial or lower third (1495/3537 cases, 42.2%) and that was also the level discovered in our case-series (21/76, 27.6%). From our systematic review it occurred that the level of bifurcation presents great variation as it ranges from L3U to S1U, with the most frequent levels being between L3 and L5 (Table 3).

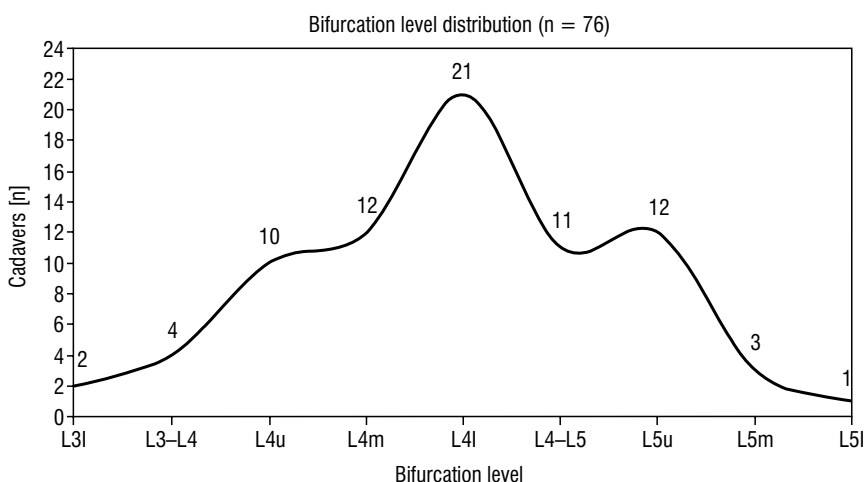


Figure 2. The abdominal aorta bifurcation levels in relation to the lumbar vertebral bodies and the relevant intervertebral discs in the total of the cadaveric specimens; U — upper; m — middle; l — lower.

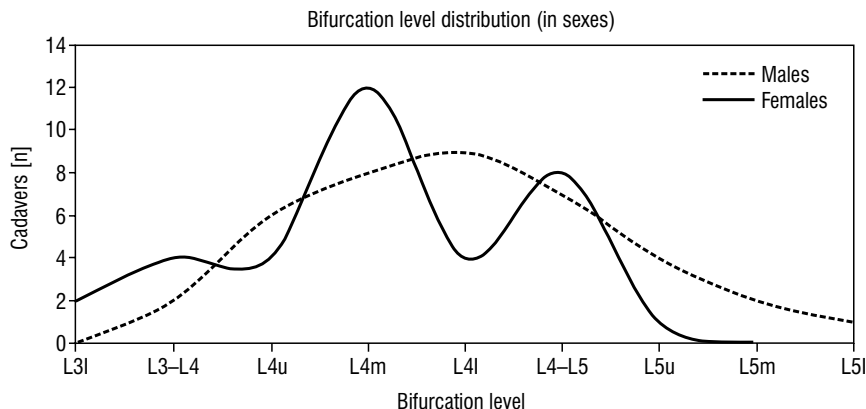


Figure 3. The abdominal aorta bifurcation levels in relation to the lumbar vertebral bodies and the relevant intervertebral discs between the sexes; U — upper; m — middle; l — lower.

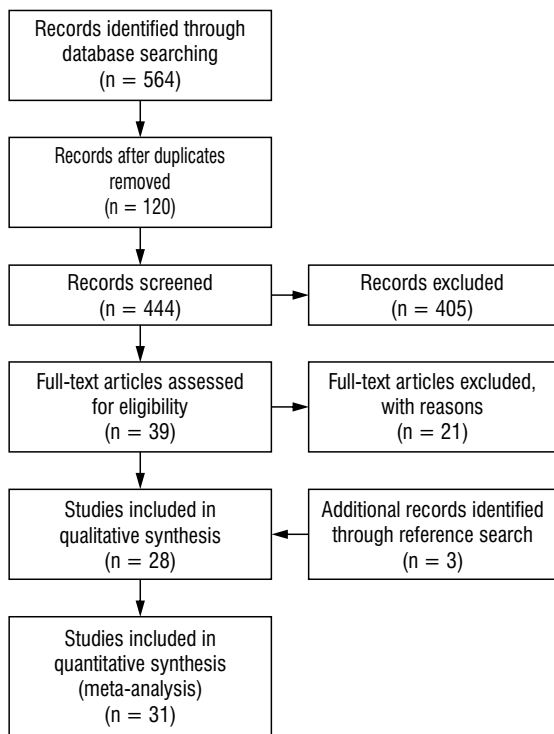


Figure 4. Flow diagram of the studies (according to PRISMA guidelines); the diagram describes the steps followed during the selection of the eligible studies.

Kawahara et al. 1996 [19] reported that the level of termination of great vessels shifted significantly downwards with age and this observation is justified by the loss of overall height due to dehydration of intervertebral discs as well as osteoporosis in the elderly. The present case series was performed in rather aged cadavers (mean age 75.4 ± 11.23 years) and the level of their aortic bifurcation ranged between L3L and L5L. The studies retrieved from the systematic

Table 3. Mean and range level of abdominal aorta (AA) bifurcation according to the retrieved studies

Mean level of AA bifurcation	Range of AA bifurcation
L3-L4: 132/3537 — 3.7%	L3U to S1U 1286/1866
L4: 1495/3537 — 42.2%	L4 to L5: 121/1866
L4 body, n = 993	— 52.8%
L4U, n = 194	L4 to L5-S1: 4/1866
L4M, n = 159	L3 to S1: 176/1866
L4L, n = 149	L4 to S1: 9/1866
L4-L5: 23/3537 — 0.65%	L3-L4 to L4-L5: 53/1866
L5: 21/3537 — 0.59%	L3 to L5-S1: 152/1866
	L3-L4 to L5: 65/1866

review showed a variable age range (Table 1). Moreover, many of them included both youngsters as older people as well [8, 9, 14, 25, 29, 35, 37]. However, both range and mean level of aortic bifurcation did not seem to differ according to age. Additionally, in the two studies which were conducted exclusively in children [15, 38] a great range was also recorded (L4 to L5-S1 and L3 to L5, respectively). Nevertheless, all above mentioned facts, combined with the lack of age details in some studies [1, 2, 7, 12, 18, 22, 36] could not lead to a safe result concerning the correlation between age and level range of AA bifurcation.

The same mean level of AA bifurcation was observed in both sexes in our case series. That was also the case in the study of Molinares et al. [29], Bečulić et al. [5], and Goyal et al. [14], while in most of the remaining studies, details about sexes were not provided and or when present, the presence of a statistically significant difference between sexes was not discussed at all. Consequently, it seems that the level of aortic bifurcation does not differ according to gender. Moreover, is worth to mention that Bečulić et al. [5] concluded in their

study that the level of AA bifurcation was independent on gender, height or body mass index.

Concerning the limitations of the present study, the most important was the lack of demographic characteristics of most of the studies. The majority did not provide detailed data about age and gender. Another limitation was the fact that there was a wide age range and that some studies consisted of live patients while others were conducted on cadavers. Radiographic studies may also have limitations in detecting the level of aortic bifurcation. Nevertheless, not important differences have been observed between the two types of studies.

Knowledge of the exact level of AA bifurcation is important for the planning of a great number of laparoscopic, transcatheter arterial chemoembolisation and radioembolisation procedures, as well in view of surgery in the area involved as it will minimize the risk of injury and complications [2, 14, 29]. The fact that the mean level of bifurcation is at L4 vertebra and the range is over S1, is helpful information in the planning of approach during surgery, especially when the area of operation involves L4–L5 [14, 31]. Another field of medicine where the familiarity with the level of AA bifurcation is necessary is radiation therapy planning [14, 29]. Finally, it could help in the identification of the vertebral level in imaging [14, 29].

CONCLUSIONS

Knowledge of the mean level of AA bifurcation and its probable ranges is important for a number of surgical and radiologic procedures. Our systematic review, combined with a case series study concluded that the mean level of AA corresponds to the body of L4 and presents a great range (from L3U to S1U). Aging might cause a caudal shift of AA, nevertheless different ranges and low levels might occur in any age. Finally, there is no indication of a different level according to gender.

REFERENCES

1. Anson B, McVay C. The topographical positions and the mutual relations of the visceral branches of the abdominal aorta. A study of 100 consecutive cadavers. *Anat Rec*. 1936; 67(1): 7–15, doi: [10.1002/ar.1090670103](https://doi.org/10.1002/ar.1090670103).
2. Appaji AC, Kulkarni R, Pai D. Level of Bifurcation of Aorta and Iliac Confluence and Its Clinical Relevance. *IOSR-JDMS*. 2014; 13(7): 56–60, doi: [10.9790/0853-13725660](https://doi.org/10.9790/0853-13725660).
3. Attwell L, Rosen S, Upadhyay B, et al. The umbilicus: a reliable surface landmark for the aortic bifurcation? *Surg Radiol Anat*. 2015; 37(10): 1239–1242, doi: [10.1007/s00276-015-1500-1](https://doi.org/10.1007/s00276-015-1500-1), indexed in Pubmed: [26044782](https://pubmed.ncbi.nlm.nih.gov/26044782/).
4. Barrey C, Ene B, Louis-Tisserand G, et al. Vascular anatomy in the lumbar spine investigated by three-dimensional computed tomography angiography: the concept of vascular window. *World Neurosurg*. 2013; 79(5-6): 784–791, doi: [10.1016/j.wneu.2012.03.019](https://doi.org/10.1016/j.wneu.2012.03.019), indexed in Pubmed: [22480981](https://pubmed.ncbi.nlm.nih.gov/22480981/).
5. Bečulić H, Sladojević I, Jusić A, et al. Morphometric study of the anatomic relationship between large retroperitoneal blood vessels and intervertebral discs of the distal segment of the lumbar spine: a clinical significance. *Med Glas (Zenica)*. 2019 [Epub ahead of print]; 16(2), doi: [10.17392/1011-19](https://doi.org/10.17392/1011-19), indexed in Pubmed: [31077124](https://pubmed.ncbi.nlm.nih.gov/31077124/).
6. Bergman RA, Afifi AK, Miyauchi R. Illustrated Encyclopedia of Human Anatomic Variation. <http://www.anatomyatlases.org/AnatomicVariants/AnatomyHP.shtml> (last revised: 2006).
7. Butoi G, Iliescu DM, Baz R, et al. Morphology of the terminal aorta. *ARS Medica Tomitana*. 2013; 19(2): 61–111, doi: [10.2478/arsm-2013-0011](https://doi.org/10.2478/arsm-2013-0011).
8. Cauldwell E, Anson B. The visceral branches of the abdominal aorta: Topographical relationships. *Am J Anat*. 2005; 73(1): 27–57, doi: [10.1002/aja.1000730103](https://doi.org/10.1002/aja.1000730103).
9. Chithrithi M, Jaibaji M, Steele RD. The anatomical relationship of the aortic bifurcation to the lumbar vertebrae: a MRI study. *Surg Radiol Anat*. 2002; 24(5): 308–312, doi: [10.1007/s00276-002-0036-3](https://doi.org/10.1007/s00276-002-0036-3), indexed in Pubmed: [12497222](https://pubmed.ncbi.nlm.nih.gov/12497222/).
10. Clemente C, Clemente C. Clemente's anatomy dissector. Lippincott Williams & Wilkins, Philadelphia, Pa 2010: 131–160.
11. Datta JC, Janssen ME, Beckham R, et al. The use of computed tomography angiography to define the prevertebral vascular anatomy prior to anterior lumbar procedures. *Spine (Phila Pa 1976)*. 2007; 32(1): 113–119, doi: [10.1097/01.brs.0000250991.02387.84](https://doi.org/10.1097/01.brs.0000250991.02387.84), indexed in Pubmed: [17202901](https://pubmed.ncbi.nlm.nih.gov/17202901/).
12. Deswal A, Tamang BK, Bala A. Study of aortic-common iliac bifurcation and its clinical significance. *J Clin Diagn Res*. 2014; 8(7): AC06–AC08, doi: [10.7860/JCDR/2014/8767.4559](https://doi.org/10.7860/JCDR/2014/8767.4559), indexed in Pubmed: [25177553](https://pubmed.ncbi.nlm.nih.gov/25177553/).
13. George R. Topography of the unpaired visceral branches of the abdominal aorta. *J Anat*. 1935; 69(Pt 2): 196–205, indexed in Pubmed: [17104532](https://pubmed.ncbi.nlm.nih.gov/17104532/).
14. Goyal R, Aggarwal A, Gupta T, et al. Reappraisal of the classical abdominal anatomical landmarks using in vivo computerized tomography imaging. *Surg Radiol Anat*. 2020; 42(4): 417–428, doi: [10.1007/s00276-019-02326-4](https://doi.org/10.1007/s00276-019-02326-4), indexed in Pubmed: [31511961](https://pubmed.ncbi.nlm.nih.gov/31511961/).
15. Gregory LS, McGifford OJ, Jones LV. Differential growth patterns of the abdominal aorta and vertebrae during childhood. *Clin Anat*. 2019; 32(6): 783–793, doi: [10.1002/ca.23400](https://doi.org/10.1002/ca.23400), indexed in Pubmed: [31056783](https://pubmed.ncbi.nlm.nih.gov/31056783/).
16. Henry BM, Tomaszewski KA, Ramakrishnan PK, et al. Development of the anatomical quality assessment (AQUA) tool for the quality assessment of anatomical studies included in meta-analyses and systematic reviews. *Clin Anat*. 2017; 30(1): 6–13, doi: [10.1002/ca.22799](https://doi.org/10.1002/ca.22799), indexed in Pubmed: [27718281](https://pubmed.ncbi.nlm.nih.gov/27718281/).
17. Henry BM, Tomaszewski KA, Walocha JA. Methods of evidence-based anatomy: a guide to conducting systematic reviews and meta-analysis of anatomical

- studies. *Ann Anat.* 2016; 205: 16–21, doi: [10.1016/j.aanat.2015.12.002](https://doi.org/10.1016/j.aanat.2015.12.002), indexed in Pubmed: [26844627](https://pubmed.ncbi.nlm.nih.gov/26844627/).
18. Inamasu J, Kim DH, Logan L. Three-dimensional computed tomographic anatomy of the abdominal great vessels pertinent to L4-L5 anterior lumbar interbody fusion. *Minim Invasive Neurosurg.* 2005; 48(3): 127–131, doi: [10.1055/s-2004-830262](https://doi.org/10.1055/s-2004-830262), indexed in Pubmed: [16015487](https://pubmed.ncbi.nlm.nih.gov/16015487/).
 19. Kawahara N, Tomita K, Baba H, et al. Cadaveric vascular anatomy for total en bloc spondylectomy in malignant vertebral tumors. *Spine (Phila Pa 1976).* 1996; 21(12): 1401–1407, doi: [10.1097/00007632-199606150-00001](https://doi.org/10.1097/00007632-199606150-00001), indexed in Pubmed: [8792515](https://pubmed.ncbi.nlm.nih.gov/8792515/).
 20. Keskinöz E, Salbacak A, Akin D, et al. Morphometric analysis of the inferior vena cava related to lumbar vertebra and the aortic bifurcation on multidetector computed tomography (MDCT). *Int J Morphol.* 2016; 34(2): 620–627, doi: [10.4067/s0717-95022016000200033](https://doi.org/10.4067/s0717-95022016000200033).
 21. Khamanarong K, Sae-Jung S, Supa-Adirek C, et al. Aortic bifurcation: a cadaveric study of its relationship to the spine. *J Med Assoc Thai.* 2009; 92(1): 47–49, indexed in Pubmed: [19260243](https://pubmed.ncbi.nlm.nih.gov/19260243/).
 22. Kornreich L, Hadar H, Sulkes J, et al. Effect of normal ageing on the sites of aortic bifurcation and inferior vena cava confluence: a CT study. *Surg Radiol Anat.* 1998; 20(1): 63–68, doi: [10.1007/BF01628118](https://doi.org/10.1007/BF01628118), indexed in Pubmed: [9574492](https://pubmed.ncbi.nlm.nih.gov/9574492/).
 23. Lakchayapakorn K, Siriprakarn Y. Anatomical variations of the position of the aortic bifurcation, ilioacava junction and iliac veins in relation to the lumbar vertebra. *J Med Assoc Thai.* 2008; 91(10): 1564–1570, indexed in Pubmed: [18972901](https://pubmed.ncbi.nlm.nih.gov/18972901/).
 24. Lee CH, Seo BoK, Choi YC, et al. Using MRI to evaluate anatomic significance of aortic bifurcation, right renal artery, and conus medullaris when locating lumbar vertebral segments. *Am J Roentgenol.* 2004; 182(5): 1295–1300, doi: [10.2214/ajr.182.5.1821295](https://doi.org/10.2214/ajr.182.5.1821295), indexed in Pubmed: [15100135](https://pubmed.ncbi.nlm.nih.gov/15100135/).
 25. Lerona PT, Tewfik HH. Bifurcation level of the aorta: landmark for pelvic irradiation. *Radiology.* 1975; 115(3): 735, doi: [10.1148/15.3.735](https://doi.org/10.1148/15.3.735), indexed in Pubmed: [1129492](https://pubmed.ncbi.nlm.nih.gov/1129492/).
 26. Marchi L, Oliveira L, Amaral R, et al. Morphometric study of the areolar space between the great vessels and the lumbar spine. *Coluna/Columna.* 2015; 14(4): 271–275, doi: [10.1590/s1808-185120151404152843](https://doi.org/10.1590/s1808-185120151404152843).
 27. McHanwell S, Brenner E, Chirculescu ARM, et al. The legal and ethical framework governing Body Donation in Europe: a review of current practice and recommendations for good practice. *Eur J Anat.* 2008; 12: 1–24.
 28. Mirjalili SA, McFadden SL, Buckenham T, et al. A reappraisal of adult abdominal surface anatomy. *Clin Anat.* 2012; 25(7): 844–850, doi: [10.1002/ca.22119](https://doi.org/10.1002/ca.22119), indexed in Pubmed: [22744875](https://pubmed.ncbi.nlm.nih.gov/22744875/).
 29. Molinares DM, Davis TT, Fung DA. Retroperitoneal oblique corridor to the L2-S1 intervertebral discs: an MRI study. *J Neurosurg Spine.* 2016; 24(2): 248–255, doi: [10.3171/2015.3.SPINE13976](https://doi.org/10.3171/2015.3.SPINE13976), indexed in Pubmed: [26451662](https://pubmed.ncbi.nlm.nih.gov/26451662/).
 30. Moon MS. Anatomical location, running pattern, and bifurcation level of abdominal aorta over the lumbosacral spine: computed tomography angiographic study. *J Spinal Surg.* 2017; 4(3): 97–101, doi: [10.5005/jp-journals-10039-1138](https://doi.org/10.5005/jp-journals-10039-1138).
 31. Ogeng'o J, Olabu B, Ongeti K, et al. Topography of aortic bifurcation in a black kenyan population. *Anat J Africa.* 2014; 3(2).
 32. Panagouli E, Lolis E, Venieratos D. A morphometric study concerning the branching points of the main arteries in humans: relationships and correlations. *Ann Anat.* 2011; 193(2): 86–99, doi: [10.1016/j.aanat.2010.10.009](https://doi.org/10.1016/j.aanat.2010.10.009), indexed in Pubmed: [21169000](https://pubmed.ncbi.nlm.nih.gov/21169000/).
 33. Pennington N, Soames RW. The anterior visceral branches of the abdominal aorta and their relationship to the renal arteries. *Surg Radiol Anat.* 2005; 27(5): 395–403, doi: [10.1007/s00276-005-0026-3](https://doi.org/10.1007/s00276-005-0026-3), indexed in Pubmed: [16177834](https://pubmed.ncbi.nlm.nih.gov/16177834/).
 34. Pirró N, Ciampi D, Champsaur P, et al. The anatomical relationship of the ilioacava junction to the lumbosacral spine and the aortic bifurcation. *Surg Radiol Anat.* 2005; 27(2): 137–141, doi: [10.1007/s00276-004-0301-8](https://doi.org/10.1007/s00276-004-0301-8), indexed in Pubmed: [15611835](https://pubmed.ncbi.nlm.nih.gov/15611835/).
 35. Rajini T, Mokhasi V, Geethanjali BS, et al. The abdominal aorta and its branches: anatomical variations and clinical implications. *Folia Morphol.* 2011; 70(4): 282–286, indexed in Pubmed: [22117246](https://pubmed.ncbi.nlm.nih.gov/22117246/).
 36. Sharma M, Sharma T, Singh R. Variations in the aortic — common iliac bifurcation in man: a cadaveric study. *Nat J Clin Anat.* 2020; 02(02): 056–060, doi: [10.1055/s-0039-3401703](https://doi.org/10.1055/s-0039-3401703).
 37. Vaccaro AR, Kepler CK, Rihn JA, et al. Anatomical relationships of the anterior blood vessels to the lower lumbar intervertebral discs: analysis based on magnetic resonance imaging of patients in the prone position. *J Bone Joint Surg Am.* 2012; 94(12): 1088–1094, doi: [10.2106/JBJS.K.00671](https://doi.org/10.2106/JBJS.K.00671), indexed in Pubmed: [22717827](https://pubmed.ncbi.nlm.nih.gov/22717827/).
 38. Watt I, Park WM. The abdominal aorta in spina bifida cystica. *Clin Radiol.* 1978; 29(1): 63–68, doi: [10.1016/s0009-9260\(78\)80167-6](https://doi.org/10.1016/s0009-9260(78)80167-6), indexed in Pubmed: [624204](https://pubmed.ncbi.nlm.nih.gov/624204/).
 39. White HJ, Bordes S, Borger J. Anatomy, Abdomen and Pelvis, Aorta. In: StatPearls. StatPearls Publishing, Treasure Island (FL) 2020.

Morphological particularities and morphometry of rats' kidneys under the effect of experimental mild traumatic brain injury

R. Prus¹, P. Pokotylo², M. Logash², T. Zvir³

¹Department of Pathological Anatomy with Section Course, Odessa National Medical University, Odessa, Ukraine

²Department of Normal Anatomy, Danylo Halytsky Lviv National Medical University, Lviv, Ukraine

³Liaison Librarian, the Catholic University of America, Washington, United States

[Received: 18 February 2020; Accepted: 7 April 2020]

Background: Traumatic brain injury (TBI) is one of the most serious problems of modern medicine that plays the dominant role in the morbidity and mortality of population of the economically developed countries. This article presents the findings of the experimental study of the effect of a mild TBI on the morphology of rats' kidney.

Materials and methods: The experiment was performed on 70 adult white rats 3 months of age. The mild TBI was modelled by the Impact-Acceleration Model — free fall of weight in the parieto-occipital area. For histopathological comparison, the samples were taken on the 1st, 3rd, 5th, 7th, 14th, 21st days after TBI.

Results: Examination of the rat's kidney histological slides on the 1st, 3rd, 5th, 7th, 14th, and 21st days after the TBI showed manifested changes in the bloodstream and structural changes in the kidney parenchyma, particularly, dilatation of the capillaries and veins in the initial period. It also showed perivascular lymphocytic infiltration, dystrophic and necrotic processes in the form of the focal destruction of the renal tubule, and renal corpuscles with diapedesis and perivascular haemorrhages on the 5th and 7th days after the TBI. There were also the focal signs of perivascular and glomerular sclerosis observed on the 14th and 21st days after the injury.

Conclusions: The greatest changes in the rats' kidneys appear on the 5th–7th days after the injury, which have a clear tendency to decrease after that. (Folia Morphol 2021; 80, 2: 310–316)

Key words: traumatic brain injury, kidney, rat, nephron

INTRODUCTION

Traumatic brain injury (TBI) is one of the most important problems of modern medicine, which plays a major role in the morbidity and mortality of the population even in the most economically developed countries [3, 7, 8, 10, 11, 20, 23, 25, 26]. This medical

problem is multidisciplinary in the field of practical and experimental medicine and biology, which, in addition to medical, has an important social significance, given the young age of patients traumatized, and the significant cost of their treatment [9, 24].

Address for correspondence: L. Maksim, Assistant Professor, Danylo Halytsky Lviv National Medical University, Pekarska str. 69, 79010 Lviv, Ukraine, tel: +38 0975524441, e-mail: maxlohash@gmail.com

This article is available in open access under Creative Common Attribution-Non-Commercial-No Derivatives 4.0 International (CC BY-NC-ND 4.0) license, allowing to download articles and share them with others as long as they credit the authors and the publisher, but without permission to change them in any way or use them commercially.

Traumatic brain injury has a global effect on the body, causing a general adaptive response, which is manifested by a complex of pathophysiological and pathomorphological changes not only in the area of direct mechanical damage but also in various organs and systems of the body, in particular in the kidneys [4, 5]. Currently, there is a small amount of experimental research that would reveal the content of morphological disorders of the internal organs of pubescent and immature rats due to TBI, especially in the advanced period. As for the paediatric TBI, it is known that a distinctive feature of the dynamics and clinical picture of TBI in children is the impact of a traumatic factor on the brain, the growth and development of which has not yet completed [6]. In addition, the intensity of metabolic processes, low tolerance to blood loss, hypoxia and hypotension, prevalence of generalised reactions over local, high compensatory opportunities with a fast transition to decompensation, should be taken into account in a case of TBI in children [22]. This is the reason why the TBIs of even mild severity caused in childhood do not go away without a trace.

It has been shown that in severe TBI, especially in its acute period, liver and renal failure are among the most common disorders, as well as individual disorders in the coronary vessels and myocardium [15]. Extracranial complications, including acute kidney injury, are highly influential in determining the outcome from severe head injury [2, 12, 13, 17, 19] and may contribute to morbidity and mortality. However, there is neither a clear understanding of the pathogenesis of such effects nor experimental work that would confirm or refute the assumption of morphological changes in the kidney, as a result of TBI, particularly — mild TBI. The purpose of this study was to reveal the content of internal organ morphology, particularly the kidneys, in rats affected by TBI of mild severity with particular focus on pubescent rats. Thus, the first stage of this study was to investigate such changes in pubescent rats immediately after the injury and in the more advanced period after the injury.

MATERIALS AND METHODS

The study was performed on 70 adult white rats aged 3 months with the bodyweight of 180–230 g. All animals were divided into two groups: 1 — healthy animals (control group, 10 animals), 2 — animals with simulated mechanical TBI of mild severity (60 animals). Animals in group 2 were removed from the

experiment on days 1, 3, 5, 7, 14, and 21 after the TBI modelling (10 animals on each day). Rats were kept on a standard laboratory diet with free unrestricted access to water at the vivarium of the Odessa National Medical University. All experiments were carried out in compliance with the provisions of the European Convention for the Protection of Vertebrate Animals used for research and other scientific purposes (Strasbourg, 18.03.1986), Council of Europe Directive 86/609/EEC (1986), resolutions of the First National Congress on Bioethics (Kyiv, 2001), and the Ministry of Health of Ukraine Order No. 690 (Kyiv, 23.09.2009). All stages of the experiments were approved by the ONMEDU Bioethics Commission (Minutes No. 109-A, 4.11. 2016). Mild TBI was inflicted by using the Impact-Acceleration Model, a free fall of weight onto the parieto-occipital area according to Meretskyi [16]. Reproduction of TBI a vertically mounted tripod metal guide tube was used with an inner diameter of 1 mm and a height of 65 cm. The tube served as a guide for a freely moving weight inside. The latter represented a circular metal rod, to which a solid rubber strip 3 mm thick and 0.5 cm² in area was glued to the lower end. The tripod stand was also glued with a sturdy rubber gasket. By means of light ether anaesthesia, the animals were placed under the tube so that the head was clearly below the opening and fixed by the experimenter. Then the tractor performed a free fall with a subsequent blow to the skull of the animal. Thus, the centre of impact was clearly on the sagittal line forward 3–5 mm from the intraauricular line. For reproduction of the TBI of a mild severity in mature rats, a 34.5 g tractor was used, which produced impact energy of 0.220 J. The animals were removed from the experiment by an overdose of ether anaesthesia, after which the kidney samples were prepared and obtained for further histological examination. Histological slides were stained with the haematoxylin and eosin and Mallory's trichrome, examined, and photographed using the Leica-DMLS microscope while all the measurements were done with the ImageJ software (ver.1.51j8).

Statistical analysis

The obtained results were tested for the normality of distribution with Shapiro-Wilk test. All the data were presented as $M \pm SD$ where "M" stands for average and "SD" for standard deviation. The differences between the groups were analysed using analysis of variance (ANOVA) with Tukey's post-hoc test. The

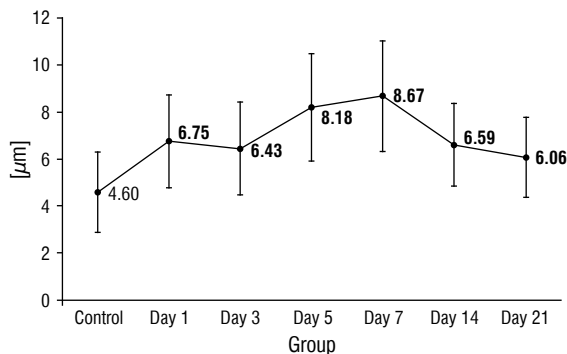


Figure 1. Diameter variation of the rats' peritubular capillaries.

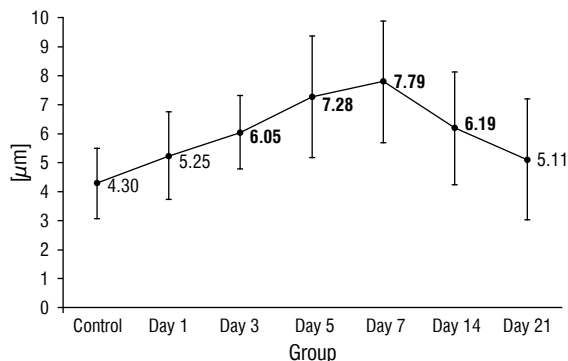


Figure 2. Diameter variation of the rats' glomerular capillaries.

Table 1. Rats' nephron glomerulus measurements

Group	Mean	SD	SEM	Min	Max	N
Control	66.46	10.57	1.53	48.33	90.69	48
Day 1	67.76	14.15	2.24	44.57	95.95	40
Day 3	74.24	10.74	1.87	50.65	93.50	33
Day 5	76.85*	15.19	2.11	48.77	105.35	52
Day 7	77.78**	15.31	2.12	49.02	105.49	52
Day 14	76.23*	10.52	1.66	57.71	97.55	40
Day 21	73.97	10.23	1.62	54.10	95.99	40

*p < 0.05, **p < 0.001; SD — standard deviation; SEM — standard error of mean; Min — minimum value; Max — maximum value; N — total numbers of measurements

Table 2. Rats' nephron capsule measurements

Group	Mean	SD	SEM	Min	Max	N
Control	79.90	12.30	2.32	63.23	112.81	28
Day 1	86.55	12.89	2.06	58.43	120.63	39
Day 3	90.14	10.90	1.99	70.38	114.85	30
Day 5	93.07*	14.76	1.97	62.85	122.43	56
Day 7	94.06*	14.82	1.98	63.47	123.14	56
Day 14	85.20	11.85	1.87	66.73	115.24	40
Day 21	83.20	11.87	1.88	66.39	112.74	40

*p < 0.001; SD — standard deviation; SEM — standard error of mean; Min — minimum value; Max — maximum value; N — total numbers of measurements

differences turned out to be statistically significant with the p-value < 0.05. All statistical computing was done with the RStudio software (ver. 1.1.442).

RESULTS

After the TBI modelling, no fatalities, behavioural, or dietary changes were recorded in the animals. On the 1st day after the inflicted experimental injury, hyperaemia of the tubular capillaries with the stasis of erythrocytes in their lumen in all examined histological specimens was observed. The mean diameter increased up to $6.75 \pm 1.98 \mu\text{m}$ (index of the control group $4.60 \pm 1.72 \mu\text{m}$, $p < 0.001$; Fig. 1) while the diameter of the dilated afferent arterioles was in the range of 10–15 μm . Some veins were dilated with the stasis of erythrocytes in their lumen with 40–60 μm in diameter. Erythrocytic stasis was also observed in the lumen of the medium-sized arteries. Nephron glomeruli were fragmented, and their diameter remains in the range of control group value, as well as the capsule diameter (Tables 1, 2). Capillaries of glomeruli had narrowed down to 2.44 μm and dilated — with the maximal value up to 9.91 μm as opposed to the control group where the maximal value remained at

7.80 μm . The mean value was $5.25 \pm 1.51 \mu\text{m}$ (Fig. 2), which is significantly higher than of the control group ($p < 0.05$).

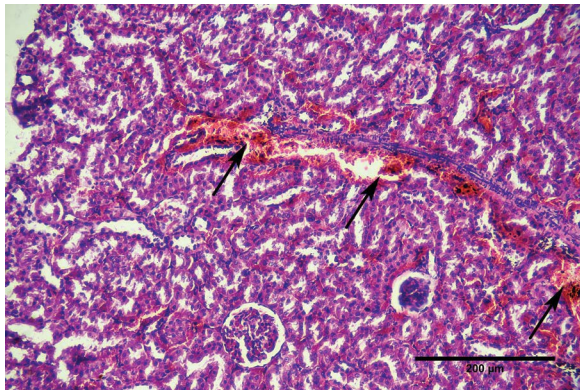
On the 3rd day of the experiment, in all of the samples dilatation of the tubular capillaries with erythrocytic stasis in their lumen continued to persist. Their diameter in certain areas was up to 12.12 μm with the mean value of $6.43 \pm 1.98 \mu\text{m}$, the diameter of glomerular capillaries increased too (Table 3). Erythrocytic stasis was observed in the veins of all calibres with their dilatation in separate areas reaching up to 40–50 μm . This was especially the case for the area between the cortical layer and the medullary area. Dilatation of vasa recta was also observed with diameter reaching up to 12–15 μm with erythrocytic stasis in their lumen.

On the 5th and 7th days of the TBI, renal corpuscles of various sizes were observed in the majority of examined specimens. The diameter of the glomerulus on the 5th day was $76.85 \pm 15.19 \mu\text{m}$ and $77.78 \pm 15.31 \mu\text{m}$ on the 7th day. The diameter of the capsule of the renal corpuscle also had reached its maximal value — $93.07 \pm 14.76 \mu\text{m}$ on the 5th day and $94.06 \pm 14.82 \mu\text{m}$ on the 7th day. The diameter of

Table 3. Measurements of glomerular capillaries.

Group	Mean	SD	SEM	Min	Max	N
Control	4.30	1.22	0.17	2.41	7.80	52
Day 1	5.25	1.51	0.18	2.44	9.91	70
Day 3	6.05*	1.29	0.14	4.09	11.93	82
Day 5	7.28*	2.10	0.26	3.44	12.68	67
Day 7	7.79*	2.12	0.26	3.91	13.11	67
Day 14	6.19*	1.94	0.23	3.09	15.92	73
Day 21	5.11	2.08	0.25	1.82	15.03	72

* $p < 0.001$; SD — standard deviation; SEM — standard error of mean; Min — minimum value; Max — maximum value; N — total numbers of measurements

**Figure 3.** Perivascular haemorrhage (arrow); 5th day after traumatic brain injury; haematoxylin and eosin.

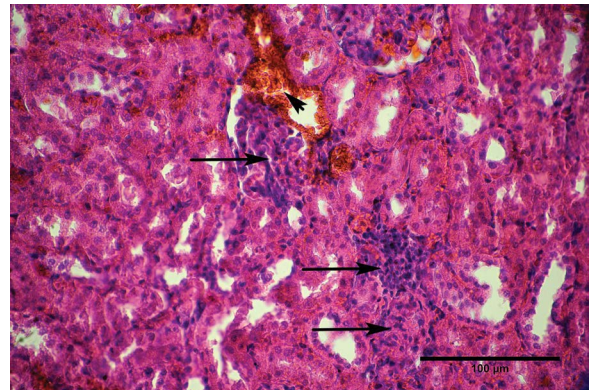
the tubular capillaries and capillaries of the nephron glomeruli had reached their maximum throughout the experiment on the 7th day (Figs. 1, 2, Tables 3, 4). This was predominantly due to dilatation of the cortical capillaries that were close to the renal capsule while the diameter of some capillaries was 15.46 μm . In some places, renal corpuscles were partially destroyed and there was a dilation of the space between the glomeruli and the capsule. Small arteries were congested, mainly, with aggregated erythrocytes (sludge). Perivascular space showed impregnation of the blood cells and massive lymphocytic infiltrates with perivascular haemorrhage in some areas (Fig. 3). The renal medulla showed the areas with the signs of renal infarction and destruction of the proximal and distal tubules. One of the characteristic features of this period was dilatation of the arcuate veins with the blood stasis in their lumen, the diameter of which reached 50–80 μm .

On the 14th–21st days after the TBI the sclerotic changes of the renal corpuscles were focally observed (Fig. 4) as well as the massive perivascular infiltrates

Table 4. Measurements of tubular capillaries

Group	Mean	SD	SEM	Min	Max	N
Control	4.60	1.72	0.29	1.14	7.78	36
Day 1	6.75**	1.98	0.27	2.98	11.84	53
Day 3	6.43**	1.98	0.23	2.63	12.12	72
Day 5	8.18**	2.30	0.23	4.09	15.46	97
Day 7	8.67**	2.36	0.24	4.25	16.32	97
Day 14	6.59**	1.75	0.20	3.00	12.52	80
Day 21	6.06*	1.73	0.19	2.34	11.96	80

* $p < 0.05$, ** $p < 0.001$; SD — standard deviation; SEM — standard error of mean; Min — minimum value; Max — maximum value; N — total numbers of measurements

**Figure 4.** Destruction of renal corpuscle with lymphocytic infiltrate and sclerosis (arrow). Blood clot near renal corpuscle (arrowhead); 14th day after traumatic brain injury; haematoxylin and eosin.

and initial signs of sclerosing of perivascular spaces in the renal medulla (Fig. 5). Infiltrates were observed in all specimens, while the signs of sclerosis were detected in 6 animals. The renal corpuscles focally were fragmented with infiltrates taking their place and the signs of formation of the connective tissue (Figs. 4, 6). Lumen of the vessels, especially veins, was filled with the red blood cells occasionally sticking to their intima. The diameter of capillaries and the size of glomeruli tended to decrease, though all their values remained significantly greater than those of the control group. Venous dilatation and blood cells aggregation were especially manifested in the area between the renal cortex and the medulla similarly to the previous periods.

DISCUSSION

According to the research literature, the dysfunctional disorders caused by a heavy craniocerebral injury are manifested in the form of the acute renal insufficiency that develops as a result of the dience-

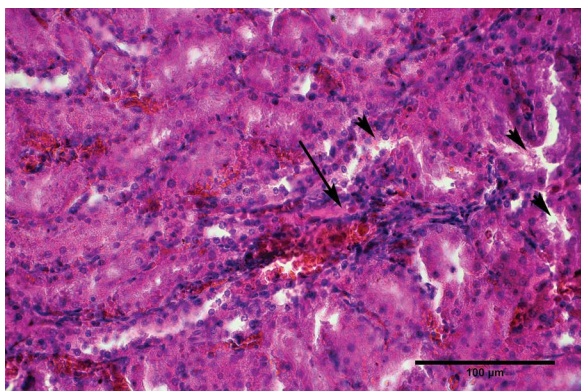


Figure 5. Perivascular infiltrate and sclerosis (arrow). Destruction of the renal tubules (arrowhead); 14th day after traumatic brain injury; haematoxylin and eosin.

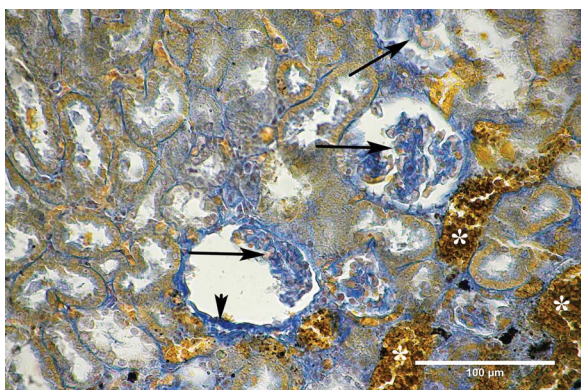


Figure 6. Fragmented renal glomeruli (arrow) with sclerosis (arrowhead) and blood stasis (asterisk); 21st day after traumatic brain injury; trichrome.

phalic-catabolic syndrome [4, 5]. In clinical treatment of patients with severe TBI described are dyscirculatory functional changes in the form of spasm of the arteries, arterioles, and venous plethora and diapedetic haemorrhages. In the future, this leads to metabolic, dystrophic, and necrotic changes. The first clinical sign of this is the appearance of red blood cells, protein, and cylinders in the urine.

The trigger mechanism of it could be, most likely, a massive adrenalin rush in the bloodstream with subsequent spasm of the microcirculatory bed that leads to the acute hepatorenal insufficiency. But such as complications is explained not only by the stress, but also by the activation of the cytokine system in response to brain damage leading to a systemic inflammatory response [14, 18]. Due to a prolonged spasm and influence of catecholamines the signs of hypoxic damage of the vascular endothelium started to develop along with the formation of sludges

and thrombi, increased endothelial permeability, and expression of endothelial adhesion molecules [18] which in the more prolonged periods of the experiment lead to the infarct of the renal parenchyma, destruction of the renal corpuscles, formation of sclerotic changes, and development of chronic renal insufficiency. The central dysregulation mechanisms after brain injury could contribute to the development and progression of extracerebral organ dysfunction by promoting systemic inflammation that may cause medical complications.

Microscopic studies of the kidneys in the first hour after the heavy TBI showed absolute dyscirculatory changes manifested by the spasm of vessels, congestion, and areas of the diapedesis haemorrhages on the border between the kidney cortex and the medulla [1, 15]. On the 3rd day after the injury, pathomorphological processes are complicated by the dystrophic and necrotic processes with manifestation of the ischaemic necrosis of the tubular epithelium and the interstitial oedema with disorganisation of the connective tissue [1, 15]. In the case of the severe TBI, observed were dyscirculatory changes in the liver, myocardium, and kidneys. They were accompanied by ischaemia, congestion, macrophagal and lymphocytic infiltration with dilatation of the vessels of various calibres, which in the more prolonged period after the TBI (5th day) were complicated by the pathomorphological processes in the form of dystrophic and necrotic changes in all organs [15, 21].

In the course of this study, the following pattern in the development of pathological changes in the rats' kidneys resulting from the mild TBI was found:

- on the 1st–3rd days, the development of mostly dyscirculatory changes manifested by the spasm of arterioles, dilatation of capillaries and venous bed were observed;
- on the 5th–7th days, the dyscirculatory changes are growing and are accompanied by the areas of destruction of the convoluted tubules and renal corpuscles. Such changes along with congestion and the areas of diapedesis and perivascular haemorrhages are best manifested between the cortex and medulla and in the areas close to the renal capsule. These pathological changes can explain the disorders of the filtration processes and urine reabsorption and are typical of the stage of the acute kidney failure;
- on the 14th–21st days, the intensity of the dyscirculatory and destructive changes decreases,

although there are indications of the focal perivascular sclerosis, perivascular infiltrates and indications of sclerosis of some renal corpuscles.

In the context of the clinical application of the results of experimental studies of the effects of TBI on rats, it should be noted that a rat's kidney structurally and functionally has similarities to the human kidney. Minor differences are mainly at the macrostructural level; the rat kidney, unlike humans, contains one pyramid.

The structure of the vascular grid also differs. But nephron structure, hierarchy of kidney layers, and their functioning are similar as to those found in humans. This similarity allows us to make assumptions about the similarity of pathological changes caused by TBI. The limitation of full conclusions from the results of this work is its exclusively morphological character. For a full and voluminous conclusion, the physiological aspects of these changes also need to be investigated to evaluate a possible strategy for the treatment and prevention of urinary tract complications from TBI. However, the assured conclusion for the clinicians may be that attention is needed not only for patients with severe TBI but also those with mild head injuries as well. Particularly if mild TBI is part of the polytrauma, or if such patients have concomitant renal pathology.

CONCLUSIONS


Summarising the data from these experiments and considering the relevant reports contained in the research literature, it is reasonable to conclude that there is a clear dependence of developmental dynamics and notable degree of pathological changes in kidneys on the severity of the TBI. In case of a mild TBI, the greatest changes in the rats' kidneys appear on the 5th–7th days after the injury, which have a consistent tendency to decrease after that. However, morphological changes in the form of a perivascular sclerosis and focal changes in the renal corpuscles show the signs of a possible development of a chronic kidney failure even after a mild TBI.

REFERENCES

- Aarabi B, Simard J. Traumatic brain injury. *Curr Opin Crit Care*. 2009; 15(6): 548–553, doi: [10.1097/mcc.0b013e-32833190da](https://doi.org/10.1097/mcc.0b013e-32833190da).
- Ahmed M, Sriganesh K, Vinay B, et al. Acute kidney injury in survivors of surgery for severe traumatic brain injury: Incidence, risk factors, and outcome from a tertiary neuroscience center in India. *Br J Neurosurg*. 2015; 29(4): 544–548, doi: [10.3109/02688697.2015.1016892](https://doi.org/10.3109/02688697.2015.1016892), indexed in Pubmed: [25796992](https://pubmed.ncbi.nlm.nih.gov/25796992/).
- Bailes JE, Petraglia AL, Omalu BI, et al. Role of subconcussion in repetitive mild traumatic brain injury. *J Neurosurg*. 2013; 119(5): 1235–1245, doi: [10.3171/2013.7.JNS121822](https://doi.org/10.3171/2013.7.JNS121822), indexed in Pubmed: [23971952](https://pubmed.ncbi.nlm.nih.gov/23971952/).
- Chepkij L, Minov S, Chernyshov V. Pathogenesis, clinic, prognosis and prophylactics of poliorganic insufficiency at cranio-cerebral trauma. *Ukr Neurosurgi J*. 2011; 0(2): 56–59, doi: [10.25305/unj.57892](https://doi.org/10.25305/unj.57892).
- Fursov I, Mogila V. Extracranial complications of severe head injury. *Tavrisheskiy Medico-Biol Vestn*. 2013; 16: 146–149.
- Guzeva V, Ochrim I, Maksimova N, et al. Characteristics of acute period of traumatic brain injury in children with hemophilia. *Pediatrician (St. Petersburg)*. 2017; 8(3): 158–163, doi: [10.17816/ped83158-163](https://doi.org/10.17816/ped83158-163).
- Harting MT, Jimenez F, Adams SD, et al. Acute, regional inflammatory response after traumatic brain injury: Implications for cellular therapy. *Surgery*. 2008; 144(5): 803–813, doi: [10.1016/j.surg.2008.05.017](https://doi.org/10.1016/j.surg.2008.05.017), indexed in Pubmed: [19081024](https://pubmed.ncbi.nlm.nih.gov/19081024/).
- Heegaard W, Biros M. Traumatic brain injury. *Emerg Med Clin North Am*. 2007; 25(3): 655–78, viii, doi: [10.1016/j.emc.2007.07.001](https://doi.org/10.1016/j.emc.2007.07.001), indexed in Pubmed: [17826211](https://pubmed.ncbi.nlm.nih.gov/17826211/).
- Humphreys I, Wood RL, Phillips CJ, et al. The costs of traumatic brain injury: a literature review. *Clinicoecon Outcomes Res*. 2013; 5: 281–287, doi: [10.2147/CEOR.S44625](https://doi.org/10.2147/CEOR.S44625), indexed in Pubmed: [23836998](https://pubmed.ncbi.nlm.nih.gov/23836998/).
- Kyrychenko A. Clinical and epidemiological aspects of primary disablement under craniocerebral trauma. *Probl Ecol Med*. 2012; 16: 30–33.
- Lekhan V, Huk A. Specifics of traumatic brain injury epidemiology in aine. *Ukr Nation's Health*. 2010; 2: 7–14.
- Li N, Zhao WG, Zhang WF. Acute kidney injury in patients with severe traumatic brain injury: implementation of the acute kidney injury network stage system. *Neurocrit Care*. 2011; 14(3): 377–381, doi: [10.1007/s12028-011-9511-1](https://doi.org/10.1007/s12028-011-9511-1), indexed in Pubmed: [21298359](https://pubmed.ncbi.nlm.nih.gov/21298359/).
- Mascia L, Sakr Y, Pasero D, et al. Extracranial complications in patients with acute brain injury: a post-hoc analysis of the SOAP study. *Intensive Care Med*. 2008; 34(4): 720–727, doi: [10.1007/s00134-007-0974-7](https://doi.org/10.1007/s00134-007-0974-7), indexed in Pubmed: [18175107](https://pubmed.ncbi.nlm.nih.gov/18175107/).
- McKeating EG, Andrews PJ, Signorini DF, et al. Transcranial cytokine gradients in patients requiring intensive care after acute brain injury. *Br J Anaesth*. 1997; 78(5): 520–523, doi: [10.1093/bja/78.5.520](https://doi.org/10.1093/bja/78.5.520), indexed in Pubmed: [9175965](https://pubmed.ncbi.nlm.nih.gov/9175965/).
- Meretskiy V. Structural and morphological disorders of internal organs of rats with craniocerebral injury and diabetes mellitus. *Hosp Surg*. 2012: 56–60.
- Meretskiy VM. Method for simulation of traumatic brain injury. 2012. <http://uapatents.com/5-74935-sposib-modelyuvannya-cherepno-mozkovo-travmi.html>.
- Moore EM, Bellomo R, Nichol A, et al. The incidence of acute kidney injury in patients with traumatic brain injury. *Ren Fail*. 2010; 32(9): 1060–1065, doi: [10.3109/0886022X.2010.510234](https://doi.org/10.3109/0886022X.2010.510234), indexed in Pubmed: [20863210](https://pubmed.ncbi.nlm.nih.gov/20863210/).
- Ott L, McClain CJ, Gillespie M, et al. Cytokines and metabolic dysfunction after severe head injury. *J Neurotrauma*. 1994; 11(5): 447–472, doi: [10.1089/neu.1994.11.447](https://doi.org/10.1089/neu.1994.11.447), indexed in Pubmed: [7861440](https://pubmed.ncbi.nlm.nih.gov/7861440/).

19. Piek J, Chesnut RM, Marshall LF, et al. Extracranial complications of severe head injury. *J Neurosurg.* 1992; 77(6): 901–907, doi: [10.3171/jns.1992.77.6.0901](https://doi.org/10.3171/jns.1992.77.6.0901), indexed in Pubmed: [1432133](https://pubmed.ncbi.nlm.nih.gov/1432133/).
20. Pinto FC, Capone-Neto A, Prist R, et al. Volume replacement with lactated Ringer's or 3% hypertonic saline solution during combined experimental hemorrhagic shock and traumatic brain injury. *J Trauma.* 2006; 60(4): 758–763, doi: [10.1097/01.ta.0000214581.89316.73](https://doi.org/10.1097/01.ta.0000214581.89316.73), indexed in Pubmed: [16612295](https://pubmed.ncbi.nlm.nih.gov/16612295/).
21. Puras U, Talypov A, Krylov V, et al. Factors of secondary ischemic cerebral damage at craniocerebral trauma. Part 1. Intracranial and extracranial factors of secondary cerebral damage. *Russ Sklifosovsky J Emerg Med Care.* 2012; 1: 56–65.
22. Semenova Z, Melnikov A, Savin I, et al. Recommendations for treatment of children with craniocerebral trauma. *Russ J Pediatr Surg Anesth Intensive Care.* 2016; 6: 112–127.
23. Skowronek R, Kobek M, Jankowski Z, et al. Traumatic basal subarachnoid haemorrhage or ruptured brain aneurysm in 16-year-old boy? — case report. *Arch Med Sadowej Kryminol.* 2016; 66(1): 32–40, doi: [10.5114/amsik.2016.62333](https://doi.org/10.5114/amsik.2016.62333), indexed in Pubmed: [28155987](https://pubmed.ncbi.nlm.nih.gov/28155987/).
24. Tagliaferri F, Compagnone C, Korsic M, et al. A systematic review of brain injury epidemiology in Europe. *Acta Neurochir (Wien).* 2006; 148(3): 255–68; discussion 268, doi: [10.1007/s00701-005-0651-y](https://doi.org/10.1007/s00701-005-0651-y), indexed in Pubmed: [16311842](https://pubmed.ncbi.nlm.nih.gov/16311842/).
25. Van Beek JGM, Mushkudiani NA, Steyerberg EW, et al. Prognostic value of admission laboratory parameters in traumatic brain injury: results from the IMPACT study. *J Neurotrauma.* 2007; 24(2): 315–328, doi: [10.1089/neu.2006.0034](https://doi.org/10.1089/neu.2006.0034), indexed in Pubmed: [17375996](https://pubmed.ncbi.nlm.nih.gov/17375996/).
26. Verchère J, Blanot S, Vergnaud E, et al. Mortality in severe traumatic brain injury. *Lancet Neurol.* 2013; 12(5): 426–427, doi: [10.1016/S1474-4422\(13\)70073-5](https://doi.org/10.1016/S1474-4422(13)70073-5), indexed in Pubmed: [23602158](https://pubmed.ncbi.nlm.nih.gov/23602158/).

Types of left brachiocephalic vein aberrations detected during cardiac implantable electronic device implantation procedures

R. Steckiewicz¹ , P. Stolarz², E.B. Świętoń¹

¹1st Department of Cardiology, Central University Hospital in Warsaw, Poland

²1st Chair and Department of Cardiology, Medical University of Warsaw, Poland

[Received: 10 January 2020; Accepted: 28 May 2020]

Background: Cardiac implantable electronic device (CIED) implantation procedures with transvenous lead placement afford an opportunity to observe vascular anatomic variations. The course of CIED implantation depends largely on morphometric and topographic characteristics of the relevant brachiocephalic vein (BCV), which is the left BCV in the case of lead insertion via the left clavipectoral triangle. This study aims to present left BCV anomalies arising from abnormal systemic vein embryogenesis and encountered during CIED implantation.

Materials and methods: Venograms obtained during CIED implantation procedures and illustrating left BCV topography/morphometry were analysed retrospectively for two types of anomalies: anomalies of the left BCV itself (data from the period 2014–2018) and a combination of left BCV variations with a persistent left superior vena cava (PLSVC); since the latter instances are rare, the analysed period was longer (2003–2018).

Results: Analysis of data from the first, 5-year-long, period included data from a group of 1812 patients and revealed 5 (0.3%) cases of developmental left-BCV anomalies (3 double left BCV and 2 cases of a single subaortic left BCV). The 16-year-long analysed period included 6110 CIED implantation procedures, which showed 12 (0.2%) cases of PLSVC including 4 (33%) cases of left BCV agenesis.

Conclusions: The analysed venograms rarely showed isolated left-BCV aberrations (0.3%), with the combination of left-BCV agenesis and PLSVC being much more common (33%). The morphometry and/or topography of aberrant left-BCV may result in difficulties during cardiac lead insertion. (Folia Morphol 2021; 80, 2: 317–323)

Key words: aberrant left brachiocephalic vein, persistent left superior vena cava, venography, lead implantation, cardiac implantable electronic device (CIED)

INTRODUCTION

Procedures utilising transvenous catheter insertion, including cardiac implantable electronic device (CIED) implantation, afford an opportunity to detect

vascular anatomy variations, such as the natural physiological individual variations in the shape or course of vessels and vascular anomalies due to disturbances during embryogenesis [1, 5, 11, 17]. The normal

Address for correspondence: R. Steckiewicz, MD, PhD, 1st Department of Cardiology, Central University Hospital in Warsaw, ul. Banacha 1A, 02–097 Warszawa, Poland, e-mail: r.steckiewicz@pro.onet.pl

This article is available in open access under Creative Common Attribution-Non-Commercial-No Derivatives 4.0 International (CC BY-NC-ND 4.0) license, allowing to download articles and share them with others as long as they credit the authors and the publisher, but without permission to change them in any way or use them commercially.

course of said procedures depends on favourable morphometry and topography of the brachiocephalic vein (BCV), also known as the innominate vein, which is a systemic vein.

Disturbances in systemic vein embryogenesis result in vascular anomalies. In the case of left BCV such anomalies exhibit considerable anatomical variations in comparison with a normal left BCV. These anomalies may manifest as variations in the course of the vein through the anterior mediastinum and its spatial relationship to adjacent anatomical structures. Another result of disturbed venous embryogenesis can be the presence of an accessory vessel which is a doubled version of the left BCV [4, 15, 18, 29].

The rates of detected left-BCV anomalies depend on the evaluated population and the used imaging technique. Left-BCV anomalies are detected in approximately 1% of patients with congenital heart defects, such as tetralogy of Fallot, atrial septal defect, and ventricular septal defect. In the population without heart defects the estimated prevalence of left-BCV anomalies is below 0.4%. Developmental anomalies of the left BCV may occur in isolation or coexist with various variations of the persistent left superior vena cava (PLSVC). This type of systemic vein aberrations is found in 0.3–0.5% of individuals from the general population [3, 12, 14, 19, 26].

Unlike in the case of left BCVs with a typical topography, anatomical variations of this vessel (depending on their nature and extent), may facilitate inflicting inadvertent damage to the vessel itself and to the adjacent structures during certain transvascular procedures [2, 9, 10, 13, 22]. This is particularly likely if the vascular variation had been asymptomatic prior to the procedure and is detected only during a CIED implantation procedure, as was the case in the examples presented below.

This paper presents our records on rare, and sometimes very rare, developmental anomalies of the left BCV observed over a number of years. The enclosed images illustrate the nature of the detected anomalies (i.e. they are a radiographic representation of vascular morphometry and topography).

MATERIALS AND METHODS

This study is a retrospective assessment of the imaging records from venography procedures performed during de-novo CIED implantation procedures involving cardiac lead insertion through the systemic veins via a venous access in the left clavipectoral

triangle. The indication for contrast-enhanced venography had been intra-operative problems with lead advancement, which needed to be explained and solved.

The material presented below has been classified into two types of disturbed left BCV embryogenesis: — developmental anomalies involving only the left BCV, detected over the period 2014–2018; — developmental anomalies of the left BCV in combination with the presence of PLSVC, detected over the period of 2003–2018.

The images of left-BCV variations presented in this paper have been selected to best illustrate characteristic examples of the relevant vascular anatomical variants.

During most of the procedures, venography involved selective contrast administration, directly via cephalic vein cutdown or axillary vein/subclavian vein puncture. This helped limit the volume of the contrast agent being administered while at the same time ensuring a more thorough filling of mediastinal vein lumina.

Our statistical analysis used numerical variables in the form of mean values, standard deviations. This study had been approved by the Institutional Review Board.

RESULTS

Table 1 provides an overview of the types of left-BCV anomalies presented in this paper in terms of: patients' age at the time of first CIED implantation, procedure date, electrocardiographic indications for CIED implantation and the CIED types.

Analysis of data from the first, 5-year-long (2014–2018), period included CIED implantation procedures performed in a total of 1812 patients. Among those, there were 5 (0.3%) cases of developmental left-BCV anomalies.

Over the analysed 5-year period, there were 3 cases of a double left BCV, 2 of which were detected during de-novo CIED implantation procedures (including that illustrated in Fig. 1A). The third case of a double left BCV was detected during a procedure involving the addition of another cardiac lead to a CIED that had been implanted years earlier. The venography in this case additionally showed the patency of the vein in whose lumen the previous cardiac lead resided (Fig. 1B).

In the detected cases of double left BCV, the main and duplicated vessel differed in their diameters, with only the main ('upper') vessel's course and morpho-

Table 1. Venous anomaly types

Type of BCV anomaly	Sex	Age*	ECG-based indications	Procedure date	CIED type
Double BCV	Female	78	VT	2014	ICD VR
	Male	74	AF, AVB	2015	VI
	Male	82	SSS+PAF	2017	DDD
Subaortal BCV	Male	87	AF, AVB, EF 17%	2017 (ineffective procedure)	Indications for ICD VR
	Male	81	SF, AVB	2018	VI
Left BCV + Double SVC	Male	41	SSS	2003	AAI
	Female	90	AF+CHB	2004	VI
	Male	63	SR+CHB	2015	DDD
	Male	67	VT	2016	ICD VR
Double SVC without BCV	Female	77	TBS	2006	DDD
	Female	80	SR+CHB	2006	VI
	Male	61	TBS	2007	DDD
	Female	67	AF+CHB	2017	VI
	Female	52	SR+CHB	2009	DDD
Single persistent left SVC	Male	67	SR+CHB	2013	VI
	Female	66	VT+AF	2014	ICD VR
	Male	63	AF+CHB	2015	VI

*Patients' age at the time of first cardiac implantable electronic device (CIED) implantation; AAI — single-chamber atrial pacemaker; AF — atrial fibrillation; AVB — atrioventricular block (I°/II°); BCV — brachiocephalic vein; CHB — complete heart block; DDD — dual-chamber (atrioventricular) pacemaker; EF — ejection fraction; ECG — electrocardiogram; ICD VR — single-chamber implantable cardioverter-defibrillator; PAF — paroxysmal atrial fibrillation; SVC — superior vena cava; SR — sinus rhythm; SSS — sick sinus syndrome; TBS — tachycardia-bradycardia syndrome; VT — ventricular tachycardia; VI — single-chamber ventricular pacemaker

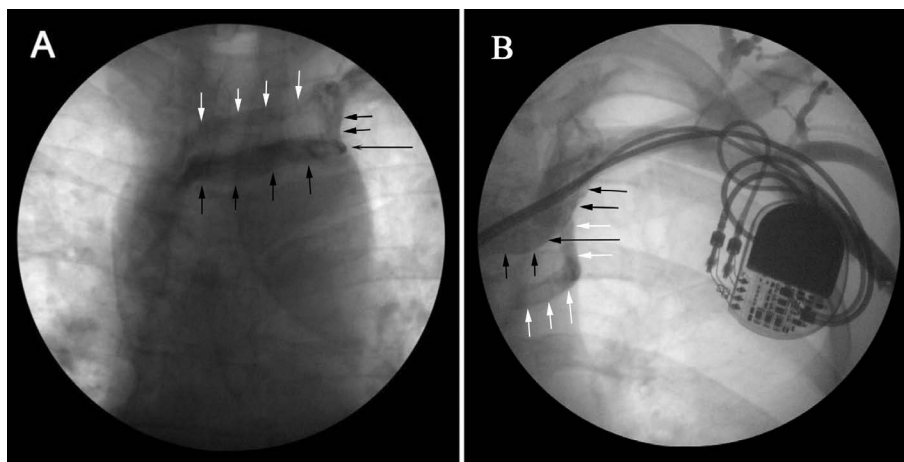


Figure 1. Differences in the lumina of the double left brachiocephalic vein variants: the main vessel (with a larger diameter and greater venous blood flow) — black arrows; the vessel with a smaller diameter and blood flow — white arrows; **A.** The blood/contrast agent flowing through the lower vessel in an 82-year-old male (black arrows). The cardiac leads were later successfully threaded through the upper vessel (white arrows); **B.** Cardiac leads threaded through the upper vessel in a 74-year-old male (black arrows), with the lower vessel exhibiting unfavourable morphometry and topography for lead advancement (white arrows).

metry allowing cardiac leads to be threaded towards the heart.

Throughout the evaluated period, we detected 2 cases of a subaortal left BCV (Fig. 2A, B). In 1 of those patients (Fig. 2A), who had undergone aortic valve replacement in the past, the altered venous

lumen morphometry precluded threading a cardiac lead beyond the site of stenosis and, thus, it was impossible to implant the CIED via a left-sided approach.

In the years 2003–2018, PLSVC was detected in 12 cases (6 women and 6 men), which constituted 0.2% of the 6110 CIED implantation procedures

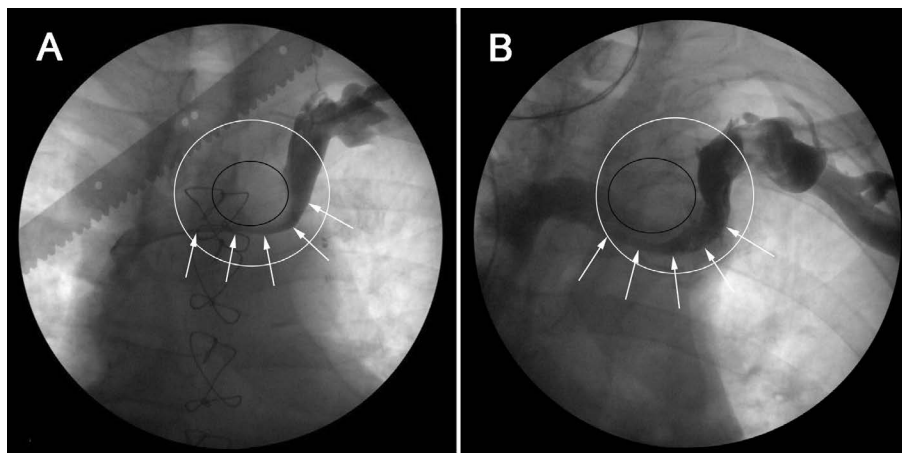


Figure 2. The general radiographic location of a subaortic left brachiocephalic vein (BCV) (white circles), including the location of the aortic arch (aortic cross-section marked with a black oval); the compressed subaortic left BCV segment (marked with arrows); **A.** Venous lumen compression by a dilated aorta in a 87-year-old male with a documented anatomical variation in aortic-arch arteries, involving both carotid arteries and the right subclavian artery branching off a common vessel (CT), status post aortic valve implantation, and an ascending aortic aneurysm. The oblique radiopaque stripe with a notched margin is a measuring scale; **B.** A radiogram from the successful implantation of a VVI pacemaker in an 81-year-old male, illustrating the venous configuration.

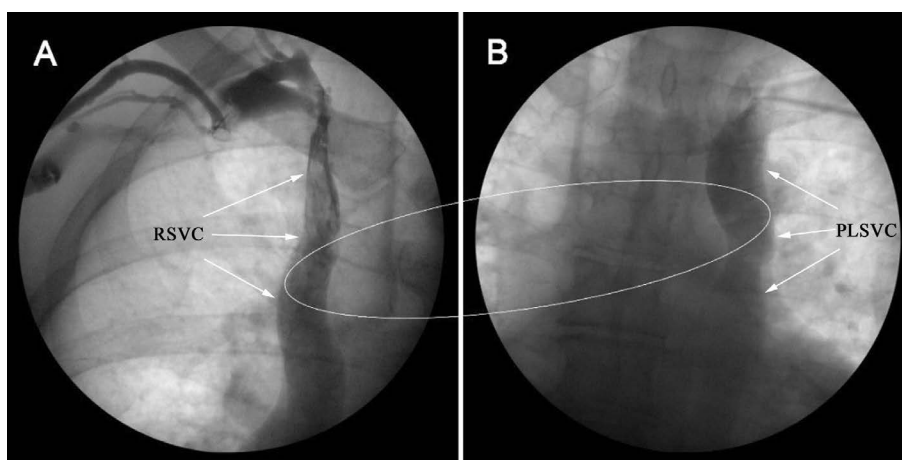


Figure 3. Persistent left superior vena cava (PLSVC) with left brachiocephalic vein (BCV) agenesis in a 61-year-old male. Intraoperative bilateral venography illustrates a lack of contrast enhancement in the left BCV potentially connecting the two superior venae cavae; **A.** Right superior vena cava (RSVC) morphometry illustrated with a contrast agent shows a lack of the left BCV. The site where the left BCV can be typically visualised if the vessel forms during normal embryogenesis (white oval). Marking the exact topography and morphometry of the vessel would be difficult due to inter-individual anatomical variations; **B.** Contrast-enhanced PLSVC also shows a lack of contrast flow through a left BCV in a situation where a left BCV bridge could be potentially present.

involving transvenous cardiac lead placement performed over this period.

In 4 PLSVC patients (3 women and 1 man; mean age 71 ± 9 years; $< 0.1\%$) there was concomitant left BCV agenesis (Fig. 3), with each of the two superior venae cavae having independent venous drainage.

The presence of a left BCV forming a bridge between the two superior venae cavae was detected in 4 cases (including 3 men and 1 woman; mean age 65 ± 20 years; one example is illustrated in Fig. 4).

In the remaining 4 cases (2 men and 2 women; mean age 62 ± 7 years), we observed a single PLSVC providing right-side thoracic drainage via an arching left BCV located in the superior mediastinum (Fig. 5).

The aberrant anatomy of systemic vessels (shown in the cases presented above and due to abnormal systemic vessel embryogenesis) proved problematic during CIED implantation procedures and lengthened procedure duration; however, there were no intraoperative complications.

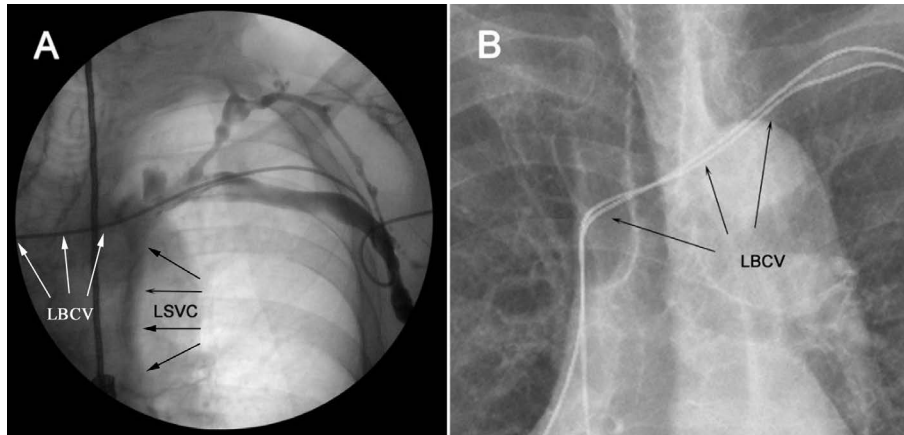


Figure 4. Persistent left superior vena cava (LSVC) with a left brachiocephalic vein (LBCV) in a 90-year-old female; **A.** Venogram showing the course of the cardiac lead and demonstrating a typical course of the LBCV through the mediastinum (obliquely and inferiorly) and the presence of two superior venae cavae (fluoroscopic image obtained during intra-procedure venography); **B.** LBCV patency can be verified when threading a new lead is required several years after the first procedure. Post-procedure chest X-ray film illustrating the location of both cardiac leads within the LBCV.

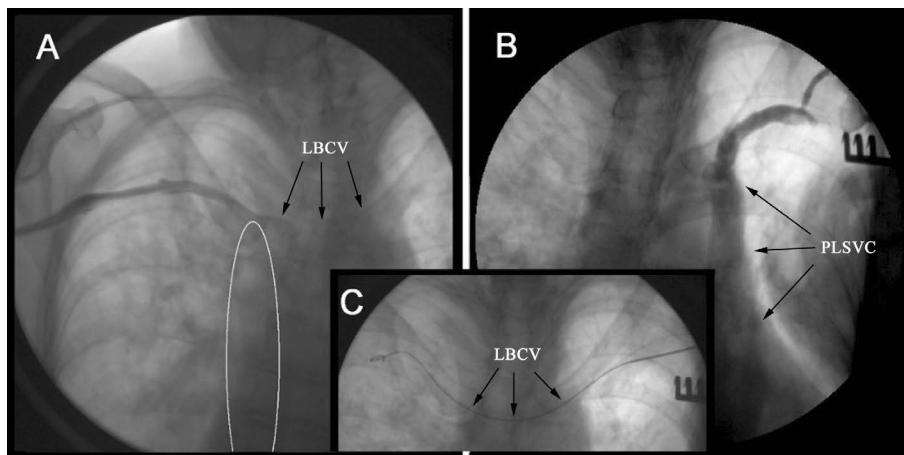


Figure 5. Single persistent left superior vena cava in a 66-year-old female; **A.** Right superior vena cava agenesis — documented by a lack of contrast enhancement in the vessel's potential location (white oval); **B.** Persistent left superior vena cava (PLSVC) morphometry poorly visualised by a retrograde flow of contrast; **C.** The position of a guidewire, arching between the left and the right subclavian veins, unequivocally proves the presence of a patent left brachiocephalic vein (LBCV).

DISCUSSION

In normally developing human embryos, the initially symmetrical venous system consists of paired anterior and posterior cardinal veins that drain the cephalic and caudal areas of the embryo, respectively. During further stages of physiological embryogenesis, the left and right pairs of cardinal veins anastomose inferiorly to form the left and right common cardinal veins (ducts of Cuvier). At 8 weeks of gestation, anastomoses between the left and right anterior cardinal veins lead to BCV formation. The physiological development of the systemic veins of the superior mediastinum ends with the left BCV being nearly 3 times longer than the right BCV. Each BCV, which is

an anatomical continuation of the ipsilateral internal jugular vein and subclavian vein, drains blood from the ipsilateral side of the body.

The left-BCV is typically positioned superior to the aortic arch and anterior to the aortic arch branches (the brachiocephalic trunk, left common carotid artery, and left subclavian artery). Having crossed to the right side of the superior mediastinum, the left BCV merges with the right BCV to form the superior vena cava (SVC) [21, 25]. During CIED implantation procedures, cardiac leads are typically inserted via the veins of the left clavipectoral triangle. This is also the approach preferred at our centre (utilised in approximately 97% of de novo CIED implantation procedures).

The presence of left BCV anomalies may pose a challenge in performing transvascular procedures employing this vessel and increase the risk of their complications [10, 13, 14]. Moreover, the left BCVs that are not anomalous themselves may sometimes have tributaries, whose configurations and confluence angles differ dramatically from those typically observed. This usually poses problems during anaesthesiology procedures, such as central venous catheter placement [8, 22].

An abnormal, supraaortic variant of the typically subaortic course of the left BCV in the superior mediastinum was first described by Takada et al. [28]. Other left-BCV variants due to the vessel's abnormal embryogenesis have also been described: a double left BCV, formed when a doubled branch of the left BCV courses inferoposteriorly to the ascending aorta before anastomosing with the right BCV or when the accessory vessel courses posteriorly to the trachea and oesophagus and merges with the azygos vein before draining into the SVC [24, 31]. In our study, we encountered the following left-BCV variants: subaortic left BCV, double left BCV, and another, previously unreported, variant where both vessels (the upper and lower one) coursed parallel to each other above the aortic arch [27]. Our records over a 5-year period showed left-BCV-only anomalies in 1.6% of the analysed CIED implantation procedures involving contrast venography.

During normal embryogenesis, the mature form of the right anterior cardinal vein forms the right SVC, whereas the left-sided vessel undergoes involution up to the 20th week of gestation and, consequently, blood flow is redistributed to the right side. During abnormal embryogenesis the left anterior cardinal vein may not undergo involution, which leads to the presence of PLSVC. Over the last 16 years, during which CIED implantation procedures were conducted at our centre, this type of systemic vein anomaly was detected in 12 (0.2%) cases, slightly less commonly than reported in other, comparable populations [1, 7, 30].

Approximately 85% of adults diagnosed with PLSVC have two coexisting venous drainages. In our study, the PLSVC anomaly with two developed venous drainages (double SVC) was detected in 67% of cases. Out of these PLSVC cases, concomitant left-BCV agenesis with two independent SVC drainages due to a failure in the formation of the physiological bridge between the two anterior cardinal veins, was

observed less commonly (50%) than reported by other authors [7, 16, 20, 30].

A double SVC with the two vessels bridged by the left BCV was found in 4 (33%) cases, out of all 12 detected cases of PLSVC. However, we believe that this type of double SVC may be more common due to the fact that some cases remain undetected; for instance, those cases where the continuation of the left subclavian vein into the left BCV favours smooth advancement of a cardiac lead into the right SVC, cases where cardiac leads are introduced via the right SVC, or cases that lack any diagnostic imaging that would visualise the presence of a double SVC [26].

In 10–20% of PLSVC cases, abnormal development of the right cardinal vein leads to right SVC agenesis. In our study, this type of venous drainage from both sides of the chest via a single PLSVC (naturally, via the left BCV) was observed in 4 (33%) out of all cases of detected PLSVC [6, 23].

Having knowledge on the prevalence of left BCV anomalies along with the morphometric and topographic characteristics helps predict potential problems during transvenous procedures, such as central venous catheter and CIED, which employ systemic thoracic veins.

Limitations of the study

Our evaluation of the prevalence of presented left-BCV variations was confined to a selected group of patients, namely those undergoing CIED implantation procedures with an accompanying venography. This may have caused the proportion of detected venous anomalies to be lower than their actual prevalence, both in populations undergoing CIED implantation and in the general population.

Failure to detect some of the developmental anomalies of mediastinal veins may be associated with the fact that venography of the left BCV is less common than that of its tributaries coursing through the left clavipectoral triangle. Moreover, during some procedures, the leads are advanced via the right BCV.

CONCLUSIONS



The analysis of our study population of patients undergoing a CIED implantation procedure showed developmental anomalies of the left BCV alone to be rare, whereas left BCV agenesis in combination with PLSVC was more common. The asymptomatic

character of left-BCV aberrations is usually the reason why they are detected only during certain transvenous procedures. Such aberrations in venous topography and morphometry may pose a challenge during CIED implantation procedures involving transvenous cardiac lead insertion.

REFERENCES

- Biffi M, Bertini M, Ziacchi M, et al. Left superior vena cava persistence in patients undergoing pacemaker or cardioverter-defibrillator implantation: a 10-year experience. *Chest*. 2001; 120(1): 139–144, doi: [10.1378/chest.120.1.139](#), indexed in Pubmed: [11451829](#).
- Bowdle A. Vascular complications of central venous catheter placement: evidence-based methods for prevention and treatment. *J Cardiothorac Vasc Anesth*. 2014; 28(2): 358–368, doi: [10.1053/j.jvca.2013.02.027](#), indexed in Pubmed: [24008166](#).
- Chen SJ, Liu KL, Chen HY, et al. Anomalous brachiocephalic vein: CT, embryology, and clinical implications. *Am J Roentgenol*. 2005; 184(4): 1235–1240, doi: [10.2214/ajr.184.4.01841235](#), indexed in Pubmed: [15788602](#).
- Curtil A, Tronc F, Champsaur G, et al. The left retro-aortic brachiocephalic vein: morphologic data and diagnostic ultrasound in 27 cases. *Surg Radiol Anat*. 1999; 21(4): 251–254, doi: [10.1007/BF01631395](#), indexed in Pubmed: [10549081](#).
- Demos TC, Posniak HV, Pierce KL, et al. Venous anomalies of the thorax. *Am J Roentgenol*. 2004; 182(5): 1139–1150, doi: [10.2214/ajr.182.5.1821139](#), indexed in Pubmed: [15100109](#).
- Gibelli G, Biasi S. Persistent left superior vena cava and absent right superior vena cava: not only an anatomic variant. *J Cardiovasc Echogr*. 2013; 23(1): 42–44, doi: [10.4103/2211-4122.117985](#), indexed in Pubmed: [28465883](#).
- Goyal SK, Punnam SR, Verma G, et al. Persistent left superior vena cava: a case report and review of literature. *Cardiovasc Ultrasound*. 2008; 6: 50, doi: [10.1186/1476-7120-6-50](#), indexed in Pubmed: [18847480](#).
- Granata A, Zanolli L, Trezzi M, et al. Anatomical variations of the left anonymous trunk are associated with central venous catheter dysfunction. *J Nephrol*. 2018; 31(4): 571–576, doi: [10.1007/s40620-017-0465-z](#), indexed in Pubmed: [29270845](#).
- Haq AA, Restrepo CS, Lamus D, et al. Thoracic venous injuries: an imaging and management overview. *Emerg Radiol*. 2016; 23(3): 291–301, doi: [10.1007/s10140-016-1386-1](#), indexed in Pubmed: [26965007](#).
- Bachleda JP. Iatrogenic injury to the superior vena cava and brachiocephalic vein. *J Infect Dis Ther*. 2014; 02(06), doi: [10.4172/2332-0877.1000169](#).
- Kahkouee S, Sadr M, Pedarzadeh E, et al. Anomalous left brachiocephalic vein: important vascular anomaly concomitant with congenital anomalies and heart diseases. *Folia Morphol*. 2017; 76(1): 51–57, doi: [10.5603/FM.a2016.0031](#), indexed in Pubmed: [27830886](#).
- Ko SF, Huang CC, Ng SH, et al. Imaging of the brachiocephalic vein. *Am J Roentgenol*. 2008; 191(3): 897–907, doi: [10.2214/AJR.07.3552](#), indexed in Pubmed: [18716126](#).
- Ko SF, Ng SH, Fang FM, et al. Left brachiocephalic vein perforation: computed tomographic features and treatment considerations. *Am J Emerg Med*. 2007; 25(9): 1051–1056, doi: [10.1016/j.ajem.2007.06.013](#), indexed in Pubmed: [18022501](#).
- Kobayashi M, Ichikawa T, Koizumi J, et al. Aberrant left brachiocephalic vein versus persistent left superior vena cava without bridging vein in adults: evaluation on computed tomography. *Ann Vasc Dis*. 2018; 11(4): 535–541, doi: [10.3400/avd.18-00098](#), indexed in Pubmed: [30637011](#).
- Kondrachuk O, Yalynska T, Tammo R. Double left brachiocephalic vein. *Pediatr Cardiol*. 2013; 34(3): 767–768, doi: [10.1007/s00246-012-0542-y](#), indexed in Pubmed: [23052674](#).
- Kula S, Cevik A, Sanli C, et al. Persistent left superior vena cava: experience of a tertiary health-care center. *Pediatr Int*. 2011; 53(6): 1066–1069, doi: [10.1111/j.1442-200X.2011.03443.x](#), indexed in Pubmed: [21810152](#).
- Loukas M, Tobola MS, Tubbs RS, et al. The clinical anatomy of the internal thoracic veins. *Folia Morphol*. 2007; 66(1): 25–32, indexed in Pubmed: [17533591](#).
- Nagashima M, Shikata F, Okamura T, et al. Anomalous subaortic left brachiocephalic vein in surgical cases and literature review. *Clin Anat*. 2010; 23(8): 950–955, doi: [10.1002/ca.21046](#), indexed in Pubmed: [20830788](#).
- Povoski SP, Khabiri H. Persistent left superior vena cava: review of the literature, clinical implications, and relevance of alterations in thoracic central venous anatomy as pertaining to the general principles of central venous access device placement and venography in cancer patients. *World J Surg Oncol*. 2011; 9: 173, doi: [10.1186/1477-7819-9-173](#), indexed in Pubmed: [22204758](#).
- Ratliff HL, Yousufuddin M, Lieving WR, et al. Persistent left superior vena cava: case reports and clinical implications. *Int J Cardiol*. 2006; 113(2): 242–246, doi: [10.1016/j.ijcard.2005.08.067](#), indexed in Pubmed: [16318881](#).
- Ruano CA, Marinho-da-Silva A, Donato P. Congenital thoracic venous anomalies in adults: morphologic MR imaging. *Curr Probl Diagn Radiol*. 2015; 44(4): 337–345, doi: [10.1067/j.cpradiol.2015.01.002](#), indexed in Pubmed: [25953438](#).
- Salik E, Daftary A, Tal MG. Three-dimensional anatomy of the left central veins: implications for dialysis catheter placement. *J Vasc Interv Radiol*. 2007; 18(3): 361–364, doi: [10.1016/j.jvir.2006.12.721](#), indexed in Pubmed: [17377181](#).
- Sheikh AS, Mazhar S. Persistent left superior vena cava with absent right superior vena cava: review of the literature and clinical implications. *Echocardiography*. 2014; 31(5): 674–679, doi: [10.1111/echo.12514](#), indexed in Pubmed: [24460570](#).
- Shim MS, Kang MJ, Kim J, et al. Circumaortic left brachiocephalic vein: CT findings. *J Korean Soc Radiol*. 2010; 62(3): 207, doi: [10.3348/jksr.2010.62.3.207](#).
- Standing S. Gray's anatomy. 39th ed. Hearts and great vessels. Chapter 60. Elsevier, Churchill, Livingstone, Edinburgh 2005: 1027.
- Steckiewicz R, Kosior DA, Rosiak M, et al. The prevalence of superior vena cava anomalies as detected in cardiac implantable electronic device recipients at a tertiary cardiology centre over a 12-year period. *HJC*. 2016; 57(2): 101–106, doi: [10.1016/j.hjc.2016.03.003](#), indexed in Pubmed: [27445024](#).
- Steckiewicz R, Świętoń EB, Stolarz P. A rare vascular anomaly in the form of double left brachiocephalic vein detected incidentally during cardiac implantable electronic device (CIED) placement. *Folia Morphol*. 2018; 77(1): 161–165, doi: [10.5603/FM.a2017.0065](#), indexed in Pubmed: [28703852](#).
- Takada Y, Narimatsu A, Kohno A, et al. Anomalous left brachiocephalic vein: CT findings. *J Comput Assist Tomogr*. 1992; 16(6): 893–896, doi: [10.1097/00004728-199211000-00012](#), indexed in Pubmed: [1430437](#).
- Topcuoglu OM, Atceken Z, Ariyurek OM. Circumaortic doubled left brachiocephalic vein: a rare confusing variation. *Surg Radiol Anat*. 2015; 37(3): 315–318, doi: [10.1007/s00276-014-1345-z](#), indexed in Pubmed: [25037739](#).
- Webb WR, Gamsu G, Speckman JM, et al. Computed tomographic demonstration of mediastinal venous anomalies. *Am J Roentgenol*. 1982; 139(1): 157–161, doi: [10.2214/ajr.139.1.157](#), indexed in Pubmed: [6979850](#).
- Yigit AE, Haliloglu M, Karcaaltincaba M, et al. Retrotracheal aberrant left brachiocephalic vein: CT findings. *Pediatr Radiol*. 2008; 38(3): 322–324, doi: [10.1007/s00247-007-0663-2](#), indexed in Pubmed: [17962930](#).

Variations in the gonadal artery with a single common trunk: embryological hypotheses by observation

H. Terayama¹, Y. Miyaki¹, N. Qu¹, S. Katsuki^{1,2}, R. Tanaka^{1,2}, K. Umemoto¹, N. Kosemura¹, K. Suyama¹, O. Tanaka¹, K. Sakabe¹

¹Department of Anatomy, Division of Basic Medicine, Tokai University School of Medicine, Kanagawa, Japan

²Department of Rehabilitation, Kanto Rosai Hospital, 1-1 Kizuki Sumiyoshi-cho, Nakahara-ku, Kawasaki-si, Kanagawa, Japan

[Received: 5 March 2020; Accepted: 31 March 2020]

Background: A gonadal artery originates as a branch of the abdominal aorta and renal artery inferior to the level of origin of the renal arteries. Variations in multiple right testicular arteries (RTAs) arising from the abdominal aorta are common. We aimed to re-evaluate the unusual courses of gonadal arteries with a single common trunk in relation to the inferior vena cava and left renal vein and explain the developmental anatomy.

Materials and methods: The observational cross-sectional study was performed on 54 Japanese adult cadavers (29 men and 25 women). We examined the literature and developed embryological hypotheses on the single common trunk of the gonadal artery.

Results: The gonadal artery, testicular artery, and ovarian artery arose from the abdominal aorta in 93.1%, 96.3%, and 89.6% of cases, respectively, and from the renal artery in 4.9%, 3.7%, and 6.3% of cases, respectively. We found two rare variations in the RTAs observed during the routine dissection of two male cadavers; in these two cases, a single common trunk of the RTAs originated from the abdominal aorta. A single common trunk was found in 3.7% of cadavers, 2.0% of sides, and 2.0% of arteries in the gonadal artery and in 6.9% of cadavers, 3.8% of sides, and 3.7% of arteries in the testicular artery. All cases of the single common trunk, including those in past reports, were observed only in men.

Conclusions: Knowledge of the variations in RTAs has important clinical consequences for invasive and non-invasive arterial procedures. In addition, this variation provides a new interpretation of the embryology of the gonadal artery. Variations similar to our findings have not been previously reported. Therefore, different variations concerning the RTA should be considered during surgical and non-surgical evaluations. (Folia Morphol 2021; 80, 2: 324–330)

Key words: single common trunk, right testicular artery, vascular development, cadaver

Address for correspondence: H. Terayama, PhD, Department of Anatomy, Division of Basic Medicine, Tokai University School of Medicine, 143 Shimokasuya, Isehara-si, Kanagawa 259-1193, Japan, tel: +81-463-931121 (ext. 2513), e-mail: terahaya@tokai-u.jp

This article is available in open access under Creative Common Attribution-Non-Commercial-No Derivatives 4.0 International (CC BY-NC-ND 4.0) license, allowing to download articles and share them with others as long as they credit the authors and the publisher, but without permission to change them in any way or use them commercially.

INTRODUCTION

The gonadal artery (GA) originates separately on the left and right sides as a lateral branch of the abdominal aorta (AA), inferior to the level of origin of the renal arteries and veins. On the right side, the artery commonly passes anterior to the inferior vena cava (IVC), while on the left, it passes posterior to the inferior mesenteric vein. It descends inferolaterally toward the pelvis along the psoas major muscle, under the parietal peritoneum, and then enters into the ipsilateral deep inguinal ring [11].

Variations of the renal, adrenal, and inferior phrenic arteries, among others, are reported to occur at the origin of the GA as well as at the AA [1, 5, 7–9, 12]. In addition, variations of the courses of multiple GAs are reported [1, 5–10, 12, 15, 17]. Even the occurrence of many GAs with multiple origins has been discussed. Multiple GAs have a single origin, and the multiple branches pass through several blood vessels.

The course of GAs is important not only for identifying the structures of the gonadal anatomy but also for facilitating safer gonadal and renal surgeries. It is unclear whether the single common trunk can be included for multiple arteries or single arteries, and no study so far has focused on GAs with a single common trunk. In addition, the embryological considerations for the development of GAs with a single common trunk have not been reported.

In the present study, we re-evaluated the unusual courses of GAs with a single common trunk with respect to the IVC and left renal vein and attempted to explain the developmental anatomy.

MATERIALS AND METHODS

All cadavers were selected from the bodies used for research and anatomy practice at Tokai University School of Medicine in 2017 and 2018. This observational cross-sectional study was performed on 54 Japanese adult cadavers (29 men and 25 women) and on 98 sides (53 male and 45 female sides) and on 102 arteries (54 testicular and 48 ovarian arteries), with an average age of 88.6 ± 7.46 years (88.0 ± 6.32 years in men and 89.1 ± 8.29 years in women). Some left and right sides of the cadavers were not observable by human error. In addition, there were cadavers with multiple gonadal arteries. Therefore, the results are presented in terms of cadavers, sides, and arteries. Cadavers that underwent urogenital surgery were excluded from this study. The single common trunks were treated as one artery.

We also presented case results from the dissection of 94-year-old (No. 2026) and 87-year-old (No. 2028) Japanese adult male cadavers as the first and second cases (cause of death: hepatic cancer and pancreatic cancer, respectively).

The cadavers were free from other diseases of the liver, stomach, and related vessels. Gross dissection was performed using the customary procedure. The vascular anatomical relationship around the kidney was specifically observed. For this purpose, we removed the branches of the coeliac trunk and the upper mesenteric arteries and carefully examined the structures.

RESULTS

The two cadavers with the single common trunk were referred to as first and second cases (Figs. 1 and 2, respectively). In Figure 1, the right testicular arteries (RTAs) of the single common trunk arose from the AA at the second lumbar vertebral level below the level of the left renal vein and ran 4 mm toward the IVC. Afterward, the single common trunk divided into two testicular arteries (TAs) passing through the lateral (dorsal) side (IRTA) and the medial (ventral) side (mRTA) of the IVC. The IRTA travelled in an arch shape from the dorsal side to the ventral side with respect to the right renal vein and descended to the caudal side. The mRTA passed through the ventral side of the right renal artery and descended to the caudal side. The IRTA and mRTA joined at the inferior pole of the right kidney and descended ventrally to the psoas major muscle. In other words, the IVC passed through the hiatus of the RTA. The left testicular arteries (LTAs) arose from the AA at the second lumbar vertebral level and descended ventrally to the psoas major muscle. The single common trunk of the RTAs, mRTA, IRTA, and LTA had an external diameter of approximately 1.8 mm, 0.8 mm, 1.8 mm, and 3.6 mm, respectively (Fig. 1). The right renal artery arose from the AA at the third lumbar vertebral level and passed through the ventral side of the IVC. The other abdominal arteries displayed normal courses.

In Figure 2, RTAs of the single common trunk arose from the AA at the third lumbar vertebral level below the level of the left renal vein and then ran 30 mm toward the IVC in the second case. Afterward, the single common trunk divided into two testicular arteries on the ventral side of the IVC and passed through the IRTA and the mRTA of the right testicular vein. The IRTA and mRTA did not join but dropped

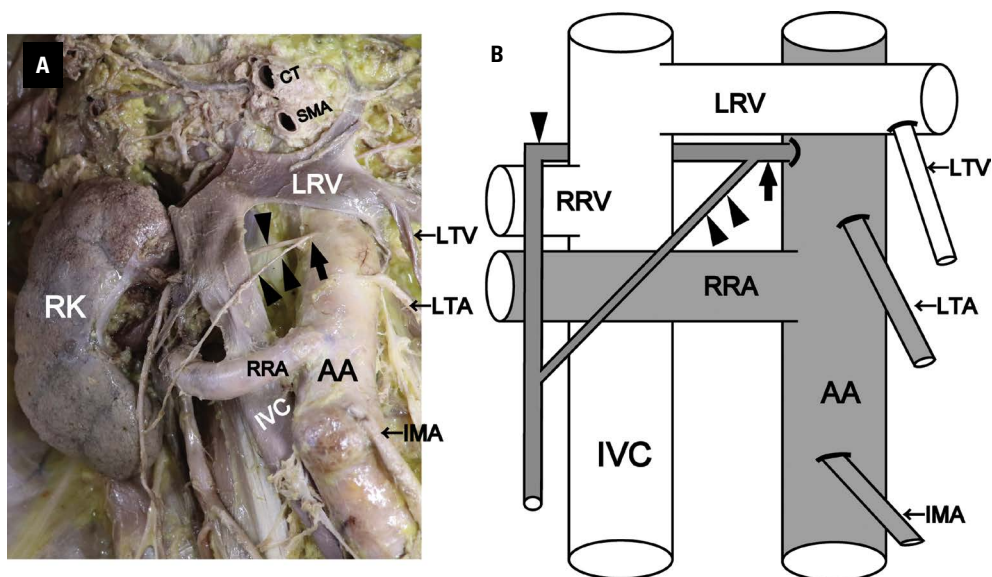


Figure 1. Photograph and schematic of the right testicular artery with the single common trunk in the first cadaver; **A.** Anterolateral view of a formaldehyde-fixed abdominal cavity of a 94-year-old man (cause of death: hepatic cancer; No. 2026); **B.** Graphical schematic of the same view. The black arrow points to the single common trunk of the right testicular artery. The single and double black arrowheads point to the lateral right testicular artery and medial testicular artery, respectively; AA — abdominal aorta; CT — coeliac trunk; IMA — inferior mesenteric artery; IVC — inferior vena cava; LRV — left renal vein, LTA — left testicular artery; LTV — left testicular vein; RK — right kidney; RRA — right renal artery; RRV — right renal vein; RTV — right testicular vein; SMA — superior mesenteric artery.

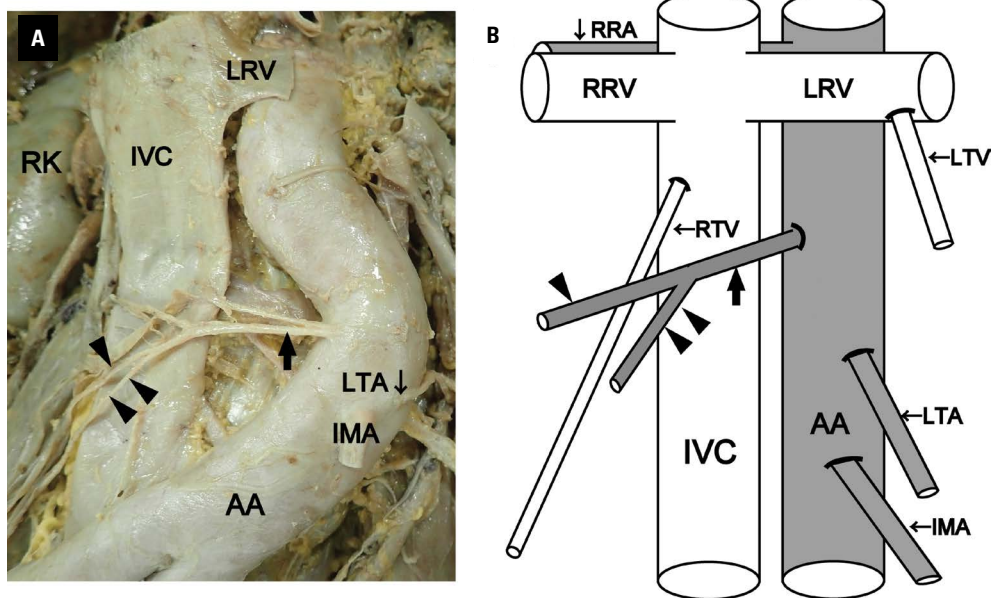


Figure 2. Photograph and schematic illustration of the right testicular artery with the single common trunk in the second cadaver; **A.** Anterolateral view of a formaldehyde-fixed abdominal cavity of an 87-year-old man (cause of death: pancreatic cancer; No. 2028); **B.** Graphical schematic of the same view. The black arrow points to the single common trunk of the right testicular artery. The single and double black arrowheads point to the lateral right testicular artery and medial testicular artery, respectively; AA — abdominal aorta; IMA — inferior mesenteric artery; IVC — inferior vena cava; LRV — left renal vein; LTA — left testicular artery; LTV — left testicular vein; RK — right kidney; RRA — right renal artery; RRV — right renal vein.

separately toward the deep inguinal ring. The left testicular arteries arose from the AA at the fourth

lumbar vertebral level and descended ventrally to the psoas major muscle. The single common trunk of the

Table 1. Observed anatomical variations in the origin of gonadal arteries of the present study

Origin of gonadal artery	Male (testicular artery)			Female (ovarian artery)			Total (gonadal artery)		
	Body	Side (left, right)	Artery (left, right)	Body	Side (left, right)	Artery (left, right)	Body	Side (left, right)	Artery (left, right)
Abdominal aorta	27	51 (25, 26)	52 (26, 26)	20	40 (20, 20)	43 (23, 20)	47	91 (45, 46)	95 (49, 46)
Renal artery	2	2 (2, 0)	2 (2, 0)	3	3 (2, 1)	3 (2, 1)	5	5 (4, 1)	5 (4, 1)
Other	Not observed	Not observed	Not observed	2	2 (0, 2)	2 (0, 2)	2	2 (0, 2)	2 (0, 2)

Table 2. Description of the gonadal artery with a single common trunk in the published literature

References	Sex	Origin	Side	Remark
Rusu (2006) [15]	Male	Abdominal aorta	Left	Doubled right testicular arteries arose from the abdominal aorta and renal artery Single common trunk run arching with respect to the left renal vein
Tanyeli et al. 2006 [17]	Male	Renal artery	Right	Normal course of a left testicular artery
Kotian et al. 2016 [6]	Male	Abdominal aorta	Left	Normal course of a right testicular artery
Mao and Li 2017 [10]	Male	Abdominal aorta	Right	Right testicular vein passed through the hiatus of the right testicular artery
First cadaver	Male	Abdominal aorta	Right	Normal course of a left testicular artery Lateral right testicular artery run arching with respect to the right renal vein Inferior vena cava passed through the hiatus of the right testicular artery
Second cadaver	Male	Abdominal aorta	Right	Normal course of a left testicular artery

RTA, mRTA, IRTA, and LTA had an external diameter of approximately 2.4 mm, 1.1 mm, 1.3 mm, and 1.9 mm, respectively (Fig. 2). The other abdominal arteries displayed normal courses.

The details of the origin of all GAs are shown in Table 1. The details for men and women are shown separately in Table 1 because the gonadal arteries are different in testicular and ovarian arteries. Given that the testicular artery with a single common trunk originates from the AA and then branches into two, it was included in the group branching from the AA in this study. In addition, the single common trunk was included in the ratio of origin as one artery. The GA, testicular artery, and ovarian artery arose from the AA in 93.1%, 96.3%, and 89.6% of cadavers, respectively, and from the renal artery in 4.9%, 3.7%, and 6.3% of cadavers, respectively.

As shown in Table 2, all previous reports of the single common trunk were from case reports of men. There were two testicular arteries with a single common trunk on the right side in the specimens of this study. Therefore, the incidence rate of the single common trunk is 3.7% of cadavers, 2.0% of sides, and 2.0% of arteries in the GA. Moreover, the incidence rate of a single common trunk is 6.9% of cadavers, 3.8% of sides, and 3.7% of arteries in the testicular artery.

DISCUSSION

Herein, we have described variations at the origin of the GAs in 54 cadavers. In addition, we examined the single common trunk in two cadavers and correlated our observations with related literature. Moreover, we discuss the embryological hypothesis of GAs with a single common trunk.

The GA, testicular, and ovarian arteries arose from the AA in 77.7% of arteries, 76.5% of arteries, and 79.3% of arteries, respectively, and from the renal artery in 21.8% of arteries, 22.6% of arteries, and 20.7% of arteries, respectively [8, 9]. Our data show that the percentage of vessels arising from the AA was higher than those arising from the renal artery. This result may be due to the limited number of cases. Double testicular arteries existed in 1.6% and 1.4% of the right and left sides, respectively. They originated from the same artery in 2 of 8 and 3 of 7 cases at the right and left sides, respectively, and originated from different arteries in 6 of 8 and 4 of 7 cases at the right and left sides, respectively [8, 9]. In another report [12], double testicular arteries were present in 25/1,167 (2.14%) cases on the left side; of these, 14 had both arteries arising from the AA (1.19%), 9 originated from the AA (0.77%). The other one had double testicular arteries originating from arteries other than the AA, and 2 had both arteries originating

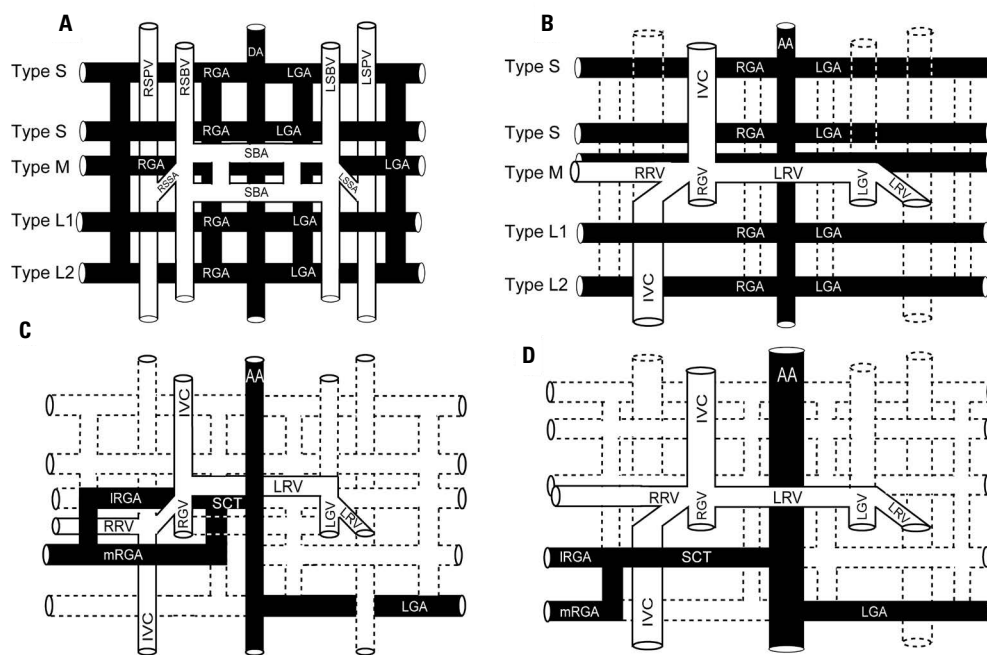


Figure 3. The proposed scheme of the formation of the single common trunk (SCT) of the right testicular artery (modified from the figure of Terayama et al. [18]'s report); **A, B.** Anastomosis of the right supracardinal vein (RSPV) and right sub-cardinal vein (RSBV) is important to determine the course of the right gonadal artery (RGA); **C.** Proposed developmental anatomy of the first cadaver (Fig. 1); **D.** Proposed developmental anatomy of the second cadaver (Fig. 2). Right gonadal arteries (GAs) arising from the dorsal aorta (DA) pass dorsally to the RSPV or pass between the RSBV and RSPV: type S of RGA pass dorsally to IVC and type M and type L of RGA pass dorsally or ventrally to inferior vena cava (IVC); AA — abdominal aorta; mRGA — medial right gonadal artery; LGA — left gonadal artery; LGV — left gonadal vein; LRV — left renal vein; LSBV — left sub-cardinal vein; LSPV — left supracardinal vein; LSSA — left sub-supracardinal anastomosis; lRGA — lateral right gonadal artery; RGV — right gonadal vein; RSSA — right sub-supracardinal anastomosis; RRV — right renal vein; SBA — sub-cardinal anastomosis.

from the vessels other than the AA (0.17%, both from the RA). On the right side, 19/1,229 cases showed a double testicular artery (1.54%), 9 had both arteries arising from the AA (0.77%), and 10 had both arteries originating from vessels other than the AA (0.81%). It is unclear whether the single common trunk can be included in multiple arteries or single arteries, and the original ratio may be masked. Therefore, a detailed ratio of single common trunk structures of the study specimens is useful for classifying the arteries.

The arterial running pattern of the single common trunk is one of the two types: type A divides into the right and left sides of GAs on the different side and type B divides into the medial and lateral sides of GAs on the same side. The single common trunk structure of type A is reported "in < 0.1% of cases a common trunk originated from the AA, which later divided into right and left testicular arteries" by statistical processing of the previous literature [7]. However, the details of type B are unknown. In this study, the incidence rate was 3.7% of cadavers and 6.9% of bodies, 2.0% of sides and 3.8% of sides, and 2.0% of arteries and 3.7% of arteries in the GA and testicular artery,

respectively. Moreover, all single common trunks of type B were present in men, which was consistent with previous literature [6, 10, 15, 17]. However, it is unclear whether the single common trunk only exists in men. The testis may be associated with longer migration than the ovary. At any rate, to the best of our knowledge, this report is the first detailed study of the single common trunk of type B.

As shown in Table 2, the RTA with a single common trunk was observed in the cadaveric specimens of this study; however, the embryological significance of the presence of these varieties of the right GAs remains unclear. In general, the variations in the origin, course, and branching out of the right GAs are attributed to the development of the IVC. Only Terayama et al. [18] reported on the development of the RTA and IVC system together. Several successive networks participate in the formation of the IVC through the initial appearance of complex capillary plexuses and preferential utilisation and expansion or regression of individual channels within the plexus [2, 18]. The sub-cardinal veins arise in association with the ventral margin of the mesonephros and form

the sub-cardinal anastomosis, which is the origin of the gonadal and renal veins [4, 18]. Thereafter, the supracardinal veins appear dorsal to the sub-cardinal veins, and the supracardinal and sub-cardinal veins anastomose (Fig. 3A). The sub-cardinal and sub-supracardinal anastomoses, as well as the sub-cardinal and supracardinal veins, are important for the development of the GAs, gonadal veins, renal veins, and IVC (Fig. 3B) [3, 14, 18].

As shown in Figure 3, we assumed that the right gonadal arteries (RGAs) arise from the dorsal arteries and then pass either dorsally to both the sub-cardinal and supracardinal veins or dorsally to the sub-cardinal veins and ventrally to the supracardinal veins (Fig. 3A). Moreover, several previous reports also showed that the lateral artery of the dorsal aorta, including the right GA, had a longitudinal anastomosis (Fig. 3A) [13, 16]. Terayama et al. [18] reported that the course of the GA is of one of the four subtypes based on the relationship to the left renal vein and the IVC, of superior (S), middle (M) and lower types (L1 = ventrally, L2 = dorsal of IVC). Type S ultimately passes dorsally to the IVC (Fig. 3B). Type L can be divided into types L1 and L2 during the development of the IVC (Fig. 3B). Finally, one or two of types S, M, L1, and L2 become the remaining RGA (Fig. 3B). In the first case, it is assumed that a longitudinal anastomosis with type L1 remained after type M passed through the dorsal side of the IVC (Fig. 3C). It is also presumed that in the second case, a longitudinal anastomosis with type L2 remained after type L1 passed through the ventral side of the IVC (Fig. 3D). The hypotheses of type S, M and L embryology, including the longitudinal anastomosis, are useful in discussing the development of the right GA, including the IVC. The left GA does not need to consider IVC, so either the grid-like vascular network remains partially or not.

Part of the discussion explains the embryological hypothesis of GA based on observations and past literature. Therefore, the limitation of this research is that it has not been proved experimentally.

CONCLUSIONS

Our findings revealed that the GA, testicular artery, and ovarian artery arose from the AA in 93.1%, 96.3%, and 89.6% of cadavers, and from the renal artery in 4.9%, 3.7%, and 6.3% of cadavers, respectively. A single common trunk was found in 3.7% of cadavers, 2.0% of sides, and 2.0% of arteries in the

GA and in 6.9% of cadavers, 3.8% of sides, and 3.7% of arteries in the testicular artery. Varying morphological anomalies of GAs may be clinically significant while considering the influence of the blood flow from the gonadal glands and the development of new operative techniques (especially in the laparoscopic surgery field) within the abdominal cavity [13]. The knowledge of these common variations can serve as a reference for avoiding clinical complications, especially during surgery in this region.

Ethical approval and informed consent

The ethics committee of the Tokai University School of Medicine (No. 17R-309) approved this study.

All the cadavers were donors who had provided direct and informed consent for their bodies to be used for teaching or research projects at the Department of Anatomy.

Acknowledgements

The authors thank Ms. Kyoko Endo and Ms. Yuko Furuya (both from Tokai University School of Medicine, Kanagawa, Japan) for the excellent secretarial support and Dr. Tsutomu Sato and Dr. Satoshi Kawakami (both from Tokai University School of Medicine, Kanagawa, Japan) for advice. We would like to thank Editage for English language editing.

Funding

This work was supported by a Grant-in-Aid for Scientific Research (JSPS KAKENHI Grant Numbers 18K10031). The funders had no role in study design, data collection and analysis, decision to publish, or preparation of the manuscript.

REFERENCES

1. Çiçekcibaşı AE, Salbacak A, Seker M, et al. The origin of gonadal arteries in human fetuses: anatomical variations. *Ann Anat.* 2002; 184(3): 275–279, doi: [10.1016/S0940-9602\(02\)80126-1](https://doi.org/10.1016/S0940-9602(02)80126-1), indexed in Pubmed: [12056759](https://pubmed.ncbi.nlm.nih.gov/12056759/).
2. Gray SW, Skandala JE. The superior and inferior venae cavae. In: Skandala JE (ed.). *Embryology for surgeons*. Saunders Company, Philadelphia 1972: 862–876.
3. Itoh M, Moriyama H, Tokunaga Y, et al. Embryological consideration of drainage of the left testicular vein into the ipsilateral renal vein: analysis of cases of a double inferior vena cava. *Int J Androl.* 2001; 24(3): 142–152, doi: [10.1046/j.1365-2605.2001.00286.x](https://doi.org/10.1046/j.1365-2605.2001.00286.x), indexed in Pubmed: [11380703](https://pubmed.ncbi.nlm.nih.gov/11380703/).
4. Jordan HE, Kindred JA. The inferior vena cava. In: HE Jordan, JA Kindred (ed.). *Textbook of embryology*. Appleton-Century, New York 1932: 220–235.

5. Kayalvizhi I, Narayan RK, Kumar P. Anatomical variations of testicular artery: a review. *Folia Morphol.* 2017; 76(4): 541–550, doi: [10.5603/FM.a2017.0035](https://doi.org/10.5603/FM.a2017.0035), indexed in Pubmed: [28394009](https://pubmed.ncbi.nlm.nih.gov/28394009/).
6. Kotian SR, Pandey AK, Padmashali S, et al. A cadaveric study of the testicular artery and its clinical significance. *J Vasc Bras.* 2016; 15(4): 280–286, doi: [10.1590/1677-5449.007516](https://doi.org/10.1590/1677-5449.007516), indexed in Pubmed: [29930605](https://pubmed.ncbi.nlm.nih.gov/29930605/).
7. Lippert H, Pabst R. Arterial variations in man: classification and frequency. 1st Ed. J F Bergman Verlag, Munich 1985.
8. Machnicki A, Grzybiak M. Variations in testicular arteries in fetuses and adults. *Folia Morphol.* 1997; 56(4): 277–285, indexed in Pubmed: [9635363](https://pubmed.ncbi.nlm.nih.gov/9635363/).
9. Machnicki A, Grzybiak M. Variations in ovarian arteries in fetuses and adults. *Folia Morphol.* 1999; 58(2): 115–125, indexed in Pubmed: [10598404](https://pubmed.ncbi.nlm.nih.gov/10598404/).
10. Mao QH, Li J. Double right testicular arteries passing through the hiatus in the trifurcated testicular vein. *Indian J Surg.* 2017; 79(1): 73–74, doi: [10.1007/s12262-016-1576-9](https://doi.org/10.1007/s12262-016-1576-9), indexed in Pubmed: [28331273](https://pubmed.ncbi.nlm.nih.gov/28331273/).
11. Moore KL, Dalley AF. Clinically oriented anatomy, 4th ed. Lippincott Williams and Wilkins, Philadelphia 1999.
12. Nallikuzhy TJ, Rajasekhar SS, Malik S, et al. Variations of the testicular artery and vein: a meta-analysis with proposed classification. *Clin Anat.* 2018; 31(6): 854–869, doi: [10.1002/ca.23204](https://doi.org/10.1002/ca.23204), indexed in Pubmed: [29737575](https://pubmed.ncbi.nlm.nih.gov/29737575/).
13. Onderoğlu S, Yüksel M, Arik Z. Unusual branching and course of the testicular artery. *Ann Anat.* 1993; 175(6): 541–544, doi: [10.1016/s0940-9602\(11\)80219-0](https://doi.org/10.1016/s0940-9602(11)80219-0), indexed in Pubmed: [8297041](https://pubmed.ncbi.nlm.nih.gov/8297041/).
14. Pansky B. Development of the venous system. In: Pansky B (ed). Review of medical embryology. Macmillan Publishing, New York 1932: 328–329.
15. Rusu MC. Human bilateral doubled renal and testicular arteries with a left testicular arterial arch around the left renal vein. *Rom J Morphol Embryol.* 2006; 47(2): 197–200, indexed in Pubmed: [17106531](https://pubmed.ncbi.nlm.nih.gov/17106531/).
16. Shinohara H, Nakatani T, Fukuo Y, et al. Case with a high-positioned origin of the testicular artery. *Anat Rec.* 1990; 226(2): 264–266, doi: [10.1002/ar.1092260216](https://doi.org/10.1002/ar.1092260216), indexed in Pubmed: [2301743](https://pubmed.ncbi.nlm.nih.gov/2301743/).
17. Tanyeli E, Uzel M, Soyloğlu AI. Complex renal vascular variation: a case report. *Ann Anat.* 2006; 188(5): 455–458, doi: [10.1016/j.aanat.2006.05.013](https://doi.org/10.1016/j.aanat.2006.05.013), indexed in Pubmed: [16999210](https://pubmed.ncbi.nlm.nih.gov/16999210/).
18. Terayama H, Yi SQ, Naito M, et al. Right gonadal arteries passing dorsally to the inferior vena cava: embryological hypotheses. *Surg Radiol Anat.* 2008; 30(8): 657–661, doi: [10.1007/s00276-008-0378-6](https://doi.org/10.1007/s00276-008-0378-6), indexed in Pubmed: [18584112](https://pubmed.ncbi.nlm.nih.gov/18584112/).

Origin and main ramifications of coeliac artery in *Cerdocyon thous*

S. Viana-Peçanha¹, E.C. Souza¹, D.M.L. Guerra¹, F.C.S. Bernardes¹, R.B.J. Carvalho¹, P. de Souza Junior¹, M. Abidu-Figueiredo¹

Laboratory of Animal Anatomy, Federal University of Pampa (UNIPAMPA), Campus Uruguaiiana, RS, Brazil

[Received: 28 May 2020; Accepted: 3 July 2020]

Background: *Cerdocyon thous* is the canid with the greatest geographical coverage in South America. The aim of this study was to describe the origin, skeletopy, length and main branches of the coeliac artery in *C. thous*.

Materials and methods: The dissections were performed on 14 cadavers of adult specimens, 6 males and 8 females, with a rostrorsacral length average of 67.00 ± 4.7 cm and 62.09 ± 5.7 cm, respectively. The specimens were collected dead on highways on the banks of the Atlantic Forest (Rio de Janeiro) and the Pampa biome (Rio Grande do Sul) in Brazil. The cadavers were fixed and preserved in a formaldehyde solution until dissection. The coeliac artery was dissected, the length was measured “in situ” and its main branches were recorded. The coeliac artery emerged as a single artery in all dissected animals.

Results: The average length of the coeliac artery was 1.43 ± 0.17 cm in males and 1.39 mm ± 0.24 cm in females, with no significant difference in this measurement between sexes. The predominant skeletopy was at the level of the second lumbar vertebra (57.1%), positioned on average 1.43 cm cranially to the cranial mesenteric artery. In most individuals (92.9%), the classic trifurcation was formed: the coeliac artery branched into the hepatic, left gastric, and lienal arteries. Only 1 male animal presented a bifurcation formed between the hepatic artery and a gastrolienal trunk.

Conclusions: These anatomical characteristics are similar to those of other species of the Canidae family, possibly due to their phylogenetic proximity. (Folia Morphol 2021; 80, 2: 331–335)

Key words: animal anatomy, cardiovascular system, crab-eating-fox, wild carnivorans

INTRODUCTION

Cerdocyon thous (*C. thous*), known as “crab-eating-fox”, is the most widely distributed wild canid on the South American continent, populating Colombia to Uruguay. With great adaptability, it inhabits closed and open vegetation areas [8, 9, 18, 19]. Body mass

ranges from 5 to 9 kg and can measure up to 1.2 m from the tip of the snout to the tail [19]. The diet is based on fruits, small vertebrates, eggs, insects, and crustaceans, characterising an opportunistic omnivorous diet [9, 18]. *Cerdocyon thous* is threatened by hunting, hit-and-run, and diseases transmitted by

Address for correspondence: Prof. P. de Souza Junior, Laboratory of Animal Anatomy, Rodovia BR-472, Km 595, Uruguaiiana, RS, Brazil, Postal code 97501-970, tel/fax: +55 55 3911-0200, e-mail: paulosouza@unipampa.edu.br

This article is available in open access under Creative Common Attribution-Non-Commercial-No Derivatives 4.0 International (CC BY-NC-ND 4.0) license, allowing to download articles and share them with others as long as they credit the authors and the publisher, but without permission to change them in any way or use them commercially.

Canis familiaris (*C. familiaris*), although its conservation is not a concern [9, 18, 19].

The high occurrence of free-ranging *C. thous* and its high frequency in zoos and private collections makes it frequently subject to veterinary care [8, 32].

The coeliac artery (CA) is one of the most important arteries in the abdominal part of aorta; it is a short vessel that emerges ventrally from the abdominal aorta, at the level of the aortic hiatus of the diaphragm muscle [20]. Close to its origin, this vessel is surrounded by the coeliac plexus and ganglia. On the left, the CA forms a syntopic relationship with the stomach; on the right, with the liver and adrenal gland, and caudally with the left lobe of the pancreas [17, 20]. The CA emits the hepatic, left gastric and lienal arteries [17].

In mixed-breed *C. familiaris*, the CA presents two morphological arrangements distinct from branches: classical trifurcation (formed by the hepatic artery, left gastric, and lienal), and hepatic artery and gastrolenal trunk [1]. Anatomy knowledge and possible variations in branches of the main splanchnic vessels is fundamental for planning surgeries and supports comparative studies on vascular arrangement in different species.

The aim of this study was to describe the origin, skeletopy, and main branches of the CA in *Cerdocyon thous*.

MATERIALS AND METHODS

Adult specimens of *C. thous* were collected dead on highways of the Atlantic Forest biome (State of Rio de Janeiro, Brazil) and in the Pampa biome (Rio Grande do Sul, Brazil) under authorisation of the Ethics Committee on Animal Experimentation (protocol 018/2017) and IBAMA/SISBIO (number 33667). Since most of the cadavers collected on highways had abdominal vessels and viscera ruptured, only specimens in perfect condition were selected for the dissection of the CA and its main branches. Thus, 14 cadavers (6 males and 8 females), 7 from each biome, were dissected.

Initially, the cadavers were thawed under running water, sexed, and identified by placing a plastic tag attached to the common calcaneal tendon using a string. The rostrum-sacral length of each animal was measured using a precision metal measuring tape. The tip of the snout was used as a reference for the proximal insertion of the tail. The cadavers were placed in right lateral decubitus position to access

the thoracic aorta through an incision made between the 6th and 10th left intercostal spaces. The artery was cannulated with a number 8 or 10 urethral probe, depending on the diameter of the vessel, and was attached with a string to prevent leakage and maintain intravascular pressure. Fixation was performed by injecting a 10% formaldehyde solution through the probe in a caudal direction.

Immediately following the fixation of the cadavers, petrolatex S65 (Petrobrás Duque de Caxias Refinery [RE-DUC], Duque de Caxias/RJ) solution was injected and stained with Suvinil pigment for repletion of the arterial system. Then, the cadavers were immersed in polyethylene boxes containing 10% formaldehyde solution for to complete the latex fixation and polymerisation process.

Seven days after the latex injection, the cadavers were dissected in order to determine the origin, skeletopy, and main branches of the CA. After skin removal, two incisions were made in the abdominal wall: the first in the linea alba, starting from the xiphoid cartilage to the pubic region; the second transversely at the level of the last rib in both antimers, starting from the transverse process of the first lumbar vertebra to the linea alba. The cranial coeliac and mesenteric arteries were dissected after locating the abdominal aorta.

A digital calliper (ZAAS Precision, Amatools®) was used to measure the distance between the centres of the origins of the coeliac and cranial mesenteric arteries and the CA length until it originated its first branch.

The mean and standard deviation of the animals' rostrum-sacral length, CA length, and the distance between CA and cranial mesenteric artery were calculated. These values were compared for both sexes and considered significant when $p < 0.05$ using the unpaired "t" test. The data were analysed using the Graphpad Prism 5® Software.

RESULTS

The rostrum-sacral and CA length averages were higher in males (Table 1), while the distance between the coeliac and cranial mesenteric arteries was higher in females, although there was no significant difference in any comparison between sexes ($p > 0.05$).

In all dissected specimens, the CA originated ventrally from the abdominal aorta. The predominant skeletopy of the CA in *C. thous* occurred at the level of the second lumbar vertebra (Table 2).

Table 1. Mean and standard deviation (cm) of the rostrum-sacral length, length of the coeliac artery (CA) and the distance between the coeliac and cranial mesenteric arteries in *Cerdocyon thous*. The p value corresponds to that obtained in the unpaired t-test of comparison of means between sexes

	<i>Cerdocyon thous</i> (n = 14)		
	Males (n = 6)	Females (n = 8)	P
Rostrum-sacral length	67.0 ± 4.79	62.09 ± 5.78	0.11
CA length	1.43 ± 0.17	1.39 ± 0.24	0.78
Distance between CA and cranial mesenteric artery	1.48 ± 0.20	1.60 ± 0.26	0.36

Table 2. Absolute and percentage frequencies of the skeletopy of the coeliac artery in *Cerdocyon thous*

Skeletopy	Males (n = 06)	Females (n = 08)	Total (n = 14)
L1	2 (33.3%)	–	2 (14.3%)
L1–L2	1 (16.7%)	3 (37.5%)	4 (28.6%)
L2	3 (50.0%)	5 (62.5%)	8 (57.1%)

Although the CA in *C. thous* presented a variable skeletopy between the individuals, there was no statistical difference between sexes ($p = 0.05$).

In 13 specimens, the classic trifurcation was formed: the CA originated the hepatic, left gastric and lienal arteries (Fig. 1). Only 1 male animal presented a bifurcation formed between the hepatic artery and a gastrolial trunk (Fig. 2).

DISCUSSION

Origin

The CA emerged ventrally from the abdominal aorta, close to the aortic hiatus of the diaphragm, similar to what is described in different mammals [1–3, 10, 22, 23, 27, 33]. However, in *Bubalus bubalis* foetuses [24] and in 33% of *Lycalopex gymnocercus* specimens [22], the origin of the CA occurred in the thoracic aorta. Despite phylogenetic proximity to *Lycalopex gymnocercus*, no coeliac arteries originating in the thoracic aorta were found in the sampling of *C. thous* from the present study.

Some studies have noted variations in the emergence of the CA in some species of mammals and mention the presence of a common trunk formed by the coeliac and cranial mesenteric arteries called the coeliac-mesenteric trunk. It was reported with *Ovis aries* [21], *Bubalus bubalis* [24], *Capra aegagrus hircus* [13], *Myocastor coypus* [23], *C. familiaris* [30], *Felis catus* [29], *Didelphis albiventris* [11], and humans [15].

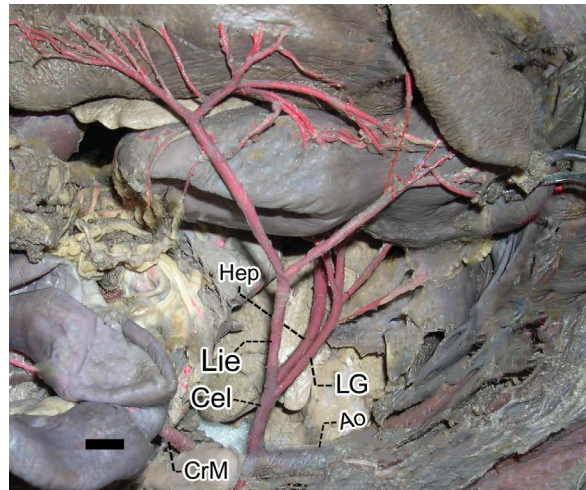


Figure 1. The aorta (Ao), cranial mesenteric (CrM) artery and coeliac artery (Cel) and its main branches (classic trifurcation): hepatic (Hep), left gastric (LG) and lienal (Lie) arteries in a female, adult, specimen of *Cerdocyon thous*. Scale bar: 10 mm.

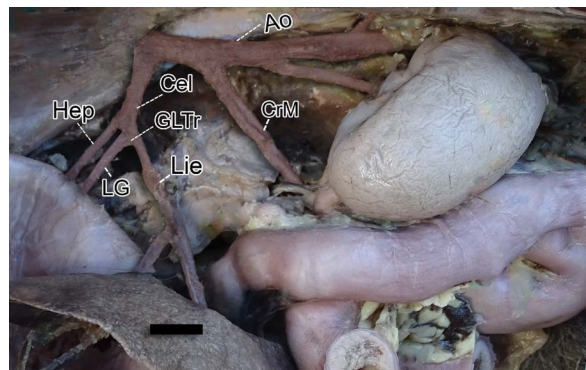


Figure 2. The aorta (Ao), cranial mesenteric (CrM) artery and coeliac artery (Cel) and its main branches. In this specimen, an adult male *Cerdocyon thous*, coeliac artery originated a gastrolial trunk (GLTr) and a hepatic artery (Hep); the gastrolial trunk bifurcated into lienal (Lie) and left gastric (LG) arteries. Scale bar: 10 mm.

In humans, another arrangement has been described: the formation of the coeliac-bimesenteric trunk, formed by the coeliac, superior mesenteric, and inferior mesenteric arteries [7, 26].

Regarding the incidence in mammals, the coeliac-mesenteric trunk was divided into three groups: a group with a regular or preponderant incidence, observed in *Cavia porcellus*; a group with frequent incidence, observed in *Ovis aries*; and a group with a low or zero incidence observed in *Castor fibre*, *Erinaceus europaeus*, *Mesocricetus auratus*, and *Mus musculus* [31]. In canids, the occurrence of coeliac-mesenteric trunk is described only in *C. familiaris* [30], not being found in *L. gymnocercus* [22] or *C. thous*.

Table 3. Summarisation of common skeletopy, average length and primary branches of coeliac artery in species of the order Carnivora

Species	Family	N	Common skeletopy	Length	Branches
<i>C. thous</i>	Canidae	14	L2	1.41 cm	Hepatic, left gastric and lienal arteries
<i>L. gymnocercus</i> [22]	Canidae	15	L2	–	Hepatic, left gastric and lienal arteries
<i>V. vulpes</i> [12]	Canidae	06	L1	–	Gastrolienal trunk and hepatic artery
<i>C. familiaris</i> [1]	Canidae	30	L1	0.98 cm	Gastrolienal trunk and hepatic artery or hepatic, left gastric and lienal arteries
<i>M. martes</i> [34]	Mustelidae	01	-	–	Gastrolienal trunk and hepatic artery
<i>M. p. furo</i> [13]	Mustelidae	–	–	–	Hepatic, left gastric and lienal arteries
<i>N. nasua</i> [5]	Procyonidae	04	L1	–	Hepatic, left gastric and lienal arteries
<i>F. catus</i> [33]	Felidae	30	L1	1.30 cm	Gastrolienal trunk and hepatic artery or hepatic, left gastric and lienal arteries
<i>L. pardalis</i> [28]	Felidae	02	–	–	Hepatic, left gastric and lienal arteries

Skeletopy

In domestic carnivores, the coeliac artery has a predominant origin at the level of the first lumbar vertebra (Table 3) [1, 29, 33], although origin points as cranial as the 13th thoracic vertebra or as caudal as the 2nd lumbar vertebra are often described [1, 25, 33]. In the wild canid *L. gymnocercus*, the predominant skeletopy of the CA was at the level of the 2nd lumbar vertebra, varying cranially to the 1st lumbar [22], similar to the results obtained in the sampling of *C. thous* in this research. In other carnivores, including *C. familiaris* and *Felis catus* as well as wild canids *Vulpes vulpes* and procyonid *Nasua nasua*, the skeletopy was at the level of the first lumbar [1, 5, 12, 33].

Getty et al. [17] reported that the CA appears at the level of the 17th and 18th thoracic vertebra in *Equus ferus caballus*, at the level of the 1st lumbar vertebra in *Bos taurus* and *Ovis aries*, between the 1st and 2nd lumbar vertebra in goat [16], and between the last thoracic vertebra and the 1st lumbar vertebra in *Sus domesticus*. In *Oryctolagus cuniculus*, the coeliac artery's level predominates between the 13th thoracic vertebra and the 1st lumbar [2], ventrally to the 1st lumbar vertebra in *Cavia porcellus* [17], and the coeliac trunk appears at the level of the 12th thoracic vertebra in humans [26].

Reports of CA length measurements are still scarce. In the *C. familiaris* it measures around 2 cm [14], 1.3 cm in *Felis catus* [33], and about 1.4 cm in *C. thous*. Regarding the distance between the origins of the coeliac and cranial mesenteric arteries, it was described as 3 mm in *Bubalus bubalis* foetuses, ranging from 1.8 to 5 mm [24]. In humans, it was 12 mm, ranging from 3 to 23 mm [4]. The mean value found in *Lycalopex gymnocercus* was 6.66 mm, had a moderate correlation with the animal's length [22], and was smaller than in the *C. thous* specimens analysed.

Main branches

The classic trifurcation of the CA into hepatic, left gastric and lienal arteries was the most prevalent arrangement in *C. thous*, similar to that registered in *C. familiaris*, *Oryctolagus cuniculus*, *Myocastor coypus*, and *Galea spixii* [1, 2, 10, 27]. The bifurcation in a hepatic artery and gastrolienal trunk found in a single specimen of *C. thous* of this sampling was also reported as sporadic in *C. familiaris* [1, 14]. However, this bifurcation was found in almost half of *Felis catus* [33]. In *Oryctolagus cuniculus*, unlike in other species, the CA emitted only one arrangement: the lienal artery and then the left gastric artery, which continued to be hepatic [2]. In *Hystrix cristata* and *Didelphis albiventris*, the CA was divided into only two branches: the lienal artery and the hepatic artery in all animals studied [6, 11].

CONCLUSIONS

It can be concluded that the CA in *C. thous* originates as a single artery in the ventral face of the abdominal aorta, predominantly at the level of the second lumbar vertebra, about 1.5 cm from the cranial mesenteric artery, cranially. The artery measures about 1.4 cm until the predominant classic trifurcation occurs, although a bifurcation variant can be verified. These anatomical characteristics are similar to those described in other canids, possibly as an expression of the evolutionary proximity of these species.

Funding

Research Support Foundation of Rio Grande do Sul (FAPERGS), National Council of Technological and Scientific Development (CNPq), Rio de Janeiro State Research Foundation (FAPERJ) and Coordination of Superior Level Staff Improvement (CAPES) Finance Code 001.

REFERENCES

- Abidu-Figueiredo M, Dias GP, Cerutti S, et al. Variations of celiac artery in dogs: anatomic study for experimental, surgical and radiological practice. *Int J Morphol*. 2005; 23(1), doi: [10.4067/s0717-95022005000100007](https://doi.org/10.4067/s0717-95022005000100007).
- Abidu-Figueiredo M, Xavier-Silva B, Cardinot T, et al. Celiac artery in New Zealand rabbit: anatomical study of its origin and arrangement for experimental research and surgical practice. *Pesquisa Veterinária Brasileira*. 2008; 28(5): 237–240, doi: [10.1590/s0100-736x2008000500002](https://doi.org/10.1590/s0100-736x2008000500002).
- Amadori A, Birck AJ, Fidelpho AL, Guimarães GC, Peres JÁ, Souza RAM. Origem e distribuição da artéria celiaca em veado catigueiro (*Mazama gouazoubira*). *Revista Científica Eletrônica Medicina Veterinária [Internet]*. 2012 Jul. 10(19) [Portuguese]. http://faef.revista.inf.br/imagens_arquivos/arquivos_destaque/NnwiPElvFhC-S7oy_2013-6-24-12-3-16.pdf (cited 2020 Mar 03).
- Araujo Neto SA, Franca HA, de Mello Júnior CF, et al. Anatomical variations of the celiac trunk and hepatic arterial system: an analysis using multidetector computed tomography angiography. *Radiol Bras*. 2015; 48(6): 358–362, doi: [10.1590/0100-3984.2014.0100](https://doi.org/10.1590/0100-3984.2014.0100), indexed in Pubmed: [26811552](https://pubmed.ncbi.nlm.nih.gov/26811552/).
- Assunção M, Oliveira T, Oliveira T, et al. Comparative Anatomy of Abdominal Aorta in Coati (*Nasua nasua*). *Int J Adv Engineer Res Sci*. 2019; 6(2): 259–267, doi: [10.22161/ijaers.6.2.32](https://doi.org/10.22161/ijaers.6.2.32).
- Atalar O, Yilmaz S. The branches of the arteria celiaca in the porcupine (*Hystrix cristata*). *Vet Med*. 2012; 49(No. 2): 52–56, doi: [10.17221/5675-vetmed](https://doi.org/10.17221/5675-vetmed).
- Bergman RA, Thompson SA, Afifi AK, Saadeh FA. Compendium of human anatomic variation: Catalog, Atlas and World Literature. Urban & Schwarzenberg, Munich 1988.
- Cheida CC, Nakano-Oliveira E, Fusco-Costa R, Rocha-Mendes F (eds). *Ordem Carnivora*. In: Reis NR, Perachi AL, Pedro WA, Lima IP (eds). *Mamíferos do Brasil*. Nelio R. dos Reis, Londrina 2006: 231–276.
- Courtenay O, Maffei L. Crab-eating fox *Cerdocyon thous* (Linnaeus, 1766). In: Sillero-Zubiri C, Hoffmann M, Macdonald DW, editors. *Canids: Foxes, Wolves, Jackals and Dogs. Status Survey and Conservation Action Plan*. IUCN/SSC Canid Specialist Group, Cambridge 2004: 32–38.
- Culau POV, Azambuja RC, Campos R. Ramos colaterais viscerais da aorta abdominal em *Myocastor coypus* (nutria). *Acta Scientiae Veterinariae*. 2008; 36(3): 241–247.
- Culau P, Reckziegel S, Goltz L, et al. A artéria celiaca em *Didelphis albiventris* (gambá). *Acta Scientiae Veterinariae*. 2018; 38(2): 121, doi: [10.22456/1679-9216.16589](https://doi.org/10.22456/1679-9216.16589).
- Dogan GK, Dalga S, Akbulut Y, et al. Kızıl Tilkilerde (*Vulpes vulpes*) Arteria Celiaca ve Dalları Üzerinde Bir Çalışma. *Harran Üniversitesi Veteriner Fakültesi Dergisi*. 2019; 8(2): 168–172, doi: [10.31196/huvfd.667680](https://doi.org/10.31196/huvfd.667680).
- Evans H, An MQ. Anatomy of the Ferret. In: Fox JG, Marini RP (eds) *Biology and Diseases of the Ferret*, 3rd ed. John Wiley & Sons, Philadelphia 2014: 23–67.
- Evans HE, Lahunta A. *Miller's anatomy of the dog*. 4th ed. Elsevier Health Sciences, New York 2013.
- Fakoya AO, Aguinaldo E, Velasco-Nieves NM, et al. A unique communicating arterial branch between the celiac trunk and the superior mesenteric artery: a case report. *Open Access Maced J Med Sci*. 2019; 7(13): 2138–2141, doi: [10.3889/oamjms.2019.562](https://doi.org/10.3889/oamjms.2019.562), indexed in Pubmed: [31456840](https://pubmed.ncbi.nlm.nih.gov/31456840/).
- Ferreira F, Miglino M, Silva F, et al. Origens e ramificações das artérias mesentéricas cranial e caudal em fetos de caprinos da raça Saanen (*Capra hircus* — Linnaeus, 1758). *Braz J Vet Res Animal Sci*. 2001; 38(2), doi: [10.1590/s1413-95962001000200005](https://doi.org/10.1590/s1413-95962001000200005).
- Getty R, Sisson S, Grossman JD. *Anatomia dos animais domésticos*. 5th ed. Vol. 1. Guanabara Koogan, Rio de Janeiro 1986.
- Hunter L. *Carnivores of the World*. Princeton University Press, Princeton 2011.
- Kasper CB, Trinca CS, Sanfelice D, Mazim FD, Trigo TC. Os carnívoros. In: Gonçalves GL, Quintela FM, Freitas TRO (eds). *Mamíferos do Rio Grande do Sul*. Pacartes,, Porto Alegre 2014: 161–190.
- König HE, Liebich HG. *Anatomia dos animais domésticos: texto e atlas colorido*. 6th ed. Artmed, Porto Alegre 2016.
- Langenfeld M, Pastea E. Anatomical variants of the celiac artery in the sheep, with special reference to the celiomesenteric arterial trunk. *Anat Anz*. 1977; 142(3): 168–174, indexed in Pubmed: [603064](https://pubmed.ncbi.nlm.nih.gov/603064/).
- Leão-Neto LF, Souza EC, Rodriguez E, et al. Esqueletopia e topografia da artéria celiaca no *Lycalopex gymnocercus* (Fischer, 1814). *Revista Acadêmica Ciência Animal*. 2019; 17: 1, doi: [10.7213/1981-4178.2019.17007](https://doi.org/10.7213/1981-4178.2019.17007).
- Machado GV, Souza JR, Gonçalves PR, et al. artéria celiaca e seus ramos no rato-do-banhado (*Myocastor coypus* — Rodentia: Mammalia). *Biotemas*. 2002; 15(2): 44–52, doi: [10.5007/%25x](https://doi.org/10.5007/%25x).
- Machado M, Miglino M, Carbal V, et al. Origem das artérias celiaca e mesentérica cranial em bubalinos (*Bubalus bubalis*, L. 1758). *Braz J Vet Res Animal Sci*. 2000; 37(2), doi: [10.1590/s1413-9596200000200002](https://doi.org/10.1590/s1413-9596200000200002).
- Niza MM, Vilela CL, Ferreira AJA, et al. Irrigação arterial hepática em canídeo. *Revista Portuguesa de Ciências Veterinárias*. 2003; 98(546): 69–76.
- Nonent M, Larroche P, Forlodu P, et al. Celiac-bimesenteric trunk: anatomic and radiologic description — case report. *Radiology*. 2001; 220(2): 489–491, doi: [10.1148/radiology.220.2.r01au34489](https://doi.org/10.1148/radiology.220.2.r01au34489), indexed in Pubmed: [11477258](https://pubmed.ncbi.nlm.nih.gov/11477258/).
- Oliveira G, Oliveira R, Bezerra F, et al. Origem e distribuição da artéria celiaca em preás (*Galea spixii* Wagler, 1831). *Ciência Animal Brasileira*. 2017; 18(0), doi: [10.1590/1089-6891v18e-32918](https://doi.org/10.1590/1089-6891v18e-32918).
- Pinheiro L, Araújo E, Lima A, et al. Os ramos colaterais da aorta abdominal em jaguatirica (*Leopardus pardalis*). *Pesquisa Veterinária Brasileira*. 2014; 34(5): 491–495, doi: [10.1590/s0100-736x2014000500018](https://doi.org/10.1590/s0100-736x2014000500018).
- Roza MS, Pestana FM, Silva BX, et al. Tronco Celiaco-Mesentérico em Gato. *Revista Portuguesa de Ciências Veterinárias*. 2009; 104(569): 83–86.
- Schmidt D, Schoenau L. Origem das artérias celiaca e mesentérica cranial por tronco comum em cão. *Ciência Rural*. 2007; 37(2): 408–411, doi: [10.1590/s0103-84782007000200017](https://doi.org/10.1590/s0103-84782007000200017).
- Schultz W. Der Magen-Darm-Kanal der Monotremen und Marsupialier. In: Helmeke JG, Starck D, Wermuth H. (eds). *Handbuch der Zoologie*. Walter de Gruyter, Berlin 1976: 1–117.
- Silva A, Feliciano M, Motheo T, et al. Mode B ultrasonography and abdominal Doppler in crab-eating-foxes (*Cerdocyon thous*). *Pesquisa Veterinária Brasileira*. 2014; 34(suppl. 1): 23–28, doi: [10.1590/s0100-736x2014001300005](https://doi.org/10.1590/s0100-736x2014001300005).
- Xavier-Silva B, Roza MS, Babinski MA, et al. Morfometria, origem e esqueletopia da artéria celiaca no gato doméstico. *Rev Bras Med Vet*. 2013; 35(3): 253–259.
- Yousefi M. Ramification of Celiac artery in the pine marten (*Martes martes*). *Iranian J Vet Sci Tech*. 2016; 8(2): 60–65, doi: [10.22067/veterinary.v8i2.54842](https://doi.org/10.22067/veterinary.v8i2.54842).

Determination of anomalous pulmonary venous return with high-pitch low-dose computed tomography in paediatric patients

E. Gözgeç¹, M. Kantarci¹, F. Guven¹, H. Ogul¹, N. Ceviz², S. Eren¹

¹Department of Radiology, School of Medicine, Ataturk University, Erzurum, Turkey

²Department of Paediatric Cardiology, School of Medicine, Ataturk University, Erzurum, Turkey

[Received: 12 January 2020; Accepted: 14 March 2020]

Background: In this study, we aimed to image pulmonary venous return anomalies and associated cardiovascular and pulmonary abnormalities by high-pitch low-dose computed tomography (CT) in children.

Materials and methods: Forty-one patients with total or partial anomalous pulmonary venous return anomalous between May 2012 and June 2019 were retrospectively reviewed. The anomalies were determined using high-pitch low-dose CT. The patients' mean age was 3 years (6 months to 15 years), and 24 of them were female.

Results: There were 10 patients with total pulmonary venous return anomalies (TPVRA) and 31 patients with partial pulmonary venous return anomalies (PPVRA). Six (60%) patients with TPVRA had the supracardiac type, 2 (20%) had the cardiac type, and 2 (20%) had the mixed type. All patients with TPVRA had a large atrial septal defect (ASD), 1 patient also had patent ductus arteriosus, and 1 patient had right cardiac hypertrophy. Forty cases of PPVRA were found in 31 patients. Twenty-seven (67%) of them were right-sided, and 13 were left-sided (33%). Twenty (65%) patients also had an additional cardiovascular anomaly (ASD in 12 patients, persistent superior vena cava in 4 patients, patent ductus arteriosus in 3 patients, and aortic coarctation in 2 patients). Of the 27 patients with right-sided PPVRA, it drained into the superior vena cava in 19 patients, the right atrium in 5 patients, and the inferior vena cava in 3 patients. In left-sided cases, the anomalous pulmonary vein drained into the left innominate vein in 9 patients, and in 4 patients, there were accessory pulmonary veins that drained into the left innominate vein. Many of the patients had additional lung anomalies, including pneumonic infiltration ($n = 12$), atelectasis ($n = 8$), and lobar emphysema ($n = 5$), and some of these findings coexisted.

Conclusions: Anomalous pulmonary venous drains and associated cardiac and extra-cardiac anomalies can be detected reliably and quickly with high-pitch low-dose CT without sedation in paediatric patients. (Folia Morphol 2021; 80, 2: 336–343)

Key words: anomalous pulmonary venous return, high-pitch, low-dose computed tomography, paediatric patients

Address for correspondence: M. Kantarci, MD, PhD, Selcuklu Mah. Kanarya Sok. No 17, Dadaskent, Erzurum, Turkey, tel: +90 442 5023435 (home), +90 533 5686625 (Cellular), fax: +90 (442) 2361301, e-mail: akkanrad@hotmail.com

This article is available in open access under Creative Common Attribution-Non-Commercial-No Derivatives 4.0 International (CC BY-NC-ND 4.0) license, allowing to download articles and share them with others as long as they credit the authors and the publisher, but without permission to change them in any way or use them commercially.

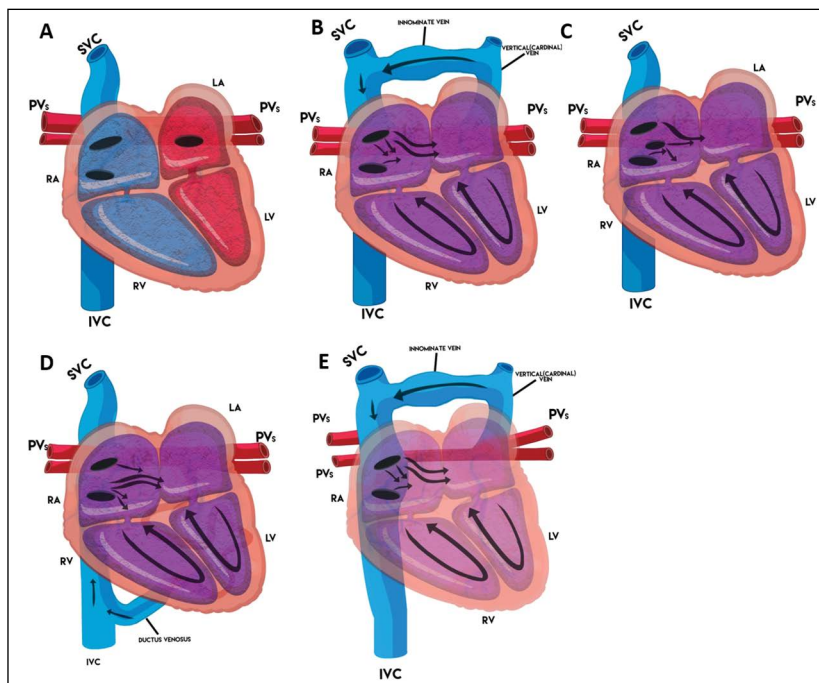


Figure 1. A–E. The types of total pulmonary venous return anomaly. Normal (A), supracardiac type (B), cardiac type (C), infracardiac type (D) and mixed type (E); SVC — superior vena cava; PVs — pulmonary veins; RA — right atrium; LA — left atrium; RV — right ventricle; LV — left ventricle; IVC — inferior vena cava.

INTRODUCTION

Pulmonary venous return anomalies (PVRA) result from one or more pulmonary veins draining into the systemic circulation instead of the left atrium. PVRA constitutes 1.5–5% of all congenital heart diseases and is divided into two main groups: total and partial. In total pulmonary venous return anomalies (TPVRA), all of the pulmonary veins drain into the systemic circulation rather than the left atrium. This condition causes left-to-right shunt and often cyanosis. Although it is usually isolated, it may also be a part of complex heart diseases, such as heterotaxis [8, 15, 17].

Total pulmonary venous return anomalies are divided into four groups depending on where it is drained: supracardiac, cardiac, infracardiac, and mixed. The supracardiac form is the most common type of TPVRA (45–49%). In this type, all pulmonary veins merge in a confluence and then drain through the vertical vein to the innominate vein, superior vena cava (SVC), or other veins above the heart. The vertical vein is often seen in front of the left pulmonary vein, but if it passes behind, it causes obstruction. In the cardiac type, commonly, the confluence is connected to the right atrium via the coronary sinus. In the infracardiac type, which is a less common form of TPVRA (11%), the confluence drains into any vein below the diaphragm, the most common being the portal vein. This form is frequently associated with obstruction

(> 90%), so patients have respiratory distress and a high mortality rate. The mixed type TPVRA comprises different combinations of the other three anomalies (Fig. 1A–E) [8, 18, 21].

Partial pulmonary venous return anomalies (PPVRA) involve the connection of one or more pulmonary veins (but not all) to systemic veins. The prevalence of PPVRA is 0.4–0.7% in children and it is usually asymptomatic [5, 10]. Patients with PPVRA usually have the sinus venosus type of atrial septal defect (ASD) (42%), and up to 80–90% of patients with this ASD have PPVRA [3, 11]. PPVRA most commonly occurs on the right side, and the anomalous vein drains to the SVC in children [1]. Left-side PPVRA are seen more in adult patients, and they occasionally drain into the left brachiocephalic vein. Schimitzer syndrome is a less common type of PPVRA and occurs when the right inferior or right common pulmonary vein continues with the inferior vena cava [16]. The determination of venous return anomalies and especially concomitant cardiovascular and pulmonary anomalies is important to determine the course of patients.

Traditionally, echocardiography is the most commonly used diagnostic method, and catheter angiography is the gold standard. Cardiac magnetic resonance imaging also provides good structural and functional information. However, all these imaging modalities have various advantages, disadvantages,

and different limitations in paediatric patients [4, 17, 19]. In recent years, multidetector computed tomography (CT) has been used more frequently in congenital heart disease to evaluate cardiac and extra-cardiac structures, but radiation is a known disadvantage. To overcome this drawback, a number of filtering and low-dose techniques have been developed. One of these is the high-pitch and low-dose technique, which gives important information in a short time without utilising sedation. These features provide an important advantage, especially in very sick or uncooperative children [6, 7, 9, 12, 14].

In this study, we aimed to investigate the value of high-pitch low-dose CT in demonstrating cardiac anomalies, as well as associated vascular and pulmonary pathologies in children with PVRA. To the best of our knowledge, this is one of the largest studies to show both TPVRA and PPVRA by high-pitch low-dose CT.

MATERIALS AND METHODS

In this study, we retrospectively examined the records of patients who were diagnosed with PVRA using CT angiography at our institution between May 2012 and June 2019. The mean age of the 41 patients was 3 years (6 months to 15 years old), and 24 of them were female. Catheter angiography was also performed in some patients (14 patients). Ethics committee approval was obtained in accordance with the ethical considerations set out in the Declaration of Helsinki.

Patients underwent high-pitch low-dose CT for extra-cardiac, lung, or other pathologies with a three-dimensional configuration in preoperative preparation. All CT angiography examinations were performed using a dual-source CT system (Definition Flash, Siemens Healthcare). All scans were performed with free breathing. The imaging parameters included a gantry time of 280 ms and sectional collimation of 128×0.6 mm by the z-flying focal spot technique. The table speed was 411 mm/s, and the high pitch was 3.4 for the examinations. The tube current and voltage were adapted to the patient's weight. The scan field was started under the neck and extended below the diaphragm.

The contrast agent (iopromide, 350 mg I/mL Ultravist, Bayer HealthCare) was administered at a rate of 1 mL/sn via the peripheral vein at a dose of 1.5 mL/kg. A chaser saline solution was injected at 1.0 mL/kg body weight after the contrast material. Vacuum-lock

cushions were utilized to immobilise the patient. After the contrast and chaser saline solution were injected, the scan was started when the left ventricular cavity was clearly visualised. None of the patients required sedation or beta-blocker therapy.

Image reconstructions were conducted with a slice thickness of 0.75 mm. All shots were completed without any complications. Images were processed on a Workstation (Syngo Via, Siemens HealthCare). Retrospectively, two radiologists and a paediatric cardiologist who had more than 10 years of experience reviewed all of the images, and decisions were made together. Pulmonary venous return anomalies were compared with catheter angiography results.

RESULTS

Pulmonary venous return anomalies were determined in 41 patients. TPVRA occurred in 10 patients, 6 (60%) patients had the supracardiac type, 2 (20%) of them had the cardiac type, and 2 (20%) of them had the mixed type. In the supracardiac cases, the right and left pulmonary veins were connected posterior to the left ventricle, and this confluence was drained to the left innominate vein via a vertical vein in all patients (Fig. 2). One of these 6 patients also had right ventricular hypertrophy.

In the cardiac TPVRA cases, all of pulmonary veins were connected to the right atrium directly by a confluence (Fig. 3). Large ASDs were found in all patients with the cardiac and supracardiac forms of TPVRA, and the SVC was dilated in supracardiac cases. In mixed-type patients, the right upper vein was drained to the SVC, and the other veins were drained to the left innominate vein through a vertical vein (Fig. 4). One of patients with mixed-type TPVRA had patent ductus arteriosus (PDA), and one of them also had ASD.

Forty cases of PPVRA were imaged in 31 patients, and 27 of them were right-sided (67%), while 13 were left-sided (33%). Twenty-one patients had one anomalous pulmonary vein, and 10 patients had two. Of the 27 patients right-sided PPVRA, it drained into the SVC in 19 patients (Fig. 5), the right atrium in 5 patients, and the inferior vena cava in 3 patients (Fig. 6). Among the 13 left-sided cases, the anomalous pulmonary vein drained into the left innominate vein in 9 patients (Fig. 7), and there were accessory pulmonary veins draining into the left innominate vein in 4 patients (Fig. 8). The anomalies found in CT correlated with the catheter angiography results.

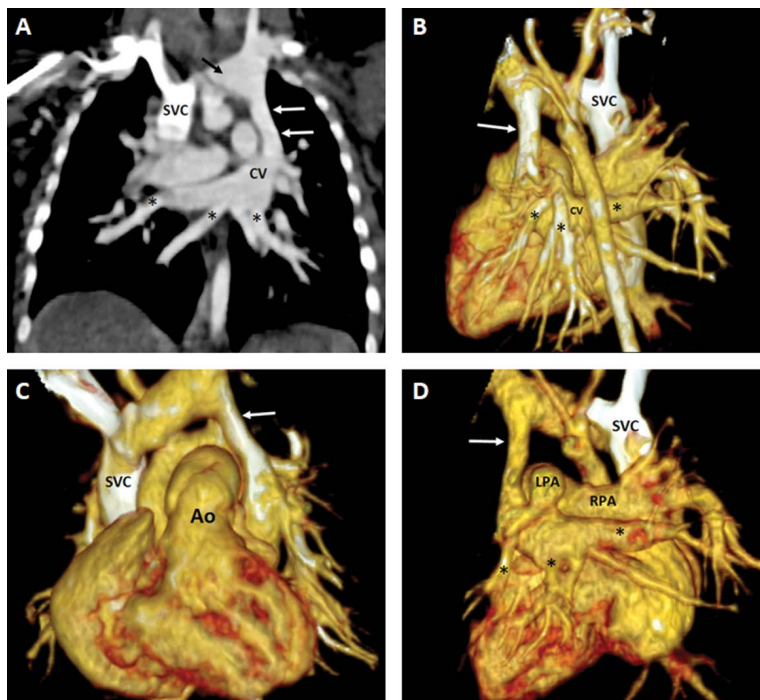


Figure 2. A–D. A 6-month-old male patient with supracardiac type total pulmonary venous return anomaly. Coronal maximum intensity projections computed tomography image (A) shows confluence of pulmonary veins (CV), vertical vein (white arrows) and left innominate vein (black arrow). Lateral-posterior (B), anterolateral (C) and posterior (D) three-dimensional volume-rendered computed tomography image demonstrates vertical vein (white arrow) and confluence vein (CV); SVC — superior vena cava; asterisks — pulmonary veins; Ao — aorta; LPA — left pulmonary artery; RPA — right pulmonary artery.

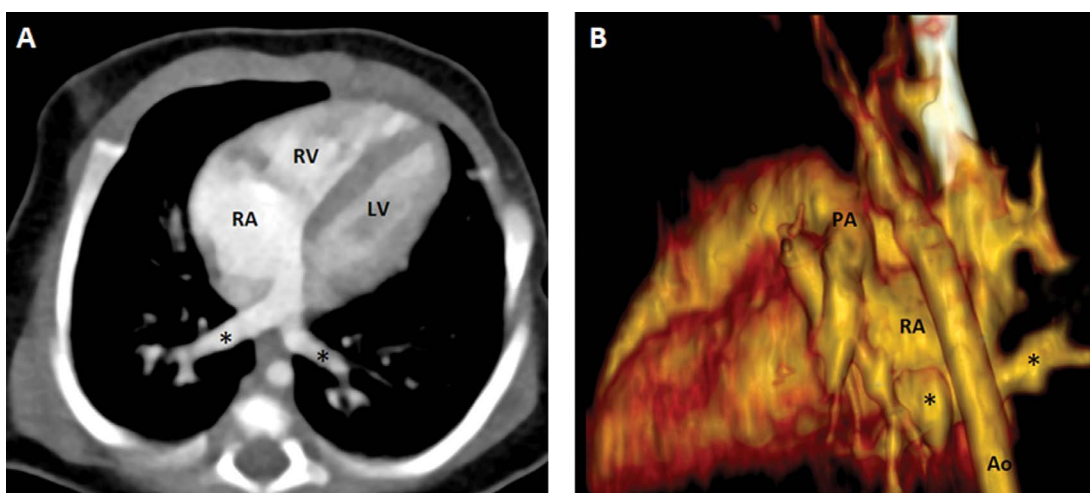


Figure 3. A, B. A 7-month-old male patient with cardiac type total pulmonary venous return anomaly. Axial computed tomography image (A) demonstrates right and left pulmonary veins drain into the right atrium. Posterior-lateral three-dimensional volume-rendered computed tomography image (B) shows anomalous of pulmonary drainage; asterisks — pulmonary veins; PA — pulmonary artery; RA — right atrium; RV — right ventricle; LV — left ventricle; Ao — aorta.

Eleven patients had only PPVRA, while the other ones had additional cardiovascular anomalies. There was ASD in 12 patients, persistent SVC (PSVC) in 4 patients, PDA in 3 patients, and aortic coarctation in 2 patients. Only 2 patients who were left-sided had additional cardiovascular anomalies.

Most of the patients with PVRA had different pulmonary findings. Additional lung anomalies included pneumonic infiltration (n = 12), atelectasis (n = 8), and lobar emphysema (n = 5), and some of these

findings coexisted. Lung findings were detected in 4 of the patients with TPVRA and 11 of the patients with PPVRA (Table 1). The effective radiation dose was determined as 1.01 mSv (range: 0.12–4.06 mSv), but 0.55 mSv (range: 0.15–0.68 mSv) was used for patients under 1 year old.

DISCUSSION

The detection of PVRA and associated cardiovascular and lung anomalies is very important in deter-

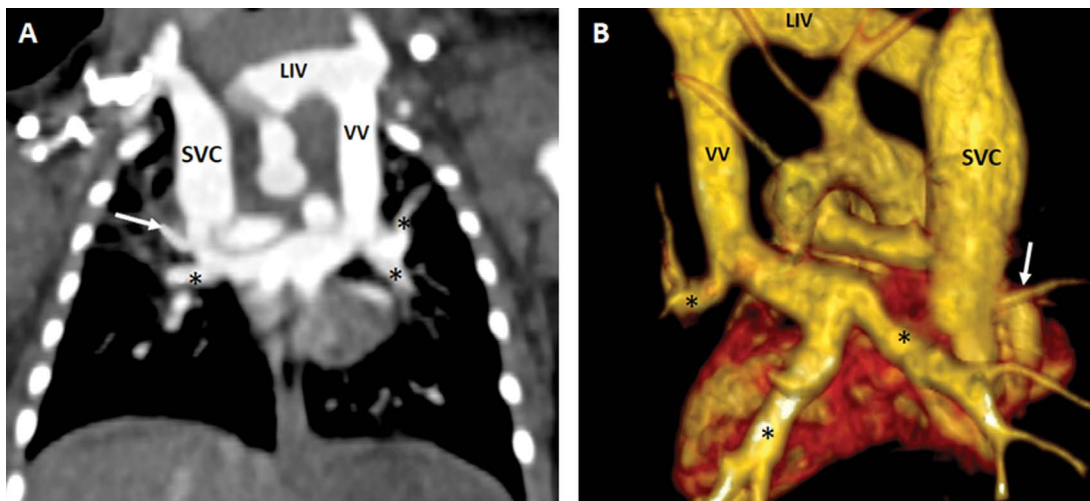


Figure 4. A, B. A female patient with mixed type total pulmonary venous return anomaly. Coronal maximum intensity projections computed tomography image (A) and posterior three-dimensional volume rendered images (B) demonstrates right upper pulmonary vein (white arrow) directly drain to superior vena cava (SVC) and other pulmonary veins (asterisks) drained to left innominate vein (LIV) via a vertical vein (VV).

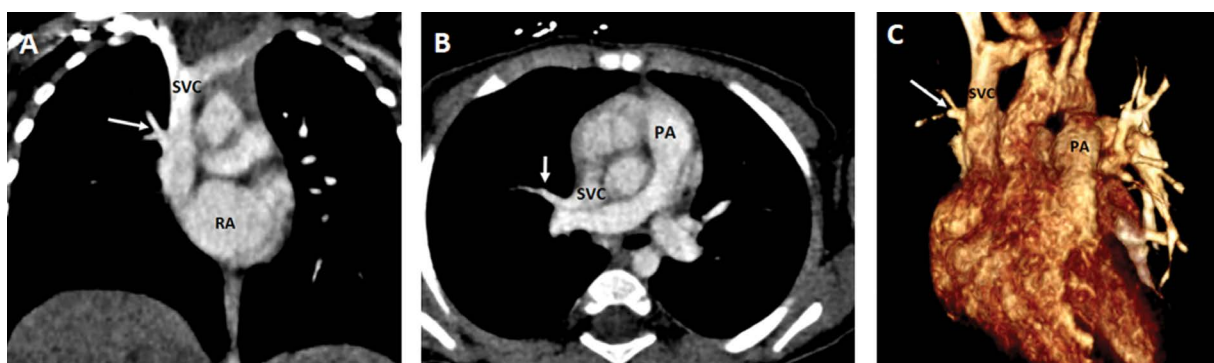


Figure 5. A–C. Right upper pulmonary vein directly drains into superior vena cava in 8-year-old male patient with partial pulmonary venous return anomaly. Coronal (A), axial (B) and anterior three-dimensional volume rendered images show anomalous pulmonary vein (white arrow); SVC — superior vena cava; RA — right atrium; PA — pulmonary artery.

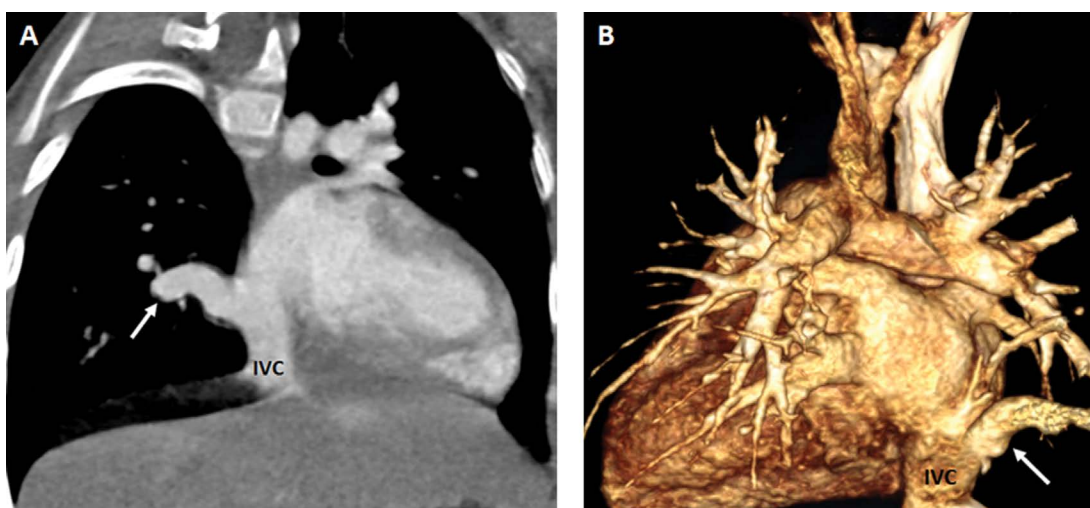


Figure 6. A, B. A 9-year-old female patient with partial pulmonary venous return anomaly. Curved coronal and posterior-lateral three-dimensional volume rendered computed tomography images show anomalous right lower pulmonary vein (white arrow) drains into inferior vena cava (IVC).

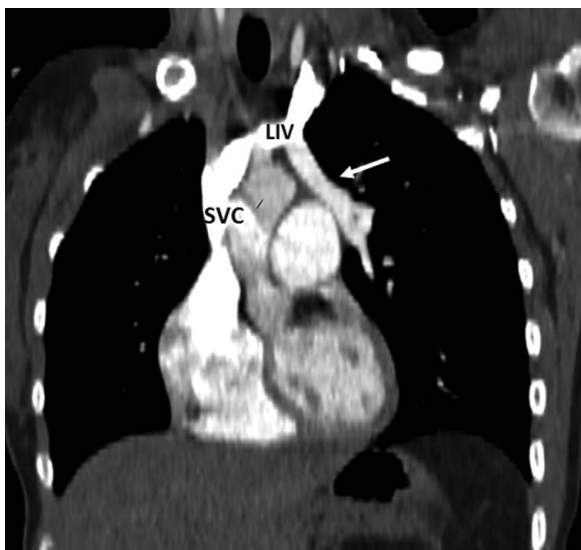


Figure 7. Partial pulmonary venous return anomaly at left upper pulmonary vein in a 7-year-old female patient. Coronal computed tomography image shows anomalous pulmonary vein (white arrow); LIV — left innominate vein; SVC — superior vena cava.

mining treatment plans for children. PPVRA should be examined because it changes the surgical treatment plan, especially in patients with ASD. Although plain X-ray images are notoriously typical in patients with TPVRA, further imaging is required to detect additional anomalies and confirm the diagnosis. Echocardiography is the first and most commonly used method to

detect PVRA, but this method is inadequate due to the fact that the veins draining into the SVC are distant from the chest wall, as well as the method being user dependent and having a poor acoustic window.

The use of catheter angiography, which is the gold standard in the diagnosis, is limited because it requires sedation and high radiation in paediatric patients. In addition, complications are important limitations as the procedure is invasive. Magnetic resonance imaging is highly advantageous in that it is non-invasive and is free of ionising radiation. It also provides accurate information about cardiac and extra-cardiac structures and provides flow measurement. But the long duration of the shots and the necessity of sedation and breath holding create significant limitations.

Children are more susceptible to radiation than adults. Since radiation exposure is the most important problem in CT imaging, attempts have been made to minimise it with high-pitch low-dose screening. In recent years, the use of high-pitch low-dose CT has increased considerably in the demonstration of cardiac and extra-cardiac structures, especially in paediatric patients. The most important advantage is that it provides more and more accurate information quickly and reliably. Due to the high spatial resolution and large imaging area, the drainage location of the abnormal veins can be determined easily, along

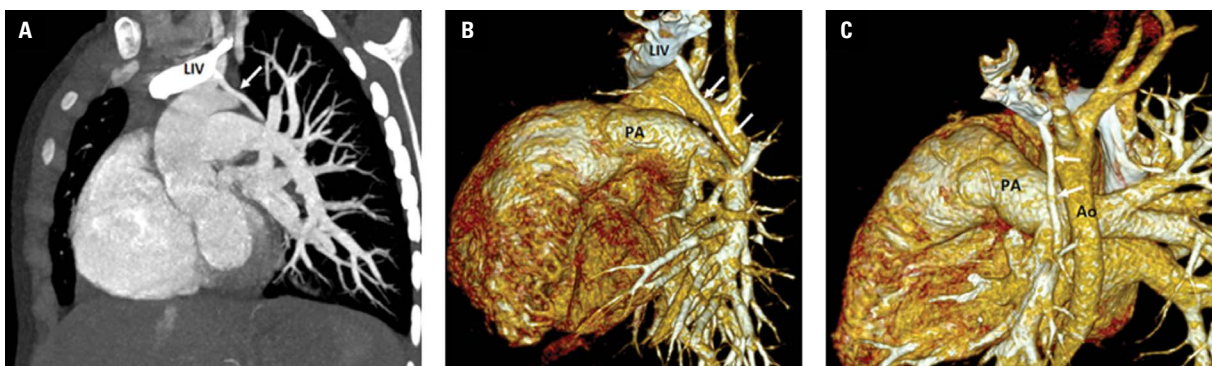


Figure 8. A–C. In a 10-year-old female patient an accessory left pulmonary vein drains into left innominate vein. Sagittal maximum intensity projections computed tomography image (A), lateral (B) and posterior three-dimensional volume rendered images demonstrate accessories pulmonary vein (white arrows) drains into left innominate vein (LIV); PA — pulmonary artery; Ao — aorta.

Table 1. Additional cardiac and pulmonary findings in patients with total and pulmonary venous return anomalies

	Patient number	ASD	PDA	PSVC	Aortic coarctation	Pulmonary infiltration	Atelectasis	Lobar emphysema
TPVRA	10	10	1	–	–	2	2	1
PPVRA	31	12	3	4	2	10	7	5

ASD — atrial septal defect; PDA — patent ductus arteriosus; PPVRA — partial pulmonary venous return anomaly; PSVC — persistent superior vena cava; TPVRA — total pulmonary venous return anomaly

with complex cardiac anomalies and lung disease. Furthermore, it is a non-invasive technique and does not require sedation like catheter angiography.

In a study published by Huang et al. [12], the effective radiation dose was 1.6 ± 0.3 mSv (range: 1.1–2.5 mSv) in infants with congenital heart disease. Bonelli-Sica et al. [2] reported that the overall effective radiation dose was 1.01 mSv (range: 0.13–6.43 mSv) for older children and 0.78 mSv (range: 0.13–4.16 mSv) for patients younger than 1 year old. In another study performed by Turkvatan et al. [20], the effective radiation dose was 1.12 mSv (range: 0.15–4.17 mSv) for older children and 0.58 mSv (range: 0.15–0.73 mSv) for patients younger than 1 year old among paediatric patients with PPVRA. In our study, the effective radiation dose was slightly less than in previous studies.

All pulmonary veins are drained to the right circulation in TPVRA, and the most common type is supracardiac. The presence of obstruction is very important in the diagnosis of patients with TPVRA. In this study, the rate of supracardiac TPVRA was most frequently correlated with previous studies [13]. However, the rates of the other types were found to be slightly higher since no cases of the infracardiac type were seen, which was probably because of the small number of patients. PPVRA occurs as a result of abnormal drainage of one or more pulmonary veins, but not all. An abnormal pulmonary vein can drain into any systemic vein from the SVC to the portal vein, and the most common on the right is the drainage into the SVC. The most common form on the left is one in which the left upper lobe drains into the innominate vein.

The lobar distribution of pulmonary anomalies in our study was the most frequent right anomalous vein draining into SVC, similar to other studies [2, 7]. The findings were the same as CT findings in patients undergoing catheter angiography. This suggests that although catheter angiography is the gold standard, high-pitch CT angiography could assume the diagnostic role of this invasive procedure. PPVRA is usually asymptomatic in children. According to the degree of anomaly, symptoms may develop in the following years due to the left-to-right shunt.

Pulmonary venous return anomaly can be accompanied by many cardiac anomalies, and ASD is the most common. Although the presence of different anomalies has been shown, the most common was ASD, which was present in 39% of the cases in the present study, similar to the study by Turkvatan et

al. [20]. In this study, we evaluated lung anomalies together with cardiac anomalies, in contrast to other studies. The detection of lung diseases was especially important for patients who would undergo surgery. In these patients, medical treatment was applied, and then surgery was performed.

Limitations of the study

There were some limitations in our study. Firstly, the technique involves radiation, albeit a reduced amount. Secondly, only CT scans were examined retrospectively in some patients. Therefore, false negatives in CT could not be determined. Third, the number of patients was low, although this is one of the largest studies to evaluate both TPVRA and PPVRA.

CONCLUSIONS







In conclusion, this study confirms that high-pitch low-dose CT is an easy, robust, and rapid diagnostic method for detecting abnormal venous return anomaly in paediatric patients. In addition, other types of cardiac and great vascular anomalies can be detected very quickly by the high-pitch low-dose CT. This important information may change treatment strategies for patients with suspected PVRA.

REFERENCES

1. Alsoufi B, Cai S, Van Arsdell GS, et al. Outcomes after surgical treatment of children with partial anomalous pulmonary venous connection. *Ann Thorac Surg.* 2007; 84(6): 2020–6; discussion 2020, doi: [10.1016/j.athoracsur.2007.05.046](https://doi.org/10.1016/j.athoracsur.2007.05.046), indexed in Pubmed: [18036929](https://pubmed.ncbi.nlm.nih.gov/18036929/).
2. Bonelli-Sica JM, de la Mora-Cervantes R, Diaz-Zamudio M, et al. Dual-source 256-MDCT for diagnosis of anomalous pulmonary venous drainage in pediatric population. *Am J Roentgenol.* 2013; 200(2): W163–W169, doi: [10.2214/AJR.11.8348](https://doi.org/10.2214/AJR.11.8348), indexed in Pubmed: [23345380](https://pubmed.ncbi.nlm.nih.gov/23345380/).
3. Davia J, Cheitlin M, Bedynek J. Sinus venosus atrial septal defect: Analysis of fifty cases. *Am Heart J.* 1973; 85(2): 177–185, doi: [10.1016/0002-8703\(73\)90458-4](https://doi.org/10.1016/0002-8703(73)90458-4).
4. Delisle G, Ando M, Calder AL, et al. Total anomalous pulmonary venous connection: Report of 93 autopsied cases with emphasis on diagnostic and surgical considerations. *Am Heart J.* 1976; 91(1): 99–122, doi: [10.1016/s0002-8703\(76\)80440-1](https://doi.org/10.1016/s0002-8703(76)80440-1), indexed in Pubmed: [1244724](https://pubmed.ncbi.nlm.nih.gov/1244724/).
5. Dillman JR, Yarram SG, Hernandez RJ. Imaging of pulmonary venous developmental anomalies. *Am J Roentgenol.* 2009; 192(5): 1272–1285, doi: [10.2214/AJR.08.1526](https://doi.org/10.2214/AJR.08.1526), indexed in Pubmed: [19380552](https://pubmed.ncbi.nlm.nih.gov/19380552/).
6. Fourdrain A, De Dominicis F, Bensussan M, et al. Three-dimensional computed tomography angiography of the pulmonary veins and their anatomical variations: involvement in video-assisted thoracoscopic surgery-lobectomy for lung cancer. *Folia Morphol.* 2017; 76(3): 388–393, doi: [10.5603/FM.a2016.0081](https://doi.org/10.5603/FM.a2016.0081), indexed in Pubmed: [28026848](https://pubmed.ncbi.nlm.nih.gov/28026848/).

7. Gao Y, Lu B, Hou Z, et al. Low dose dual-source CT angiography in infants with complex congenital heart disease: a randomized study. *Eur J Radiol.* 2012; 81(7): e789–e795, doi: [10.1016/j.ejrad.2012.03.023](https://doi.org/10.1016/j.ejrad.2012.03.023), indexed in Pubmed: [22525595](https://pubmed.ncbi.nlm.nih.gov/22525595/).
8. Gathman GE, Nadas AS. Total anomalous pulmonary venous connection: clinical and physiologic observations of 75 pediatric patients. *Circulation.* 1970; 42(1): 143–154, doi: [10.1161/01.cir.42.1.143](https://doi.org/10.1161/01.cir.42.1.143), indexed in Pubmed: [5425587](https://pubmed.ncbi.nlm.nih.gov/5425587/).
9. Han BK, Lindberg J, Grant K, et al. Accuracy and safety of high pitch computed tomography imaging in young children with complex congenital heart disease. *Am J Cardiol.* 2011; 107(10): 1541–1546, doi: [10.1016/j.amjcard.2011.01.065](https://doi.org/10.1016/j.amjcard.2011.01.065), indexed in Pubmed: [21539949](https://pubmed.ncbi.nlm.nih.gov/21539949/).
10. Herlong JR, Jagers JJ, Ungerleider RM. Congenital Heart Surgery Nomenclature and Database Project: pulmonary venous anomalies. *Ann Thorac Surg.* 2000; 69(4 Suppl): S56–S69, doi: [10.1016/s0003-4975\(99\)01237-0](https://doi.org/10.1016/s0003-4975(99)01237-0), indexed in Pubmed: [10798417](https://pubmed.ncbi.nlm.nih.gov/10798417/).
11. Ho ML, Bhalla S, Bierhals A, et al. MDCT of partial anomalous pulmonary venous return (PAPVR) in adults. *J Thorac Imaging.* 2009; 24(2): 89–95, doi: [10.1097/RTI.0b013e318194c942](https://doi.org/10.1097/RTI.0b013e318194c942), indexed in Pubmed: [19465830](https://pubmed.ncbi.nlm.nih.gov/19465830/).
12. Huang Mp, Liang Ch, Zhao Zj, et al. Evaluation of image quality and radiation dose at prospective ECG-triggered axial 256-slice multi-detector CT in infants with congenital heart disease. *Pediatr Radiol.* 2011; 41(7): 858–866, doi: [10.1007/s00247-011-2079-2](https://doi.org/10.1007/s00247-011-2079-2), indexed in Pubmed: [21534003](https://pubmed.ncbi.nlm.nih.gov/21534003/).
13. Kim TH, Kim YM, Suh CH, et al. Helical CT angiography and three-dimensional reconstruction of total anomalous pulmonary venous connections in neonates and infants. *Am J Roentgenol.* 2000; 175(5): 1381–1386, doi: [10.2214/ajr.175.5.1751381](https://doi.org/10.2214/ajr.175.5.1751381), indexed in Pubmed: [11044048](https://pubmed.ncbi.nlm.nih.gov/11044048/).
14. Klink T, Müller G, Weil J, et al. Cardiovascular computed tomography angiography in newborns and infants with suspected congenital heart disease: retrospective evaluation of low-dose scan protocols. *Clin Imaging.* 2012; 36(6): 746–753, doi: [10.1016/j.clinimag.2012.01.043](https://doi.org/10.1016/j.clinimag.2012.01.043), indexed in Pubmed: [23154004](https://pubmed.ncbi.nlm.nih.gov/23154004/).
15. Muñoz Castellanos L, Sánchez Vargas CA, Kuri Nivon M. [Morphopathologic study of total anomalous pulmonary venous connection]. *Arch Cardiol Mex.* 2007; 77(4): 265–274, indexed in Pubmed: [18361070](https://pubmed.ncbi.nlm.nih.gov/18361070/).
16. Roehm JO, Jue KL, Amplatz K. Radiographic features of the scimitar syndrome. *Radiology.* 1966; 86(5): 856–859, doi: [10.1148/86.5.856](https://doi.org/10.1148/86.5.856), indexed in Pubmed: [5936095](https://pubmed.ncbi.nlm.nih.gov/5936095/).
17. Seale AN, Uemura H, Webber SA, et al. British Congenital Cardiac Association. Total anomalous pulmonary venous connection: morphology and outcome from an international population-based study. *Circulation.* 2010; 122(25): 2718–2726, doi: [10.1161/CIRCULATIONAHA.110.940825](https://doi.org/10.1161/CIRCULATIONAHA.110.940825), indexed in Pubmed: [21135364](https://pubmed.ncbi.nlm.nih.gov/21135364/).
18. Shen Q, Pa M, Hu X, et al. Role of plain radiography and CT angiography in the evaluation of obstructed total anomalous pulmonary venous connection. *Pediatr Radiol.* 2013; 43(7): 827–835, doi: [10.1007/s00247-012-2609-6](https://doi.org/10.1007/s00247-012-2609-6), indexed in Pubmed: [23341089](https://pubmed.ncbi.nlm.nih.gov/23341089/).
19. Sreeram N, Walsh K. Diagnosis of total anomalous pulmonary venous drainage by Doppler color flow imaging. *J Am Coll Cardiol.* 1992; 19(7): 1577–1582, doi: [10.1016/0735-1097\(92\)90620-3](https://doi.org/10.1016/0735-1097(92)90620-3).
20. Türkvatan A, Tola HT, Kutlutürk N, et al. Low-Dose computed tomographic imaging of partial anomalous pulmonary venous connection in children. *World J Pediatr Congenit Heart Surg.* 2017; 8(5): 590–596, doi: [10.1177/2150135117723903](https://doi.org/10.1177/2150135117723903), indexed in Pubmed: [28901235](https://pubmed.ncbi.nlm.nih.gov/28901235/).
21. Vyas HV, Greenberg SB, Krishnamurthy R. MR imaging and CT evaluation of congenital pulmonary vein abnormalities in neonates and infants. *Radiographics.* 2012; 32(1): 87–98, doi: [10.1148/rg.321105764](https://doi.org/10.1148/rg.321105764), indexed in Pubmed: [22236895](https://pubmed.ncbi.nlm.nih.gov/22236895/).

Revisiting the anatomy of the cephalic vein, its origin, course and possible clinical correlations in relation to the anatomical snuffbox among Jordanian

M.A. Salameh¹, A.T. Shatarat², D.H. Badran³, M.A. Abu-Abeeleh⁴, T.M. Kanaan⁵,
A.M. Bani-Hani⁴, M.Q. Hamdan⁵

¹Department of Basic Medical Science, Faculty of Medicine, Al Balqa Applied University, Al Salt, Jordan

²Department of Anatomy and Histology, Faculty of Medicine, University of Jordan, Amman, Jordan

³Dean of the Faculty of Medicine, Hashemite University, Zarqa, Jordan

⁴Department of General Surgery, Faculty of Medicine, University of Jordan, Amman, Jordan

⁵Department of Special Surgery, Faculty of Medicine, University of Jordan, Amman, Jordan

[Received: 11 January 2020; Accepted: 27 March 2020]

Background: The cephalic vein is one of the most distinguished superficial veins of the upper limb. Its clinical value lies in venous access. There is little known about the variation of its formation in relation to the anatomical snuffbox. Hence, anatomical variants in the origin of the cephalic vein are important in clinical practice. Subsequently, this study was designed to examine the variation of the cephalic vein formation in relation to the anatomical snuffbox.

Materials and methods: A cross-sectional study of 438 subjects (722 hands), was prepared to study the cephalic vein among Jordanian students and staff of one of the major governmental Medical College in Jordan, by using infrared illumination system. The obtained data was analysed according to; gender, sidedness, and handedness.

Results: Four sites for the formation of the cephalic vein in relation to the anatomical snuffbox were found. There was a significant relation between gender and sidedness, and the sites of formation of the cephalic vein ($p < 0.0001$ and $p = 0.048$, respectively).

Conclusions: For the first time this study identified different sites for the formation of the cephalic vein in relation to the anatomical snuffbox. However, regardless of its sites of formation, the cephalic vein was running in 98% of the examined hands in the anatomical snuffbox. (Folia Morphol 2021; 80, 2: 344–351)

Key words: anatomic variation, cannulation, hand, veins, venous access

INTRODUCTION

The cephalic vein (CV) as a term originates from the Arabic word al-kefal, which means “outer” and was first used by Muslim physician Ibn Sina, when the

term was translated to Latin, cephalic inaccurately was selected to replace the Arabic origin of the term [3]. The CV is a superficial vein that originates from the radial aspect of the dorsal venous network of the

Address for correspondence: Dr. S.T. Amjad, Department of Anatomy and Histology, Faculty of Medicine, University of Jordan, Amman, 11942, Jordan, tel: 00962 6 5355000, ext. 23434, e-mail: a.shatarat@ju.edu.jo

This article is available in open access under Creative Common Attribution-Non-Commercial-No Derivatives 4.0 International (CC BY-NC-ND 4.0) license, allowing to download articles and share them with others as long as they credit the authors and the publisher, but without permission to change them in any way or use them commercially.

hand. It is formed when the dorsal digital vein from the radial side of the index finger and the two dorsal digital veins of the thumb join each other. It arises on the roof of the anatomical snuffbox (AS) then crosses the radial styloid process and courses upward on the anterolateral side over the forearm. Then it passes upwards over the antecubital region, where it may receive blood from the median cubital vein, and continues to ascend on the anterolateral side of arm lateral to the biceps muscle in the deltopectoral groove. Later on, the vein passes through the axilla, by piercing the clavipectoral fascia to drain and end into the axillary vein. Throughout its course, the CV has three clinically important regions; its origin on the hand in the AS, in the cubital fossa and its termination in the axillary vein. The latter two regions were studied and it has been concluded that the CV has different anatomical patterns in those regions [6, 8, 13, 22]. However, the anatomical patterns of the CV in the AS seemed to be overlooked.

The AS is a descriptive anatomical term for the triangular hollow on the radial part of the dorsum of the hand, which is formed by depressing skin of muscle contraction; the base is directed to the wrist while the apex is directed to the thumb. The impression is most apparent when the thumb is abducted and extended. It is limited on the ulnar (posterior) side by the extensor pollicis longus (EPL) tendon, whereas on the radial (anterior) side by tendons of the abductor pollicis longus (APL) and extensor pollicis brevis (EPB). The base is formed by the distal margin of the extensor retinaculum, while the apex is created by the attachment of EPL and EPB tendons [5]. The terminal part of the superficial branch of the radial nerve (SBRN) and the CV pass through the superficial fascia that forms in addition to the skin the roof of the AS. The floor is formed by the base of the first metacarpal bone, trapezium, scaphoid and the distal radius [5]. The radial artery (RA) and the extensor carpi radialis tendons are at the bottom of AS [2].

The relation between the CV and the AS has always been underestimated regardless of its clinical value. For example, clinical procedures such as venous cannulation of the CV in the AS is a well known site [12]. Placing an arteriovenous fistula which is applied surgically to obtain vascular access between the RA and CV in patients on haemodialysis is another procedure used in this area [10, 19, 25]. Also, it has been shown that, maintaining satisfactory venous drainage of the hand using neurovascular pedicles,

which include the transferred digit or the reimplanted digit gives the CV another clinical importance [9, 14, 21]. The large diameter of the distal part of the CV has been suggested for vein puncture, especially; because this part is easier to view and palpate [9]. Furthermore, it was reported that the vein puncture of CV adjacent to the AS is the ideal site beside the cubital fossa [9]. However, other studies have challenged the access of the CV in the AS and the distal part of the forearm, for example, Robson et al. [15] and Samarakoon et al. [18] stated that cannulation of the CV in the distal third of the forearm should be avoided; to prevent any possible injury of the SBRN. Besides, Vialle et al. [24] recommended that CV puncture must be at least 12 cm above the styloid process of the radius to avoid injury to SBRN.

This valuable relationship between the CV and AS has been mentioned in some studies as findings but not as a full study about these two valuable anatomical structures. For example, it has been reported that sometimes the origin of the CV from the dorsal venous network of the hand can be recognized in the roof of the AS. Another study has demonstrated that the SBRN was largely related to the CV in 80% of the studied forearms, which underlay the CV [14]. Furthermore, within the AS there were connections between the vena comitantes of the RA and the CV, and the CV was found considerably in the ulnar part of the AS [16, 20]. A case study for dissecting upper limbs of 2 months infant showed normal beginning of CV in the roof of the AS, no variation in the vein of the right upper limb, while the left upper limb showed abnormal running up and continuation of CV [15]. A cadaveric study of 10 cadavers was carried out to demonstrate the variations in the tendons of the AS in a Malaysian, it was found that 2 hands of different specimens showed the CV in the AS [23]. Therefore, the present study aimed to study and describe in details the origin of the CV in relation to AS. Also, to characterize any possible anatomical patterns for CV in the AS.

MATERIALS AND METHODS

Subjects

A total number of 438 subjects were included in the study; 217 males and 221 females. A total number of 722 hands were examined. They were chosen randomly from the Hashemite University. The age group considered was from 18–35 years. A total of 239 hands with injuries, scars, burns and hairy skin, were excluded (exclusion rate 33%). In females; 39 right hands

and 49 left hands were excluded, while in males; 69 right hands and 84 left hands were excluded.

Subjects were informed in detail about the procedure and written consent was signed. The study was approved by the Institution Review Board of the Hashemite University (IRB#) P.O/222/1704841.

Instruments

The infrared (IR) vein illumination system (Sure vein ZD-JM-260-01) has been used to identify the formation of the CV. It utilises 750–980 nm wavelength of infrared light, with an effective distance of projection by 29–31 cm.

Study design

The procedure was conducted in a dark room with a temperature between 24–26°C. Subjects instructed to sit and rest their fist hand in midprone position on the enhancer. Before exposing the hand to the IR beam, the targeted area was carefully identified. The targeted area was the AS includes the medial and lateral boundaries. It is limited on the medial side by EPL tendon, whereas on the lateral side by tendons of APL and EPB, the styloid process of the radial bone which was taken as the proximal boundary and the tendons of the AS they approximate to form the apex. The apex, which directed into the first metacarpophalangeal joint considered the distal boundary of the targeted area.

The EPL and APL tendons were identified and were marked by putting a dot by a pen on both of them. The targeted area of the examined hand was then exposed to the IR beam. The CV was followed in the AS and at the proximal forearm on the lateral side to be assured that it was the CV.

The targeted area of the examined hand was then exposed to the IR beam. Each subject had two photos for the right and left hands; the CV was photographed by a mobile phone camera. Images were carefully analysed and grouped according to the formation of the CV in relation to the AS.

Statistical analysis

Data analysis was performed using IBM SPSS Statistics version 22 software. Chi-square test was used to test the association between gender, sidedness and handedness, and the sites of formation of the CV. Statistical comparisons were made by Student's unpaired t-test. The association was considered statistically significant if $p < 0.05$.

Table 1. Demographic and experimental characteristics of the final population of the formation of the cephalic vein in relation to anatomical snuffbox

Characteristic	Number of subjects	Total number of hands in the study	Hands excluded from the study
Gender:			
Male	217 (49%)	368 (51%)	151 (63%)
Female	221 (51%)	354 (49%)	88 (37%)
Hand:			
Right		368 (51%)	108 (45%)
Left		354 (49%)	131 (55%)
Symmetry:			
Yes		196 (45%)	
No		242 (55%)	

RESULTS

The final population of the study consisted of 438 subjects; 217 males and 221 females (Table 1). The total number of the hands was 722 hands. The number of the hands included in this study was 368 in males and 354 in females (Table 1). The number of right hands included in this study was 368 and the number of left hands was 354. Two hundred and eighty three hands were excluded (exclusion rate of 33%).

It was found during the examination of the CV, the formation of the CV was variable in relation to the AS (Fig. 1). Thus, the CV was formed either inside the AS (type A) or outside it (type B), type A was found in 305 (63%) of the examined hands and type B was found in 178 (37%) of the examined hands. Further examination showed that the CV was not only formed in the AS (type A) but also was formed at different levels (Table 2). Type A1 was present in 87 (18%) of the examined hands, where the CV was formed in the distal part of the AS (Fig. 2). Type A2 was the most common being in 218 (45%) of the examined hands (the CV was formed in the proximal part of the AS (Fig. 3).

Also, there were two types of Bs (according to their location medial or lateral to the AS): type B1 ($n = 170$, 35%) of the examined hands, where the CV was formed medially to the EPL tendon (Fig. 4), and type B2 ($n = 8$, 2%) of the examined hands, which was the least common, (the CV was formed lateral to the APL tendon) (Fig. 5).

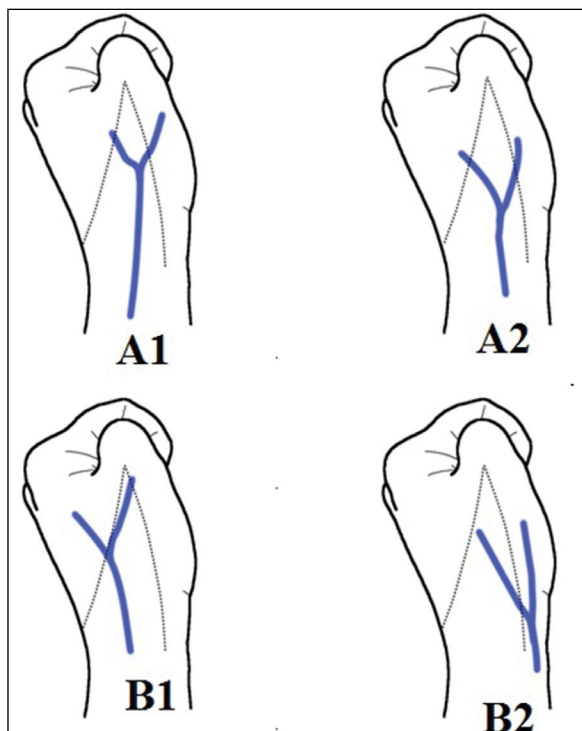


Figure 1. Illustration shows the different sites of formation of the cephalic vein in relation to the anatomical snuffbox.

Table 2. Subtotal frequencies of the anatomic variants under study of the formation of cephalic vein (CV) in relation to the anatomical snuffbox (AS) (n = 483)

The formation of the CV in relation to the AS	Subtotal (% total)
Inside the AS:	305 (63%)
Distally	87 (18%)
Proximally	218 (45%)
Outside the AS:	178 (37%)
Medially	170 (35%)
Laterally	8 (2%)

The most common site of formation of the CV was in the AS proximally in both males 98 (48%) and females 120 (43%), but not in both hands, where the formation of the CV in AS proximally was proportionally greater in right hands 120 (46%) compared with left hands 98 (44%) (Table 3). While the formation of the CV outside the AS medially was greater in left hands 100 (45%) (Table 3). In males, the most common site of formation of the CV was in the AS proximally in right and left hands 55 (50%) and 43 (46%), respectively, while in females, the most common site of formation of the CV was different in both hands; was in the AS

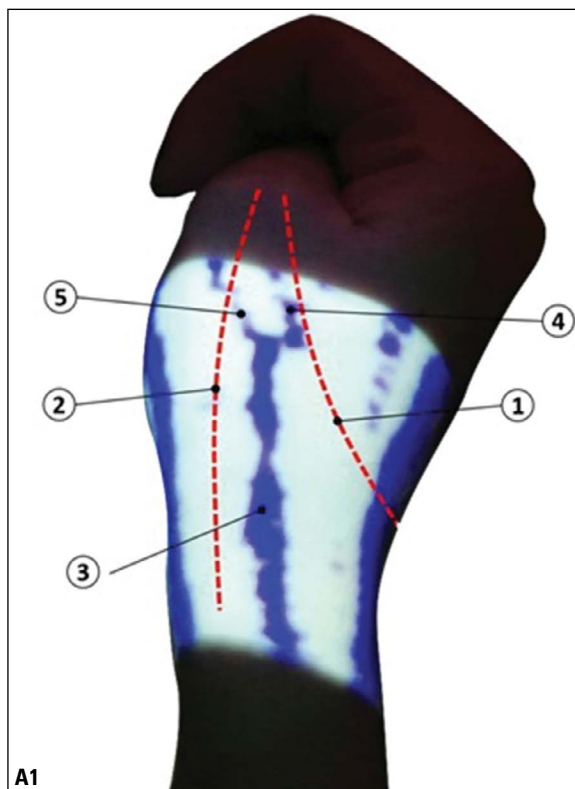


Figure 2. Right hand shows the presumed position of the tendon of extensor pollicis longus muscle (1), the presumed position of the tendons of abductor pollicis longus and extensor pollicis brevis muscles (2), the cephalic vein as it begins in the distal part of the anatomical snuffbox (3), continuation of the medial digital vein of the thumb (4) and continuation of the lateral digital vein of the thumb (5) where they resemble the origin of the cephalic vein.

proximally in right hands 65 (43%), but was outside the AS medially in left hands 64 (49%) (Table 4). Also, the formation of the CV in AS proximally was proportionally greater in left handed 98 (44%) compared with right handed 83 (41%) (Table 3). Moreover, it was noted that the symmetry of the site of formation of the CV between both hands in the same subject (in the total sample) was 107 (25%), the symmetry in females was 64 (15%), which is greater than the symmetry in males 43 (10%) (Table 5).

Statistical analysis using the chi-square test, there was a significant relation between both right and left hands, and site of the CV formation ($p = 0.048$). There was a significant relation between both females and males, and the site of the CV formation ($p < 0.0001$). Also, there was significant relation between sidedness and site of CV formation in males ($p = 0.01$), and in females ($p = 0.009$). There was not a significant relation between right handed and left handed subjects and the site of the CV formation ($p = 0.081$).

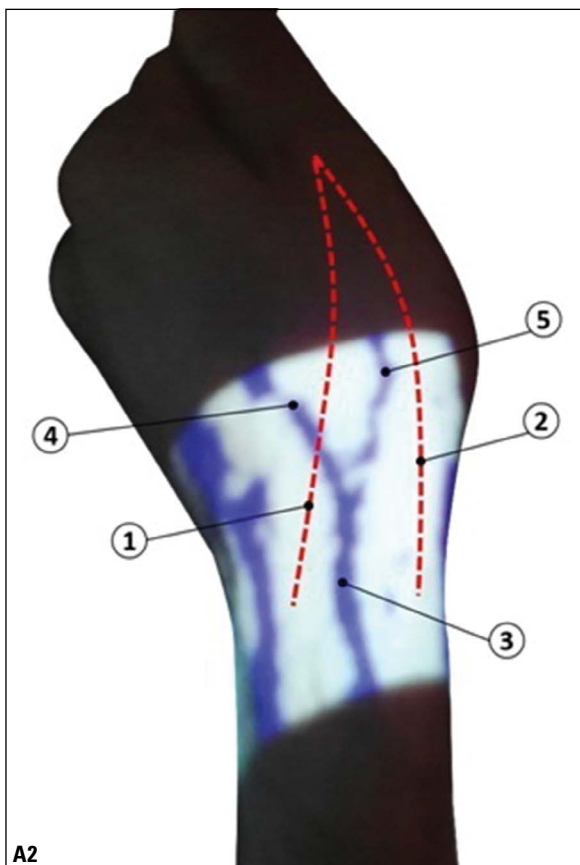


Figure 3. Left hand shows the presumed position of the tendon of extensor pollicis longus muscle (1), the presumed position of the tendons of abductor pollicis longus and extensor pollicis brevis muscles (2), and the cephalic vein (3) as it begins in the proximal part of the anatomical snuffbox, (4) continuation of the medial digital vein of the thumb (4) and continuation of the lateral digital vein of the index (5) where they resemble the origin of the cephalic vein.

DISCUSSION

The main finding of the present study was the characterisation of the course of the CV in relation to the AS. Two main origins have been demonstrated; the first one was identified within the AS either in its proximal or in its distal parts. The second origin, however, was identified outside the AS either in its medial or lateral sides. However, despite these different origins of the CV, it was running in the AS in 98% of the examined hands.

The IR illuminator has been used before in recognition of different veins in different areas, like the veins on the cubital fossa and the veins on the dorsum of the hand [4, 7, 17]. It should be noted that the present study did not examine the course of veins that formed the CV as it was not one of the aims of this study and because these veins cannot be imaged at

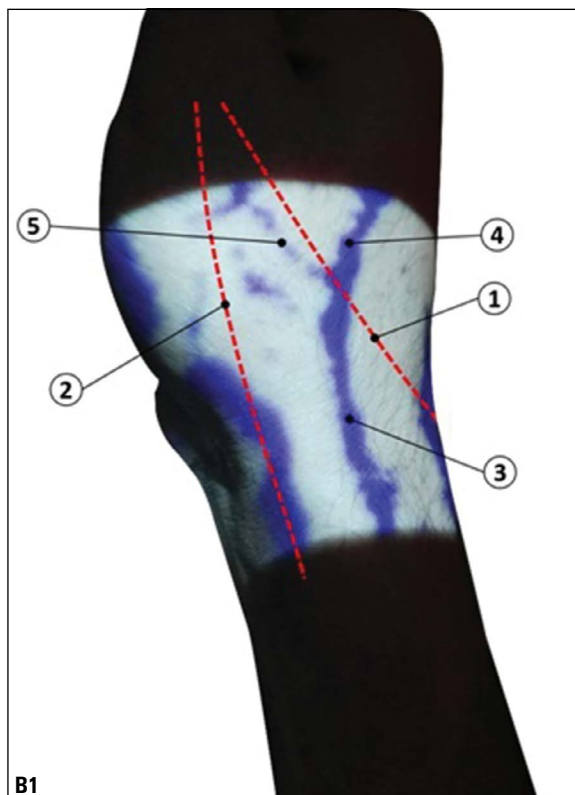


Figure 4. Right hand shows the presumed position of the tendon of extensor pollicis longus muscle (1), the presumed position of the tendons of abductor pollicis longus and extensor pollicis brevis muscles (2), and the cephalic vein (3) which begins outside the anatomical snuffbox, medial to the extensor pollicis longus tendon, continuation of the medial digital vein of the thumb (4) and continuation of the lateral digital vein of the index (5) where they resemble the origin of the cephalic vein.

the same time with CV due to the limited area that can be measured by IR illuminator. However, it has been reported that the origin of the CV is usually from the dorsal superficial venous network of the hand, specifically from the radial side, also the veins receive both dorsal digital veins from the thumb [24]. It is also worth mentioning that, in each examined hand the course of the CV was traced, separately, on the distal part of the lateral aspect of the forearm to confirm that the examined vein was the CV. The courses of the veins that formed the CV and its course proximal to the AS could be part of future projects as they need further examinations.

One of the most important findings in the present study is the demonstration of the relation of the CV and the AS. Despite the different sites of formation of the CV, it was running in the AS in 98% of the examined hands. These results are in agreement with another study in which the presence of the CV in the

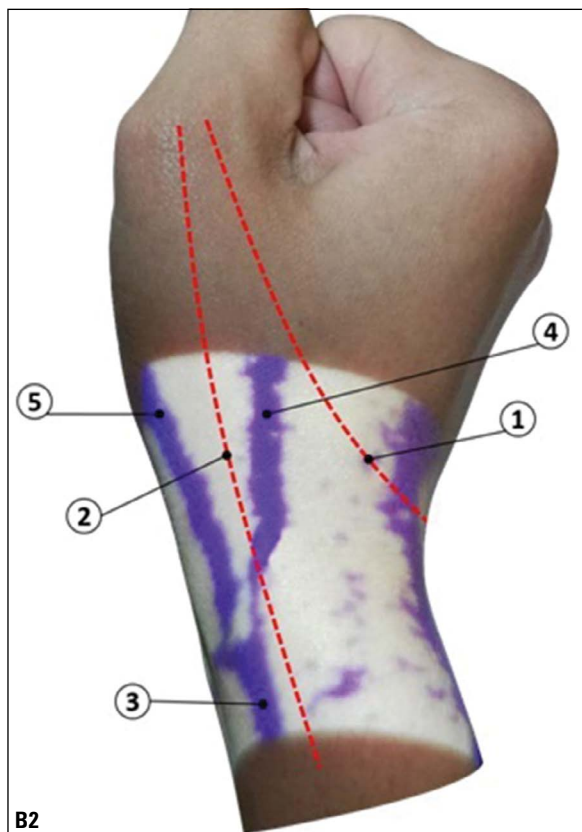


Figure 5. Right hand shows the presumed position of the tendon of extensor pollicis longus muscle (1), the presumed position of the tendons of abductor pollicis longus and extensor pollicis brevis muscles (2), and the cephalic vein (3) which originates outside the anatomical snuffbox, lateral to the abductor pollicis longus tendon, continuation of the medial digital vein of the thumb (4) and continuation of the lateral digital vein of the thumb (5) where they resemble the origin of the cephalic vein.

AS has been identified during arteriovenous fistula procedures in all patients [10]. Another anatomical study that revisited the anatomy of the AS and its contents also found and described the CV and its communications in the AS [20]. The present study did not investigate the reasons behind this very well established a relationship between the CV and AS. However, we may suggest that based on the anatomical course of the veins that participate in the formation of the CV, that they have no other options but to run through the AS or near to it. The dorsal digital vein from the radial side of the index finger which lies on the lateral side of the hand and the two dorsal digital veins of the thumb coming from the most lateral side of the hand (the thumb) find the nearest point to join each other in the AS to form the CV on the dorsum of the hand. In fact, this should not be surprising as it has been reported that superficial veins of the hand are running in radial and ulnar groups [4]. The radial group drains a much

Table 3. Frequency and number of sites of formation of the cephalic vein (CV) in relation to the anatomical snuffbox (AS), according to gender (n = 483), sidedness (n = 483) and handedness (laterality) (n = 228)

The formation of the CV in relation to the AS	Male	Female	Right hand	Left hand	Right handed	Left handed
Inside the AS distally	42 (21%)	45 (16%)	64 (25%)	23 (10%)	55 (27%)	2 (8%)
Inside the AS proximally	98 (48%)	120 (43%)	120 (46%)	98 (44%)	83 (41%)	12 (44%)
Outside the AS medially	58 (29%)	112 (40%)	70 (27%)	100 (45%)	60 (30%)	13 (48%)
Outside the AS laterally	5 (3%)	3 (1%)	6 (2%)	2 (1%)	3 (2%)	0 (0%)
Subtotal	203 (42%)	280 (58%)	260 (54%)	223 (46%)	201 (88%)	27 (12%)

Table 4. Right and left hands frequency and number of sites of formation of the cephalic vein (CV) in relation to the anatomical snuffbox (AS) according to gender

The formation of the CV in relation to the AS	Male		Female	
	Right hand	Left hand	Right hand	Left hand
Inside the AS distally	30 (27%)	12 (13%)	34 (23%)	11 (9%)
Inside the AS proximally	55 (50%)	43 (46%)	65 (43%)	55 (42%)
Outside the AS medially	22 (20%)	36 (39%)	48 (32%)	64 (49%)
Outside the AS laterally	3 (3%)	2 (2%)	3 (2%)	0 (0%)
Subtotal	110	93	150	130

Table 5. The possible symmetry of site of formation of the cephalic vein (CV) in relation to the anatomical snuffbox (AS) between both hands in the same subject

The formation of the CV in relation to the AS	Total hands frequency	Female hands frequency	Male hands frequency
Inside the AS distally	15 (3%)	8 (12.5%)	7 (16%)
Inside the AS proximally	51 (12%)	26 (40.5%)	25 (58%)
Outside the AS medially	41 (10%)	30 (47%)	11 (26%)
Outside the AS laterally	0 (0%)	0 (0%)	0 (0%)
Total	107 out of 430 (25%)	64 out of 430 (15%)	43 out of 430 (10%)

larger portion of the hand and forms the CV which is running on the lateral side of the forearm. Therefore, the AS seems to be located right in the dorsum

between the hand and the forearm. In addition, we have demonstrated that only in 2% of the examined hands the CV was neither formed inside the AS nor ran in the AS which has also been demonstrated in a different study where the CV in some cases was not found in the AS but in the first web space beside the RA and its branches [1, 18].

The present study has also investigated any possible patterns for the origin of the CV in relation to the AS. We have identified two anatomical patterns; one inside the AS named, (pattern A) with 67% and another pattern outside the AS, named (pattern B) with 37%. Furthermore, pattern A was running either in the proximal or distal parts of the AS. Pattern B was outside the AS either medial or lateral to the AS. These patterns have not been described before to the best of our knowledge and it should be mentioned that they might have been taken as the CV rather than its origin especially, in the pattern A. Thus, while we indicate that the CV is almost in 98% of all examined hands was found in AS in the current study, it should be highlighted that both sides (the distal and proximal) of the AS have to be avoided when cannulating or operating the CV, because in these parts of the AS may run the origins of the CV but not the CV itself.

An observational study of 200 hands (in 100 living subjects) using tourniquet to study the digital veins, metacarpal veins, dorsal venous arch, cephalic and basilic veins, CV has been observed in three different sites of formation; at first inter digital cleft (in our study it is B1), at AS (in our study it is A1 and A2), and at lateral end of wrist (in our study it is B2). We added a new description of CV location in AS whether it was proximally or distally. The findings of their study confirm ours in that, the most common site of CV formation according to sidedness was in AS, and least common site was outside AS laterally. They found that, in the right hands, 53 (53%) of the hands the CV site of formation was at first inter digital cleft, in 36 (36%) of the hands was at AS, in 11 (11%) of the hands was at lateral end of wrist. While in the left hands, 51 (51%) of the hands CV site of formation was at first inter digital cleft, in 31 (31%) of the hands was at AS, in 18 (18%) of the hands was at lateral end of wrist [18]. The observation of the present study was unlike that of a study carried by Matsuo et al. [12]; a study of 32 hands and forearms from 18 cadavers, showed constant existence of the CV, which consistently derived from a collateral vein of the deep palmar arch [11]. The variation of the results

between the present study and an aforementioned study could be due to the ethnic variation, as one of the studies confirmed the potential changeable role of ethnicity on the frequency distribution of certain patterns of the superficial veins on the hand [4].

CONCLUSIONS

The present study has fully examined whether the location of CV in relation to the AS is different in both sexes and both hands. Data obtained in the present study have indicated that the formation of the CV in the proximal part of the AS was the most common one for the CV in both sexes. However, when the course of CV in the AS was evaluated in both hands in the general population, it was also found that the formation of the CV in the proximal part of the AS is proportionally greater in the right hands. On the contrary, the formation of the CV outside and medial to the AS which was greater in left hands.




The current study has for the first time scrutinized the origin of the CV and its relationship with the AS and demonstrated that the CV was running within the AS in almost 98% of the examined hands. In addition, the CV has shown two anatomical patterns in its origin; within or outside the AS. These data may help and guide medical personal to better understand the course of the CV and its different patterns of origin which may help in better cannulation and setting up arteriovenous fistula.

REFERENCES

1. Canale ST, Beaty JH. Campbell's operative orthopaedics e-book. Elsevier Health Sciences, Philadelphia 2012.
2. Cerda A, del Sol M. Anatomical snuffbox and its clinical significance: a literature review. *Int J Morphol.* 2015; 33(4): 1355–1360, doi: [10.4067/s0717-95022015000400027](https://doi.org/10.4067/s0717-95022015000400027).
3. Tanea C, Younus M, Howale D. The study of dorsal venous arch of hand in living adult males in udaipur district of raasthan. *Int J Curr Res Rev.* 2012; 4(5): 89–89.
4. Diab M. *Lexicon of orthopaedic etymology.* 1st ed. Harwood Academic Pub, Newark 1999.
5. Elmegarhi SS, Amarin JZ, Hadidi MT, et al. Dorsal metacarpal veins: anatomic variation and potential clinical implications. *Anat Sci Int.* 2018; 93(2): 238–243, doi: [10.1007/s12565-017-0403-0](https://doi.org/10.1007/s12565-017-0403-0), indexed in Pubmed: [28417223](https://pubmed.ncbi.nlm.nih.gov/28417223/).
6. Grechenig W, Peicha G, Fellinger M, et al. Anatomical and safety considerations in establishing portals used for wrist arthroscopy. *Clin Anat.* 1999; 12(3): 179–185, doi: [10.1002/\(sici\)1098-2353\(1999\)12:3<179::aid-ca6>3.0.co;2-9](https://doi.org/10.1002/(sici)1098-2353(1999)12:3<179::aid-ca6>3.0.co;2-9).
7. Hamzah AA, Ramasamy S, Adnan AS. Pattern of superficial venous of the cubital fossa among volunteers in a tertiary hospital. *Trop Med Surg.* 2014; 2(2): 104–109, doi: [10.4172/2329-9088.1000164](https://doi.org/10.4172/2329-9088.1000164).

8. Lee SH, Chun KJ, Lee DS, et al. Right cardiac catheterization using the antecubital fossa vein in Korean patients. *Korean Circ J.* 2016; 46(2): 207–212, doi: [10.4070/kcj.2016.46.2.207](https://doi.org/10.4070/kcj.2016.46.2.207), indexed in Pubmed: [27014351](https://pubmed.ncbi.nlm.nih.gov/27014351/).
9. Loukas M, Myers CS, Wartmann ChT, et al. The clinical anatomy of the cephalic vein in the deltopectoral triangle. *Folia Morphol.* 2008; 67(1): 72–77, indexed in Pubmed: [18335417](https://pubmed.ncbi.nlm.nih.gov/18335417/).
10. Loukas M, Tubbs RS, Feldman J. *Netter's introduction to clinical procedures e-book.* Elsevier Health Sciences, Philadelphia 2016.
11. Mehigan J, McAlexander R. Snuffbox arteriovenous fistula for hemodialysis. *Am J Surg.* 1982; 143(2): 252–253, doi: [10.1016/0002-9610\(82\)90080-0](https://doi.org/10.1016/0002-9610(82)90080-0).
12. Matsuo M, Honma S, Sonomura T, et al. Clinical anatomy of the cephalic vein for safe performance of venipuncture. *JA Clin Rep.* 2017; 3(1): 50, doi: [10.1186/s40981-017-0121-6](https://doi.org/10.1186/s40981-017-0121-6), indexed in Pubmed: [29457094](https://pubmed.ncbi.nlm.nih.gov/29457094/).
13. Naeem R, Soueid A, Lahiri A. The dangers of intravenous cannulation within the anatomical snuffbox. *J Hand Surg Eur Vol.* 2012; 37(4): 362–363, doi: [10.1177/1753193411433524](https://doi.org/10.1177/1753193411433524), indexed in Pubmed: [22190567](https://pubmed.ncbi.nlm.nih.gov/22190567/).
14. Radkowski CA, Richards RS, Pietrobon R, et al. An anatomic study of the cephalic vein in the deltopectoral shoulder approach. *Clin Orthop Relat Res.* 2006; 442: 139–142, doi: [10.1097/01.blo.0000181146.78434.da](https://doi.org/10.1097/01.blo.0000181146.78434.da), indexed in Pubmed: [16394752](https://pubmed.ncbi.nlm.nih.gov/16394752/).
15. Robson AJ, See MS, Ellis H. Applied anatomy of the superficial branch of the radial nerve. *Clin Anat.* 2008; 21(1): 38–45, doi: [10.1002/ca.20576](https://doi.org/10.1002/ca.20576), indexed in Pubmed: [18092362](https://pubmed.ncbi.nlm.nih.gov/18092362/).
16. Sadeghi A, Setayesh Mehr M, Esfandiari E, et al. Variation of the cephalic and basilic veins: A case report. *J Cardiovasc Thorac Res.* 2017; 9(4): 232–234, doi: [10.15171/jcvtr.2017.40](https://doi.org/10.15171/jcvtr.2017.40), indexed in Pubmed: [29391938](https://pubmed.ncbi.nlm.nih.gov/29391938/).
17. Salameh MA, Shatarat AT, Badran DH, et al. The best vein to be accessed based on descriptive study of dorsal metacarpal vein. *Anat Cell Biol.* 2019; 52(4): 390–396, doi: [10.5115/acb.19.142](https://doi.org/10.5115/acb.19.142), indexed in Pubmed: [31949977](https://pubmed.ncbi.nlm.nih.gov/31949977/).
18. Samarakoon LB, Lakmal KC, Thillainathan S, et al. Anatomical relations of the superficial sensory branches of the radial nerve: a cadaveric study with clinical implications. *Patient Saf Surg.* 2011; 5(1): 28, doi: [10.1186/1754-9493-5-28](https://doi.org/10.1186/1754-9493-5-28), indexed in Pubmed: [22054296](https://pubmed.ncbi.nlm.nih.gov/22054296/).
19. Tao W, Dong-Yang G, Meng W, et al. Anatomical snuffbox versus forearm internal arteriovenous fistula for 214 hemodialysis patients with chronic renal failure: Which is the better method for permanent vascular access prior to kidney transplantation. *J Clin Rehab Tissue Eng Res.* 2010; 14(31): 5837–5840, doi: [10.3969/j.issn.1673-8225.2010.31.034](https://doi.org/10.3969/j.issn.1673-8225.2010.31.034).
20. Tubbs RS, Salter EG, Oakes WJ. *The tabatière anatomique.* *Clin Anat.* 2006; 19(4): 299–303, doi: [10.1002/ca.20151](https://doi.org/10.1002/ca.20151), indexed in Pubmed: [16283634](https://pubmed.ncbi.nlm.nih.gov/16283634/).
21. Tubiana R. *The hand.* Vol. 1. Sanders, Philadelphia, Penn 1981.
22. Ukoha UU, Oranusi CK, Okafor JI, et al. Patterns of superficial venous arrangement in the cubital fossa of adult Nigerians. *Niger J Clin Pract.* 2013; 16(1): 104–109, doi: [10.4103/1119-3077.106777](https://doi.org/10.4103/1119-3077.106777), indexed in Pubmed: [23377482](https://pubmed.ncbi.nlm.nih.gov/23377482/).
23. Thwin SS, Fazlin F, Than M. Multiple variations of the tendons of the anatomical snuffbox. *Singapore Med J.* 2014; 55(1): 37–40, doi: [10.11622/smedj.2013216](https://doi.org/10.11622/smedj.2013216), indexed in Pubmed: [24452976](https://pubmed.ncbi.nlm.nih.gov/24452976/).
24. Vialle R, Pietin-Vialle C, Cronier P, et al. Anatomic relations between the cephalic vein and the sensory branches of the radial nerve: How can nerve lesions during vein puncture be prevented? *Anesth Analg.* 2001; 93(4): 1058–1061, doi: [10.1097/0000539-200110000-00052](https://doi.org/10.1097/0000539-200110000-00052), indexed in Pubmed: [11574383](https://pubmed.ncbi.nlm.nih.gov/11574383/).
25. Wolowczyk L, Williams AJ, Donovan KL, et al. The snuffbox arteriovenous fistula for vascular access. *Eur J Vasc Endovasc Surg.* 2000; 19(1): 70–76, doi: [10.1053/ejvs.1999.0969](https://doi.org/10.1053/ejvs.1999.0969), indexed in Pubmed: [10706839](https://pubmed.ncbi.nlm.nih.gov/10706839/).

Hypothyroidism: morphological and metabolic changes in the testis of adult albino rat and the amelioration by alpha-lipoic acid

A.A. Ibrahim¹, N.A. Mohammed², K.A. Eid³ , M.M. Abomughaid⁴, A.M. Abdelazim^{4, 5} , A.M. Aboregela^{1, 6} 

¹Human Anatomy and Embryology Department, Faculty of Medicine, Zagazig University, Zagazig, Egypt

²Medical Physiology Department, Faculty of Medicine, Zagazig University, Zagazig, Egypt

³House Officer, Faculty of Medicine, Zagazig University, Zagazig, Egypt

⁴Laboratory Medical Sciences, College of Applied Medical Sciences, University of Bisha, Saudi Arabia

⁵Biochemistry Department, Faculty of Veterinary Medicine, Zagazig University, Zagazig, Egypt

⁶Basic Medical Sciences, College of Medicine, University of Bisha, Saudi Arabia

[Received: 6 June 2020; Accepted: 29 June 2020]

Background: The objective of this study is to evaluate the influence of carbimazole-induced hypothyroidism on the testes of adult albino rats and the probable protective effect of alpha-lipoic acid (ALA).

Materials and methods: The rats were divided into four groups; control group, ALA group, carbimazole, and carbimazole + ALA groups. Rats were exposed to ALA (60 mg/kg body weight) or carbimazole (1.35 mg/kg body weight), or both, administered via gavages for 30 days.

Results: Morphometric analysis revealed a significant decrease in tubular diameter, germinal epithelium thickness, and interstitial space as compared to the controls. Also, rats exposed to carbimazole showed a significant decline in testicular weight, sperm motility, and count. Additionally, deterioration of the testicular architecture was observed. ALA supplementation resulted in a significant improvement in the tubular diameter and germinal epithelium thickness, but no significant improvement regarding interstitial space was observed. Another observation was the significant decline in serum testosterone and follicle-stimulating hormone (FSH) in the carbimazole group, indicating reduced steroidogenesis. A significant reduction in reduced glutathione content was detected in the testes of the carbimazole group compared with the controls, while malonaldehyde concentration significantly increased. Conversely, ALA supplementation ameliorated the toxicity induced by hypothyroidism as illustrated by enhanced reproductive organ weights, testosterone, luteinizing hormone, and FSH levels, testicular steroidogenesis, and oxidative stress parameters.

Conclusions: Hypothyroidism altered testicular antioxidant balance and negatively affected spermatogenesis. On the other hand, ALA through its antioxidant properties alleviated testicular toxicity in carbimazole-exposed rats. (Folia Morphol 2021; 80, 2: 352–362)

Key words: alpha-lipoic acid, carbimazole, hypothyroidism, testis, rat

Address for correspondence: Dr. A.M. Aboregela, Faculty of Medicine, Zagazig University, 44519, Egypt; College of Medicine, University of Bisha, 61992, Kingdom Saudi Arabia, tel: +966505163578/+201001498234, e-mail: amaboregela@zu.edu.eg; aaboregela@ub.edu.sa

This article is available in open access under Creative Common Attribution-Non-Commercial-No Derivatives 4.0 International (CC BY-NC-ND 4.0) license, allowing to download articles and share them with others as long as they credit the authors and the publisher, but without permission to change them in any way or use them commercially.

INTRODUCTION

In the past decades, clinical studies revealed that the thyroid hormone plays a mandatory role in spermatogenesis and steroidogenesis. It is now known that T3 regulates the testicular growth and maturation, in different mammals [27]. The efficiency of spermatogenesis is directly correlated to the number of functional Sertoli cells entrenched during adulthood [40]. Thyroid hormones have a well-known physiological role in modulating the process of oxidative stress caused by reactive oxygen species [28]. Its deficiency is known to induce hypothyroidism and oxidative stress and perhaps might lead to testicular dysfunction and infertility [20]. In males, hypothyroidism is accompanied by hypogonadism and other abnormalities, like a declined serum testosterone [24]. Furthermore, hypothyroidism can alter sperm morphology and motility [23]. Carbimazole mode of action is through its active form methimazole (1-methyl-2-mercaptoimidazole), which inhibits the iodination of tyrosine catalysed by thyroid peroxidase inducing lowering of circulating thyroid hormones [31]. In this regard, carbimazole has been used to induce experimental hypothyroidism [6]. Alpha-lipoic acid (ALA), is one of the cofactors for multi-enzyme complexes in mitochondria, enhances the uptake of glucose by the cells, and modulates the activity of various signalling molecules and transcription factors [41]. Moreover, ALA has a lipophilic character, it is can cross cell membranes, and, with dihydrolipoic acid (DHLA), it can overcome free radicals efficiently in both lipid and watery phases [16]. Various reports in the literature suggested that ALA can improve body resistance to free radicals [42]. Also, ALA can recycle other important antioxidants, including glutathione and vitamin C [21]. To date, less attention has been directed towards identifying the precise role of ALA in ameliorating the toxic effects caused by oxidative stress, especially in the hypothyroid state. From this perspective, we designed this study to determine the effects of carbimazole-induced hypothyroidism on testicular structure and function and the possible ameliorating role of ALA supplementation.

MATERIALS AND METHODS

Animal models and groups treatment

Forty healthy adult males (21 weeks old and weighing 200 to 250 g) albino rats of Wister strain were obtained from Zagazig Veterinary Medicine Animal House, Egypt. All rats were fed *ad libitum*

and were grouped (n = 5 per cage) in standard special cages made from plastic. Before experimentation, all animals were accommodated for 2 weeks at temperature: 24–26°C and in a 12 h light/12 h dark cycle. Then, rats were divided into four main groups (10/group). Group 1 (control) received 2 mL of distilled water with 2 mL of olive oil orally. Group 2 (ALA group) was administered 2 mL of distilled water plus ALA (60 mg/kg body weight) [11] dissolved in 2 mL of olive oil. Group 3 (carbimazole group) was administered 2 mL of olive oil plus carbimazole (1.35 mg/kg body weight) [32] dissolved in 2 mL of distilled water. Group 4 (carbimazole + ALA group) was administered ALA (60 mg/kg body weight) dissolved in 2 mL of olive oil and carbimazole (1.35 mg/kg body weight) dissolved in 2 mL distilled water. Each rat was administered daily a fresh single oral dose via gavages for 30 days. The Guide for the Care and Use of Laboratory Animals, 8th edition was our guide during all experimental processes [1]. The Institutional Animal Care and Use Committee at Zagazig University (ZU-IACUC/3/F/29/2018) approved the present study. All chemicals were purchased from Sigma Chemicals Company (St. Louis, MO).

Blood collection

The rats were sacrificed under ethyl ether anaesthesia after 24 hours of the last dose [13]. Blood samples were obtained by cardiac puncture and then centrifuged at 4000 rpm for a quarter of an hour after allowing the blood to clot for 2 hours at room temperature. The sera from all rats were kept at –20°C till the proceeding of the biochemical determinations. We take in mind, to avoid the repeated freezing and thawing of preserved samples.

Extraction and preparation of gonads

The testes were removed from all groups by laparotomy and the epididymis was obtained, removed, and homogenised at 37°C in 2 mL of Hank's buffer solution. Then caudal epididymis sperms numbers were detected by haemocytometry technique [37].

The right testes were weighed and washed in cold physiologic saline and dried with filter paper. The volume of the testes was estimated. Next, the testes were fixed in 10% buffered formaldehyde solution, and then processed and embedded in paraffin wax. The left testes from all animals were weighed and their volume was estimated and recorded. Testes of all groups were homogenised in 50 mM phosphate

buffer (pH 7) containing 0.1 mM EDTA to give 10% homogenate (w/v). The testicular homogenates were centrifuged for 10 min at 1000 rpm and the supernatant was separated and then after used for oxidative stress evaluation [37].

Light microscopic analysis

Sections from the testis at 4–5 μm thickness were obtained and stained with eosin and haematoxylin to assess general histological architecture [3]. Thirty different testicular sections from 10 different rats in each group were processed for immunohistochemistry [39]. In brief, 3% H_2O_2 in phosphate buffered saline was used to block the endogenous peroxidase activity. Immersing the slides in citrate sodium solution (10 mM, pH 6.0) for 15 min at 95°C was done for antigenic retrieval. The sections were kept in diluted primary antibodies overnight at 4°C; (myoid cell marker) rabbit polyclonal anti- α -smooth muscle actin (SMA) (diluted 1:3000; Catalogue No. ab5694, Abcam, Cambridge, UK), (androgen receptor antibody) mouse anti-“androgen receptor” (N-20, sc-816; Santa Cruz Biotechnology, Inc., Santa Cruz, CA, USA) diluted 1:100, and mice anti-Vimentin as (Sertoli cell marker, 1:50, Santa Cruz, CA, USA). After addition of avidin-biotin complex, Mayer’s haematoxylin was used as a counterstain. All sections were photographed and examined using a photomicroscope (Leica DM500, German).

Morphometry

ImageJ software was used for image analysis and morphometry according to Wayne Rasband — National Institute of Mental Health (Bethesda, Maryland, USA). Seminiferous tubule diameter, germinal epithelium thickness, and interstitial space thickness (μm) were measured in six sections per testis from ten different rats in each group at magnification power $\times 400$. Numbers of Sertoli cells and Leydig cells were also counted in the same slides. In addition, the area percentages of androgen receptor, α -SMA, and vimentin expression were assessed.

Biochemical analysis

Blood samples from 10 different rats in each group were used to determine the hormone levels in the serum. Serum levels of triiodothyronine (T3) (mouse/rat ELISA Kit) (Abnova, Taiwan), and thyroxin (T4) (rat ELISA Kit) (MyBioSource, Inc. USA) were determined by colorimetric method according to the

manufacturer instructions. rTSH kit — Biotrak Assay System was used to determine thyroid-stimulating hormone (TSH) levels. The sensitivity of the rTSH assay was 0.05 ng/tube, with cross-reactivity 100% with rat TSH and 15% non-specific binding. The procedures were performed following the specifications of the manufacturer’s manual. Follicle-stimulating hormone (FSH) level was estimated using rat FSH ELISA Kit, Novus Biologicals (KA2330) by colorimetric method [33]. Luteinizing hormone (LH) level was estimated using rat LH ELISA kit, Novus Biologicals (NBP2-61257) by colorimetric method range from 1.2 to 280 mIU/m according to the manufacturer instructions. Testosterone level was estimated using rat testosterone ELISA Kit, Aviva Systems Biology (OKCA00179) by a colourimetric method (OD450 nm) [4]. Malondialdehyde (MDA) level was assessed by incubating the testis homogenate at 100°C in 1 mL of trichloroacetic acid (10%) and 1 mL of thiobarbituric acid (0.67%) for a half of an hour. The amount of MDA concentration was expressed by the coloured complex obtained at 535 nm absorbance [30]. Reduced glutathione (GSH) content in the tissue homogenate was determined, where a mixture formed from 250 μL of testicular homogenate (10%), 250 μL distilled water, 50 μL of trichloroacetic acid (50%). The mixture was shaken for 15 min and centrifuged for 10 min at 3000 rpm. The 10 μL of supernatant was mixed with 400 μL Tris buffer (0.4 M) and (pH = 8.9) and 10 μL of 5,5-dithio-bis-2 nitrobenzoic acid (DTNB). The obtained colour complex was detected by a spectrophotometer at 512 nm [38].

Statistical analysis

The obtained data of our results were statistically analysed by Graph Pad Prism 5.01 (GraphPad Software, San Diego, CA, USA). Quantitative data were tabulated as mean and standard deviation when normally distributed or median and interquartile range if not normally distributed. Analysis of variance (ANOVA) used to test mean values differences for all experimental groups and Bonferroni’s multiple comparison test was used as a *post hoc* test. The statistical significance of the results was considered at (p-value < 0.05).

RESULTS

Hypothyroidism was induced by administering carbimazole (1.35 mg/kg body weight). This resulted in a decrease in serum concentrations of total T3, and T4.

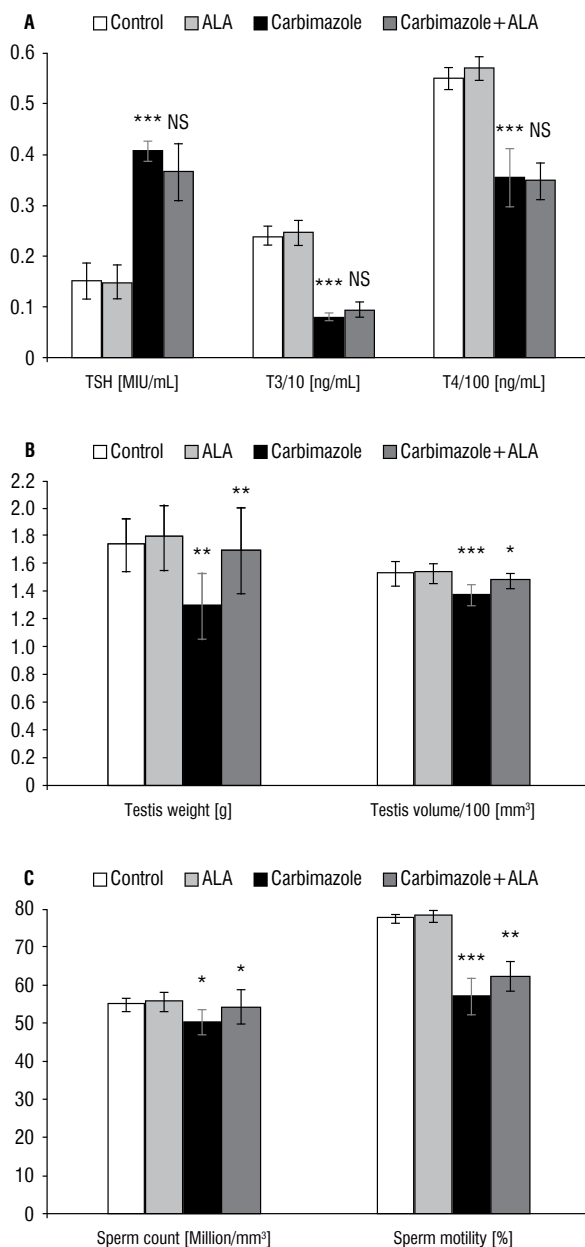


Figure 1. A. Histogram showing thyroid function tests after different treatment strategies confirming the hypothyroid state; **B, C.** Histograms representing the effects of carbimazole-induced hypothyroidism and alpha-lipoic acid (ALA) on gross measurements and semen analysis, respectively. Data are presented as mean \pm standard deviation; TSH — thyroid-stimulating hormone; T3 — thyroxine 3; T4 — thyroxine 4; NS — no significance; * $p < 0.05$; ** $p < 0.01$; *** $p < 0.001$.

Also, this was accompanied by a significant increase in the serum TSH levels. Moreover, ALA supplementation did not affect the hypothyroid state in the carbimazole + ALA group (Fig. 1A). A decrease in testicular weight and volume of hypothyroid rats was observed (Fig. 1B).

Gross measurements and semen analysis

The average testicular sperm count was significantly reduced in the carbimazole group when compared to the control group. Supplementation of ALA significantly restored the sperm count in the testis of the carbimazole + ALA group (Fig. 1C). The mean sperm motility in the carbimazole group was significantly low when compared to the control group. However, a significant elevation was detected in the carbimazole + ALA group after ALA supplementation.

Light microscopic analysis

In the control group, the testicular sections expressed normal architecture with average sperm density (Fig. 2A, B). However, in the carbimazole group, there was a deposition of homogenous substance in the interstitial spaces, which was associated with congestion and disturbance in the tubular contour. Also, destruction in some tubular walls was noted. Besides, testicular sections expressed a remarkable detachment of germinal epithelium with decreased spermatocytes density. Furthermore, vacuolations in the interstitial space and in between spermatocytes, and scarce Sertoli cells with scattering and stripping off spermatids were observed and Leydig cells nearly disappeared (Fig. 2C, D). Moreover, the tubular diameter, germinal epithelium thickness, and interstitial space were decreased when compared to the control group. On the other hand, the supplementation of ALA resulted in a significant improvement in the tubular diameter and germinal epithelium thickness. However, no significant improvement regarding interstitial space was observed (Table 1). In the carbimazole + ALA group, the integrity of germinal epithelium was maintained with minute areas of detachment and Leydig cell clusters were preserved. Besides, refinement in spermatocyte density was noted. However, any deposition of homogenous substance and the regularity and maintenance of the tubular contour were not observed. Also, spermatids appeared scattered (Fig. 2E, F). Sertoli cell and Leydig cell numbers were significantly decreased in the carbimazole group when compared to the control. Moreover, their numbers were significantly higher in the group receiving combination of carbimazole and ALA than in the carbimazole group (Table 1).

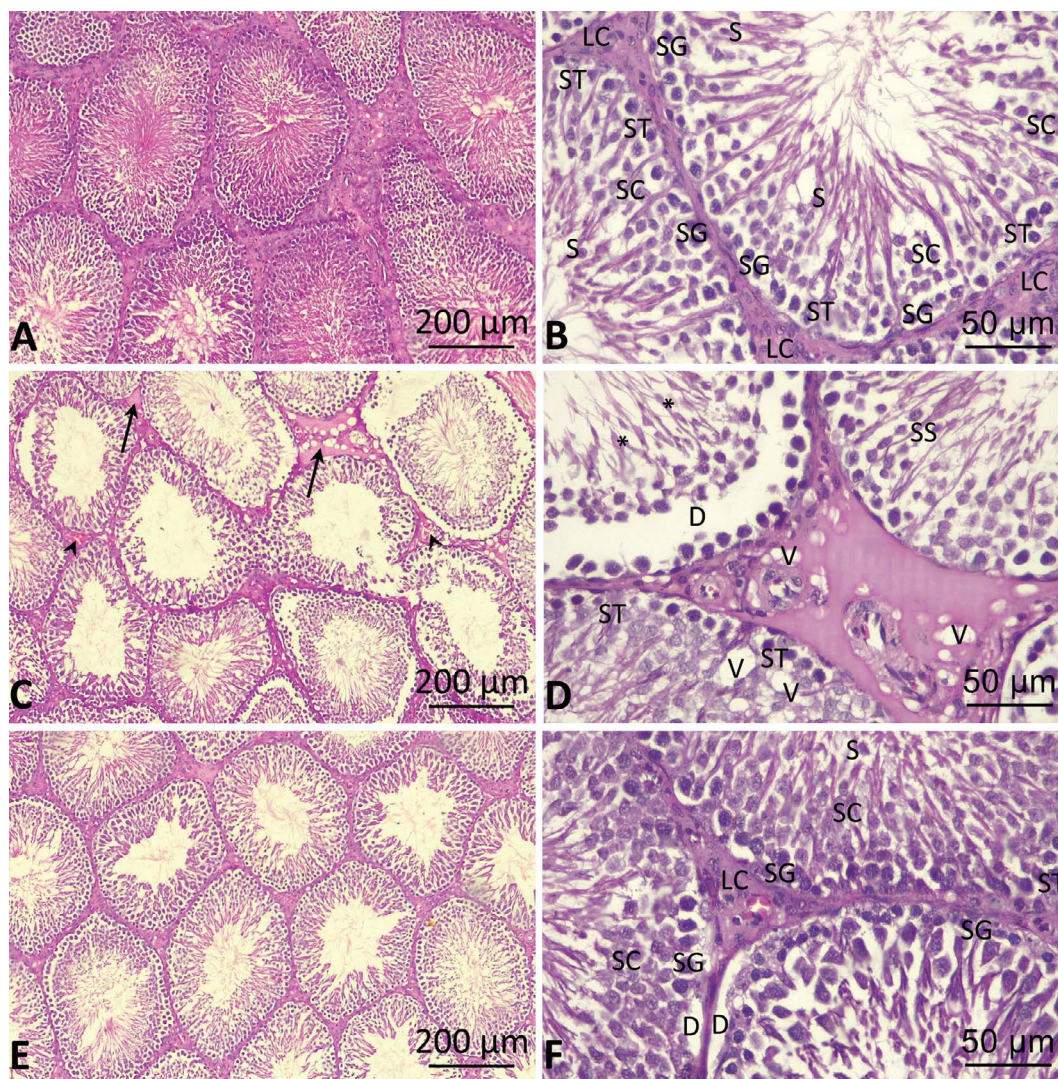


Figure 2. Representative microphotograph of the testis in different groups. **A, B.** Control group. The testis shows different types of cells; LC — Leydig cells; ST — Sertoli cells; SG — spermatogonia; SC — spermatocyte; S — spermatid; **C, D.** Hypothyroid group (carbimazole-treated) the testis represents homogenous substance in the interstitial space (straight arrow), congestion (arrowhead), vacuolation (V), scarce Sertoli cells (ST), stripped off spermatids (SS), scattered spermatids (*) and detached germinal epithelium (D); **E, F.** Carbimazole + α -lipoic acid group expressing few Sertoli cells (ST), Leydig cells (LC), spermatogonia (SG), spermatocyte (SC), spermatid (S) and detached germinal epithelium (D) (H&E, bars = 200 and 50 μ m).

Immunohistochemistry

In the testes of the control group, androgen receptor expression was prominent in interstitial cells of Leydig and the peritubular myoid cells, but it was weak in the Sertoli cells in all stages of spermatogenesis. In contrast, the androgen receptor expression was limited to certain interstitial cells with a decrease in the area per cent in the carbimazole group. The decrease in androgen receptor expression in Sertoli cells was prominent in all stages of spermatogenesis especially stage IV–VIII. Interestingly, the group that received carbimazole + ALA showed maintenance of the androgen receptor expression in Leydig cells and some peritubular myoid

cells with improvement in the area percentage (Table 1, Fig. 3A–C). Regarding α -SMA expression, it was limited to the peritubular myoid cells and it appeared as a very thin bilaminar line with very potential space in between laminae, and in the wall of the interstitial blood vessels in the control group. In contrast, α -SMA expression in the carbimazole group showed areas of thickening and fusion between the laminae. Besides, it was associated with prominent thickening in the wall of blood vessels, which in turn increased the surface area percentage. However, the testes of the carbimazole + ALA group displayed maintenance of the control expression pattern (Table 1, Fig. 3D–F). We also

Table 1. Effects of carbimazole-induced hypothyroidism and alpha-lipoic acid (ALA) on the histomorphometry and immunomorphometry of the testis in albino rats

Parameter	Control	ALA	Carbimazole	Carbimazole + ALA	ANOVA
Seminiferous tubule diameter [μm]	241.80 \pm 34.47	242.90 \pm 29.80 ^{NS}	181.40 \pm 12.06 ^{***}	218.7 \pm 5.554 [*]	< 0.0001 ^{***}
Germinal epithelium thickness [μm]	52.42 \pm 6.505	54.66 \pm 5.685 ^{NS}	29.26 \pm 3.760 ^{***}	38.46 \pm 3.068 ^{**}	< 0.0001 ^{***}
Interstitial space [μm]	12.25 \pm 2.639	13.13 \pm 3.052 ^{NS}	6.74 \pm 1.346 ^{***}	7.15 \pm 1.215 ^{NS}	< 0.0001 ^{***}
Sertoli cell number/tubule	33.63 \pm 2.973	34.25 \pm 3.196 ^{NS}	11.13 \pm 2.232 ^{***}	21.5 \pm 2.449 ^{***}	< 0.0001 ^{***}
Leydig cell number/cluster	14.75 \pm 1.282	15.13 \pm 1.885 ^{NS}	2.38 \pm 1.408 ^{***}	9.88 \pm 1.458 ^{***}	< 0.0001 ^{***}
Androgen receptor area [%]	1.20 \pm 0.345	1.13 \pm 0.195 ^{NS}	0.60 \pm 0.119 ^{***}	0.93 \pm 0.102 [*]	< 0.0001 ^{***}
Alpha smooth muscle actin area [%]	2.03 \pm 0.388	2.09 \pm 0.234 ^{NS}	4.76 \pm 0.305 ^{***}	3.88 \pm 0.678 ^{**}	< 0.0001 ^{***}
Vimentin area [%]	14.63 \pm 2.547	15.25 \pm 1.949 ^{NS}	7.74 \pm 1.516 ^{***}	10.65 \pm 0.611 [*]	< 0.0001 ^{***}

Values are expressed in mean \pm standard deviation. One-way ANOVA and post-hoc Bonferroni's multiple comparison test (ALA and carbimazole vs. control, carbimazole + ALA vs. carbimazole); * p < 0.05, ** p < 0.01, *** p < 0.001; NS — no significance

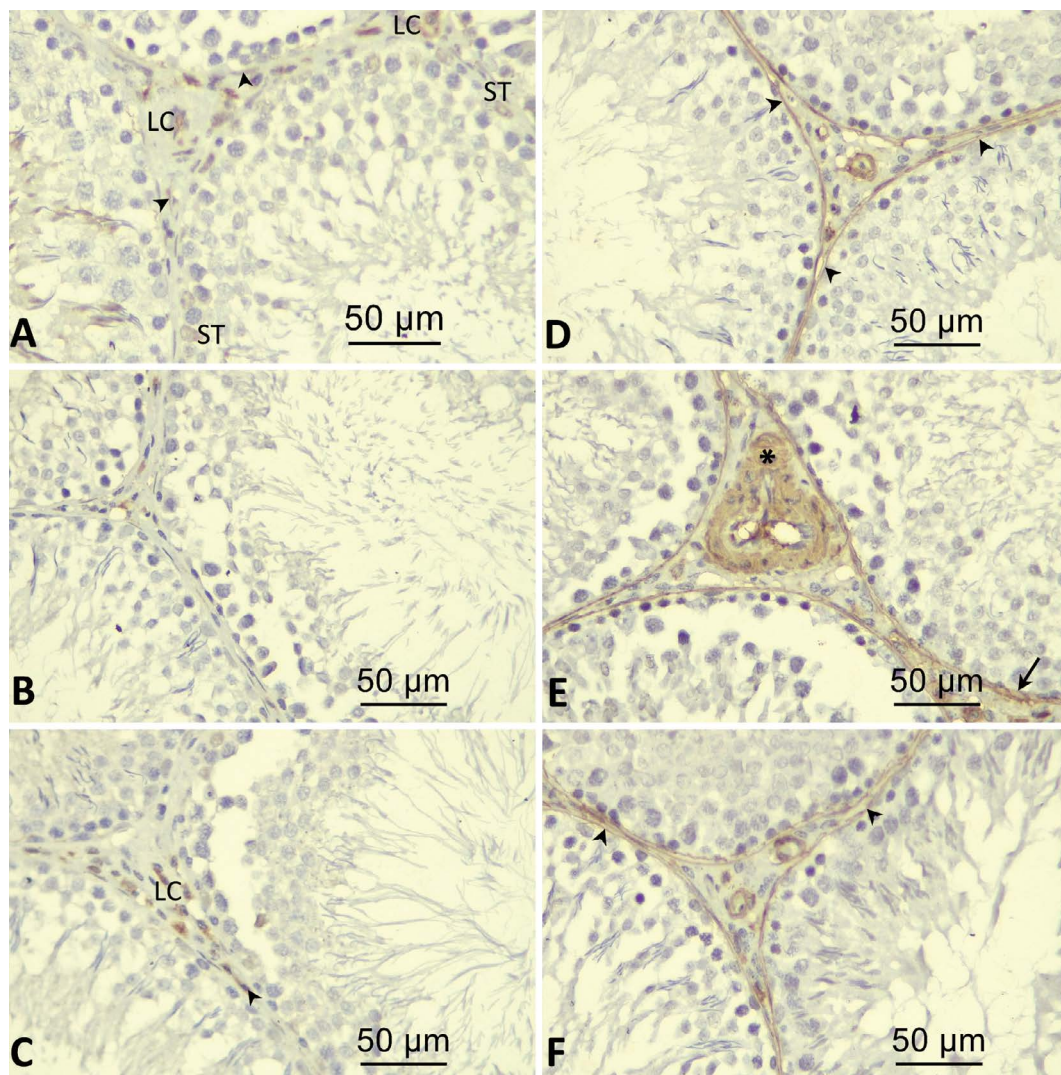


Figure 3. Representative microphotograph of the immunohistochemical expression in the testis. The groups are arranged as control, carbimazole-treated and carbimazole + alpha-lipoic acid-treated group, respectively. **A, B, C.** Androgen receptor. The testis shows Leydig cells (LC), Sertoli cells (ST), and peritubular myoid cells (arrowhead); **D, E, F.** Alpha-smooth muscle actin. The testis represents bilaminar peritubular myoid cells expression (arrowhead), thickening and fusion of the two laminae (arrow), and thickening in the interstitial vessel wall (*). (Bars = 50 μm).

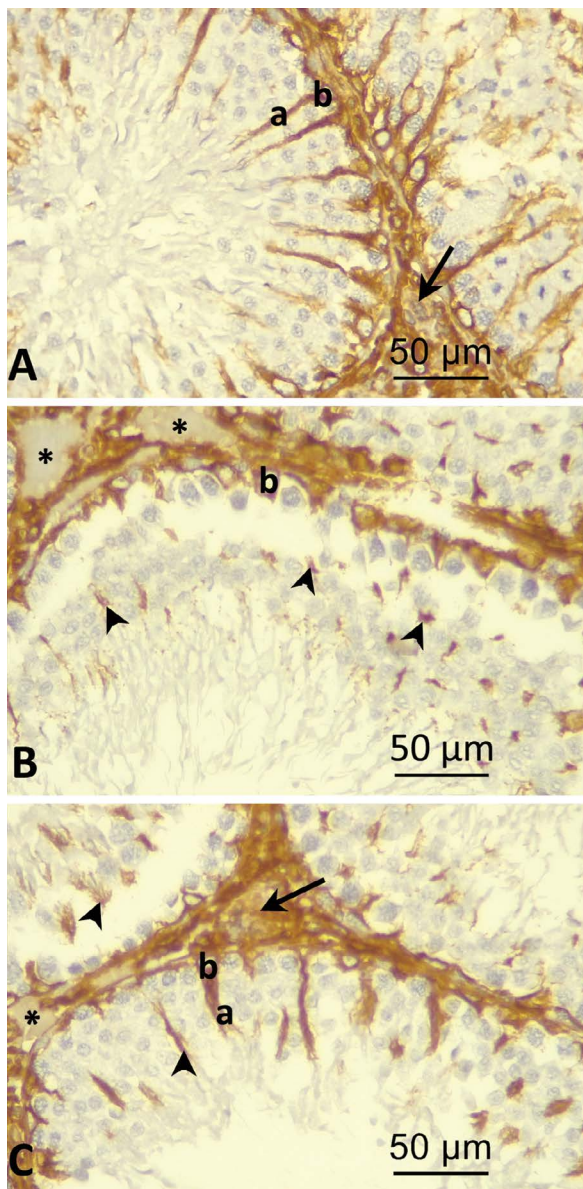


Figure 4. Representative microphotograph of vimentin expression in the testis in different groups. **A, B, C.** Control, carbimazole-treated and carbimazole + alpha-lipoic acid-treated group, respectively. The testis shows different segments of Sertoli cells; a — apical segment; b — basal segment, destroyed detached apical segment of Sertoli cells (arrowhead), interstitial tissue (arrow) empty areas in the interstitial space (*). (Bars = 50 μm).

analysed the immunocontent of vimentin expression. The results showed that vimentin was prominently expressed in the cytoplasm of the Sertoli cells with clear continuity between both apical and basal segments and the interstitial tissue in the control group. On the contrary, Sertoli cells' destruction was elucidated by the pattern of vimentin expression in the carbimazole group. There was a destruction of the apical segment of Sertoli cells with the scarce appearance of the basal segment in most of the tubules. Besides, there was

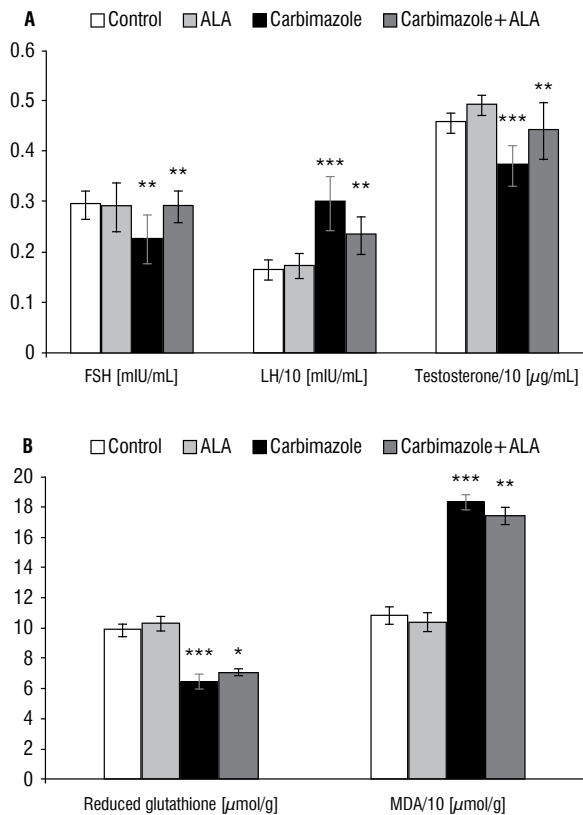


Figure 5. A, B. Histograms representing the effects of carbimazole-induced hypothyroidism and alpha-lipoic acid (ALA) on reproductive hormones, reduced glutathione, and malondialdehyde (MDA). Data are presented as mean ± standard deviation; FSH — follicle-stimulating hormone; LH — luteinizing hormone; NS — no significance; *p < 0.05; **p < 0.01; ***p < 0.001.

a lack of expression in certain areas of the interstitial tissue which appeared empty of cells. This resulted in a decrease in the area percentage of vimentin expression. On the other hand, limited conservation of the expression pattern of the control in some Sertoli cells was detected in the carbimazole + ALA group. Also, the interstitial tissue was partially protected showing fractional improvement in area percentage of vimentin expression (Table 1, Fig. 4A–C).

Biochemical analysis

Serum levels of testosterone were significantly decreased in the carbimazole group compared to the control group. Also, FSH concentrations showed a significant decline in the carbimazole group when compared to the control group. In contrast, the level of LH showed a significant increase in the carbimazole group compared to the control group. The results were improved after ALA administration in the carbimazole + ALA group, with a significant increase in testosterone and FSH levels (Fig. 5A). GSH contents

in the carbimazole group showed a significant decline when compared to the control group (Fig. 5B). A comparison of the MDA contents of the testis showed a significant increase in the carbimazole group when compared to the control group. Interestingly, the results improved in the carbimazole + ALA group, and a significant decrease was observed in MDA (Fig. 5B).

DISCUSSION

The impact of thyroid diseases on male reproduction has been an area of controversy for many years ago, due to the reports of the inability of the testis to respond metabolically to thyroid hormones [15]. Yet, in the last decades, some clinical trials have concluded that thyroid hormones have a great role in the process of testicular spermatogenesis even at and after puberty [14]. However, some authors suggested that hypothyroidism does not influence the functions or the size of the testis or seminiferous tubules [10]. Thyroid hormones are considered to be one of the main factors in cell metabolism regulation and thus play a significant role in oxidative stress [8]. The impetus of the present study is to determine the ameliorating role of ALA supplementation on the damage caused by carbimazole-induced hypothyroidism on testicular tissue of the experimental animal model. The obtained data of the present study confirmed that carbimazole can decrease the testicular volume and tubular diameter, germinal epithelium thickness, sperm count as compared to the control group. Besides, congestion and disturbance in tubular contour with damage to some tubular wall and very limited expression of androgen receptor to certain interstitial cells were observed. Moreover, detachment of germinal epithelium decreased spermatocytes density, and destruction in Sertoli cells was recorded. The above-obtained data came in accordance with Prathima et al. [32] who reported that rats exposed to carbimazole showed major histological deterioration such as congestion of blood vessels, haemorrhage, and destruction of interstitial cells with degeneration of spermatogenic cells with the irregular cell membrane. The report of Yousofvand et al. [43] revealed that hypothyroidism induced by a chemical called propylthiouracil was able to induce a significant reduction in testicular weight [43]. In another study, administration of carbimazole at a dose of 1.35 mg/kg for 3 or 6 weeks resulted in the disorganisation of germinal cells, a decrease in the diameters of the seminiferous tubules and the height of testicular

tissue epithelium. This was associated with congestion of interstitial blood vessels and oedema [35]. This may be related to the increased blood endotoxins and the state of oxidative stress that lead to capillary destruction, exudation and apoptosis. This is in accordance with Jalilvand et al.'s [19] observation that hypothyroidism increases TUNEL-positive cells in the testis. Examination of the testes of rats treated with carbimazole and ALA showed improvement in tubular diameter and germinal epithelium thickness, and no change was seen in interstitial space regularity. Also, maintenance of tubular contour with nearly normal expression of androgen receptors, vimentin, and α -SMA was observed. These data are consistent with a previous result [5] which revealed that ALA works at two levels intracellular and extracellular (at cell membrane level). Thus, giving double protection and improving the pathology of testicular tissue with normal expression of different immune markers. Gawish [11] concluded that the ALA has an ameliorative role against toxicity induced by hypothyroidism. Also, Prathima et al. [32] reported that ALA acts as a potent antioxidant and can reverse the histological changes in the testicular tissue of adult rats induced by carbimazole. Androgen receptor expression in Sertoli cells was reduced due to the state of oxidative stress induced by admission of ethanol [17]. This agreed with the finding of this experiment in which androgen receptor expression was limited to certain interstitial cells with a decrease in the area per cent in the carbimazole group. The decrease in androgen receptor expression in Sertoli cells was prominent in all stages of spermatogenesis, especially stage IV–VIII. As reported by Horibe et al. [18], marked decrease in androgen receptor expression was evident in all stages of the spermatogenic cycle in the testes of rats treated with ethanol. Reduction in androgen receptor expression can affect the pattern of α -SMA expression [29]. In the current study α -SMA expression showed prominent thickening in the wall of blood vessels, which in turn increased the surface area percentage after carbimazole supplementation. On the other hand O'Hara and Smith [29] showed reduction in α -SMA expression following androgen receptor expression in transgenic mice. Also Gosteli-Peter et al. [12] mentioned that T3 increased dramatically α -SMA mRNA and protein accumulation. Vimentin can be considered as Sertoli cell marker. It is dependent on spermatocytes renewal and attachment to Sertoli cells which is altered by oxidative stress induced by busul-

phan [22]. This goes with the pattern noticed in this experiment regarding vimentin expression in the control group as well as the destruction in the apical segment of Sertoli cells with the scarce appearance of the basal segment in most of the tubule after carbimazole treatment. On the contrary, Zamoner et al. [44] mentioned that there was no change in vimentin expression by real time-quantitative polymerase chain reaction in the testis of hypothyroid rats; however, increase in its phosphorylation and its content in the cytoskeleton of the testis was observed. In the present study, administration of carbimazole (1.35 mg/kg) for a month resulted in a significant decline in serum levels of free T3, T4, testosterone and FSH while there was a significant increase in TSH and LH levels. These findings are consistent with those of Yousofvand et al. [43] who reported a significant reduction in serum levels of testosterone hormone induced by hypothyroidism, with non-significant changes in LH and FSH serum levels. Similarly, another study showed that rats with hypothyroidism presented with high serum levels of LH hormone. Also, there was a significant decline in total serum testosterone levels. These results highlighted the great role of thyroid hormones in the regulation of FSH biosynthesis [34]. Moreover, in hypothyroidism, the serum level of the LH hormone was increased, while serum level of testosterone was decreased [25]. The authors correlated these findings to the decrease in liver synthesis of sex hormone-binding globulin (SHBG) in a hypothyroid state. SHBG is accountable for the transfer of testosterone from the testis to brain tissue, where free testosterone is dissociated and crosses the blood-brain barrier, to induce negative feedback on LH biosynthesis and its secretion [26]. Propylthiouracil-induced hypothyroidism significantly decreased serum levels of both T3 and T4 while increasing TSH level [36]. To better understand the pathological effects of hypothyroidism on testicular tissues, the oxidant-antioxidant state was studied in the testicular tissues. It seems that hypothyroidism can induce a disruption in the thiol redox status of mitochondria, which resulted in testicular structural and functional abnormalities. Our data regarding these above-mentioned data showed a significant decrease in the GSH content in testicular tissue homogenate. There was also a decrease in sperm count and motility. However, a significant improvement in the level of GSH was recorded after ALA supplementation. This may aid in

confirmation of the antioxidant system failure in the testes of carbimazole-treated rats. The results also revealed that carbimazole-induced hypothyroidism was able to increase MDA contents in the testicular tissue. In contrast, a partial improvement was noted in the carbimazole + ALA group. The testes have a defence mechanism that is composed of the enzymatic and non-enzymatic antioxidant defence system, but its potential is limited. Furthermore, the testes contain a high amount of polyunsaturated fatty acids subjected to peroxidation by many oxidative radicals. In this regard, it has been proven that the production of high amounts of free radicals is harmful to sperm structure and function due to the bad effects on both the quality and quantity of DNA content of spermatozoa [7]. Taking into consideration these above-mentioned facts, the oxidative damage of testes tissue may play a main role in the obtained results of this study. The results obtained from previous reports indicated the alterations in thyroid hormone concentrations impaired mitochondrial GSH regulation mechanism, antioxidant defence mechanism, and their ratio to the functions of testes of adult rats [2]. On the other hand, the administration of ALA with carbimazole (1.35 mg/kg body weight) resulted in a significant increase in GSH level, increase in sperm number and motility while a significant decrease in MDA testicular level was noted when compared with the carbimazole group. In agreement with our results, ALA proved to be a potent factor to restore the deteriorated antioxidants in testicular rats exposed to cadmium [9].

CONCLUSIONS

Based on the obtained data, we can conclude that ALA as an antioxidant, can ameliorate the toxic effects of hypothyroidism on spermatogenesis and improved the structural and physiological processes in the testes of hypothyroidism-induced rats. Furthermore, it can protect testicular tissues against oxidative damage. One of the limitations which we faced was the inability to add *in situ* hybridisation as a confirmatory tool for our data.

Acknowledgements

The authors would like to thank the Zagazig Scientific and Medical Research Centre (ZSMRC) team for their support and permission for performing experimentation procedures in their laboratories.

REFERENCES

- Albus U. Guide for the Care and Use of Laboratory Animals (8th Ed). In Laboratory Animals. 2012.
- Asadi N, Bahmani M, Kheradmand A, et al. The impact of oxidative stress on testicular function and the role of anti-oxidants in improving it: a review. *J Clin Diagn Res.* 2017; 11(5): IE01–IE05, doi: [10.7860/JCDR/2017/23927.9886](https://doi.org/10.7860/JCDR/2017/23927.9886), indexed in Pubmed: [28658802](https://pubmed.ncbi.nlm.nih.gov/28658802/).
- Bancroft JD, Gamble M. Theory and practice of histological techniques. Elsevier Health Sciences. 2008.
- Bell CA. Clinical guide to laboratory tests. Norbert W Tietz (3rd edn). Transfusion. 1995; 35(11): 972.
- Cronan JE, Zhao X, Jiang Y. Function, attachment and synthesis of lipoic acid in *Escherichia coli*. *Adv Microb Physiol.* 2005; 50: 103–146, doi: [10.1016/S0065-2911\(05\)50003-1](https://doi.org/10.1016/S0065-2911(05)50003-1), indexed in Pubmed: [16221579](https://pubmed.ncbi.nlm.nih.gov/16221579/).
- Delitala AP, Capobianco G, Cherchi PL, et al. Thyroid function and thyroid disorders during pregnancy: a review and care pathway. *Arch Gynecol Obstet.* 2019; 299(2): 327–338, doi: [10.1007/s00404-018-5018-8](https://doi.org/10.1007/s00404-018-5018-8), indexed in Pubmed: [30569344](https://pubmed.ncbi.nlm.nih.gov/30569344/).
- Divakaruni AS, Wiley SE, Rogers GW, et al. Thiazolidinediones are acute, specific inhibitors of the mitochondrial pyruvate carrier. *Proc Natl Acad Sci U S A.* 2013; 110(14): 5422–5427, doi: [10.1073/pnas.1303360110](https://doi.org/10.1073/pnas.1303360110), indexed in Pubmed: [23513224](https://pubmed.ncbi.nlm.nih.gov/23513224/).
- El Hassani RA, Buffet C, Leboulleux S, et al. Oxidative stress in thyroid carcinomas: biological and clinical significance. *Endocr Relat Cancer.* 2019; 26(3): R131–R143, doi: [10.1530/ERC-18-0476](https://doi.org/10.1530/ERC-18-0476), indexed in Pubmed: [30615595](https://pubmed.ncbi.nlm.nih.gov/30615595/).
- El-Maraghy SA, Nassar NN. Modulatory effects of lipoic acid and selenium against cadmium-induced biochemical alterations in testicular steroidogenesis. *J Biochem Mol Toxicol.* 2011; 25(1): 15–25, doi: [10.1002/jbt.20354](https://doi.org/10.1002/jbt.20354), indexed in Pubmed: [20957662](https://pubmed.ncbi.nlm.nih.gov/20957662/).
- Gautam DK, Misro MM, Chaki SP, et al. H₂O₂ at physiological concentrations modulates Leydig cell function inducing oxidative stress and apoptosis. *Apoptosis.* 2006; 11(1): 39–46, doi: [10.1007/s10495-005-3087-1](https://doi.org/10.1007/s10495-005-3087-1), indexed in Pubmed: [16374549](https://pubmed.ncbi.nlm.nih.gov/16374549/).
- Gawish AM. The protective role of alpha lipoic acid against pesticides induced testicular toxicity- histopathological and histochemical studies. *J Aquaculture Res Development.* 2010; 1(1): 101, doi: [10.4172/2155-9546.1000101](https://doi.org/10.4172/2155-9546.1000101).
- Gosteli-Peter MA, Harder BA, Eppenberger HM, et al. Triiodothyronine induces over-expression of alpha-smooth muscle actin, restricts myofibrillar expansion and is permissive for the action of basic fibroblast growth factor and insulin-like growth factor I in adult rat cardiomyocytes. *J Clin Invest.* 1996; 98(8): 1737–1744, doi: [10.1172/JCI118972](https://doi.org/10.1172/JCI118972), indexed in Pubmed: [8878423](https://pubmed.ncbi.nlm.nih.gov/8878423/).
- Ha AeW, Kim WK. The effect of fucoxanthin rich power on the lipid metabolism in rats with a high fat diet. *Nutr Res Pract.* 2013; 7(4): 287–293, doi: [10.4162/nrp.2013.7.4.287](https://doi.org/10.4162/nrp.2013.7.4.287), indexed in Pubmed: [23964316](https://pubmed.ncbi.nlm.nih.gov/23964316/).
- Hernandez A, Martinez ME. Thyroid hormone action in the developing testis: intergenerational epigenetics. *J Endocrinol.* 2020; 244(3): R33–R46, doi: [10.1530/JOE-19-0550](https://doi.org/10.1530/JOE-19-0550), indexed in Pubmed: [31977317](https://pubmed.ncbi.nlm.nih.gov/31977317/).
- Hofstee P, McKeating DR, Bartho LA, et al. Maternal selenium deficiency in mice alters offspring glucose metabolism and thyroid status in a sexually dimorphic manner. *Nutrients.* 2020; 12(1): 267, doi: [10.3390/nu12010267](https://doi.org/10.3390/nu12010267), indexed in Pubmed: [31968625](https://pubmed.ncbi.nlm.nih.gov/31968625/).
- Holmquist L, Stuchbury G, Berbaum K, et al. Lipoic acid as a novel treatment for Alzheimer's disease and related dementias. *Pharmacol Ther.* 2007; 113(1): 154–164, doi: [10.1016/j.pharmthera.2006.07.001](https://doi.org/10.1016/j.pharmthera.2006.07.001), indexed in Pubmed: [16989905](https://pubmed.ncbi.nlm.nih.gov/16989905/).
- Horibe A, Eid N, Ito Y, et al. Upregulated autophagy in sertoli cells of ethanol-treated rats is associated with induction of inducible nitric oxide synthase (inos), androgen receptor suppression and germ cell apoptosis. *Int J Mol Sci.* 2017; 18(5), doi: [10.3390/ijms18051061](https://doi.org/10.3390/ijms18051061), indexed in Pubmed: [28505146](https://pubmed.ncbi.nlm.nih.gov/28505146/).
- Horibe A, Eid N, Ito Y, et al. Ethanol-Induced autophagy in sertoli cells is specifically marked at androgen-dependent stages of the spermatogenic cycle: potential mechanisms and implications. *Int J Mol Sci.* 2019; 20(1), doi: [10.3390/ijms20010184](https://doi.org/10.3390/ijms20010184), indexed in Pubmed: [30621351](https://pubmed.ncbi.nlm.nih.gov/30621351/).
- Jalilvand N, Hosseini M, Beheshti F, et al. Protective effect of PPAR γ agonist pioglitazone, on testicular tissue and sperm parameters in hypothyroid rats. *Toxin Reviews.* 2019; 24: 1–10, doi: [10.1080/15569543.2018.1564775](https://doi.org/10.1080/15569543.2018.1564775).
- Kamel A, Hamouli-Said Z. Neonatal exposure to T3 disrupts male reproductive functions by altering redox homeostasis in immature testis of rats. *Andrologia.* 2018; 50(9): e13082, doi: [10.1111/and.13082](https://doi.org/10.1111/and.13082), indexed in Pubmed: [29968296](https://pubmed.ncbi.nlm.nih.gov/29968296/).
- Karafakioğlu YS. Effects of α lipoic acid on noise induced oxidative stress in rats. *Saudi J Biol Sci.* 2019; 26(5): 989–994, doi: [10.1016/j.sjbs.2018.08.008](https://doi.org/10.1016/j.sjbs.2018.08.008), indexed in Pubmed: [31303830](https://pubmed.ncbi.nlm.nih.gov/31303830/).
- Kopecky M, Semecky V, Nachtigal P. Vimentin expression during altered spermatogenesis in rats. *Acta Histochem.* 2005; 107(4): 279–289, doi: [10.1016/j.acthis.2005.06.007](https://doi.org/10.1016/j.acthis.2005.06.007), indexed in Pubmed: [16139876](https://pubmed.ncbi.nlm.nih.gov/16139876/).
- Krassas GE, Markou KB. The impact of thyroid diseases starting from birth on reproductive function. *Hormones (Athens).* 2019; 18(4): 365–381, doi: [10.1007/s42000-019-00156-y](https://doi.org/10.1007/s42000-019-00156-y), indexed in Pubmed: [31734887](https://pubmed.ncbi.nlm.nih.gov/31734887/).
- Krysiak R, Szkróbka W, Okopień B. The impact of testosterone on metformin action on hypothalamic-pituitary-thyroid axis activity in men: a pilot study. *J Clin Pharmacol.* 2020; 60(2): 164–171, doi: [10.1002/jcph.1507](https://doi.org/10.1002/jcph.1507), indexed in Pubmed: [31389032](https://pubmed.ncbi.nlm.nih.gov/31389032/).
- Krytskyy T, Pasyechko N. Correction of androgen deficiency in men with hypothyroidism. *Georgian Med News.* 2019(286): 77–82, indexed in Pubmed: [30829594](https://pubmed.ncbi.nlm.nih.gov/30829594/).
- La Vignera S, Vita R, Condorelli RA, et al. Impact of thyroid disease on testicular function. *Endocrine.* 2017; 58(3): 397–407, doi: [10.1007/s12020-017-1303-8](https://doi.org/10.1007/s12020-017-1303-8), indexed in Pubmed: [28429281](https://pubmed.ncbi.nlm.nih.gov/28429281/).
- La Vignera S, Vita R. Thyroid dysfunction and semen quality. *Int J Immunopathol Pharmacol.* 2018; 32: 2058738418775241, doi: [10.1177/2058738418775241](https://doi.org/10.1177/2058738418775241), indexed in Pubmed: [29737216](https://pubmed.ncbi.nlm.nih.gov/29737216/).
- Naseem Z, Iqbal MA, Ahmad S, et al. Inflammatory markers as prognosticators of cardiovascular dysfunction in hypothyroid patients. *J Biol Regul Homeost Agents.* 2019; 33(6): 1891–1895, doi: [10.23812/19-334-L](https://doi.org/10.23812/19-334-L), indexed in Pubmed: [31823594](https://pubmed.ncbi.nlm.nih.gov/31823594/).

29. O'Hara L, Smith LB. Androgen receptor roles in spermatogenesis and infertility. *Best Pract Res Clin Endocrinol Metab.* 2015; 29(4): 595–605, doi: [10.1016/j.beem.2015.04.006](https://doi.org/10.1016/j.beem.2015.04.006), indexed in Pubmed: [26303086](https://pubmed.ncbi.nlm.nih.gov/26303086/).
30. Ohkawa H, Ohishi N, Yagi K. Assay for lipid peroxides in animal tissues by thiobarbituric acid reaction. *Anal Biochem.* 1979; 95(2): 351–358, doi: [10.1016/0003-2697\(79\)90738-3](https://doi.org/10.1016/0003-2697(79)90738-3), indexed in Pubmed: [36810](https://pubmed.ncbi.nlm.nih.gov/36810/).
31. Panait N, Michel F, D'Ercole C, et al. Esophageal atresia, small omphalocele and ileal prolapse through a patent omphalomesenteric duct: a methimazole embryopathy? [Corrected]. *J Pediatr Surg.* 2013; 48(6): E9–E11, doi: [10.1016/j.jpedsurg.2013.03.073](https://doi.org/10.1016/j.jpedsurg.2013.03.073), indexed in Pubmed: [23845657](https://pubmed.ncbi.nlm.nih.gov/23845657/).
32. Prathima P, Venkaiah K, Pavani R, et al. α -lipoic acid inhibits oxidative stress in testis and attenuates testicular toxicity in rats exposed to carbimazole during embryonic period. *Toxicol Rep.* 2017; 4: 373–381, doi: [10.1016/j.toxrep.2017.06.009](https://doi.org/10.1016/j.toxrep.2017.06.009), indexed in Pubmed: [28959662](https://pubmed.ncbi.nlm.nih.gov/28959662/).
33. Rebar RW, Morandini IC, Petze JE, et al. Hormonal basis of reproductive defects in athymic mice: reduced gonadotropins and testosterone in males. *Biol Reprod.* 1982; 27(5): 1267–1276, doi: [10.1095/biolreprod27.5.1267](https://doi.org/10.1095/biolreprod27.5.1267), indexed in Pubmed: [6819011](https://pubmed.ncbi.nlm.nih.gov/6819011/).
34. Romano RM, Bargi-Souza P, Brunetto EL, et al. Hypothyroidism in adult male rats alters posttranscriptional mechanisms of luteinizing hormone biosynthesis. *Thyroid.* 2013; 23(4): 497–505, doi: [10.1089/thy.2011.0514](https://doi.org/10.1089/thy.2011.0514), indexed in Pubmed: [23240964](https://pubmed.ncbi.nlm.nih.gov/23240964/).
35. Sakr SR, ELnaby SH, Okdah Y, et al. Impact of ginger aqueous extract on carbimazole induced testicular degenerative alterations and oxidative stress in albino rats. *J Coastal Life Med.* 2017; 5(4): 167–173, doi: [10.12980/jclm.5.2017j6-219](https://doi.org/10.12980/jclm.5.2017j6-219).
36. Saha I, Chakraborty SB, Chatterjee A, et al. Arecoline inhibits pineal-testis function in experimentally induced hypothyroid rats. *Arch Physiol Biochem.* 2020; 126(1): 7–16, doi: [10.1080/13813455.2018.1486428](https://doi.org/10.1080/13813455.2018.1486428), indexed in Pubmed: [30145920](https://pubmed.ncbi.nlm.nih.gov/30145920/).
37. Schlorff EC, Husain K, Somani SM. Dose and time dependent effects of ethanol on antioxidant system in rat testes. *Alcohol.* 1999; 18(2-3): 203–214, doi: [10.1016/s0741-8329\(99\)00004-x](https://doi.org/10.1016/s0741-8329(99)00004-x), indexed in Pubmed: [10456572](https://pubmed.ncbi.nlm.nih.gov/10456572/).
38. Sedlak J, Lindsay RH. Estimation of total, protein-bound, and nonprotein sulfhydryl groups in tissue with Ellman's reagent. *Anal Biochem.* 1968; 25(1): 192–205, doi: [10.1016/0003-2697\(68\)90092-4](https://doi.org/10.1016/0003-2697(68)90092-4), indexed in Pubmed: [4973948](https://pubmed.ncbi.nlm.nih.gov/4973948/).
39. Shalaby AM, Ibrahim MA, Aboregela AM. Effect of aspartame on the placenta of adult albino rat. A histological and immunohistochemical study. *Ann Anat.* 2019; 224: 133–141, doi: [10.1016/j.aanat.2019.04.007](https://doi.org/10.1016/j.aanat.2019.04.007), indexed in Pubmed: [31108189](https://pubmed.ncbi.nlm.nih.gov/31108189/).
40. Sharpe RM. Environmental/lifestyle effects on spermatogenesis. *Philos Trans R Soc Lond B Biol Sci.* 2010; 365(1546): 1697–1712, doi: [10.1098/rstb.2009.0206](https://doi.org/10.1098/rstb.2009.0206), indexed in Pubmed: [20403879](https://pubmed.ncbi.nlm.nih.gov/20403879/).
41. Tutelyan VA, Makhova AA, Pogozheva AV, et al. [Lipoic acid: physiological role and prospects for clinical application]. *Vopr Pitan.* 2019; 88(4): 6–11, doi: [10.24411/0042-8833-2019-10035](https://doi.org/10.24411/0042-8833-2019-10035), indexed in Pubmed: [31722135](https://pubmed.ncbi.nlm.nih.gov/31722135/).
42. Xiang W, Wang Li, Cheng S, et al. Protective effects of α -lipoic acid on vascular oxidative stress in rats with hyperuricemia. *Curr Med Sci.* 2019; 39(6): 920–928, doi: [10.1007/s11596-019-2124-1](https://doi.org/10.1007/s11596-019-2124-1), indexed in Pubmed: [31845223](https://pubmed.ncbi.nlm.nih.gov/31845223/).
43. Yousofvand N, Kazemi M, Mohammadizadeh E. Effect of induced hypothyroidism by propiltiouracil (PTU) on serum levels of testosterone, luteinizing hormone, follicle stimulating hormone in adult rat. *Scientific J Ilam University Med Sci.* 2013; 21(6): 1–8.
44. Zamoner A, Barreto KP, Filho DW, et al. Propylthiouracil-induced congenital hypothyroidism upregulates vimentin phosphorylation and depletes antioxidant defenses in immature rat testis. *J Mol Endocrinol.* 2008; 40(3): 125–135, doi: [10.1677/JME-07-0089](https://doi.org/10.1677/JME-07-0089), indexed in Pubmed: [18316471](https://pubmed.ncbi.nlm.nih.gov/18316471/).

Protective effect of *Coriandrum sativum* extract against inflammation and apoptosis in liver ischaemia/reperfusion injury

A. Kükner¹, G. Söyler², P. Toros¹, G. Dede³, F. Meriçli⁴, S. Işık⁵, O. Edebal⁶, C. Özoğul⁷

¹Department of Histology and Embryology, Faculty of Medicine, Near East University, Nicosia, Cyprus

²Koç University, Graduate School of Health Sciences and School of Medicine, Istanbul, Turkey

³Department of Histology and Embryology, Faculty of Medicine, Abant İzzet Baysal University, Bolu, Turkey

⁴Department of Phytotherapy, Faculty of Pharmacy, Near East University, Nicosia, Cyprus

⁵Department of Analytic Chemistry, Faculty of Pharmacy, Near East University, Nicosia, Cyprus

⁶Department of Biochemistry, Medical Hospital, Near East University, Nicosia, Cyprus

⁷Department of Histology and Embryology, Faculty of Medicine, Girne University, Kyrenia, Cyprus

[Received: 6 April 2020; Accepted: 13 May 2020]

Background: The aim of this study was to investigate the anti-inflammatory and antioxidant effects of *Coriandrum sativum* extract on liver ischaemia reperfusion injury at light microscopic and biochemical levels.

Materials and methods: Sham, ischaemia/reperfusion injury (IRI), IRI + *Coriandrum sativum* extract and only *Coriandrum sativum* extract groups were formed. Sixty minutes of ischaemia and 60 minutes of reperfusion were performed. In the treatment group, 300 mg/kg/day *Coriandrum sativum* was given by gavage. Hepatic tissues were fixed in 4% paraformaldehyde. Serum alanine aminotransferase (ALT), aspartate aminotransferase (AST) and alkaline phosphatase (ALP) enzymes were measured. Nuclear factor-kappa beta (NF-κB), tumour necrosis factor-alpha (TNF-α) and caspase-3 immunohistochemistry staining was performed. Microscopic scoring was performed in terms of sinusoidal congestion, vacuolisation, and necrosis.

Results: Sinusoidal enlargement and diffuse congestion, Kupffer cell increase, neutrophil increase in necrotic areas, vacuolisation in hepatocytes, and bile duct proliferation in the portal triad were observed in ischaemia/reperfusion hepatic tissue. Very rare, necrotic areas were observed in the *Coriandrum sativum* treatment group, while congestion and vacuolisation and bile duct proliferation were decreased compared to the ischaemic group. The AST and ALT levels were increased in the IRI and IRI + *Coriandrum sativum* groups. When compared to the IRI group, the AST and ALT levels of the *Coriandrum sativum* were considerably decreased. The IRI and IRI + *Coriandrum sativum* groups had statistically significant differences in ALP compared to that of the *Coriandrum sativum* and Sham groups. There was no significant difference between the ALP levels of the IRI and IRI + *Coriandrum sativum* groups. TNF-α, NF-κB and caspase-3 immune positive stained hepatocytes were numerous and widely observed in the injury group. There were positive TNF-α immunohistochemical staining Kupffer cells in the IRI group. In the group treated with *Coriandrum sativum*, Kupffer cells were

Address for correspondence: Prof. A. Kükner, MD, Near East University, Medicine Faculty, Histology and Embryology Department, 99138, Nicosia, Cyprus, tel: +90 533 873 4460 (Mobile); +90 392 675 1000, ext 3012 (Office), e-mail: akukner@hotmail.com

This article is available in open access under Creative Common Attribution-Non-Commercial-No Derivatives 4.0 International (CC BY-NC-ND 4.0) license, allowing to download articles and share them with others as long as they credit the authors and the publisher, but without permission to change them in any way or use them commercially.

not stained, while TNF- α , NF- κ B and caspase-3 expressing hepatocytes were found to be decreased compared to the IRI group. When the expression values of the TNF- α , NF- κ B and caspase-3 groups were evaluated statistically, it was seen that there was a significant decrease in the group treated with *Coriandrum sativum*. **Conclusions:** It was found that *Coriandrum sativum* extract decreased proinflammatory cytokine TNF- α and apoptotic cell death and liver enzymes in liver ischaemia/reperfusion injury. (Folia Morphol 2021; 80, 2: 363–371)

Key words: liver ischaemia, *Coriandrum sativum*, nuclear factor-kappa beta, tumour necrosis factor-alpha, caspase-3

INTRODUCTION

Liver ischaemia/reperfusion injury (IRI) is a clinical problem that increases morbidity and mortality after trauma, hepatectomy or liver transplantation [13, 14]. The ischaemic period is described as a blockage of oxygen and nutrient transportations which, in turn, obstructs the cellular metabolism. Once the blood supply is restored by reperfusion, the sudden increase in the blood flow to the tissue increases the concentration of the free oxygen radicals and results in inflammatory cell infiltration at the site of the damage [14, 22]. The acute phase of the reperfusion lasts between three to 6 hours. During this time, T-cell and Kupffer cell activation as well as the activation of adhesion molecules are increased. The late (subacute) phase is 18 to 24th h of reperfusion, and neutrophil infiltration reaches its peak level during this time. The activated Kupffer cells and other hepatic cells also initiate secretion of inflammatory mediators, such as tumour necrosis factor-alpha (TNF- α), interleukin 6 (IL-6), increasing the expression levels of intercellular adhesion molecule (ICAM), vascular cell adhesion protein (VCAM) and P-selectins [10, 27]. TNF- α expression is regulated by nuclear factor kappa beta (NF- κ B). NF- κ B is a transcription factor that plays an important role in liver ischaemia reperfusion damage, inflammation response, and the protection and regeneration of hepatocytes [33]. Hepatic apoptosis is directly proportional to the severity of IRI [5, 6]. Necrotic cell death in hepatic cells with apoptosis may also occur [35]. The pathophysiology of IRI has numerous determinative factors and it is essential to understand and identify these factors to develop new therapeutic strategies in preventive medicine [14]. *Coriandrum sativum* is an important medicinal plant that originated in the Eastern Mediterranean and subsequently spread to India, China and is now cultivated all over the world. *Coriandrum sativum*

is frequently used in medicines, natural treatment, and the food preservative industry [16, 18, 26, 29]. To the best of the authors' knowledge, this is the first study to extensively investigate the biochemical and anti-inflammation and antiapoptotic effects of *Coriandrum sativum* use on hepatic ischaemia reperfusion in a rat model. The aim of this study was to investigate the biochemical and microscopic effects of methanol extract of *Coriandrum sativum* on liver ischaemic reperfusion injuries in rats.

MATERIALS AND METHODS

Plant material and extraction

Leaves of *Coriandrum sativum* were collected from the Alayköy region in North Cyprus and then dried. Dried leaves were extracted with methanol using the maceration method and the extract was evaporated. According to the HPLC analysis (realised using Agilent Technologies 1200 series HPLC and separated with Eclipse XDB-C18 column, 150 mm \times 4.6 mm, 5 μ m). As mobile phases, (A): water with 0.5% formic acid and (B): methanol were used at a flow rate of 1 mL/min. The gradient was initially 90–70% A for 18 min, then 55–80% A for 5 min and finally, 90% A for 5 min. The detection wavelength was set at 254 nm. The injection volume was 10 μ L for each sample and standard solutions, and according to the results of data validation, the percentage of isoquercitrin was found to contain 139.25 ppm (0.21%).

Animals and experimental design

All experimental protocols were performed according to the Guide for Care and Use of Laboratory Animals and were approved by the Animal Care and Use Local Ethics Committee of Near East University (2019/01-57). Six–seven months female Wistar Albino rats (450–500 g weight) were housed at a constant room temperature (22 \pm 2°C) under a 12-h

light/dark cycle. They were fed standard rat chow (210 kcal/100 g/day) and drank tap water ad libitum. All surgical interventions were performed between 9:00 am and 12:00 pm to minimise diurnal effects.

Animals were randomly divided into four groups:

- Sham group (n = 10): A midline incision was made, and the hepatic pedicle (contains ductus hepaticus, hepatic portal vein and proper hepatic artery) was mobilised. No blood supply blocked;
- Ischaemia/reperfusion injury (IRI) group (n = 10): Ischaemia was achieved by clamping the hepatic pedicle with a vascular clamp for 1 hour after the ischaemic period, the clamp was opened and 1 hour reperfusion of the liver was provided;
- IRI + *Coriandrum sativum* group (n = 10): *Coriandrum sativum* extract was given by gavage 300 mg/kg/day for 3 days before ischaemia and 1 hour before ischaemia [24];
- *Coriandrum sativum* group (n = 10): *Coriandrum sativum* extract was given by gavage 300 mg/kg/day for 3 days.

Ischaemia/reperfusion

All animals were given ketamine HCl 90 mg/kg (Ketalar R, Pfizer Drug Company, Istanbul, Turkey) + xylazine hydrochloride 10 mg/kg (Rompun R 23.32 mg/mL, Bayer Drug Company, Istanbul, Turkey) after 15 hours fasting. The animals were placed on the operating table in the supine position, immobilised at four points, and a midline abdominal laparotomy was performed to expose the abdominal cavity. Hepatic IRI was performed by Pringle manoeuvre. After detaching of liver from the ligaments and hepatic pedicle (ductus hepaticus, hepatic portal vein and proper hepatic artery) was clamped with an atraumatic microvascular clamp and hepatic ischaemia in the lobus hepatis mediana and lobus hepatis sinister. After 60 minutes of ischaemia, the clamp was removed and 1 mL NaCl 0.9% was administered intraperitoneally, then the abdomen was closed and we waited 1 hour for reperfusion [2]. The other hepatic lobes had taken whole portal and arterial blood supply. Colour change appeared in the ischaemic lobes; however, the colour of the lobes returned to normal in reperfusion. Rats were kept on heated tables during ischaemia and reperfusion. In IRI and IRI + *Coriandrum sativum* groups, rats were under anaesthesia for 60 minutes with reperfusion duration and no substance was given. At the end of the reperfusion

period, blood was taken from the hearts of the rats and euthanased with the exsanguination method. Tissue samples were taken from the reperfused lobus hepatis sinister for histological examinations. Rats in Sham and *Coriandrum sativum* groups were euthanased by the same method and tissue samples were taken from lobus hepatis sinister. During the reperfusion period, 3 rats from the IRI group and 2 rats from the IRI + *Coriandrum sativum* group died.

Blood sample analyses

Serum alanine aminotransferase (ALT), aspartate aminotransferase (AST) and alkaline phosphatase (ALP) measurements were made by using an Abbott Architect c8000 clinical chemistry analyser (Abbott Instruments–Abbott Diagnostics, Abbott Park, IL, A.B.D.).

Light microscopy

All rats were euthanased, and tissue samples were fixed in paraformaldehyde 4% for 48 hours, embedded in paraffin, and cut into 5 μ m sections. Haematoxylin and eosin staining was carried out to assess the general structure of the liver. Tissue sections were examined, with 10 fields per section, and scored from 0 to 4 for vacuolisation, sinusoidal congestion, and hepatocyte necrosis, which were evaluated semi-quantitatively according to the modified Suzuki scoring system [32].

Immunohistochemical staining

Immunohistochemical evaluation of the hepatic tissue samples were performed by the following stains: caspase-3 (anti-caspase-3 antibody, ab 2302, Abcam), TNF- α (anti-TNF- α antibody, ab183896, Abcam), NF- κ B p65 (anti-NF- κ B p65 antibody, ChIP Grade ab7970, Abcam). The cells stained positively with caspase-3, TNF- α and NF- κ B were counted in a light microscope with a magnification of 40 \times in 20 different areas.

Statistical analyses

All the statistical analyses were performed with SPSS 17.0. Data obtained from the groups were compared using the non-parametric Kruskal-Wallis test within each group, whereas the groups were compared with each other using the Mann-Whitney U test. A value of $p < 0.05$ was considered to be statistically significant.

Table 1. The mean values of liver enzymes in groups

	ALT	AST	ALP
Sham	36.33 ± 10.19 ^a	74.00 ± 14.93 ^a	46.50 ± 10.21
<i>Coriandrum sativum</i>	39.33 ± 3.77 ^b	73.17 ± 17.75 ^b	54.50 ± 9.57
IRI	1297.50 ± 357.30 ^c	1127.83 ± 177.09 ^c	71.67 ± 22.38 ^a
IRI + <i>Coriandrum sativum</i>	801.83 ± 241.86 ^c	765.17 ± 242.87 ^c	66.33 ± 14.71 ^a
P value	0.000*	0.000*	0.048*

*Kruskal-Wallis test significant value $p < 0.05$; ^{ab}Significance according to Mann-Whitney U test ($p < 0.05$); ^aSignificance between Sham group and IRI, IRI + *Coriandrum sativum*; ^bSignificance between *Coriandrum sativum* group and IRI, IRI + *Coriandrum sativum*; ^cSignificance between IRI group and IRI + *Coriandrum sativum*; IRI — ischaemia/reperfusion injury; ALT — alanine aminotransferase; AST — aspartate aminotransferase; ALP — alkaline phosphatase

Table 2. Injury scoring in groups

	Congestion	Vacuolisation	Necrosis
Sham	0.00 ± 0.00 ^a	0.00 ± 0.00 ^a	0.00 ± 0.00 ^a
<i>Coriandrum sativum</i>	0.17 ± 0.41 ^b	0.00 ± 0.00 ^b	0.00 ± 0.00 ^b
IRI	2.33 ± 0.82 ^{abc}	1.50 ± 0.55 ^{abc}	0.67 ± 0.52 ^{abc}
IRI + <i>Coriandrum sativum</i>	0.83 ± 0.75 ^c	0.33 ± 0.52 ^c	0.17 ± 0.41 ^c
P value	0.001*	0.000*	0.000*

*Kruskal-Wallis test significant value $p < 0.05$; ^{ab}Significance according to Mann-Whitney U test ($p < 0.05$); ^aSignificance between Sham group and IRI group; ^bSignificance between *Coriandrum sativum* group and IRI group; ^cSignificance between IRI + *Coriandrum sativum* and IRI group; IRI — ischaemia/reperfusion injury

RESULTS

Biochemical results

The AST and ALT levels were increased in the IRI and IRI + *Coriandrum sativum* groups. When compared to the IRI group, the AST and ALT levels of the *Coriandrum sativum* were considerably decreased. The IRI and IRI + *Coriandrum sativum* groups had statistically significant differences in ALP compared to that of the *Coriandrum sativum* and Sham groups. There was no significant difference between the ALP levels of the IRI and IRI + *Coriandrum sativum* groups (Table 1).

Light microscopic results

Congestion, vacuolisation, and necrosis were observed to be considerably higher in the IRI group when compared with the results of the Sham and *Coriandrum sativum* groups. The IRI + *Coriandrum sativum* group showed decreased congestion, vacuolisation, and necrosis. Nevertheless, the levels were still higher than those of the Sham and IRI groups (Table 2). Compared to the Sham group (Fig. 1A), dilatation and congestion of sinusoids (Fig. 1B), increased number of Kupffer cells (Fig. 1C), necrotic areas with hepatocyte degeneration and increased number of neutrophils (Fig. 1D), vacuolisation of hepatocytes especially around the portal triads (Fig. 1E), and proliferation of the bile ducts (Fig. 1F) were confirmed in the IRI group. The IRI + *Coriandrum sa-*

tivum group showed decreased congestion (Fig. 1G), decreased Kupffer cell activation and, although lessened, a still discernible proliferation of the bile ducts (Fig. 1H). TNF- α , NF- κ B and caspase-3 expressions were very common and there was strong expression in hepatocytes in the IRI group compared to the sham groups. It was observed that there was no TNF- α , NF- κ B and caspase-3 immunohistochemical staining in the liver sham group (Fig. 2A), but there were positive TNF- α immunohistochemical staining Kupffer cells (Fig. 2B) and hepatocytes (Fig. 2C) in the IRI group. In the group treated with *Coriandrum sativum*, Kupffer cells were not stained, while TNF- α expressing hepatocytes were found to be decreased compared to the IRI group (Fig. 2D). It was found that there was NF- κ B staining in the IRI group (Fig. 2E). The severity of immunohistochemical staining and number of stained cells decreased in the group treated with *Coriandrum sativum* (Fig. 2F). It was observed that many hepatocytes were expressed caspase-3 in the IRI group (Fig. 2G), and the caspase-3 expression was very low in the *Coriandrum sativum* treatment group (Fig. 2H). When the expression values of the TNF- α , NF- κ B and caspase-3 groups were evaluated statistically, it was seen that there was a significant decrease in the group treated with *Coriandrum sativum*, in which the expressions increased in the IRI group. These results were positive correlated with the microscopic findings (Table 3).

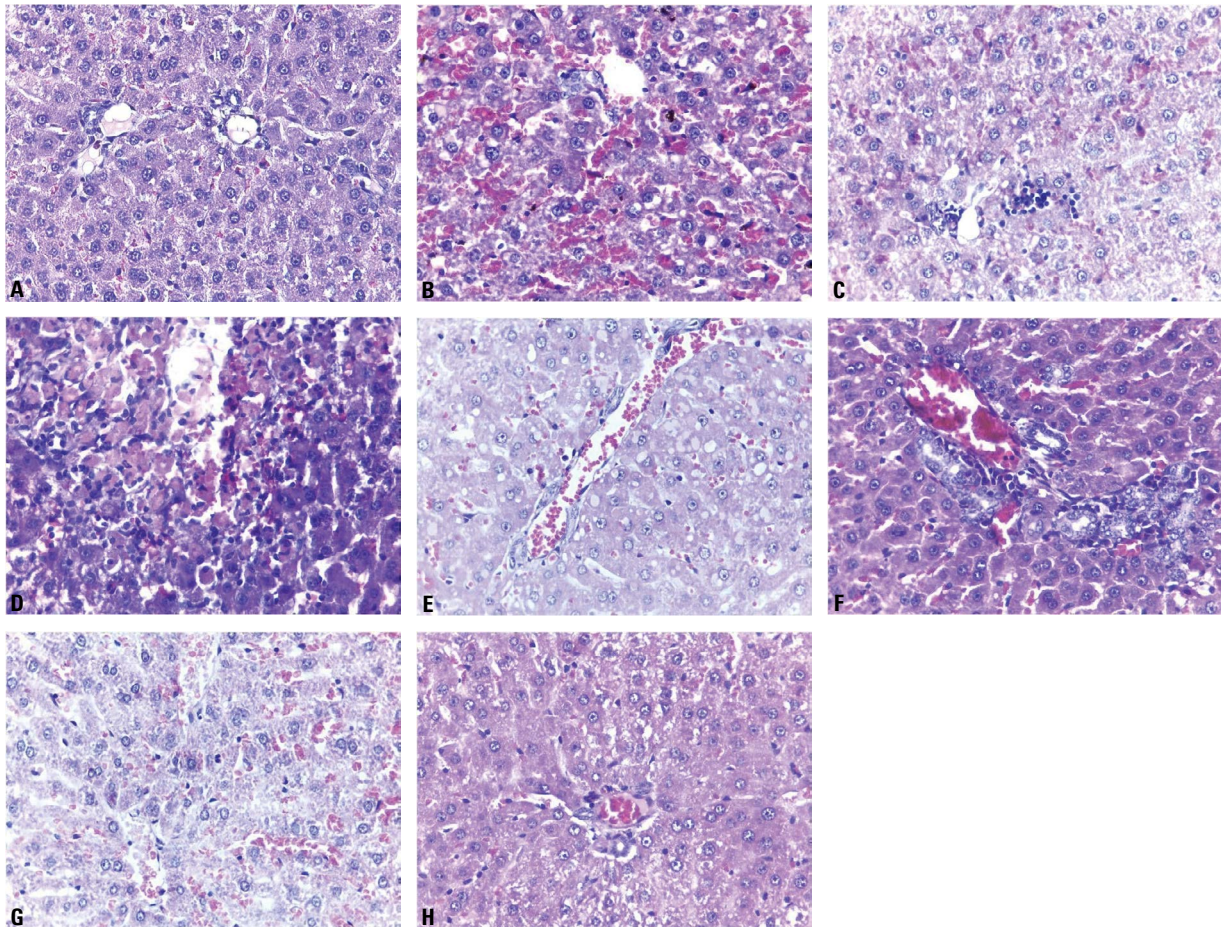


Figure 1. Liver tissue in experimental groups. **A.** Sham group. Dilatation of sinusoids, congestion (**B**), increased Kupffer cells (**C**), necrotic area and increased neutrophil number (**D**), vacuolisation in hepatocytes around the portal triads (**E**) and bile duct proliferation are observed in ischaemia/reperfusion injury (IRI) group (**F**). Congestion is less common than IRI group, when vacuolisation is not common (**G**), and bile duct proliferation continues to exist in portal triads as decreased (**H**) in *Coriandrum sativum* treated IRI group. Haematoxylin and eosin $\times 40$.

DISCUSSION

The results obtained throughout this study indicate that *Coriandrum sativum* has therapeutic effects on the histological and biochemical outcomes of liver IRI during the acute phase. During liver transplantations or surgeries, IRI can have a negative impact on regeneration. Many different factors can trigger this, and one of them is the duration of the ischaemic period [3]. The preventive or therapeutic effects of various plant extracts or components in IRI have been studied. The blockage of endothelial adhesion molecules, reduction of cytokines released from cells, free oxygen radicals and hepatocyte apoptosis have been discussed [1]. The *Coriandrum sativum* plant has antioxidant and anti-inflammatory effects and the protective effect of *Coriandrum sativum* on liver damage caused by various hepatotoxic substances has been reported [20, 21, 24, 30]. Studies have shown that *Coriandrum sativum* extract dosage

is not toxic up to 3000 mg/kg [25]. In our study, we have identified the anti-inflammatory effect of *Coriandrum sativum* sourced from the Cyprus-Nicosia region at low doses in rats treated with 300 mg/kg. It has been determined that *Coriandrum sativum* extract obtained from this region contains 139.25 ppm isoquercitrin as the active substance. Isoquercitrin (quercetin-3-O- β -D-glucopyranoside) is one of the major glycosidic forms of quercetin and is commonly found in many medicinal plants. It has antioxidant, anti-inflammatory, antiapoptotic effects [17]. It is the major bioactive component of the Coriander (*Coriandrum sativum* L.) and is commonly found in coriander leaves and roots. In recent years, isoquercitrin has a great potential due to the discovery of new biological activities and its ability to be obtained by enzymatic modification of rutin [34].

Upon reperfusion injury during the first few hours, Kupffer cells are activated and they release cytokines.

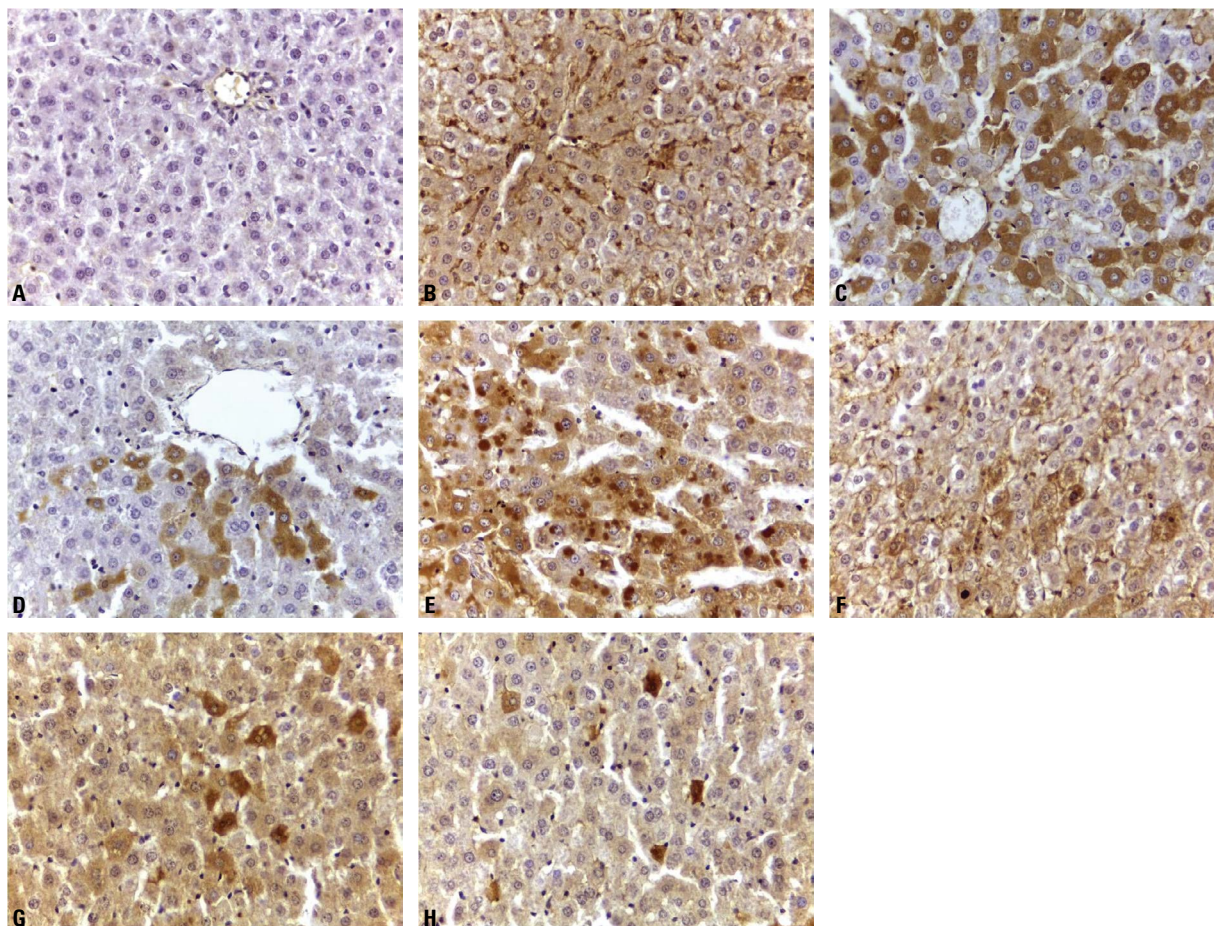


Figure 2. Tumour necrosis factor-alpha (TNF- α), nuclear factor-kappa beta (NF- κ B) and caspase-3 were negative in the immunohistochemical stained liver tissue belonging to Sham group (A). It appears to be TNF- α positive in Kupffer cells (B) and hepatocytes (C) in the ischaemia/reperfusion injury (IRI) group. In the *Coriandrum sativum* treated IRI group, there is no staining in Kupffer cells and it is observed that hepatocytes expressing TNF- α are decreased compared to IRI group (D). Commonly in hepatocytes NF- κ B expression appears to be positive in the IRI group (E). The severity of NF- κ B immunohistochemical staining and the number of stained cells decreased in the *Coriandrum sativum* treated IRI group (F). Caspase-3 is expressed in a large number of hepatocytes in the IRI group (G), it is seen that the number of immune positive hepatocytes decreased in the *Coriandrum sativum* treated IRI group (H). TNF- α , NF- κ B and caspase-3 immunohistochemistry staining $\times 40$.

Table 3. Nuclear factor-kappa beta (NF- κ B), tumour necrosis factor-alpha (TNF- α) and caspase-3 expression in groups

	TNF- α	NF- κ B	Caspase-3
Sham	0.05 \pm 0.21 ^{ab}	0.00 \pm 0.00 ^{ab}	0.00 \pm 0.00 ^{ab}
<i>Coriandrum sativum</i>	0.10 \pm 0.31 ^{cd}	0.10 \pm 0.31 ^{cd}	0.05 \pm 0.22 ^{cd}
IRI	11.05 \pm 2.82 ^{bc}	10.45 \pm 3.35 ^{bc}	5.30 \pm 2.60 ^{bc}
IRI + <i>Coriandrum sativum</i>	2.65 \pm 1.76 ^{bde}	5.20 \pm 2.59 ^{bde}	1.35 \pm 0.49 ^{bde}
P value	0.000*	0.000*	0.000*

*Kruskal-Wallis test significant value $p < 0.05$. ^{abcd}Significance according to Mann-Whitney U test ($p < 0.05$); ^aSignificance between Sham group and IRI group; ^bSignificance between Sham group and IRI + *Coriandrum sativum* group; ^cSignificance between *Coriandrum sativum* group and IRI group; ^dSignificance between *Coriandrum sativum* group and IRI + *Coriandrum sativum* group; ^eSignificance between IRI group and IRI + *Coriandrum sativum* group; IRI — ischaemia/reperfusion injury

There is a positive correlation between Kupffer cell activation and liver IRI [9, 11]. On the other hand, neutrophils play the main role in the stimulation process of the inflammatory cascade mechanisms [7]. During reperfusion, selectin receptors on the endothelial cells increase in number; leukocytes adhere

to the endothelial cells and then migrate to the site of the injury [9, 22]. Nuclear pyknosis of hepatocytes, scattering of the hepatic cords and hepatic sinusoid dilation can be observed. It was observed that diffuse local necrosis in reperfusion, vacuolisation in hepatocytes and inflammatory cell increase were significantly

increased; these findings decreased on the 3rd day and decreased to the minimal level on the 7th day [9]. Although the cause of hepatocyte fats due to IRI is not fully understood, may be multifactorial and involve both parenchymal and nonparenchymal dysfunction, a large amount of lipid accumulation occurs in hepatocytes due to metabolic changes in ischaemia during the reperfusion stage. Intracellular triglycerides accumulate due to deterioration of hepatocyte metabolism and vacuolisation is observed on a light microscope [28]. The presence of steatosis is associated with an increased mortality risk between 2% and 14%, following liver resection surgery [19].

In our study, congestion of sinusoids was very prominent and widespread in the IRI group. Areas of necrosis were not common but numerous necrotic hepatocytes and vacuolisation were detected. Bile duct proliferation in portal areas was detected as a result of ligation of the bile duct in the hepatic pedicle. In the IRI + *Coriandrum sativum* group, there were a few mitotic hepatocytes around the portal area. Kupffer cell activation was observed in fewer areas. Decrease in the Kupffer cells affected metabolic changes and the necrotic hepatocyte count. In addition, the decreased vacuolisation due to lipid accumulation in the hepatocytes in the treatment group depends on the hypolipidaemic effect of *Coriandrum sativum*.

Tumour necrosis factor-alpha is the primary inflammatory cytokine secreted from Kupffer cells in ischaemia/reperfusion injuries. TNF- α and NF- κ B levels increase significantly in the reperfusion stage after ischaemia. Excessive increase of TNF- α activity in ischaemia and reperfusion injuries stimulates cell death or apoptosis by direct toxic effects on the mitochondria [8, 36]. NF- κ B is thought to act as a proinflammatory. Therefore, inhibition of NF- κ B is expected to suppress the inflammatory response [15, 27]. The expression of NF- κ B was seen in the hepatocyte cytoplasm after warm ischaemia (35–37°C); there was no nuclear staining [15]. Our study results are compatible with the literature. A positive correlation was observed between increased TNF- α expression and increased NF- κ B expression in the IRI group. In IRI group, the increase in neutrophils is very evident. It was determined that inflammation markers and inflammation decreased in the group treated with *Coriandrum sativum*. In the *Coriandrum sativum* group, NF- κ B reduction was significantly detected in hepatocytes and Kupffer cells due to decreased TNF- α expression. As our experimental model is a warm ischaemia model,

NF- κ B staining was seen in hepatocyte cytoplasm. In addition to inflammation in liver ischaemia reperfusion injuries, apoptotic cell death and necrosis are observed in hepatocytes [4, 12]. In our study, both necrotic and apoptotic cell death were observed. It was determined that the number of apoptotic and necrotic cells decreased in the *Coriandrum sativum* treatment group, and this was due to decreased neutrophil caused by the anti-inflammatory effect of *Coriandrum sativum*.

In ischaemia/reperfusion studies, AST and ALT values increased in IRI [23, 24, 31]. AST and ALT levels were significantly increased in the ischaemic group and decreased in the *Coriandrum sativum* treated group but did not reach the control level in our study. In the ALP level, no significant difference was observed between IRI and IRI + *Coriandrum sativum* groups. One of the main causes of the ALP increase is bile duct obstruction and proliferation. While bile duct proliferation was common in portal triads in IRI, proliferation was found to be less in the IRI + *Coriandrum sativum* group. This result explained the high ALP level.

There is a complex series of complicated events involving parenchymal and non-parenchymal cells in hepatic IR injuries resulting from trauma, cancer surgery, and transplantation. The levels of TNF- α and NF- κ B, inflammatory factors, increase and NF- κ B causes an increase in inflammation-associated cell adhesion molecules, cytokines, anti-apoptotic and pro-apoptotic proteins. Therefore, it is very important to prevent inflammation to prevent and/or reduce ischaemia reperfusion damage. Our aim, in this study, was to investigate the possible protective effect of *Coriandrum sativum* against hepatic IRI-induced inflammation, oxidative stress, apoptosis, and hyperlipidaemia in the hepatic tissue. In the acute phase, 300 mg/kg *Coriandrum sativum* was used to reduce the damage, decrease liver enzymes, inflammation, and apoptosis. The hepatoprotective effect of *Coriandrum sativum* could be partly due to inhibition of the expression of pro-inflammatory cytokines. Anti-inflammatory and anti-apoptotic effect of *Coriandrum sativum* was demonstrated immunohistochemically. In addition, lipid accumulation in the hepatocytes of the group treated with *Coriandrum sativum*, vacuolisation decreased. This finding was an indication of the anti-lipidaemic effect of *Coriandrum sativum*. Isoquercetin, the active ingredient in *Coriandrum sativum* extract, is thought to play an important role. According

to the literature review, no previous study has used *Coriandrum sativum* against liver ischaemia reperfusion injuries. To the best of the authors' knowledge, this is the first time such data has been provided.

Limitations of the study

The limitation of the study is the absence of oxidative stress data. Also, showing protein expressions with Western blotting method will strengthen our study results. Increasing the dose used and prolonged use before ischaemia, prolonging the reperfusion period and continuing *Coriandrum sativum* use will provide more effective results. Study of the effects of *Coriandrum sativum* on other cytokines at a molecular level will increase the knowledge on this subject. These study results will be the source of the studies to be done with *Coriandrum sativum*. In particular, the antioxidant effect of a certain amount of *Coriandrum sativum* consumed in daily life will prevent or delay the emergence of some diseases.

CONCLUSIONS

It was found that *Coriandrum sativum* extract decreased proinflammatory cytokine TNF- α , apoptotic cell death and liver enzymes in liver ischaemia/reperfusion injury.

REFERENCES

1. Aćimović M, Milić N. Perspectives of the apiaceae hepatoprotective effects: a review. *Nat Prod Commun.* 2017; 12(2): 1934578X1701200, doi: [10.1177/1934578x1701200241](https://doi.org/10.1177/1934578x1701200241).
2. Barlas AM, Kismet K, Erel S, et al. Erdosteine ameliorates the harmful effects of ischemia-reperfusion injury on the liver of rats. *Acta Cir Bras.* 2017; 32(10): 796–806, doi: [10.1590/s0102-865020170100000001](https://doi.org/10.1590/s0102-865020170100000001), indexed in Pubmed: [29160366](https://pubmed.ncbi.nlm.nih.gov/29160366/).
3. Casillas-Ramírez A, Mosbah IB, Ramalho F, et al. Past and future approaches to ischemia-reperfusion lesion associated with liver transplantation. *Life Sci.* 2006; 79(20): 1881–1894, doi: [10.1016/j.lfs.2006.06.024](https://doi.org/10.1016/j.lfs.2006.06.024), indexed in Pubmed: [16828807](https://pubmed.ncbi.nlm.nih.gov/16828807/).
4. Chattopadhyay P, Shukla G, Wahi AK. Protective effect of L-arginine against necrosis and apoptosis induced by experimental ischemic and reperfusion in rat liver. *Saudi J Gastroenterol.* 2009; 15(3): 156–162, doi: [10.4103/1319-3767.45356](https://doi.org/10.4103/1319-3767.45356), indexed in Pubmed: [19636175](https://pubmed.ncbi.nlm.nih.gov/19636175/).
5. Ge Y, Zhang Q, Li H, et al. Adipose-derived stem cells alleviate liver apoptosis induced by ischemia-reperfusion and laparoscopic hepatectomy in swine. *Sci Rep.* 2018; 8(1): 16878, doi: [10.1038/s41598-018-34939-x](https://doi.org/10.1038/s41598-018-34939-x), indexed in Pubmed: [30442976](https://pubmed.ncbi.nlm.nih.gov/30442976/).
6. Go KL, Lee S, Zendejas I, et al. Mitochondrial dysfunction and autophagy in hepatic ischemia/reperfusion injury. *Biomed Res Int.* 2015; 2015: 183469, doi: [10.1155/2015/183469](https://doi.org/10.1155/2015/183469), indexed in Pubmed: [26770970](https://pubmed.ncbi.nlm.nih.gov/26770970/).
7. Honda M, Takeichi T, Asonuma K, et al. Intravital imaging of neutrophil recruitment in hepatic ischemia-reperfusion injury in mice. *Transplantation.* 2013; 95(4): 551–558, doi: [10.1097/TP.0b013e31827d62b5](https://doi.org/10.1097/TP.0b013e31827d62b5), indexed in Pubmed: [23423266](https://pubmed.ncbi.nlm.nih.gov/23423266/).
8. Iimuro Y, Nishiura T, Hellerbrand C, et al. NFkappaB prevents apoptosis and liver dysfunction during liver regeneration. *J Clin Invest.* 1998; 101(4): 802–811, doi: [10.1172/JCI483](https://doi.org/10.1172/JCI483), indexed in Pubmed: [9466975](https://pubmed.ncbi.nlm.nih.gov/9466975/).
9. Jaeschke H, Farhood A. Neutrophil and Kupffer cell-induced oxidant stress and ischemia-reperfusion injury in rat liver. *Am J Physiol.* 1991; 260(3 Pt 1): G355–G362, doi: [10.1152/ajpgi.1991.260.3.G355](https://doi.org/10.1152/ajpgi.1991.260.3.G355), indexed in Pubmed: [2003603](https://pubmed.ncbi.nlm.nih.gov/2003603/).
10. Jaeschke H, Hasegawa T. Role of neutrophils in acute inflammatory liver injury. *Liver Int.* 2006; 26(8): 912–919, doi: [10.1111/j.1478-3231.2006.01327.x](https://doi.org/10.1111/j.1478-3231.2006.01327.x), indexed in Pubmed: [16953830](https://pubmed.ncbi.nlm.nih.gov/16953830/).
11. Jaeschke H. Mechanisms of Liver Injury. II. Mechanisms of neutrophil-induced liver cell injury during hepatic ischemia-reperfusion and other acute inflammatory conditions. *Am J Physiol Gastrointest Liver Physiol.* 2006; 290(6): G1083–G1088, doi: [10.1152/ajpgi.00568.2005](https://doi.org/10.1152/ajpgi.00568.2005), indexed in Pubmed: [16687579](https://pubmed.ncbi.nlm.nih.gov/16687579/).
12. Jiang X, Kuang Ge, Gong X, et al. Glycyrrhetic acid pretreatment attenuates liver ischemia/reperfusion injury via inhibiting TLR4 signaling cascade in mice. *Int Immunopharmacol.* 2019; 76: 105870, doi: [10.1016/j.intimp.2019.105870](https://doi.org/10.1016/j.intimp.2019.105870), indexed in Pubmed: [31493667](https://pubmed.ncbi.nlm.nih.gov/31493667/).
13. Jiménez-Castro MB, Cornide-Petronio ME, Gracia-Sancho J, et al. Inflammasome-Mediated inflammation in liver ischemia-reperfusion injury. *Cells.* 2019; 8(10), doi: [10.3390/cells8101131](https://doi.org/10.3390/cells8101131), indexed in Pubmed: [31547621](https://pubmed.ncbi.nlm.nih.gov/31547621/).
14. Konishi T, Lentsch AB. Hepatic ischemia/reperfusion: mechanisms of tissue injury, repair, and regeneration. *Gene Expr.* 2017; 17(4): 277–287, doi: [10.3727/105221617X15042750874156](https://doi.org/10.3727/105221617X15042750874156), indexed in Pubmed: [28893351](https://pubmed.ncbi.nlm.nih.gov/28893351/).
15. Kuboki S, Schuster R, Blanchard J, et al. Role of heat shock protein 70 in hepatic ischemia-reperfusion injury in mice. *Am J Physiol Gastrointest Liver Physiol.* 2007; 292(4): G1141–G1149, doi: [10.1152/ajpgi.00491.2006](https://doi.org/10.1152/ajpgi.00491.2006).
16. Laribi B, Kouki K, M'Hamdi M, et al. Coriander (*Coriandrum sativum* L.) and its bioactive constituents. *Fitoterapia.* 2015; 103: 9–26, doi: [10.1016/j.fitote.2015.03.012](https://doi.org/10.1016/j.fitote.2015.03.012), indexed in Pubmed: [25776008](https://pubmed.ncbi.nlm.nih.gov/25776008/).
17. Liang S, Xu Z, Ruan Y, et al. Isoquercitrin attenuates renal ischemia/reperfusion injury through antioxidation, anti-inflammation, and antiapoptosis in mice. *Transplant Proc.* 2020; 52(3): 1014–1019, doi: [10.1016/j.transproceed.2019.12.038](https://doi.org/10.1016/j.transproceed.2019.12.038), indexed in Pubmed: [32115238](https://pubmed.ncbi.nlm.nih.gov/32115238/).
18. Mandal S, Mandal M. Coriander (*Coriandrum sativum* L.) essential oil: Chemistry and biological activity. *Asian Pac J Trop Biomed.* 2015; 5(6): 421–428, doi: [10.1016/j.apjtb.2015.04.001](https://doi.org/10.1016/j.apjtb.2015.04.001).
19. McCormack L, Petrowsky H, Jochum W, et al. Hepatic steatosis is a risk factor for postoperative complications after major hepatectomy: a matched case-control study. *Ann Surg.* 2007; 245(6): 923–930, doi: [10.1097/01.sla.0000251747.80025.b7](https://doi.org/10.1097/01.sla.0000251747.80025.b7), indexed in Pubmed: [17522518](https://pubmed.ncbi.nlm.nih.gov/17522518/).
20. Moustafa AH, Ali EM, Moselhey SS, et al. Effect of coriander on thioacetamide-induced hepatotoxicity in rats. *Toxicol Ind Health.* 2014; 30(7): 621–629, doi:

- [10.1177/0748233712462470](https://doi.org/10.1177/0748233712462470), indexed in Pubmed: [23042592](https://pubmed.ncbi.nlm.nih.gov/23042592/).
21. Nishio R, Tamano H, Morioka H, et al. Intake of heated leaf extract of coriandrum sativum contributes to resistance to oxidative stress via decreases in heavy metal concentrations in the kidney. *Plant Foods Hum Nutr.* 2019; 74(2): 204–209, doi: [10.1007/s11130-019-00720-2](https://doi.org/10.1007/s11130-019-00720-2), indexed in Pubmed: [30783906](https://pubmed.ncbi.nlm.nih.gov/30783906/).
 22. Oliveira TH, Marques PE, Proost P, et al. Neutrophils: a cornerstone of liver ischemia and reperfusion injury. *Lab Invest.* 2018; 98(1): 51–62, doi: [10.1038/labinvest.2017.90](https://doi.org/10.1038/labinvest.2017.90), indexed in Pubmed: [28920945](https://pubmed.ncbi.nlm.nih.gov/28920945/).
 23. Osman AS, Osman AH, Kamel MM. Study of the protective effect of ischemic and pharmacological preconditioning on hepatic ischemic reperfusion injury induced in rats. *JGH Open.* 2017; 1(3): 105–111, doi: [10.1002/jgh3.12018](https://doi.org/10.1002/jgh3.12018), indexed in Pubmed: [30483545](https://pubmed.ncbi.nlm.nih.gov/30483545/).
 24. Pandey A, Bigoniya P, Raj V, et al. Pharmacological screening of *Coriandrum sativum* Linn. for hepatoprotective activity. *J Pharm Bioallied Sci.* 2011; 3(3): 435–441, doi: [10.4103/0975-7406.84462](https://doi.org/10.4103/0975-7406.84462), indexed in Pubmed: [21966166](https://pubmed.ncbi.nlm.nih.gov/21966166/).
 25. Patel D, Desai S, Devkar R, et al. Acute and sub-chronic toxicological evaluation of hydro-methanolic extract of *Coriandrum sativum* L. seeds. *EXCLI J.* 2012; 11: 566–575, indexed in Pubmed: [27847445](https://pubmed.ncbi.nlm.nih.gov/27847445/).
 26. Prachayasittikul V, Prachayasittikul S, Ruchirawat S, et al. Coriander (*Coriandrum sativum*): A promising functional food toward the well-being. *Food Res Int.* 2018; 105: 305–323, doi: [10.1016/j.foodres.2017.11.019](https://doi.org/10.1016/j.foodres.2017.11.019), indexed in Pubmed: [29433220](https://pubmed.ncbi.nlm.nih.gov/29433220/).
 27. Quesnelle KM, Bystrom PV, Toledo-Pereyra LH. Molecular responses to ischemia and reperfusion in the liver. *Arch Toxicol.* 2015; 89(5): 651–657, doi: [10.1007/s00204-014-1437-x](https://doi.org/10.1007/s00204-014-1437-x), indexed in Pubmed: [25566829](https://pubmed.ncbi.nlm.nih.gov/25566829/).
 28. Schleicher J, Dahmen U. Computational modeling of oxidative stress in fatty livers elucidates the underlying mechanism of the increased susceptibility to ischemia/reperfusion injury. *Comput Struct Biotechnol J.* 2018; 16: 511–522, doi: [10.1016/j.csbj.2018.10.013](https://doi.org/10.1016/j.csbj.2018.10.013), indexed in Pubmed: [30505404](https://pubmed.ncbi.nlm.nih.gov/30505404/).
 29. Silva F, Domingues FC. Antimicrobial activity of coriander oil and its effectiveness as food preservative. *Crit Rev Food Sci Nutr.* 2017; 57(1): 35–47, doi: [10.1080/10408398.2013.847818](https://doi.org/10.1080/10408398.2013.847818), indexed in Pubmed: [25831119](https://pubmed.ncbi.nlm.nih.gov/25831119/).
 30. Sreelatha S, Padma PR, Umadevi M. Protective effects of *Coriandrum sativum* extracts on carbon tetrachloride-induced hepatotoxicity in rats. *Food Chem Toxicol.* 2009; 47(4): 702–708, doi: [10.1016/j.fct.2008.12.022](https://doi.org/10.1016/j.fct.2008.12.022), indexed in Pubmed: [19146910](https://pubmed.ncbi.nlm.nih.gov/19146910/).
 31. Sun L, Wu Q, Nie Y, et al. A role for MK2 in enhancing neutrophil-derived ROS production and aggravating liver ischemia/reperfusion injury. *Front Immunol.* 2018; 9: 2610, doi: [10.3389/fimmu.2018.02610](https://doi.org/10.3389/fimmu.2018.02610), indexed in Pubmed: [30483268](https://pubmed.ncbi.nlm.nih.gov/30483268/).
 32. Suzuki S, Toledo-Pereyra LH, Rodriguez FJ, et al. Neutrophil infiltration as an important factor in liver ischemia and reperfusion injury. Modulating effects of FK506 and cyclosporine. *Transplantation.* 1993; 55(6): 1265–1272, doi: [10.1097/00007890-199306000-00011](https://doi.org/10.1097/00007890-199306000-00011), indexed in Pubmed: [7685932](https://pubmed.ncbi.nlm.nih.gov/7685932/).
 33. Uchinami H, Yamamoto Y, Kume M, et al. Effect of heat shock preconditioning on NF-kappaB/I-kappaB pathway during I/R injury of the rat liver. *Am J Physiol Gastrointest Liver Physiol.* 2002; 282(6): G962–G971, doi: [10.1152/ajpgi.00466.2001](https://doi.org/10.1152/ajpgi.00466.2001), indexed in Pubmed: [12016121](https://pubmed.ncbi.nlm.nih.gov/12016121/).
 34. Wang J, Sun GX, Yu L, et al. Enhancement of the selective enzymatic biotransformation of rutin to isoquercitrin using an ionic liquid as a co-solvent. *Bioresour Technol.* 2013; 128: 156–163, doi: [10.1016/j.biortech.2012.10.098](https://doi.org/10.1016/j.biortech.2012.10.098), indexed in Pubmed: [23201508](https://pubmed.ncbi.nlm.nih.gov/23201508/).
 35. Yang M, Antoine DJ, Weemhoff JL, et al. Biomarkers distinguish apoptotic and necrotic cell death during hepatic ischemia/reperfusion injury in mice. *Liver Transpl.* 2014; 20(11): 1372–1382, doi: [10.1002/lt.23958](https://doi.org/10.1002/lt.23958), indexed in Pubmed: [25046819](https://pubmed.ncbi.nlm.nih.gov/25046819/).
 36. Zapolska-Downar D, Naruszewicz M. Propionate reduces the cytokine-induced VCAM-1 and ICAM-1 expression by inhibiting nuclear factor-kappa B (NF-kappa B) activation. *J Physiol Pharmacol.* 2009; 60(123): 131, indexed in Pubmed: [19617655](https://pubmed.ncbi.nlm.nih.gov/19617655/).

Computer-assisted measurements of the histological structure of the tibial nerve and its terminal branches

Ł. Warchoń¹, J.A. Walocha¹, E. Mizia¹, H. Liszka¹, M. Bonczar², I. Zamojska¹

¹Department of Anatomy, Jagiellonian University Medical College, Krakow, Poland

²Intermed Medical Clinic, Zabierzow, Poland

[Received: 21 April 2020; Accepted: 7 June 2020]

Background: The aim of this study was to analyse the histological structure (cross-sectional area [CSA] and number of nerve bundles) of the distal part of the tibial nerve and its terminal branches (medial plantar nerve, lateral plantar nerve) using computer-assisted image analysis.

Materials and methods: The tibial nerve and its distal branches (medial and lateral plantar nerves) were dissected from the fresh cadavers. Each nerve was harvested 5 mm proximally and respectively 5 mm distally from the tibial nerve bifurcation, marked, dehydrated, embedded in paraffin, sectioned at 2 µm slices and stained with haematoxylin and eosin. Then photographed and analysed using Olympus cellSens software.

Results: The studied group comprised 28 female and 32 male feet (mean age 68.1 ± 15.2 years). The mean CSA and the number of nerve bundles were respectively 17.86 ± 4.57 mm², 33.88 ± 6.31 for the tibial nerve, 9.58 ± 1.95 mm², 23.41 ± 7.37 for the medial plantar nerve and 7.17 ± 2.36 mm², 15.06 ± 5.81 for the lateral plantar nerve in males and 12.27 ± 2.45 mm², 26.32 ± 8.87 for the tibial nerve, 7.81 ± 1.41 mm², 17.71 ± 5.28 for the medial plantar nerve and 5.83 ± 1.25 mm², 11.50 ± 3.72 for the lateral plantar nerve in females. Both CSA and number of nerve bundles of the tibial, medial plantar and lateral plantar nerves revealed no statistical differences when comparing foot side of the individual. The statistical difference was related to the gender, showing significantly bigger CSA and number of nerve bundles in males (CSA: $p = 0.000$, $p = 0.000$, $p = 0.016$; number of nerve bundles: $p = 0.01$, $p = 0.003$, $p = 0.004$, respectively). A positive correlation was found between the donor age and the tibial nerve CSA ($r = 0.44$, $p = 0.000$). A significant statistical difference was found between the medial and lateral plantar nerves both in CSA and number of nerve bundles ($p < 0.001$, $p < 0.001$, respectively).

Conclusions: The CSA and the number of nerve bundles in the distal part of the tibial nerve and its branches are significantly larger in males with no differences between right and left foot of the individual. The tibial nerve shows increasing CSA with advanced age. The medial plantar nerve has larger CSA and more nerve bundles than the lateral plantar nerve. (Folia Morphol 2021; 80, 2: 372–379)

Key words: tibial nerve, cross-sectional area, nerve bundles, medial and lateral plantar nerves, computer-assisted image analysis, histology

Address for correspondence: Dr. Ł. Warchoń, Department of Anatomy, Jagiellonian University Medical College, ul. Kopernika 12, 31–034 Kraków, Poland, tel: +48 601 865 239, e-mail: l.warchon@uj.edu.pl

This article is available in open access under Creative Common Attribution-Non-Commercial-No Derivatives 4.0 International (CC BY-NC-ND 4.0) license, allowing to download articles and share them with others as long as they credit the authors and the publisher, but without permission to change them in any way or use them commercially.

INTRODUCTION

The tibial nerve is a peripheral sensorimotor nerve which is derived from the L4, L5 and S1–S3 spinal nerve roots [32]. It is the larger of the two terminal branches of the sciatic nerve arising in the popliteal fossa. It runs vertically on the tibialis posterior muscle together with the posterior tibial vessels. Postero-inferiorly to the medial malleolus it terminates emitting medial plantar nerve and lateral plantar nerve [26]. The tibial nerve bifurcation level shows a great variability with the most common occurrence below the tip of the medial malleolus, inside the tarsal tunnel [33].

Through its course the tibial nerve emits motor branches to the muscles of the posterior lower leg as well as sensory branches: medial sural cutaneous nerve and medial calcaneal nerve(s) innervating the skin of the posterolateral inferior third of the leg together with the lateral side of the foot and the skin of the heel, accordingly [10]. Medial calcaneal branches show diversity in terms of number (range from 1 to 4), location and nerve of origin [9, 17]. Both plantar nerves enter the sole of the foot supplying its muscles and skin. The medial plantar nerve innervates the skin medial to the line splitting fourth digit whilst the lateral plantar nerve the skin lateral to the line [20].

Tarsal tunnel syndrome is one of the entrapment conditions affecting the tibial nerve and its terminal branches in the medial ankle. It causes heel and sole burning pain and paraesthesia [2]. Such disorders together with other peripheral nerve pathologies may be examined by the ultrasound [24]. The cross-sectional area (CSA) is a parameter measured by the ultrasound which increasing value confirms the diagnosis [7].

The aim of this study was to assess the histological structure of the tibial nerve, medial plantar nerve and lateral plantar nerve as well as to determine the distribution of the nerve bundles of the distal tibial nerve to its terminal branches.

MATERIALS AND METHODS

The study was conducted on 60 lower limbs of the fresh cadavers in the Department of Anatomy of the Jagiellonian University Medical College between December 2016 and December 2019. The exclusion criteria were any deformation of the lower limb or the lower limb trauma, surgical or radiotherapeutic procedures of the lower limb, chronic disease of the lower limb in the medical record of the donor.

The research protocol was approved by the local Ethics Committee (registry no. 122.6120.315.2016).

The study has been performed in accordance with the ethical standards established in the 1964 Declaration of Helsinki and its later amendments.

Dissection technique

The incision was made in the midline between the tip of the medial malleolus and the Achilles tendon. It was continued 10 cm proximally along the Achilles tendon and 10 cm distally curving anteriorly 2 cm below the tip of the medial malleolus. Upon dissecting the skin and the subcutaneous tissue, the tibial nerve was visualised together with the posterior tibial artery and two posterior tibial veins. After meticulous dissection, the tibial nerve, its bifurcation and lateral and medial plantar nerves were exposed. The plantar nerves were marked 2 cm distally from the tibial nerve bifurcation point with the following pattern: blue thread — lateral plantar nerve, white thread — medial plantar nerve. The tibial nerve was left without any marking. Then 3 cm proximally to the bifurcation the tibial nerve was cut out from the main nerve trunk. Accordingly, 3 cm distally the medial and lateral plantar nerves were cut out. The excised tibial nerve and its terminal branches were removed *en bloc* from the cadaver. The incision was closed with the running subcuticular suture. The harvesting was carried out by the same surgeon.

Preparation of histological slide

The excised block of nerves was fixed in a 10% solution of the formaldehyde (pH 7.4). After 2–5 days it was removed from the formaldehyde. The tibial nerve was cut transverse to the nerve axis 5 mm and 10 mm proximally to the tibial nerve bifurcation point as were the medial and lateral plantar nerves 5 mm and 10 mm distally to the tibial nerve bifurcation point. Obtained 5 mm long nerve fragments were dehydrated separately and embedded in paraffin according to its initial marking. Each paraffin cube was transverse sectioned with the microtome providing one 2 μ m thick slice. Subsequently each slice was stained with haematoxylin and eosin (Fig. 1).

Micromorphometry

The CSA and the number of nerve bundles of the tibial nerve, the medial plantar nerve and the lateral plantar nerve were assessed using a light microscope (Olympus BX53, 20 \times magnification). Each cross-section was photographed (20 \times magnification). Afterwards, the CSA was measured semi-automatically using Olympus cellSens Standard 2.3 software with the producer's

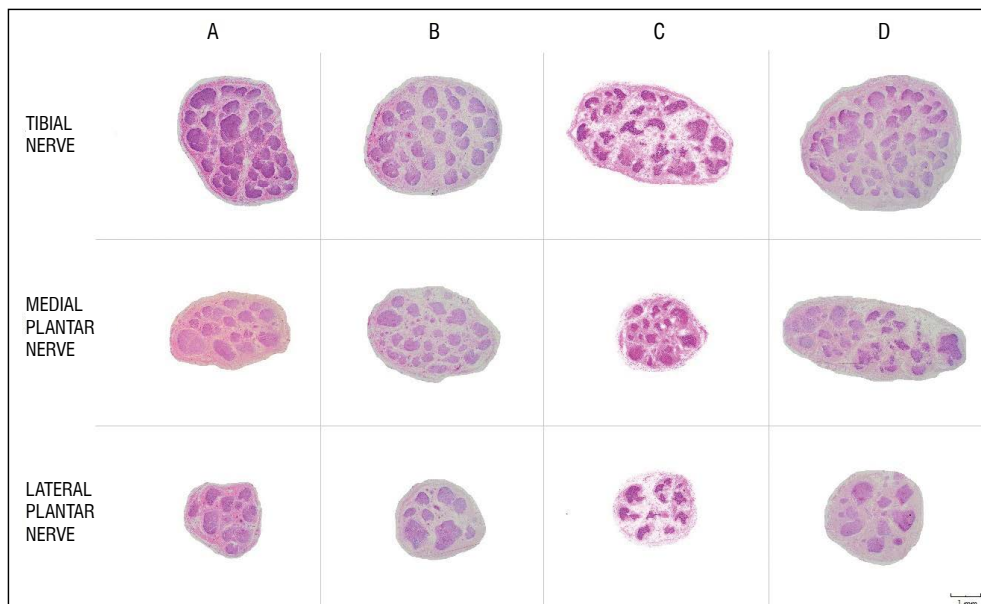


Figure 1. Cross-section of the tibial nerves (TN), the medial plantar nerves (MPN) and the lateral plantar nerves (LPN). Haematoxylin and eosin staining. 20 × magnification; **A.** 58-year-old male, right foot — cross-sectional area (CSA): TN — 12.76 mm², MPN — 6.79 mm², LPN — 4.37 mm²; number of nerve bundles: TN — 35, MPN — 18, LPN — 12; **B.** 58-year-old male (same individual as in panel A), left foot CSA: TN — 12.83 mm², MPN — 9.92 mm², LPN — 5.47 mm²; number of nerve bundles: TN — 29, MPN — 26, LPN — 8; **C.** 63-year-old male, right foot — CSA: TN — 13.92 mm², MPN — 5.63 mm², LPN — 5.05 mm²; number of nerve bundles: TN — 34, MPN — 14, LPN — 12; **D.** 84-year-old male, left foot — CSA: TN — 18.39 mm², MPN — 10.32 mm², LPN — 7.09 mm²; number of nerve bundles: TN — 44, MPN — 34, LPN — 13.

Table 1. The tibial nerve and its terminal branches measurements

Measurement		N	Mean ± standard deviation	Median	Minimum	Maximum	Lower quartile (Q1)	Upper quartile (Q3)
Cross-sectional area [mm ²]	Tibial nerve	60	15.25 ± 4.65	14.66	7.22	30.82	11.77	17.29
	Medial plantar nerve	60	8.76 ± 1.93	8.45	5.53	14.22	7.19	9.90
	Lateral plantar nerve	60	6.54 ± 2.02	6.44	3.90	16.06	5.12	7.41
Number of nerve bundles	Tibial nerve	60	30.35 ± 8.45	31.00	7.00	50.00	25.00	35.25
	Medial plantar nerve	60	20.75 ± 7.04	20.00	5.00	38.00	16.00	25.00
	Lateral plantar nerve	60	13.40 ± 5.22	14.00	3.00	38.00	10.75	15.00

precision of 10 μm, whilst the number of nerve bundles was calculated manually. Each slice was assessed once by the same pathologist. Then the values of the CSA and the number of nerve bundles were tabulated.

Statistics

Obtained data were statistically processed using descriptive statistics such as percentage, mean, median, standard deviation, upper and lower quartiles. A p-value of < 0.05 was considered as statistically significant. Two groups were compared using the Mann-Whitney test and t-test for non-normally and normally distributed data, accordingly. Levene’s test was used to check for homogeneity of variance. Two-way analysis of variance and possible interactions

between the sex and age (> 70/< 70 years old) were checked in selected nerve parameters. Post-hoc analysis was performed using HSD test. To compare the nerve features between the left and right foot, the paired t-test or Wilcoxon rang test was used depending on whether data were normally or non-normally distributed. Correlation coefficients were calculated to establish any statistical dependence between parameters. All analyses were performed using MedCalc version 16.8.

RESULTS

There were 30 fresh cadavers dissected (n = 60 lower limbs) with a mean age of 68.1 ± 15.2 (range from 27 to 91 years). 28 (46.7%) feet were female and

Table 2. The tibial nerve and its terminal branches measurements — comparison by gender

Measurement	Women					Men					P	
	N	Mean ± SD	Median	Q1	Q3	N	Mean ± SD	Median	Q1	Q3		
Cross-sectional area [mm ²]	Tibial nerve	28	12.27 ± 2.45	11.85	10.35	14.31	32	17.86 ± 4.57	17.10	15.02	19.90	0.000
	Medial plantar nerve	28	7.81 ± 1.41	7.37	6.70	9.10	32	9.58 ± 1.95	9.16	8.40	10.66	0.000
	Lateral plantar nerve	28	5.83 ± 1.25	5.77	4.61	6.86	32	7.17 ± 2.36	7.08	5.18	8.35	0.016
Number of nerve bundles	Tibial nerve	28	26.32 ± 8.87	25.00	19.50	34.00	32	33.88 ± 6.31	34.00	28.50	38.00	0.001
	Medial plantar nerve	28	17.71 ± 5.28	18.00	14.50	20.50	32	23.41 ± 7.37	23.00	17.50	29.50	0.003
	Lateral plantar nerve	28	11.50 ± 3.72	12.00	9.00	14.00	32	15.06 ± 5.81	15.00	12.50	16.50	0.004

Numbers in bold indicate statistically significant differences between males and females ($p < 0.05$); SD — standard deviation; Q1 — lower quartile; Q3 — upper quartile

Table 3. The tibial nerve and its terminal branches measurements — comparison by foot side

Measurement	Left foot					Right foot					P	
	N	Mean ± SD	Median	Q1	Q3	N	Mean ± SD	Median	Q1	Q3		
Cross-sectional area [mm ²]	Tibial nerve	30	15.82 ± 5.08	15.64	11.73	17.79	30	14.67 ± 4.19	14.14	11.91	16.64	0.229
	Medial plantar nerve	30	8.80 ± 1.98	8.32	7.21	9.88	30	8.71 ± 1.90	8.78	7.08	9.92	0.805
	Lateral plantar nerve	30	7.05 ± 2.48	6.99	5.05	8.30	30	6.03 ± 1.28	5.91	5.12	7.08	0.075
Number of nerve bundles	Tibial nerve	30	30.43 ± 8.36	31.00	25.00	35.00	30	30.27 ± 8.67	32.00	24.00	37.00	0.989
	Medial plantar nerve	30	20.37 ± 6.77	20.00	17.00	23.00	30	21.13 ± 7.39	21.00	15.00	26.00	0.412
	Lateral plantar nerve	30	14.20 ± 6.37	14.00	11.00	16.00	30	12.60 ± 3.68	13.00	10.00	15.00	0.296

Statistically significant differences between left and right foot when $p < 0.05$; SD — standard deviation; Q1 — lower quartile; Q3 — upper quartile

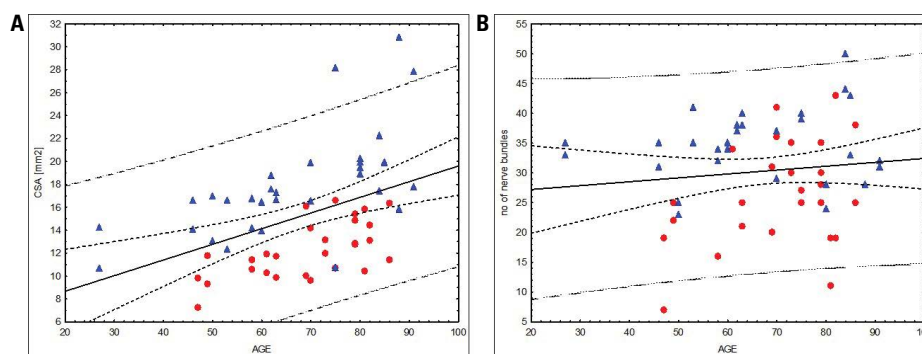


Figure 2. **A.** A scatter plot of donors age correlation with tibial nerve cross-sectional area (CSA). Triangles represent males ($r = 0.69$, $p = 0.000$), dots represent females ($r = 0.60$, $p = 0.001$); **B.** A scatter plot of donors age correlation with number of tibial nerve bundles. Triangles represent males ($r = -0.04$, $p = 0.846$), dots represent females ($r = 0.31$, $p = 0.110$). The continuous line represents progression. The dash lines represent the 95% confidence intervals of the progression. The dash-dot lines represent the 95% prediction intervals.

32 (53.3%) were male. The mean CSA and number of nerve bundles of the tibial nerve, the medial plantar nerve and the lateral plantar nerve are presented in Table 1. Differences between the gender and foot side are shown in Tables 2 and 3, respectively. Males showed larger CSA and more nerve bundles than females. No statistically significant differences between the right and left foot of the individual were found ($p > 0.05$). There was a statistically significant

difference between medial and lateral plantar nerve both in CSA and number of nerve bundles ($p < 0.001$, $p < 0.001$, respectively). The medial plantar nerve was confirmed to have 1.3 times larger CSA and 1.5 times more nerve bundles than the lateral plantar nerve. A positive correlation was noted between the age of donors and CSA of the tibial nerve ($r = 0.44$, $p = 0.000$) (Fig. 2). No statistically significant correlation was found between the age of donors and CSA

Table 4. Studies of the tibial nerve cross-sectional area (CSA) measured at the level of medial malleolus

	Group (n)	Mean age [years]	CSA of the tibial nerve at the level of medial malleolus [mm ²]	Reference range [mm ²]	Type of study
He et al., 2019 [13]	40	55.2	11.6 ± 1.6	–	US 4–15 MHz
Lothet et al., 2019 [24]	15	21.7	12.3	–	US 18 MHz
Singh et al., 2019 [30]	45	30–68	6.0 ± 1.8	–	US 5–18 MHz
Bedewi et al., 2018 [3]	138	38.3	12.7 ± 4.5	2.0–30.0	US 18.5 MHz
Grimm et al., 2018 [12]	100	51.2	10.2 ± 2.0	–	US 14 MHz
Kronlage et al., 2017 [21]	60	30.5	8.1 ± 2.0*	4.0–12.1	MRI
Singh et al., 2017 [29]	75	39.5	12.4 ± 1.1	10.0–14.0	US 7–18 MHz
Kang et al., 2016 [18]	20	65.0	12.4 ± 2.9	–	US 7–12 MHz
Yiu et al., 2015 [35]	29	11.3	6.3 ± 1.9	8.6–14.1	US 7–13 MHz
Boehm et al., 2014 [5]	56	50.2	9.6 ± 2.2	9.0–10.2	US 12–15 MHz
Seok et al., 2014 [28]	94	43.9	12.1 ± 3.1	8.5–22.8	US 5–12 MHz
Kerasnoudis et al., 2013 [19]	75	53.5	6.3 ± 1.5	3.5–9.3	US 18 MHz
Riazi et al., 2012 [27]	43	46.8	17.7 ± 6.5	–	US 6–13 MHz
Tagliafico et al., 2012 [31]	58	47.0	9.6 ± 4.0	7.2–13.7	US 17.5 MHz
Cartwright et al., 2008 [7]	60	45.9	13.7 ± 4.3	5.1–22.3	US 15 MHz
Ito et al., 2007 [16]	35	52.8	7.9 ± 1.5	5.0–10.7	US 7.5 MHz
Lee et al., 2005 [22]	24	57.4	12.0	–	US 10–12 MHz

*Measured at the proximal third of the calf; US — ultrasonography; MRI — magnetic resonance imaging

of medial or lateral plantar nerves as well as number of nerve bundles. In the two-way analysis of variance, the mean CSA of the tibial nerve in males below 70 years of age was $15.37 \pm 0.80 \text{ mm}^2$ and $20.35 \pm 0.80 \text{ mm}^2$ for those above 70 years old, whilst in females $10.83 \pm 0.92 \text{ mm}^2$ and $13.35 \pm 0.80 \text{ mm}^2$, respectively. There was no statistically significant sex and age interactions with the CSA of the tibial nerve ($p = 0.14$). Post-hoc analysis revealed significant differences between younger and older males as well as between younger males and younger females ($p < 0.05$). Older males' CSA was significantly higher when compared to the younger and older females ($p < 0.05$).

DISCUSSION

The present study reveals data obtained using computer-assisted analysis of the histological structure of the distal tibial nerve and its terminal branches: medial and lateral plantar nerves. Literature analysis shows that the previous studies focused mostly on the variations of the topographic anatomy of the tibial nerve, its bifurcation, branching pattern and the cross-sectional area measured by the ultrasound imaging [33]. A limited number of studies concentrated on the histological structure of the tibial nerve

and its distal branches. To the best of the authors' knowledge this is the first publication analysing histological structure of the medial and lateral plantar nerves as well as tibial nerve bundles distribution to its terminal branches. As the previous publications of the cross-sectional area were based on the ultrasound or magnetic resonance imaging, the present study is the first to reveal the CSA measured directly on the nerves harvested from the fresh cadavers, which shows greater accuracy.

In the present study, 60 lower limbs of the fresh cadavers were dissected. The majority of donors presented advanced age (mean age 68.1 years) and relatively equal gender distribution (53% males). The mean CSA of the tibial nerve measured with the computer-assisted image analysis is 15.25 mm^2 , which is comparable with the results obtained in the previous studies collected in Table 4. Nonetheless, it needs to be noticed that majority of those measurements are slightly below 15.25 mm^2 as well as the mean age is lower than 68.1 years. It confirms the positive correlation between the age of the donors and the CSA observed in the present study. Despite different methodology (micromorphometry vs. ultrasound vs. magnetic resonance imaging) the obtained results showed insignificant differences in CSA of the tibial

nerve. Thus, it proves the reliability and usefulness of those imagining methods.

Analysing the results summarised in Table 4, the authors found that the average cross-sectional area of the tibial nerve (15.25 mm²) is almost identical with Riazi et al. [27] — 17.7 mm² and Cartwright et al. [6] — 13.7 mm². At the same time it is more than two times larger than the values provided by Singh et al. [30] — 6.0 mm², Yiu et al. [35] — 6.3 mm² and Kerasnoudis et al. [19] — 6.3 mm². The differences may be the result of the average age of the examined patients. Namely, Yiu et al. [35] examined children with the mean age of 11.3 mm², which probably is the reason for the small CSA. The other cause of slight variation may be related to a different level of measurements. Lothet et al. [24] together with Kang et al. [18], Kerasnoudis et al. [19], Cartwright et al. [7], Bedewi et al. [3], Boehm et al. [5] and Grimm et al. [12] performed the examination at the level of the ankle whilst He et al. [13] and Singh et al. [30] measured the CSA 3 cm above the medial malleolus and Riazi et al. [27] 1 cm, 3 cm and 5 cm above the medial malleolus. As the tibial nerve bifurcation level shows great topographic variability, such inaccuracy may bring different results. Its location was subject of many studies and frequently referred to the medial or lower located lateral malleolus [23, 34]. For the sake of comparison in the present study, all publications mentioned in Table 4 were qualified as if the measurements were at the level of medial malleolus. The other sources of the differences may be the reliability and accuracy of the researchers as well as the ultrasound resolution or the ethnical groups which was not comprised in the study.

To the best of the authors' knowledge, no previous studies of the cross-sectional area of the tibial, medial and lateral plantar nerves harvested from the fresh cadavers have been reported. The first report of the tibial nerve measurements dates back to 1938 when Horwitz [15] performed a dissection on 100 cadavers reporting the average diameter of tibial nerve to be between 6 and 10 mm. Unfortunately, there is no information about the level of assessment. In 2006 Joshi and Joshi [17] examined 112 cadavers describing an average width of the tibial nerve above its bifurcation to be 8.23 mm. The authors also measured the width of the medial plantar nerve to be 5.32 mm and the lateral plantar nerve to be 4.61 mm. Since the tibial nerve shows clear flattening at the level of its bifurcation it would be wrong to assess the CSA

using the circle area formula ($\pi \times r^2$). These are the only measurements of the medial and lateral plantar nerves found in the literature. Complementing the available data with the mean CSA of 8.76 mm² and the average number of nerve bundles to be 20.75 in the medial plantar nerve and 6.54 mm² and 13.40 in the lateral plantar respectively should serve as a starting point for future researchers.

According to Alshami et al. [1], one of the causes of the foot pain is the tarsal tunnel syndrome. As the tibial nerve and its divisional branches pass through tarsal tunnel it may be entrapped or compressed. Joshi and Joshi [17] together with Bilge et al. [4] state that in the majority of cases the tibial nerve bifurcation is located inside the tarsal tunnel. As Heimkes et al. [14] point out, it is a tight, stretch resistant osteofibrous canal between talus, calcaneus and flexor retinaculum. It may be suggested that the larger the size (CSA) of the nerves (tibial, medial and lateral plantar), the higher the risk of its entrapment. Therefore the prevalence of the foot pain and paraesthesia among older people is higher.

Lothet et al. [24] together with Cartwright et al. [7] proved that in the medial ankle ultrasound examination the tibial nerve CSA remains uninfluenced by the patient's height and weight. In the present study the authors confirm that CSA of the tibial nerve increases with the advanced age, which is consistent with the findings of Grimm et al. [12] and Cartwright et al. [6]. It needs to be mentioned that according to Kerasnoudis et al. [19] and Mizia et al. [25] other peripheral nerves such as median nerve, radial nerve or sural nerve present an age-related decrease in the CSA values. This exceptional finding was explained by Ceballos et al. [8] in 1999 on the mouse model. The authors observed the age-related increase in mastocytes and macrophages depositing in the endoneurium as well as collagen accumulation in the perineurium, causing the enlargement of the cross-sectional area. Tibial nerve age-related thickening was also described by Grimm et al. [12] as a higher fibrous tissue deposition in the nerve.

In the present study, the number of nerve bundles in the tibial, medial plantar and lateral plantar nerves was also counted, finding respectively 30.35 ± 8.45 , 20.75 ± 7.04 , 13.40 ± 5.22 nerve bundles. Interestingly the number of nerve bundles of the tibial nerve is lower than the summative number of its two terminal branches (medial and lateral plantar nerves). The similar finding was reported by Delgado-Martinez

et al. [11] who counted the number of nerve bundles of the median nerve. Despite the muscle and cutaneous branches sprouting from the main trunk of the median nerve along its course, the authors found the increasing number of nerve bundles in distal part of the forearm (11.81 ± 0.32 in the proximal upper arm, 12.81 ± 0.73 in the distal upper arm, 21.87 ± 0.58 in the forearm). Although there is no study explaining this finding available in the literature, the authors suggest that the increased summative number of nerve bundles in the medial and lateral plantar nerves might result from the split of (some) nerve bundles of the tibial nerve at the bifurcation level. Therefore, finding out the branching pattern of the tibial nerve bundles and its distribution to the medial and lateral plantar nerves (by measuring the CSA of each nerve bundle or by counting the number of axons) at the bifurcation level might be an interesting subject for the future studies.

Limitations of the study

The fact that the cross-sectional area and number of nerve bundles were assessed on the nerves harvested from the fresh cadavers donated to the Department of the Anatomy results in the high average age of the examined group. Because of the technical difficulties no weight and height of the donors were obtained which might have been beneficial for this study. The other limitation of the present study is the fact that only one slice of each nerve was prepared for the micromorphometric assessment. Single pathologist, performing all measurements only once also biased the possibility to ascertain the inter-observer and intra-observer variabilities. Another restriction is a diverse level of the tibial nerve CSA measurements presented in available studies as well as lack of medial and lateral plantar nerve assessments which handicapped the comparison possibility.

CONCLUSIONS

To conclude, the authors of the present study proved that CSA and number of nerve bundles of the tibial nerve, medial plantar nerve and lateral plantar nerve are larger among males whilst shows no differences comparing to the side of the lower limb. This study also confirms that the CSA and number of nerve bundles of the medial plantar nerve is higher than the lateral plantar nerve. The authors proved the increasing CSA and number of nerve bundles among older donors. This work also contributes to

the establishment of reference values for the medial and lateral plantar nerves.

REFERENCES

1. Alshami AM, Souvlis T, Coppieters MW. A review of plantar heel pain of neural origin: differential diagnosis and management. *Man Ther.* 2008; 13(2): 103–111, doi: [10.1016/j.math.2007.01.014](https://doi.org/10.1016/j.math.2007.01.014), indexed in Pubmed: [17400020](https://pubmed.ncbi.nlm.nih.gov/17400020/).
2. Bailie DS, Kelikian AS. Tarsal tunnel syndrome: diagnosis, surgical technique, and functional outcome. *Foot Ankle Int.* 1998; 19(2): 65–72, doi: [10.1177/107110079801900203](https://doi.org/10.1177/107110079801900203), indexed in Pubmed: [9498577](https://pubmed.ncbi.nlm.nih.gov/9498577/).
3. Bedewi MA, Abodonya A, Kotb M, et al. Estimation of ultrasound reference values for the lower limb peripheral nerves in adults: A cross-sectional study. *Medicine (Baltimore).* 2018; 97(12): e0179, doi: [10.1097/MD.00000000000010179](https://doi.org/10.1097/MD.00000000000010179), indexed in Pubmed: [29561431](https://pubmed.ncbi.nlm.nih.gov/29561431/).
4. Bilge O, Ozer MA, Govsa F. Neurovascular branching in the tarsal tunnel. *Neuroanatomy.* 2003; 2: 39–41.
5. Boehm J, Scheidl E, Bereczki D, et al. High-resolution ultrasonography of peripheral nerves: measurements on 14 nerve segments in 56 healthy subjects and reliability assessments. *Ultraschall Med.* 2014; 35(5): 459–467, doi: [10.1055/s-0033-1356385](https://doi.org/10.1055/s-0033-1356385), indexed in Pubmed: [24764211](https://pubmed.ncbi.nlm.nih.gov/24764211/).
6. Cartwright MS, Mayans DR, Gillson NA, et al. Nerve cross-sectional area in extremes of age. *Muscle Nerve.* 2013; 47(6): 890–893, doi: [10.1002/mus.23718](https://doi.org/10.1002/mus.23718), indexed in Pubmed: [23670837](https://pubmed.ncbi.nlm.nih.gov/23670837/).
7. Cartwright MS, Passmore LV, Yoon JS, et al. Cross-sectional area reference values for nerve ultrasonography. *Muscle Nerve.* 2008; 37(5): 566–571, doi: [10.1002/mus.21009](https://doi.org/10.1002/mus.21009), indexed in Pubmed: [18351581](https://pubmed.ncbi.nlm.nih.gov/18351581/).
8. Ceballos D, Cuadras J, Verdú E, et al. Morphometric and ultrastructural changes with ageing in mouse peripheral nerve. *J Anat.* 1999; 195 (Pt 4): 563–576, doi: [10.1046/j.1469-7580.1999.19540563.x](https://doi.org/10.1046/j.1469-7580.1999.19540563.x), indexed in Pubmed: [10634695](https://pubmed.ncbi.nlm.nih.gov/10634695/).
9. Davis TJ, Schon LC. Branches of the tibial nerve: anatomic variations. *Foot Ankle Int.* 1995; 16(1): 21–29, doi: [10.1177/107110079501600105](https://doi.org/10.1177/107110079501600105), indexed in Pubmed: [7697149](https://pubmed.ncbi.nlm.nih.gov/7697149/).
10. De Maeseneer M, Madani H, Lenchik L, et al. Normal anatomy and compression areas of nerves of the foot and ankle: US and MR imaging with anatomic correlation. *Radiographics.* 2015; 35(5): 1469–1482, doi: [10.1148/rg.2015150028](https://doi.org/10.1148/rg.2015150028), indexed in Pubmed: [26284303](https://pubmed.ncbi.nlm.nih.gov/26284303/).
11. Delgado-Martínez I, Badia J, Pascual-Font A, et al. Fascicular topography of the human median nerve for neuroprosthetic surgery. *Front Neurosci.* 2016; 10: 286, doi: [10.3389/fnins.2016.00286](https://doi.org/10.3389/fnins.2016.00286), indexed in Pubmed: [27445660](https://pubmed.ncbi.nlm.nih.gov/27445660/).
12. Grimm A, Axer H, Heiling B, et al. Nerve ultrasound normal values: Readjustment of the ultrasound pattern sum score UPSS. *Clin Neurophysiol.* 2018; 129(7): 1403–1409, doi: [10.1016/j.clinph.2018.03.036](https://doi.org/10.1016/j.clinph.2018.03.036), indexed in Pubmed: [29729596](https://pubmed.ncbi.nlm.nih.gov/29729596/).
13. He Y, Xiang Xi, Zhu BH, et al. Shear wave elastography evaluation of the median and tibial nerve in diabetic peripheral neuropathy. *Quant Imaging Med Surg.* 2019; 9(2): 273–282, doi: [10.21037/qims.2019.02.05](https://doi.org/10.21037/qims.2019.02.05), indexed in Pubmed: [30976551](https://pubmed.ncbi.nlm.nih.gov/30976551/).

14. Heimkes B, Posel P, Stotz S, et al. The proximal and distal tarsal tunnel syndromes. An anatomical study. *Int Orthop.* 1987; 11(3): 193–196, doi: [10.1007/BF00271447](https://doi.org/10.1007/BF00271447), indexed in Pubmed: [3623755](https://pubmed.ncbi.nlm.nih.gov/3623755/).
15. Horwitz M. Normal anatomy and variations of the peripheral nerves of the leg and foot application in operations for vascular diseases: study of one hundred specimens. *Arch Surg.* 1938; 36(4): 626–636, doi: [10.1001/archsurg.1938.01190220068005](https://doi.org/10.1001/archsurg.1938.01190220068005).
16. Ito T, Kijima M, Watanabe T, et al. Ultrasonography of the tibial nerve in vasculitic neuropathy. *Muscle Nerve.* 2007; 35(3): 379–382, doi: [10.1002/mus.20673](https://doi.org/10.1002/mus.20673), indexed in Pubmed: [17058272](https://pubmed.ncbi.nlm.nih.gov/17058272/).
17. Joshi SS, Joshi SD, Athavale AS. Anatomy of tarsal tunnel and its applied Significance. *J Anat Soc India.* 2006; 55(1): 52–56.
18. Kang S, Kim SeH, Yang SN, et al. Sonographic features of peripheral nerves at multiple sites in patients with diabetic polyneuropathy. *J Diabetes Complications.* 2016; 30(3): 518–523, doi: [10.1016/j.jdiacomp.2015.12.008](https://doi.org/10.1016/j.jdiacomp.2015.12.008), indexed in Pubmed: [26782023](https://pubmed.ncbi.nlm.nih.gov/26782023/).
19. Kerasnoudis A, Pitarokoili K, Behrendt V, et al. Cross sectional area reference values for sonography of peripheral nerves and brachial plexus. *Clin Neurophysiol.* 2013; 124(9): 1881–1888, doi: [10.1016/j.clinph.2013.03.007](https://doi.org/10.1016/j.clinph.2013.03.007), indexed in Pubmed: [23583024](https://pubmed.ncbi.nlm.nih.gov/23583024/).
20. Koo GB, Lee JH, Jang JH, et al. Superficial course of the medial plantar nerve: case report. *Anat Cell Biol.* 2019; 52(1): 87–89, doi: [10.5115/acb.2019.52.1.87](https://doi.org/10.5115/acb.2019.52.1.87), indexed in Pubmed: [30984458](https://pubmed.ncbi.nlm.nih.gov/30984458/).
21. Kronlage M, Schwehr V, Schwarz D, et al. Magnetic resonance neurography: normal values and demographic determinants of nerve caliber and T2 relaxometry in 60 healthy individuals. *Clin Neuroradiol.* 2019; 29(1): 19–26, doi: [10.1007/s00062-017-0633-5](https://doi.org/10.1007/s00062-017-0633-5), indexed in Pubmed: [29030674](https://pubmed.ncbi.nlm.nih.gov/29030674/).
22. Lee D, Dauphinée D. Morphological and functional changes in the diabetic peripheral nerve. *J Am Podiatr Med Assoc.* 2005; 95(5): 433–437, doi: [10.7547/0950433](https://doi.org/10.7547/0950433).
23. Lijoi F, Lughì M, Baccarani G. Posterior arthroscopic approach to the ankle: an anatomic study. *Arthroscopy.* 2003; 19(1): 62–67, doi: [10.1053/jars.2003.50003](https://doi.org/10.1053/jars.2003.50003), indexed in Pubmed: [12522404](https://pubmed.ncbi.nlm.nih.gov/12522404/).
24. Lothet EH, Bishop TJ, Walker FO, et al. Ultrasound-derived nerve cross-sectional area in extremes of height and weight. *J Neuroimaging.* 2019; 29(3): 406–409, doi: [10.1111/jon.12590](https://doi.org/10.1111/jon.12590), indexed in Pubmed: [30582247](https://pubmed.ncbi.nlm.nih.gov/30582247/).
25. Mizia E, Tomaszewski KA, Rutowicz B, et al. Computer-assisted assessment of the histological structure of the human sural nerve. *Folia Morphol.* 2014; 73(3): 292–297, doi: [10.5603/FM.2014.0046](https://doi.org/10.5603/FM.2014.0046), indexed in Pubmed: [25242156](https://pubmed.ncbi.nlm.nih.gov/25242156/).
26. Moore KL. *Clinically Oriented Anatomy.* 8th Ed, LWW 2017.
27. Riazì S, Bril V, Perkins BA, et al. Can ultrasound of the tibial nerve detect diabetic peripheral neuropathy? A cross-sectional study. *Diabetes Care.* 2012; 35(12): 2575–2579, doi: [10.2337/dc12-0739](https://doi.org/10.2337/dc12-0739), indexed in Pubmed: [23033242](https://pubmed.ncbi.nlm.nih.gov/23033242/).
28. Seok HY, Jang JH, Won SJ, et al. Cross-sectional area reference values of nerves in the lower extremities using ultrasonography. *Muscle Nerve.* 2014; 50(4): 564–570, doi: [10.1002/mus.24209](https://doi.org/10.1002/mus.24209), indexed in Pubmed: [24639103](https://pubmed.ncbi.nlm.nih.gov/24639103/).
29. Singh K, Gupta K, Kaur S. High resolution ultrasonography of the tibial nerve in diabetic peripheral neuropathy. *J Ultrason.* 2017; 17(71): 246–252, doi: [10.15557/JoU.2017.0036](https://doi.org/10.15557/JoU.2017.0036), indexed in Pubmed: [29375899](https://pubmed.ncbi.nlm.nih.gov/29375899/).
30. Singh Y, Dixit R, Singh S, et al. High resolution ultrasonography of peripheral nerves in diabetic peripheral neuropathy. *Neurol India.* 2019; 67(Suppl): S71–S76, doi: [10.4103/0028-3886.250719](https://doi.org/10.4103/0028-3886.250719), indexed in Pubmed: [30688237](https://pubmed.ncbi.nlm.nih.gov/30688237/).
31. Tagliafico A, Cadoni A, Fiscì E, et al. Reliability of side-to-side ultrasound cross-sectional area measurements of lower extremity nerves in healthy subjects. *Muscle Nerve.* 2012; 46(5): 717–722, doi: [10.1002/mus.23417](https://doi.org/10.1002/mus.23417), indexed in Pubmed: [23055313](https://pubmed.ncbi.nlm.nih.gov/23055313/).
32. Tomaszewski KA, Graves MJ, Henry BM, et al. Surgical anatomy of the sciatic nerve: A meta-analysis. *J Orthop Res.* 2016; 34(10): 1820–1827, doi: [10.1002/jor.23186](https://doi.org/10.1002/jor.23186), indexed in Pubmed: [26856540](https://pubmed.ncbi.nlm.nih.gov/26856540/).
33. Warchol Ł, Walocha JA, Mizia E, et al. Ultrasound guided topographic anatomy of the medial calcaneal branches of the tibial nerve. *Folia Morphol.* 2020 [Epub ahead of print], doi: [10.5603/FM.a2020.0062](https://doi.org/10.5603/FM.a2020.0062), indexed in Pubmed: [32488855](https://pubmed.ncbi.nlm.nih.gov/32488855/).
34. Warchol Ł, Mróz I, Mizia E, et al. Vascular density of inferior tibiofibular joint: cadaveric experimental study. *Folia Med Cracov.* 2017; 57(1): 47–54, indexed in Pubmed: [28608862](https://pubmed.ncbi.nlm.nih.gov/28608862/).
35. Yiu EM, Brockley CR, Lee KJ, et al. Peripheral nerve ultrasound in pediatric Charcot-Marie-Tooth disease type 1A. *Neurology.* 2015; 84(6): 569–574, doi: [10.1212/WNL.0000000000001236](https://doi.org/10.1212/WNL.0000000000001236), indexed in Pubmed: [25576636](https://pubmed.ncbi.nlm.nih.gov/25576636/).

Effect of genistein and oestradiol on the adrenal cortex of the ovariectomised adult female albino rats

H.D. Yassa¹, N.M. Safwat², R.M. Ahmed¹, M.Z. Fathy³, H.L. Metry⁴

¹Department of Anatomy and Embryology, Faculty of Medicine, Beni-Suef University, Beni-Suef, Egypt

²Department of Pathology, Faculty of Veterinary Medicine, Beni-Suef University, Beni-Suef, Egypt

³Department of Surgery, Faculty of Veterinary Medicine, Beni-Suef University, Beni-Suef, Egypt

⁴Department of Anatomy and Embryology, Faculty of Medicine, Cairo University, Cairo, Egypt

[Received: 3 April 2020; Accepted: 3 May 2020]

Background: Genistein, a naturally occurring soy isoflavone, attracts interest as an effective and safe alternative to hormone replacement therapy for menopausal problems. The aim of the current study was to compare between the effect of genistein and oestradiol on the adrenal cortex of the ovariectomised adult female albino rats.

Materials and methods: Twenty rats were used in the current study and divided into four groups, 5 rats in each group; group 1 (control non-ovariectomised), group 2 (ovariectomised), group 3 (ovariectomised + genistein) and group 4 (ovariectomised + oestradiol). The rats were sacrificed after 4 weeks. Both adrenal glands were removed for light microscope using haematoxylin and eosin stain, ultrastructural study and immunohistochemical examination using proliferating cell nuclear antigen, caspase-3, and oestrogen receptor- β .

Results: Ovariectomised rats showed signs of degeneration in all zones of adrenal cortex. On the other hand, treatment with genistein showed restoration of the adrenal cortex with less proliferative effect than oestradiol.

Conclusions: So, genistein can be used as effective therapy to decrease the symptoms of menopause without fear of cancer development. (Folia Morphol 2021; 80, 2: 380–391)

Key words: adrenal, menopause, genistein, oestradiol, rat

INTRODUCTION

The adrenal glands are paired organs lying near the superior poles of both kidneys. They are embedded in the perirenal adipose tissue and their weight and size vary with the age and physiological conditions [20]. Each gland has two distinct components: a yellowish peripheral cortex (80% to 90% of the gland) and a reddish brown central medulla [6, 32]. The adrenal cortex

is uniquely formed of three major layers organised into concentric zones. The cells of the different zones are generally distinguished by their characteristic cellular arrangement, their ultrastructure as well as their position within the gland. The three zones of the adrenal cortex are the outermost zona glomerulosa (ZG), the middle zona fasciculata (ZF) and the innermost zona reticularis (ZR). These zones are named according to

Address for correspondence: Dr. R.M. Ahmed, Department of Anatomy and Embryology, Faculty of Medicine, Beni-Suef University, Beni-Suef, Egypt, tel: 002-01226655590, e-mail: rowayda_g@yahoo.com

This article is available in open access under Creative Common Attribution-Non-Commercial-No Derivatives 4.0 International (CC BY-NC-ND 4.0) license, allowing to download articles and share them with others as long as they credit the authors and the publisher, but without permission to change them in any way or use them commercially.

the arrangement of their secretory cells. In human, the limits of these cortical zones are usually not sharply defined [8]. The adrenal cortical hormones play vital roles in different physiological processes, including: fluid and electrolyte balance, cardiovascular homeostasis, carbohydrate, lipid and protein metabolism, immune and inflammatory reactions, reproductive function and sexual development [10].

Menopause is the period in a woman's life when hormonal alterations cause menstruation to stop permanently and may be followed by psychological and physical symptoms. This is due to ovarian failure and oestrogen deficiency which will influence the quality of life. Thus, although menopause appears to be a natural process, it is a period that must be followed and treated. The menopause experiences vary greatly from one female to another [22]. Menopause can occur spontaneously on average around 51 years of age or may be induced by medical intervention (surgery, pelvic radiation therapy or chemotherapy) [18]. It has been reported that bilateral ovariectomy can result in a decrease in the adrenal cortical activity, and oestradiol is used for treatment of this condition [25]. Gaete et al. [9] reported that hormonal therapy with oestrogen was related to the induction of proliferation in the uterus and mammary gland cells, increasing the hazard of cancer development. To prevent these adverse effects, isoflavones are being investigated as alternatives to hormone replacement therapy for menopausal women [19].

Isoflavones are a type of isoflavonoids, which act as phyto-oestrogens in mammals. Genistein, a phyto-oestrogen that belongs to isoflavones, is structurally similar to 17 β -oestradiol, and selective oestrogen receptor modulator. On that account, there has been intense interest in the isoflavones as substitutes for oestrogen for postmenopausal women and as preventive therapy for premenopausal women [19].

MATERIALS AND METHODS

Animals and experimental protocols

Twenty adult female albino rats (Sprague-Dawley) weighing 180–200 g were used in the present work. Rats were provided by Faculty of Veterinary Medicine, Beni-Suef University Animal House and bred in specific pathogen free condition. Rats were housed and maintained in an air-conditioned animal house under standard laboratory and environmental conditions, and were subjected to a 12:12 hours daylight/darkness and allowed free access to food and water. Before carrying

out the drug administration, rats were acclimatised in the laboratory for 2 weeks. All the ethical protocols and guidelines for animal handling and treatment were followed and supervised by the animal facilities, Faculty of Veterinary Medicine, Beni-Suef University in compliance with the national standards published in the Guide for the Care and Use of Laboratory Animals.

Rats were divided into four groups; 5 rats each; group 1 — the control group received standard diet only; group 2 — the ovariectomised group (OVX), rats were subjected to ovariectomy operation; group 3 — ovariectomised and treated with genistein group (OVX + genistein); group 4 — ovariectomised and treated with oestradiol group (OVX + oestradiol).

Ovariectomy operation

Rats were anaesthetised with intraperitoneal injection of ketamine (15 mg/kg body weight). The lower abdomen of the rats was shaved and incised to identify the Fallopian tubes and ovaries. The Fallopian tubes below the ovaries were tied using absorbable vicryl sutures. Then, the ovaries were removed [26].

Drugs

Genistein: was obtained from Sigma Chemical Company (St. Louis, Missouri, USA). Each 100 mg of genistein was dissolved in 10 mL distilled water (10 mg/mL) and given orally by gastric tube. The dose was adjusted on the basis of a previous work [31].

Oestradiol: Cyclo-Progynova (oestradiol valerate 2 mg, Bayer Weimar Pharma, AG, Germany), 1 mg/kg/day, orally [29].

Drugs were daily ingested by gastric intubation and by the end of application; the gavage tube was left for seconds to avoid regurgitation and to assure supplying the calculated dose completely. All the medications were supplied at a fixed time for the whole period of the experiment.

By the end of the experimental period after 4 weeks, rats were sacrificed by CO₂ narcosis. Both adrenal glands of each rat were collected and used for the following methods. One was used for haematoxylin and eosin (H&E) stain and immunohistochemistry study. The other gland was fixed in glutaraldehyde solution for electron microscopic examination.

Haematoxylin and eosin [7]

Specimens were fixed in 10% neutral buffered formalin for 48 h and were processed to prepare 5 μ m thick paraffin sections.

Immunohistochemical stains using

Proliferating cell nuclear antigen (PCNA) [24]: using PCNA antibody (Clone PC-10). It is a mouse anti-rat monoclonal antibody (Santa Cruz Biotechnology, catalogue number sc-56). It was supplied as (7.0 mL) of antibody (200 µg/mL) prediluted 1:2000 using phosphate buffered saline (PBS) based antibody diluent, PH: 7.4 to reduce background and unspecific staining. It was stored at 2–8°C. No special pretreatment was required for immunohistochemical staining of formalin-fixed tissues

Caspase-3 [2]: using caspase-3 (CPP 32) Ab-4. It is a rabbit polyclonal antibody (Lab Vision Corporation Laboratories, USA, RB-1197-R7). It was supplied as prediluted ready-to-use antibody for staining formalin fixed paraffin-embedded tissues. It was stored at 2–8°C.

Oestrogen receptors (ER-β) [3]: it is a rabbit polyclonal antibody; catalogue number RB-10658-R7 (ready to use for immunohistochemical staining). This antibody labels oestrogen which is detected in human thymus, spleen, ovary and testis and in rat ovary and prostate. It reacts in human and rat and is characterised by nuclear cellular localisation. It was supplied as antibody fraction purified from rabbit anti-serum. Prepared as prediluted antibody which is ready to use for staining of formalin-fixed and paraffin embedded tissues. It's stored at 4°C. When stored at 2–8°C, this antibody is stable for 24 months. Staining of formalin-fixed tissues requires boiling tissue sections in 10 mM citrate buffer, pH 6.0 for 10–20 min followed by cooling at room temperature for 20 min.

Electron microscopy [4]

After dissecting the rats, 5–10 small pieces 1 × 1 mm in size were taken from each specimen and then fixed in 5% cold glutaraldehyde for 24–48 h. Then, the specimens were washed in cacodylate buffer (pH 7.2) 3–4 times for 20 min every time and post fixed in 1% osmium tetroxide (O₄S₄) for 2 hours. After that, specimens were washed in the same buffer four times. Ascending grades of alcohol (30–50–70–90 and 100%) were used dehydrate the sections (2 h each) and then they were embedded in epon-araldite mixture according to the protocol of E.M. unit, Assiut University. Semi thin sections by LKB ultramicrotome in thickness of 0.5–1 micron were prepared from the embedded blocks for orientation of the tissue and photographed by sc30 Olympus camera. Ultrathin section in thickness of 500–700 Å were made using

Leica AG ultramicrotome and contrasted in uranyl acetate and lead citrate, as usual. Examination was performed by JEM 100 CXII electron microscope at 80 KV and photographed by CCD digital camera Model XR-41.

Morphometric study

Measurements of the width of the 3 cortical zones in all groups were performed using image J programme at the Faculty of Medicine, Beni-Suef University.

Statistical analysis

Analysis of variance (ANOVA) was used to compare between the different groups in morphometric results and followed by post hoc Tukey test. The results were expressed as means ± standard deviation. The differences were considered statistically significant when p-value was < 0.05.

RESULTS

Light microscopy with H&E stain

The control group showed the normal histological architecture. The adrenal cortex is covered with thin capsule and an outer layer of adipose connective tissue. It consists of three main zones; the first, ZG is a narrow zone just under the capsule formed of columnar cells with vacuolated cytoplasm and rounded vesicular nuclei. The cells are arranged in arched groups (Fig. 1A). The second, ZF is the widest zone formed of polyhedral cells having clear cell membranes, vacuolated cytoplasm with lipid droplets and large rounded nuclei. The cells are arranged in narrow straight cords (fascicles) separated by straight capillaries (Fig. 2A). The last one, ZR is the deepest zone and is formed of polyhedral cells in branching and anastomosing cords separated by blood sinusoids (Fig. 3A).

In the OVX group, most of the cells in ZG are comparable to control with vesicular nuclei and vacuolated cytoplasm. Few cells have hypochromatic or ghost nuclei (Fig. 1B). The nuclei of the affected cells in both ZF and ZR showed different degrees of pathologic lesions, pyknotic with shrunken and darkly stained nuclei, hypochromatic or had ghost figures. The blood capillaries and sinusoids in between the cortical cells were dilated (Figs. 2B, 3B).

In the OVX + genistein group, a marked amelioration of the degenerative effects were seen in

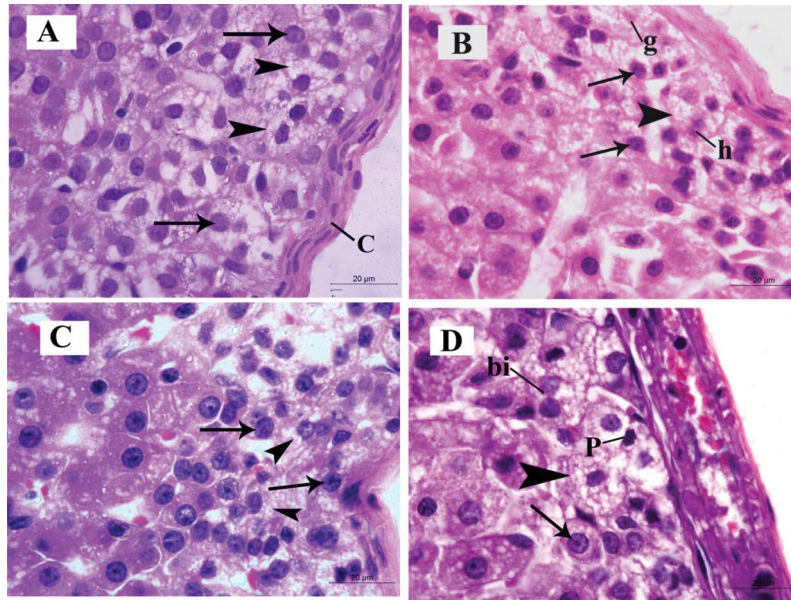


Figure 1. Haematoxylin and eosin-stained sections of zona glomerulosa (ZG) of different studied groups; **A.** Control group; **B.** Ovariectomised group (OVX); **C.** OVX + genistein group; **D.** OVX + oestradiol group; **A.** The ZG is covered by capsule (C) and the cells are columnar with vesicular nuclei (arrows) and vacuolated cytoplasm (arrow heads); **B.** Glomerulosa cells have vesicular nuclei (arrows) and vacuolated cytoplasm (arrow head) and some cells have hypochromatic (h) or ghost (g) nuclei; **C.** The cells became comparable to control with vesicular nuclei (arrows) and vacuolated cytoplasm (arrow heads); **D.** Glomerulosa cells have vesicular nuclei (arrow) and vacuolated cytoplasm (arrow head) and some cells are pyknotic (p) and others are binucleated (bi). Scale bar = 20 µm.

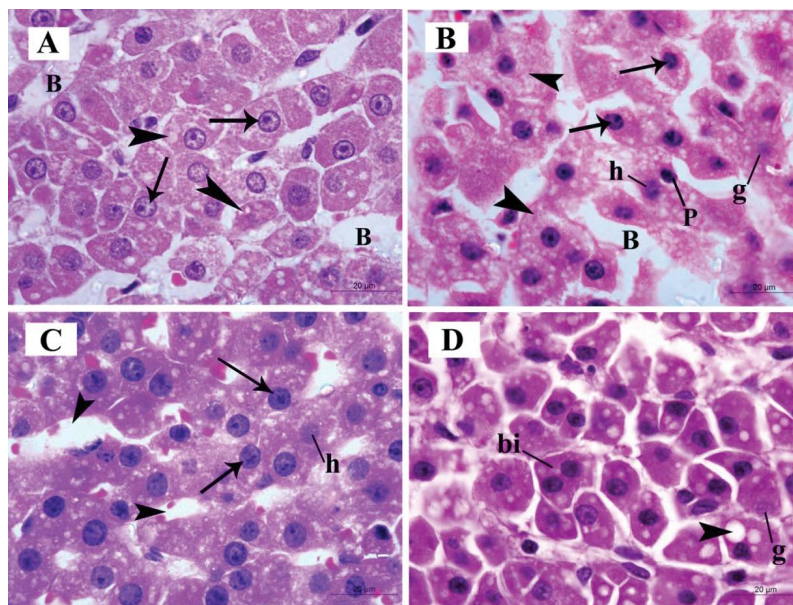


Figure 2. Haematoxylin and eosin-stained sections of zona fasciculata (ZF) of different studied groups; **A.** Control group; **B.** Ovariectomised group (OVX); **C.** OVX + genistein group; **D.** OVX + oestradiol group; **A.** The cells in this zone are polyhedral with vesicular nuclei (arrows) and the cytoplasm has few vacuolations (arrow heads). The cells are separated by blood capillaries (B); **B.** The cells have vesicular nuclei (arrows) and vacuolated cytoplasm (arrow heads) and some cells have pyknotic (p), hypochromatic (h) or ghost (g) nuclei. Fasciculata cells are separated by dilated blood capillaries (B); **C.** Fasciculata cells became comparable to control with vesicular nuclei (arrows) and few cells have hypochromatic nuclei (h). The blood capillaries between the cells are mildly congested (arrow heads); **D.** Fasciculata cells are pleomorphic having vacuolated cytoplasm (arrow head). Some cells have ghost figures (g) and others are binucleated (bi). Scale bar = 20 µm.

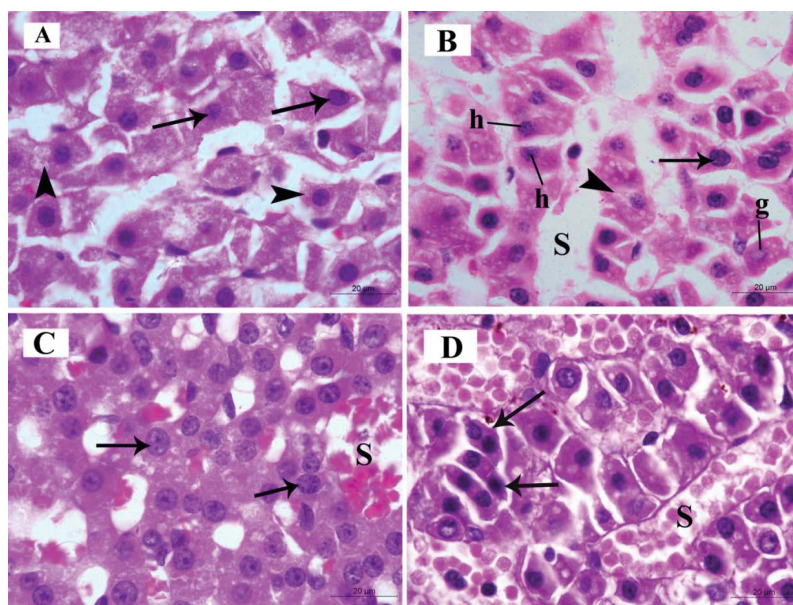


Figure 3. Haematoxylin and eosin-stained sections of zona reticularis (ZR) of different studied groups; **A.** Control group; **B.** Ovariectomised group (OVX); **C.** OVX + genistein group; **D.** OVX + oestradiol group; **A.** The cells in this zone are polyhedral with vesicular nuclei (arrows) and the cytoplasm has few vacuolations (arrow heads); **B.** The cells have vesicular nuclei (arrow) and vacuolated cytoplasm (arrow head) and some cells have hypochromatic (h) or ghost (g) nuclei. Reticularis cells are separated by dilated blood sinusoids (S); **C.** The cells became comparable to control with vesicular nuclei (arrows) and the blood sinusoids between the cells are mildly congested (S); **D.** Reticularis cells are pleomorphic and binucleated (arrows). They are separated by congested blood sinusoids. Scale bar = 20 μm .

the majority of rats in the three zones with only few degenerated cells having hypochromatic nuclei and few congested blood capillaries were detected (Figs. 1C, 2C, 3C).

In the OVX + oestradiol group, there was generalised hyperplasia. The cells were pleomorphic with high mitotic activity. Numerous cells were binucleated and others had pyknotic or ghost nuclei. The blood sinusoids in between the cortical cells were dilated and congested (Figs. 1D, 2D, 3D).

Immunohistochemical staining with PCNA

Proliferating cell nuclear antigen stained sections of group 1 (control) and group 2 (OVX) revealed negative immunoreaction (Fig. 4A, B). While, group 3 (OVX + genistein) revealed positive immunoreaction (Fig. 4C). Group 4 (OVX + oestradiol) revealed strong positive immunoreaction (Fig. 4D).

Immunohistochemical staining with caspase-3

Caspase-3 stained sections of group 1 (control), group 3 (OVX + genistein) and group 4 (OVX + oestradiol) revealed negative immunoreaction (Fig. 5A, C, D), while group 2 (OVX) revealed positive immunoreaction (Fig. 5B).

Immunohistochemical staining with ER- β

Oestrogen receptor- β stained sections of group 1 (control), group 3 (OVX + genistein) and group 4 (OVX + oestradiol) revealed positive immunoreaction (Fig. 6A, C, D), while group 2 (OVX) revealed negative immunoreaction (Fig. 6B).

Ultrastructural study of the adrenal cortex

In the control group, ZG cells had rounded or oval nuclei with finely dispersed euchromatin and the nuclear envelope and nuclear pores were easily discerned. The cytoplasm had variable sized numerous lipid globules, medium-sized, rounded or oval mitochondria (Fig. 7A). The fasciculata cells appeared with rounded or oval euchromatic nuclei with clear nuclear envelope rounded mitochondria and variable amount of lipid globules (Fig. 8A). Cells of ZR had vesicular nucleus and abundant cytoplasm which contains few lipid globules and mitochondria (Fig. 9A).

In the OVX group, the adrenal cortical cells showed signs of degeneration. The ZG cells contained vesicular nucleus and the cytoplasm showed few lipid globules which vary in size and electron density. The cytoplasm of the cells also revealed numerous vacu-

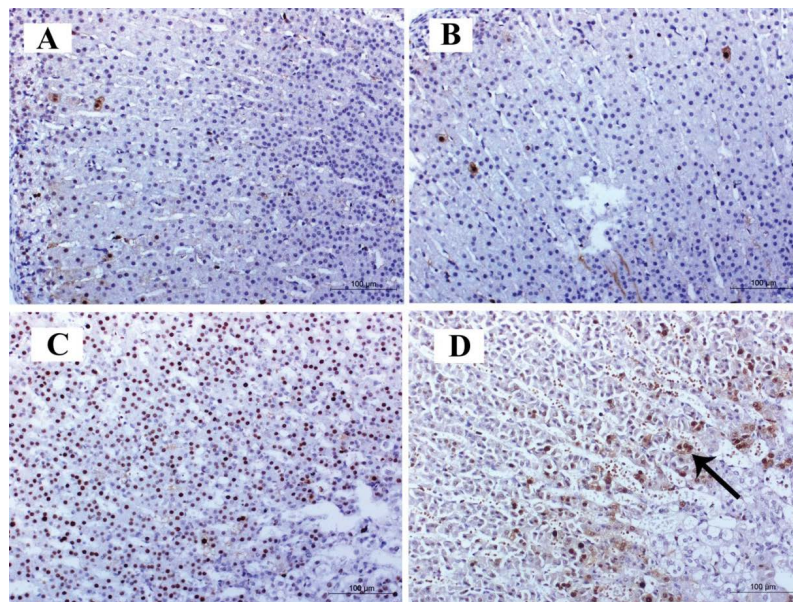


Figure 4. Proliferating cell nuclear antigen-stained sections of different studied groups; **A.** Control group; **B.** Ovariectomised group (OVX) are showing negative immunoreaction; **C.** OVX + genistein group is revealing positive immune reaction; **D.** OVX + oestradiol group showing strong positive immune reaction (arrow). Scale bar = 100 µm.

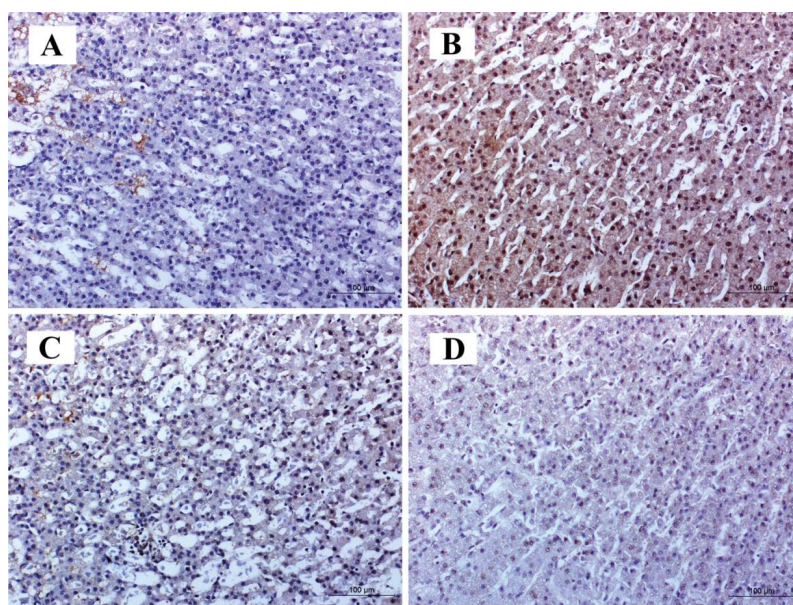


Figure 5. Caspase-3-stained sections of different studied groups; **A.** Control group; **B.** Ovariectomised (OVX) group showing strong positive immune reaction; **C.** OVX + genistein group; **D.** OVX + oestradiol group showing negative immunoreaction. Scale bar = 100 µm.

oles and small electron dense lysosomes (Fig. 7B). The ZF cells showed irregular nucleus with thick and irregular nuclear envelope and indistinguishable pores and the cytoplasm contained numerous vacuoles (Fig. 8B). The ZR cells showed irregular nucleus with thick and irregular nuclear envelope and indistinguishable pores and the cytoplasm contained vacuoles and lipofuscin granules (Fig. 9B).

The OVX + genistein group almost regained the normal ultrastructure of cells. The ZG cells showed large amount of electron dense lipid globules, mitochondria, less vacuoles and the nucleus showed normal and regular nuclear membrane, well discerned nuclear pores and finely dispersed euchromatin. Few nuclei became small and condensed (Fig. 7C). The ZF cells showed rounded or oval euchromatic nucleus

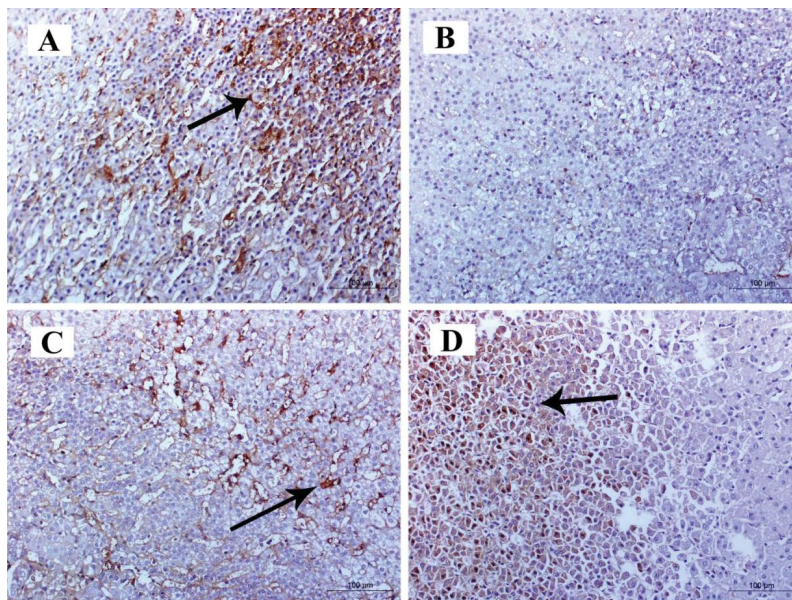


Figure 6. Oestrogen receptor- β -stained sections of different studied groups; **A.** Control group; **B.** Ovariectomised (OVX) group is showing negative immune reaction; **C.** OVX + genistein group; **D.** OVX + oestradiol group showing positive immunoreaction (arrows). Scale bar = 100 μ m.

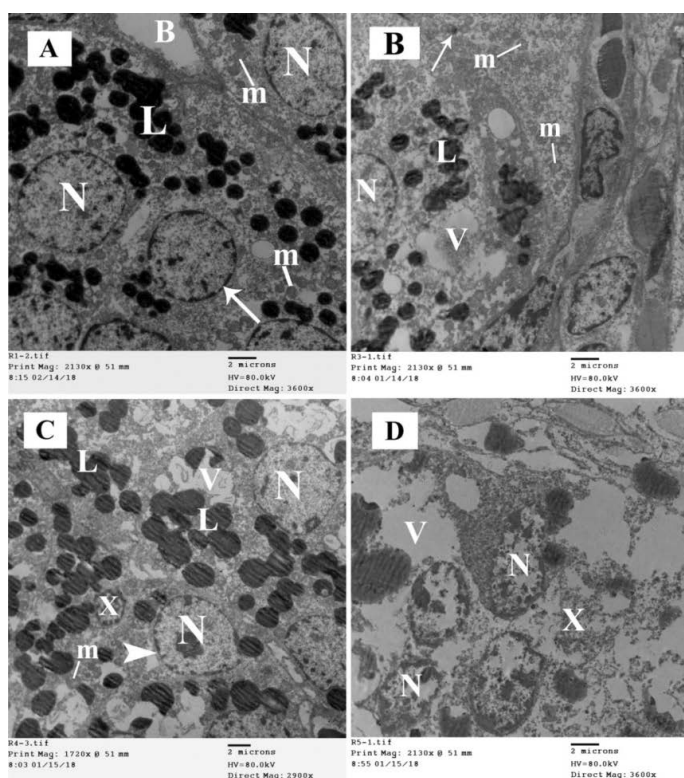


Figure 7. Electron micrographs of the zona glomerulosa (ZG) of the adrenal cortex of different studied groups; **A.** Control group; **B.** Ovariectomised (OVX) group; **C.** OVX + genistein group; **D.** OVX + oestradiol group; **A.** Glomerulosa cells have rounded or oval nuclei (N) with finely dispersed euchromatin and the nuclear envelope and nuclear pores are easily discerned (arrow) and the cytoplasm contains spherical or rounded mitochondria (m) and lipid globules (L). The cells are separated by blood capillaries (B); **B.** The nuclei of the glomerulosa cells are rounded or oval (N) and the cytoplasm contains rounded mitochondria (m), less lipid globules compared to the control group (L), numerous vacuoles (V) and small electron dense lysosomes (arrow); **C.** The nuclei (N), lipid globules (L) and mitochondria (m) are comparable to control. Few vacuoles (V) are detected and few nuclei became small and condensed (X); **D.** Glomerulosa cells have condensed nuclei (N) and the cytoplasm contains vacuoles (V) with dispersion of the cell organelles (X). Scale bars: E = 2 μ m.

and the cytoplasm contained variable amount of lipid globules, mitochondria and few lysosomes (Fig. 8C). The cells of ZR appeared of normal structure containing euchromatic nucleus and few lipid globules. Apoptotic cell was seen with loss of its architecture.

Some cells showed condensation of the nucleus chromatin (Fig. 9C).

In the OVX + oestradiol group, the cells forming the ZG had condensed nuclei and the cytoplasm contained large amount of vacuoles with dispersion

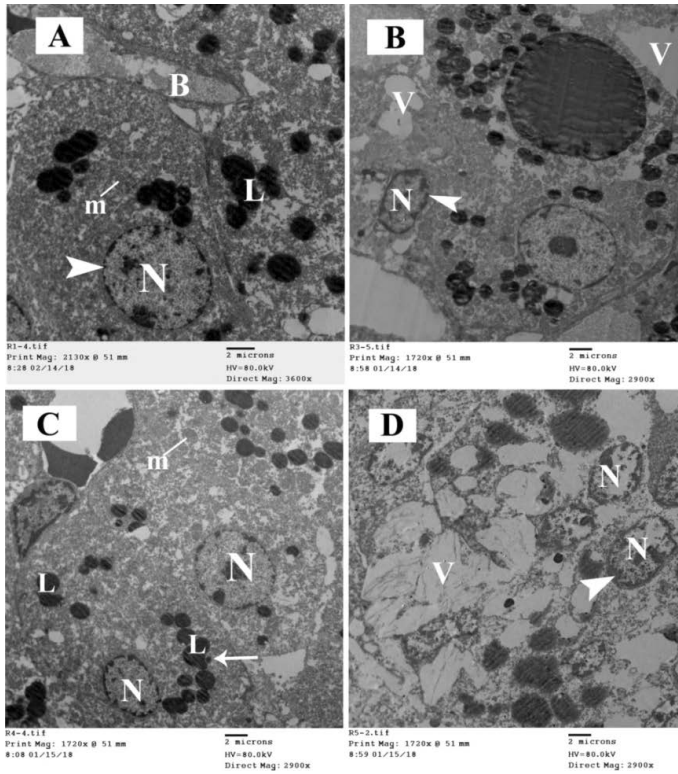


Figure 8. Electron micrographs of the zona fasciculata (ZF) of the adrenal cortex of different studied groups; **A.** Control group; **B.** Ovariectomised (OVX) group; **C.** OVX + genistein group; **D.** OVX + oestradiol group; **A.** Fasciculata cells have rounded or oval euchromatic nuclei (N) with regular nuclear envelope and nuclear pores are easily discerned (arrow head) and the cytoplasm contains spherical or rounded mitochondria (m) and lipid globules (L). The cells are separated by blood capillaries (B); **B.** The cells contain irregular nucleus (N (with thick and irregular nuclear envelope and indistinguishable pores (arrow head) and the cytoplasm contains vacuoles (V); **C.** The cells show rounded or oval euchromatic nuclei (N) and the cytoplasm contains variable amount of lipid globules (L) and rounded mitochondria (m); **D.** The nuclei of the fasciculata cells (N) are condensed with thick and irregular nuclear envelope and indistinguishable pores (arrow head) and the cytoplasm has large amount vacuoles communicating with each other (V). Scale bars: E = 2 µm.

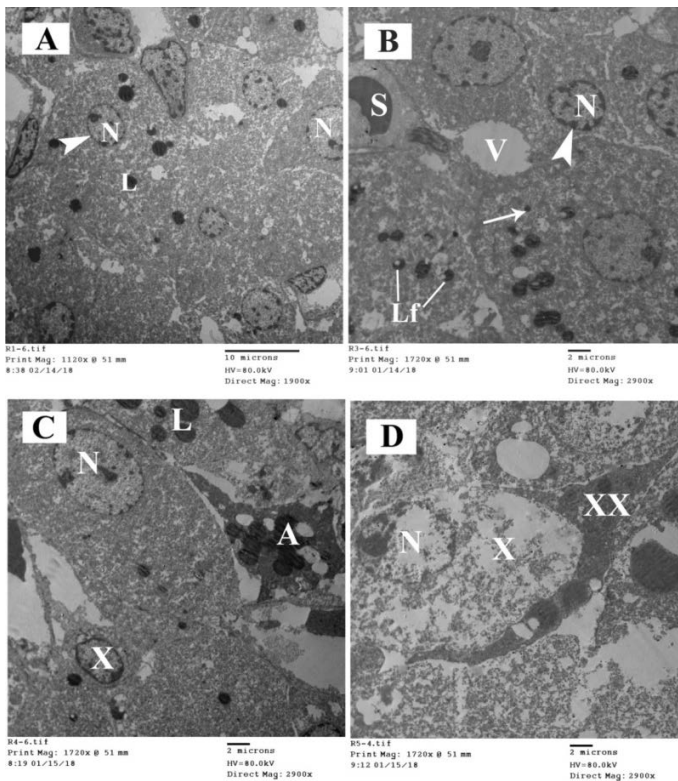


Figure 9. Electron micrographs of the zona reticularis (ZR) of the adrenal cortex of different studied groups; **A.** Control group; **B.** Ovariectomised (OVX) group; **C.** OVX + genistein group; **D.** OVX + oestradiol group; **A.** The ZR cells have rounded or oval euchromatic nuclei (N) with regular nuclear envelope and nuclear pores are easily discerned (arrow head) and the cytoplasm contains few lipid globules (L); **B.** Reticularis cells contain irregular nucleus (N (with thick and irregular nuclear envelope and indistinguishable pores (arrow head) and the cytoplasm of the cells contains vacuoles (V), lysosomes (arrow) and lipofuscin granules (Lf). The cells are separated by blood sinusoids (S); **C.** In this zone, the cells contain variable amount of lipid globules (L) and euchromatic nuclei (N). Some cells show condensation of the nucleus chromatin (X) Apoptotic cell (A) is seen with loss of its architecture; **D.** The cells show dispersion of the cytoplasmic cell organelles (X).The nuclei of the cells (N) are small and electron dens. Apoptotic cell appear electron dens and compressed in between the cells (XX). Scale bars: A = 10 µm; B, C, D = 2 µm.

of the cell organelles (Fig. 7D). The ZF cells had large amount of vacuoles communicating with each other and their nuclei were condensed (Fig. 8D).

The ZR cells showed dispersion of the cytoplasmic organelles. The nuclei of the cells were small and electron dens. Also, electron dens apoptotic

Table 1. Morphometric data of zona glomerulosa thickness in all groups

Groups	Mean \pm standard deviation	Pairwise comparison between groups		
		This group	Other groups	P-value (significance)
Group 1	104.45 \pm 12.68	1	2	0.0083
			3	0.4344
			4	0.528
Group 2	83.80 \pm 3.86	2	1	0.0083
			3	0.0144
			4	0.006
Group 3	98.53 \pm 9.86	3	1	0.4344
			2	0.0144
			4	0.192
Group 4	110.45 \pm 15.91	4	1	0.528
			2	0.006
			3	0.192

P < 0.05 is considered significant

Table 2. Morphometric data of zona fasciculata thickness in all groups

Groups	Mean \pm standard deviation	Pairwise comparison between groups		
		This group	Other groups	P-value (significance)
Group 1	685.09 \pm 41.52	1	2	0.0001
			3	0.0886
			4	0.0001
Group 2	371.69 \pm 28.30	2	1	0.0001
			3	0.0001
			4	0.0001
Group 3	752.15 \pm 65.27	3	1	0.0886
			2	0.0001
			4	0.0003
Group 4	959.52 \pm 39.61	4	1	0.0001
			2	0.0001
			3	0.0003

P < 0.05 is considered significant

cells were seen compressed between the cells (Fig. 9D).

Morphometric results

The ZG thickness was significantly decreased after ovariectomy operation ($p < 0.05$) and became comparable to control after treatment with both genistein and oestradiol (Table 1). The thicknesses of ZF (Table 2) as well as ZR (Table 3) were significantly decreased after ovariectomy operation and they were comparable to control after treatment with genistein. In contrast, oestradiol treatment significantly increased ZF and ZR thicknesses compared to group 1, 2 and 3.

DISCUSSION

In the present study, we examined the effect of ovariectomy on the adult rat adrenal cortex. Additionally, the therapeutic effects of genistein and

oestradiol on the adrenal cortex of ovariectomised adult female albino rats were compared. In this experimental study, adult female albino rats aged 3 months old were chosen to be in the reproductive period of life. According to Suckow et al. [27], female rats reach sexual maturity at 2 months of age, their reproductive system is fully functioning and their maximum fertility is reached between 3 and 10 months of age.

In the present study, specimens taken from rats subjected to ovariectomy operation and stained with H&E showed signs of degeneration in the form of irregular ZF cells and degenerated cortical cells in the form of pyknotic, hypochromatic and ghost nuclei. These findings were in agreement with the findings of Saruhan and Ozdemir [25]. The dilated blood capillaries and sinusoids were also detected. These findings usually accompany the vacuolated cells as reported by Laast et al. [15].

Table 3. Morphometric data of zona reticularis thickness in all groups

Groups	Mean \pm standard deviation	Pairwise comparison between groups		
		This group	Other groups	P-value (significance)
Group 1	317.98 \pm 24.97	1	2	0.0001
			3	0.0510
			4	0.0001
Group 2	178.15 \pm 13.74	2	1	0.0001
			3	0.0001
			4	0.0001
Group 3	366.14 \pm 39.76	3	1	0.0510
			2	0.0001
			4	0.0022
Group 4	481.50 \pm 42.55	4	1	0.0001
			2	0.0001
			3	0.0022

P < 0.05 is considered significant

Marked improvement was noticed after treatment with genistein in the degeneration of the cortical cells as they were comparable to control with only few degenerated cells having pyknotic nuclei. On the other hand, treatment with oestradiol showed trophic changes in the form of marked increase in the thickness of the cortical adrenal gland layers with proliferation of the cells compared to ovariectomised rats and rats treated with genistein. This was in agreement with previous findings in the uterus [5, 16]. Saruhan and Ozdemir [25] determined that ovariectomy resulted in a decrease in the activity of the adrenal cortex. In contrast, they found that oestrogen supplementation caused a significant increase in the activity of the adrenal cortex and medulla. Lo et al. [17] indicated that oestrogens may enhance corticosterone feedback by stimulating corticosterone production at the adrenal gland or by reducing corticosterone metabolism.

In the current study, immunohistochemistry using PCNA revealed moderate proliferation in group 3, while group 4 showed marked +ve immunoreaction. These findings were in agreement with Marinho et al. [19] who used vascular endothelial growth factor (VEGF) and Ki67 gene expression in the adrenal tissue as proliferative markers and stated that oestrogen induced an increase in the expression of both the VEGF and the Ki67 in rat adrenal glands. On the other hand, the results of the current study showed that treatment with genistein was less effective than with 17 β -oestradiol. They emphasized that genistein has an antagonistic effect, thus supporting the decreased gene expression of VEGF and Ki67 and of

proliferation-related genes. VEGF is an important regulated angiogenic molecule and is considered a prognostic factor for various tumours. Thus, these results indicate that genistein may cause less stimulation of VEGF expression than does oestrogen. In fact, some authors have shown that isoflavone may have a weaker effect on tumour induction compared to oestrogen [12, 13, 21].

In the present study, there was a significant decrease in the thickness of the three adrenal cortical zones in group 2 compared to the control group. These changes may be explained by decreased adrenal cortical activity as reported by Saruhan and Ozdemir [25]. In contrast, non-significant changes were observed in group 3 compared to the control group. This could be explained by the improvement noticed in the adrenal cortical cells after treatment with genistein. Moreover, treatment with oestradiol caused significant increase in the thickness of the adrenal cortical zones compared to group 1, 2 and 3. These findings were going well with the results obtained by Marinho et al. [19] who reported that treatment with soy isoflavone extract induces fewer changes in the thickness of all zones of the adrenal cortex than treatment with oestrogen compared to ovariectomised rats.

In the current work, immunohistochemistry using caspase-3 revealed that +ve reaction appeared only with the group 2 but were -ve in group 3 and 4. Marinho et al. [19] analysed the expression of caspase-3 gene in order to verify the protective potential of isoflavones. Animals treated with isoflavones showed an expression of caspase-3 more than the

group treated with oestradiol. This may be related to the proliferative potential of oestradiol, which to some extent can prevent cell death by apoptosis.

Data from many experiments indicate that gonadal hormones have a direct effect on the physiology of the adrenal tissue. ER expression had been demonstrated in the adrenal glands of several species such as rodents [14] and monkeys [11]. In the present study, group 1 exhibited +ve ER- β immuno-staining. On the other hand, group 2 showed down-regulation of ER- β expression, with -ve ER- β immuno-reactivity. After treatment with genistein and oestradiol, many cells exhibited strong +ve ER- β immuno-reactivity. Such down regulation of ER- β in group 2 probably explains the degenerative changes induced in the cortical cells. Then, the up-regulation of ER- β in the groups treated with genistein and oestradiol clearly indicates that ER- β expressed by the adrenal cortical cells mediate oestrogen-induced cell proliferation in these cells. These findings postulate that ER- β isoform plays an essential role in modifying the effect of oestrogen and thus, further improvement of the adrenal cortex. This was matching with Teng et al. [28] who suggested that ER- β isoform plays an important role in modulating the urinary bladder urothelial proliferation.

In the reviewed literature there were no electron microscopic studies observing the ultrastructure of the adrenal cortex in OVX rats and their treatment with either genistein or oestradiol.

Comparable to L.M. examination, the E.M. examination of the adrenal cortex of group 2 showed marked signs of degeneration. The lipofuscin pigments were the most obvious finding in ZR. These results were in agreement with the demonstration carried by Rebuffat et al. [23] and Almeida et al. [1] who observed these findings in aged rats.

Lipofuscin pigments are common structures found in aged ZF and ZR cells and are frequently observed as a classic marker of ageing. Ward and Reznik-Schuller [30] stated that lipofuscin pigments may have originated from degradation of lipid droplets of epithelial cells. Almeida et al. [1] demonstrated that lipofuscin does not exert any noticeable damaging effect on cells but it is possible that, at a certain moment, this accumulation may interfere with cellular function.

The genistein treated group almost regained the normal ultrastructure. While, the oestradiol treated group showed dispersion of the cytoplasmic orga-

nelles and apoptotic cells were detected. Similar data have not been reported in the reviewed literature.

CONCLUSIONS

It could be concluded that ovariectomy decreases the adrenal gland activity due to decreased oestrogen levels in blood. On the other hand, administration of genistein ameliorates the adrenal gland injury without producing trophic effect. Moreover, oestradiol treatment induces an intense cell proliferation as proved histologically, immunohistochemically and ultrastructurally. So, genistein found naturally in soy may have less effect on cell proliferation and cancer risk than oestradiol.

REFERENCES

1. Almeida H, Magalhães MC, Magalhães MM. Age-related changes in lipid peroxidation products in rat adrenal gland. *Age (Omaha)*. 1998; 21(3): 119–121, doi: [10.1007/s11357-998-0018-4](https://doi.org/10.1007/s11357-998-0018-4), indexed in Pubmed: [23604369](https://pubmed.ncbi.nlm.nih.gov/23604369/).
2. Bancroft JD, Gamble M. *Theory and practice of histological techniques*. 6th ed. Churchill Livingstone Elsevier, China 2008: 433–472.
3. Bancroft JD, Cook HC. *Immunocytochemistry*. In: *Manual of Histological Techniques and Diagnostic Applications*. 1st ed., Churchill Livingstone, Edinburgh, London, Madrid, Melbourne, New York, Tokyo 1994: 263–325.
4. Bozzola J, Russell L. *Electron microscopy principles and techniques for biologists*: Jones and Bartlett publishers 20 park plaza, Boston Mao 1991: 2116.
5. Budhathoki S, Iwasaki M, Sawada N, et al. Soy food and isoflavone intake and endometrial cancer risk: the Japan Public Health Center-based prospective study. *BJOG*. 2015; 122(3): 304–311, doi: [10.1111/1471-0528.12853](https://doi.org/10.1111/1471-0528.12853), indexed in Pubmed: [24941880](https://pubmed.ncbi.nlm.nih.gov/24941880/).
6. Chang SP, Mullins JJ, Morley SD, et al. Transition from organogenesis to stem cell maintenance in the mouse adrenal cortex. *Organogenesis*. 2011; 7(4): 267–280, doi: [10.4161/org.7.4.18060](https://doi.org/10.4161/org.7.4.18060), indexed in Pubmed: [22198434](https://pubmed.ncbi.nlm.nih.gov/22198434/).
7. Drury R, Wallington E. *Carleton's Histological techniques*. 5th ed. Oxford 1980: 183–185.
8. Eroschenko VP. *DiFiore's atlas of histology with functional correlations*. 12th ed. Lippincott Williams and Wilkins, Philadelphia 2013: 402–407.
9. Gaete L, Tchernitchin AN, Bustamante R, et al. Daidzein-estrogen interaction in the rat uterus and its effect on human breast cancer cell growth. *J Med Food*. 2012; 15(12): 1081–1090, doi: [10.1089/jmf.2011.0322](https://doi.org/10.1089/jmf.2011.0322), indexed in Pubmed: [23216111](https://pubmed.ncbi.nlm.nih.gov/23216111/).
10. Hart KA, Barton MH. Adrenocortical insufficiency in horses and foals. *Vet Clin North Am Equine Pract*. 2011; 27(1): 19–34, doi: [10.1016/j.cveq.2010.12.005](https://doi.org/10.1016/j.cveq.2010.12.005), indexed in Pubmed: [21392651](https://pubmed.ncbi.nlm.nih.gov/21392651/).
11. Hirst JJ, West NB, Brenner RM, et al. Steroid hormone receptors in the adrenal glands of fetal and adult rhesus monkeys. *J Clin Endocrinol Metab*. 1992; 75(1): 308–314,

- doi: [10.1210/jcem.75.1.1619023](https://doi.org/10.1210/jcem.75.1.1619023), indexed in Pubmed: [1619023](https://pubmed.ncbi.nlm.nih.gov/1619023/).
12. Hyder SM, Huang JC, Nawaz Z, et al. Regulation of vascular endothelial growth factor expression by estrogens and progestins. *Environ Health Perspect.* 2000; 108 Suppl 5: 785–790, doi: [10.1289/ehp.00108s5785](https://doi.org/10.1289/ehp.00108s5785), indexed in Pubmed: [11035983](https://pubmed.ncbi.nlm.nih.gov/11035983/).
 13. Jarzabek K, Koda M, Walentowicz-Sadlecka M, et al. Altered expression of ERs, aromatase, and COX2 connected to estrogen action in type 1 endometrial cancer biology. *Tumour Biol.* 2013; 34(6): 4007–4016, doi: [10.1007/s13277-013-0991-9](https://doi.org/10.1007/s13277-013-0991-9), indexed in Pubmed: [23873111](https://pubmed.ncbi.nlm.nih.gov/23873111/).
 14. Kuiper GG, Carlsson B, Grandien K, et al. Comparison of the ligand binding specificity and transcript tissue distribution of estrogen receptors alpha and beta. *Endocrinology.* 1997; 138(3): 863–870, doi: [10.1210/endo.138.3.4979](https://doi.org/10.1210/endo.138.3.4979), indexed in Pubmed: [9048584](https://pubmed.ncbi.nlm.nih.gov/9048584/).
 15. Laast VA, Larsen T, Allison N, et al. Distinguishing cystic degeneration from other aging lesions in the adrenal cortex of Sprague-Dawley rats. *Toxicol Pathol.* 2014; 42(5): 823–829, doi: [10.1177/0192623313502258](https://doi.org/10.1177/0192623313502258), indexed in Pubmed: [24970856](https://pubmed.ncbi.nlm.nih.gov/24970856/).
 16. Liu J, Yuan F, Gao J, et al. Oral isoflavone supplementation on endometrial thickness: a meta-analysis of randomized placebo-controlled trials. *Oncotarget.* 2016; 7(14): 17369–17379, doi: [10.18632/oncotarget.7959](https://doi.org/10.18632/oncotarget.7959), indexed in Pubmed: [26967050](https://pubmed.ncbi.nlm.nih.gov/26967050/).
 17. Lo MJ, Chang LL, Wang P. Effects of estradiol on corticosterone secretion in ovariectomized rats. *J Cell Biochem.* 2000; 77(4): 560–568, doi: [10.1002/\(sici\)1097-4644\(20000615\)77:4<560::aid-jcb4>3.0.co;2-d](https://doi.org/10.1002/(sici)1097-4644(20000615)77:4<560::aid-jcb4>3.0.co;2-d).
 18. Manson JE, Bassuk SS. The menopause transition and postmenopausal hormone therapy. In: Fauci AS, Braunwald E, Kasper DL, eds. *Harrison's Principles of Internal Medicine*, 17th ed. McGrawHill, New York 2008: 2334–2339.
 19. Marinho SD, Cali3 ML, Santos MA, et al. Evaluation of the isoflavones and estrogen effects on the rat adrenal. *Gynecol Endocrinol.* 2017; 33(10): 811–815, doi: [10.1080/09513590.2017.1318371](https://doi.org/10.1080/09513590.2017.1318371), indexed in Pubmed: [28454492](https://pubmed.ncbi.nlm.nih.gov/28454492/).
 20. Mescher AL. *Adrenal Glands in: Junqueira's Basic Histology: Text and Atlas*. 13th ed. McGraw-Hill Medical, New York 2013: 414–417.
 21. Nagata C, Mizoue T, Tanaka K, et al. Soy intake and breast cancer risk: an evaluation based on a systematic review of epidemiologic evidence among the Japanese population. *Jpn J Clin Oncol.* 2014; 44(3): 282–295, doi: [10.1093/jjco/hyt203](https://doi.org/10.1093/jjco/hyt203), indexed in Pubmed: [24453272](https://pubmed.ncbi.nlm.nih.gov/24453272/).
 22. Parhizkar S, Abdul Latiff L, Parsa A. Effect of *Nigella sativa* on reproductive system in experimental menopause rat model. *Avicenna J Phytomed.* 2016; 6(1): 95–103.
 23. Rebuffat P, Belloni AS, Rocco S, et al. The effects of ageing on the morphology and function of the zonae fasciculata and reticularis of the rat adrenal cortex. *Cell Tissue Res.* 1992; 270(2): 265–272, doi: [10.1007/BF00328012](https://doi.org/10.1007/BF00328012), indexed in Pubmed: [1333363](https://pubmed.ncbi.nlm.nih.gov/1333363/).
 24. Sabry MM, Elkalawy SAE, Abo-Elnour RKD, et al. Histological and immunohistochemical study on the effect of stem cell therapy on bleomycin induced pulmonary fibrosis in albino rat. *Int J Stem Cells.* 2014; 7(1): 33–42, doi: [10.15283/ijsc.2014.7.1.33](https://doi.org/10.15283/ijsc.2014.7.1.33), indexed in Pubmed: [24921026](https://pubmed.ncbi.nlm.nih.gov/24921026/).
 25. Saruhan BG, Ozdemir N. Effect of ovariectomy and of estrogen treatment on the adrenal gland and body weight in rats. *Saudi Med J.* 2005; 26(11): 1705–1709.
 26. Seko K, Kagami H, Senga K, et al. Effects of ovariectomy and estrogen replacement on rat oral mucosa. *Maturitas.* 2005; 50(1): 44–51, doi: [10.1016/j.maturitas.2004.03.015](https://doi.org/10.1016/j.maturitas.2004.03.015), indexed in Pubmed: [15590213](https://pubmed.ncbi.nlm.nih.gov/15590213/).
 27. Suckow M, Weisbroth S, Franklin C. *The laboratory Rat*, 2nd ed. American College of Laboratory Animal Medicine, Academic Press, Toronto 2005.
 28. Teng J, Wang ZY, Jarrard DF, et al. Roles of estrogen receptor alpha and beta in modulating urothelial cell proliferation. *Endocr Relat Cancer.* 2008; 15(1): 351–364, doi: [10.1677/erc.1.01255](https://doi.org/10.1677/erc.1.01255), indexed in Pubmed: [18310301](https://pubmed.ncbi.nlm.nih.gov/18310301/).
 29. Vinicius Carvalho DC, Silveira VÁ, do Prado RF, et al. Effect of estrogen therapy, soy isoflavones, and the combination therapy on the submandibular gland of ovariectomized rats. *Pathol Res Pract.* 2011; 207(5): 300–305, doi: [10.1016/j.prp.2011.01.002](https://doi.org/10.1016/j.prp.2011.01.002), indexed in Pubmed: [21514062](https://pubmed.ncbi.nlm.nih.gov/21514062/).
 30. Ward JM, Reznik-Schüller H. Morphological and histochemical characteristics of pigments in aging F344 rats. *Vet Pathol.* 1980; 17(6): 678–685, doi: [10.1177/030098588001700604](https://doi.org/10.1177/030098588001700604), indexed in Pubmed: [7423828](https://pubmed.ncbi.nlm.nih.gov/7423828/).
 31. Yang W, Wang S, Li Li, et al. Genistein reduces hyperglycemia and islet cell loss in a high-dosage manner in rats with alloxan-induced pancreatic damage. *Pancreas.* 2011; 40(3): 396–402, doi: [10.1097/MPA.0b013e318204e74d](https://doi.org/10.1097/MPA.0b013e318204e74d), indexed in Pubmed: [21206328](https://pubmed.ncbi.nlm.nih.gov/21206328/).
 32. Young B, Woodford P, O'Dowd G. *Adrenal Gland*. In: *Wheater's functional histology: a text and colour atlas*. 6th ed. Elsevier Health Sciences, Philadelphia 2013: 328–331.

Febuxostat ameliorates methotrexate-induced lung damage

S.M. Zaki^{1,2}, G.H.A. Hussein³, H.M.A. Khalil⁴, W.A. Abd Algaleel¹

¹Department of Anatomy and Embryology, Faculty of Medicine, Cairo University, Cairo, Egypt

²Fakeeh College for Medical Sciences, Jeddah, Saudi Arabia

³Department of Anatomy and Embryology, Faculty of Medicine, Beni Suef University, Beni Suef, Egypt

⁴Department of Veterinary Hygiene and Management, Faculty of Veterinary Medicine, Cairo University, Cairo, Egypt

[Received: 17 June 2020; Accepted: 1 July 2020]

Background: The intention of the present study was to assess the structural affection of the lung following methotrexate (MTX) overdose. The proposed underlying mechanisms involved in lung affection were studied. The possible modulation role of febuxostat over such affection was studied.

Materials and methods: Twenty-four rats were divided into three groups: control, MTX-treated, febuxostat-treated. The study was continued for 2 weeks. Lung was processed for histological and immunohistochemical (inducible nitric oxide synthase [iNOS] and cyclooxygenase [COX]-2) studies. Inflammatory markers (tumour necrosis factor alpha [TNF- α], interleukin 1 [IL-1]), Western blot evaluation of nuclear factor kappa B (NF- κ B) and oxidative/antioxidative markers were done.

Results: Methotrexate-treated group exhibited inflammatory cellular infiltrations, thickened interalveolar septa, dilated congested blood vessels, extravasated blood, and apoptosis. The collagen fibres content increased 3-fold. MTX induced lung affection through oxidative stress (increase MDA/decrease GSH, SOD) and apoptosis. It induced sterile inflammation through an increase of NF- κ B (2-fold), IL-1 (3-fold) and TNF- α (3-fold), COX-2 cells (2.5-fold) and iNOS (6-fold). With the use of febuxostat, the normal lung architecture was observed with a bit thickened interalveolar septum and extravasated blood. The collagen fibres content was minimal. Decrement of oxidative stress and sterile inflammation (COX-2 cells and iNOS were comparable to the control group. NF- κ B, IL-1 and TNF- α became higher by 34%, 64% and 100%).

Conclusions: The overdose of MTX displays inflammatory lung affection with residual fibrosis. It induces lung affection through oxidative stress, apoptosis and sterile inflammation. With the use of febuxostat, the normal lung architecture was preserved with a little structural affection or fibrotic residue. Febuxostat exerts its lung protection through its anti-inflammatory and antioxidant features. (Folia Morphol 2021; 80, 2: 392–402)

Key words: febuxostat, methotrexate, lung

INTRODUCTION

Methotrexate (MTX) has displayed effectiveness in treating several diseases, including rheumatoid

arthritis, psoriatic arthritis, systemic lupus erythematosus, inflammatory bowel disease, psoriasis, and small-vessel vasculitis [11, 32]. It is commonly used

Address for correspondence: Dr. S.M. Zaki, Fakeeh College for Medical Sciences, Jeddah, Saudi Arabia, e-mail: zakysheerf1@gmail.com

This article is available in open access under Creative Common Attribution-Non-Commercial-No Derivatives 4.0 International (CC BY-NC-ND 4.0) license, allowing to download articles and share them with others as long as they credit the authors and the publisher, but without permission to change them in any way or use them commercially.

as a treatment for some types of cancer, including breast, ovaries, brain, and leukaemia [26]. It is used as an alternative to surgical management of ectopic pregnancy in selected patients with small, unruptured tubal pregnancies [34]. In addition, it is recommended for induction and maintenance of remission in Crohn's disease [13].

The therapeutic application of MTX is usually limited by its severe toxicity [38]. It is involved as a causative agent in lung toxicity [9, 33]. The prevalence of MTX-related lung disease and MTX-related interstitial lung disease (in rheumatoid arthritis) are 7.6% and 11.6%, respectively [4, 9].

Several mechanisms have been studied to recognise the mechanism of MTX-induced lung damage. One of these mechanisms is oxidative stress [2]. MTX interferes with the antioxidant defence enzymes, depletes glutathione content, and causes lipid peroxidation [2]. Diminution of antioxidant defences enhances the production of reactive oxygen species (ROS) that result in parenchymal lung injury and interstitial, alveolar fibrosis [24]. Other possible mechanism of MTX-induced lung damage is inflammatory reaction of MTX. MTX increases the levels of interleukin 1beta (IL-1 β), and tumour necrosis factor alpha (TNF- α), which are indicators of inflammatory response [1]. Adding, overdose of MTX can lead to proinflammatory cytokine release [19].

Febuxostat is a selective xanthine oxidase inhibitor that is used to reduce urate levels in diseases that involve hyperuricemia such as gout and tumour lysis syndrome [28, 31]. The focus on xanthine oxidase inhibitors has increased due to their anti-inflammatory, antioxidant and immune-modulatory features which might be beneficial in the treatment of different auto-inflammatory diseases [27]. Febuxostat showed anti-inflammatory effects in different experimental models [15]. It has an antioxidative stress effect and suppressed ROS production in the rat model of renal ischemia-reperfusion injury [36].

The intention of the present study was to assess the structural affection of the lung following MTX overdose. The proposed underlying mechanisms involved in lung affection were studied. The possible modulation role of febuxostat over such affection was studied.

MATERIALS AND METHODS

Animals

Twenty-four Sprague-Dawley adult albino rats were used. The sample size was based according to

resource equation method [10, 16]. The rats were housed in a temperature of $22 \pm 2^\circ\text{C}$, relative humidity of $55 \pm 5\%$, and 12/12 h light/dark cycle. The study was conducted in Experimental Animal Centre, Cairo University. The experiment was carried out in accordance to ARRIVE guidelines (Animal Research: Reporting of In-Vivo Experiments) with the approval of the local IACUC Research Ethics Committee and according to ethical standards of National Institutes of Health guide for care and use of Laboratory Animals (8th edition, revised in 2011).

Experimental design

The rats were divided into three groups. Each group consisted of 8 rats:

- Control group: 100 mg/kg physiological saline/ intraperitoneally;
- MTX-treated group;
- Febuxostat-treated group (concomitant MTX + febuxostat).

Test materials

Methotrexate was obtained from Pfizer Pharmaceutical Company and Chemical industries (Egypt) and given as a single dose of 20 mg/kg, intraperitoneally [2]. The used dose of MTX was a high dose to evaluate the role of ROS formation and apoptosis [21].

Febuxostat was obtained from Hikma Pharmaceutical Co. (Egypt). It was dissolved in 0.9% saline and given at a dose of 15 mg/kg, orally: 2 drops of Tween 80 [15] for 14 successive days.

General toxicological profile

The general toxicological data were recorded including food and water consumption, health status, body weight and behavioural measures.

Behavioural measures (anxiety-like behaviour)

Two days before the end of the experiment, the rats were subjected to behavioural observation to measure anxiety-like behaviour using two behavioural tests. The rats were accustomed to the presence of the experimenter before the behavioural observation. The tests were carried out between 9 a.m. and 12 p.m. for 2 days.

Light/dark box. This test based on the innate fear of the rat to bright spaces. It is composed of a box divided into equal compartment, bright and dark compartments separated by a partition with a door. The rat was placed at the bright compartment and

allowed to explore for 5 min. Frequency of entry into dark and light compartments and the time spent in these compartments were measured [7].

Elevated plus maze [37]. This test is based on the rat's conflict between exploring novel places, and avoiding heights and dangerous places. It is composed of wooden two open and enclosed arms connected by central platform. The apparatus elevated 60 cm above the ground. The rats were placed in the open arm and allowed to explore for 5 min. Frequency of entry to the open and closed arms as well as the time spent in each arm were measured.

Tissue sampling

The lung was dissected and fixed immediately in 10% formalin saline. To randomise selection, the entire lung was cut starting at the superior border; every 10th section (5 μ m thick) was put aside for staining.

Preparation of tissue extracts

A portion of lungs was homogenised in 10 volumes (1:10; w/v) of ice-cold 10 mM phosphate buffered saline (PBS, pH 7.4) in an Ultra Turrax tissue homogenizer for 30 s. Homogenates were centrifuged at 10,000 rpm for 10 min at 4°C. The supernatant was pipetted into clean centrifuge tubes and stored in aliquots (-80°C) until analysis [12].

Light microscopic study

Haematoxylin and eosin stain

The technique of haematoxylin and eosin stain was done according to Suvarna et al. [35].

Masson's trichrome stain [35]

The paraffin sections were dewaxed, rehydrated then stained in acid fuchsin solution for 5 min, rinsed in distilled water, placed in phosphomolybdic acid solution for 3 min, washed in distilled water, stained with methyl blue solution for 2–5 min, rinsed in distilled water, and treated in acetic acid for 2 min. Finally, the sections were dehydrated in absolute alcohol, cleared in xylol, and mounted in Canada balsam. The nuclei appeared dark red, the cytoplasm appeared pale red and, the collagen fibres appeared blue.

Immunohistochemistry [30]

Immunohistochemical staining using the streptavidin-biotin-peroxidase technique for inducible nitric oxide synthase (iNOS), and cyclooxygenase (COX)-2 (markers of inflammation). Briefly, 10 sections/group

were deparaffinised, rehydrated, and rinsed in tap water, treated with 3% hydrogen peroxide for 10 min then, immersed in antigen retrieval solution. Non-specific protein binding was blocked by incubating the sections in 10% normal goat serum in phosphate buffer solution (PBS). Then, the sections were incubated in a humid chamber at 4°C with primary anti-iNOS antibody (rabbit polyclonal antibody, 1:100 dilution, ab15323, Abcam, Cambridge, Massachusetts, USA), anti-nuclear factor kappa B (NF- κ B) antibody (rabbit polyclonal anti-rat antibody against P65 subunit of NF- κ B; 1:20 dilution, ab86299, Abcam, Cambridge, Massachusetts, USA) and anti-COX-2 (rabbit polyclonal antibody, 1:100 dilution, ab15191, Abcam, Cambridge, Massachusetts, USA) overnight. After washing in PBS, the corresponding biotinylated secondary antibody was added to lung sections for 1 h at room temperature. Streptavidin peroxidase was added for 10 min and then washed in PBS. Finally, the sections were counterstained by Mayer's haematoxylin. For negative control sections, the primary antibodies were excluded. All the slides were assessed in triplicates to confirm the accuracy of the obtained results.

Oxidative/antioxidative markers

Lung lipid peroxidation. Malondialdehyde (MDA), a marker for lipid peroxidation, was measured by monitoring thiobarbituric reactive substances formation. Briefly, 500 mL of lung homogenate was added to 200 mL of PBS (10 Mm, pH 7.4) and 500 μ L of heat trichloroacetic acid-butylated hydroxytoluene (20% TCA, 1% BHT) solution. The resultant was mixed and centrifuged at 3000 rpm for 10 min at 4°C. To 800 mL of supernatant, 160 μ L of 0.6 M HCL and 640 μ L of 1.73% thiobarbituric acid were added. This suspension was mixed and heated in a boiling water bath for 15 min. After cooling, the thiobarbituric reactive substances were measured in the supernatant at 530 nm against a blank containing all reagents except the tissue homogenate. The concentration of MDA was calculated and expressed in Nano-moles per milligram of protein.

Lung SOD activity. Superoxide dismutase activity (SOD) was determined at room temperature (RT) according to the modified Misra and Fridovich's method [23]. 5 μ L of 10% lung homogenate was added to 1965 μ L of sodium carbonate buffer and to 10 μ L of bovine catalase. 20 μ L of 30 mM epinephrine (dissolved in 0.05% acetic acid) was added to the mixture. Superoxide dismutase activity was measured at

480 nm for 5 min on a spectrophotometer. The activity was expressed as the amount of the enzyme that inhibits the oxidation of epinephrine by 50%, which is equal to 1 U/mg of protein.

Lung glutathione (GSH). Glutathione was measured spectrophotometrically in the bronchoalveolar lavage fluid (BALF) and lung tissue [29]. GSH was measured by adding the standard or sample to 100 μ L of a 1:1 mixture of 3 U/mL glutathione reductase with 0.67 mg/mL 5,5'-dithiobis(2-nitro benzoic acid) (DTNB). The reaction was initiated by the addition of 20 μ L of 0.67 mg/mL nicotinamide adenine dinucleotide phosphate (NADPH) and the increase in absorbance at 412 nm was monitored by using a commercial kit (Biodiagnostic, Cairo, Egypt). Values measured in BALF were normalised to urea, values in lung tissue were normalised to protein content. For in vitro samples both the media and lysate were normalised to the lysate protein. The limit of detection for GSH was 0.2 μ M. The concentration of the lung GSH was calculated using the standard curve and expressed per mg of protein. The level of epithelial lining fluid GSH (ELF GSH) was expressed in μ M.

Western blot assay

Nuclear factor kappa B was estimated by the enzyme-linked immunosorbent assays (ELISA), according to the manufacturer's guide (R&D System Inc.). Lung tissue was standardised (1:10) in saline and stockpiled at -80°C . Models were preserved with cell lysis buffer, adjusted with PMSF and PIC former to the measures. Samples were extra watered down in assay buffer. After pipetting 100 μ L assay buffer, 100 μ L of sample/standard were supplemented to the pits.

The plate was incubated at RT for 1 h. The wells were splashed 5 times with rinse buffer. After 1 h incubation, the plate was splashed 5 times with shower buffer and 100 μ L of conjugate were supplemented to all wells. The plate was vacuum-packed and incubated for 30 min at RT. Well matters were let down and rinsed 5 times in buffer. 100 μ L of substrate was auxiliary to all wells and colour endorsed to progress. 30 min later, halt solution was substituted. The plate was delivered on an ELISA Plate Reader (OD 450 nm). Rectilinear average curves were created in assay buffer to estimate the values of NF- κ B.

Image analysis and morphometric measurements

The area per cent of collagen fibres and immune expression of iNOS, and COX-2 were done using Leica

LAS V3.8 image analyser computer system (Switzerland). The measurements were obtained by an independent blinded observer. The data was obtained in ten non-overlapping microscopic fields taken randomly from each slide and were examined within the standard measuring frame.

Biochemical assay

The serum level of the inflammatory markers TNF- α , and IL-1 were assayed by the commercially ELISA kits supplied by Biopsies, China according to manufacturer instructions.

Protein assay

The protein concentration in the lung homogenate was measured by Bradford's method using bovine serum albumin as standard [8].

Statistical analysis

Statistical analysis was performed using statistical package for the social sciences (SPSS) version 21.0 (IBM Corporation, Somers, NY, USA) statistical software. Data were expressed as means \pm standard deviation (SD). Statistical evaluation was done using one-way analysis of variance (ANOVA) followed by Bonferroni pairwise comparisons. Significance was considered when the p-value was less than 0.05.

The percentage of increase or decrease (difference) of all study parameters were calculated with the following formula: Percentage of difference = (Mean difference value between two groups)/(Value of the compared group) \times 100.

RESULTS

The general toxicological data

No mortalities were noticed in the studied groups. The food and water intake and health status were relatively excellent.

At the beginning of study, the body weight was 150 ± 3.6 g. By the end of study, the body weight of MTX-treated group decreased by 22% compared to the control group. With use of febuxostat, the body weight became 12% less than the control group (Table 1).

Behavioural measures (anxiety-like behaviour)

Light/dark box. There was non-significant difference among the different groups concerning time spent in the dark or light compartments. A significant increase (130%) in the number of entries of the MXT-treated rats into the dark compartment as compared to the control

Table 1. Body weight in the different groups at the end of study

Group	Body weight [g]	Versus group
Control	185 ± 5	
MTX-treated	145 ± 5	Control* Febuxostat-treated*
Febuxostat-treated	162.6 ± 2.5	Control* MTX-treated*

*P-value significant. Data are shown as mean ± standard deviation. The body weight at the beginning of the study was 150 ± 3.6 g. MTX — methotrexate

rats. Non-significant entry difference was detected in febuxostat-treated group into dark and light compartments as compared to the control group (Fig. 1).

Elevated plus maze. As compared to the other groups, MXT-treated rats entered the open arm of the elevated plus maze less frequent and spent less time. They entered more frequent the closed arm of the elevated plus maze and spent more time (Fig. 2A, B).

Febuxostat-treated rats entered more frequent and spent more time in the open arm (Fig. 2C, D).

Structure of lung as revealed by haematoxylin and eosin staining

The control group presented normal lung morphology. MTX-treated rats exhibited inflammatory cellular infiltrations, thickened interalveolar septa (with oedema), dilated congested blood vessels, extravasated blood, and apoptotic pneumocytes. With the use of febuxostat, normal lung architecture was observed with a bit thickened interalveolar septum and extravasated blood (Figs. 3, 4).

The content of collagen fibres

The collagen fibres were minimum in the control group. The fibres content increased three-fold in MTX-treated group when compared to the control group. Much improvement was noticed in febux-

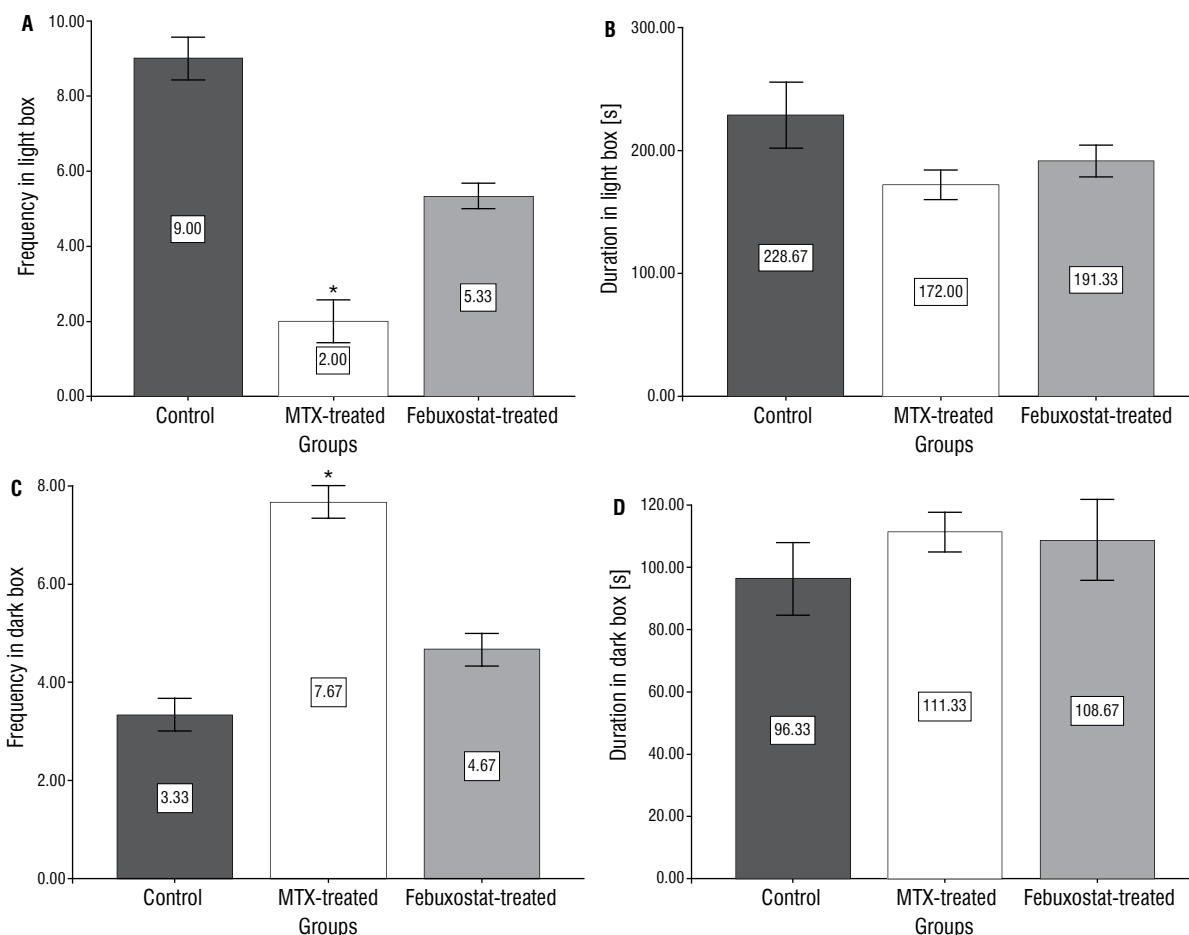


Figure 1. Anxiety-like behaviour in the light/dark box test; **A.** Frequency of entry into the light compartment; **B.** Time spent in the light compartment; **C.** Frequency of entry into the dark compartment; **D.** Time spent in the dark compartment; *Significant from control group; $p = 0.006$.

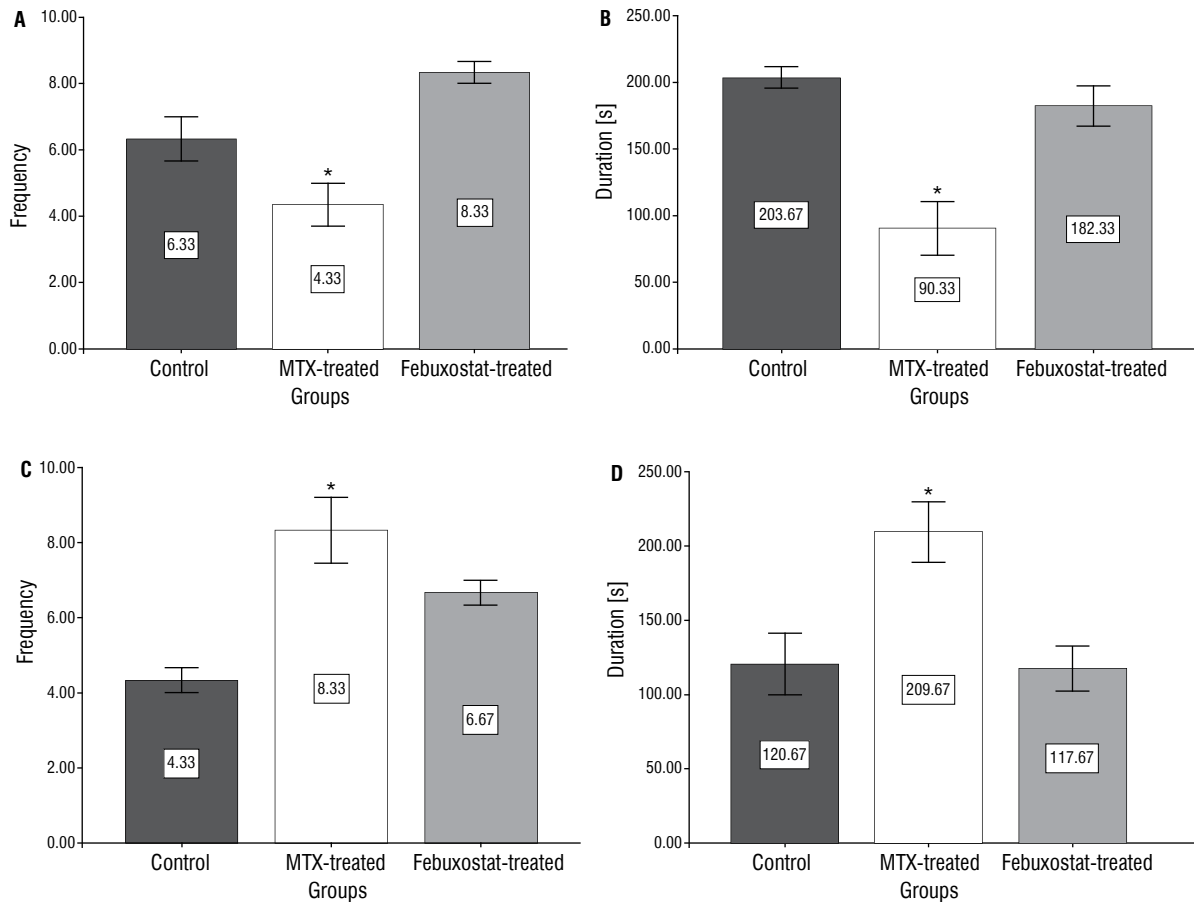


Figure 2. Anxiety-like behaviour in the elevated plus maze test; **A.** Open arm entry; **B.** Open arm duration; **C.** Close arm entry; **D.** Close arm duration; *Significant from control group; $p = 0.000$.

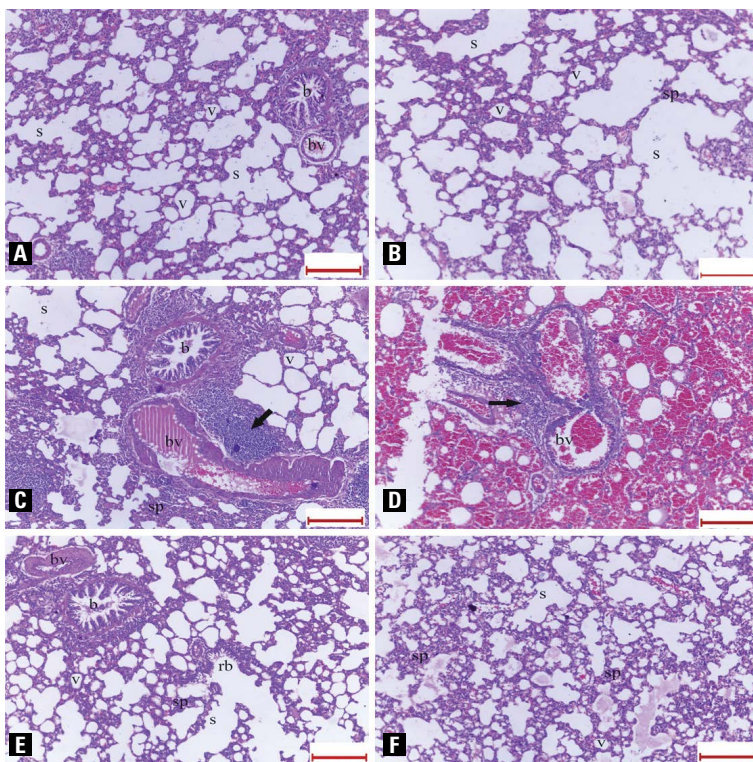


Figure 3. Lung morphology of the different studied groups. Note respiratory bronchiole (rb), terminal bronchiole (b), alveolar sac (s), alveoli (v), interalveolar septa (sp) and blood vessels (bv); **A, B.** Normal lung architecture of the control rats; **C, D.** Inflammatory cellular infiltrations (arrows), thickened interalveolar septa, dilated congested blood vessels and extravasated blood of methotrexate-treated rats; **E, F.** Normal lung architecture with a pit thickened interalveolar septum and extravasated blood of febuxostat-treated rats. Haematoxylin and eosin, scale bar, 200 μm (A–F).

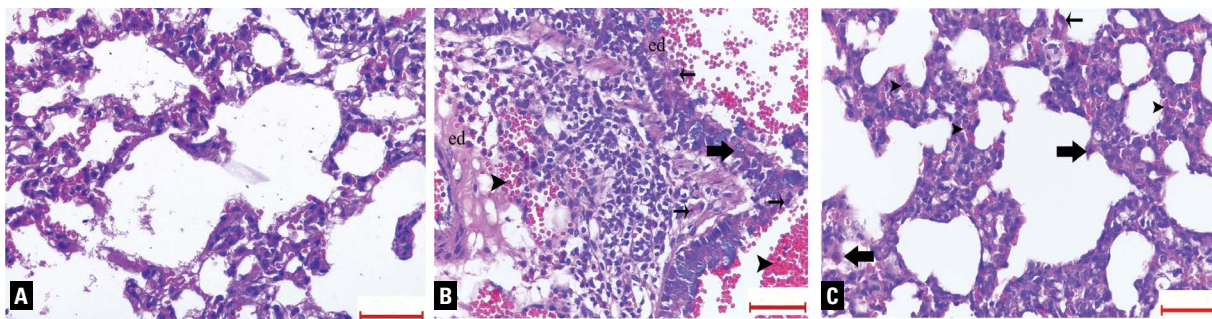


Figure 4. **A.** Normal lung architecture of the control rats; **B.** Inflammatory cellular infiltration, extravasated blood (arrowheads), oedema (ed), macrophages (thick arrows) and apoptotic pneumocytes (thin arrows) of methotrexate-treated rats; **C.** Normal lung architecture with a slight congestion (arrowheads), macrophages (thick arrows) and apoptotic pneumocytes (thin arrows) of februxostat-treated rats. Haematoxylin and eosin, scale bar, 50 μm (A–C).

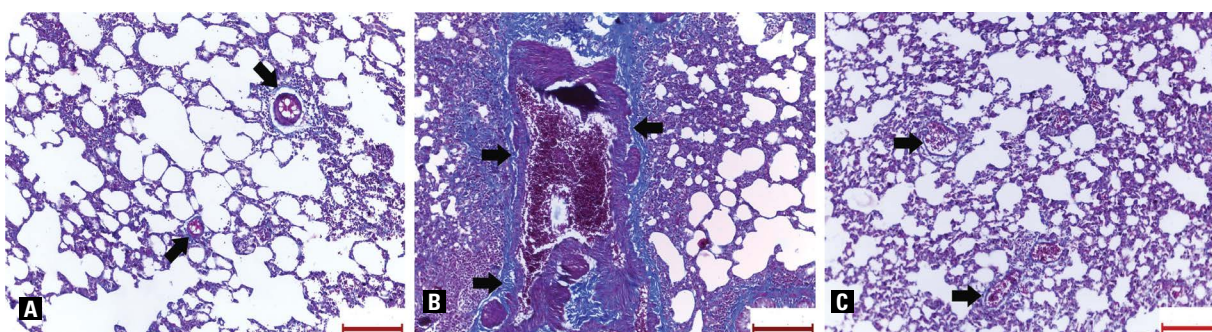


Figure 5. **A.** The collagen fibres (arrows) in the control rats; **B.** Increased collagen fibres (arrows) in methotrexate-treated rats; **C.** Minimal collagen fibres (arrows) in februxostat-treated rats. Masson's trichrome, scale bar, 200 μm (A–C).

Table 2. Area per cent (%) of collagen fibres, inducible nitric oxide synthase (iNOS) and cyclooxygenase-2 (COX-2)

Group		Area % of collagen fibres	COX-2 [cells/mm ²]	iNOS
Control	Mean \pm SD	1.47 \pm 0.54	40 \pm 5	3.1 \pm 0.8
MTX-treated	Mean \pm SD	6.0 \pm 0.55	150 \pm 30	18.0 \pm 2.0
	Versus control	*	*	*
	Versus februxostat-treated	*	*	*
Februxostat-treated	Mean \pm SD	2.5 \pm 0.38	55 \pm 8	5.1 \pm 1.7
	Versus control	NS	NS	*
	Versus MTX-treated	*	*	*

*P-value significant. MTX — methotrexate; NS — not significant; SD — standard deviation

ostat-treated group as its fibres contents were comparable to the control group (Fig. 5, Table 2).

Immunohistochemical evaluation

The COX-2 (cells/mm²) in the control and februxostat-treated groups were comparable. The immunostained COX-2 cells increased in MTX-treated rats by > 2.5-fold (275%) compared to the control group (Fig. 6, Table 2).

The immunohistochemical reaction of iNOS was poor in both control and februxostat-treated groups. With use of MXT, the reaction in MXT-treated group became 6-fold higher than in the control group (Fig. 7, Table 2).

Western blot assay

Nuclear factor kappa B was 2-fold higher than in the control group. With use of februxostat, NF- κ B be-

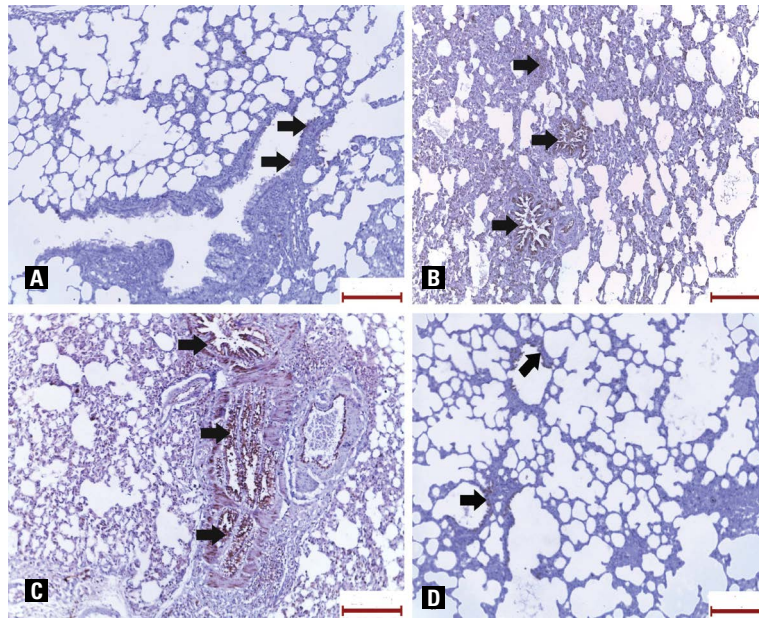


Figure 6. A. Minimal immunostaining of cyclooxygenase-2 (COX-2) (arrows) in the control rats; B, C. Increased staining (arrows) in methotrexate-treated rats; D. Minimal immunostaining of COX-2 (arrows) in febuxostat-treated rats. COX-2 immunostaining, scale bar, 200 μ m (A–D).

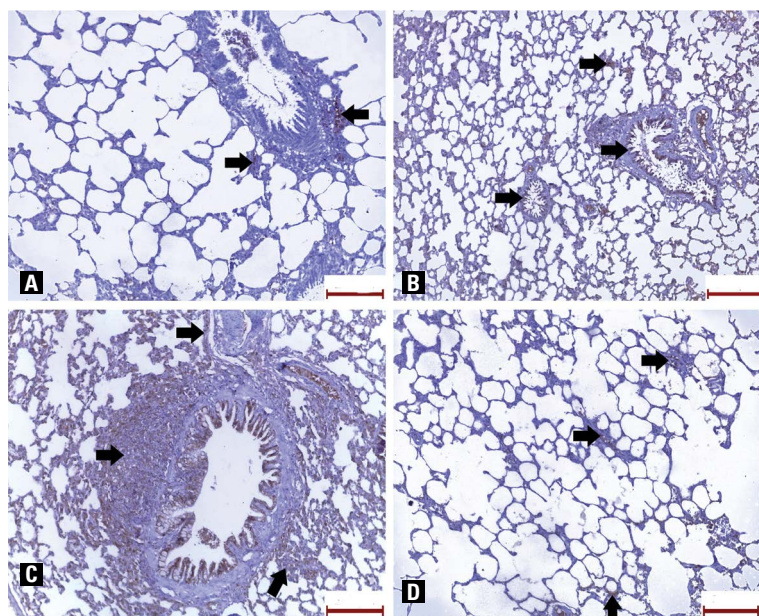


Figure 7. A. Poor immunohistochemically reaction of inducible nitric oxide synthase (iNOS) (arrows) in the control rats; B, C. Increase immunohistochemically reaction of iNOS (arrows) in methotrexate-treated rats; D. Immunohistochemically reaction (arrows) in febuxostat-treated rats. iNOS immunostaining, scale bar, 50 μ m (A–D).

came 34% higher than in the control group (Table 3, Fig. 8).

Inflammatory and oxidative/antioxidative markers evaluation (Table 3)

Interleukin 1 and TNF- α were three-fold higher in MTX-treated group than in the control group.

Improvement was noticed with use of febuxostat as IL-1 and TNF- α were 64% and 100% higher than in the control group.

Malondialdehyde was two and half-fold higher than in the control group. With use of febuxostat, MDA became half fold higher than in the control group.

Table 3. Inflammatory and oxidative/antioxidative markers

Group		NF-κB	IL-1 [pg/mg protein]	TNF-α [pg/mg protein]	MDA [nmol/mg protein]	GSH [μg/mg protein]	SOD [nmol/mg protein]
Control	Mean ± SD	1.17 ± 0.05	149.0 ± 22.8	123.3 ± 43.1	1.48 ± 0.17	1.65 ± 0.07	8.02 ± 0.39
MTX-treated	Mean ± SD	3.80 ± 0.06	604.0 ± 17.6	506.6 ± 28.4	5.22 ± 0.38	0.66 ± 0.10	3.07 ± 0.24
	Versus control	*	*	*	*	*	*
	Versus febuxostat-treated	*	*	*	*	*	*
Febuxostat-treated	Mean ± SD	1.57 ± 0.15	245.0 ± 21.7	256.6 ± 19.0	2.22 ± 0.07	1.69 ± 0.13	7.10 ± 0.72
	Versus control	*	*	*	*	NS	NS
	Versus MTX-treated	*	*	*	*	*	*

*P-value significant. NF-κB — nuclear factor kappa B; IL-1 — interleukin 1; TNF-α — tumour necrosis factor alpha; MDA — malondialdehyde; GSH — glutathione; SOD — superoxide dismutase activity; MTX — methotrexate; NS — not significant; SD — standard deviation

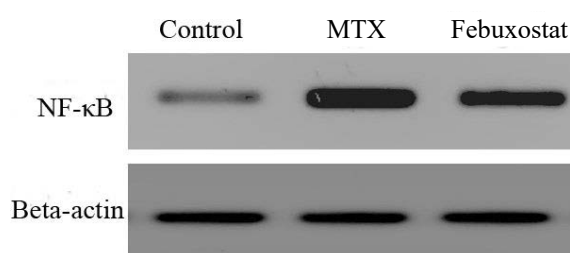


Figure 8. Western blot assay of nuclear factor kappa B (NF-κB) in the different groups. NF-κB was higher in methotrexate (MTX)-treated group than the control group. NF-κB was a bit higher in febuxostat-treated rats than the control rats. Beta-actin was used as internal control to measure the relative quantitation of the expression of the target gene.

Superoxide dismutase activity and GSH and decreased by 60% compared to the control group. Both markers in the control and febuxostat-treated groups were alike.

DISCUSSION

Body weight of MTX-treated rats decreased by 22%. The loss of weight in rats' model of MTX is due to anorexia, cachexia, intestinal mucositis, impairment of absorption and digestive functions, alteration of the gut barrier, and diarrhoea [6, 22].

Methotrexate-treated rats showed a significant increase in the anxiety-like behaviour, expressed by an increase in the number of entries to the dark compartments of the light/dark box, and an increase in the frequency and duration of closed arm entries in the elevated plus maze. The anxiety-like behaviour is explained in mice by the association of MTX with acute brain toxicity and by its ability to induce folate depletion [17]. The anxiety-like behaviour was reported with MTX administration in cancer patients [14]. Much improvement was in the febuxostat-treated group which attributed to the antidepressant activity of the febuxostat [20].

Methotrexate-treated rats exhibited an acute inflammatory process (cellular infiltrations, dilated congested blood vessels, thickened interalveolar septa with alveolar oedema). Because of severe congestion, blood extravasation occurred. Additionally, apoptotic pneumocytes were detected.

The cause of lung affection in the MTX-treated group is multifactorial. The major cause is oxidative stress [21]. Oxidative stress is defined as the shift in the balance between oxidants and antioxidants in favour of oxidants [5]. The oxidant marker (MDA) was higher, while the antioxidant markers (SOD and GSH) were lower in MTX-treated rats. It is used for measuring oxidative damage to lipids resulting from free radicals [3]. Analysis of MDA is sufficient to prove and assess the oxidative stress [21]. The elevated MDA is a consequence of the higher level of IL-1 and the toxic dose of MTX [21].

The sterile inflammation in the MTX-treated group was caused by an increase of NF-κB (2-fold), IL-1 (3-fold) and TNF-α (3-fold), COX-2 cells (2.5-fold) and iNOS (6-fold). The present neutrophils result in ROS formation and tissue damage through the release of chemical mediators [21]. The higher level of IL-1 and higher dose of MTX increase the secretion of proinflammatory cytokines TNF-α [21]. TNF-α is crucially responsible for the pathogenesis of oxidative stress and increases ROS [21]. It regulates growth, proliferation, differentiation, and viability of activated leukocytes [25]. TNF-α also provokes the cellular release of other cytokines, chemokines, or inflammatory mediators [25]. So, excessive TNF-α secretion leads to lung damage by inducing oxidative stress and directly inducing apoptosis.

Fibrosis was observed in the MTX-treated group (the collagen fibres content increased 3-fold) as a consequence of oxidative stress and sterile inflammation.

The third major cause of lung damage in the overdose MTX-treated group is apoptosis. Apoptosis is multifactorial. It is induced by higher level of TNF- α which activates the caspase enzyme system [21]. Apoptosis is also induced by lipid peroxidation (higher MDA) as MDA is the end product of the lipid peroxidation process [5]. Lipid peroxidation results in organ and cell damage [21]. The increased observed apoptosis results in excessive release of cytokines and enhanced ROS which finally damage the lung tissue [21].

Another possible cause of lung injury in MXT-treated group is the elevation of iNOS. The nitric oxide-derived from iNOS appears to induce inflammatory infiltration and oxidative stress. These events create a deleterious environment that ultimately leads to cellular damages. It seems that disruption of COX-2 activity aggravates the resultant lung damage [18].

With the use of febuxostat, the normal lung architecture was observed with a bit thickened interalveolar septum and extravasated blood. The collagen fibres content was minimal. Decrement of oxidative stress and sterile inflammation (COX-2 cells and iNOS were comparable to the control group. NF- κ B, IL-1 and TNF- α became higher by 34%, 64% and 100%). The protective role of febuxostat is due to its anti-inflammatory and antioxidant features [27]. Febuxostat showed anti-inflammatory effects in different experimental models [15]. Its antioxidative stress effect was proved in the rat model of renal ischaemia-reperfusion injury [36].

CONCLUSIONS

In conclusion, the overdose of MTX displays inflammatory lung affection with residual fibrosis. It induces lung affection through oxidative stress, apoptosis and sterile inflammation. With the use of febuxostat, the normal lung architecture was preserved with a little structural affection or fibrotic residue. Febuxostat exerts its lung protection through its anti-inflammatory and antioxidant features.

Acknowledgements

Acknowledgements to all my colleagues who support me during this work.

REFERENCES

1. Alamir I, Boukhattala N, Aziz M, et al. Beneficial effects of cathepsin inhibition to prevent chemotherapy-induced intestinal mucositis. *Clin Exp Immunol*. 2010; 162(2): 298–305, doi: [10.1111/j.1365-2249.2010.04220.x](https://doi.org/10.1111/j.1365-2249.2010.04220.x), indexed in Pubmed: [20731673](https://pubmed.ncbi.nlm.nih.gov/20731673/).

2. Arpag H, Gül M, Aydemir Y, et al. Protective effects of alpha-lipoic acid on methotrexate-induced oxidative lung injury in rats. *J Invest Surg*. 2018; 31(2): 107–113, doi: [10.1080/08941939.2017.1296513](https://doi.org/10.1080/08941939.2017.1296513), indexed in Pubmed: [28340320](https://pubmed.ncbi.nlm.nih.gov/28340320/).
3. Atug Özcan SS, Ceylan I, Ozcan E, et al. Evaluation of oxidative stress biomarkers in patients with fixed orthodontic appliances. *Dis Markers*. 2014; 2014: 597892, doi: [10.1155/2014/597892](https://doi.org/10.1155/2014/597892), indexed in Pubmed: [24864131](https://pubmed.ncbi.nlm.nih.gov/24864131/).
4. Barrera P, Laan RF, van Riel PL, et al. Methotrexate-related pulmonary complications in rheumatoid arthritis. *Ann Rheum Dis*. 1994; 53(7): 434–439, doi: [10.1136/ard.53.7.434](https://doi.org/10.1136/ard.53.7.434), indexed in Pubmed: [7944614](https://pubmed.ncbi.nlm.nih.gov/7944614/).
5. Birben E, Sahiner UM, Sackesen C, et al. Oxidative stress and antioxidant defense. *World Allergy Organ J*. 2012; 5(1): 9–19, doi: [10.1097/WOX.0b013e3182439613](https://doi.org/10.1097/WOX.0b013e3182439613), indexed in Pubmed: [23268465](https://pubmed.ncbi.nlm.nih.gov/23268465/).
6. Boukhattala N, Leblond J, Claeysens S, et al. Methotrexate induces intestinal mucositis and alters gut protein metabolism independently of reduced food intake. *Am J Physiol Endocrinol Metab*. 2009; 296(1): E182–E190, doi: [10.1152/ajpendo.90459.2008](https://doi.org/10.1152/ajpendo.90459.2008), indexed in Pubmed: [18984853](https://pubmed.ncbi.nlm.nih.gov/18984853/).
7. Bourin M, Hascoët M. The mouse light/dark box test. *Eur J Pharmacol*. 2003; 463(1-3): 55–65, doi: [10.1016/s0014-2999\(03\)01274-3](https://doi.org/10.1016/s0014-2999(03)01274-3).
8. Bradford M. A rapid and sensitive method for the quantitation of microgram quantities of protein utilizing the principle of protein-dye binding. *Anal Biochem*. 1976; 72(1-2): 248–254, doi: [10.1016/0003-2697\(76\)90527-3](https://doi.org/10.1016/0003-2697(76)90527-3).
9. Carson C, Cannon G, Egger M, et al. Pulmonary disease during the treatment of rheumatoid arthritis with low dose pulse methotrexate. *Semin Arthritis Rheum*. 1987; 16(3): 186–195, doi: [10.1016/0049-0172\(87\)90021-7](https://doi.org/10.1016/0049-0172(87)90021-7).
10. Charan J, Biswas T. How to calculate sample size for different study designs in medical research? *Indian J Psychol Med*. 2013; 35(2): 121–126, doi: [10.4103/0253-7176.116232](https://doi.org/10.4103/0253-7176.116232), indexed in Pubmed: [24049221](https://pubmed.ncbi.nlm.nih.gov/24049221/).
11. Conway R, Low C, Coughlan RJ, et al. Methotrexate use and risk of lung disease in psoriasis, psoriatic arthritis, and inflammatory bowel disease: systematic literature review and meta-analysis of randomised controlled trials. *BMJ*. 2015; 350: h1269, doi: [10.1136/bmj.h1269](https://doi.org/10.1136/bmj.h1269), indexed in Pubmed: [25770113](https://pubmed.ncbi.nlm.nih.gov/25770113/).
12. Dhoub H, Jallouli M, Draief M, et al. Oxidative damage and histopathological changes in lung of rat chronically exposed to nicotine alone or associated to ethanol. *Pathol Biol (Paris)*. 2015; 63(6): 258–267, doi: [10.1016/j.pat-bio.2015.10.001](https://doi.org/10.1016/j.pat-bio.2015.10.001), indexed in Pubmed: [26586280](https://pubmed.ncbi.nlm.nih.gov/26586280/).
13. Dignass A, Van Assche G, Lindsay JO, et al. The second European evidence-based Consensus on the diagnosis and management of Crohn's disease: Current management. *J Crohns Colitis*. 2010; 4(1): 28–62, doi: [10.1016/j.crohns.2009.12.002](https://doi.org/10.1016/j.crohns.2009.12.002), indexed in Pubmed: [21122489](https://pubmed.ncbi.nlm.nih.gov/21122489/).
14. Elens I, Dekeyser E, Moons L. Methotrexate affects cerebrospinal fluid folate and tau levels and induces late cognitive deficits in mice. *Neuroscience*. 2019; 404: 62–70, doi: [10.1016/j.neuroscience.2019.01.024](https://doi.org/10.1016/j.neuroscience.2019.01.024), indexed in Pubmed: [30703509](https://pubmed.ncbi.nlm.nih.gov/30703509/).
15. Fahmi AN, Shehatou GS, Shebl AM. Febuxostat protects rats against lipopolysaccharide-induced lung inflammation

- in a dose-dependent manner, Naunyn Schmiedebergs. Arch Pharmacol, 389(3), pp. 2016; 389(3): 269–278, doi: [10.1007/s00210-015-1202-6](https://doi.org/10.1007/s00210-015-1202-6), indexed in Pubmed: [26713331](https://pubmed.ncbi.nlm.nih.gov/26713331/).
16. Festing MF, Altman DG. Guidelines for the design and statistical analysis of experiments using laboratory animals. ILAR J, 43(4), pp. 2002; 43(4): 244–258, doi: [10.1093/ilar.43.4.244](https://doi.org/10.1093/ilar.43.4.244), indexed in Pubmed: [12391400](https://pubmed.ncbi.nlm.nih.gov/12391400/).
 17. François M, Takagi K, Legrand R, et al. Increased ghrelin but low ghrelin-reactive immunoglobulins in a rat model of methotrexate chemotherapy-induced anorexia. Front Nutr. 2016; 3: 23, doi: [10.3389/fnut.2016.00023](https://doi.org/10.3389/fnut.2016.00023), indexed in Pubmed: [27508207](https://pubmed.ncbi.nlm.nih.gov/27508207/).
 18. Fukunaga K, Kohli P, Bonnans C, et al. Cyclooxygenase 2 plays a pivotal role in the resolution of acute lung injury. J Immunol. 2005; 174(8): 5033–5039, doi: [10.4049/jimmunol.174.8.5033](https://doi.org/10.4049/jimmunol.174.8.5033), indexed in Pubmed: [15814734](https://pubmed.ncbi.nlm.nih.gov/15814734/).
 19. Huang C, Hsu P, Hung Y, et al. Ornithine decarboxylase prevents methotrexate-induced apoptosis by reducing intracellular reactive oxygen species production. Apoptosis, 2005; 10(4): 895–907, doi: [10.1007/s10495-005-2947-z](https://doi.org/10.1007/s10495-005-2947-z), indexed in Pubmed: [16133879](https://pubmed.ncbi.nlm.nih.gov/16133879/).
 20. Karve AV, Jagtiani S, Chitnis KSA. Evaluation of effect of allopurinol and febuxostat in behavioral model of depression in mice. Indian J Pharmacol. 2013; 45(3): 244–247, doi: [10.4103/0253-7613.111922](https://doi.org/10.4103/0253-7613.111922), indexed in Pubmed: [23833366](https://pubmed.ncbi.nlm.nih.gov/23833366/).
 21. Kurt A, Tumkaya L, Turut H, et al. Protective effects of infliximab on lung injury induced by methotrexate. Arch Bronconeumol. 2015; 51(11): 551–557, doi: [10.1016/j.arbr.2015.05.012](https://doi.org/10.1016/j.arbr.2015.05.012).
 22. Leblond J, Le Pessot F, Hubert-Buron A, et al. Chemotherapy-induced mucositis is associated with changes in proteolytic pathways. Exp Biol Med (Maywood). 2008; 233(2): 219–228, doi: [10.3181/0702-RM-49](https://doi.org/10.3181/0702-RM-49), indexed in Pubmed: [18222977](https://pubmed.ncbi.nlm.nih.gov/18222977/).
 23. Misra H, Fridovich I. The role of superoxide anion in the autoxidation of epinephrine and a simple assay for superoxide dismutase. J Biol Chem. 1972; 247(10): 3170–3175, doi: [10.1016/s0021-9258\(19\)45228-9](https://doi.org/10.1016/s0021-9258(19)45228-9).
 24. Mohamed DI, Khairy E, Tawfek SS, et al. Coenzyme Q10 attenuates lung and liver fibrosis via modulation of autophagy in methotrexate treated rat. Biomed Pharmacother. 2019; 109: 892–901, doi: [10.1016/j.biopha.2018.10.133](https://doi.org/10.1016/j.biopha.2018.10.133), indexed in Pubmed: [30551543](https://pubmed.ncbi.nlm.nih.gov/30551543/).
 25. Nair MP, Mahajan S, Reynolds JL, et al. The flavonoid quercetin inhibits proinflammatory cytokine (tumor necrosis factor alpha) gene expression in normal peripheral blood mononuclear cells via modulation of the NF-kappa beta system. Clin Vaccine Immunol. 2006; 13(3): 319–328, doi: [10.1128/CVI.13.3.319-328.2006](https://doi.org/10.1128/CVI.13.3.319-328.2006), indexed in Pubmed: [16522772](https://pubmed.ncbi.nlm.nih.gov/16522772/).
 26. Ohbayashi M, Kubota S, Kawase A, et al. Involvement of epithelial-mesenchymal transition in methotrexate-induced pulmonary fibrosis. J Toxicol Sci. 2014; 39(2): 319–330, doi: [10.2131/jts.39.319](https://doi.org/10.2131/jts.39.319), indexed in Pubmed: [24646714](https://pubmed.ncbi.nlm.nih.gov/24646714/).
 27. Pacher P, Nivorozhkin A, Szabó C. Therapeutic effects of xanthine oxidase inhibitors: renaissance half a century after the discovery of allopurinol. Pharmacol Rev. 2006; 58(1): 87–114, doi: [10.1124/pr.58.1.6](https://doi.org/10.1124/pr.58.1.6), indexed in Pubmed: [16507884](https://pubmed.ncbi.nlm.nih.gov/16507884/).
 28. Pui CH, Pei D, Pappo AS, et al. Treatment outcomes in black and white children with cancer: results from the SEER database and St Jude Children’s Research Hospital, 1992 through 2007. J Clin Oncol. 2012; 30(16): 2005–2012, doi: [10.1200/JCO.2011.40.8617](https://doi.org/10.1200/JCO.2011.40.8617), indexed in Pubmed: [22547602](https://pubmed.ncbi.nlm.nih.gov/22547602/).
 29. Rahman I, Kode A, Biswas SK. Assay for quantitative determination of glutathione and glutathione disulfide levels using enzymatic recycling method. Nat Protoc. 2006; 1(6): 3159–3165, doi: [10.1038/nprot.2006.378](https://doi.org/10.1038/nprot.2006.378), indexed in Pubmed: [17406579](https://pubmed.ncbi.nlm.nih.gov/17406579/).
 30. Ramos-Vara JA, Kiupel M, Baszler T. Suggested guidelines for immunohistochemical techniques in veterinary diagnostic laboratories. J Vet Diagn Invest. 2008; 20(4): 393–413, doi: [10.1177/104063870802000401](https://doi.org/10.1177/104063870802000401), indexed in Pubmed: [18599844](https://pubmed.ncbi.nlm.nih.gov/18599844/).
 31. Robinson PC, Dalbeth N. Febuxostat for the treatment of hyperuricaemia in gout. Expert Opin Pharmacother. 2018; 19(11): 1289–1299.
 32. Sakthiswary R, Suresh E. Methotrexate in systemic lupus erythematosus: a systematic review of its efficacy. Lupus. 2014; 23(3): 225–235, doi: [10.1177/0961203313519159](https://doi.org/10.1177/0961203313519159), indexed in Pubmed: [24399812](https://pubmed.ncbi.nlm.nih.gov/24399812/).
 33. Sathi N, Chikura B, Kaushik VV, et al. How common is methotrexate pneumonitis? A large prospective study investigates. Clin Rheumatol. 2012; 31(1): 79–83, doi: [10.1007/s10067-011-1758-6](https://doi.org/10.1007/s10067-011-1758-6), indexed in Pubmed: [21638023](https://pubmed.ncbi.nlm.nih.gov/21638023/).
 34. Sivalingam VN, Duncan WC, Kirk E, et al. Diagnosis and management of ectopic pregnancy. J Fam Plann Reprod Health Care. 2011; 37(4): 231–240, doi: [10.1136/jfprhc-2011-0073](https://doi.org/10.1136/jfprhc-2011-0073), indexed in Pubmed: [21727242](https://pubmed.ncbi.nlm.nih.gov/21727242/).
 35. Suvarna SK, Layton C, Bancroft JD. Bancroft’s theory and practice of histological techniques. Eighth edition. Oxford, Elsevier 2019.
 36. Tsuda H, Kawada N, Kaimori Jy, et al. Febuxostat suppressed renal ischemia-reperfusion injury via reduced oxidative stress. Biochem Biophys Res Commun. 2012; 427(2): 266–272, doi: [10.1016/j.bbrc.2012.09.032](https://doi.org/10.1016/j.bbrc.2012.09.032), indexed in Pubmed: [22995295](https://pubmed.ncbi.nlm.nih.gov/22995295/).
 37. Walf AA, Frye CA. The use of the elevated plus maze as an assay of anxiety-related behavior in rodents. Nat Protoc. 2007; 2(2): 322–328, doi: [10.1038/nprot.2007.44](https://doi.org/10.1038/nprot.2007.44), indexed in Pubmed: [17406592](https://pubmed.ncbi.nlm.nih.gov/17406592/).
 38. Zhu H, Deng FY, Mo XB, et al. Pharmacogenetics and pharmacogenomics for rheumatoid arthritis responsiveness to methotrexate treatment: the 2013 update. Pharmacogenomics. 2014; 15(4): 551–566, doi: [10.2217/pgs.14.25](https://doi.org/10.2217/pgs.14.25), indexed in Pubmed: [24624921](https://pubmed.ncbi.nlm.nih.gov/24624921/).

Normal and five-fingered hand: comparative X-ray morphometry in the post-natal age

M.P. Bondioni¹, L. Casati², A.G. Salvi³, A. Minini³, E. Zini¹, U.E. Pazzaglia³

¹Department of Radiology, Department of Medical and Surgical Specialties, Radiological Sciences and Public Health, University of Brescia, Italy

²Department of Medical Biotechnology and Translational Medicine, University of Milano, Italy

³Orthopaedic Clinic, Department of Medical and Surgical Specialties, Radiological Sciences and Public Health, University of Brescia, Italy

[Received: 18 June 2020; Accepted: 1 July 2020]

Background: Five-fingered hand (5-FH) with completely developed phalanges is a rare phenotype observed so far only in humans and characterised by three phalanges of the 1st ray. A long-lasting, debated question is if the missing element of the normal hand 1st ray is the metacarpal or the phalanx. In this study, comparative X-rays morphometry of long bones in normal and 5-FH is carried out with the aim to face this question through homology analysis of long bone segments in the transverse and longitudinal line of normal hand and 5-FH.

Materials and methods: In the normal hand X-rays ($n = 20$) and in a 5-FH X-rays series ($n = 9$) the relative length of each segment on the ray total length and the index of growth rate (IGR) were assessed. The calculation of the first parameter in normal hand bi-phalangeal thumb was carried out on the 3rd ray total length in the same hand.

Results: The parameters of relative length and the proximal/distal growth rate asymmetry in the post-natal period (assessed through the IGR) confirmed in 5-FH the homology of all the five segment on the transverse line. In the normal control hand, the relative length assessment methodology was biased by the missing segment of the thumb, therefore, the reference to the 3rd ray total length in the same hand (instead of the 1st), allowed the homology analysis of the thumb metacarpal and 1st phalanx with the lateral segments (2nd–5th ray) of the same hand. The 5-FH analysis was used to choose the more appropriate reference ray for the normal hand group.

Conclusions: The comparative analysis of relative lengths and IGRs in the two groups suggested homology of the (anatomical) 1st metacarpal with the 2nd–5th proximal phalanges in the same hand and that of the (anatomical) 1st proximal phalanx with the 2nd–5th mid phalanges. These data suggest that the missing segment of the normal hand thumb is the metacarpal. (Folia Morphol 2021; 80, 2: 403–409)

Key words: five-fingered hand, triphalangeal thumb, hand post-natal ossification pattern, hand segments morphometry homology

Address for correspondence: M.P. Bondioni, MD, Department of Medical and Surgical Specialties, Radiological Sciences and Public Health, University of Brescia, Piazzale Spedali Civili Brescia, 25123 Brescia, Italy, tel: 0039 0303996291, fax: 0039 0303996034, e-mail: mariapiabondioni@gmail.com

This article is available in open access under Creative Common Attribution-Non-Commercial-No Derivatives 4.0 International (CC BY-NC-ND 4.0) license, allowing to download articles and share them with others as long as they credit the authors and the publisher, but without permission to change them in any way or use them commercially.

INTRODUCTION

In the foetal period and after the formation of the primary ossification centres, it is possible to document that the length increment of the long bone cartilage anlagen in the hand occurs with a symmetric proximal and distal growth of the meta-epiphyses [12, 13]. This process is controlled by the chondrocyte proliferation rate and orientation in the transition zones between the primary ossification centre of the diaphysis and the epiphyses [12]. In a more advanced developmental stage (late foetal and post-natal period), a distinct ossification centre is formed transforming the interposed cartilage layer between the ossified diaphysis and the epiphyseal ossification centre into the metaphyseal growth plate cartilage. This provides the longitudinal growth until the skeletal maturity is reached. The opposite epiphyseal end undergoes a different type of ossification indicated with the term of "pseudo-epiphysis" [5]. Therefore the pattern of longitudinal growth changes becoming asymmetric, with a higher distal growth rate in the 2nd–5th metacarpals and an inverted proximal growth in the 1st metacarpal and in all the phalanges.

Five-fingered hand (5-FH) with completely developed phalanges (excluding delta or severely underdeveloped phalanges) is a rare phenotype. To the best of our knowledge, it has been observed only in the human species. X-ray morphometry of this phenotype has been used to compare length, shape and index of growth rate (IGR) of each ray bone element without the bias of the missing segment of the thumb. The result of this study are considered in the context of the long lasting question if the missing 1st ray segment of the normal, human hands a metacarpal or a phalanx [10, 15]. No morphometric analysis of this type has

been so far carried out on 5-FH phenotype because its uncommon occurrence prevented the collection of a sufficient number of X-rays for the analysis. The aim of this paper is to document through published X-ray images of 5-FH reported cases [6, 14, 20–22] the length homology of the hand segments in the transverse line, the length proportions along the ray longitudinal line, and the pattern of growth which determine the overall shape of each segment class. These data were compared with the normal hand population. In this context, the 5-FH phenotype deserves a remarkable interest because it can be related to the evolution of the opposable thumb in hominids and some anthropoid species.

MATERIALS AND METHODS

The search of published articles on the topic was carried out on PubMed data base using the terms "triphalangeal thumb" or "five-fingered hands". Five papers provided X-ray of image quality, which should allow reliable measurements: in all 9 hands in 8 reported cases were analysed (Table 1). The low number of studied cases was due to the rarity of this mutation (basically a normal hand with three phalanges associated to a variable limitation of the opposition). A further limit was represented by the quality of the printed X-ray images, which required a further selection for a reliable morphometry. The selected X-ray images were digitalized in JPEG format with a scanner (when no PDF was available). Elaboration with Adobe Photoshop was carried out using only the brightness/contrast or the "relief" function of the program. Twenty normal hand X-rays of children between 8 and 15 years old was selected from the Paediatric Radiology archives (ASST Spedali

Table 1. Selected case reports of five-fingered hand and data available from the articles (columns 1st–3rd), total number of subjects (column 4th), total number of scanned hand X-rays where measurements and calculation of relative length and growth rate index assessment were carried out (column 5th)

Selected case reports	Subject age	Parentage	Number of cases	Number of analysed X-rays
Heiss (1957)	Adult	Mother	1	1
	New-born	Son	1	0
Qazi and Kassner (1988)	Adult		1	2
	Child		1	1
Zuidam et al. (2006)	Adult		1	1
Zuidam et al. (2010)	Adult		1	1
Zguricas et al. (1997)	Adult		1	2
	Adult		1	1
Total			8	9

Civili di Brescia). The radiographic survey had been carried out for trauma of wrist/finger because of a dubious fracture, which was not confirmed by X-rays; otherwise, for assessment of the skeletal age. X-rays were taken in anterior-posterior hand projection at the standard distance of 50 cm from the radiogenic tube. The research was approved by University of Brescia DSMC Council.

Length analysis

The length assessment of each hand segment (metacarpals and phalanges) was carried out on digitalised images measuring the distance from the proximal to the distal end along the longitudinal mid axis with the programme "Cell" (Soft Imaging System GmbH, Munster, Germany). The epiphyseal ossification centres were included in the measurement: most of the selected X-rays were of adolescents or young adults, therefore with the full developed series of epiphyseal nuclei. The total ray length was calculated as the sum of the metacarpal and of the same ray phalanges. The relative length of each segment in the same 5-FH was calculated on the total length of its own ray. In the normal hand population, the relative length of the thumb segments was calculated on the 3rd ray total length in the same hand, those of the other fingers on the total length of the corresponding ray.

Longitudinal fingers' growth rate index (IGR)

In metacarpals' and phalanges' X-rays, the narrower circumference of the diaphysis (deduced from the narrower A-P diameter in 2D view) did not correspond to mid-point of the segment length. In the early foetal period, the primary ossification centre develops at the mid-point of the cartilage anlage and only later in the ensuing developmental stage become manifest the different longitudinal growth rate of the bone proximal and distal end. This specific character of long bone anlagen development was used to assess the longitudinal growth index of each hand segment: the narrower, transverse diameter of the diaphysis was traced on the digitalised X-ray image and the distance between this line and the proximal and distal ends was measured. When the definition of the narrower transverse diameter was uncertain, the proximal and distal boundaries of the narrow, central segment were traced: the mid-point of the central segment was assumed as the level of the narrower diameter (Fig. 1). The ratio between the distance of the mid-point and the proximal/distal ends (IGR)



Figure 1. Method for the index of growth rate (IGR) measurement in long bones of post-natal hand X-rays. The narrower, transverse diameter of the diaphysis was traced in on the digitalised X-ray image and its distance from the distal and proximal end epiphyseal ends measured: $AB/AC = IGR$. When the definition of the narrower diameter was uncertain, the proximal and distal boundaries of the narrower central segment were traced: the mid-point of the latter was assumed as the narrower diameter (examples of measurement in metacarpal, mid and distal phalanx).

expressed the differential growth after cessation of the bidirectional growth pattern which characterises the growth phase of the post-natal age.

Statistical analysis

Repeated measurements of 20 normal hand X-ray images and of 9 5-FH X-rays were obtained independently by two investigators (A.G.S. and A.M.). Each data set was measured twice at interval of 1 month in two series of paired measurements. The difference of each paired measurements (intra-observer and inter-observer) was plotted against difference in individual segments and total ray length. By analysing the differences between the paired measurements, the variation in the differences for both the two series of measurements was wider in the inter-observed paired data set than in the corresponding intra-observer set; however, with a degree of agreement above 95% of confidence interval for both [11]. The finger segments relative length and the IGR was expressed as mean \pm standard error of mean (SEM).

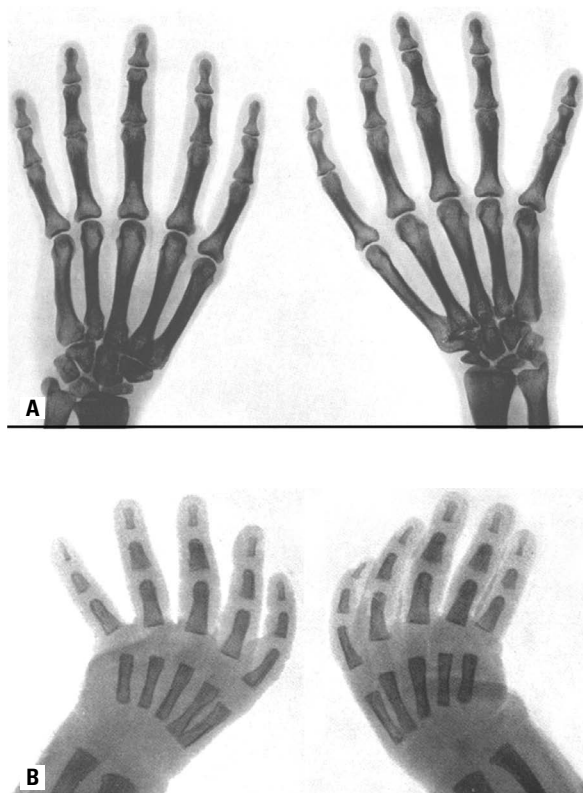


Figure 2. Five-fingered hand of the right and left hand of the mother (A) and of her new-born (B) reported by Heiss (1957) (reproduced from *Zeitschrift für Anatomie und Entwicklungsgeschichte* with permission of Springer Nature; license n. 4334811065195).

Statistical analysis was performed with a statistical package (Graph Pad prism 5, Graph Pad Software, San Diego, CA, USA). Non parametric data were analysed by a Kruskal-Wallis test followed by Dunn's test or Mann-Whitney test when appropriate.

RESULTS

The genetic transmission of 5-FH phenotype has been documented by the study of gene mutations in several cases with a large genealogical tree [1, 3, 7, 18, 19]; one of these hands X-ray image entered into the criteria of this study and could be analysed with morphometry. A further case reported by Heiss [6] documented bilateral 5-FH either in the mother (Fig. 2) and her new-born, confirming the genetic transmission. The relative length measurements of the 5-FH segments showed along each ray longitudinal axis same progression with $MC > Php > Phm > Phd$ (metacarpal; proximal phalanx; mid phalanx; distal phalanx). The comparison between the corresponding segment relative lengths in the transverse line (from ray 1 to ray 5) was variable, but with no-significant

differences (Table 2, relative length). The IGR variance was wider among the distal phalanges, not significant among mid/proximal phalanges and metacarpals. The index of all metacarpals was > 1 in contrast with that of all the phalanges which resulted < 1 (Table 2, IGR). Comparing 5-FH and normal hand segments, the 2nd–5th ray showed no significant difference of relative length and IGR between corresponding segments (Table 3, relative length). The normal hand thumb ray (with the missing segment) was obviously much shorter than the 5-FH 1st ray. Correction of the “missing element bias” of the normal hand 1st ray segments with calculation of the relative length on the 3rd of the same hand (instead of the 1st), homology resulted between the normal hand thumb metacarpal (anatomical) and the lateral proximal phalanges as well as between the thumb proximal phalanx (anatomical) and the lateral mid-phalanges (Table 3, relative length).

The IGR of normal hand 2nd–5th metacarpals was > 1 , that of the 1st < 1 , such as all the phalanges (Table 3, IGR). Both relative length and IGR of the thumb parameters were significantly different in the normal hand and in 5-FH series. In the latter ($n = 9$), three cases were reported as not-opposable thumb, in the remaining 6 hands this character was not reported. In the Heiss [6] case report the hands of the mother showed a synostosis of the right hand trapezius-metacarpal joint; however, also the flat and enlarged joint between the trapezius and the 1st–2nd left hand proximal metacarpals (Fig. 3) indicated a not-opposable thumb.

DISCUSSION

The concept of homology and its application in developmental biology is a cornerstone in the study of organismic diversity and evolution [16]. The issue of the limb bone segment development in the vertebrates offers an ideal field for the application of X-ray morphometry, in particular for what concerns the most distal limb sector, (the autopod) and the evolution of primates and the hominin family.

The measurement of the hand segment relative lengths on the total ray length was an unavoidable methodology to apply morphometry to published X-ray images of 5-FH because of the rare observation of this human phenotype and the consequent difficulty to collect the original documentation of old cases. Moreover, the morphometric comparison with the normal-hand population was complicated

Table 2. Morphometric analysis of the hand segment relative lengths in the five-fingered hand (5-FH) series (n = 9 hands). The segment mean relative lengths along the ray longitudinal axis decreased from the metacarpal to the distal phalanx (MC): proximal phalanx (Php), mid phalanx (Phm), distal phalanx (Phd). Only statistical comparison of the mean relative lengths between corresponding segments in the transverse line was carried out and resulting not significant. Analysis of the hand segments' index of growth rate (IGR) in the 5-FH series (n = 9 hands). All metacarpals (1th–5th) have IGR > 1, all phalanges IGR < 1. This observation is relevant in the comparison with the normal human hand, whose thumb metacarpal (anatomical) has always IGR < 1, like that of all the phalanges. It corresponds to the asymmetrical growth pattern of the human autopod segments, which is characterised by the development of a unique, epiphyseal ossification centre (see text). No other index inversions in the transversal line

	MC	P	Php	P	Phm	P	Phd	P
Relative length								
R1	0.42 ± 0.05	NS	0.32 ± 0.05	NS	0.14 ± 0.02	NS	0.12 ± 0.01	NS
R2	0.49 ± 0.04		0.27 ± 0.02		0.17 ± 0.01		0.07 ± 0.02	
R3	0.44 ± 0.01		0.28 ± 0.02		0.18 ± 0.01		0.10 ± 0.02	
R4	0.42 ± 0.02		0.30 ± 0.02		0.18 ± 0.02		0.11 ± 0.03	
R5	0.46 ± 0.02		0.29 ± 0.01		0.17 ± 0.01		0.15 ± 0.03	
IGR								
R1	0.92 ± 0.06		0.84 ± 0.05		0.63 ± 0.03		0.33 ± 0.04	
R2	1.28 ± 0.10		0.82 ± 0.06		0.61 ± 0.04		0.32 ± 0.07	
R3	1.31 ± 0.08		0.83 ± 0.05		0.62 ± 0.06		0.32 ± 0.07	
R4	1.32 ± 0.08		0.78 ± 0.08		0.61 ± 0.04		0.31 ± 0.05	
R5	1.35 ± 0.08		0.82 ± 0.05		0.62 ± 0.05		0.32 ± 0.05	

Data are show as mean ± standard deviation; NS — not significant

Table 3. Relative length comparison in five-fingered hand (5-FH) (TPT; n = 9) and normal hand series (NH; n = 20). The relative length of the 1st ray segments normal hands was calculated on the total length of the 3rd ray in the same hand. Comparison of index of growth rate (IGR) in normal hand and in 5-FH series. In the first series the thumb metacarpal is < 1, the 2nd–5th > 1, in the second all metatarsals IGR is > 1. All phalanges have IGR < 1 with an index gradient corresponding to metacarpal (MC) ≈ proximal phalanx (Php) ≈ middle phalanx (Phm) ≈ distal phalanx (Phd)

	R1			R2			R3			R4			R5		
	TPT	NH	P	TPT	NH	P	TPT	NH	P	TPT	NH	P	TPT	NH	P
Relative length															
MC	0.42 ± 0.05	0.28 ± 0.1	NS	0.49 ± 0.04	0.48 ± 0.05	NS	0.44 ± 0.01	0.43 ± 0.01	NS	0.42 ± 0.02	0.4 ± 0.01	NS	0.46 ± 0.02	0.44 ± 0.02	NS
Php	0.32 ± 0.05	0.19 ± 0	***	0.27 ± 0.02	0.25 ± 0.08	NS	0.28 ± 0.02	0.29 ± 0.01	NS	0.3 ± 0.02	0.29 ± 0.01	NS	0.29 ± 0.01	0.27 ± 0.01	NS
Phm	0.14 ± 0.02			0.17 ± 0.01	0.16 ± 0.02	NS	0.18 ± 0.01	0.18 ± 0.01	NS	0.18 ± 0.02	0.18 ± 0.01	NS	0.17 ± 0.01	0.15 ± 0.01	NS
Phd	0.12 ± 0.01	0.14 ± 0		0.07 ± 0.02	0.11 ± 0.02	*	0.1 ± 0.02	0.11 ± 0.01	NS	0.11 ± 0.03	0.13 ± 0.01	NS	0.15 ± 0.03	0.14 ± 0.01	NS
IGR															
MC	0.92 ± 0.06	0.91 ± 0.1	NS	1.28 ± 0.1	1.18 ± 0.06	**	1.31 ± 0.08	1.11 ± 0.07	**	1.32 ± 0.08	1.15 ± 0.12	NS	1.35 ± 0.08	0.99 ± 0.04	***
Php	0.84 ± 0.05	0.87 ± 0.1	NS	0.82 ± 0.06	0.87 ± 0.06	NS	0.83 ± 0.05	0.85 ± 0.11	NS	0.78 ± 0.08	0.83 ± 0.1	NS	0.82 ± 0.05	0.87 ± 0.07	NS
Phm	0.63 ± 0.03			0.61 ± 0.04	0.86 ± 0.09	***	0.62 ± 0.06	0.83 ± 0.11	**	0.61 ± 0.04	0.92 ± 0.15	***	0.62 ± 0.05	0.84 ± 0.1	***
Phd	0.33 ± 0.04	0.84 ± 0.2	***	0.32 ± 0.07	0.35 ± 0.1	NS	0.32 ± 0.07	0.74 ± 0.19	***	0.31 ± 0.05	0.4 ± 0.06	**	0.32 ± 0.05	0.32 ± 0.13	NS

Data are show as mean ± standard deviation; NS — not significant; *p < 0.05; **p < 0.01; ***p < 0.001



Figure 3. Detail of Figure 2, elaborated with the “relief” function to enhance the relationship between trapezium-1st and 2nd proximal metacarpals: synostosis trapezium-1st metacarpal in the right hand and a flat/enlarged trapezium joint surface with the 1st and 2nd metacarpals in the left hand. Both correspond to a not-opposable thumb.

by the “thumb missing segment bias” of the latter population which reduced the total length of the 1st ray (thus increasing the relative lengths of the ray segments). Therefore, a correction factor was introduced in the normal-hands population calculating the relative length of the thumb segments on the 3rd ray of the same hand total length. The choice of the 3rd ray was based on the observation that in the 5-FH series the 3rd ray total length gave the best approximation to that of the thumb without a missing element.

Shape and topology were the currently used criteria to recognise the individuality of the hand segments as the metacarpals and respectively the proximal, mid and distal phalanges. The morphometric analysis of 5-FH confirmed with the parameters of relative length and IGR the homology of the segments at the same level in the transverse line of metacarpals and phalanges. In the human hand evolution, the loss of one segment of the 1st ray and the acquired ability of the thumb opposition has raised a long lasting discussion on the thumb segments homology with that of the lateral four metacarpals and phalanges [4, 15].

The unanswered question in this discussion was if the proximal segment of the thumb should be considered as a true metapodial or a phalanx and if the missing segment was the metacarpal or alternatively the proximal or the mid phalanx.

The 5-FH phenotype has been considered the result of a repeated, occasional gene mutation in the

chromosomal region 7q36 [2, 7] and it was suggested that it could be an ancestral phenotype in the evolution of anthropoids and hominids [8, 9, 11, 17]. However, to the best of our knowledge no observations of this autopod pattern have been reported in palaeontology or in the phylogenesis of vertebrates. These considerations were used to support the theory that the proximal thumb segment in the modern humans was a modified metapodial [4], but it does not give an explanation of the thumb missing segment (accordingly to this theory the proximal or the mid phalanx).

The comparative relative length analysis between the 1st ray segments of normal-hand and that of the 5-FH series suggested homology between metacarpal \neq proximal-phalanx and proximal-phalanx \neq mid-phalanx.

In this context, the IGR (which can be easily determined in the human hands post-natal X-rays) offered further insights in this discussion. The development of the human autopod was characterised by two different growth patterns. The first with a symmetric proximal and distal length growth of the cartilage anlage and the formation of the primary ossification centre in the embryonic and early foetal phase. The second with the appearance of the epiphyseal ossification centre in the late foetal and post-natal age [12, 13]. The narrower mid-transverse section of the primary ossification centre corresponded to the mid-point of the cartilage anlage characterised by the symmetric length growth of both ends during the whole foetal phase and until the epiphyseal centres development. Therefore, the post-natal X-rays of both 5-FH and normal hands after the formation of the single epiphyseal centre (and of the related growth plate cartilage) can be used to measure the distal and proximal segmental growth. It is worth to underscore that this parameter is independent from the relative length measurement.

Since $IGR > 1$ in 5-FH was the typical pattern of metacarpals, opposed to $IGR < 1$ of all the phalanges, the observation of the ratio < 1 in the normal-hand series 1st ray proximal segment (a metacarpal accordingly to the current anatomical nomenclature), further reinforced the homology suggested by the thumb relative length measurement, that is a correspondence metacarpal \approx proximal phalanx and proximal phalanx \approx mid phalanx.

This study presents some limitations, as frequently observed in comparative meta-analysis. First of

all, and since the topic refers to a rather infrequent condition, some papers included in this analysis are not very recent and thus include older elaboration techniques for X-ray images which may influence the included data. Secondly, we opted for the measurement of the 3rd ray together with a correction factor in order to achieve the most accurate approximation measurement.

CONCLUSIONS

The comparative analysis of relative lengths and IGRs in the two groups suggested homology of the (anatomical) thumb metacarpal with the 2nd–5th ray proximal phalanges in the same hand and that of the (anatomical) thumb proximal phalanx with the 2nd–5th ray mid-phalanges. These data suggest that in the human hand the missing segment of the thumb is the metacarpal.

REFERENCES

- Bland JM, Altman DG, Elsner JJ, et al. Statistical methods for assessing agreement between two methods of clinical measurement. *Lancet*. 1986; 1(8476): 307–310, indexed in Pubmed: [2868172](#).
- Dobbs MB, Dietz FR, Gurnett CA, et al. Localization of dominantly inherited isolated triphalangeal thumb to chromosomal region 7q36. *J Orthop Res*. 2000; 18(3): 340–344, doi: [10.1002/jor.1100180303](#), indexed in Pubmed: [10937618](#).
- Girisha KM, Bidchol AM, Kamath PS, et al. A novel mutation (g.106737G>T) in zone of polarizing activity regulatory sequence (ZRS) causes variable limb phenotypes in Werner mesomelia. *Am J Med Genet A*. 2014; 164A(4): 898–906, doi: [10.1002/ajmg.a.36367](#), indexed in Pubmed: [24478176](#).
- Guillem P, Demondion X, Drizenko A, et al. La bio phalange du pouce. *Revue générale de la littérature. Morphologie*. 1999; 83: 27–31.
- Haines RW. The pseudo epiphysis of the first metacarpal of man. *J Anat*. 1974; 117: 145–158.
- Heiss H. [Bilateral congenital thumbless five-finger hand in mother and child]. *Z Anat Entwicklungsgesch*. 1957; 120(3): 226–231, indexed in Pubmed: [13531207](#).
- Heutink P, Zguricas J, van Oosterhout L, et al. The gene for triphalangeal thumb maps to the subtelomeric region of chromosome 7q. *Nat Genet*. 1994; 6(3): 287–292, doi: [10.1038/ng0394-287](#), indexed in Pubmed: [8012392](#).
- Marzke MW, Marzke RF. Evolution of the human hand: approaches to acquiring, analysing and interpreting the anatomical evidence. *J Anat*. 2000; 197 (Pt 1): 121–140, doi: [10.1046/j.1469-7580.2000.19710121.x](#), indexed in Pubmed: [10999274](#).
- Marzke MW. Precision grips, hand morphology, and tools. *Am J Phys Anthropol*. 1997; 102(1): 91–110, doi: [10.1002/\(SICI\)1096-8644\(199701\)102:1<91::AID-AJPA8>3.0.CO;2-G](#), indexed in Pubmed: [9034041](#).
- Ogden JA, Ganey TM, Light TR, et al. Ossification and pseudoepiphysis formation in the “nonepiphyseal” end of bones of the hands and feet. *Skeletal Radiol*. 1994; 23(1): 3–13, doi: [10.1007/BF00203694](#), indexed in Pubmed: [8160033](#).
- Patel B, Maiolino S. Morphological diversity in the digital rays of primate hands. In Kivell TL, Lemelin, P, Richmond, BG, et al (eds). *The evolution of the primate hand*. Springer Science New York. *The Evolution of the Primate Hand*. 2016: 55–100, doi: [10.1007/978-1-4939-3646-5_4](#).
- Pazzaglia UE, Congiu T, Sibilia V, et al. Growth and shaping of metacarpal and carpal cartilage anlagen: application of morphometry to the development of short and long bone. A study of human hand anlagen in the fetal period. *J Morphol*. 2017; 278(7): 884–895, doi: [10.1002/jmor.20681](#), indexed in Pubmed: [28386944](#).
- Pazzaglia UE, Congiu T, Sibilia V, et al. Relationship between the chondrocyte maturation cycle and the endochondral ossification in the diaphyseal and epiphyseal ossification centers. *J Morphol*. 2016; 277(9): 1187–1198, doi: [10.1002/jmor.20568](#), indexed in Pubmed: [27312928](#).
- Qazi Q, Kassner EG. Triphalangeal thumb. *J Med Genet*. 1988; 25(8): 505–520, doi: [10.1136/jmg.25.8.505](#), indexed in Pubmed: [3050097](#).
- Reno PL, Horton WE, Lovejoy CO. Metapodial or phalanx? An evolutionary and developmental perspective on the homology of the first ray’s proximal segment. *J Exp Zool B Mol Dev Evol*. 2013; 320(5): 276–285, doi: [10.1002/jez.b.22506](#), indexed in Pubmed: [23640850](#).
- Rieppel O. Homology, topology, and typology: the history of modern debates. In Hall BK (ed). *Homology: the hierarchical basis of comparative biology*. Academic Press Inc. *Homology*. 1994: 63–100, doi: [10.1016/b978-0-12-318920-2.50008-1](#).
- Tocheri MW, Orr CM, Jacofsky MC, et al. The evolutionary history of the hominin hand since the last common ancestor of Pan and Homo. *J Anat*. 2008; 212(4): 544–562, doi: [10.1111/j.1469-7580.2008.00865.x](#), indexed in Pubmed: [18380869](#).
- Warm A, Di Pietro C, D’Agrosa F, et al. Non-opposable triphalangeal thumb in an Italian family. *J Med Genet*. 1988; 25(5): 337–339, doi: [10.1136/jmg.25.5.337](#), indexed in Pubmed: [3385742](#).
- Wieczorek D, Pawlik B, Li Y, et al. A specific mutation in the distant sonic hedgehog (SHH) cis-regulator (ZRS) causes Werner mesomelic syndrome (WMS) while complete ZRS duplications underlie Haas type polysyndactyly and preaxial polydactyly (PPD) with or without triphalangeal thumb. *Hum Mutat*. 2010; 31(1): 81–89, doi: [10.1002/humu.21142](#), indexed in Pubmed: [19847792](#).
- Zguricas J, Dijkstra PF, Gelsema ES, et al. Metacarpophalangeal pattern (MCP) profile analysis in a family with triphalangeal thumb. *J Med Genet*. 1997; 34(1): 55–62, doi: [10.1136/jmg.34.1.55](#), indexed in Pubmed: [9032651](#).
- Zuidam JM, Dees EEC, Lequin MH, et al. The effect of the epiphyseal growth plate on the length of the first metacarpal in triphalangeal thumb. *J Hand Surg Am*. 2006; 31(7): 1183–1188, doi: [10.1016/j.jhsa.2006.03.025](#), indexed in Pubmed: [16945724](#).
- Zuidam JM, Dees EEC, Selles RW, et al. Implications for treatment of variations in length of the first metacarpal in different types of triphalangeal thumbs. *J Hand Surg Eur Vol*. 2010; 35(1): 65–69, doi: [10.1177/1753193408095881](#), indexed in Pubmed: [20100712](#).

Morphology of sesamoid bones in keyboard musicians

K.P. Dąbrowski¹, H. Stankiewicz-Jóźwicka², A. Kowalczyk¹, J. Wróblewski², B. Cizek^{1,3}

¹Department of Descriptive and Clinical Anatomy, Medical University of Warsaw, Poland

²The Instrumental Department, The Fryderyk Chopin University of Music, Warsaw, Poland

³Department of Neurosurgery in Bogdanowicz Children's Hospital, Warsaw, Poland

[Received: 7 April 2020; Accepted: 29 May 2020]

Background: The sesamoid bones are small, usually oval bone structures often found in joints and under the tendons. Although their precise function is not fully understood, it is agreed upon that they protect the joints and make movements faster and less energy consuming. Sesamoid bones are found in hands, especially around first, second and fifth metacarpophalangeal joint and the interphalangeal joint of the thumb.

Materials and methods: This study compares a group of 32 young musicians to 30 non-musicians of similar age and posture. The hands of the subjects were examined by ultrasound imaging for the presence of sesamoid bones. The results were noted and observed sesamoids were measured.

Results: The results seem to prove that although there are no difference in the amount or the location of the sesamoid bones between the musicians and the non-musicians, there is statistically significant tendency for the musicians to have bigger sum of the sesamoid's volume per hand (Fisher's test p -value = 0.034 < 0.05).

Conclusions: There was also observed an unusually shaped "Bactrian" sesamoid bone at the interphalangeal joint of the thumb in 8 cases in the musicians' group and 1 case in the control group. All participants with the aforementioned structure were female. (Folia Morphol 2021; 80, 2: 410–414)

Key words: sesamoid, wrist, hand, musician, morphology, adaptation

INTRODUCTION

First known descriptions of the Sesamoid bones come from Galen's works on Old World monkeys, most likely macaques, in the late second century. More reliable account comes from Versalis' *De Humani Corporis Fabrica Libri Septem* of 1542. Both authors, however, describe the Sesamoid bones as small, oval, bony structures forming in close vicinity of joints — either within the joint capsule walls or under or within tendons of nearby muscles, most noticeably on palmar side of a hand and plantar side

of a foot. Their name comes from resemblance in size and shape to sesamoid seeds, although they are also being compared to halves of peas or grains of rice [2, 9, 12, 22, 23, 25].

The prevalence of Sesamoid bones seems to vary greatly depending on ethnicity, it is safe to say, however, that in over 99% of cases there are two bones present in the first metacarpophalangeal joint, vast majority of population possesses Sesamoid bones in the fifth metacarpophalangeal joint and first interphalangeal joint and approximately 50% of peo-

Address for correspondence: Dr. K. Dąbrowski, ul. Indirji Gandhi 37/15, 02–776 Warszawa, Poland, tel: +48 888 363 320, e-mail: k.p.dabr@gmail.com

This article is available in open access under Creative Common Attribution-Non-Commercial-No Derivatives 4.0 International (CC BY-NC-ND 4.0) license, allowing to download articles and share them with others as long as they credit the authors and the publisher, but without permission to change them in any way or use them commercially.

ple have a sesamoid bone in the second metacarpophalangeal joint. They can also occur in other joints of the hand and fingers, but that remains very rare [1, 2, 9, 10, 12, 13, 17, 19, 25].

The precise function of Sesamoid bones remains a subject of discussions. It is generally agreed that they play part in protecting the joint, reducing pressure and friction of the tendon and modifying the vector of the muscular pull [1, 5, 8, 9, 12, 18, 25].

MATERIALS AND METHODS

The study was performed on the group of 62 healthy adults: a study group of 32 students of keyboard instruments and a control group of 30 students without any extended musical training.

The study group included 16 females and 16 males between the ages of 18 and 38, with a mean age of 23.7 years, mean height of 172.8 cm and mean weight of 67.3 kg. Five of them were noted as left-handed. All of the participants were healthy and had no history of serious trauma or surgical procedures in the area of the hand. All the participants underwent multiple years of instrumental training.

The control group included 17 females and 13 males between the ages of 20 and 33, with a mean age of 22.8 years, mean height of 174.3 cm and mean weight of 69.2 kg. Four of them noted as left-handed. All of the participants were healthy and had no history of serious trauma or surgical procedures in the area of the hand. None of the participants underwent any form of prolonged, systematic musical education.

All of the examined signed the form of informed consent. All participants were interviewed and had the anthropological measurements of their upper extremities taken. Afterwards all of the participants' hands were examined by an ultrasound imaging (LOGIQ F8 GE with L6–12, 6–13 MHz probe) for presence of the sesamoid bones. Found bones were described regarding their amount, location and three-dimensional measurements (anterior-posterior, radial-ulnar and proximal-distal in relation to anatomical position). To facilitate comparison, the formula of the volume of the sesamoid bones was rounded to the product of the measurements. All the measurements and calculations were performed by the same team. All the findings were examined with the use of Fisher's exact test and t-Student's test.

The examination was completely non-invasive and the research does have the approval of the Ethics Committee.

RESULTS

The amount of sesamoid bones found in one hand varied from 2 to 6 with no significant differences between sides and groups (Fisher's test p-value for control group sides, study group sides, left hands of both groups and right hands of both groups, respectively: 0.654, 0.683, 0.398, and 0.926) with 26 out of 32 musicians showing symmetry in the pattern, and 23 out of 30 non-musicians showing symmetry in the pattern. There was also no noticeable difference between the groups in the location of the sesamoid bones.

The mean of the sum of the sesamoid bones' volume in one hand for musicians was 83.2351 mm³ (78.3774 mm³ for the left hand and 88.0928 mm³ for the right hand) and for non-musicians was 74.8420 mm³ (73.5829 mm³ for the left hand and 76.1010 mm³ for the right hand). Fisher's test p-value for the mean volumes from both hands was: p-value = 0.033618274 (p-value = 0.168077962 for only left hands and p-value = 0.024897613 for only right hands) which does reach the threshold of statistical significance ($\alpha = 0.05$).

In case of 27 musicians it was possible to acquire information regarding the length of their musical education and the starting age. The mean age of the beginning of the musical education was 7.7 years and the mean length of education to the point of examination was 15.4 years. Both of those variables, when tested against mean sum of the volumes of the sesamoids in one hand with paired t-Student's test has returned p-value < 0.0001 which would suggest a strong correlation.

Sexual dimorphism proved to be statistically significant (p-value < 0.05) in musicians (Fisher's test p-value for mean, left hands and right hands respectively 0.003094, 0.025887, and 0.001637), with males having greater volume sum of sesamoid bones, and non-significant in control group (Fisher's test p-value for mean, left hands and right hands, respectively 0.636599, 0.668857, 0.110638).

An unusually shaped, "Bactrian" sesamoid bone was observed in the first interphalangeal joint in musician's hand in 8 cases (5 females), 6 of which (3 females) occurred symmetrically. Only 1 case (left hand of a 23-year-old left handed female) was observed in the control group (Figs. 1, 2).

DISCUSSION

The features of a "perfect musician's hand" remain a subject of discussion. Most authors seem to focus

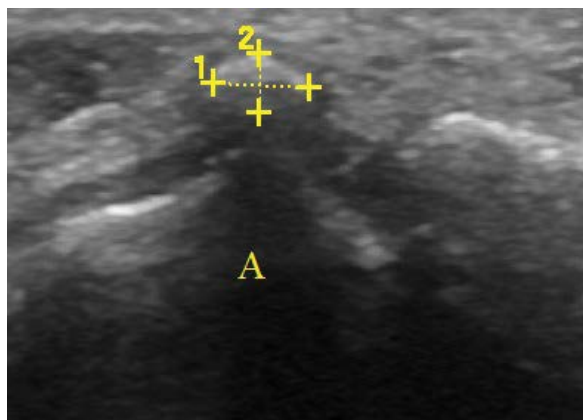


Figure 1. A sesamoid bone over the 5th metacarpophalangeal joint (A) of the left hand of the female pianist — sagittal view. Estimated volume based on the measurements for this sesamoid bone was 19.2 mm³.

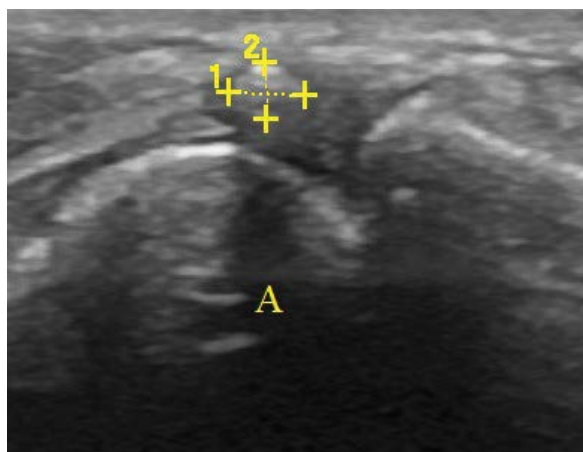


Figure 2. A sesamoid bone over the 5th metacarpophalangeal joint (A) of the left hand of the female non-pianist of similar age, built and height as the aforementioned female pianist — sagittal view. Estimated volume based on the measurements for this sesamoid bone was 10.9 mm³.

primarily on the hand's size and the hand's span, with assumption that the bigger the hand and the hand span, the better. Wristen claims that throughout history small-handed musicians remained rather devoted amateurs than professionals [24]. Some authors point out that the group most commonly suffering from trauma and performance related misuse of the hands are women [16] who statistically have 15% smaller hand than the men [4]. However, there seems to be a lot of research putting this seemingly obvious matter in question. The results of Sang-Hie Lee's research suggests that the size of the hand is not as important as it's mobility and hand's span, which seems to be less important of the two. She quotes Kentner saying

that there were just as many famous pianists with big hands (like Sauer, Richter, Rachmaninoff) as those whose hands were considered small (Patchmann, Hoffmann, d'Albert). Both Sang-Hie [15, 16] and Sakai [14] bring up Wagner's analysis — that hands of the male pianists are on average bigger but less mobile than female, both when it comes to active and passive range of motion, and that left hand has statistically greater hand's span than the right one. Interestingly enough there is research suggesting that more sesamoid bones occur both in females than males and in the left hand compared to the right hand [3, 14–16, 20].

This research focused on the sesamoid bones, due to them being one of the most morphologically variable structures of the human hand as well as sesamoid bones starting to ossify at the beginning of the puberty, which would be between 11 and 13 years of age for females and between 13 and 15 age for males [21], which seem to overlap with the typical beginning of the intense musical training for future students of the musical universities.

There was no significant difference between the groups of musicians and non-musicians regarding the amount of the sesamoid bones in the hand, as well as there was only approximately 12% difference between the groups in the symmetry which lines up with Miller's opinion [11] that there are no morphological differences in the structures of the hand. However, upon a closer inspection, there appears to be a tendency in the sesamoids' volume. It seems that musicians tend to have bigger sesamoid bones on average than non-musicians. The mean sum of all the sesamoid bones in one hand was 83.2351 mm³ in the study group compared to 74.8420 mm³ in the control group, which does meet the criteria of statistical significance (p -value of the Fisher's test = 0.034 < 0.05). When, in order to remove the potential confounding variable, the results were accounted for body type by dividing by body mass index of each participant, the p -value only decreased, further underlining the results.

There also seems to be a noticeable tendency regarding sexual dimorphism. Despite general tendency for women to have more sesamoid bones than men [3, 9, 20, 25], the men in the musicians' group proved to have statistically significantly (p -value = 0.003094) bigger sum of the volume of the sesamoid bones in one hand than women. Such dimorphism did not occur in the group of non-musicians

(p -value = 0.636599). The participants were questioned regarding their history of past regular physical activity, and the suspected reason for such phenomenon could not be found, therefore it needs to be assumed that the primary reason for aforementioned dimorphism was the musical training.

Considering that both groups consisted of people in similar age (mean: 23.7 years for the study group and 22.8 years for the control group), and similar built (mean height: 172.8 cm for the study group and 174.3 cm for the control group, mean weight: 67.3 kg for the study group and 69.2 kg for the control group) with very small differences that could only possibly favour the control group (statistically bigger body mass should translate for the bigger mass of the skeletal structures), and that the sexual make-up of the control group was proven not to influence the outcome (no significant sexual dimorphism in the control group), it could be speculated that the main reason for the differences in the mean sum of the volume of the sesamoid bones was the musical training during the age of sesamoids' ossification. It would agree with the assumption that the sesamoid bones function as a pulley for the muscular tendons, therefore making the movement faster, stronger and safer for the joint underneath [2, 3, 8, 9, 12, 22, 25]. It could be speculated that the time when the hand undergoes most significant morphological adaptation to the task of playing the keyboard instrument, and therefore possibly most important time for regular musical training is the time of sesamoids' ossification which starts during early stages of puberty.

This idea seems to be supported by the results of the Student's t -test between the age of the beginning of the musical education or length of the musical education and volume of the sesamoid bones. This was tested on 27 out of 32 musicians due to limited availability of the information. However, this should not have an impact on the results since the sexual proportion remained the same. The length of education varied from 7 to 29 years with a mean of 15.4 years. The beginning age varied from 4 to 13 years of age with a mode of 6 mean of 7.7 years of age. In both cases the p -value of the test showed to be $p < 0.0001$ which would suggest a very strong correlation.

Another interesting outcome of this research was finding of the unusually shaped sesamoid bone in the interphalangeal joint of the pollex. This bone, instead of typical oval shape, displayed two slight elevations on the palmar site, with a furrow between them. There

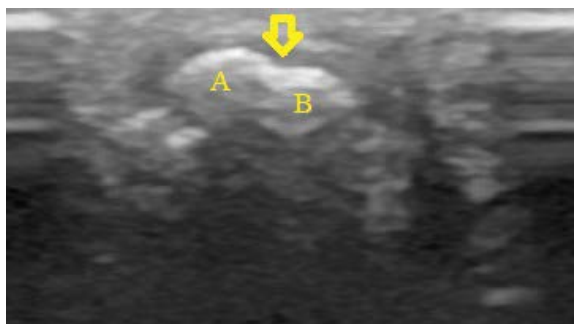


Figure 3. A "Bactrian" sesamoid bone found in the interphalangeal joint of the thumb of a female musician — horizontal view. There are two distinctive elevations (A, B) and a sulcus between them (arrow).

was no proof that such "Bactrian" sesamoid occurred due to damage, or conjunction of two smaller bones, moreover similar sesamoid bones were observed by Jones [7] in smaller mammals, such as rabbits. Since there were 8 cases of such sesamoid found in the study group (25% of cases), most of which symmetrical (6 cases), and only 1 case in the control group (3% of cases) it could be speculated that this variability is also a form of adaptation to the musical training on the keyboard instrument, especially since there is evidence that the sesamoid bones are being shaped by the action of the tendons above them (Fig. 3) [6].

Interestingly, all of the cases of "Bactrian" sesamoid occurred in female hands only. It might be related to the fact that the pattern of sesamoids' development in females seems to be tied to menarche [21]. Unfortunately, this concept is unverifiable based on this particular research.

CONCLUSIONS

There were no significant differences in the amount or localisation of the sesamoid bones of the hand between the musicians and the non-musicians.

The trained keyboard musicians tend to have significantly bigger sesamoid bones than non-musicians. It may be related to the fact that both sesamoid ossification and typical beginning of musical training intensification happens at the early stages of puberty.

There seems to be a strong correlation ($p < 0.0001$) between the age of the beginning of the musical education or length of the musical education and volume of the sesamoid bones.

The male musicians proved to have significantly bigger sesamoid bones than the female musicians. Such tendency did not occur in the control group.

Unusually shaped "Bactrian" sesamoid bone on the interphalangeal joint of the pollex was observed 8 times in the musicians' group and only once in the control group. All the cases occurred in the female's hand.

REFERENCES

1. Becciolini M, Bonacchi G. Fracture of the sesamoid bones of the thumb associated with volar plate injury: ultrasound diagnosis. *J Ultrasound*. 2015; 18(4): 395–398, doi: [10.1007/s40477-015-0166-1](https://doi.org/10.1007/s40477-015-0166-1), indexed in Pubmed: [26550076](https://pubmed.ncbi.nlm.nih.gov/26550076/).
2. Chen W, Cheng J, Sun R, et al. Prevalence and variation of sesamoid bones in the hand: a multi-center radiographic study. *Int J Clin Exp Med*. 2015; 8(7): 11721–11726, indexed in Pubmed: [26380010](https://pubmed.ncbi.nlm.nih.gov/26380010/).
3. Dąbrowski K, Stankiewicz-Józwicka H, Kowalczyk A, et al. Ossa Sesamoidea — prevalence of sesamoid bones in human hands. *Folia Morphol*. 2019 [Epub ahead of print], doi: [10.5603/FM.a2019.0123](https://doi.org/10.5603/FM.a2019.0123), indexed in Pubmed: [31750538](https://pubmed.ncbi.nlm.nih.gov/31750538/).
4. Donison C. Hand Size vs the Standard Piano Keyboard. *Med Problems Performing Artists*. 2000; 15(3): 111–114, doi: [10.21091/mppa.2000.3022](https://doi.org/10.21091/mppa.2000.3022).
5. Egerci OF, Kose O, Turan A, et al. Prevalence and distribution of the fabella: a radiographic study in Turkish subjects. *Folia Morphol*. 2017; 76(3): 478–483, doi: [10.5603/FM.a2016.0080](https://doi.org/10.5603/FM.a2016.0080), indexed in Pubmed: [28026849](https://pubmed.ncbi.nlm.nih.gov/28026849/).
6. Jin ZW, Shibata S, Abe H, et al. A new insight into the fabella at knee: the foetal development and evolution. *Folia Morphol*. 2017; 76(1): 87–93, doi: [10.5603/FM.a2016.0048](https://doi.org/10.5603/FM.a2016.0048), indexed in Pubmed: [27665955](https://pubmed.ncbi.nlm.nih.gov/27665955/).
7. Jones FW. The principles of Anatomy as seen in hand. 2nd ed. Bailliere Tindall and Cox 1944.
8. Koo BS, Song Y, Sung YK, et al. Prevalence and distribution of sesamoid bones in the hand determined using digital tomosynthesis. *Clin Anat*. 2017; 30(5): 608–613, doi: [10.1002/ca.22881](https://doi.org/10.1002/ca.22881), indexed in Pubmed: [28340518](https://pubmed.ncbi.nlm.nih.gov/28340518/).
9. Kose O, Guler F, Turan A, et al. Prevalence and distribution of sesamoid bones of the hand: a radiographic study in Turkish subjects. *Int J Morphol*. 2012; 30(3): 1094–1099, doi: [10.4067/s0717-95022012000300055](https://doi.org/10.4067/s0717-95022012000300055).
10. Kwon HH, Koo BS, Song Y, et al. AB1028 Prevalence and distribution of sesamoid bones in the hand determined using digital tomosynthesis. Abstracts Accepted for Publication. *Clin Anat*. 2017; 30(5): 608–613, doi: [10.1136/annrheumdis-2017-eular.4553](https://doi.org/10.1136/annrheumdis-2017-eular.4553).
11. Miller G, Peck F, Watson J. Pain disorders and variations in upper limb morphology in music students. *Med Problems Performing Artists*. 2002; 17(4): 169–172, doi: [10.21091/mppa.2002.4016](https://doi.org/10.21091/mppa.2002.4016).
12. Ozcanli H, Sekerci R, Keles N. Sesamoid disorders of the hand. *J Hand Surg Am*. 2015; 40(6): 1231–1232, doi: [10.1016/j.jhssa.2015.01.029](https://doi.org/10.1016/j.jhssa.2015.01.029), indexed in Pubmed: [25771478](https://pubmed.ncbi.nlm.nih.gov/25771478/).
13. Rosengarten E. Occurrence of Sesamoid bones in the hands of the Polish population. *Folia Morphol*. 1967; XXVI: 2.
14. Sakai N. Keyboard span in old musical instruments: concerning hand span and overuse problems in pianists. *Med Problems Performing Artists*. 2008; 23(4): 169–171, doi: [10.21091/mppa.2008.4034](https://doi.org/10.21091/mppa.2008.4034).
15. Sang-Hie L. Hand biomechanics in skilled pianists playing a scale in thirds. *Med Problems Performing Artists*. 2010; 25(4): 167–174, doi: [10.21091/mppa.2010.4034](https://doi.org/10.21091/mppa.2010.4034).
16. Sang-Hie L. Pianists' hand ergonomics and touch control. *Med Problems Performing Artists*. 1990; 5: 72–78.
17. Seki Y, Hoshino Y, Kuroda H. Locking of the ring finger at proximal interphalangeal joint due to a sesamoid bone: a case report. *Hand (N Y)*. 2012; 7(1): 119–120, doi: [10.1007/s11552-011-9386-9](https://doi.org/10.1007/s11552-011-9386-9), indexed in Pubmed: [23450978](https://pubmed.ncbi.nlm.nih.gov/23450978/).
18. Seki Y, Hoshino Y, Kuroda H. Prevalence of sesamoid bones in the interphalangeal joint of the thumb and fingers: a radiographic study. *Clin Anat*. 2013; 26(7): 823–826, doi: [10.1002/ca.22201](https://doi.org/10.1002/ca.22201), indexed in Pubmed: [23255267](https://pubmed.ncbi.nlm.nih.gov/23255267/).
19. Sokołowska-Pituchowa J, Miaśkiewicz C. The Sesamoid bones in Negros. *Folia Morphol*. 1969; XXVIII: 2.
20. Sokołowska-Pituchowa J, Miaśkiewicz C. Studies on the Sesamoid bones in the hands of women. *Folia Morphol*. 1967; XXVI: 1.
21. Szmurło J, Szwaykowski W, Olczak A. Time of appearance of the ossification centre in the metacarpophalangeal sesamoid bone of the thumb in girls during puberty. *Folia Morphol*. 1975; XXXIV(3): 259–265.
22. Ting L, San C, Ben Ng, et al. Distribution of sesamoid bones in the hand: a study in the Chinese population. *J Orthopaedics Trauma Rehabilitation*. 2017; 23(1): 45–48, doi: [10.1016/j.jotr.2017.03.001](https://doi.org/10.1016/j.jotr.2017.03.001).
23. Versalis A, De HuA, Garrison DH. De Humani Corporis Fabrica Libri Septem - An annotated translation of 1542 and 1555 editions. Garrison DH., Hast MH., Karger 2014.
24. Wristen BG, Jung MC, Wismer A, et al. Assessment of muscle activity and joint angles in small-handed pianists: a pilot study on the 7/8-sized keyboard versus the full-sized keyboard. *Med Problems Performing Artists*. 2006; 21(1): 3–9, doi: [10.21091/mppa.2006.1002](https://doi.org/10.21091/mppa.2006.1002).
25. Yammine K. The prevalence of the sesamoid bones of the hand: a systematic review and meta-analysis. *Clin Anat*. 2014; 27(8): 1291–1303, doi: [10.1002/ca.22378](https://doi.org/10.1002/ca.22378), indexed in Pubmed: [24615762](https://pubmed.ncbi.nlm.nih.gov/24615762/).

Surface localisation of master knot of Henry, *in situ* and *ex vivo* length of flexor hallucis longus tendon: pertinent data for tendon harvesting and transfer

P. Wan-ae-loh¹, P. Danginthawat², T. Huanmanop³, S. Agthong³, V. Chentanez³

¹PhD Candidate, Medical Science Programme, Faculty of Medicine, King Chulalongkorn Memorial Hospital, Chulalongkorn University, Bangkok, Thailand

²Faculty of Physical Therapy, Huachiew Chalermprakiet University, Samutprakan, Thailand

³Department of Anatomy, Faculty of Medicine, King Chulalongkorn Memorial Hospital, Chulalongkorn University, Bangkok, Thailand

[Received: 19 February 2020; Accepted: 30 March 2020]

Background: Length of flexor hallucis longus (FHL), localisation of master knot of Henry (MKH) and relationship between MKH and neurovascular bundle are essential for the achievement of FHL tendon transfer. The purpose of this study is to define the localisation of MKH in reference to bony landmarks of the foot, its relationship to plantar neurovascular bundle and to investigate *in situ* and *ex vivo* length of FHL tendon in single incision, double incision and minimally invasive techniques.

Materials and methods: Foot length was examined in 62 feet of 31 soft cadavers (9 males, 22 females). Various parameters including the relationship between MKH and neurovascular bundle, the distances from MKH to medial malleolus (MM), navicular tuberosity (NT) and the first interphalangeal joint of great toe (IP) were measured. Surface localisation of MKH in relation to a line joining the medial end of plantar flexion crease at the base of great toes (MC) to NT (MC-NT line) was determined. Lengths of FHL tendon graft from three surgical techniques were examined. *In situ* length was measured in the plantar surface of foot and *ex vivo* length was measured after tendon was cut from its insertion.

Results: The mean length of foot was 230.98 ± 15.35 mm with a statistically significant difference between genders in both sides ($p < 0.05$). No distance was found between medial plantar neurovascular bundle (MPNVB) and MKH. Mean distance of 17.13 ± 3.55 mm was found between lateral plantar neurovascular bundle (LPNVB) and MKH. MKH was located at a mean distance of 117.11 ± 1.00 mm proximal to IP, 26.28 ± 4.75 mm under NT and 59.58 ± 7.51 mm distal to MM with a statistically significant difference of MKH-IP distance between genders in both sides and MKH-NT in right side. MKH was located anterior to NT (66.1%), at NT (27.4%) and posterior to NT (6.5%) on the MC-NT line. Surface localisation of MKH was $94.75 \pm 8.43\%$ of MC-NT line from MC with a perpendicular distance of 25.11 ± 5.37 mm below MC-NT line. The *in situ* and *ex vivo* tendon lengths from MTJ to ST₁ to MKH and to IP were 39.05 ± 10.88 mm and 34.43 ± 10.23 mm,

Address for correspondence: V. Chentanez, MD, PhD, Department of Anatomy, Faculty of Medicine, King Chulalongkorn Memorial Hospital, Chulalongkorn University, Bangkok 10330, Thailand, tel: 66-860701084, e-mail: fmedvct@gmail.com

This article is available in open access under Creative Common Attribution-Non-Commercial-No Derivatives 4.0 International (CC BY-NC-ND 4.0) license, allowing to download articles and share them with others as long as they credit the authors and the publisher, but without permission to change them in any way or use them commercially.

73.45 ± 9.91 mm and 68.63 ± 9.43 mm, 197.98 ± 13.89 and 191.79 ± 14.00 mm, respectively. A statistically significant difference between genders was found in MTJ-IP of *in situ* and *ex vivo* length of both sides ($p < 0.05$). The mean length of tendon between *in situ* and *ex vivo* was significantly different in all techniques ($p < 0.05$). A moderate positive correlation between foot length and tendon length was found in MTJ-IP of both *in situ* and *ex vivo* tendon length.

Conclusions: A statistically significant difference between *in situ* and *ex vivo* tendon length was shown in all harvesting techniques. Surface location of MKH was approximately at 95% of MC-NT line from MC with a perpendicular distance of 25 mm from MC-NT line. (Folia Morphol 2021; 80, 2: 415–424)

Key words: flexor hallucis longus, master knot of Henry, tendon transfer

INTRODUCTION

Flexor hallucis longus (FHL) tendon transfer is a widely used technique for reconstruction of the Achilles tendinopathies [17, 20]. This technique proposes to repair the length, to strengthen the injured tendon with additional tendon, and to incorporate more muscle force to the plantar flexor [6]. FHL is appropriate for transfer because of its strength, axis and amplitude of contraction, and its concomitant action with triceps surae muscles [32]. Moreover, FHL transfer can also reduce the pain by normalising vascularity [1, 6]. FHL transfer is also used for the treatment of posterior tibial insufficiency with a good to excellent clinical outcome [8, 19].

There are many techniques for harvesting FHL tendon grafts including single incision, double incision, and minimally invasive techniques [13]. The differences among these techniques are the indication and sites of incision. Importantly, the length of harvested tendon from each technique is vastly different [13]. The single incision approach is used to harvest the FHL within the tarsal tunnel. Although, this technique yields a shorter graft but it is long enough to be inserted on the calcaneus. When the additional length is required, the double incision technique at the medial aspect of foot near master knot of Henry (MKH) is considered. The added 3 cm of tendon length is obtained from this technique if the FHL is cut at MKH [4, 27, 29]. The minimally invasive technique provides the longest length [17]. Although, previous reports revealed good results following FHL transfer, complications such as serious injury of the distal branches of the posterior tibial artery and nerve, cock-up deformity, and functional loss of toe have been reported [1, 7, 13, 26].

Anatomically, medial and lateral plantar neurovascular bundles (MPNVB, LPNVB) reside near the incision

line. In consequence, they might be at risk during harvesting. The other structure which affects tendon harvesting is MKH. MKH is where the tendon of flexor digitorum longus (FDL) crosses over the tendon of FHL. It has been used as a surgical landmark for the tendon graft harvesting [2, 17]. Therefore, the precise location of the MKH is crucial for better results [2].

Knowledge of the length of FHL tendon available for harvesting, the relationship between tendon and neurovascular bundle, and the anatomical locations of MKH are essential for guiding the surgeon during operation and decreasing potential morbidity [13]. The length of FHL tendon after cutting for harvesting, which might be different from the length of attached tendon, should be elucidated. This anatomical study aims to clarify these issues in soft cadavers.

MATERIALS AND METHODS

This study was performed in 62 legs from 31 Thai soft cadavers (9 male and 22 female) supported by the Chula Soft Cadaver Surgical Training Centre, Faculty of Medicine, Chulalongkorn University. The average age of the cadavers was 78.39 ± 10.60 years (age range 53–100). All cadaveric ankles and feet had no deformities, damage and history of previous surgery.

Foot length measurement and surface marking

The foot was aligned to neutral position by fixing with a supporting frame. The foot length was measured from the most posterior portion of the calcaneus to the end of the longest toe [30]. The line joining the medial end of plantar flexion crease at the base of the great toes (MC) and the most prominent point of navicular tuberosity (NT) by palpation was created to be a reference line for locating the MKH surface landmark (Fig. 1A).

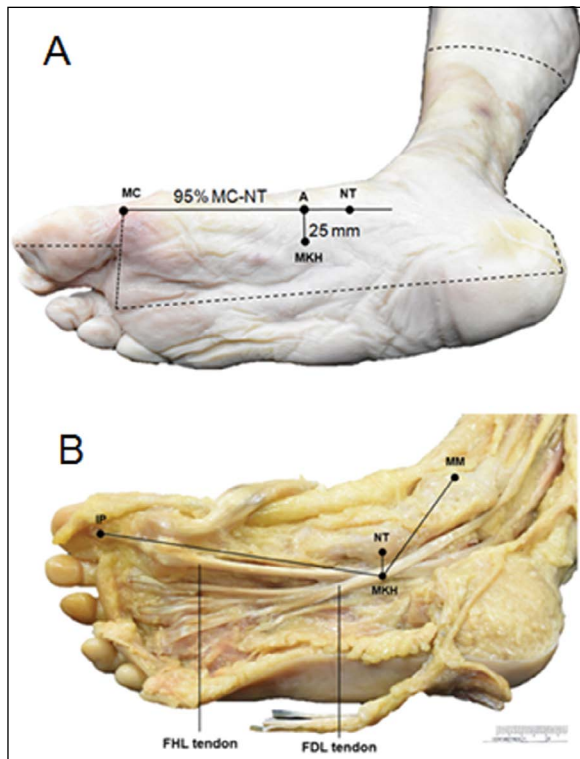


Figure 1. Plantar surface of right foot showing the skin incision and surface landmark of master knot of Henry (MKH); **A.** Skin incision line (dot line), the line joining between the medial end of plantar flexion crease at the base of the great toes (MC) and the most prominent point of navicular tuberosity (NT) (MC-NT line), the surface location of MKH on MC-NT line; **B.** The distance from MKH to the most prominent point of medial malleolus (MM), navicular tuberosity (NT) and first interphalangeal joint (IP); A — the perpendicular point of MKH on MC-NT line; FDL — flexor digitorum longus; FHL — flexor hallucis longus.

Cadaveric dissection

The skin incision along the dotted line as shown in Figure 1A was performed. The skin was dissected. Subcutaneous fatty tissue, flexor digitorum brevis and abductor hallucis muscle were removed to expose FHL tendon, FDL tendon and MKH in the plantar surface of foot (Fig. 1B). FHL was dissected further to its musculotendinous junction (MTJ) proximally and its insertion distally. The skin flap was turned down to cover the plantar surface of the foot and the location of MKH was marked on the skin surface. The perpendicular line from MKH to MC-NT line (MKH-A) was created (Fig. 1A). Point A might be located at NT, anterior to NT or posterior to NT on MC-NT line (Fig. 2). The most prominent point of medial malleolus (MM), sustentaculum tali (ST) and the midpoint of first interphalangeal joint of great toe (IP) were marked (Figs. 1B, 4A).

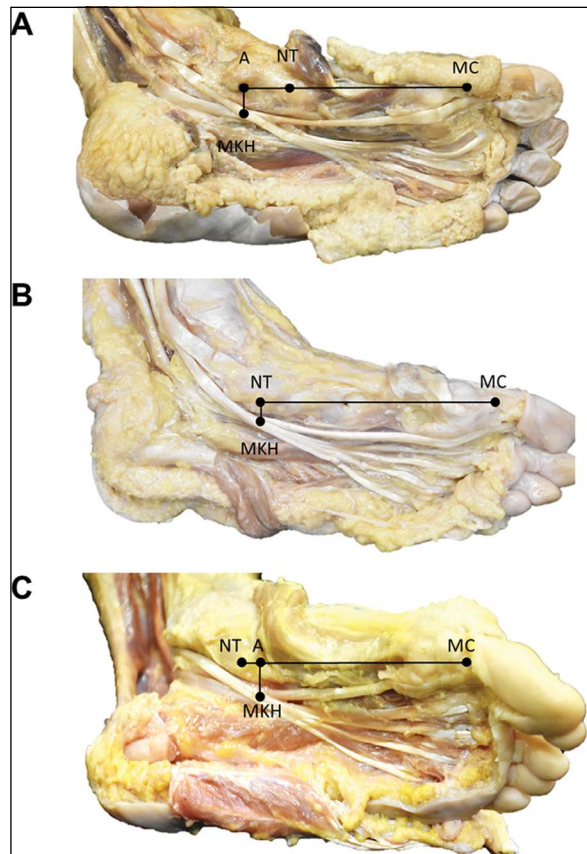


Figure 2. Plantar surface of left feet showing the surface location of master knot of Henry (MKH) on MC-NT line (point A); **A.** Posterior to NT; **B.** At NT; **C.** Anterior to NT; A — the perpendicular point of MKH on MC-NT line; MC — medial end of plantar flexor crease at the base of great toe; NT — navicular tuberosity.

Observations and measurements

Surface landmark and location of MKH, its relationship to the neurovascular bundle. The surface landmark of MKH was determined by measuring the length of MC-NT, MKH-A and MC-A lines (Fig. 1A). The MC-A length was calculated into percentage of MC-NT length. To determine the location of MKH in the dissected specimen, the distances from MKH to MM, to NT and to IP was measured (Fig. 1B). The anatomical relationship between MKH and neurovascular bundle, including MPNVB and LPNVB were evaluated and the distance between their midpoints were recorded (Fig. 3). All distances were measured by standardised digital Vernier calliper (Mitutoyo® 0–150 mm; range 150 mm, resolution 0.01 mm).

In situ and ex vivo lengths of FHL tendon. To determine the *in situ* length of FHL tendon, the lengths from MTJ to ST, MTJ to MKH and MTJ to IP represent the length harvested through a single incision, dou-

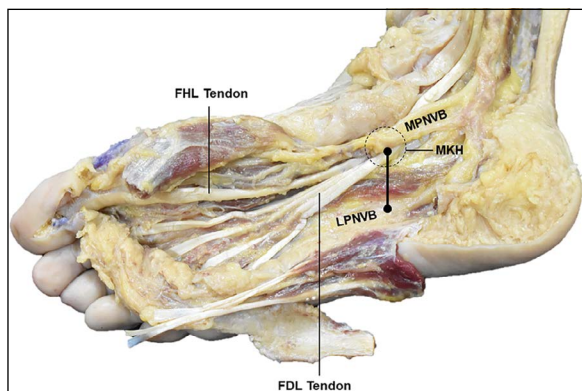


Figure 3. Plantar surface right foot showing the distance between master knot of Henry (MKH) and the midpoint of lateral plantar neurovascular bundle (LPNVB); MPNVB — medial plantar neurovascular bundle; FDL — flexor digitorum longus; FHL — flexor hallucis longus.

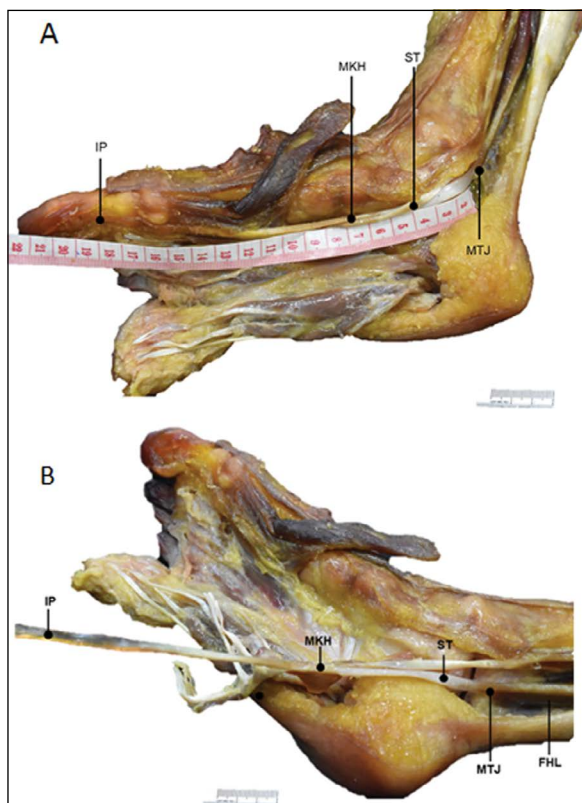


Figure 4. Plantar surface right foot showing the distances between musculotendinous junction (MTJ) of flexor hallucis longus (FHL) and first interphalangeal joint (IP), master knot of Henry (MKH), sustentaculum tali (ST); **A.** *In situ* tendon length; **B.** *Ex vivo* tendon length.

ble-incision and the minimally invasive technique, respectively (Fig. 4A).

To define the *ex vivo* length of FHL tendon, three points were marked on the FHL tendon at the level of ST,

MKH and IP. FHL tendon was cut at its insertion. *Ex vivo* length was measured from MTJ to those three points on FHL tendon by using a measuring tape (Butterfly® 0–150 cm; range 150 cm, resolution 1 mm) (Fig. 4B).

Each parameter was measured twice. The same digital Vernier calliper and measuring tape were used to ensure the consistency. All measurements were done by the same investigator.

Statistical analysis

Statistical analysis was performed by SPSS software version 22.0. All data from measurements were statistically analysed to demonstrate range, mean and standard deviation. To compare between genders, unpaired t-test (for parametric test) or Mann-Whitney U test (for nonparametric test) was used. The difference between *in situ* and *ex vivo* tendon length was examined with paired t-test (for parametric test) or Wilcoxon signed-rank test (for nonparametric test). A p-value of less than 0.05 was statistically significant. Pearson correlation test was used to assess the associative relationship between the foot length and the tendon length.

Ethical consideration

This cadaveric study has been approved by the Institutional Review Board (IRB) of the Faculty of Medicine, Chulalongkorn University (IRB No. 636/62).

RESULTS

Foot length

Results and analyses of the foot length are illustrated in Table 1. The mean length of foot in male and female was 246.50 ± 12.02 mm and 224.64 ± 11.63 mm, respectively. A statistically significant difference was found between genders in both sides.

Surface landmark and location of MKH

Master knot of Henry location and surface landmark results and analyses are shown on Tables 2 and 3. The location of MKH was identified at 117.11 ± 1.00 mm proximal to IP, 26.28 ± 4.75 mm under NT and 59.58 ± 7.51 mm distal to MM. A statistically significant difference between genders was observed in MKH-IP of both sides and MKH-NT on right side.

Point A could be resided anterior to NT (66.1%), at NT (27.4%) and posterior to NT (6.5%) (Table 3). The mean length of MC-NT and MC-A line were 107.36 ± 8.60 and 101.72 ± 12.01 mm, respectively. Point A was located at $94.75 \pm 8.43\%$ of MC-NT line from

Table 1. The mean foot length in male and female

Gender	Foot length [mm] — mean ± standard deviation (minimum-maximum)			P
	Left	Right	Total	
Male	N = 9 246.44 ± 12.22 (225.00–268.00)	N = 9 246.56 ± 12.54 (228.00–270.00)	N = 18 246.50 ± 12.02 (225.00–270.00)	0.937
Female	N = 22 223.77 ± 12.18 (200.00–250.00)	N = 22 225.50 ± 11.27 (203.00–248.00)	N = 44 224.64 ± 11.63 (200.00–250.00)	0.026
Total	N = 31 230.35 ± 15.91 (20.00–26.80)	N = 31 231.61 ± 15.01 (203.00–270.00)	N = 62 230.98 ± 15.35 (200.00–270.00)	–
P	0.00	0.00	–	

Table 2. Location of MKH from IP, NT and MM, surface landmark of MKH, distances between MKH and NVB, location of MKH in term of percentage of the length of MC-NT line

Parameters	Male — mean ± standard deviation (minimum-maximum)			Female — mean ± standard deviation (minimum-maximum)			Total
	Left	Right	Total	Left	Right	Total	
Location of MKH [mm]:							
MKH-IP	124.69 ± 9.04 (106.56–137.88)	126.39 ± 12.39 (110.24–151.27)	125.54 ± 10.55 (106.56–151.27)	113.30 ± 8.11 (93.14–129.50)	114.03 ± 6.95 (100.27–128.20)	113.66 ± 7.47 (93.14–129.50)	117.11 ± 1.00 (93.14–151.27)
MKH-NT	29.45 ± 7.06 (21.38–40.91)	27.88 ± 4.15 (19.53–33.16)	28.67 ± 5.68 (19.53–40.91)	26.21 ± 3.51 (17.93–33.73)	24.40 ± 4.32 (18.30–35.87)	25.31 ± 3.99 (17.93–35.87)	26.28 ± 4.75 (17.93–40.91)
MKH-MM	63.32 ± 9.80 (47.02–78.71)	60.02 ± 11.02 (34.59–75.27)	61.67 ± 10.26 (34.59–78.71)	60.36 ± 6.49 (48.91–78.07)	57.10 ± 5.06 (44.43–67.05)	58.72 ± 5.98 (44.43–78.07)	59.58 ± 7.51 (34.59–78.71)
Surface landmark of MKH [mm]:							
MC-NT	113.11 ± 10.21 (91.75–124.12)	113.13 ± 7.44 (101.49–122.19)	113.12 ± 8.67 (91.75–123.37)	102.57 ± 8.09 (87.18–116.74)	107.45 ± 6.01 (97.26–117.65)	105.01 ± 7.46 (87.18–117.65)	107.36 ± 8.60 (87.18–124.12)
MKH-A	29.10 ± 8.83 (19.39–41.85)	27.89 ± 4.86 (25.11–35.53)	28.49 ± 6.94 (19.39–41.85)	24.18 ± 3.33 (17.26–32.27)	23.26 ± 4.39 (16.89–34.15)	23.72 ± 3.88 (16.89–34.15)	25.11 ± 5.37 (16.89–41.85)
MC-A	111.59 ± 11.01 (90.62–126.71)	110.87 ± 15.39 (87.26–139.77)	111.23 ± 12.99 (87.26–139.77)	95.92 ± 10.55 (76.05–116.74)	99.75 ± 7.40 (86.91–115.63)	97.83 ± 9.21 (76.05–116.74)	101.72 ± 12.01 (76.05–139.77)
Distance between MKH and NVB [mm]:							
MKH-LPNVB	17.98 ± 6.09 (9.59–30.29)	19.91 ± 5.32 (13.05–28.85)	18.94 ± 5.64 (9.59–30.29)	15.17 ± 3.84 (8.44–22.05)	17.61 ± 3.56 (7.11–24.38)	16.39 ± 3.86 (7.11–24.38)	17.13 ± 3.55 (7.11–30.29)
MKH-MPNVB	0	0	0	0	0	0	0
Location of MKH in term of percentage of MC-NT length (%)	98.84 ± 7.77 (87.77–110.28)	98.34 ± 15.90 (82.21–137.72)	98.56 ± 11.98 (82.21–137.72)	93.47 ± 6.36 (75.83–107.16)	92.89 ± 5.65 (79.82–100.00)	93.18 ± 5.95 (75.83–107.16)	94.75 ± 8.43 (75.83–137.72)

A — perpendicular point of MKH on MC-NT line; IP — first interphalangeal joint of great toe; LPNVB — lateral plantar neurovascular bundles; MC — medial end of plantar flexion crease at the base of great toes; MKH — master knot of Henry; MM — medial malleolus; MPNVB — medial plantar neurovascular bundles; NT — navicular tuberosity

MC (Table 2). The mean perpendicular length from MKH to A (MKH-A) was 25.11 ± 5.37 mm (Table 2). A statistically significant difference between genders was present in MC-A on both sides and MKH-A on right side.

Relationship between MKH and plantar neurovascular bundle

The MPNVB lied very closely to MKH in all cases; therefore, no distance could be measured. In contrast,

a mean distance of 17.13 ± 3.55 mm was observed between LPNVB and MKH without a statistically significant difference between genders (Table 2).

Length of FHL tendon

The mean *in situ* and *ex vivo* length of FHL tendon graft, harvested by three different incision techniques, are shown on Table 4. A statistically significant difference was found between genders in MTJ-IP of *in situ* and *ex vivo* length of both sides ($p < 0.05$). The

Table 3. Prevalence of master knot of Henry (MKH) location on MC-NT line

Location of MKH	Male			Female			Total (n = 62)
	Left (n = 9)	Right (n = 9)	Total (n = 18)	Left (n = 22)	Right (n = 22)	Total (n = 44)	
At NT	4 (44.4%)	3 (33.3%)	7 (38.9%)	4 (18.2%)	6 (27.3%)	10 (22.7%)	17 (27.4%)
Anterior to NT	3 (33.33%)	5 (55.6%)	8 (44.4%)	17 (77.3%)	16 (72.7%)	33 (75.0%)	41 (66.1%)
Posterior to NT	2 (22.22%)	1 (11.1%)	3 (16.7%)	1 (4.5%)	0 (0%)	1 (2.3%)	4 (6.5%)

MC — medial end of plantar flexion crease at the base of great toes; MM — medial malleolus; NT — navicular tuberosity

Table 4. *In situ* and *ex vivo* length of harvested flexor hallucis longus tendon from single incision (MTJ-ST), double incision (MTJ-MKH) and minimally invasive techniques (MTJ-IP)

Techniques	Genders						Total (n = 62)
	Male — mean ± standard deviation (minimum–maximum)			Female — mean ± standard deviation (minimum–maximum)			
	Left (n = 9)	Right (n = 9)	Total (n = 18)	Left (n = 22)	Right (n = 22)	Total (n = 44)	
<i>In situ</i> length:							
MTJ-ST	43.22 ± 12.14 (21.00–60.00)	41.56 ± 8.35 (30.00–55.00)	42.39 ± 10.15 (21.00–60.00)	37.50 ± 10.15 (15.00–62.00)	37.86 ± 12.01 (19.00–71.00)	37.68 ± 11.00 (15.00–71.00)	39.05 ± 10.88 (15.00–71.00)
MTJ-MKH	76.78 ± 9.55 (67.00–95.00)	75.78 ± 10.19 (60.00–91.00)	76.28 ± 9.60 (60.00–95.00)	71.00 ± 8.09 (59.00–92.00)	73.59 ± 11.51 (54.00–95.00)	72.29 ± 9.92 (54.00–95.00)	73.45 ± 9.91 (54.00–95.00)
MTJ-IP	209.44 ± 17.67 (181.00–240.00)	209.56 ± 15.32 (188.00–240.00)	209.50 ± 16.00 (181.00–240.00)	192.22 ± 9.12 (174.00–215.00)	194.32 ± 10.33 (179.00–215.00)	193.27 ± 9.68 (174.00–215.00)	197.98 ± 13.89 (174.00–240.00)
<i>Ex vivo</i> length:							
MTJ-ST	38.33 ± 10.22 (19.00–50.00)	36.67 ± 7.36 (25.00–46.00)	37.50 ± 8.68 (19.00–50.00)	33.00 ± 10.64 (11.00–57.00)	33.36 ± 10.88 (15.00–58.00)	33.18 ± 10.63 (11.00–58.00)	34.43 ± 10.23 (11.00–58.00)
MTJ-MKH	71.67 ± 8.90 (64.00–90.00)	70.44 ± 9.36 (57.00–87.00)	71.06 ± 8.88 (57.00–90.00)	66.45 ± 8.73 (54.00–89.00)	68.82 ± 10.40 (51.00–84.00)	67.64 ± 9.56 (51.00–89.00)	68.63 ± 9.43 (51.00–90.00)
MTJ-IP	203.56 ± 18.77 (174.00–236.00)	203.78 ± 14.94 (184.00–235.00)	203.67 ± 16.46 (174.00–236.00)	186.36 ± 9.21 (167.00–209.00)	187.50 ± 9.69 (173.00–205.00)	186.93 ± 9.36 (167.00–209.00)	191.79 ± 14.00 (167.00–236.00)

IP — first interphalangeal joint of great toe; MKH — master knot of Henry; MTJ — musculotendinous junction; NT — navicular tuberosity; ST — sustentaculum tali

Table 5. Length of harvested flexor hallucis longus tendon in term of percentage of the foot length

Techniques	Genders						Total (n = 62)
	Male — mean ± standard deviation (minimum–maximum)			Female — mean ± standard deviation (minimum–maximum)			
	Left (n = 9)	Right (n = 9)	Total (n = 18)	Left (n = 22)	Right (n = 22)	Total (n = 44)	
<i>In situ</i> length:							
MTJ-ST	17.45 ± 4.64 (9.33–24.29)	16.84 ± 3.27 (12.24–22.82)	17.14 ± 3.90 (9.33–24.29)	16.84 ± 4.72 (6.38–28.84)	16.92 ± 5.77 (8.19–33.81)	16.88 ± 5.21 (6.38–33.81)	16.96 ± 4.84 (6.38–33.81)
MTJ-MKH	31.18 ± 3.69 (27.31–35.56)	30.76 ± 2.91 (26.15–36.93)	30.97 ± 3.79 (26.15–36.93)	31.81 ± 3.89 (25.11–39.07)	32.70 ± 5.36 (23.40–45.24)	32.26 ± 4.65 (23.40–45.24)	31.88 ± 4.43 (23.40–45.24)
MTJ-IP	84.89 ± 3.89 (74.58–88.06)	84.97 ± 3.90 (80.77–93.36)	84.93 ± 3.78 (78.75–93.36)	86.02 ± 3.91 (75.74–92.09)	85.83 ± 3.51 (79.91–93.75)	85.92 ± 3.67 (75.74–93.75)	85.63 ± 3.70 (75.74–93.75)
<i>Ex vivo</i> length:							
MTJ-ST	15.47 ± 3.85 (8.44–20.24)	14.87 ± 2.91 (12.24–18.67)	15.17 ± 3.33 (8.44–20.24)	14.83 ± 4.91 (4.78–26.51)	14.91 ± 5.15 (6.47–27.62)	14.87 ± 4.97 (4.78–27.62)	14.96 ± 4.53 (4.78–27.62)
MTJ-MKH	29.09 ± 3.31 (25.77–33.58)	28.59 ± 3.70 (24.23–34.80)	28.84 ± 3.41 (24.23–34.80)	29.77 ± 4.07 (23.20–37.21)	30.57 ± 4.78 (23.18–40.00)	32.26 ± 4.65 (23.18–40.00)	29.79 ± 4.16 (23.18–40.00)
MTJ-IP	82.48 ± 4.49 (74.58–88.06)	82.61 ± 3.34 (79.62–89.21)	82.55 ± 3.84 (74.58–89.21)	83.38 ± 3.71 (74.89–90.23)	83.38 ± 3.71 (74.89–90.23)	83.31 ± 3.95 (74.89–94.76)	83.09 ± 3.90 (74.58–94.76)

IP — first interphalangeal joint of great toe; MKH — master knot of Henry; MTJ — musculotendinous junction; NT — navicular tuberosity; ST — sustentaculum tali

mean length of tendon between *in situ* and *ex vivo* was significantly different in all techniques ($p < 0.05$). Moreover, a moderate positive correlation between foot length and tendon length was found in MTJ-IP of both *in situ* and *ex vivo* tendon length ($r = 0.52$ and 0.56 , respectively).

The length of FHL tendon was calculated in term of percentage of foot length as shown in Table 5. *In situ* and *ex vivo* tendon lengths were 16.96 ± 4.84 and $14.96 \pm 4.53\%$, 31.88 ± 4.43 and $29.79 \pm 4.16\%$, 85.63 ± 3.70 and $83.09 \pm 3.90\%$ of foot length in single incision, double incision, and minimally invasive techniques, respectively.

DISCUSSION

Achilles tendinopathy is a painful condition that can occur in both active and inactive people [11]. Despite of noninvasive treatments such as physical therapy, orthotics and drugs, surgical intervention might be necessary when clinical outcome remained disappointing [6, 12]. FHL tendon is a common tendon used in the augmentation of the Achilles tendon because it is easy to harvest and provides good to excellent functional outcomes and pain relief regardless of the technique used to harvest the tendon [4, 6, 29].

The shape and morphology of the foot vary among ethnicities, genders, and individuals [10, 15, 21, 24, 31]. Foot length was used in this study to anticipate anatomical data which is significant for FHL tendon transfer. Asian foot length is shorter than that of North American and European. In Asians, the most frequent length was 255 mm for male and 235 mm for female [9]. In this study, the mean foot lengths were 246 mm and 225 mm in male and female respectively. A significant difference between genders was found similar to the previous reports [3, 22].

Master knot of Henry has been widely utilized as a surgical landmark for the FHL tendon graft harvesting especially in double incision technique [2]. The first IP joint and NT were used to localize MKH by Mao et al. [13], in Asian embalmed cadavers. Moreover, Beger et al. [2] and Vasudha et al. [28] further investigated the precise location of the MKH from MM, NT and first IP joint in Turkish and Indian formalin fixed cadavers, respectively. According to the results of this study, the location of MKH resided proximal to the first IP joint, inferior to NT and distal to MM which resembled findings of previous reports (Table 6) [2, 28].

Although there were several reports about the location of the MKH, they did not take surface landmarks for localizing MKH into account. Medial end of plantar flexion crease at the base of great toe (MC) and navicular tuberosity (NT), which could be clearly identified and palpated, were used to determine the surface localization of MKH in this study. For accuracy and easy application in clinical practice, MC-NT line and A which is the perpendicular point of MKH on MC-NT line were defined. Approximately, MKH located at 95% of MC-NT line from MC with a perpendicular distance of 25 mm from MC-NT line. However, our results revealed that point A could be located anterior, posterior and at the NT on MC-NT line. Nevertheless, MKH was located posterior to NT in only 6.5% of cases.

Medial and lateral plantar nerves (MPN and LPN) are the branches of posterior tibial nerve which supply skin and intrinsic muscle of the sole. Anatomically, MPN travels along the plantar surface of FDL tendon and passes through MKH [16]. LPN passes obliquely between flexor digitorum brevis and quadratus plantae to the lateral side of the foot. The anatomical relationship between plantar nerves and MKH was reported by Mao et al. [14] in embalmed cadavers. They found a mean distance of 5.26 mm between MPN and MKH, and 15.50 mm between LPN and MKH which was different from the result of this study. In all specimens of this study, there was no distance between MPNVB and MKH and a longer distance of 17.13 ± 3.55 mm was observed between LPNVB and MKH. This might be due to the different methods of cadaveric fixation. In embalmed cadaver, most tissues are rigid and joints cannot be moved freely which may affect the location of anatomical structures [23]. The proximity of MKH and MPNVB might lead to neurovascular bundle injury. The injuries of the distal branches of the posterior tibial nerve and artery were reported previously [7, 13, 14, 18]. The transection of tendon that was performed near MKH in double incision technique may cause MPN or LPN injury [13]. In the literature, it was hypothesized that difficult harvesting might be the cause of nerve injury [16]. Nerve injury might be partial but not significant enough to cause clinical symptoms and long periods of casting after surgery could prohibit the detection of symptoms [16]. Nevertheless, caution is required to preserve this neurovascular bundle especially when distal transection is performed blindly [25, 27]. More-

Table 6. Comparison of the distances from master knot of Henry (MKH) to anatomical landmarks and *in situ* flexor hallucis longus tendon length

	This study, 2020	Vasudha et al., 2019 [28]	Beger et al., 2018 [2]	Mao et al., 2015 [13]	Tashjian et al., 2003 [27]
Ethnic	Thai	Indian	Turkish	Asian	United States
Cadaveric type	Soft	Formalin fixed	Formalin fixed	Embalmed	Fresh frozen
Number of specimen	62	L: 36; R: 36	20	64	14
Distances from MKH to landmarks [cm]:					
MM	5.96 ± 0.75 (3.46–7.87)	L: 6.07 ± 1.25 (4.03–9.00) R: 6.10 ± 1.17 (4.26–8.50)	5.93 ± 0.74 (4.72–7.35)	–	–
NT	2.63 ± 0.48 (1.79–4.09)	L: 2.99 ± 0.96 (1.50–5.50) R: 3.24 ± 0.93 (1.64–5.00)	1.75 ± 0.39 (1.11–2.44)	2.21 ± 0.34 (1.59–3.04)	–
IP	11.71 ± 1.00 (9.31–15.13)	L: 11.97 ± 1.11 (9.32–14.2) R: 12.50 ± 0.89 (9.77–14.46)	12.61 ± 1.11 (10.33–14.09)	10.89 ± 1.08 (13.04–9.22)	–
Tendon length [cm]:					
Single incision technique	3.90 ± 1.09 (1.50–7.10)	–	5.75 ± 0.63 (4.52–6.86)	5.08 ± 1.09 (3.32–10.35)	5.16 ± 1.29 (3.4–6.9)
Double incision technique	7.34 ± 0.99 (5.40–9.50)	–	7.03 ± 0.86 (5.77–8.80)	6.72 ± 1.02 (4.69–12.09)	8.09 ± 1.63 (5.1–11.1)
Minimally invasive technique	19.80 ± 1.39 (17.40–24.00)	–	20.22 ± 1.32 (16.82–21.97)	17.49 ± 1.80 (13.51–20.52)	–

IP — first interphalangeal joint of great toe; L — left; MM — medial malleolus; NT — navicular tuberosity; R — right

over, tendon disease in the region of MKH may lead to the entrapment of MPN [5].

In this study, the length of tendon graft with three different incision techniques (single incision, double incision and minimally invasive technique) was quantified. Previous researches reported that the *in situ* length of harvested FHL tendon were different between techniques (Table 6) [2, 13, 27]. The length of tendon graft from single incision technique in this study was shorter than previous studies. In double incision technique, our result was longer when compared to those of Mao et al. [13] and Beger et al. [2], but shorter than that of Tashjian et al. [27]. Furthermore, the length of tendon graft from minimally invasive technique was found to be longer when compares with Mao et al. [13]. Nevertheless, it was shorter than the mean length from Beger et al. [2]. These differences might be caused by the different ethnic backgrounds, cadaveric preservation technique and position of foot and ankle during measurement.

Ex vivo length of tendon graft has never been reported previously. *Ex vivo* length refers to the length of tendon after it is cut from the insertion point,

which may be more similar to the length of harvested tendon for transfer. Our results revealed significant differences between *in situ* and *ex vivo* length of tendon from all techniques. *Ex vivo* tendon length was shorter than *in situ* tendon length by about 4.5 mm in single incision and double incision techniques and 6.0 mm in minimally invasive technique. The shorter tendon might result from loss of tension after it was cut from the insertion site in the foot. The correlation between tendon length and foot length was analysed for clinical benefit. Our results showed a moderate positive correlation between them. The lengths of harvested tendon from single incision, double incision and minimally invasive technique were about 15%, 30%, and 85% of foot length, respectively. Thus, it might be possible to estimate the length of harvested tendon from the foot length.

This study offers some benefits as it identifies the precise surface location of MKH which will make it easier to identify the incision site and improve the clinical efficacy of the surgery. Understanding the relation between MKH and neurovascular bundle can assist the clinician to avoid iatrogenic injury. The *in*

situ and *ex vivo* length of FHL tendon could guide surgeons to designs personalized operation techniques that are appropriate for each patient. Therefore, the knowledge of this investigation can enhance the clinical efficacy of foot and ankle surgery and help minimize potential complications.

CONCLUSIONS

Master knot of Henry resides distal to MM, under NT and proximal to IP with MPNVB residing closely to MKH. Surface localisation of MKH can be located at 95% of MC-NT line from MC with a perpendicular distance of 25 mm from MC-NT line. The *ex vivo* lengths of tendon graft in all techniques were significantly shorter than *in situ* length. Foot length, MKH-IP, MKH-NT, MC-A, MKH-A and the lengths of FHL tendon graft from minimally invasive technique had statistically significant differences between genders.

Acknowledgements




This study was supported by the 100th Anniversary Chulalongkorn University Fund for Doctoral Scholarship. The authors would like to thank and offer sincere gratitude to all those who have donated their bodies for research. Authors would like to thank Dr. Jiran Apinun from Department of Orthopaedics for providing clinical information. Special thanks are extended to the technical staffs of the Chula Soft Cadaver Surgical Training Centre, Department of Anatomy, Faculty of Medicine, Chulalongkorn University for their support in cadaveric care.

REFERENCES

- Alhaug OK, Berdal G, Husebye EE, et al. Flexor hallucis longus tendon transfer for chronic Achilles tendon rupture. A retrospective study. *Foot Ankle Surg.* 2019; 25(5): 630–635, doi: [10.1016/j.fas.2018.07.002](https://doi.org/10.1016/j.fas.2018.07.002), indexed in Pubmed: [30321934](https://pubmed.ncbi.nlm.nih.gov/30321934/).
- Beger O, Elvan Ö, Keskinbora M, et al. Anatomy of Master Knot of Henry: A morphometric study on cadavers. *Acta Orthop Traumatol Turc.* 2018; 52(2): 134–142, doi: [10.1016/j.aott.2018.01.001](https://doi.org/10.1016/j.aott.2018.01.001), indexed in Pubmed: [29366540](https://pubmed.ncbi.nlm.nih.gov/29366540/).
- Chaiwanichsiri D, Tantisriwat N, Janchai S. Proper shoe sizes for Thai elderly. *Foot (Edinb).* 2008; 18(4): 186–191, doi: [10.1016/j.foot.2008.05.001](https://doi.org/10.1016/j.foot.2008.05.001), indexed in Pubmed: [20307435](https://pubmed.ncbi.nlm.nih.gov/20307435/).
- Coughlin MJ, Saltzman CL, Anderson RB. *Mann's surgery of the foot and ankle.* 9th ed. Elsevier Inc., Philadelphia 2014: 1617–1620.
- Donovan A, Rosenberg ZS, Bencardino JT, et al. Plantar tendons of the foot: MR imaging and US. *Radiographics.* 2013; 33(7): 2065–2085, doi: [10.1148/rg.337125167](https://doi.org/10.1148/rg.337125167), indexed in Pubmed: [24224599](https://pubmed.ncbi.nlm.nih.gov/24224599/).
- Hahn F, Meyer P, Maiwald C, et al. Treatment of chronic achilles tendinopathy and ruptures with flexor hallucis tendon transfer: clinical outcome and MRI findings. *Foot Ankle Int.* 2008; 29(8): 794–802, doi: [10.3113/FAI.2008.0794](https://doi.org/10.3113/FAI.2008.0794), indexed in Pubmed: [18752777](https://pubmed.ncbi.nlm.nih.gov/18752777/).
- Herbst SA, Miller SD. Transection of the medial plantar nerve and hallux cock-up deformity after flexor hallucis longus tendon transfer for Achilles tendinitis: case report. *Foot Ankle Int.* 2006; 27(8): 639–641, doi: [10.1177/107110070602700814](https://doi.org/10.1177/107110070602700814), indexed in Pubmed: [16919220](https://pubmed.ncbi.nlm.nih.gov/16919220/).
- Hockenbury R, Sammarco G. Medial sliding calcaneal osteotomy with flexor hallucis longus transfer for the treatment of posterior tibial tendon insufficiency. *Foot and Ankle Clinics.* 2001; 6(3): 569–581, doi: [10.1016/s1083-7515\(03\)00114-1](https://doi.org/10.1016/s1083-7515(03)00114-1).
- Jurca A, Žabkar J, Džeroski S. Analysis of 1.2 million foot scans from North America, Europe and Asia. *Sci Rep.* 2019; 9(1): 19155, doi: [10.1038/s41598-019-55432-z](https://doi.org/10.1038/s41598-019-55432-z), indexed in Pubmed: [31844106](https://pubmed.ncbi.nlm.nih.gov/31844106/).
- Kouchi M. Foot dimensions and foot shape: differences due to growth, generation and ethnic origin. *Anthropol Sci.* 1998; 106(Suppl.): 161–188, doi: [10.1537/ase.106.supplement_161](https://doi.org/10.1537/ase.106.supplement_161).
- Lake JE, Ishikawa SN. Conservative treatment of Achilles tendinopathy: emerging techniques. *Foot Ankle Clin.* 2009; 14(4): 663–674, doi: [10.1016/j.fcl.2009.07.003](https://doi.org/10.1016/j.fcl.2009.07.003), indexed in Pubmed: [19857840](https://pubmed.ncbi.nlm.nih.gov/19857840/).
- Lopez RG, Jung HG. Achilles tendinosis: treatment options. *Clin Orthop Surg.* 2015; 7(1): 1–7, doi: [10.4055/cios.2015.7.1.1](https://doi.org/10.4055/cios.2015.7.1.1), indexed in Pubmed: [25729512](https://pubmed.ncbi.nlm.nih.gov/25729512/).
- Mao H, Shi Z, Wapner KL, et al. Anatomical study for flexor hallucis longus tendon transfer in treatment of Achilles tendinopathy. *Surg Radiol Anat.* 2015; 37(6): 639–647, doi: [10.1007/s00276-014-1399-y](https://doi.org/10.1007/s00276-014-1399-y), indexed in Pubmed: [25542244](https://pubmed.ncbi.nlm.nih.gov/25542244/).
- Mao H, Dong W, Shi Z, et al. Anatomical study of the neurovascular in flexor hallucis longus tendon transfers. *Sci Rep.* 2017; 7(1): 14202, doi: [10.1038/s41598-017-13742-0](https://doi.org/10.1038/s41598-017-13742-0), indexed in Pubmed: [29079740](https://pubmed.ncbi.nlm.nih.gov/29079740/).
- Mauch M, Grau S, Krauss I, et al. A new approach to children's footwear based on foot type classification. *Ergonomics.* 2009; 52(8): 999–1008, doi: [10.1080/00140130902803549](https://doi.org/10.1080/00140130902803549), indexed in Pubmed: [19629814](https://pubmed.ncbi.nlm.nih.gov/19629814/).
- Mulier T, Rummens E, Dereymaeker G. Risk of neurovascular injuries in flexor hallucis longus tendon transfers: an anatomic cadaver study. *Foot Ankle Int.* 2007; 28(8): 910–915, doi: [10.3113/FAI.2007.0910](https://doi.org/10.3113/FAI.2007.0910), indexed in Pubmed: [17697656](https://pubmed.ncbi.nlm.nih.gov/17697656/).
- Murphy RL, Womack JW, Anderson T. Technique tip: a new technique for harvest of the flexor hallucis longus tendon. *Foot Ankle Int.* 2010; 31(5): 457–459, doi: [10.3113/FAI.2010.0457](https://doi.org/10.3113/FAI.2010.0457), indexed in Pubmed: [20460076](https://pubmed.ncbi.nlm.nih.gov/20460076/).
- Myerson MS, Corrigan J. Treatment of posterior tibial tendon dysfunction with flexor digitorum longus tendon transfer and calcaneal osteotomy. *Orthopedics.* 1996; 19(5): 383–388, indexed in Pubmed: [8727331](https://pubmed.ncbi.nlm.nih.gov/8727331/).
- O'Sullivan E, Carare-Nnadi R, Greenslade J, et al. Clinical significance of variations in the interconnections between

- flexor digitorum longus and flexor hallucis longus in the region of the knot of Henry. *Clin Anat.* 2005; 18(2): 121–125, doi: [10.1002/ca.20029](https://doi.org/10.1002/ca.20029), indexed in Pubmed: [15696523](https://pubmed.ncbi.nlm.nih.gov/15696523/).
20. Pichler W, Tesch NP, Grechenig W, et al. Anatomical variations of the flexor hallucis longus muscle and the consequences for tendon transfer. A cadaver study. *Surg Radiol Anat.* 2005; 27(3): 227–231, doi: [10.1007/s00276-005-0314-y](https://doi.org/10.1007/s00276-005-0314-y), indexed in Pubmed: [15789138](https://pubmed.ncbi.nlm.nih.gov/15789138/).
 21. Razeghi M, Batt M. Foot type classification: a critical review of current methods. *Gait Posture.* 2002; 15(3): 282–291, doi: [10.1016/s0966-6362\(01\)00151-5](https://doi.org/10.1016/s0966-6362(01)00151-5), indexed in Pubmed: [11983503](https://pubmed.ncbi.nlm.nih.gov/11983503/).
 22. Romphothonga M, Traithepchanapai P. Sex determination through anthropometry of hand and foot in Thais. *Chula Med J.* 2019; 63(1): 47–55, doi: [10.14456/clmj.1476.9](https://doi.org/10.14456/clmj.1476.9).
 23. Sangchay N. The soft cadaver (thiel's method): the new type of cadaver of department of anatomy, siriraj hospital. *Siriraj Med J.* 2014; 66(Suppl): S228–S231.
 24. Shu Y, Mei Q, Fernandez J, et al. Foot morphological difference between habitually shod and unshod runners. *PLoS One.* 2015; 10(7): e0131385, doi: [10.1371/journal.pone.0131385](https://doi.org/10.1371/journal.pone.0131385), indexed in Pubmed: [26148059](https://pubmed.ncbi.nlm.nih.gov/26148059/).
 25. Sigvard T, Hansen J. Functional reconstruction of the foot and ankle. Lippincott Williams & Wilkins, a Wolters Kluwer Business, Philadelphia 2000: 422–429.
 26. Suttinark P, Suebpongsiri P. Clinical outcomes of flexor hallucis longus transfer for the treatment of Achilles tendinosis rupture. *J Med Assoc Thai.* 2009; 92 Suppl 6: S226–S231, indexed in Pubmed: [20120691](https://pubmed.ncbi.nlm.nih.gov/20120691/).
 27. Tashjian RZ, Hur J, Sullivan RJ, et al. Flexor hallucis longus transfer for repair of chronic achilles tendinopathy. *Foot Ankle Int.* 2003; 24(9): 673–676, doi: [10.1177/107110070302400903](https://doi.org/10.1177/107110070302400903), indexed in Pubmed: [14524515](https://pubmed.ncbi.nlm.nih.gov/14524515/).
 28. Vasudha TK, Vani PC, Sankaranarayanan G, et al. Communications between the tendons of flexor hallucis longus and flexor digitorum longus: a cadaveric study. *Surg Radiol Anat.* 2019; 41(12): 1411–1419, doi: [10.1007/s00276-019-02311-x](https://doi.org/10.1007/s00276-019-02311-x), indexed in Pubmed: [31541272](https://pubmed.ncbi.nlm.nih.gov/31541272/).
 29. Wapner KL, Pavlock GS, Hecht PJ, et al. Repair of chronic Achilles tendon rupture with flexor hallucis longus tendon transfer. *Foot Ankle.* 1993; 14(8): 443–449, doi: [10.1177/107110079301400803](https://doi.org/10.1177/107110079301400803), indexed in Pubmed: [8253436](https://pubmed.ncbi.nlm.nih.gov/8253436/).
 30. Williams D, McClay I. Measurements used to characterize the foot and the medial longitudinal arch: reliability and validity. *Physl Ther.* 2000; 80(9): 864–871, doi: [10.1093/ptj/80.9.864](https://doi.org/10.1093/ptj/80.9.864).
 31. Wong CK, Weil R, de Boer E. Standardizing foot-type classification using arch index values. *Physiother Can.* 2012; 64(3): 280–283, doi: [10.3138/ptc.2011-40](https://doi.org/10.3138/ptc.2011-40), indexed in Pubmed: [23729964](https://pubmed.ncbi.nlm.nih.gov/23729964/).
 32. Wulker N, Stephens MM, Cracchiolo A. An atlas of foot and ankle surgery. 2nd ed. Talor & Francis, London 2005: 377–386.

Evaluation of the relationship between the maxillary third molars and pterygomaxillary fissure by cephalometric radiographs

S. Sadry¹, C.G. Koca², I. Kaya²

¹DDS/PhD, Assistant Professor, Department of Orthodontics, Faculty of Dentistry, Istanbul Aydin University, Istanbul, Turkey

²DDS/PhD, Assistant Professor, Department of Oral and Maxillofacial Surgery, Faculty of Dentistry, Usak University, Usak, Turkey

[Received: 11 June 2020; Accepted: 27 July 2020]

Background: The aim of this study is to evaluate the relationship between the third molars which are determined to be closely related to pterygomaxillary fissure (PTM) in cephalometric radiographs.

Materials and methods: The material of this study was panoramic from 200 individuals (101 male, 99 female, mean age 19.02 ± 1.62) with three different skeletal malocclusion in the sagittal direction (class I: 109; class II: 66; class III: 25) and lateral cephalometric radiographs. It was observed that 151 of the patients included in this study had unilateral, 49 bilateral impacted maxillary third molars teeth. Angular and millimetric measurements (SNA° , SNB° , ANB° , PTM [Height-x], PTM [Width-y]) were made in accordance with the parameters determined on the lateral cephalometric radiographs of individuals. In this retrospective study, the relation of impaction with PTM evaluated on cephalometric radiographs, whether the impaction was unilateral or bilateral, was investigated in terms of skeletal anomaly. Chi-square test was used for the analysis.

Results: Of the 200 individuals with impacted maxillary third molar, 99 were female and 101 were male. There is no statistical difference between them in terms of unilateral and bilateral impacted third molars ($p > 0.05$). Of the 200 patients, 109 patients were class I, 66 patients were class II, and 25 patients were class III. There is no statistical difference between unilateral and bilateral impacted cases in facial skeletal classification ($p > 0.05$). According to chi-square test results, the relationship between genders and PTM variable width and height (PTM-x and PTM-y) measurements were not statistically significant ($p > 0.05$).

Conclusions: The fact that the third molar teeth are impacted bilaterally or unilaterally is not affected by PTM change. (Folia Morphol 2021; 80, 2: 425–431)

Key words: cephalometric radiography, maxillary third molar, pterygomaxillary fissure, panoramic radiograph

INTRODUCTION

Maxillary complex is affected by not only face components but also skull base and neurocranium [4]. The functional matrix hypothesis tries to explain the adaptation of skeletal tissues and organs during modification of craniofacial growth. According to this hypothesis, the two main units are skeletal structure and functional elements. Therefore, in the development of craniofacial skeletal structures, some adaptive responses can be influenced by functional components [16–18]. Functional components refer to soft tissues surrounding skeletal units, organs, and operational volumes that perform a given function [4, 7]. The interaction between the skeletal unit and functional matrices may also have an effect on the spaces between skeletal units such as the pterygopalatine fossa [11]. The pterygopalatine fossa is a space between the maxilla, palatine, and sphenoid bones [3, 25]. The pterygomaxillary fissure (PTM), on the other hand, forms the lateral boundary of the pterygopalatine fossa. In clinical terms, the PTM is in an important landmark for orthognathic surgical procedures such as Le Fort I osteotomy, and extraoral and intraoral maxillary nerve blockage [3, 11]. Furthermore, during surgically assisted rapid maxillary expansion, the PTM and the remaining posterior connection of the maxilla with the pterygoid process region can improve blood circulation and also provide symmetrical openings of the maxillary shelves [26].

With the influence of the development of the maxillary complex, differences in anatomical formations and structures can be observed in the maxillary complex. Especially with the maxillary deficiency, the progression of third molar teeth can also be affected.

The third molars are the teeth to become most frequently impacted. The most common reason for the third molar teeth to become impacted is the fact that they are the last teeth to erupt, which leaves them with insufficient space for eruption. Impacted teeth can cause pathologies such as tooth decay, root resorption, pericoronitis, pains of unknown origin, orthodontic and prosthetic problems, infections, odontogenic cysts and tumours [13, 14]. In cases of inadequate space on the dental arch, tooth eruption can be obstructed by the gingiva, bone or other adjacent teeth.

The relationship between the cranium and various anomalies has been previously studied [8, 10, 19]. The PTM seems to have an effect on both growth and

developmental stages of the face. In addition to this knowledge of the PTM morphology also seems to be essential during surgical procedures. Therefore, the aim of this study was to investigate the PTM length and possible correlation between maxillary third molars existence using cephalometric radiographs.

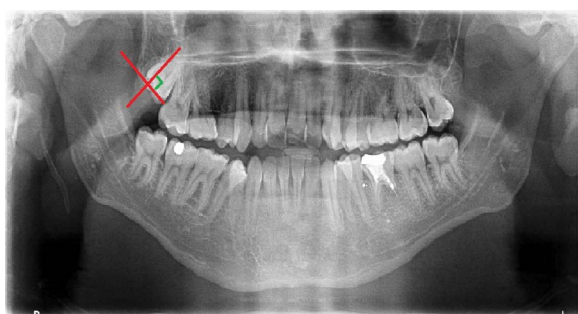
MATERIALS AND METHODS

The study conducted on the patients who were admitted to Istanbul Aydin University Faculty of Dentistry Department of Orthodontic to undergo orthodontic treatment. Ethical approval was obtained from Istanbul Aydin University Faculty of Dentistry "Ethics Committee on Non-Interventional Clinical Research-Research Not Involving Pharmaceuticals and Medical Devices" (Number: B.30.2AYD.0.00.00-50.06.04/67). The present study included 200 patients, 101 males and 99 females, between the ages of 19 and 39 (mean age 24.9), with the indications of impacted third molar dental surgery who were admitted to Istanbul Aydin University Faculty of Dentistry Department of Orthodontics from 2015–2018. The sample size was calculated based on a power analysis and 90% strength using G * Power Software version 3.1.9.2 (Universität Düsseldorf, Germany) for the sella turcica classification with an alpha error probability of 0.05. Power analysis showed that 134 samples were absolutely necessary. During the acquisition of lateral cephalometric radiographs, the patient's head was fixed on the cephalostat, and the Frankfort horizontal plane was adjusted parallel to the ground. Radiographs were taken with the central beam perpendicular to the patient's mid-axial plane and the teeth in centric occlusion. It was paid attention to see clearly the PTM. The individuals in the study were classified according to the ANB angle determined on the lateral cephalometric radiograph as class I, class II and class III in the sagittal direction, with the unilateral or bilateral impaction of the maxillary third molar teeth (Table 1). Skeleton classification was done according to ANB angle as shown in Table 1. It was paid attention to see clearly the PTM in lateral cephalometric films (Fig. 1). The width (W), depth (D) and interclenoid (I) determined by Costa et al. [6] with respect to the dimensions of sella turcica on each radiograph are shown in Figure 2. Patients with unilaterally and/or bilaterally impacted teeth, completed bone retention, with no local factors that would cause impaction, and with no missing teeth. The data from the patients

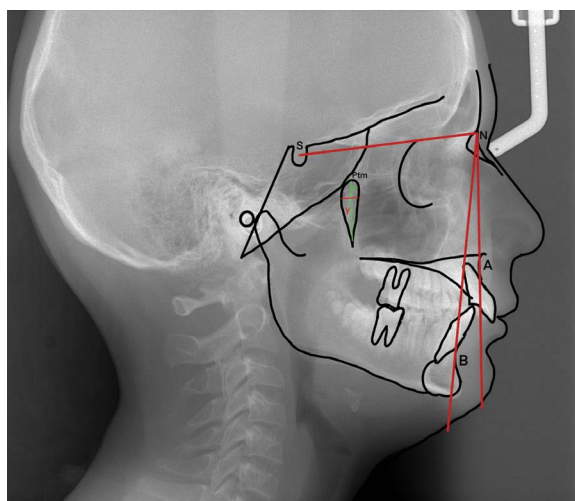
Table 1. Relationship of impacted molar with gender and facial skeletal classification

		Maxillary third molar teeth			P
		Unilateral impacted	Bilateral impacted	Total	
Gender	Female	80 (53.3%)	19 (38.7%)	99 (46.2%)	0.172; NS
	Male	71 (46.6%)	30 (61.2%)	101 (53.8%)	
Facial skeletal classification	Class I	81 (46.6%)	28 (50.1%)	109 (47.7%)	0.356; NS
	Class II	50 (41.6%)	16 (43.7%)	66 (42.8%)	
	Class III	20 (12.0%)	5 (6.2%)	25 (9.5%)	
Total		151 (100.0%)	49 (100.0%)	200 (100.0%)	

NS — not significant

**Figure 1.** Class III and class C groups according to Archer (1975) classification. In panoramic images, it is seen that two lines intersect at 90 degrees, parallel to the long axis and occlusal plane of the third molar tooth impacted in the maxillary.

under 18 years of age who had suffered a trauma or accident in the head and neck region, undergone previous surgery on the sinus or skull base, and suffer from any syndromes or congenital anomalies (cranio-cytosis, hemi-facial microstomy) were excluded from the study (Fig. 1). A clear visualisation of the PTM was ensured in lateral cephalometric images. All radiographs were taken using the same cephalometry device (Morita Veraviewpocs Dental X-ray 2D [Type: J. Morita, Kyoto, Japan]) with the Frankfort plane parallel to the ground, teeth in centric occlusion, and lips in resting position. Cephalometric radiographs were evaluated by the same researcher using the NemoCeph NX 9.0 software program (Nemotech, Imaging and Management Solutions, Chatsworth, Madrid, Spain) (Fig. 2). To evaluate the method error, 50 films were redrawn and measured again by the same researcher 2 weeks later. Paired t test was applied between the first and second measurements and no statistically significant difference was found between the two measurements. These results show that our drawings and measurements are repeatable.

**Figure 2.** Cephalometric angular measurements used in the research; SNA — the angle between the anterior skull base (S-N plane) and point A; SNB — it is the angle between the front head base (S-N plane) and point B; ANB — angle between NA and NB lines. Determines the relation of the apical bases of the lower and upper jaw relative to each other. According to Steiner analysis, its normal value is between 0 and 4 degrees; PTM-x [mm] — height of pterygomaxillary fissure; PTM-y [mm] — width of the pterygomaxillary fissure.

Statistical analysis

The data were evaluated in SPSS 21.0 (Statistical Package for Social Sciences, Chicago, Illinois, USA) statistical package programme. The analysis of the data was evaluated using the χ^2 test. The significance level was considered statistically significant for $p < 0.05$.

RESULTS

This study was performed on 249 maxillary third molar teeth in a total of 200 patients, 99 (49.5%) women and 101 (50.5%) men. Of the 200 patients included in the study, 49 had bilateral and 151 were

unilateral maxillary third molar teeth. According to the results of χ^2 analysis, the relationship between gender and molar variable was not statistically significant ($p > 0.05$). 53.3% of female had unilateral (unilateral) molar, 38.7% of female had bilateral (bilateral) maxillary molars. 46.6% of male had unilateral molar and 61.2% of male had bilateral molar. In both gender categories, unilateral molar status was found higher than bilateral molar status, so gender has no relation with molar status (Tables 1–3).

Since the variables are not normally distributed, the non-parametric test used in the comparison of two independent groups was used in the χ^2 test. According to the χ^2 test results, no variables were found statistically significant according to the molar status (Table 4). In the comparison of skeletal subgroups in facial skeletal classification, there was no statistically significant difference in the vertical and width distance (PTM-x, PTM-y) between the peak and the lower point of the PTM ($p > 0.05$) (Table 5). According to this test result, PTM variables did not differ by gender (Table 6).

DISCUSSION

The third molars are the most frequently impacted teeth. The most common reason of impaction of the third molars is to be last teeth and not enough space to continue. The hard placement of these teeth on the back of the tooth depends on the fact that the conditions of dentition and eruption as well as the distance and direction travelled during riding differ from other teeth. With the increasing need for orthodontic treatment, especially the need for orthodontic surgery, consensus is needed for the relationship of third molar with anatomical structures. This study was performed on lateral cephalographs from untreated patients. Again, in order to reduce errors in anatomical point definition, anatomical points were checked again by the same researcher. Anatomical points used in steiner analysis were marked on the lateral cephalographs obtained and related measurements were made. This analysis includes measurements that define dental and skeletal relationships that are important for orthodontists, and partially for oral and maxillofacial surgeons. The maxillary third molars are not included in the scope of orthodontic theory and complete the process of riding with a completely opposite movement. Impacted teeth; It is a common problem with a prevalence of 18–32%, affecting a large population in the world. In order

Table 2. Relationship of unilateral impacted molar with gender and facial skeletal classification

Facial skeletal classification	Unilateral impacted molar			P
	Female n (%)	Male n (%)	Total n (%)	
Class I	28 (35.0%)	30 (42.2%)	58 (38.4%)	0.451; NS
Class II	33 (41.2%)	24 (33.8%)	57 (37.7%)	
Class III	19 (23.7%)	17 (23.7%)	36 (23.8%)	
Total	80 (100.0%)	71 (100.0%)	129 (100.0%)	

n — number of individuals; NS — not significant

Table 3. Relationship of bilateral impacted molar with gender and facial skeletal classification

Facial skeletal classification	Bilateral impacted molar			P
	Female n (%)	Male n (%)	Total n (%)	
Class I	10 (52.6%)	15 (50.0%)	25 (51.0%)	0.448; NS
Class II	9 (47.3%)	12 (40.0%)	21 (42.8%)	
Class III	0 (0.0%)	3 (10.0%)	3 (6.8%)	
Total	19 (100.0%)	30 (100.0%)	71 (100.0%)	

n — number of individuals; NS — not significant

Table 4. Relationship of impacted molar and pterygomaxillary fissure

	Unilateral impacted molar — mean \pm SD	Bilateral impacted molar — mean \pm SD	P
PTM-x	25.18 \pm 3.24	25.2 \pm 3.2	0.420; NS
PTM-y	5.22 \pm 1.2	5.15 \pm 1.18	0.445; NS

PTM-x [mm] — height of pterygomaxillary fissure; PTM-y [mm] — width of the pterygomaxillary fissure; SD — standard deviation; NS — not significant

Table 5. Relationship of pterygomaxillary fissure and facial skeletal classification

	PTM-x — mean \pm SD	PTM-y — mean \pm SD	P
Class I	25.64 \pm 3.24	5.18 \pm 1.14	0.420; NS
Class II	25.55 \pm 3.2	5.1 \pm 1.1	0.330; NS
Class III	25.42 \pm 3.04	5.22 \pm 1.02	0.433; NS

PTM-x [mm] — height of pterygomaxillary fissure; PTM-y [mm] — width of the pterygomaxillary fissure; SD — standard deviation; NS — not significant

Table 6. Relationship of gender and pterygomaxillary fissure

	Female (n = 101) — mean \pm SD	Male (n = 99) — mean \pm SD	P
PTM-x	25.68 \pm 3.16	25.79 \pm 3.09	0.576; NS
PTM-y	5.19 \pm 1.03	5.21 \pm 1.02	0.258; NS

PTM-x [mm] — height of pterygomaxillary fissure; PTM-y [mm] — width of the pterygomaxillary fissure; SD — standard deviation; NS — not significant

to determine the appropriate treatment method of impacted teeth, to prevent complications that may occur during or after treatment, the positions of the impacted teeth in the jaw should be evaluated in detail with their adjacent anatomical structures.

Radiological evaluation plays an important role on the treatment plan [28]. Impacted teeth can cause pathologies such as pericoronitis, cystic lesions, tumours, periapical lesions and resorption in the adjacent tooth. For this reason, third molars must be removed when they are associated with pathological findings or for prophylactic reasons [2, 15, 20, 21]. For this reason, it is planned that the maxillary third molars will remain bilaterally or unilaterally, and the relationship between the base length of the maxilla and the anatomical structures will be examined. Therefore, the present study is a unique study that will bring a different perspective to the impaction pattern of the maxillary third molars. Since the known average impaction age of the third molars is 17 to 21, we set an age limit of 18 and found the mean age to be 24.9 for our study. There was no difference between the genders in our study. Tuğsel et al. [27] did not mention a difference in the distribution of impacted third molars between the genders in parallel with other information in the literature [13, 24]. In the study of Dural et al. [9], the incidence of impacted teeth was found to be higher in female than in male and it was statistically confirmed. According to the results of the χ^2 test used in comparing the two independent groups, age and PTM variables did not differ by gender. In the present study, it was observed that in the majority of the impacted maxillary third molars, the teeth were on the border of the PTM and no bone septa were observed between the PTM and third molars. According to this result, the vast majority of these teeth may be related to the development of the base length of the maxilla and it is likely that any complications occur during tooth extraction. As a result of cephalometric analysis in the present study, it is thought that the increase in anterior face height and PTM length measurement in female is characterised by an increase in the maxilla skeletal unit. In their three-dimensional cone-beam computed tomography studies, Costa et al. [6] recorded findings indicating no correlation between the anterior face height and maxillary posterior vertical alveoli, and thereby, PTM, which is in contradiction with our findings.

On the other hand, Rothstein and Yoon-Tarlie [23] found a statistically positive relationship between the anterior facial heights and the maxilla posterior heights of individuals in the age group of 10 and 12, similar to the results, in their longitudinal study. The reason for this is thought to be population differences. In the retrospective evaluation performed in our study, the relationship between the variables was determined by considering the differences in the lateral projection with anatomical structures in PTM, which was not previously evaluated in English or foreign literature. In the present study, no statistical difference was found in the evaluation of PTM variable according to gender, localisation and the condition of the third molars ($p > 0.05$). Rothstein and Yoon-Tarlie [23] determined the length of the PTM by measuring the distance from the deepest point of the buccal sulcus to the peak of the fissure. To know the difference in measurements between PTM lengths; in anaesthesia to be performed in the region, it is thought that paying attention to the penetration depth of the needle according to localisation is important in terms of ophthalmic or intracranial complications that may occur due to providing sufficient anaesthesia and advancing deeper than necessary. In the present study, a negative correlation was found between age and PTM variable. There was no statistically significant difference in terms of PTM variable in patients according to age groups ($p > 0.05$). Although the age progression causes changes in the fissure area, it suggests that the fissure does not cause macro changes in the overall morphology. Considering the results obtained by Albert et al. [1] in their studies, it was observed that the growth in both soft and hard tissues continued after adolescence. As a result of the reshaping of the alveolar bone in the craniofacial complex, PTM, which is located behind the tuber region, is also thought to be affected by these changes. However, as mentioned earlier, it is thought that it will not be appropriate to use this point orthodontically as a fixed reference [5, 12, 22].

CONCLUSIONS

In groups formed according to unilaterally or bilaterally impacted maxillary third molars, anatomical structures were found not to affect the impacted teeth rather than the significant differences. Regarding PTM in both genders, unilateral and bilateral impacted third molars were not found to differ

significantly between groups. It was also found that there were no significant differences between the groups of skeletal anomalies and embedded upper third molars with respect to PTM. It is thought that further studies should be supported by a larger number of patients.

Acknowledgements

The authors would like to thank Elif Eren for her valuable help with the cephalometric tracing.

Funding

The study was financially supported by the researcher and authors.

REFERENCES

- Albert AM, Ricanek K, Patterson E. A review of the literature on the aging adult skull and face: implications for forensic science research and applications. *Forensic Sci Int.* 2007; 172(1): 1–9, doi: [10.1016/j.forsciint.2007.03.015](https://doi.org/10.1016/j.forsciint.2007.03.015), indexed in Pubmed: [17434276](https://pubmed.ncbi.nlm.nih.gov/17434276/).
- Alling JJ, Helfrick JF, Alling RD. *Impacted teeth*. WB Saunders, Philadelphia 1993.
- Breeze J, Vereia Linares C, Stockton P. Is an osteotome necessary for pterygomaxillary dysjunction or dysjunction through the tuberosity during Le Fort I osteotomy? A systematic review. *Br J Oral Maxillofac Surg.* 2016; 54(3): 248–252, doi: [10.1016/j.bjoms.2015.11.014](https://doi.org/10.1016/j.bjoms.2015.11.014), indexed in Pubmed: [26687554](https://pubmed.ncbi.nlm.nih.gov/26687554/).
- Carlson D. Theories of craniofacial growth in the post-genomic era. *Semin Orthod.* 2005; 11(4): 172–183, doi: [10.1053/j.sodo.2005.07.002](https://doi.org/10.1053/j.sodo.2005.07.002).
- Cevidanes LHS, Franco AA, Gerig G, et al. Comparison of relative mandibular growth vectors with high-resolution 3-dimensional imaging. *Am J Orthod Dentofacial Orthop.* 2005; 128(1): 27–34, doi: [10.1016/j.ajodo.2004.03.033](https://doi.org/10.1016/j.ajodo.2004.03.033), indexed in Pubmed: [16027622](https://pubmed.ncbi.nlm.nih.gov/16027622/).
- Costa HN, Slavicek R, Sato S. A computerized tomography study of the morphological interrelationship between the temporal bones and the craniofacial complex. *J Anat.* 2012; 220(6): 544–554, doi: [10.1111/j.1469-7580.2012.01499.x](https://doi.org/10.1111/j.1469-7580.2012.01499.x), indexed in Pubmed: [22458595](https://pubmed.ncbi.nlm.nih.gov/22458595/).
- Dargaud J, Cotton F, Buttin R, et al. [The maxillary sinus: evolution and function in aging]. *Morphologie.* 2003; 87(276): 17–22, indexed in Pubmed: [12793110](https://pubmed.ncbi.nlm.nih.gov/12793110/).
- Dibbets JM. Morphological associations between the Angle classes. *Eur J Orthod.* 1996; 18(2): 111–118, doi: [10.1093/ejo/18.2.111](https://doi.org/10.1093/ejo/18.2.111), indexed in Pubmed: [8670923](https://pubmed.ncbi.nlm.nih.gov/8670923/).
- Dural S, Avcı N, Karabıyıkoğlu T. Gömük dişlerin görülme sıklığı, çenelere göre dağılımları ve gömülü kalma nedenleri. *Sağ Bil Arş Derg.* 1996; 7: 127–133.
- Hwang SeH, Seo JH, Joo YH, et al. An anatomic study using three-dimensional reconstruction for pterygopalatine fossa infiltration via the greater palatine canal. *Clin Anat.* 2011; 24(5): 576–582, doi: [10.1002/ca.21134](https://doi.org/10.1002/ca.21134), indexed in Pubmed: [21400608](https://pubmed.ncbi.nlm.nih.gov/21400608/).
- Icen M, Orhan K. Cone-beam computed tomography evaluation of the pterygomaxillary fissure and pterygopalatine fossa using 3D rendering programs. *Surg Radiol Anat.* 2019; 41(5): 513–522, doi: [10.1007/s00276-019-02201-2](https://doi.org/10.1007/s00276-019-02201-2), indexed in Pubmed: [30725218](https://pubmed.ncbi.nlm.nih.gov/30725218/).
- Iseri H, Solow B. Average surface remodeling of the maxillary base and the orbital floor in female subjects from 8 to 25 years. An implant study. *Am J Orthod Dentofacial Orthop.* 1995; 107(1): 48–57, doi: [10.1016/s0889-5406\(95\)70156-7](https://doi.org/10.1016/s0889-5406(95)70156-7), indexed in Pubmed: [7817961](https://pubmed.ncbi.nlm.nih.gov/7817961/).
- Kruger E, Thomson WM, Konthasinghe P. Third molar outcomes from age 18 to 26: findings from a population-based New Zealand longitudinal study. *Oral Surg Oral Med Oral Pathol Oral Radiol Endod.* 2001; 92(2): 150–155, doi: [10.1067/moe.2001.115461](https://doi.org/10.1067/moe.2001.115461), indexed in Pubmed: [11505260](https://pubmed.ncbi.nlm.nih.gov/11505260/).
- Lim AA, Wong CW, Allen JC. Maxillary third molar: patterns of impaction and their relation to oroantral perforation. *J Oral Maxillofac Surg.* 2012; 70(5): 1035–1039, doi: [10.1016/j.joms.2012.01.032](https://doi.org/10.1016/j.joms.2012.01.032), indexed in Pubmed: [22494509](https://pubmed.ncbi.nlm.nih.gov/22494509/).
- Mollaoglu N, Cetiner S, Güngör K. Patterns of third molar impaction in a group of volunteers in Turkey. *Clin Oral Investig.* 2002; 6(2): 109–113, doi: [10.1007/s00784-001-0144-1](https://doi.org/10.1007/s00784-001-0144-1), indexed in Pubmed: [12166710](https://pubmed.ncbi.nlm.nih.gov/12166710/).
- Moss ML, Salentijn L. The capsular matrix. *Am J Orthod.* 1969; 56(5): 474–490, doi: [10.1016/0002-9416\(69\)90209-7](https://doi.org/10.1016/0002-9416(69)90209-7), indexed in Pubmed: [5261161](https://pubmed.ncbi.nlm.nih.gov/5261161/).
- Moss ML. The functional matrix hypothesis revisited. 1. The role of mechanotransduction. *Am J Orthod Dentofacial Orthop.* 1997; 112(1): 8–11, doi: [10.1016/s0889-5406\(97\)70267-1](https://doi.org/10.1016/s0889-5406(97)70267-1), indexed in Pubmed: [9228835](https://pubmed.ncbi.nlm.nih.gov/9228835/).
- Moss ML. The functional matrix hypothesis revisited. 2. The role of an osseous connected cellular network. *Am J Orthod Dentofacial Orthop.* 1997; 112(2): 221–226, doi: [10.1016/s0889-5406\(97\)70249-x](https://doi.org/10.1016/s0889-5406(97)70249-x), indexed in Pubmed: [9267235](https://pubmed.ncbi.nlm.nih.gov/9267235/).
- Oz U, Orhan K, Aksoy S, et al. Association between pterygoid hamulus length and apnea hypopnea index in patients with obstructive sleep apnea: a combined three-dimensional cone beam computed tomography and polysomnographic study. *Oral Surg Oral Med Oral Pathol Oral Radiol.* 2016; 121(3): 330–339, doi: [10.1016/j.oooo.2015.10.032](https://doi.org/10.1016/j.oooo.2015.10.032), indexed in Pubmed: [26776720](https://pubmed.ncbi.nlm.nih.gov/26776720/).
- Ozeç I, Hergüner Siso S, Taşdemir U, et al. Prevalence and factors affecting the formation of second molar distal caries in a Turkish population. *Int J Oral Maxillofac Surg.* 2009; 38(12): 1279–1282, doi: [10.1016/j.ijom.2009.07.007](https://doi.org/10.1016/j.ijom.2009.07.007), indexed in Pubmed: [19665355](https://pubmed.ncbi.nlm.nih.gov/19665355/).
- Peterson LJ, Ellis II, Hupp JR. *Contemporary oral and maxillofacial surgery*. 3rd ed. Mosby, St. Louis 1998: 215–248.
- Piva LM, Brito HHA, Leite HR, et al. Effects of cervical headgear and fixed appliances on the space available for maxillary second molars. *Am J Orthod Dentofacial Orthop.* 2005; 128(3): 366–371, doi: [10.1016/j.ajodo.2004.04.032](https://doi.org/10.1016/j.ajodo.2004.04.032), indexed in Pubmed: [16168333](https://pubmed.ncbi.nlm.nih.gov/16168333/).
- Rothstein T, Yoon-Tarlie C. Dental and facial skeletal characteristics and growth of males and females with class II, division 1 malocclusion between the ages of 10 and 14 (revisited) — part I: characteristics of size, form, and

- position. *Am J Orthod Dentofacial Orthop.* 2000; 117(3): 320–332, doi: [10.1016/s0889-5406\(00\)70237-x](https://doi.org/10.1016/s0889-5406(00)70237-x), indexed in Pubmed: [10715092](https://pubmed.ncbi.nlm.nih.gov/10715092/).
24. Schersten E, Lysell L, Rohlin M. Prevalence of impacted third molars in dental students. *Swed Dent J.* 1989; 13: 7–13.
25. Tashi S, Purohit BS, Becker M, et al. The pterygopalatine fossa: imaging anatomy, communications, and pathology revisited. *Insights Imaging.* 2016; 7(4): 589–599, doi: [10.1007/s13244-016-0498-1](https://doi.org/10.1007/s13244-016-0498-1), indexed in Pubmed: [27230518](https://pubmed.ncbi.nlm.nih.gov/27230518/).
26. Tausche E, Deeb W, Hansen L, et al. CT analysis of nasal volume changes after surgically-assisted rapid maxillary expansion. *J Orofac Orthop.* 2009; 70(4): 306–317, doi: [10.1007/s00056-009-9910-5](https://doi.org/10.1007/s00056-009-9910-5), indexed in Pubmed: [19649578](https://pubmed.ncbi.nlm.nih.gov/19649578/).
27. Tuğsel Z, Kandemir S, Küçüker F. Üniversite öğrencilerinde üçüncü molarların gömüklülük durumlarının değerlendirilmesi, *Cumhuriyet Üniv. Dişhek Fak Der.* 2001; 4: 102–105.
28. Türker M, Yücetaş Ş. *Ağız Diş Çene Hastalıkları ve Cerrahisi.* 3rd ed. Özyurt 2004.

Evaluation of facial soft tissues by stereophotogrammetry method in patients with obstructive sleep apnoea: a morphological study

B. Karadede Ünal¹, C. Hüseyin¹

Department of Orthodontics, Faculty of Dentistry, Izmir Katip Çelebi University, Izmir, Turkey

[Received: 18 February 2021; Accepted: 8 March 2021]

Background: We aimed to use the “SomnoMed MAS” device, which brings the mandible forward in obstructive sleep apnoea syndrome patients due to mandibular retrognathia, and to examine its effects on facial soft tissues by stereophotogrammetry (3dMD) method.

Materials and methods: Thirty-one patients with a mean age of 44 years and 6 months were included in the study. SomnoMed MAS, one of the splint appliances that position the mandible in front, was applied to all patients and the changes in facial soft tissues were examined by overlapping the images taken at different times with the 3dMD face system. The obtained data were analysed statistically and the level of statistical significance was determined as $p \leq 0.05$.

Results: Mouth width decreased statistically during T0–T1 period. In T0–T2 period, while crista philtri and labiale inferius points moved backwards, Mouth width, nose width decreased and nasal base width increased. In the T0–T3 period, nasal base width increased statistically, the philtrum width and the mouth width decreased, and the soft tissue nasion point came to the fore.

Conclusions: Splint treatment, which positions the mandible in front in adult obstructive sleep apnoea syndrome patients, affected the middle and lower facial soft tissues with the forward and downward translational movement of the lower jaw. (Folia Morphol 2021; 80, 2: 432–441)

Key words: appliances, obstructive sleep apnoea syndrome, stereophotogrammetry, snoring

INTRODUCTION

Obstructive sleep apnoea syndrome (OSAS) is defined as the involuntary blockage of breathing that lasts at least 10 seconds or more with a decrease in oxygen saturation in the blood due to collapse of the upper respiratory tract at varying degrees while breathing during sleep [13]. One of the most prominent features of OSAS is snoring. However, not every

snoring patient should be diagnosed with OSAS. Snoring increases due to fat accumulation in obese patients with OSAS. Sleeping position affects the severity of these symptoms [19]. OSAS characterised by recurrent partial or complete upper airway obstructions that develop during sleep in patients. More than 75% of OSAS patients have airway collapse in the velopharyngeal/retropalatal region [8, 21].

Address for correspondence: Dr. B. Karadede Ünal, Izmir Katip Çelebi Üniversitesi Diş Hekimliği Fakültesi, Aydınlikevler Mahallesi, Cemil Meriç Bulvarı, 6780 Sokak. No: 48, Çiğli, Izmir, Turkey. Address code: 1537976407, Post code: 35640, tel: +90 (232) 325 40 40, fax: +90 (232) 325 25 25, e-mail: dtbeyzaunalkaradede@gmail.com

This article is available in open access under Creative Common Attribution-Non-Commercial-No Derivatives 4.0 International (CC BY-NC-ND 4.0) license, allowing to download articles and share them with others as long as they credit the authors and the publisher, but without permission to change them in any way or use them commercially.

The traditional important diagnostic method of OSAS is the overnight polysomnography (PSG) test performed in sleep laboratories [14, 30]. In addition to sleep stages, many physiological parameters, functions of different organs, and their interactions during sleep and wakefulness are examined with PSG [3]. If the number of apnoeas observed in an hour of sleep is less than 5, simple snoring is mentioned, if 5–15 is mild, 15–30 is moderate, and if it is 30 or more, it is mentioned that there is severe sleep apnoea syndrome [23, 30]. The third edition of the International Classification of Sleep Disorders defines obstructive sleep apnoea (OSA) as a PSG-determined obstructive respiratory disturbance index (RDI) ≥ 5 events per hour associated with the typical symptoms of OSA (e.g., unrefreshing sleep, daytime sleepiness, fatigue or insomnia, awakening with a gasping or choking sensation, loud snoring, or witnessed apnoeas), or an obstructive RDI more than 15 events per hour (even in the absence of symptoms) [15].

The most commonly used method for the treatment of OSAS disease is the use of a continuous positive nasal airway pressure (nCPAP) device. It is thought that the positive changes achieved with the use of this device are the result of a decrease in upper airway oedema [28]. Continuous positive airway pressure provides a stable positive pressure across inspiration and expiration [30]. Tracheostomy, nasal septal surgery, hyoid bone suspension, partial tongue resection, mandibular surgery, maxillomandibular advancement osteotomy, inferior mandibular osteotomy, lingualplasty, hyoid myotomy and suspension combined with genioglossal advancement, laser uvuloplasty, uvulopalatopharyngoplasty methods are surgical treatment approaches of OSAS [7, 18]. Some authors recommend that sleep physicians can consider prescription of oral appliances, rather than no treatment, for adult patients with OSA who are intolerant of CPAP therapy or prefer alternate therapy [24]. Oral devices are used in patients who cannot tolerate nCPAP therapy, who cannot undergo surgery due to their systemic condition and who are diagnosed with mild and mild-moderate sleep apnoea as a result of the PSG test. With these devices, only OSA can be treated, but central and mixed apnoeas cannot be treated [13].

The appliances that position the mandible in front and the devices which have tongue retainer feature

prevent retroglossal collapse. The importance of minor tooth movements and small changes in occlusion during the use of these appliances is controversial [32]. Most important advantages of the intraoral devices are easily tolerated, non-invasive, reversible method, cheap, less patient time in the clinic, available for patients with or without teeth, are easy to carry, the use of the appliance does not affect daily life, is physiologically harmless, does not dissolve in water and is odourless [5].

Although there are studies investigating the effects of intraoral appliances used by sleep apnoea patients on the teeth and skeletal system, we have not come across a study that investigates the effect on facial soft tissues in a comprehensive way. In order to shed light on the unknowns in this field, we aimed to use the "SomnoMed MAS" device, which brings the lower jaw forward in OSAS patients due to mandibular retrognathia [4], and to examine its effects on facial soft tissues by stereophotogrammetry method including anatomical landmarks. This appliance is custom-made two-piece MAS (SomnoDent MAS, SomnoMed, Crows Nest, Australia) device. This appliance positions the lower jaw at the front as a result of the wings in the lower part sitting on the front of the upper part with the logic of the functional appliance [20]. Three-dimensional (3D) stereophotogrammetry method is safe, noninvasive and able to capture superior quality 'external surface' 3D photographs in less than 10 ms [20].

MATERIALS AND METHODS

Patient follow-up

This study was conducted on patients diagnosed with OSAS in sleep clinics, in the Department of Orthodontics, Faculty of Dentistry of Izmir Katip Celebi University. In this study, G * Power 3.1 software programme (Franz Foul, Universität Kiel, Germany) was used to determine the sample size. It was seen that 30 patients would be sufficient for this study, and a total of 31 individuals, 20 men and 11 women, with an average age of 44 years and 6 months (19 years 10 months–60 years) were included in the study. SomnoMed MAS (SomnoDent MAS, SomnoMed Ltd, Australia), one of the types of mandibular repositioner apparatus for therapeutic purposes, was applied to these patients. The approval of the ethics committee dated 07.06.2018 and numbered 68 was obtained

from Izmir Katip Celebi University Interventional Clinical Research Ethics Committee.

Inclusion criteria of the individuals were as follows:

- patients between the ages of 19–60, with mandibular retrognathia and sleep apnoea syndrome;
- having enough teeth and retention areas to apply the apparatus;
- good oral hygiene;
- absence of temporomandibular joint problems;
- absence of severe skeletal malocclusion, systemic disease and no history of operation in the head and neck region;
- not having orthodontic or orthognathic treatment.

The exclusion criteria of the individuals are as follows:

- patients not complying with the treatment protocol;
- not paying attention to oral hygiene.

Upper and lower impressions were taken from individuals. For the standardisation of the forward activation of the lower jaw in the sagittal direction, a wax was used to register a protrusive bite by 75% of the maximum amount of protrusion [9].

Facial soft tissues of patients was performed immediately before the appliance is applied (T0), after 1 hour of use (T1), 3 days (T2), and after 8 hours of use while sleeping at night for 7 days (T3) with the 3D imaging system (3dMD, Atlanta, Ga, USA). In the study, an in-group evaluation was made and the T0 group was used as the control group.

The analysis of the images obtained by the stereophotogrammetry method was made with the 3dMD Vultus analysis programme (3dMD, Atlanta, Ga, USA). Images were overlapped in order to measure point and volumetric changes in the records (Figs. 1–3). As stated Maal et al. [20], the forehead, nasal dorsum and temple areas were used to overlap. The registration process has been applied in such a way that the root mean square (RMS) value reaches the lowest possible value [29].

Statistical analysis

The data were evaluated in the IBM SPSS Statistics Standard Concurrent User V 25 (IBM Corp., Armonk, New York, USA) statistical package program. Descriptive statistics are given as unit number (n), percentage (%), mean \pm standard deviation ($\bar{x} \pm SD$) values. Normality of measurement difference was evaluated

by Shapiro-Wilk normality test and Q-Q charts. Before and after treatment measurement differences were compared with paired t test. A value of $p < 0.05$ was considered statistically significant.

Ethical committee approval and informed consent

The study protocol was approved by the Health Research Ethics Board of İzmir Katip Çelebi University, School of Medicine, a report of ethics committee decision numbered 68 and dated June, 7, 2018. The study was conducted in accordance with the principles of the Declaration of Helsinki. In this research, cone-beam computed tomography (CT) images, which was previously recorded for diagnostic and therapeutic purposes, was used from the archives of İzmir Katip Çelebi University Faculty of Dentistry Department of Radiology.

A written informed consent was obtained from each participant.

RESULTS

Images were taken from the individuals included in the study at the T0, T1, T2 and T3 periods and the differences were determined by overlapping them. Looking at the point values in Table 1, alare right and cheilion left points came to the fore statistically significantly in the T0–T1 period. In the T0–T2 period, crista philtri right, crista philtri left and labiale inferius points moved back statistically significantly. Soft tissue nasion and alare right points came to the fore significantly in the T0–T3 period ($p < 0.05$).

Looking at the linear measurements, a statistically significant decrease was observed in the mouth width in all three periods. In the T0–T2 period, while the nose width decreased, the nasal base width increased. In the T0–T3 period, while the philtrum width decreased, the nasal base width increased statistically ($p < 0.05$) (Table 2).

When the volumetric, proportional and angular parameters are examined, no statistically significant change was observed in any of the T0–T1, T0–T2 and T0–T3 periods ($p > 0.05$). The changes in the total face volume values, the upper facial volume and lower facial volume were not statistically significant at the T0–T1, T0–T2 and T0–T3 periods. In addition, we evaluated the ratio of the results obtained from the measurements we made in our study. There was no statistically significant difference in the ratio of



Figure 1. Points used in the analysis of three-dimensional face scan image data. **1) Glabella point (G')**: It is the most anterior midpoint of the fronto-orbital soft tissue contour; **2) Soft tissue nasion point (N')**: It is the most posterior point of the nasal root in the soft tissue contour; **3) Exocanthion (exr, exl)**: It is the outer edge point of both eyeballs; **4) Pronasale point (Prn')**: It is the most anterior point of the tip of the nose. If there is a bifid nasal structure, the most anterior point should be chosen; **5) Subnasale point (Sn')**: It is the point on the nasolabial soft tissue contour of the junction of columella and upper lip; **6) Alare points (Alr, All)**: The outermost points of both alar curvatures; **7) Alar curvature points (Acr, Acl)**: The junction points of both alar bases with the facial structure; **8) Columella point (C')**: It is the midpoint of Columella at the nostril top point level; **9) Soft tissue A point (A')**: It is the deepest point of philtrum; **10) Labiale superius point (Ls)**: It is the midpoint of the upper lip on the vermillion line; **11) Crista philtri points (Cphr, Cphi)**: They are the junction points of the vermillion line and the upward edges of the philtrum; **12) Stomion point (Sto)**: It is the horizontal midpoint of the joint of the two lips when the lips are closed. If the lips do not close when the patient is in the resting position, it is the point in the middle of the gap between the lips; **13) Cheilion points (Chr, Chl)**: They are the edge joints of the lips; **14) Labiale inferius point (Li)**: It is the midpoint of the lower lip on the vermillion line; **15) Soft tissue B point (B')**: It is the deepest point of the labiomental soft tissue contour between the lower lip and the tip of the chin; **16) Soft tissue pogonion point (Pog')**: It is the outermost point of the chin tip; **17) Soft tissue menton point (Me')**: It is the lowest point of the soft tissue contour of the chin tip. It corresponds to the projection of the skeletal menton point.

philtrum length to mouth width, the ratio of mouth width/total vermillion length, upper lip length/lower lip length, the ratio of upper lip vermillion length/lower lip vermillion length, and the ratio of anterior facial height/lower facial height at the T0-T1, T0-T2, and T0-T3 periods.

Some important angular measurements were also made on soft tissues in our study. Interlabial angle, the lower lip angle, and upper lip angle did not change statistically significant at the T0-T1, T0-T2, and T0-T3 stages. Similarly, we found that the nasomental angle, labiomental angle, nasolabial angle and nasofrontal angle did not show statistically significant changes in the T0-T1, T0-T2 and T0-T3 stages.

There were no statistically significant differences in the soft tissue convexity angle at the T0-T1, T0-T2, and T0-T3 periods.

DISCUSSION

There are various mandibular advancement appliances used in the treatment of OSAS patients [12]. Among the reasons we prefer the SomnoMed MAS device, which positions the mandible for 8 hours at night for all patients with OSAS, the sagittal screws placed in the upper part can be activated in the sagittal direction when necessary, the outer part of the apparatus is made of rigid acrylic that wraps all teeth rigidly and increases stabilisation, Since the inner

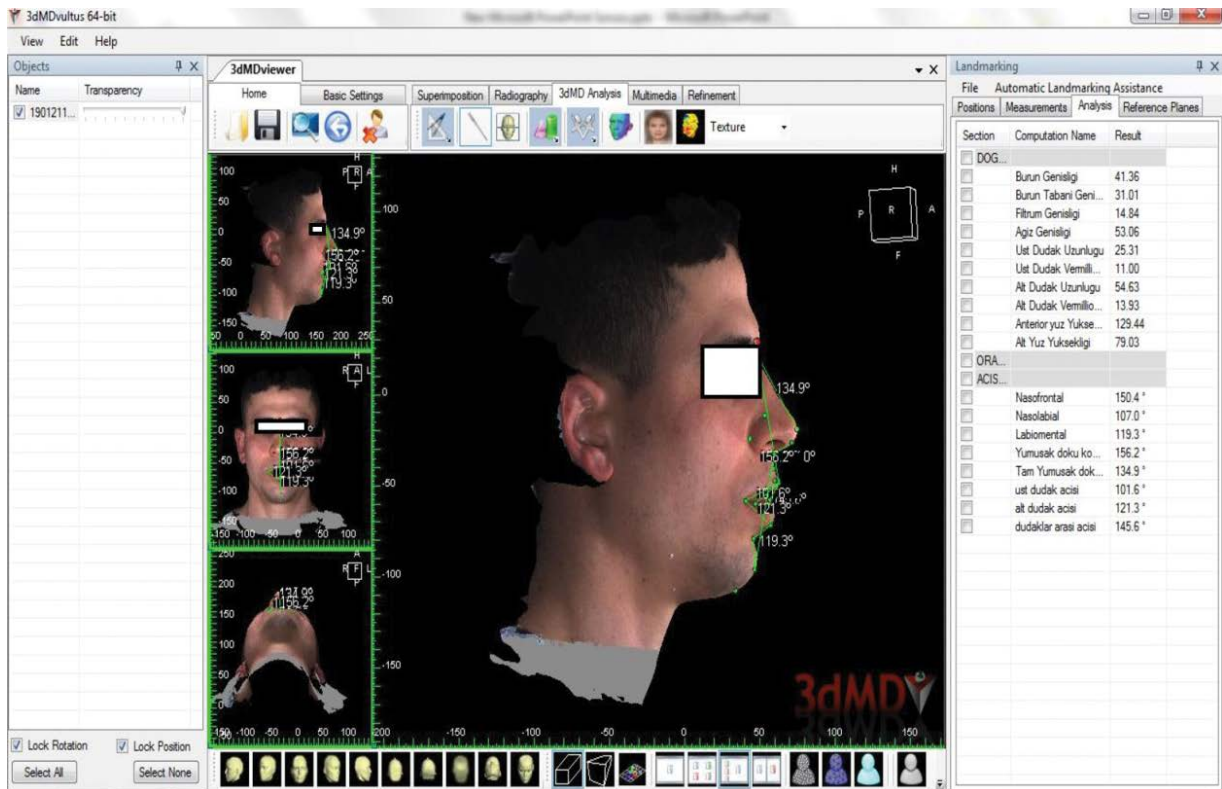


Figure 2. Linear, proportional and angular measurements used on three-dimensional face scan images. **Linear measurements:** 1) **Nasal width (Air-Air):** It is the distance between the outermost points of the right and left nasal wings; 2) **Nasal base width (Acr-Acl):** It is the distance between the right and left alar base; 3) **Philtrum width (Cphr-Cphl):** It is the distance between right and left crista philtri points; 4) **Mouth width (Chr-Chl):** It is the distance between the right and left angles of the mouth; 5) **Upper lip length (Sn'-Sto):** It is the distance between the subnasale and stomion points; 6) **Upper lip vermillion length (Ls-Sto):** It is the distance between labiale superius and stomion points; 7) **Lower lip length (Sto-Me'):** The distance between the stomion and soft tissue menton points; 8) **Lower lip vermillion length (Sto-Li):** It is the distance between stomion and labiale inferius points; 9) **Anterior face height (N'-Me'):** It is the distance between soft tissue nasion and soft tissue menton points; 10) **Lower face height (Sn'-Me'):** The distance between the subnasale and soft tissue menton points; **Proportional measurements:** 1) **N'-Me'/Sn'-Me':** It is the ratio of the height of the anterior face to the height of the lower face; 2) **Ls-Sto/Sto-Li:** It is the ratio of the vermillion length of the upper lip to the vermillion length of the lower lip; 3) **Sn'-Sto/Sto-Me':** It is the ratio of the length of the upper lip to the length of the lower lip; 4) **Chr-Chl/Ls-Li:** It is the ratio of mouth width to total vermillion length; 5) **Cphr-Cphl/Chr-Chl:** It is the ratio of the philtrum width to the mouth width; **Angular measurements:** 1) **Nasofrontal angle (G'-N'-Prn'):** It is the angle between the soft tissue glabella, nasion and pronasale points; 2) **Nasolabial angle (C'-Sn'-Ls):** It is the angle between the soft tissue columella, subnasale and labiale superius points; 3) **Labiomental angle (Li-B'-Pog'):** It is the angle between the labiale inferius, soft tissue B and soft tissue pogonion points; 4) **Soft tissue convexity angle (N'-Sn'-Pog'):** It is the angle between the soft tissue nasion, subnasale and soft tissue pogonion points; 5) **Nasomental angle (N'-Prn'-Pog'):** It is the angle between the soft tissue nasion, pronasale and soft tissue pogonion points; 6) **Upper lip angle (Chr-Ls-Chl):** It is the angle between the right cheilion, labiale superius and left cheilion points; 7) **Lower lip angle (Chr-Li-Chl):** It is the angle between the right cheilion, labiale inferius and left cheilion points; 8) **Interlabial angle (Ls-Sto-Li):** It is the angle between labiale superius, stomion and labiale inferius points.

part covering the teeth is made of soft material, it causes less discomfort to the patients, patients can use this device without the need of a physician and also allows jaw movements because the upper and lower parts are separate.

Arnett et al. [1] stated that the changes in facial soft tissues were completed at the age of 12 in girls, and that growth continued until the age of 17 in boys. In our study, individuals with an average age

of 44 years and 6 months were included in the study. Due to the disadvantages of two-dimensional (2D) imaging methods, 3D CT method, which is a more sensitive method, has been widely used [27]. There are a number of limitations of CT systems. The images captured on the detector screens are made up of multiple slices that are 'stacked' to obtain a final complete image. Furthermore, the radiation exposure to the patient has limited its usage to complex

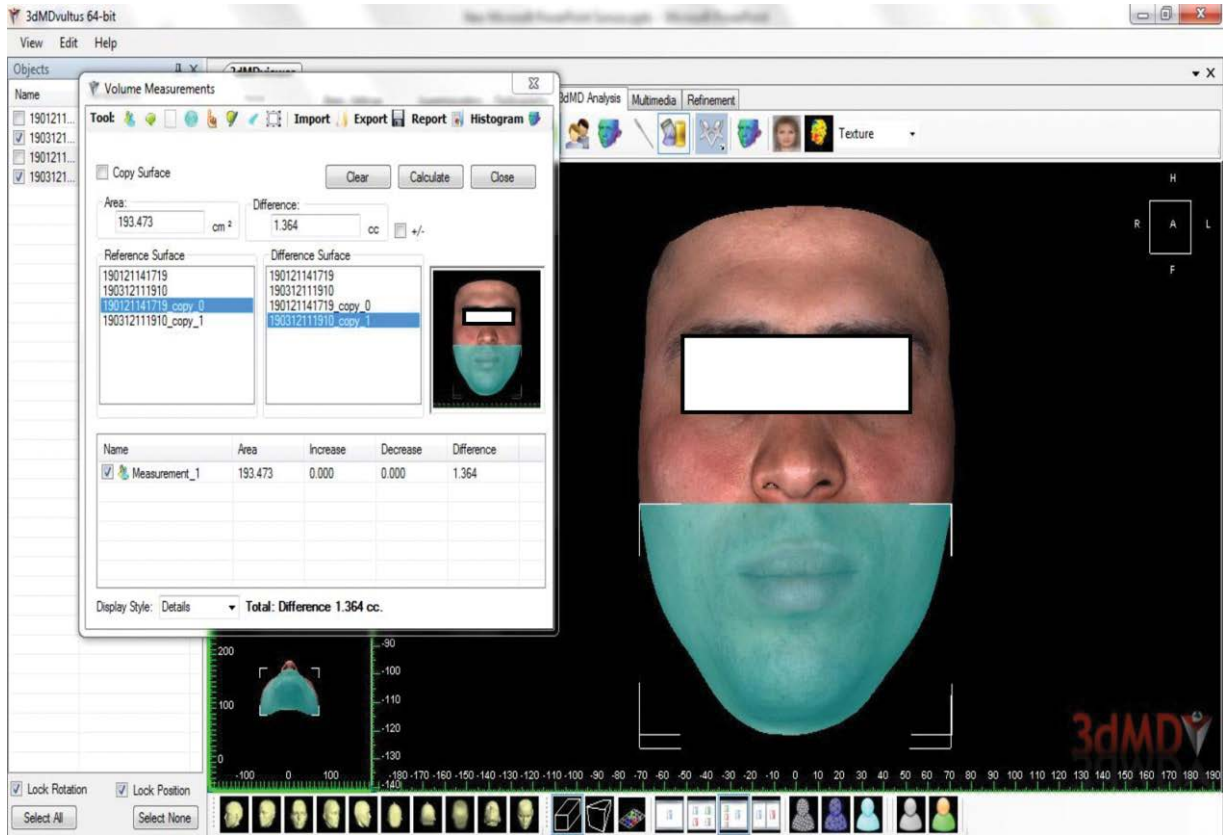


Figure 3. Calculation of volumetric measurements; **1) Total facial volume:** It covers the area from the soft tissue nasion (N') point on the top to the soft tissue pogonion (Pog') point at the bottom; **2) Upper face volume:** It covers the area from the upper soft tissue nasion (N') point to the lower subnasale (Sn) point; **3) Lower face volume:** It covers the region from the subnasale (Sn) point at the top to the soft tissue pogonion (Pog') point at the bottom.

Table 1. Point changes obtained from image registration and statistical evaluation results

Parameters	T0-T1			T0-T2			T0-T3		
	X diff. [mm]	SD	P	X diff. [mm]	SD	P	X diff. [mm]	SD	P
Soft tissue nasion (N')	-0.0729	0.49013	0.414	0.1019	0.39049	0.156	0.1916	0.45360	0.025*
Alare right (Alr)	0.1668	0.37818	0.020*	0.0916	0.34294	0.147	0.1448	0.33430	0.022*
Crista philtri right (Cphr)	-0.1623	0.84917	0.296	-0.3929	0.97084	0.032*	-0.1210	0.83410	0.426
Crista philtri left (Cphl)	-0.2119	0.81224	0.157	-0.3368	0.84081	0.033*	-0.0665	0.81022	0.651
Cheilion left (Chl)	0.3910	0.98621	0.035*	0.0426	0.95294	0.805	0.0481	1.02750	0.796
Labiale inferius (Li)	-0.2197	1.02785	0.243	-0.5761	1.11018	0.007*	-0.3145	1.15843	0.141

*Statistically significant (p < 0.05), standard deviation (SD), mean (x)

craniofacial problems and for specialised diagnostic information only. Magnetic resonance imaging has been shown to be useful in a variety of head and neck applications and is a relatively safe but costly procedure. It has been applied to the analysis of tem-

poro-mandibular joints, preoperative planning of tumour resection and maxillary sinus evaluation [16]. Magnetic resonance imaging can assess soft tissue size but this method is expensive and has relatively poor resolution for surface changes. Ideally, the

Table 2. Linear measurements

Parameters	T0-T1			T0-T2			T0-T3								
	T0 X [mm]	T1 X [mm]	X diff. [mm]	SD	P	T0 X [mm]	T2 X [mm]	X diff. [mm]	SD	P	T0 X [mm]	T3 X [mm]	X diff. [mm]	SD	P
Nasal width (Afr-All)	38.6371	38.5274	-0.10968	0.94359	0.522	38.6371	38.1416	-0.49508	0.93332	0.006*	38.6371	38.2839	-0.35323	1.17900	0.106
Nasal base width (Acr-Ac)	31.2300	31.6813	0.45129	1.40107	0.083	31.2300	31.9874	0.75742	1.30397	0.003**	31.2300	31.9206	0.69065	1.46667	0.014*
Philtrum width (Cphr-Cphl)	14.8529	14.8148	-0.03806	1.04106	0.840	14.8529	14.8519	-0.00097	1.19444	0.996	14.8529	14.4277	-0.42516	1.14426	0.047*
Mouth width (Chr-Chl)	51.1694	50.2400	-0.92935	1.75734	0.006*	51.1694	49.7029	-1.46645	2.37502	0.002*	51.1694	49.7152	-1.45419	2.29938	0.001*

*Statistically significant (p < 0.05), standard deviation (SD), mean (x)

quantitative assessment of the main characteristics of the human face should be a 3D evaluation. One such objective and quantitative method for analysing facial dimensions is 3D stereophotogrammetry system. This system uses two digital camera pods to create a 3D facial image [26]. The development of the stereophotogrammetry method has made a breakthrough in the examination of facial soft tissues. Lin et al. [17] compared these methods by taking CT, 3dMD, and 2D photograph from 38 patients diagnosed with OSA. They found that the records obtained by 3dMD and CT methods were compatible with OSA severity.

Maal et al. [20] determined variations in the face at rest; 100 3dMD photographs of the same individual were acquired at different times. Initially, 50 3dMD photographs were obtained; 25 using a wax bite to ensure similar occlusion between subsequent photographs and 25 without wax bite. This procedure was repeated 6 weeks later. Variation of the face at rest was computed. The mean error of the system (RMS) of all four groups ranged from 0.21 mm to 0.27 mm. The standard deviation ranged from 0.20 mm to 0.26 mm. The results for the different anatomical regions are illustrated in Table 2. The RMS error ranged from 0.16 mm to 0.37 mm. The 90th percentile error ranged from 0.33 mm to 0.78 mm and the 95th percentile error ranged from 0.40 mm to 1.01 mm. The values in our study were also compatible with this study. This shows the reliability of the method used.

The methodology used by Maal et al. [20] for the forehead, nose and temple areas was also applied in this study. The points, planes, angular and volumetric parameters selected in the measurements are compatible with the parameters on soft tissues in 3D of other studies [6, 10, 22, 31]. Hammond et al. [11] used the splint, which positions the mandible anteriorly in 64 patients with OSA, for 25.1 months in a study they conducted in 2007, and examined the dental and skeletal changes; they found no significant difference in mandibular length. There was a decrease in overbite and overjet. A statistically significant, clinically insignificant forward movement was observed in the mandibular incisors.

Bondemark [2] in 1999, applied splint therapy that positions the mandible in front (by 70% of its maximum protrusion; mean 5–8 mm and increased anterior vertical height by 5 mm) on 30 patients with OSA with the average age of 55.3 (between 46.5 and 79.8) and measured by overlapping lateral cephalo-

metric images taken at the start of treatment and 2 years later. It was observed that the lower jaw of the patients moved 0.4 mm anteriorly and rotated 0.3 mm clockwise. Despite these changes, there was no complaint in the patients. The researcher stated that this change may be due to remodelling or condylar position change in the condyle and/or glenoid fossa. Skeletal parameters were examined in this study. In our study, facial soft tissues were evaluated and the clockwise rotation of the lower jaw was found to be compatible with this study; contrary to this study, there was no difference in the sagittal position of the soft tissue pogonion and menton points before and after the treatment.

Robertson [25] applied splint therapy that positioned the mandible anteriorly to 100 patients with OSA and an average age of 49, and followed it up for 30 months. The sagittal activation amount of the mandible was 75% of the maximum protrusion; observed changes in the vertical position of the condyle, total anterior and posterior face height in the first 6 months. He reported changes in the vertical position of the condyle in the total and lower face height at the 18th month and found that the changes were stable at 24th month. He emphasized that the decrease in overbite in the 30th month was due to lower incisor proclination.

In 2009, Chan et al. [4] examined the lateral cephalometry images before and after treatment (6–8 weeks) by applying SomnoMed MAS to 69 patients with OSA, which positioned the mandible anteriorly, and reported an increase in lower anterior face height. In our study, our result of the increase in lower face height at a degree close to statistically significant is consistent with the results of the researchers [2, 4, 25].

Considering the linear measurements made on the T0–T1 images, it was found that there was a statistically significant decrease in the mouth width 1 hour after the appliance was applied. When the T0–T2 and T0–T3 measurements are compared, it is seen that the decrease in the mouth width continues in a similar way, and a statistically significant difference was found when the two measurement differences are compared. The reason for the occurrence of this situation is the shrinkage in the width of the mouth with the movement of the soft tissues forward as a result of the lower jaw being brought forward with the device.

It was observed that the lower labiale point and crista philtri points were positioned statistically more anteriorly in the T0–T2 time interval. The difference occurred as a result of the lower jaw positioned in front. Considering the linear measurements between T0–T2, in contrast to the T0–T1 measurements, a decrease in nose width and an increase in nasal base width in addition to the change in mouth width were found to be statistically significant. In T0–T3 measurements, changes in nose width were found to be reversible; it was found that the change in the nasal base width continued. In this situation, as a result of the lower jaw moving forward as a result of the soft tissues associated with the lower jaw dragging the soft tissues in the upper anterior region relatively forward, the nose width decreased as a result of the stretching of the upper anterior region, while the nasal base expanded.

When looking at the results of the comparison of T0 and T3 values, it was seen that the changes in labiale inferius point and crista philtri points in the T0–T2 time interval were found to be reversible. A statistically significant difference was found at the soft tissue nasion point in the measurements in the T0–T3 period. This change made us think that it may have been caused by the adaptive movement of the soft tissue nasion point. When the linear measurements were examined, it was observed that there was a statistically significant decrease in the philtrum width between the T0 and T3 periods. No statistically significant change was found in any of the proportional and angular measurements, the changes mostly occurred in the mid and lower face region as a result of the lower jaw positioned in front and below.

CONCLUSIONS

Splint (SomnoMed MAS) treatment that positioned the mandible anteriorly did not make any difference in volumetric, proportional and angular measurements in the soft tissues of the face; It was observed that the changes in the lower and upper lip were reversible. It was thought that the decrease in mouth width and the increase in the base of the nose were caused by the stretching of the soft tissues as a result of the device that brought the lower jaw forward. The use of a device that positions the mandible anteriorly in patients who have completed their growth and development has created adaptive and

compensatory changes in the lower facial soft tissues in the short term. We think that it will be beneficial to carry out new studies by keeping the follow-up period long in the future.

Acknowledgements


Thanks to Prof. Dr. Dr. Mehmet İrfan Karadede for his contribution to our work with his scientific experience.

REFERENCES

- Arnett GW, Jelic JS, Kim J, et al. Soft tissue cephalometric analysis: diagnosis and treatment planning of dentofacial deformity. *Am J Orthod Dentofacial Orthop.* 1999; 116(3): 239–253, doi: [10.1016/s0889-5406\(99\)70234-9](https://doi.org/10.1016/s0889-5406(99)70234-9), indexed in Pubmed: [10474095](https://pubmed.ncbi.nlm.nih.gov/10474095/).
- Bondemark L. Does 2 years' nocturnal treatment with a mandibular advancement splint in adult patients with snoring and OSAS cause a change in the posture of the mandible? *Am J Orthodont Dentofacial Orthopedics.* 1999; 116(6): 621–628, doi: [10.1016/s0889-5406\(99\)70196-4](https://doi.org/10.1016/s0889-5406(99)70196-4).
- Boulos MI, Jairam T, Kendzerska T, et al. Normal polysomnography parameters in healthy adults: a systematic review and meta-analysis. *Lancet Respir Med.* 2019; 7(6): 533–543, doi: [10.1016/S2213-2600\(19\)30057-8](https://doi.org/10.1016/S2213-2600(19)30057-8), indexed in Pubmed: [31006560](https://pubmed.ncbi.nlm.nih.gov/31006560/).
- Chan ASL, Sutherland K, Schwab RJ, et al. The effect of mandibular advancement on upper airway structure in obstructive sleep apnoea. *Thorax.* 2010; 65(8): 726–732, doi: [10.1136/thx.2009.131094](https://doi.org/10.1136/thx.2009.131094), indexed in Pubmed: [20685749](https://pubmed.ncbi.nlm.nih.gov/20685749/).
- Chan ASL, Sutherland K, Cistulli PA. Mandibular advancement splints for the treatment of obstructive sleep apnea. *Expert Rev Respir Med.* 2020; 14(1): 81–88, doi: [10.1080/17476348.2020.1686978](https://doi.org/10.1080/17476348.2020.1686978), indexed in Pubmed: [31663416](https://pubmed.ncbi.nlm.nih.gov/31663416/).
- Chan FC, Kawamoto HK, Federico C, et al. Soft-tissue volumetric changes following monobloc distraction procedure: analysis using digital three-dimensional photogrammetry system (3dMD). *J Craniofac Surg.* 2013; 24(2): 416–420, doi: [10.1097/SCS.0b013e31827ff296](https://doi.org/10.1097/SCS.0b013e31827ff296), indexed in Pubmed: [23524705](https://pubmed.ncbi.nlm.nih.gov/23524705/).
- Dattilo DJ. The mandibular trapezoid osteotomy for the treatment of obstructive sleep apnea: report of a case. *J Oral Maxillofac Surg.* 1998; 56(12): 1442–1446, doi: [10.1016/s0278-2391\(98\)90413-x](https://doi.org/10.1016/s0278-2391(98)90413-x), indexed in Pubmed: [9846544](https://pubmed.ncbi.nlm.nih.gov/9846544/).
- Daurat A, Sarhane M, Tiberge M. [Obstructive sleep apnea syndrome and cognition: A review]. *Neurophysiol Clin.* 2016; 46(3): 201–215, doi: [10.1016/j.neucli.2016.04.002](https://doi.org/10.1016/j.neucli.2016.04.002), indexed in Pubmed: [27321089](https://pubmed.ncbi.nlm.nih.gov/27321089/).
- Ferguson KA, Cartwright R, Rogers R, et al. Oral appliances for snoring and obstructive sleep apnea: a review. *Sleep.* 2006; 29(2): 244–262, doi: [10.1093/sleep/29.2.244](https://doi.org/10.1093/sleep/29.2.244), indexed in Pubmed: [16494093](https://pubmed.ncbi.nlm.nih.gov/16494093/).
- Ferrario VF, Sforza C, Poggio CE, et al. Preliminary evaluation of an electromagnetic three-dimensional digitizer in facial anthropometry. *Cleft Palate Craniofac J.* 1998; 35(1): 9–15, doi: [10.1597/1545-1569_1998_035_0009_peoae-t_2.3.co_2](https://doi.org/10.1597/1545-1569_1998_035_0009_peoae-t_2.3.co_2), indexed in Pubmed: [9482218](https://pubmed.ncbi.nlm.nih.gov/9482218/).
- Hammond RJ, Gotsopoulos H, Shen G, et al. A follow-up study of dental and skeletal changes associated with mandibular advancement splint use in obstructive sleep apnea. *Am J Orthod Dentofacial Orthop.* 2007; 132(6): 806–814, doi: [10.1016/j.ajodo.2005.08.047](https://doi.org/10.1016/j.ajodo.2005.08.047), indexed in Pubmed: [18068601](https://pubmed.ncbi.nlm.nih.gov/18068601/).
- Ilea A, Timuş D, Höpken J, et al. Oral appliance therapy in obstructive sleep apnea and snoring - systematic review and new directions of development. *Cranio.* 2019 [Epub ahead of print]: 1–12, doi: [10.1080/08869634.2019.1673285](https://doi.org/10.1080/08869634.2019.1673285), indexed in Pubmed: [31588866](https://pubmed.ncbi.nlm.nih.gov/31588866/).
- Ivanhoe JR, Cibirka RM, Lefebvre CA, et al. Dental considerations in upper airway sleep disorders: A review of the literature. *J Prosthet Dent.* 1999; 82(6): 685–698, doi: [10.1016/s0022-3913\(99\)70010-7](https://doi.org/10.1016/s0022-3913(99)70010-7), indexed in Pubmed: [10588805](https://pubmed.ncbi.nlm.nih.gov/10588805/).
- Jen R, Orr JE, Li Y, et al. Accuracy of watchpat for the diagnosis of obstructive sleep apnea in patients with chronic obstructive pulmonary disease. *COPD.* 2020; 17(1): 34–39, doi: [10.1080/15412555.2019.1707789](https://doi.org/10.1080/15412555.2019.1707789), indexed in Pubmed: [31965862](https://pubmed.ncbi.nlm.nih.gov/31965862/).
- Kapur VK, Auckley DH, Chowdhuri S, et al. Clinical practice guideline for diagnostic testing for adult obstructive sleep apnea: An American Academy of Sleep Medicine Clinical Practice Guideline. *J Clin Sleep Med.* 2017; 13(3): 479–504, doi: [10.5664/jcsm.6506](https://doi.org/10.5664/jcsm.6506), indexed in Pubmed: [28162150](https://pubmed.ncbi.nlm.nih.gov/28162150/).
- Kau CH, Richmond S, Incrapera A, et al. Three-dimensional surface acquisition systems for the study of facial morphology and their application to maxillofacial surgery. *Int J Med Robot.* 2007; 3(2): 97–110, doi: [10.1002/rcs.141](https://doi.org/10.1002/rcs.141), indexed in Pubmed: [17619242](https://pubmed.ncbi.nlm.nih.gov/17619242/).
- Lin SW, Sutherland K, Liao YF, et al. Three-dimensional photography for the evaluation of facial profiles in obstructive sleep apnoea. *Respirology.* 2018; 23(6): 618–625, doi: [10.1111/resp.13261](https://doi.org/10.1111/resp.13261), indexed in Pubmed: [29462843](https://pubmed.ncbi.nlm.nih.gov/29462843/).
- Lugaresi E, Plazzi G. Heavy snorer disease: from snoring to the sleep apnea syndrome--an overview. *Respiration.* 1997; 64 (Suppl 1): 11–14, doi: [10.1159/000196730](https://doi.org/10.1159/000196730), indexed in Pubmed: [9380955](https://pubmed.ncbi.nlm.nih.gov/9380955/).
- Lyons MF, Cameron DA, Banham SW. Snoring, sleep apnoea and the role of dental appliances. *Dent Update.* 2001; 28(5): 254–256, doi: [10.12968/denu.2001.28.5.254](https://doi.org/10.12968/denu.2001.28.5.254), indexed in Pubmed: [11490637](https://pubmed.ncbi.nlm.nih.gov/11490637/).
- Maal TJJ, Verhamme LM, van Loon B, et al. Variation of the face in rest using 3D stereophotogrammetry. *Int J Oral Maxillofac Surg.* 2011; 40(11): 1252–1257, doi: [10.1016/j.ijom.2011.02.033](https://doi.org/10.1016/j.ijom.2011.02.033), indexed in Pubmed: [21514117](https://pubmed.ncbi.nlm.nih.gov/21514117/).
- Maspero C, Giannini L, Galbiati G, et al. Obstructive sleep apnea syndrome: a literature review. *Minerva Stomatol.* 2015; 64(2): 97–109, indexed in Pubmed: [25747430](https://pubmed.ncbi.nlm.nih.gov/25747430/).
- Metzger TE, Kula KS, Eckert GJ, et al. Orthodontic soft-tissue parameters: a comparison of cone-beam computed tomography and the 3dMD imaging system. *Am J Orthod Dentofacial Orthop.* 2013; 144(5): 672–681, doi: [10.1016/j.ajodo.2013.07.007](https://doi.org/10.1016/j.ajodo.2013.07.007), indexed in Pubmed: [24182583](https://pubmed.ncbi.nlm.nih.gov/24182583/).

23. Osman AM, Carter SG, Carberry JC, et al. Obstructive sleep apnea: current perspectives. *Nat Sci Sleep*. 2018; 10: 21–34, doi: [10.2147/NSS.S124657](https://doi.org/10.2147/NSS.S124657), indexed in Pubmed: [29416383](https://pubmed.ncbi.nlm.nih.gov/29416383/).
24. Ramar K, Dort LC, Katz SG, et al. Clinical practice guideline for the treatment of obstructive sleep apnea and snoring with oral appliance therapy: an update for 2015. *J Clin Sleep Med*. 2015; 11(7): 773–827, doi: [10.5664/jcsm.4858](https://doi.org/10.5664/jcsm.4858), indexed in Pubmed: [26094920](https://pubmed.ncbi.nlm.nih.gov/26094920/).
25. Robertson CJ. Dental and skeletal changes associated with long-term mandibular advancement. *Sleep*. 2001; 24(5): 531–537, doi: [10.1093/sleep/24.5.531](https://doi.org/10.1093/sleep/24.5.531), indexed in Pubmed: [11480650](https://pubmed.ncbi.nlm.nih.gov/11480650/).
26. Sawyer AR, See M, Nduka C. 3D stereophotogrammetry quantitative lip analysis. *Aesthetic Plast Surg*. 2009; 33(4): 497–504, doi: [10.1007/s00266-008-9191-1](https://doi.org/10.1007/s00266-008-9191-1), indexed in Pubmed: [18584237](https://pubmed.ncbi.nlm.nih.gov/18584237/).
27. Silva MA, Wolf U, Heinicke F, et al. Cone-beam computed tomography for routine orthodontic treatment planning: a radiation dose evaluation. *Am J Orthod Dentofacial Orthop*. 2008; 133(5): 640.e1–640.e5, doi: [10.1016/j.ajodo.2007.11.019](https://doi.org/10.1016/j.ajodo.2007.11.019), indexed in Pubmed: [18456133](https://pubmed.ncbi.nlm.nih.gov/18456133/).
28. Sullivan CE, Issa FG, Berthon-Jones M, et al. Reversal of obstructive sleep apnoea by continuous positive airway pressure applied through the nares. *Lancet*. 1981; 1(8225): 862–865, doi: [10.1016/s0140-6736\(81\)92140-1](https://doi.org/10.1016/s0140-6736(81)92140-1), indexed in Pubmed: [6112294](https://pubmed.ncbi.nlm.nih.gov/6112294/).
29. Taylor HO, Morrison CS, Linden O, et al. Quantitative facial asymmetry: using three-dimensional photogrammetry to measure baseline facial surface symmetry. *J Craniofac Surg*. 2014; 25(1): 124–128, doi: [10.1097/SCS.0b013e-3182a2e99d](https://doi.org/10.1097/SCS.0b013e-3182a2e99d), indexed in Pubmed: [24406564](https://pubmed.ncbi.nlm.nih.gov/24406564/).
30. Veasey SC, Rosen IM, Veasey SC, et al. Obstructive sleep apnea in adults. *N Engl J Med*. 2019; 380(15): 1442–1449, doi: [10.1056/NEJMcp1816152](https://doi.org/10.1056/NEJMcp1816152), indexed in Pubmed: [30970189](https://pubmed.ncbi.nlm.nih.gov/30970189/).
31. Wong JY, Oh AK, Ohta E, et al. Validity and reliability of craniofacial anthropometric measurement of 3D digital photogrammetric images. *Cleft Palate Craniofac J*. 2008; 45(3): 232–239, doi: [10.1597/06-175](https://doi.org/10.1597/06-175), indexed in Pubmed: [18452351](https://pubmed.ncbi.nlm.nih.gov/18452351/).
32. Yoshida K. Oral device therapy for the upper airway resistance syndrome patient. *J Prosthet Dent*. 2002; 87(4): 427–430, doi: [10.1067/mpr.2002.123228](https://doi.org/10.1067/mpr.2002.123228), indexed in Pubmed: [12011859](https://pubmed.ncbi.nlm.nih.gov/12011859/).

A structural magnetic resonance imaging study in therapy-naïve transsexual individuals

A. Starcevic¹ , M. Dakovic², Z. Radojicic³, B. Filipovic¹

¹Institute of Anatomy, Medical Faculty, University of Belgrade, Serbia

²Faculty for Physical Chemistry, University of Belgrade, Serbia

³Faculty of Organisational Sciences, University of Belgrade, Serbia

[Received: 20 May 2020; Accepted: 1 July 2020]

Background: *Transsexuality is explained and defined as a gender-identity disorder, characterised by very strong conviction of belonging to the opposite sex and has been associated with a distinct neuroanatomical pattern.*

Materials and methods: *We performed a structural analysis in search of possible differences in grey matter structures based on magnetic resonance imaging scans of the brains of 26 individuals between 19 and 38 years of age. The participants were divided into two groups of 15 controls and 11 transgender individuals. The segmentation of subcortical grey matter was performed using FIRST model a model-based segmentation/registration tool, from FSL software package.*

Results: *The results showed that the volume of the brain region called nucleus accumbens on the left side was significantly smaller in the group of transgender individuals compared to the control. It was the most important parameter which was shown to make distinction between two examined groups.*

Conclusions: *The results also showed decreased volumes of the left thalamus, right hippocampus and right caudate nucleus. (Folia Morphol 2021; 80, 2: 442–447)*

Key words: transsexuals, magnetic resonance imaging, FSL, subcortical brain structures

INTRODUCTION

Transsexualism is defined as a gender identity inconsistency with their biologically assigned sex with a great desire for a sex reassignment therapy. It is no longer classified as a mental disorder in the International Statistical Classification of Diseases and Related Health Problems (ICD 11), but as a sexual health condition [11]. Exact and defined aetiology is still unknown, and sexual brain differentiation through embryonic development deviates from the sexual differentiation of the rest of the body. Neuroanatomy plays a crucial, highly important role in determining gender identity and therefore the investigation and

defining the anatomical substrates and correlates can help us in identifying underlying mechanisms of transsexualism. Although public awareness is dramatically increased in past few decades, our scientific understanding and explanation of transsexualism is still very poor and pretty limited, as within every psychiatric condition where morphological substrate is not defined. It has been implicated that both environmental events and innate differences can influence and tribute to this condition. Sexual brain differentiation through embryonic development deviates from the sexual differentiation of the rest of the body [21]. This statement implicates to the fact that neuroanatomy

Address for correspondence: Dr. A. Starcevic, Institute of Anatomy, Medical Faculty, University of Belgrade, Dr Subotica 6, Belgrade, Serbia, e-mail: ana.starcevic22@gmail.com

This article is available in open access under Creative Common Attribution-Non-Commercial-No Derivatives 4.0 International (CC BY-NC-ND 4.0) license, allowing to download articles and share them with others as long as they credit the authors and the publisher, but without permission to change them in any way or use them commercially.

plays a critical role in determining gender identity and therefore the investigation and defying the anatomical substrates and correlates can help us in identifying underlying mechanisms of transsexualism.

There were a number of studies that had examined brain structures in male to female (MtF) and female to male (FtM) transsexuals and some of them are postmortem studies. They gave a great tribute to the already claimed fact that brain anatomy is associated with transsexualism. Some of them did not show any significant result but two post mortem studies revealed a lot: MtF transsexuals had a female like central subdivision of the bed nucleus of the stria terminalis with respect to its size [21] and number of neurons [12]. Other post mortem study showed that MtF transsexuals had female like volumes and neuronal densities of the interstitial nucleus of the anterior hypothalamus [8]. All this findings were very crucial in defining in which direction further investigation will proceed because scientists are pretty limited by inherent pitfalls of postmortem studies and by small number of transsexual patients generally. In a voxel based morphometric study, a grey and white matter brain structures volumes were investigated in treatment naive or hormone treated transgender women, and investigators concluded that differences existed in grey matter volumes in posterior superior frontal cortex in the cisgender women group [20]. Another magnetic resonance imaging (MRI) study showed regional grey matter structure differences in transsexuals compared to controls, independent from their biological gender in cerebellum, left angular gyrus, and in the left inferior parietal lobule [19].

In order of expanding the area of research, we investigated MRI neuroanatomy analysis and applied a very sophisticated computational image analysis approach to compare regional total volumes of different subcortical grey matter structures, caudate nucleus, putamen, globus pallidus, thalamus, hippocampus, amygdala, and nucleus accumbens.

MATERIALS AND METHODS

Participants

This research was conducted in accordance with the latest version of Declaration of Helsinki and approved by the local ethics committee and all included individuals provided written informed consent. All individuals arriving from the transgender outpatient service of the psychiatry department Clinical Centre

Dragisa Misovic in Belgrade, Serbia, diagnosed with gender identity disorder (GID) based on DSM-IV TR diagnostic criteria, were approached to enter a neuroimaging study. Both MtF and FtM individuals were eligible for the research. Healthy volunteers were recruited to serve as controls from among medical students, colleagues and friends of the research team who were free from any symptoms of GID or any psychiatric disorders. The presence of symptoms of GID was evaluated based on a free clinical interview asking simple questions targeting the symptoms of GID listed in DSM-IV TR, while the presence of psychiatric symptoms was assessed by SCL-90 [3]. Control subjects were selected to represent a population matched in age and gender identity to the patient group.

Only data from the structural imaging findings are presented in this paper, results of the functional imaging findings will be reported in upcoming publications.

Diagnosis of GID

All GID individuals underwent a detailed diagnostic interview with an expert psychiatrist in the field and also filled out a test battery assessing transgender identity disorder symptoms and associated behaviours and psychiatric comorbidity in order to confirm the diagnosis and exclude the presence of other mental disorder behind the symptoms of gender identity disorder. Sexual orientation of the patients was assessed by self-report. During the clinical interview basic demographic data, family history, psychiatric history and psychiatric status were also assessed.

MRI acquisition

Magnetic resonance examination of both transsexual and control subjects was performed using Siemens Avanto 1.5 T MRI device (Siemens, Erlangen., Germany) and 8-channel head coil. The imaging protocol consisted of T2 weighted spin echo (T2W, TR = 4800 ms, TE = 94 ms) and magnetisation prepared rapid acquisition gradient echo T1 weighted sequence (MPRAGE, TR = 1850 ms, TE = 5 ms, flip angle = 12°, matrix: 512 × 512, isovoxel). T2W images were used to exclude presence of gross brain pathology in subjects. T1W images were transferred to PC workstation (Intel i5, 8GB ram, OS Ubuntu 14.04LTS) and converted to NifTI-1 (Neuroimaging Informatics Technology Initiative) using dcm2nii software. Orientation of images was checked/corrected using fsloreorient2std script.

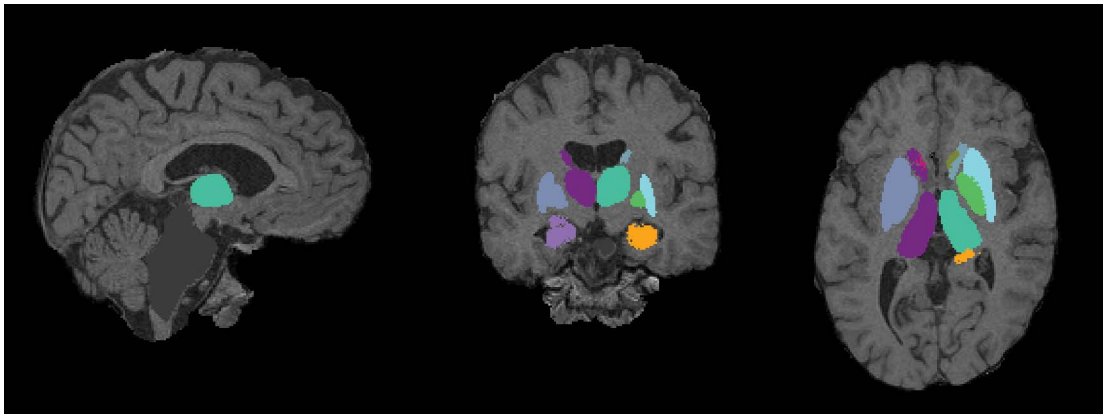


Figure 1. Example of segmentation of inner grey matter structures performed on single subject using FIRST (model based segmentation/registration tool, FSL software package).

The segmentation of subcortical grey matter was performed using the FIRST, the model based segmentation/registration tool, from FSL software package (Fig. 1) [17, 18]. The tool utilises the principles of the Active Shape and Appearance Models placed within a Bayesian framework. The models are trained for 15 different subcortical structures using 336 manually segmented and labelled T1-weighted MRI and statistical analysis was performed by R software [6].

RESULTS

We performed a structural analysis and searched for possible differences in grey matter structures based on MRI scans of the brains of 26 participants between 19 and 38 years of age, 15 controls and 11 transgender individuals. For statistical analysis, Kolmogorov-Smirnov test was used to test normal distribution of examined parameters. All parameters had a normal distribution ($p > 0.05$). To test average values of the parameters Student t-test and Levene's test for equality of variances were done. Binomial logistic regression was used to apostrophe important parameters for group prediction. Receiver operating characteristic (ROC) analysis was done for important parameters to emphasise sensitivity and specificity of each parameter and to remark cut-off values (points). All analyses were done on a level of significance $p < 0.05$. Analyses were done in SPSS 24 software package. The results showed that the volume of the brain region called nucleus accumbens on the left side was significantly smaller in the group of transgender people compared to the control. It was the

Table 1. Comparison of the groups for each examined subcortical structure

Group statistics	Group	N	Mean	Standard deviation	Standard error mean	P
Age	Trans	11	26.91	7.503	2.262	0.501
	Control	15	29.07	8.259	2.132	
Thalamus Vol L	Trans	11	8212.13	623.92	188.12	0.085
	Control	15	7673.41	838.33	216.46	
Thalamus Vol R	Trans	11	7992.21	587.19	177.05	0.025
	Control	15	7370.11	702.82	181.47	
Caudatus Vol L	Trans	11	3695.84	544.84	164.27	0.020
	Control	15	3279.72	302.52	78.11	
Caudatus Vol R	Trans	11	3653.07	574.97	173.36	0.185
	Control	15	3419.11	290.17	74.92	
Putamen Vol L	Trans	11	4924.09	363.45	109.58	0.525
	Control	15	4821.70	423.46	109.34	
Putamen Vol R	Trans	11	3921.13	859.81	259.24	0.005
	Control	15	4726.78	456.64	117.90	
Pallidum Vol L	Trans	11	1764.45	192.83	58.14	0.571
	Control	15	1711.09	259.64	67.04	
Pallidum Vol R	Trans	11	1817.34	185.10	55.81	0.746
	Control	15	1783.14	306.78	79.21	
Hippocampus Vol L	Trans	11	3562.27	461.83	139.25	0.155
	Control	15	3825.74	445.38	115.00	
Hippocampus Vol R	Trans	11	3611.82	342.21	103.18	0.010
	Control	15	3973.05	313.83	81.03	
Amygdala Vol L	Trans	11	1248.97	225.57	68.01	0.456
	Control	15	1185.74	198.32	51.20	
Amygdala Vol R	Trans	11	1338.66	402.57	121.38	0.445
	Control	15	1239.34	249.81	64.50	
Accumbens Vol L	Trans	11	514.07	68.60	20.68	0.020
	Control	15	605.47	105.74	27.30	
Accumbens Vol R	Trans	11	382.42	70.86	21.37	0.066
	Control	15	439.62	77.46	20.00	

most important parameter which was shown to make distinction between two examined groups. The results also showed decreased volumes of the left thalamus, right hippocampus and right caudate nucleus.

The Student's T test was used for the group comparison, and the results are shown in Table 1.

The groups were equal to the age structure ($p = 0.501$). Differences in the values in the values of thalamus Vol R ($p = 0.025$) and caudatus Vol R ($p = 0.020$) where the values "Trans" groups were statistically significantly higher. With the viewed parameters of putamen Vol R ($p = 0.005$), hippocampus Vol R

($p = 0.010$) and accumbens Vol L ($p = 0.020$) the values of "Trans" groups were statistically significantly reduced.

In order to discover the parameters of importance that diversify the observed groups, binomial multivariate logistics regression was used, method stepwise, from the point of view of joint action. At the start, the overall prediction was 57.5%, after four steps using forward conditional method, overall prediction showed 100%. The results of binomial logistics regression are shown in Table 2.

To confirm binomial multivariate logistic regression, for each important variable ROC analysis were done. The results confirmed the obtained logistic regression solution. In order to find breakdown values that will indicate the observed Trans group was done (Table 3), and a method P/N ratio was used to determine the cut off points. The table shows significance, value cut off and the degree of sensitivity and specificity for the given value presenting left nucleus accumbens as most important parameter (area under the curve [AUC] = 0.824) (Figs. 2, 3).

Table 2. Binomial multivariate logistics regression analysis, method stepwise forward conditional

	B	Standard error	Hazard ratio
Thalamus Vol L	-0.097	13.623	0.908
Caudatus Vol R	0.067	13.337	1.070
Hippocampus Vol R	0.054	24.948	1.055
Accumbens Vol L	0.387	60.312	1.473

Table 3. Results of area under the curve (AUC) and cut-off point with sensitivity and specificity were calculated for each given parameter

Parameter	AUC	P	95% CI L	95% CI U	Cut-off	Sensitivity	Specificity	Values*
Thalamus Vol L	0.76	0.024	0.57	0.95	7729	0.818	0.733	Bigger
Caudatus Vol R	0.74	0.040	0.53	0.95	3533	0.636	0.667	Bigger
Hippocampus Vol R	0.79	0.012	0.61	0.98	3798	0.818	0.800	Smaller
Accumbens Vol L	0.82	0.005	0.66	0.99	561	0.818	0.733	Smaller

*To the "Trans" group compared to cut off point; CI — confidence interval; L — lower; U — upper

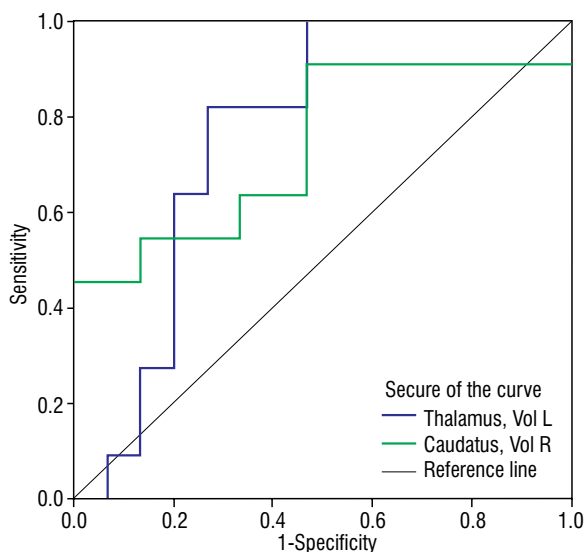


Figure 2. Receiver operating characteristic curve for left thalamus and right caudatus.

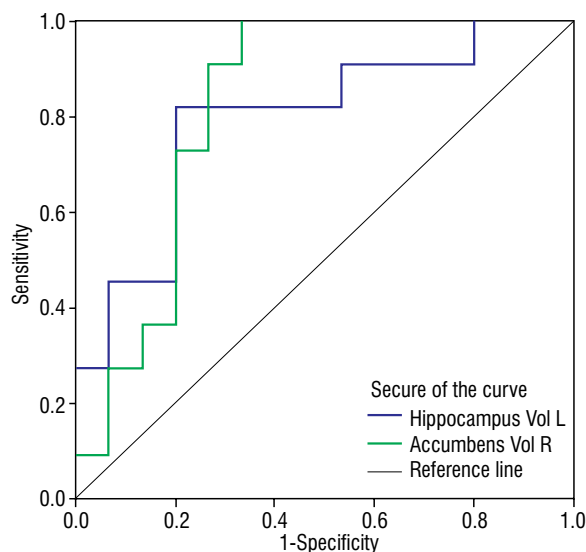


Figure 3. Receiver operating characteristic curve for left accumbens and right hippocampus.

DISCUSSION

Nucleus accumbens is, anatomically spoken, round and dorsally flattened structure located anteriorly to the anterior commissure, its posterior part, and dorsomedially into the caudate nucleus [10]. Strict delineation between these two structures is previously thought to be almost impossible, especially with MRI, but more recent studies have suggested that discerning the nucleus accumbens limits with the caudate nucleus is easier by T2-weighted MRIs due to the more intense signalling showing of nucleus accumbens than the caudate nucleus. Our study showed decreased left nucleus accumbens volume which is correlated with previous explanation [13, 15].

Many morphometric studies showed increased volume of nucleus accumbens on the left and right in males with or without gender or cerebral differences [1, 4, 13–15]. Another parameter that was included as very important was age, which was mentioned as a very important parameter when referring a decrease in specific brain structure volume correlated with age, while other structures do not pinpoint to age-related volume decrease [4, 13, 14]. Our results showed decreased volume on the left side predominantly in FtM subjects and in one MtF, and they were in their ages of 21 years, 23 years, and 39 years, which we cannot consider as age related atrophy.

The results showed that the volume of the left nucleus accumbens was smaller in transgender group consisted of both FtM and MtF than in healthy ones. Beside nucleus accumbens, we found decreased volumes of left thalamus and right hippocampus and caudate nucleus, but statistically it was shown that left nucleus accumbens was the most significant parameter. Nucleus accumbens is very important structure of ventral striatum and one of the major subcortical structures involved in emotional processes, anxiety disorders, bipolar disorder, many other neurological and psychiatric disorders as well as in addictions. It was known to be one of the key structures in addiction and drug reward circle. It would be easy to directly connect to the transgender individuals, but we can say that verification of a different volume or simply a difference in left nucleus accumbens is relevant since transgender individuals have many problems related to be accepted from their family and society, they have that strong feeling of being trapped into their own body and consequently their perception is different. Due to the fact mentioned previously, transgender people go through discrimination and

persecution and often suffer from different anxiety problems, depression, addiction issues, bipolar disorder and many others.

It is worth mentioning that an important diagnostic criterion for gender dysphoria is the distress that accompanies the incongruity between the body and gender identity, as the secondary sexual characteristics do not belong to the gender with which one identifies [7].

As for the decreased volumes of right thalamic and caudate structures, Nota et al. [16] showed that within the right working memory network, cisgender males showed significantly greater functional connectivity in the right caudate nucleus than cisgender females.

Moreover, later research has shown very similar delay of active neurons also in the posterior parietal cortex, the thalamus, the caudate, and the globus pallidus [2].

In addition to the reported regional volumetric characteristics, it is very significant to take into account human brain network connectome and morphological substrates included, which enables an investigation of interactions across brain regions and hence have provided valuable insights in fundamental human brain function. In a study investigating structural connectome of FtM and MtF, transsexuals before hormonal treatment showed differences specifically for connections between subcortical, limbic and cortical regions [5, 9]. Subcortical brain segmentation and volumetry findings put on complementary information as the evaluation on a network level between subcortical structures and cortex revealed specific characteristics for transsexuals [9].

CONCLUSIONS

Our findings support the theory that structural differences exist between transsexual individuals and controls from the same biological gender. We found that that the volume of the brain region called nucleus accumbens on the left side was significantly smaller in the group of transgender patients compared to the control. It was the most important parameter which was shown to make distinction between two examined groups. The results also showed decreased volumes of the left thalamus, right hippocampus and right caudate nucleus.


Disadvantage of this investigation is the fact of sample sizes which is modest and results are therefore yet inconclusive in details, but still significant struc-

tural differences were found between transsexuals and controls. These initial results, the results of our study, need to be further replicated and refined in future studies on larger samples, as well as followed by functional imaging studies that might clarify how these structural differences impact the process of the evolution of gender identity and its affection on specific brain structures as well as their emotional regulation, cognitive ability and brain lateralisation.

REFERENCES

- Ahsan RL, Allom R, Gousias IS, et al. Volumes, spatial extents and a probabilistic atlas of the human basal ganglia and thalamus. *Neuroimage*. 2007; 38(2): 261–270, doi: [10.1016/j.neuroimage.2007.06.004](https://doi.org/10.1016/j.neuroimage.2007.06.004), indexed in Pubmed: [17851093](https://pubmed.ncbi.nlm.nih.gov/17851093/).
- Ashby FG, Ell SW, Valentin VV, et al. FROST: a distributed neurocomputational model of working memory maintenance. *J Cogn Neurosci*. 2005; 17(11): 1728–1743, doi: [10.1162/089892905774589271](https://doi.org/10.1162/089892905774589271), indexed in Pubmed: [16269109](https://pubmed.ncbi.nlm.nih.gov/16269109/).
- Blanchard J, Brown S. Structured diagnostic interview schedules. *Comprehensive Clinical Psychology*. 1998; 4: 97–130, doi: [10.1016/b0080-4270\(73\)00003-1](https://doi.org/10.1016/b0080-4270(73)00003-1).
- Brabec J, Krásený J, Petrovický P. Volumetry of striatum and pallidum in man — anatomy, cytoarchitecture, connections, MRI and aging. *Sb Lek*. 2003; 104(1): 13–65, indexed in Pubmed: [14577136](https://pubmed.ncbi.nlm.nih.gov/14577136/).
- Cohen-Kettenis PT, van Goozen SH, Doorn CD, et al. Cognitive ability and cerebral lateralisation in transsexuals. *Psychoendocrinology*. 1998; 23(6): 631–641, doi: [10.1016/s0306-4530\(98\)00033-x](https://doi.org/10.1016/s0306-4530(98)00033-x), indexed in Pubmed: [9802133](https://pubmed.ncbi.nlm.nih.gov/9802133/).
- Development Core Team. R. A language and environment for statistical computing [Internet]. 2016; Vienna: R Foundation for Statistical Computing. <http://www.r-project.org/>.
- Fisher AD, Castellini G, Bandini E, et al. Cross-sex hormonal treatment and body uneasiness in individuals with gender dysphoria. *J Sex Med*. 2014; 11(3): 709–719, doi: [10.1111/jsm.12413](https://doi.org/10.1111/jsm.12413), indexed in Pubmed: [24330520](https://pubmed.ncbi.nlm.nih.gov/24330520/).
- García-Falgueras A, Swaab DF. A sex difference in the hypothalamic uncinate nucleus: relationship to gender identity. *Brain*. 2008; 131(Pt 12): 3132–3146, doi: [10.1093/brain/awn276](https://doi.org/10.1093/brain/awn276), indexed in Pubmed: [18980961](https://pubmed.ncbi.nlm.nih.gov/18980961/).
- Hahn A, Kranz GS, Küblböck M, et al. Structural Connectivity Networks of Transgender People. *Cereb Cortex*. 2015; 25(10): 3527–3534, doi: [10.1093/cercor/bhu194](https://doi.org/10.1093/cercor/bhu194), indexed in Pubmed: [25217469](https://pubmed.ncbi.nlm.nih.gov/25217469/).
- Johnston JB. The morphology of the septum, hippocampus, and pallial commissures in reptiles and mammals. *J Comp Neurol*. 1913; 23(5): 371–478, doi: [10.1002/cne.900230502](https://doi.org/10.1002/cne.900230502).
- Kacala A. Being Trans Is (Finally) No Longer Classified as a Mental Disorder by the WHO. 2018; Hornet.
- Kruijver FP, Zhou JN, Pool CW, et al. Male-to-female transsexuals have female neuron numbers in a limbic nucleus. *J Clin Endocrinol Metab*. 2000; 85(5): 2034–2041, doi: [10.1210/jcem.85.5.6564](https://doi.org/10.1210/jcem.85.5.6564), indexed in Pubmed: [10843193](https://pubmed.ncbi.nlm.nih.gov/10843193/).
- Mavridis I, Boviatsis E, Anagnostopoulou S. Anatomy of the human nucleus accumbens: a combined morphometric study. *Surg Radiol Anat*. 2011; 33(5): 405–414, doi: [10.1007/s00276-010-0766-6](https://doi.org/10.1007/s00276-010-0766-6), indexed in Pubmed: [21203764](https://pubmed.ncbi.nlm.nih.gov/21203764/).
- Mavridis I, Boviatsis E, Anagnostopoulou S. Stereotactic anatomy of the human nucleus accumbens: from applied mathematics to microsurgical accuracy. *Surg Radiol Anat*. 2011; 33(7): 583–594, doi: [10.1007/s00276-011-0804-z](https://doi.org/10.1007/s00276-011-0804-z), indexed in Pubmed: [21437651](https://pubmed.ncbi.nlm.nih.gov/21437651/).
- Neto LL, Oliveira E, Correia F, et al. The human nucleus accumbens: where is it? A stereotactic, anatomical and magnetic resonance imaging study. *Neuromodulation*. 2008; 11(1): 13–22, doi: [10.1111/j.1525-1403.2007.00138.x](https://doi.org/10.1111/j.1525-1403.2007.00138.x), indexed in Pubmed: [22150987](https://pubmed.ncbi.nlm.nih.gov/22150987/).
- Nota NM, Burke SM, den Heijer M, et al. Brain sexual differentiation and effects of cross-sex hormone therapy in transpeople: A resting-state functional magnetic resonance study. *Neurophysiol Clin*. 2017; 47(5-6): 361–370, doi: [10.1016/j.neucli.2017.09.001](https://doi.org/10.1016/j.neucli.2017.09.001), indexed in Pubmed: [29029883](https://pubmed.ncbi.nlm.nih.gov/29029883/).
- Patenaude B, Smith SM, Kennedy DN, et al. A Bayesian model of shape and appearance for subcortical brain segmentation. *Neuroimage*. 2011; 56(3): 907–922, doi: [10.1016/j.neuroimage.2011.02.046](https://doi.org/10.1016/j.neuroimage.2011.02.046), indexed in Pubmed: [21352927](https://pubmed.ncbi.nlm.nih.gov/21352927/).
- Patenaude BM. Bayesian statistical models of shape and appearance for subcortical brain segmentation [Internet] [Ph.D.]. 2007; University of Oxford. <http://ora.ox.ac.uk/objects/uuid:52f5fee0-60e8-4387-9560-728843e187b3>.
- Simon L, Kozák LR, Simon V, et al. Regional grey matter structure differences between transsexuals and healthy controls — a voxel based morphometry study. *PLoS One*. 2013; 8(12): e83947, doi: [10.1371/journal.pone.0083947](https://doi.org/10.1371/journal.pone.0083947), indexed in Pubmed: [24391851](https://pubmed.ncbi.nlm.nih.gov/24391851/).
- Spizzirri G, Duran FL, Chaim-Avancini TM, et al. Grey and white matter volumes either in treatment-naïve or hormone-treated transgender women: a voxel-based morphometry study. *Sci Rep*. 2018; 8(1): 736, doi: [10.1038/s41598-017-17563-z](https://doi.org/10.1038/s41598-017-17563-z), indexed in Pubmed: [29335438](https://pubmed.ncbi.nlm.nih.gov/29335438/).
- Zhou JN, Hofman MA, Gooren LJ, et al. A sex difference in the human brain and its relation to transsexuality. *Nature*. 1995; 378(6552): 68–70, doi: [10.1038/378068a0](https://doi.org/10.1038/378068a0), indexed in Pubmed: [7477289](https://pubmed.ncbi.nlm.nih.gov/7477289/).

Infrequent disposition of the first metacarpal artery related to anastomoses of the superficial and deep systems of the hand

H.F. Bianchi^{1, 2}, N.E. Ottone³ 

¹Anatomy Department, Medicine School, University of Buenos Aires, Argentina

²Anatomy Department, Instituto Universitario de Ciencias de la Salud, Fundacion Barcelo, Buenos Aires, Argentina

³Laboratory of Plastination and Anatomical Techniques, Research Centre for Dental Sciences (CICO), Department of Adults Integral Odontology, Dental School, Universidad de La Frontera, Temuco, Chile

[Received: 2 December 2019; Accepted: 30 March 2020]

There is an infrequent disposition of the first metacarpal artery which results in an anastomosis with the common palmar digital artery of the second space, forming an anastomotic system between the deep radial system and the superficial ulnar system. The radial system in turn, through the first dorsal interosseous artery, anastomoses with a collateral of the common palmar digital artery of the second space, ending as the ulnar palmar digital artery of the thumb and establishing a second anastomotic system. A third anastomosis is established in one case, between the common palmar digital artery of the fourth space and the fourth metacarpal artery. To this may be added the classic anastomosis between the superficial branch of the ulnar artery and the deep branch of the radial artery, i.e. the deep palmar arch. (Folia Morphol 2021; 80, 2: 448–454)

Key words: first metacarpal artery, superficial palmar arch, deep palmar arch, anastomosis

INTRODUCTION

In the course of an investigation into the morphology of the superficial palmar arch (SPA), we found an infrequent disposition of the first palmar metacarpal artery (1PMA), which is considered primordial in the circulation of the thumb to the point that it is called the princeps pollicis artery. We believe that surgeons must be familiar with the arterial disposition of this finger for the purposes of surgery and reconstruction procedures.

MATERIALS AND METHODS

The specimens were 28 fresh upper limbs undistinguished by sex, mean age 65 years. The specimens were injected manually, through axillary artery, with

elastomeric material (natural latex) (Meister®), using 10 mL syringes. Chemically, this elastomeric material is defined as a polymer of methylbutadiene or isoprene (C₅H₈), whose degree of polymerisation is 2500 to 4500. It is white in colour, and was coloured red with an acrylic paint (chemically, vinyl acetate) (Arcel®). Subsequently, the specimens were immersed in a 10% formalin fixative liquid container for 30 days, at room temperature. The upper limbs were dissected using appropriate instruments and stereoscopic microscopes 2×.

RESULTS

The findings reported were found in 3 cases, i.e. 10.7%, of the total sample.

Address for correspondence: Prof. Dr. N.E. Ottone, MD, PhD, Laboratory of Plastination and Anatomical Techniques, Research Centre for Dental Sciences (CICO), Dental School, Universidad de La Frontera, Francisco Salazar 01145, Casilla 54-D, Temuco, Chile, tel: +56452596935, e-mail: nicolas.ottone@ufrontera.cl

This article is available in open access under Creative Common Attribution-Non-Commercial-No Derivatives 4.0 International (CC BY-NC-ND 4.0) license, allowing to download articles and share them with others as long as they credit the authors and the publisher, but without permission to change them in any way or use them commercially.

Common characteristics were observed between cases 1 and 2. The SPAs of cases 1 and 2 may be considered of the incomplete type (Figs. 1A, 2A): the 1PMA originates in the deep palmar arch (DPA), close to the passage of the radial artery (RA) through the first dorsal interosseous muscle (1DIOM) (Figs. 1C, 2C). From this origin, the artery lies between the first dorsal interosseous muscle (1DIOM) and the adductor pollicis (AdP), emerging below its distal border, hidden by the flexor tendons of the index finger. At the point of emergence, it emits the radial artery of the index (Figs. 1A, B; 2A, B), which is seen emerging outside the flexor tendons of this finger. Located at first outside the flexor tendons, the 1PMA passes below them close to the metacarpophalangeal joint, and subsequently courses inside the flexor tendons (Figs. 1A, B; 2A, B) in the second interdigital space, where it anastomoses with the common palmar digital artery (CPDA) of the second space (CPDA2S) (Figs. 1A, B; 2A, B). It courses posterior of the palmar digital nerves of the index finger. Before it passes through the 1DIOM ring, the RA emits the first dorsal interosseous artery (1DIOA) (Figs. 1C, 2C), which anastomoses with a branch of the SPA at the edge of the first commisure. It continues its course parallel to the medial border of the thumb to become the ulnar palmar artery of the thumb (UPAT) (Figs. 1C, 2C). In case 1, shortly after its origin, the CPDA2S emits a branch which courses to proximal and divides into two branches (Fig. 1A): one distal, parallel to the medial border of the thumb, which anastomoses with the 1DIOA when it reaches the border of the first joint; and one proximal which ends up as the radial palmar artery of the thumb. Case 2 is similar (Fig. 2A), but it is the branch that anastomoses with the dorsal system that emits the radial palmar artery of the thumb. In case 1 (Fig. 1A), other arterial variations were observed: the origin of a common trunk for the CPDA of the fifth finger and the common palmar digital artery of the fourth space (CPDA4S), which has to pass below the extensor tendons and the common palmar digital nerve of this space, to arrive at the same point, receiving a fourth palmar metacarpal artery (4PMA) with which it anastomoses; and the presence of a highly developed second dorsal interosseous artery (2DIOA) located over the second dorsal interosseous muscle, which passes under the extensor tendons of the index and the junctura tendinum between this and the middle finger, and ends by joining the CPDA2S at the point where it divides into the medial

and radial proper palmar digital artery of the index and middle fingers (Fig. 1D).

Case 3 presents a complete SPA (Fig. 3A), with the thumb receiving blood supply from the ulnar proper palmar digital artery of the thumb and from radial proper palmar digital artery of the thumb, originating in the CPDA of the first space. The RA does not give origin to a 1DIOA. The 1PMA originates from the DPA and presents the same course and disposition as in the above cases (Fig. 3B, C). It also presents an arterial variation in the form of a DPA between the RA and a distal deep ulnar artery (Fig. 2C). The proximal deep ulnar artery turns over the DPA and a small anastomosis can be seen between the first and second metacarpal arteries (Fig. 3C).

DISCUSSION

Although our purpose is not to discuss the origins of the arteries of the thumb, in order to compare our findings we will say that the 1PMA has been considered the principal source of irrigation of the thumb, which is why it has been called princeps pollicis [15, 21]. Other authors argue that it should not be so called, as its contribution to the vascularisation of the thumb is inconstant [10, 15, 16, 18], or because its contribution is provided from other sources: 1DIOA [1–3, 9, 13, 15, 16, 18]; or SPA [1, 11, 15, 17]. Other authors again consider that the 1PMA and the princeps pollicis are different [8, 19]. A similar disposition to our findings appears in illustration by Dujarier [9], who calls the 1PMA as the arterial trunk of the index and — citing Farabeuf — considers this a habitual disposition, an opinion shared by Delorme [8]. Patil et al. [13] refers to a case, which we understand to be the same as those described here, in which a 1PMA is located in the second palmar space with termination as in our findings, but with the RA of the index passing under the tendons and nerves destined for the index, because the 1PMA is located in a medial position relative to these structures, while in our specimens it passes to radial. A similar disposition to ours is mentioned by Hashem et al. [12], without indicating which metacarpal artery is substituted. Occasionally a second palmar metacarpal artery (2PMA) can supply a CPDA of the second space [2], forming another anastomosis between elements of the DPA and the SPA [3, 4]. Coleman and Anson [7] say that the most developed artery destined for thumb should be called 1PMA.

Our cases confirm that it is not correct to call 1PMA as “princeps pollicis”, because it does not con-

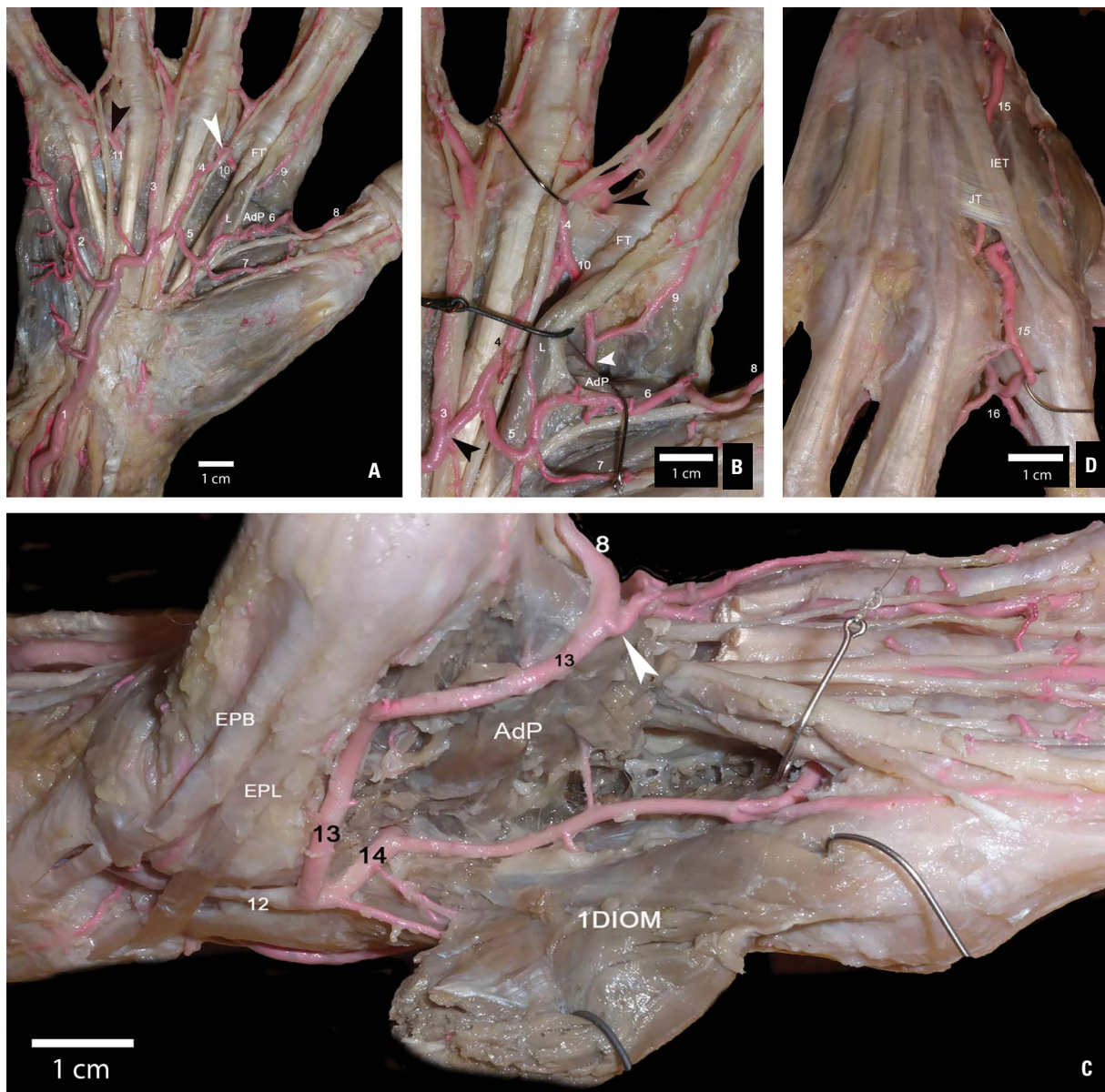


Figure 1. **A.** View of the palmar side of the hand; 1 — ulnar artery; 2 — common trunk for the common palmar digital artery of the fifth finger and the common palmar digital artery of the fourth space; 3 — common palmar digital artery of the third space; 4 — common palmar digital artery of the second space; 5 — branch of the common palmar digital artery of the second space; 6 — distal anastomotic branch of the first dorsal interosseous artery; 7 — proximal branch of the first dorsal interosseous artery; 8 — ulnar proper palmar digital artery of the index; 9 — radial artery of the index; 10 — anastomotic branch between first palmar metacarpal artery and common palmar digital artery of the second space (white arrow); 11 — common palmar digital artery of the fourth space (black arrow); FT — flexor tendons; L — lumbrical muscle; AdP — adductor pollicis muscle; **B.** Enlarged visualization of palmar side of the hand on the first and second interosseous space; white arrow — first palmar metacarpal artery; black arrow: anastomosis between second dorsal interosseous artery and common palmar digital artery of the second space; 3 — common palmar digital artery of the third space; 4 — common palmar digital artery of the second space; 5 — branch of the common palmar digital artery of the second space; 6 — distal anastomotic branch of the first dorsal interosseous artery; 7 — proximal branch of the first dorsal interosseous artery; 8 — ulnar proper palmar digital artery of the index; 9 — radial artery of the index; 10 — anastomotic branch between first palmar metacarpal artery and common palmar digital artery of the second space (white arrow); FT — flexor tendons; AdP — adductor pollicis muscle; **C.** View of the dorsal side of the hand; 12 — radial artery; 13 — first dorsal interosseous artery (white arrow: anastomosis with medial branch of common palmar digital artery of the second space); 8 — ulnar proper palmar digital artery of the index; 14 — first palmar metacarpal artery; 1DIOM — first dorsal interosseous muscle (reclined and sectioned at the level of the interosseous ring); AdP — m. adductor pollicis; EPB — m. extensor pollicis brevis; EPL — m. extensor pollicis longus; **D.** View of the dorsal side of the hand, from the first interosseous space, with recline of the first dorsal interosseous muscle; 15 — second dorsal interosseous artery; 16 — proper palmar digital arteries; IET — index extensor tendons; JT — juncturae tendineum.

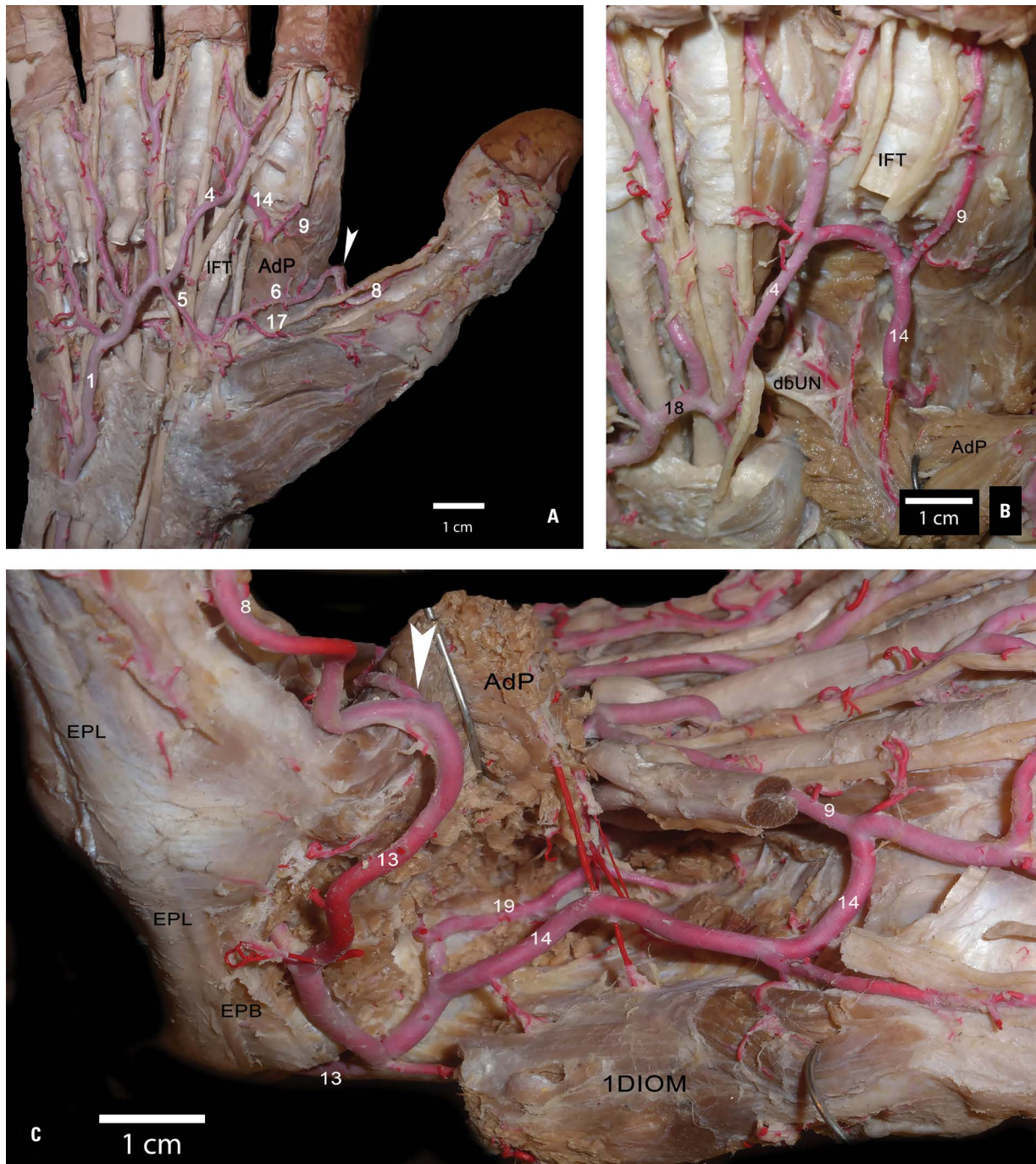


Figure 2. **A.** View of the palmar side of the hand; 1 — ulnar artery; 4 — common palmar digital artery of the second space; 5 — branch of the common palmar digital artery of the second space; 6 — distal anastomotic branch of the first dorsal interosseous artery; 8 — ulnar proper palmar digital artery of the thumb; 9 — radial artery of the index; 14 — first palmar metacarpal artery; 17 — radial proper palmar digital artery of the thumb; AdP — m. adductor pollicis; IFT — index flexor tendons; **B.** Enlarged visualization of palmar side of the hand; 4 — common palmar digital artery of the second space; 9 — radial artery of the index; 14 — first palmar metacarpal artery; 18 — superficial palmar arch; AdP — m. adductor pollicis; dbUN — deep branch of the ulnar nerve; IFT — index flexor tendons; **C.** View of the dorsal and palmar side of the hand, from the first interosseous space, with recline of the first dorsal interosseous muscle; 8 — ulnar proper palmar digital artery of the thumb; 9 — radial artery of the index; 13 — first dorsal interosseous artery; 14 — first palmar metacarpal artery; 19 — deep palmar arch; AdP — m. adductor pollicis; EPB — m. extensor pollicis brevis; EPL — m. extensor pollicis longus; 1DIOM — first dorsal interosseous muscle; white arrow — anastomosis between distal branch of the common palmar digital artery of the second space with the first dorsal interosseous artery.

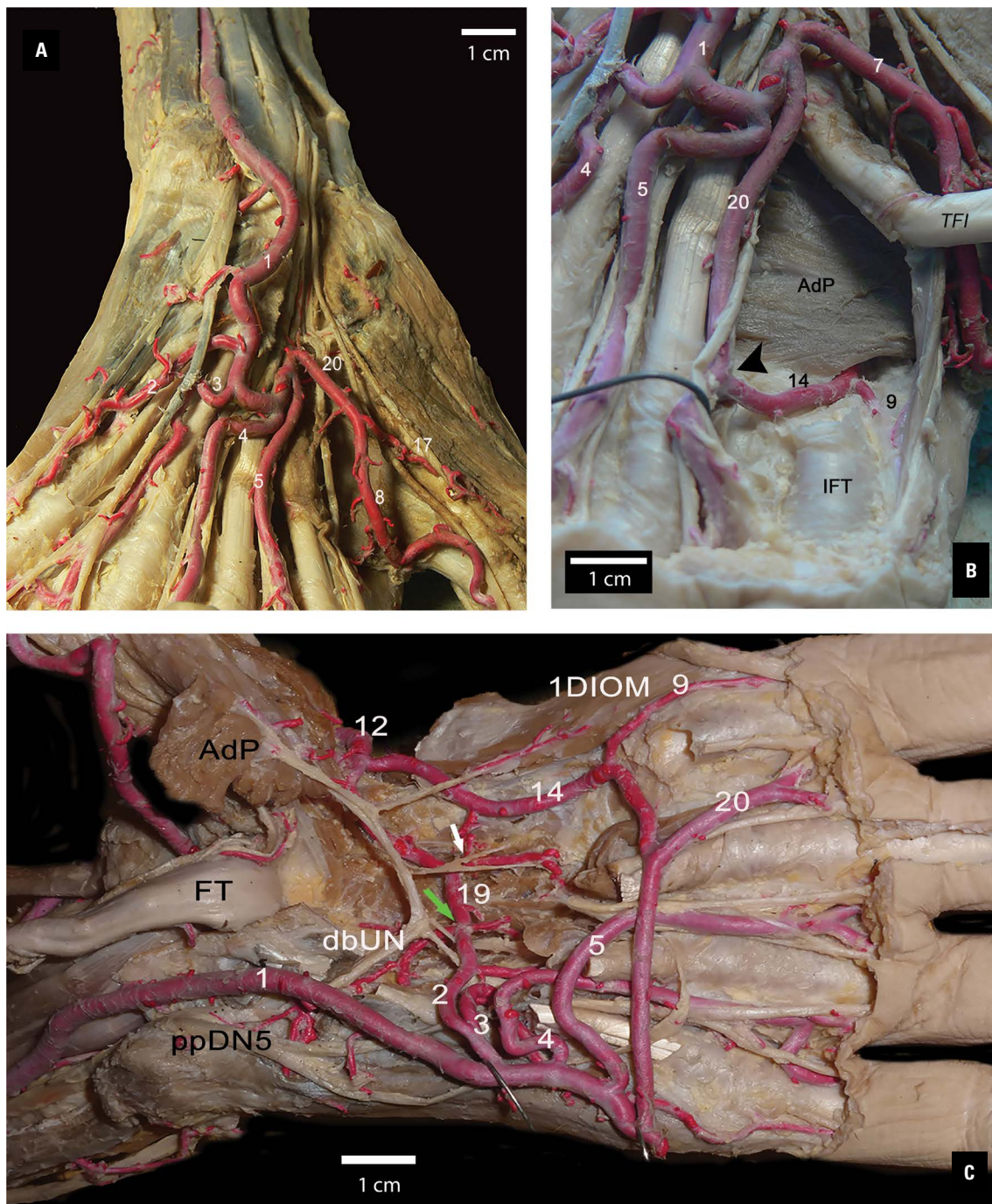


Figure 3. **A.** View of the palmar side of the hand; 1 — ulnar artery; 2 — common trunk for the common palmar digital artery of the fifth finger and the common palmar digital artery of the fourth space; 3 — common palmar digital artery of the third space; 4 — common palmar digital artery of the second space; 5 — branch of the common palmar digital artery of the second space; 8 — ulnar proper palmar digital artery of the thumb; 17 — radial proper palmar digital artery of the thumb; 20 — common palmar digital artery of the first space; **B.** Enlarged visualisation of palmar side of the hand, with recline of the index flexor tendon, and visualisation of m. adductor pollicis; 1 — ulnar artery; 4 — common palmar digital artery of the second space; 5 — branch of the common palmar digital artery of the second space; 7 — proximal branch of the first dorsal interosseous artery; 9 — radial artery of the index; 14 — first palmar metacarpal artery; 20 — common palmar digital artery of the first space; AdP — m. adductor pollicis; IFT — index flexor tendons; black arrow — anastomosis with common palmar digital artery of the second space; **C.** View of the palmar side of the hand, with recline of the thumb; 1 — ulnar artery; 2 — common trunk for the common palmar digital artery of the fifth finger and the common palmar digital artery of the fourth space; 3 — common palmar digital artery of the third space; 4 — common palmar digital artery of the second space; 5 — branch of the common palmar digital artery of the second space; 9 — radial artery of the index; 12 — radial artery; 14 — first palmar metacarpal artery; 19 — deep palmar arch; 20 — common palmar digital artery of the first space; white arrow — anastomosis between first palmar metacarpal artery and second palmar metacarpal artery; green arrow — anastomosis between deep branch of ulnar artery and deep palmar arch; ppDN5 — proper palmar digital nerve of fifth digit; dbUN — deep branch of the ulnar nerve; FT — flexor tendons; AdP — m. adductor pollicis; 1DIOM — first dorsal interosseous muscle.

tribute to the vascularisation of the thumb in any of them: in two cases this is provided by 1DIOA which ends up as ulnar proper palmar digital artery of the thumb. In case 1 the radial proper palmar digital artery of the thumb originates from the branch which has originated in the CPDA2S, and in case 2 from the distal branch from the same origin, anastomosing with the dorsal system. In case 3, both radial proper palmar digital artery of the index come from the SPA.

In all cases, the 1PMA (Fig. 1A) presents an anastomosis which differs from the classic configuration between the deep radial and the superficial ulnar systems via an indirect anastomosis between two collateral branches of those systems, the CPDA2S and the 1PMA, in the second digital space, although it originates in the first space. The same occurs in other cases of anastomosis between the radial and ulnar systems, most frequently originating in the SPA and the 1DIOA [1, 2, 15, 18]. Anastomoses between the SPA and the 1PMA or princeps pollicis were mentioned by Browning and Morton [6], but none of these cases are similar to our findings. In all the cases investigated, the 1PMA supplies the radial artery of the index [15, 16, 18]. We do not think it appropriate, even in cases like this, to call it the arterial trunk of the index as Dujarier does [9], although it could be justified in case 2, since the volume of the 1PMA is greater than that of the CPDA, which appears to be anastomosed with the 1PMA and not the other way round. The volume of the ulnar proper palmar digital artery of the thumb supplied by the 1DIOA is dominant, coinciding with other findings [15, 18]; this justifies preference for its use in implants and revascularisation [19]. In 2 of our findings, the RA was the principal source of irrigation of the thumb [1].

In specimen 1, simultaneous arterial variations were observed, such as presence of the common trunk of origin of the CPDAs for the fifth and fourth spaces, similar to that reported by Singh et al. [14] and Hasham [12]; however, these authors identified a different course of the common trunk, as well as an anastomosis of the CPDA of the fourth finger with a 4PMA, and a 2DIOA. This anastomosis reinforced the circulation of the second interdigital space instead of supplying it [3], giving rise to another indirect anastomosis between the SPA and DPA.

We agree with Rodríguez-Niedenführ et al. [20], who considered that the arteries develop from shoots, initially capillary plexuses, and that they become differentiated from proximal to distal. In this process,

some become definitive blood vessels, while others disappear or present incomplete development.

Although the incidence of modifications in arterial disposition is low, occlusions of the RA due to cannulation or trauma (Mozersky cited by Parks [18]) may have consequences such as ischaemia or acute vascular insufficiency of the thumb. We believe that caution must be exercised in surgical approaches to the radial side of the hand, where arterial variations are more frequent [4, 5], for example in aponeurotic retractions, lesions of the flexor tendons of the index, and in primary or secondary repairs. There is also a risk in the pollicisation of the index finger [12]. In some cases, the use of a Doppler ultrasound scan or angiography needs to be considered to ensure that the surgery is well planned.

CONCLUSIONS

We confirm the presence of anastomotic circuits between the superficial and deep systems of the hand, apart from the classic anastomosis between the SPA and DPA, occurring between their collateral arteries: 1PMA and CPDA2S, 1DIOA and SPA, 4PMA with CDPA4S, 2DIOA and proper palmar digital artery of the second interdigital space, in addition to those reported between the 2PMA and the CPDA. Their presence may explain why many serious hand injuries have a favourable evolution, including injuries to the thumb where the circulation is not restricted to a single artery. Considering the frequency of arterial modifications in the radial side of the hand, their possible presence must be taken in mind when carrying out both invasive and non-invasive procedures.

Ethical considerations

We complied with all the protocols and requirements established by the Government of the City of Buenos Aires, Argentina ("Protocol for the treatment of dead bodies, dead births, segments and anatomical parts in GCBA hospitals. Government of the City of Buenos Aires, Argentina, 2014").

REFERENCES

1. Ames EL, Bissonnette M, Acland R, et al. Arterial anatomy of the thumb. *J Hand Surg.* 1993; 18(4): 427–436, doi: [10.1016/0266-7681\(93\)90141-2](https://doi.org/10.1016/0266-7681(93)90141-2), indexed in Pubmed: [8409651](https://pubmed.ncbi.nlm.nih.gov/8409651/).
2. Bataineh ZM, Moqattash ST. A complex variation in the superficial palmar arch. *Folia Morphol.* 2006; 65(4): 406–409, indexed in Pubmed: [17171624](https://pubmed.ncbi.nlm.nih.gov/17171624/).
3. Bianchi HF, Leiro R. The arterial trunk of the thumb-index digital collaterals. *Surg Radiol Anat.* 1987; 9(1): 63–67, doi: [10.1007/BF02116855](https://doi.org/10.1007/BF02116855), indexed in Pubmed: [3112980](https://pubmed.ncbi.nlm.nih.gov/3112980/).

4. Bianchi H. Anatomy of the radial branches of the palmar arch. Variations and surgical importance. *Hand Clin.* 2001; 17(1): 139–146, doi: [10.1016/s0749-0712\(21\)00607-7](https://doi.org/10.1016/s0749-0712(21)00607-7), indexed in Pubmed: [11280157](https://pubmed.ncbi.nlm.nih.gov/11280157/).
5. Bianchi HF, Vargas CA, Ottone NE. Unusual ending of the second dorsal metacarpal artery as proper palmar digital arteries. *Folia Morphol.* 2018; 77(2): 393–396, doi: [10.5603/FM.a2017.0084](https://doi.org/10.5603/FM.a2017.0084), indexed in Pubmed: [28933803](https://pubmed.ncbi.nlm.nih.gov/28933803/).
6. Browning HC, Morton DE. The arterial pattern in the hand. *Yale J Biol Med.* 1955; 28(1): 37–55, indexed in Pubmed: [13257262](https://pubmed.ncbi.nlm.nih.gov/13257262/).
7. Coleman SS, Anson BJ. Arterial patterns in the hand based upon a study of 650 specimens. *Surg Gynecol Obstet.* 1961; 113: 409–424, doi: [10.1097/00006534-196201000-00028](https://doi.org/10.1097/00006534-196201000-00028), indexed in Pubmed: [13694610](https://pubmed.ncbi.nlm.nih.gov/13694610/).
8. Delorme E. De la ligature des artères de la paume de la main et en particulier des artères profondes et des artères de la plante du pied. Masson, Paris 1882.
9. Dujarier C. Anatomie des membres, dissection-anatomie topographique. G Steinheil, Paris 1905.
10. Earley M. The arterial supply of the thumb, first web and index finger and its surgical application. *J Hand Surg Br.* 1986; 11(2): 163–174, doi: [10.1016/0266-7681\(86\)90253-6](https://doi.org/10.1016/0266-7681(86)90253-6), indexed in Pubmed: [3734551](https://pubmed.ncbi.nlm.nih.gov/3734551/).
11. Erbil M, Aktekin M, Denk CC, et al. Arteries of the thumb originating from the superficial palmar arch: five cases. *Surg Radiol Anat.* 1999; 21(3): 217–220, doi: [10.1007/BF01630906](https://doi.org/10.1007/BF01630906), indexed in Pubmed: [10431337](https://pubmed.ncbi.nlm.nih.gov/10431337/).
12. Hashem AM, Knackstedt RW, Bernard S, et al. Variations in the origins and absence of the common digital arteries of the hand: a cadaveric study. *J Hand Surg Eur Vol.* 2018; 43(10): 1054–1058, doi: [10.1177/1753193418764289](https://doi.org/10.1177/1753193418764289), indexed in Pubmed: [29558847](https://pubmed.ncbi.nlm.nih.gov/29558847/).
13. Patil J, Kumar N, Aithal A, et al. An eccentric anatomical variation of palmar vascular pattern: Report of surgical challenging vascular variation. *J Med Sci.* 2016; 36(6): 240, doi: [10.4103/1011-4564.196372](https://doi.org/10.4103/1011-4564.196372).
14. Singh S, Lazarus L, De Gama BZ, et al. An anatomical investigation of the superficial and deep palmar arches. *Folia Morphol.* 2017; 76(2): 219–225, doi: [10.5603/FM.a2016.0050](https://doi.org/10.5603/FM.a2016.0050), indexed in Pubmed: [27665957](https://pubmed.ncbi.nlm.nih.gov/27665957/).
15. Miletin J, Sukop A, Baca V, et al. Arterial supply of the thumb: systemic review. *Clin Anat.* 2017; 30(7): 963–973, doi: [10.1002/ca.22973](https://doi.org/10.1002/ca.22973), indexed in Pubmed: [28791730](https://pubmed.ncbi.nlm.nih.gov/28791730/).
16. Murakami T, Takaya K, Outi H. The origin, course and distribution of arteries to the thumb, with special reference to the so-called A. princeps pollicis. *Okajimas Folia Anat Jpn.* 1969; 46(2): 123–137, doi: [10.2535/ofaj1936.46.2-3_123](https://doi.org/10.2535/ofaj1936.46.2-3_123), indexed in Pubmed: [5820050](https://pubmed.ncbi.nlm.nih.gov/5820050/).
17. Ottone N, Prum N, Dominguez M, et al. Analysis and clinical importance of superficial arterial palmar irrigation and its variants over 86 cases. *Int J Morphol.* 2010; 28(1), doi: [10.4067/s0717-95022010000100022](https://doi.org/10.4067/s0717-95022010000100022).
18. Parks B, Arbelaez J, Horner R. Medical and surgical importance of the arterial blood supply of the thumb. *J Hand Surgery Am.* 1978; 3(4): 383–385, doi: [10.1016/s0363-5023\(78\)80044-6](https://doi.org/10.1016/s0363-5023(78)80044-6), indexed in Pubmed: [681725](https://pubmed.ncbi.nlm.nih.gov/681725/).
19. Ramírez AR, Gonzalez SM. Arteries of the thumb: description of anatomical variations and review of the literature. *Plast Reconstr Surg.* 2012; 129(3): 468e–476e, doi: [10.1097/PRS.0b013e3182402d43](https://doi.org/10.1097/PRS.0b013e3182402d43), indexed in Pubmed: [22373995](https://pubmed.ncbi.nlm.nih.gov/22373995/).
20. Rodríguez-Niedenführ M, Burton GJ, Deu J, et al. Development of the arterial pattern in the upper limb of staged human embryos: normal development and anatomic variations. *J Anat.* 2001; 199(Pt 4): 407–417, doi: [10.1046/j.1469-7580.2001.19940407.x](https://doi.org/10.1046/j.1469-7580.2001.19940407.x), indexed in Pubmed: [11693301](https://pubmed.ncbi.nlm.nih.gov/11693301/).
21. Sappey CP. *Trattato di Anatomia*. Vol. 2. Detkin, Napoli 1897.

A tale of two arteries: dual posterior cerebral arteries with vascular bridges. A possible protective pattern?

Y. Mansour^{1, 2}, R. Kulesza¹

¹Department of Anatomy, Lake Erie College of Osteopathic Medicine, Erie, PA, United States

²Department of Otolaryngology and Facial Plastic Surgery, Henry Ford Macomb, Clinton Twp, MI, United States

[Received: 19 June 2020; Accepted: 1 July 2020]

Stroke is a common morbidity and a frequent cause of disability and even death. The impact of cerebrovascular events is dictated by the brain region involved and can be complicated by anatomical variations. One of the most common variations impacting the cerebral vasculature is the presence of a foetal posterior cerebral artery. This vessel arises from the internal carotid artery instead of the basilar artery and is often associated with more extensive injury in cerebrovascular events. Herein, we report the case of a 60-year-old male who had numerous arterial abnormalities, including a kink and a coil of the left internal carotid, two posterior communicating arteries on the right and two posterior cerebral arteries (PCA) on the left, one arising from the internal carotid (foetal PCA) and one from the basilar. The foetal PCA supplied the thalamus, splenium of the corpus callosum and primary visual cortex. The basilar PCA supplied the midbrain and parts of the occipital lobe. These PCA were connected to each other by a vascular bridge and the foetal PCA was connected to the middle cerebral artery by an additional vascular bridge. This vascular pattern would appear to provide collateral support around blockages in the internal carotid and main stem middle and PCA. (Folia Morphol 2021; 80, 2: 455–459)

Key words: variation, cerebral, vasculature, foetal

INTRODUCTION

Stroke is a leading cause of death and a major cause of disability [6]. Stroke, its treatment and subsequent mortality can be complicated by variations in arterial patterns. One of the most common intracranial arterial variations is persistence of the foetal posterior communicating artery (PCOM), which occurs in approximately 20% of subjects [5, 7, 8, 10]. Therefore, clinical knowledge of both normal and variant cerebrovascular patterns is important in predicting vascular risk, recognising common and atypical stroke syndromes and planning neurointerventions [2, 10, 11].

Herein, we report a rare case of a subject with two posterior cerebral arteries (PCA) on the left and two PCOMs on the right side. Additionally, this subject had two abnormalities involving his left internal carotid artery [1, 4]. We discuss the embryological origin of these vessels and their potential impacts/ consequences.

CASE REPORT

Case presentation

A 60-year-old male presented to the emergency department with the chief complaints of seeing

Address for correspondence: Dr. Y. Mansour, Department of Anatomy, Lake Erie College of Osteopathic Medicine, 1858 West Grandview Blvd, Erie, PA 16509, United States, tel: (419) 442-1354, e-mail: ymansour49902@med.lecom.edu

This article is available in open access under Creative Common Attribution-Non-Commercial-No Derivatives 4.0 International (CC BY-NC-ND 4.0) license, allowing to download articles and share them with others as long as they credit the authors and the publisher, but without permission to change them in any way or use them commercially.

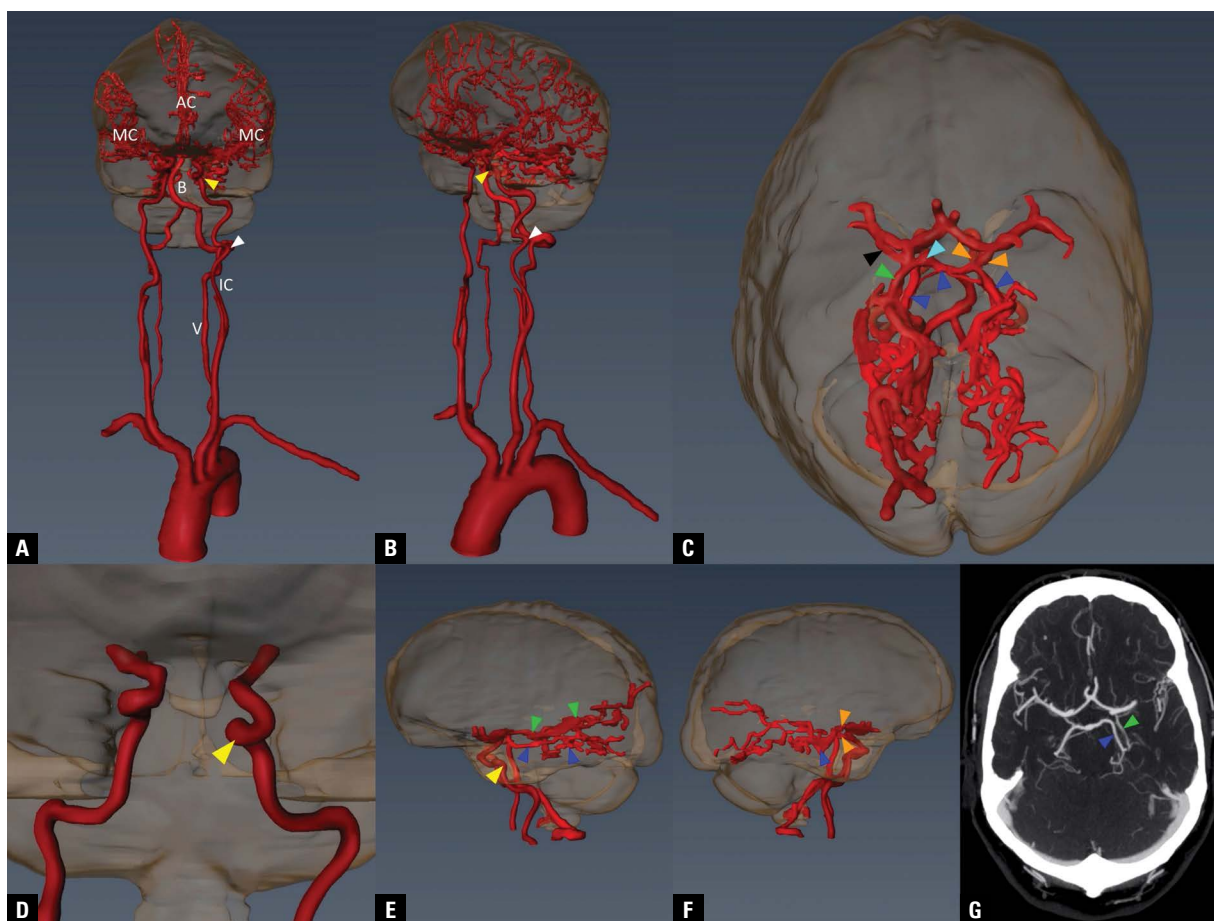


Figure 1. Images of three-dimensional reconstruction (A–F) and computed tomography angiography (G) of this patient's arterial pattern. The views in panels A and B show the carotid and vertebral arteries (V) from their origin in the neck. The formation of the basilar artery (B) appeared normal. In the neck, the left internal carotid (IC) artery (ICA) had both a coil (yellow arrowhead; observed also in panel D) and a kink (white arrowhead). The ICAs were found to give rise to the middle (MC) and anterior (AC) cerebral arteries. In panels C, E and F the abnormal posterior cerebral arteries (PCA) and posterior communicating artery (PCOM) are identified. Panel C shows a top-down view. The blue arrowheads indicate the basilar PCA [bPCA], and the orange arrowhead indicates the PCOM. On the patient's right side there were two PCOMs. On the patient's left, there were two PCAs: one from the ICA (foetal PCA [fPCA]) and one from the basilar (bPCA). There were two vascular bridges on the left: one from the fPCA to the middle cerebral artery (black arrowhead) and one from the fPCA to the bPCA. Panel E shows the two PCAs from the patient's left side. Panel F shows the double PCOM from the patient's right side. Panel G shows a slice from the computed tomography angiography study. The fPCA is indicated by the green arrowhead and the bPCA is indicated by the blue arrowhead.

flashing lights in his right eye and left arm weakness. His neurological exam was non-focal. He underwent computed tomography (CT) and computed tomography angiography (CTA) imaging to rule out possible stroke. The CT series was imported into Amira (Version 6.7.0) and a slice by slice approach was taken to create a three-dimensional (3D) rendering of both his carotid and vertebral circulations.

Imaging findings

Examination of the 3D model (Fig. 1A, B) of this subject's cerebral vasculature revealed multiple variations. On the left internal carotid artery (ICA) there was a cervical kink (Fig. 1, white arrowhead) and

a cavernous coil (Fig. 1, yellow arrowhead) [2]. On the left side there was a PCA that arose at the basilar bifurcation ("basilar PCA" [bPCA]; Fig. 1, blue arrowheads) and a foetal PCA (fPCA; Fig. 1, green arrowheads) that continued directly from the ICA. The CT and 3D reconstruction clearly showed both of these arteries wrapping around the midbrain and distributing within the occipital lobe. The fPCA had a vascular bridge to the middle cerebral artery (MCA; Fig. 1, black arrowhead) and bPCA (Fig. 1, light blue arrowhead). On the right side there were two PCOMs (Fig. 1, orange arrowheads). A video of the 3D reconstruction can be found here: <https://drive.google.com/file/d/1AfJl9W-wRe4LNhH2gNECjPqQa75hRtiY/view?usp=sharing>.

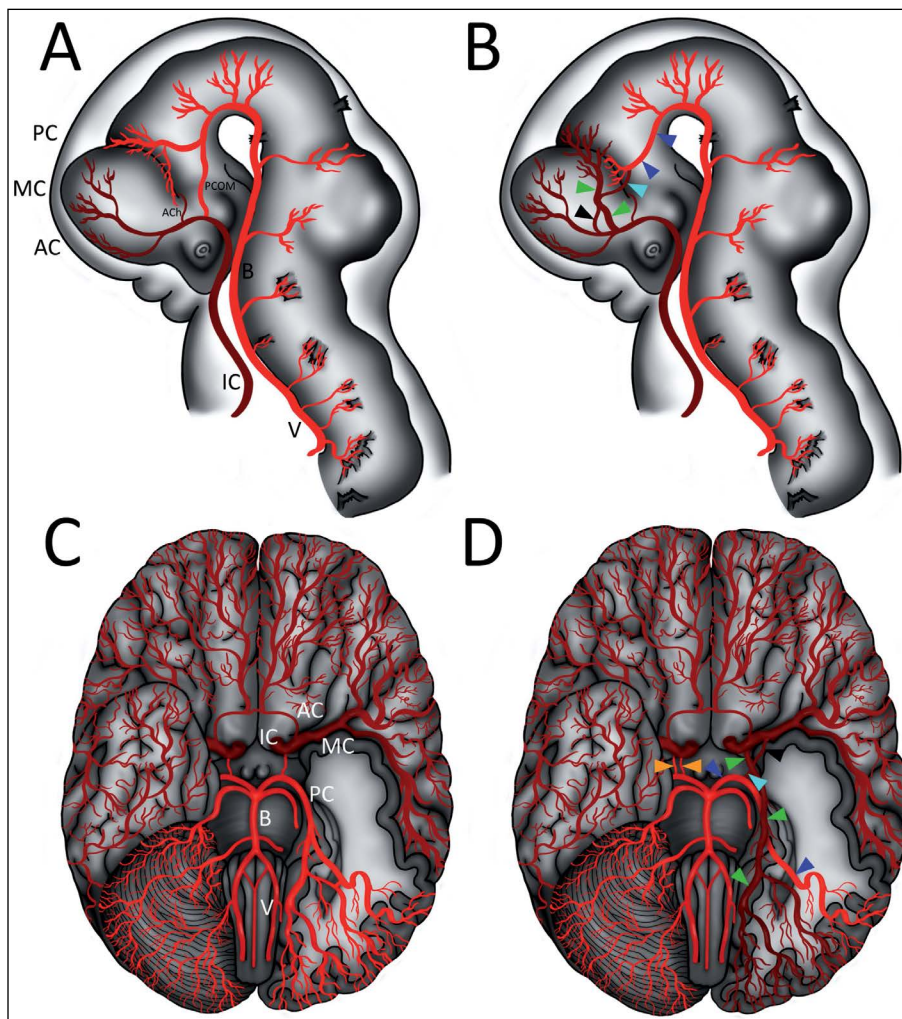


Figure 2. Proposed arterial patterns. Shown in panel **A** is the typical embryologic pattern that forms the posterior communicating artery (PCOM) and posterior cerebral arteries (PCA) and the pattern we propose developed in this subject in panel **B**. Shown in panel **C** is the typical arterial pattern and in panel **D** is the arterial pattern discovered in this case study. Key to arrowheads: green — foetal PCA, blue — basilar PCA, orange — PCOM, black — foetal PCA to middle cerebral artery vascular bridge, light blue — foetal PCA to basilar PCA vascular bridge; AC — anterior cerebral arteries; ACh — anterior choroidal; B — basilar artery; IC — internal carotid; MC — middle cerebral arteries; PC — posterior cerebral arteries; V — vertebral arteries.

Correlative anatomy

Developmentally, the arterial supply of the brain is derived from vertebral and ICAs and the PCOM initially connects these two circulations (Fig. 2A). The PCA is normally derived from the PCOM and supplies the midbrain, diencephalon and caudal telencephalon. We propose that the arterial variations identified in this subject arose from the altered embryonic vascular pattern shown schematically in Figure 2B. Careful study of the 3D reconstruction and CTA series allowed us to develop a vascular map (Fig. 2C, D). In the CTA, we carefully traced branches from both the bPCA and fPCA and constructed maps of their vascular territories. In this subject, the bPCA supplied the central aspect of the midbrain and the lateral aspect of the

PCA territory (Fig. 3). The fPCA supplied the lateral aspect of the midbrain, the entire thalamus, splenium of the corpus callosum and the medial aspect of the occipital lobe including the calcarine sulcus.

DISCUSSION

The PCA normally develops as a direct continuation of the embryonic PCOM and supplies the midbrain, thalamus and occipital lobe. The most common variant of the PCOM/PCA is an fPCA where this vessel forms as a direct branch from the ICA [5, 7, 8, 10]. When an fPCA is present, the ICA provides arterial supply to the entire cerebral hemisphere, thalamus and midbrain via anterior, middle and posterior cerebral arteries. Accordingly, if a subject with an fPCA

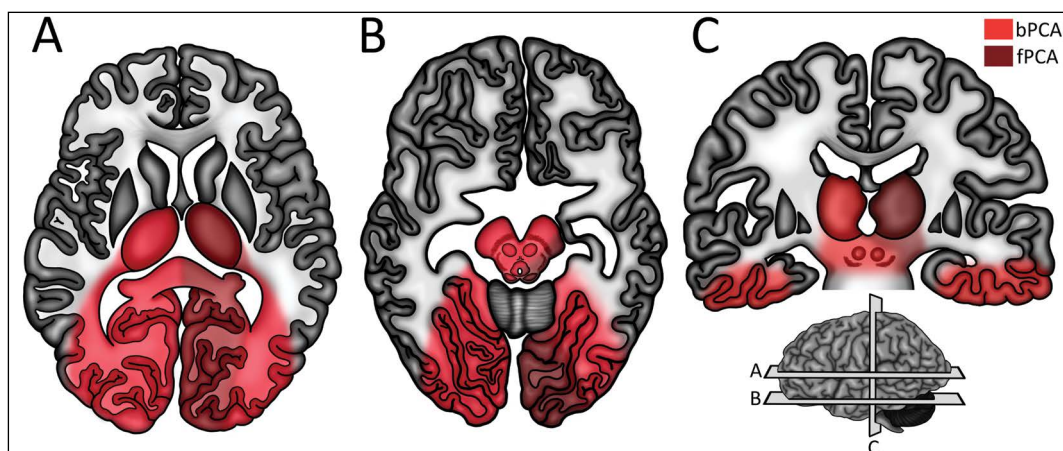


Figure 3. Shown in panels **A** and **B** are transverse slices through the brain at the level of the thalamus (**A**) and midbrain (**B**). Shown in panel **C** is a coronal slice through the brain at the level of the thalamus. On the left side of each image (the patient's right), the territory of the basilar posterior cerebral arteries (bPCA) is shown in red. On the right side of each image (the patient's left) the territory of both the bPCA and foetal posterior cerebral arteries (fPCA) are shown. Note that in the subject of this case study, the fPCA supplies the lateral and posterior midbrain, thalamus, splenium of the corpus callosum and primary visual cortex. The inset in the bottom right shows the approximate levels and locations of the slices shown in panels **A–C**.

has a blockage of the ICA, this can impair blood flow to the entire thalamus and cerebral hemisphere with often catastrophic results [5, 9]. However, the presence of an fPCA is not considered an additional risk factor for stroke [3].

The subject of this case presentation has both a bPCA and an fPCA and these vessels made major connections to other vessels in the left hemisphere through vascular bridges. In our 3D reconstruction and study of the CTA series, we found the fPCA and bPCA were connected by a small vascular bridge near their origin [8], but there were no additional connections between the two PCAs. Further, we found an additional vascular bridge connecting the fPCA and MCA. Together, we believe this arterial architecture may provide a protective support pattern. Specifically, if the subject of this case presentation were to have a thrombus in the ICA or in the main stem of fPCA, bPCA or MCA on the left, the bridging vessels could provide collateral support and potentially prevent ischaemia or infarct in PCA or MCA territories.

CONCLUSIONS

The fPCA is a fairly common anatomical variation involving arterial support of the midbrain, thalamus and occipital lobe. Vascular compromise involving the anterior circulation in a subject with an fPCA is often associated with extensive ischaemia and poor outcomes. However, the presence of vascular bridges

connecting the fPCA to surrounding main-stem vessels may provide protective anastomoses.

Acknowledgements

The authors would like to thank the University of Pittsburgh Medical Centre Hamot, Department of Neurology for the CT and CTA data.

REFERENCES

1. Benson JC, Brinjikji W, Messina SA, et al. Cervical internal carotid artery tortuosity: A morphologic analysis of patients with acute ischemic stroke. *Interv Neuroradiol.* 2020; 26(2): 216–221, doi: [10.1177/1591019919891295](https://doi.org/10.1177/1591019919891295), indexed in Pubmed: [31766962](https://pubmed.ncbi.nlm.nih.gov/31766962/).
2. Brzegowy P, Polak J, Wnuk J, et al. Middle cerebral artery anatomical variations and aneurysms: a retrospective study based on computed tomography angiography findings. *Folia Morphol.* 2018; 77(3): 434–440, doi: [10.5603/FM.a2017.0112](https://doi.org/10.5603/FM.a2017.0112), indexed in Pubmed: [29235088](https://pubmed.ncbi.nlm.nih.gov/29235088/).
3. de Monyé C, Dippel DWJ, Siepmann TAM, et al. Is a fetal origin of the posterior cerebral artery a risk factor for TIA or ischemic stroke? A study with 16-multidetector-row CT angiography. *J Neurol.* 2008; 255(2): 239–245, doi: [10.1007/s00415-008-0699-8](https://doi.org/10.1007/s00415-008-0699-8), indexed in Pubmed: [18274809](https://pubmed.ncbi.nlm.nih.gov/18274809/).
4. Griessenauer CJ, Yalcin B, Matusz P, et al. Analysis of the tortuosity of the internal carotid artery in the cavernous sinus. *Childs Nerv Syst.* 2015; 31(6): 941–944, doi: [10.1007/s00381-015-2674-x](https://doi.org/10.1007/s00381-015-2674-x), indexed in Pubmed: [25749877](https://pubmed.ncbi.nlm.nih.gov/25749877/).
5. Klimek-Piotrowska W, Kopeć M, Kochana M, et al. Configurations of the circle of Willis: a computed tomography angiography based study on a Polish population. *Folia Morphol.* 2013; 72(4): 293–299, doi: [10.5603/fm.2013.0049](https://doi.org/10.5603/fm.2013.0049), indexed in Pubmed: [24402749](https://pubmed.ncbi.nlm.nih.gov/24402749/).

6. Stroke. Centers for Disease Control and Prevention. <https://www.cdc.gov/stroke/index> (2020, April 7).
7. Uchino A, Saito N, Takahashi M, et al. Variations of the posterior cerebral artery diagnosed by MR angiography at 3 tesla. *Neuroradiology*. 2016; 58(2): 141–146, doi: [10.1007/s00234-015-1614-5](https://doi.org/10.1007/s00234-015-1614-5), indexed in Pubmed: [26553301](https://pubmed.ncbi.nlm.nih.gov/26553301/).
8. Vasović L, Trandafilović M, Jovanović I, et al. An excess vessel in the posterior part of the human cerebral arterial circle (CAC): a case series. *BMC Neurol*. 2010; 10: 53, doi: [10.1186/1471-2377-10-53](https://doi.org/10.1186/1471-2377-10-53), indexed in Pubmed: [20573186](https://pubmed.ncbi.nlm.nih.gov/20573186/).
9. Yu J, Qu L, Xu B, et al. Current understanding of dolicho-arteriopathies of the internal carotid artery: a review. *Int J Med Sci*. 2017; 14(8): 772–784, doi: [10.7150/ijms.19229](https://doi.org/10.7150/ijms.19229), indexed in Pubmed: [28824313](https://pubmed.ncbi.nlm.nih.gov/28824313/).
10. Zampakis P, Panagiotopoulos V, Petsas T, et al. Common and uncommon intracranial arterial anatomic variations in multi-detector computed tomography angiography (MDCTA). What radiologists should be aware of. *Insights Imaging*. 2015; 6(1): 33–42, doi: [10.1007/s13244-014-0381-x](https://doi.org/10.1007/s13244-014-0381-x), indexed in Pubmed: [25680324](https://pubmed.ncbi.nlm.nih.gov/25680324/).
11. Zurada A, Gielecki JS. A novel formula for the classification of blood vessels according to symmetry, asymmetry and hypoplasia. *Folia Morphol*. 2007; 66(4): 339–345, indexed in Pubmed: [18058758](https://pubmed.ncbi.nlm.nih.gov/18058758/).

Rare combined variations of the coeliac trunk, accessory hepatic and gastric arteries with co-occurrence of double cystic arteries

A. Mazurek, A. Juszczak^{ID}, J.A. Walocha^{ID}, A. Pasternak^{ID}

Department of Anatomy, Jagiellonian University Medical College, Krakow, Poland

[Received: 22 March 2020; Accepted: 29 April 2020]

Many variations of the coeliac trunk and hepatic or gallbladder arterial supply have been reported before in many cadaveric and radiologic studies. In this case we present combined anomalies observed in dissected cadaver of a 73-year-old female. The left gastric artery arises directly from the abdominal aorta and gives two branches: the right inferior phrenic artery in the proximal part and the accessory left hepatic artery in the distal part. The coeliac trunk is bifurcated into the common hepatic artery and the splenic artery. The right gastric artery emerges from the left hepatic artery. The right hepatic artery gives two cystic arteries and the accessory right hepatic artery is noticed arising from the posterior superior pancreaticoduodenal artery. The deep cystic artery and the right inferior phrenic artery give hepatic branches. Also, we noticed small accessory biliary duct going to the cystic duct. This complexity of the arterial supply with anomaly of the biliary ducts has many surgical implications which will be herein discussed. (Folia Morphol 2021; 80, 2: 460–466)

Key words: anatomical variations, accessory hepatic artery, gastric artery, double cystic arteries, right inferior phrenic artery

INTRODUCTION

The importance of the arterial supply of the liver, gallbladder and upper gastrointestinal tract has been noticed in plenty of surgical procedures. Calot (1891) [7] was the first, who emphasized the position of the cystic artery during cholecystectomy. Adachi (1928) [1] elaborated the classification of variations of the coeliac trunk, which is also used currently, and Michels [23] was one of the first researches who described and classified the variability of the hepatic arterial supply. According to recent reviews, the most common variation in types of the incomplete coeliac trunk was the hepatosplenic trunk present in 3.88% of cases with the left gastric artery (LGA) originating from the ab-

dominal aorta in 99.87% [35]. The right gastric artery (RGA) most frequently goes from the proper hepatic artery — in 53% of cases [11]. Accessory or replaced hepatic arteries are observed in 30.8%. The accessory left hepatic artery (LHA), which occurs in 8.2%, mostly arises from the LGA (7.9%) and the accessory right hepatic artery (RHA) described in 5.6% of cases with the most often origin from the superior mesenteric artery (SMA) in 5.4% [17]. Double cystic arteries (or multiple cystic arteries) are observed in 8.9% [3]. The right inferior phrenic artery most frequently originates from the abdominal aorta [32]. Our case comprises more or less frequent variations of all mentioned arteries with accessory branches to liver, which makes

Address for correspondence: A. Pasternak, MD, PhD, Department of Anatomy, Jagiellonian University Medical College, ul. Kopernika 12, 31–034 Kraków, Poland, tel: +48 12 422 95 11, fax: +48 12 422 95 11, e-mail: artur.pasternak@uj.edu.pl

This article is available in open access under Creative Common Attribution-Non-Commercial-No Derivatives 4.0 International (CC BY-NC-ND 4.0) license, allowing to download articles and share them with others as long as they credit the authors and the publisher, but without permission to change them in any way or use them commercially.

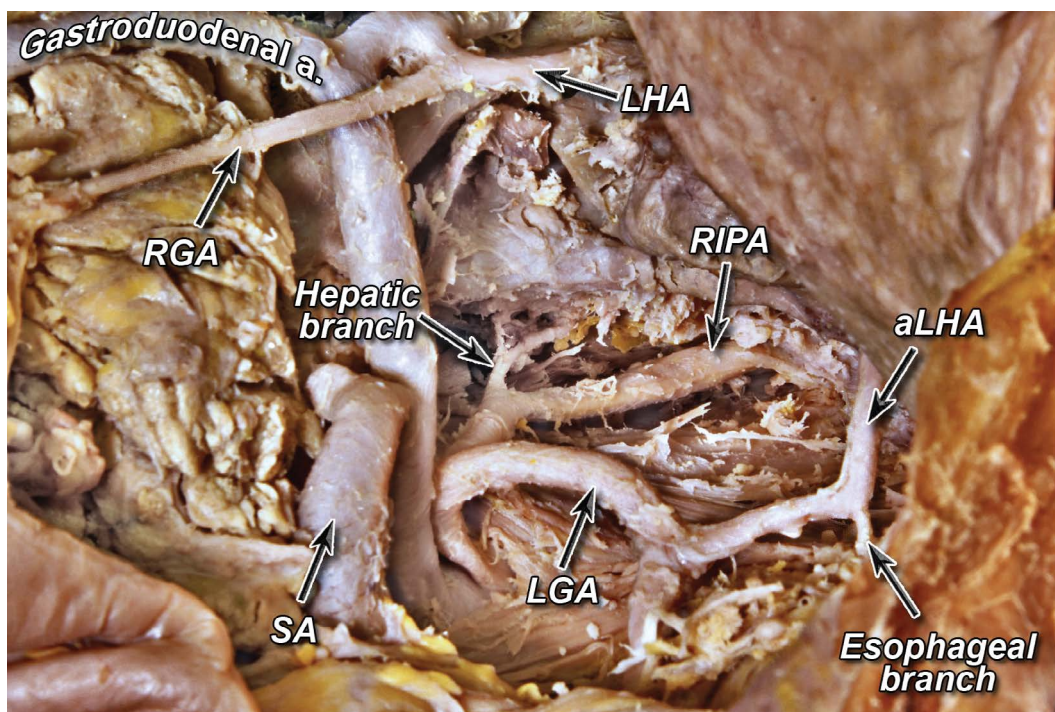


Figure 1. Emphasized small branches to the oesophagus and the liver; LHA — left hepatic artery; aLHA — accessory left hepatic artery; LGA — left gastric artery; RGA — right gastric artery; RIPA — right inferior phrenic artery; SA — splenic artery.

it unique and allows us to show the significance of them in clinical practice for example in transplantology, cholecystectomy or surgical oncology.

CASE REPORT

During a routine dissection for teaching purpose of the 73-year-old female 10% formalin-fixed cadaver many multiple anomalies were observed. In the abdominal cavity any previous surgical interventions were not noted. At the level of Th12-L1 the LGA (4.74 mm in diameter) arose separately from the abdominal aorta (18.15 mm in diameter) curving a geniculate flexure and branched off the right inferior phrenic artery (RIPA; 2.75 mm in width) at 8.51 mm from the origin and heading up gave the second branch, i.e. the accessory left hepatic artery (aLHA; 2.89 mm in diameter) after 25.15 mm in length course from the proximal branching. The small hepatic branch (1.17 mm in diameter) arose from the RIPA at 18.18 mm distal from the beginning. The aLHA gave small oesophageal branch only 1.30 mm in diameter (Fig. 1). The hepatosplenic trunk (5.33 mm in width) originated from the abdominal aorta 4.39 mm below the LGA and divided into the common hepatic artery (CHA) and the splenic artery (SA). The CHA (4.67 mm in width) coursed along the upper margin of the pancreas and branched into the

proper hepatic artery (PHA) and the gastroduodenal artery (GDA) at 27.41 mm from the beginning. The PHA (3.68 mm in diameter and 9.07 mm in length) ended up with bifurcating into the RHA and the LHA. The LHA (2.87 in width) branched to the RGA (1.79 mm diameter) at the 2.40 mm from the origin and the RGA run down 25.94 mm to the lesser curvature crossing the CHA above (Fig. 2). The RHA (3.34 mm in diameter) passed behind the common hepatic duct (CHD) at the 15.46 mm from the beginning of its course and gave rise to the superficial cystic artery (1.63 mm in width) 3.20 mm after crossing the CHD (diameter 7.07 mm), gave small branch to the liver and at the 5.24 mm from the first branching and gave the deep cystic artery (dCA; 1.48 mm in diameter) from which also arose a small hepatic branch (1.05 mm in width) (Fig. 3). The GDA at the 16.14 mm from the origin feeding branches to the right gastroepiploic artery (2.62 mm) and the anterior superior pancreaticoduodenal artery (1.95 mm diameter) and then the GDA run down as the posterior superior pancreaticoduodenal artery (PSPD) along the head of pancreas giving the proximal branch (at the 16.37 mm from the previous branching), travelled 9.89 mm and divided into the accessory right hepatic artery (aRHA) and the distal branch (1.93 mm). The aRHA (2.10 mm in diameter and 40.32 mm in length) run parallel to

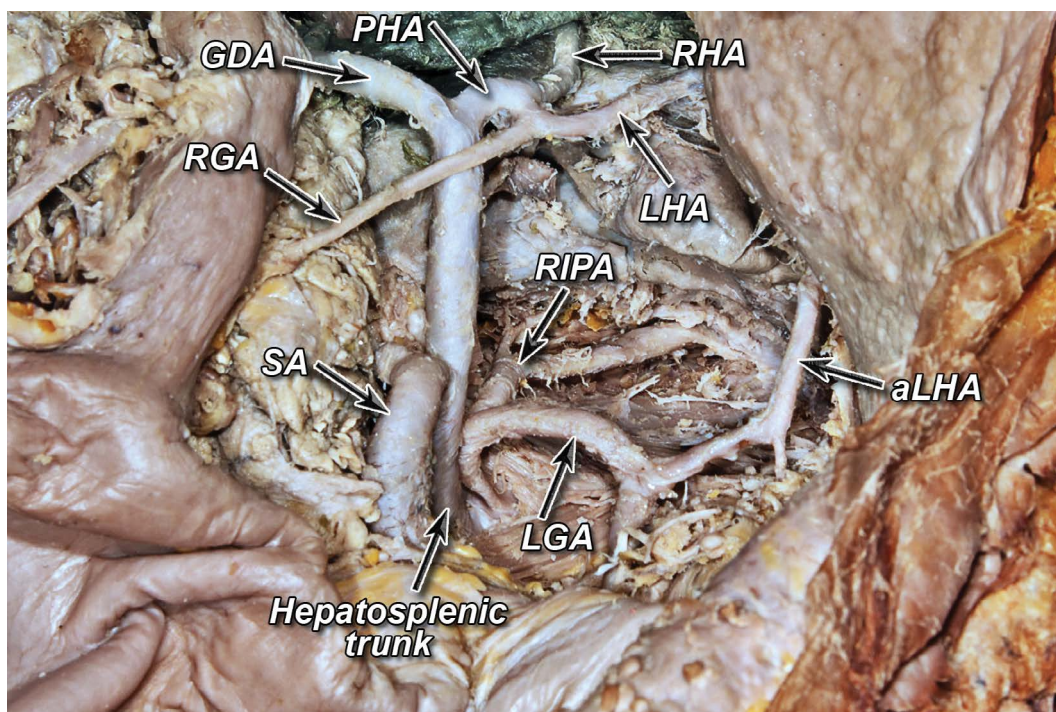


Figure 2. Complex variations of the coeliac trunk. Left gastric artery (LGA) arises independently from the abdominal aorta and branches to the right inferior phrenic artery (RIPA) which gives off small hepatic branch and in the distal course from the LGA arises the accessory left hepatic artery. Right gastric artery (RGA) originates from the left hepatic artery (LHA); aLHA — accessory left hepatic artery; GDA — gastroduodenal artery; PHA — proper hepatic artery; RHA — right hepatic artery; SA — splenic artery.



Figure 3. Cystic arteries with branches to the liver arising from the deep cystic artery (dCA) and right hepatic artery (RHA); sCA — superficial cystic artery; LHA — left hepatic artery; aLHA — accessory left hepatic artery; aRHA — accessory right hepatic artery; GDA — gastroduodenal artery; CBD — common biliary duct; CD — cystic duct; CHD — common hepatic duct.

the common bile duct and travelled to the biliary fossa dividing into two branches before entering the liver. In the vicinity of this area the small accessory biliary duct (0.52 mm in width) going directly from V segment of the liver and at 14.58 mm from the

origin merged to the cystic duct in the midway of its course (Fig. 4). Diameters of observed abnormal arteries are summarised in Table 1.

In this case, the arterial blood supply for the liver was supported by five arteries: RHA, LHA, aRHA gave

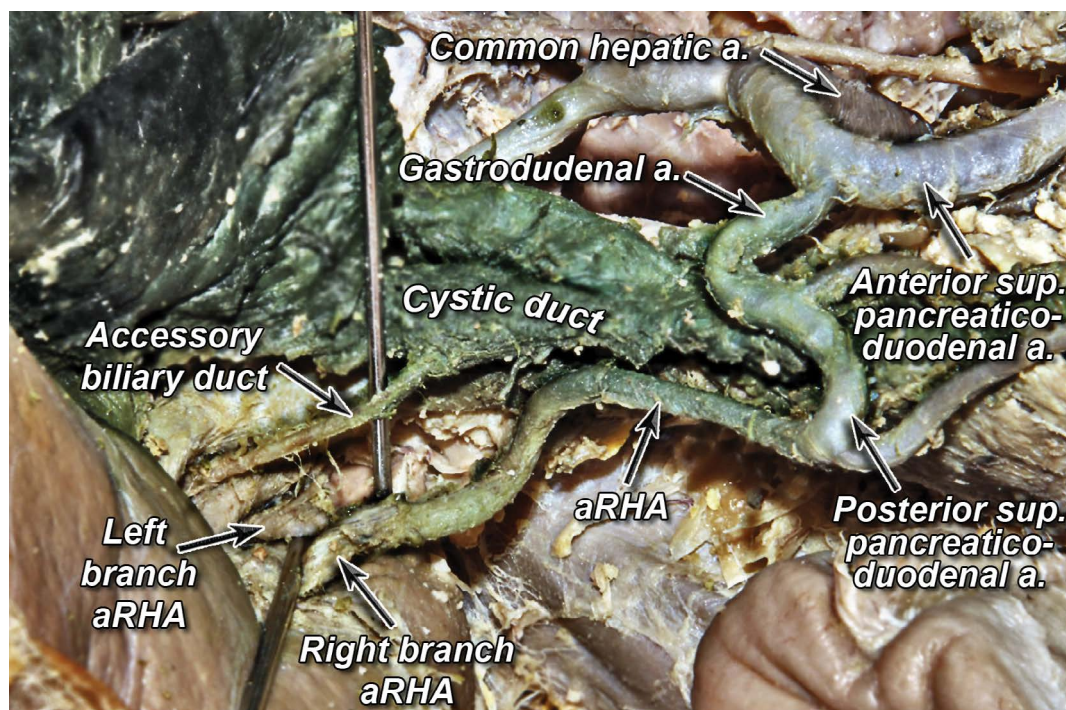


Figure 4. Accessory right hepatic artery (aRHA) emerges from the posterior superior pancreaticoduodenal artery and travels parallel to the common bile duct to the gallbladder fossa, dividing into right and left branch. Small accessory biliary duct (also known as cystohepatic duct) goes directly from the liver (V segment) and reaches the cystic duct at its halfway.

Table 1. Summarised measurements of abnormal arteries in our case

Artery	Diameter [mm]
Left gastric artery	4.74
Right gastric artery	1.79
Right inferior phrenic artery	2.75
Accessory left hepatic artery	2.89
Accessory right hepatic artery	2.10
Deep cystic artery	1.48
Superficial cystic artery	1.63

off the PSPD, aLHA from the LGA, RIPA and the small branch arising from the dCA.

DISCUSSION

The variations of the incomplete coeliac trunk were repeatedly described by researches. As we mentioned, the hepatosplenic trunk was observed in 3.88% of cases with the abdominal aorta as the origin feeding of the LGA in 99.87%. More rarely the LGA arises from the SMA (0.76%) or it is absent (0.38%) [35]. The prevalence of the cases where the LGA gave off the RIPA is estimated at 2% to 4.1% [25]. Some of the researches distinguished the gastrophrenic trunk [16,

22, 26, 28, 32, 37] as the common origin of the inferior phrenic artery and the LGA. The majority of the used classifications do not perceive it as a trunk and in most cases it is recognised in association with presence of the hepatosplenic trunk [16, 22, 26, 28] but the co-occurrence with the hepatosplenic trunk also was described [32, 37]. According to the classification proposed by Whitley et al. [35], this type of trunk is not included but we came to the conclusion that it is important to mention this fact. Inferior phrenic arteries more frequently originate asymmetrically [5]. Right inferior phrenic arteries commonly arise from the abdominal aorta (49%) or the coeliac trunk (41%), less frequently from the LGA or renal arteries (5.5%) [4, 5, 19]. Aslaner et al. [4] noted higher frequency of the RIPA arising from the renal artery with co-occurrence of the incomplete coeliac trunk.

The anomaly of the RGA arising from the LHA was observed by Yamagami et al. [36] in 25.3% of cases and the Eckmann and Krahn [11] estimated the frequency to be 15%.

Variations of the hepatic arteries were commonly described by many authors [9, 15, 17, 23]. In the review presented by the Cirrochi et al. [9], the aLHA originating from the LGA was noticed in 3.60% (694/19284) of cases (including Michels' and Hiatt's

Table 2. Prevalence of variations observed in our case

Variation	Frequency (%)
RIPA from LGA	2–4.1
Hepatosplenic trunk (LGA from abdominal aorta)	3.87
RGA from hepatic artery	15–25.3
aLHA from LGA	3.6–8.2
aRHA from GDA	0.04
Multiple CAs	8.9
Cystohepatic duct (including cholecystohepatic duct)	0.2–2.3

aLHA — accessory left hepatic artery; aRHA — accessory right hepatic artery; CA — cystic artery; GDA — gastroduodenal artery; LGA — left gastric artery; RGA — right gastric artery; RIPA — right inferior phrenic artery

findings). Jin et al. [17] estimated the prevalence of the aLHA originating from the LGA to be 8.2% (total cases 10,211). The aRHA was observed in 5.6% of cases. Although the cases of aRHA arising from the GDA were revealed in approximately 0.04% (4 of 10,211 cases which also included branches of the GDA) [17], the pancreaticoduodenal artery branched the aRHA in some of them [2]. Juszczak et al. [18] presented similar interesting case wherein also both accessory hepatic arteries were observed, aLHA arising from the LGA which arose independently from the abdominal aorta and aRHA from SMA as the feeding origin but contrary to our case the PHA did not divide into two hepatic arteries. Also, they observed both inferior phrenic arteries originating from the hepatosplenic trunk (positioned opposite to the vertebral L1 level) and both branched off superior adrenal arteries [18].

Andall et al. [3] revealed the weighted percentage of the multiple cystic arteries was circa 8.9%, with the highest noted number of arteries being four, but some researchers found this variation in 30.2% [24] and 28.3% [6] of cases. Small accessory biliary duct emerging from the liver parenchyma found in our case is classified as cystohepatic duct and the incidence of its variation (also including the cholecystohepatic duct which directly drains to the gallbladder) ranges between 0.2% and 2.3%. This variation might occur with normal CHD and common biliary duct anatomy likewise in our case [30, 31]. Frequencies of observed variations were presented in Table 2.

Variations observed in our case reflect processes during foetal development. The most common variation is trifurcation of the coeliac trunk (LGA, CHA and SA) separately to the SMA which is generated by interruption of anastomosis between third and

fourth ventral mesenteric root [33]. The interruption between 1 and 2 mesenteric roots with termination of anastomosis between 3 and 4 roots cause occurrence of LGA independently originating from abdominal aorta with hepatosplenic trunk. Higher prevalence of some variations of hepatic arteries also could be explained by analysing the embryological development. Primarily the LHA arises from the LGA and the RHA from SMA and there is an absence of the PHA which originates from the CHA after its bifurcation. If hepatic branches of the LGA or SMA with division PHA into RHA and LHA are preserved, these branches are named as accessory left hepatic artery and accessory right hepatic artery respectively. This fact clarifies high frequency of aLHA originating from the LGA and aRHA from the SMA. Grugacz et al. reported case wherein all foetal origins of hepatic arteries were preserved with presence of the middle hepatic artery feeding IV segment of the liver [14]. In our findings we observed abnormal primary right hepatic artery arising from branch of the GDA transitioned during development to the aRHA. Mahajan et al. presented similar case of preserved foetal pattern of liver's blood supply, also they reported occurrence of oesophageal branch arising from replaced LHA which emerged from LGA [21].

Doubled cystic arteries with co-occurrence of accessory hepatic arteries were reported by some authors. Loukas et al. [20] described case wherein a small accessory cystic artery (CA) arose from PSPD with aLHA originating from LGA which emerged independently from abdominal aorta and the hepatosplenic trunk also was observed. Polguy et al. [27] revealed variant of GDA which gave off both accessory CA and aRHA which also gave off CA. No other anomalies of coeliac trunk and hepatobiliary vasculature were observed in this case. Dolensšek [10] described occurrence of doubled CAs (larger sCA and small dCA) both of which arose from aRHA. Similarly to our case both accessory hepatic arteries were present but the aRHA emerged from the SMA and the PHA was trifurcated into left, middle and right hepatic arteries with coexistence of classical trifurcation of the coeliac trunk. According to Andall et al. [3], the prevalence of CA arising from abnormal RHA (replaced or accessory) is estimated at 5.58%. In this research the frequency of GDA and PSPD as origin feeding of CA was 1.94% and 0.07% respectively.

Vascular abnormalities described in this case are significant in surgical practice. Using the critical view of safety method during laparoscopic cholecystec-

tomy the surgeon has to precisely identify vascular structures in the hepatobiliary triangle. In cases, wherein the origin feeding of the cystic artery is different than the RHA (LHA or GDA) or course of the cystic artery is anteriorly to the common hepatic duct, there is a high risk of ligation. Also, in variant of multiple cystic arteries one of the CAs could be overlooked leading to uncontrolled bleeding [3]. Although the postcholecystectomy bile leaks occur in 0.2–2% of cases, the surgeon should be careful with presence of the subvesical ducts during the procedure, especially if this duct drains to the cystic duct [29, 31].

Knowledge about variations of accessory or replaced hepatic arteries is crucial in planning intra-arterial chemotherapy in treatment of cancers or metastases (mainly metastases of the colorectal cancer) in liver because it is essential to find appropriate artery feeding occupied lobe by neoplasm to accurately arrange hepatic arterial infusion pump placement and avoid infusion to arteries supplying the other organs. This procedure also include the embolisation of the extra-hepatic arteries, such as RGA, pyloric artery and GDA [8, 13] and if accessory or replaced hepatic arteries arising from the embolised artery was not recognised it could cause hepatic ischaemia. In procedures of chemo-embolisation and radio-embolisation it is significant to consider blood circulation in interested segment provided by the extra-hepatic arteries including inferior phrenic arteries which usually supply segments I, II and VII. LGA and CA are also hepatic feeders, II, III segments and peri-vesicular region, respectively [13]. The RIPA is mentioned as one of the main extrahepatic collateral arteries which are supplying the hepatocellular carcinoma and usually in this case the diameter of the RIPA is larger than the diameter of the LIPA. The width of the RIPA feeding neoplasm in the liver ranged from 2 to 3.2 mm [5] and in another research the diameter greater than 2.5 mm was considered as indication of present collateral circulation [4].

Vascular anatomy of liver is also significant in transplantology, especially in living-donor liver transplantation, wherein right (adult recipient) or left lobe (paediatric recipient) is harvested because thorough analysis of liver vessels enables to preserve proper blood circulation in retained donor's lobe and guarantees appropriate liver regeneration. In surgical practice preservation of all found anomalies of hepatic arteries is preferred [8, 34] but some of them could be difficult to find during the procedure, for example the accessory LHA arising from the LGA [34]. Also, anomalies of the

hepatic biliary vascularisation should be verified (especially in harvesting the right lobe) to avoid bile leakage in recipients, which leads to graft rejection [8, 12].

CONCLUSIONS

Anatomical variations of the arterial blood supply of upper part of the abdomen have great importance in many surgical procedures and they are strongly associated with embryological development. Acquaintance about branching patterns of cystic arteries and hepatic arteries is significant in planning cholecystectomy or liver transplantation and in these procedures existence of accessory biliary duct should be concerned to avoid postsurgical complications. Abnormal branches to liver or gallbladder arising from gastroduodenal artery or posterior superior pancreaticoduodenal artery are rarely observed and knowledge about them facilitates better understanding about vascularisation of these organs.

REFERENCES

1. Adachi B. *Das Arteriensystem der Japaner*, vol II. Maruzen, Kyoto 1928: 16–64.
2. Ahn CS, Lee SG, Hwang S, et al. Anatomic variation of the right hepatic artery and its reconstruction for living donor liver transplantation using right lobe graft. *Transplant Proc.* 2005; 37(2): 1067–1069, doi: [10.1016/j.transproceed.2005.01.068](https://doi.org/10.1016/j.transproceed.2005.01.068), indexed in Pubmed: [15848624](https://pubmed.ncbi.nlm.nih.gov/15848624/).
3. Andall RG, Matusz P, du Plessis M, et al. The clinical anatomy of cystic artery variations: a review of over 9800 cases. *Surg Radiol Anat.* 2016; 38(5): 529–539, doi: [10.1007/s00276-015-1600-y](https://doi.org/10.1007/s00276-015-1600-y), indexed in Pubmed: [26698600](https://pubmed.ncbi.nlm.nih.gov/26698600/).
4. Aslaner R, Pekcevik Y, Sahin H, et al. Variations in the origin of inferior phrenic arteries and their relationship to celiac axis variations on CT angiography. *Korean J Radiol.* 2017; 18(2): 336–344, doi: [10.3348/kjr.2017.18.2.336](https://doi.org/10.3348/kjr.2017.18.2.336), indexed in Pubmed: [28246513](https://pubmed.ncbi.nlm.nih.gov/28246513/).
5. Basile A, Tsetis D, Montineri A, et al. MDCT anatomic assessment of right inferior phrenic artery origin related to potential supply to hepatocellular carcinoma and its embolization. *Cardiovasc Intervent Radiol.* 2008; 31(2): 349–358, doi: [10.1007/s00270-007-9236-x](https://doi.org/10.1007/s00270-007-9236-x), indexed in Pubmed: [18071790](https://pubmed.ncbi.nlm.nih.gov/18071790/).
6. Browne EZ. Variations in origin and course of the hepatic artery and its branches. *Surgery.* 1940; 8: 424–445.
7. Calot JF. *De la cholecystecomie*. Dissertation, Med Frc de Paris 1891.
8. Catalano OA, Singh AH, Uppot RN, et al. Vascular and biliary variants in the liver: implications for liver surgery. *Radiographics.* 2008; 28(2): 359–378, doi: [10.1148/rq.282075099](https://doi.org/10.1148/rq.282075099), indexed in Pubmed: [18349445](https://pubmed.ncbi.nlm.nih.gov/18349445/).
9. Cirocchi R, D'Andrea V, Amato B, et al. Aberrant left hepatic arteries arising from left gastric arteries and their clinical importance. *Surgeon.* 2020; 18(2): 100–112, doi: [10.1016/j.surge.2019.06.002](https://doi.org/10.1016/j.surge.2019.06.002), indexed in Pubmed: [31337536](https://pubmed.ncbi.nlm.nih.gov/31337536/).
10. Dolenšek J. Triple arterial blood supply to the liver and double cystic arteries. *Folia Morphol.* 2017; 76(3): 523–

- 526, doi: [10.5603/FM.a2017.0008](https://doi.org/10.5603/FM.a2017.0008), indexed in Pubmed: [28150275](https://pubmed.ncbi.nlm.nih.gov/28150275/).
11. Eckmann I, Krahn V. [Frequency of different sites of origin of the right gastric artery]. *Anat Anz.* 1984; 155(1-5): 65–70, indexed in Pubmed: [6721206](https://pubmed.ncbi.nlm.nih.gov/6721206/).
 12. Fang C, Yan S, Zheng S. Bile Leakage after Liver Transplantation. *Open Med (Wars).* 2017; 12: 424–429, doi: [10.1515/med-2017-0062](https://doi.org/10.1515/med-2017-0062), indexed in Pubmed: [29318188](https://pubmed.ncbi.nlm.nih.gov/29318188/).
 13. Favelier S, Germain T, Genson PY, et al. Anatomy of liver arteries for interventional radiology. *Diagn Interv Imaging.* 2015; 96(6): 537–546, doi: [10.1016/j.diii.2013.12.001](https://doi.org/10.1016/j.diii.2013.12.001), indexed in Pubmed: [24534562](https://pubmed.ncbi.nlm.nih.gov/24534562/).
 14. Gurgacz AM, Horbaczewska A, Klimek-Piotrowska W, et al. Variations in hepatic vascularisation: lack of a proper hepatic artery. Two case reports. *Folia Morphol.* 2011; 70(2): 130–134, indexed in Pubmed: [21630235](https://pubmed.ncbi.nlm.nih.gov/21630235/).
 15. Hiatt JR, Gabbay J, Busuttill RW. Surgical anatomy of the hepatic arteries in 1000 cases. *Ann Surg.* 1994; 220(1): 50–52, doi: [10.1097/0000658-199407000-00008](https://doi.org/10.1097/0000658-199407000-00008), indexed in Pubmed: [8024358](https://pubmed.ncbi.nlm.nih.gov/8024358/).
 16. Hirai Y, Yamaki K, Saga T, et al. An anomalous case of the hepato-spleno-mesenteric and the gastro-phrenic trunks independently arising from the abdominal aorta. *Kurume Med J.* 2000; 47(2): 189–192, doi: [10.2739/kurume-medj.47.189](https://doi.org/10.2739/kurume-medj.47.189), indexed in Pubmed: [10948660](https://pubmed.ncbi.nlm.nih.gov/10948660/).
 17. Jin W, Dong M, Pan J, et al. Rare combined variations of accessory left hepatic artery and accessory right hepatic artery: a case report and literature review. *Surg Radiol Anat.* 2020; 42(4): 443–447, doi: [10.1007/s00276-019-02396-4](https://doi.org/10.1007/s00276-019-02396-4), indexed in Pubmed: [31811353](https://pubmed.ncbi.nlm.nih.gov/31811353/).
 18. Juszczak A, Solewski B, Loukas M, et al. Unusual branching pattern of celiac trunk associated with supernumerary hepatic arteries and abnormal adrenal venous drainage: case study and review of the literature. *Folia Med Cracov.* 2017; 57(3): 29–36, indexed in Pubmed: [29263452](https://pubmed.ncbi.nlm.nih.gov/29263452/).
 19. Kim HC, Chung JW, Lee W, et al. Recognizing extrahepatic collateral vessels that supply hepatocellular carcinoma to avoid complications of transcatheter arterial chemoembolization. *Radiographics.* 2005; 25 Suppl 1: S25–S39, doi: [10.1148/rg.25si055508](https://doi.org/10.1148/rg.25si055508), indexed in Pubmed: [16227494](https://pubmed.ncbi.nlm.nih.gov/16227494/).
 20. Loukas M, Fergurson A, Louis RG, et al. Multiple variations of the hepatobiliary vasculature including double cystic arteries, accessory left hepatic artery and hepatosplenic trunk: a case report. *Surg Radiol Anat.* 2006; 28(5): 525–528, doi: [10.1007/s00276-006-0138-4](https://doi.org/10.1007/s00276-006-0138-4), indexed in Pubmed: [17006621](https://pubmed.ncbi.nlm.nih.gov/17006621/).
 21. Mahajan A, Tiwari S, Mishra S. A Unique Conglomeration of Variations in the Celiac, Hepatic, and Superior Mesenteric Artery: A Clinico-Embryological Perspective. *Int J Appl Basic Med Res.* 2018; 8(4): 256–258, doi: [10.4103/ijabmr.IJABMR_395_17](https://doi.org/10.4103/ijabmr.IJABMR_395_17), indexed in Pubmed: [30598915](https://pubmed.ncbi.nlm.nih.gov/30598915/).
 22. Matusz P, Loukas M, Iacob N, et al. Common stem origin of left gastric, right and left inferior phrenic arteries, in association with a hepatospleno-mesenteric trunk, independently arising from the abdominal aorta: case report using MDCT angiography. *Clin Anat.* 2013; 26(8): 980–983, doi: [10.1002/ca.22204](https://doi.org/10.1002/ca.22204), indexed in Pubmed: [23255305](https://pubmed.ncbi.nlm.nih.gov/23255305/).
 23. Michels NA. Newer anatomy of the liver and its variant blood supply and collateral circulation. *Am J Surg.* 1966; 112(3): 337–347, doi: [10.1016/0002-9610\(66\)90201-7](https://doi.org/10.1016/0002-9610(66)90201-7), indexed in Pubmed: [5917302](https://pubmed.ncbi.nlm.nih.gov/5917302/).
 24. Mizumoto R, Suzuki H. Surgical anatomy of the hepatic hilum with special reference to the caudate lobe. *World J Surg.* 1988; 12(1): 2–10, doi: [10.1007/BF01658479](https://doi.org/10.1007/BF01658479), indexed in Pubmed: [3344582](https://pubmed.ncbi.nlm.nih.gov/3344582/).
 25. Olewnik Ł, Waśniewska A, Polguy M, et al. Rare combined variations of renal, suprarenal, phrenic and accessory hepatic arteries. *Surg Radiol Anat.* 2018; 40(7): 743–748, doi: [10.1007/s00276-018-2026-0](https://doi.org/10.1007/s00276-018-2026-0), indexed in Pubmed: [29667030](https://pubmed.ncbi.nlm.nih.gov/29667030/).
 26. Piao DX, Ohtsuka A, Murakami T. Typology of abdominal arteries, with special reference to inferior phrenic arteries and their esophageal branches. *Acta Med Okayama.* 1998; 52(4): 189–196, doi: [10.18926/AMO/31299](https://doi.org/10.18926/AMO/31299), indexed in Pubmed: [9781269](https://pubmed.ncbi.nlm.nih.gov/9781269/).
 27. Polguy M, Podgórski M, Hogendorf P, et al. Variations of the hepatobiliary vasculature including coexistence of accessory right hepatic artery with unusually arising double cystic arteries: case report and literature review. *Anat Sci Int.* 2014; 89(3): 195–198, doi: [10.1007/s12565-013-0219-5](https://doi.org/10.1007/s12565-013-0219-5), indexed in Pubmed: [24310410](https://pubmed.ncbi.nlm.nih.gov/24310410/).
 28. Prasanna LC, Alva R, Sneha GK, et al. Rare variations in the origin, branching pattern and course of the celiac trunk: report of two cases. *Malays J Med Sci.* 2016; 23(1): 77–81, indexed in Pubmed: [27540329](https://pubmed.ncbi.nlm.nih.gov/27540329/).
 29. Schnelldorfer T, Sarr MG, Adams DB. What is the duct of Luschka? A systematic review. *J Gastrointest Surg.* 2012; 16(3): 656–662, doi: [10.1007/s11605-011-1802-5](https://doi.org/10.1007/s11605-011-1802-5), indexed in Pubmed: [22215244](https://pubmed.ncbi.nlm.nih.gov/22215244/).
 30. Schofield A, Hankins J, Sutherland F. A case of cholecystohepatic duct with atrophic common hepatic duct. *HPB (Oxford).* 2003; 5(4): 261–263, doi: [10.1080/13651820310001388](https://doi.org/10.1080/13651820310001388), indexed in Pubmed: [18332999](https://pubmed.ncbi.nlm.nih.gov/18332999/).
 31. Spanos CP, Syrakos T. Bile leaks from the duct of Luschka (subvesical duct): a review. *Langenbecks Arch Surg.* 2006; 391(5): 441–447, doi: [10.1007/s00423-006-0078-9](https://doi.org/10.1007/s00423-006-0078-9), indexed in Pubmed: [16927110](https://pubmed.ncbi.nlm.nih.gov/16927110/).
 32. Terayama H, Yi SQ, Tanaka O, et al. Common and separate origins of the left and right inferior phrenic artery with a review of the literature. *Folia Morphol.* 2017; 76(3): 408–413, doi: [10.5603/FM.a2017.0025](https://doi.org/10.5603/FM.a2017.0025), indexed in Pubmed: [28281724](https://pubmed.ncbi.nlm.nih.gov/28281724/).
 33. Wang Yi, Cheng C, Wang Lu, et al. Anatomical variations in the origins of the celiac axis and the superior mesenteric artery: MDCT angiographic findings and their probable embryological mechanisms. *Eur Radiol.* 2014; 24(8): 1777–1784, doi: [10.1007/s00330-014-3215-9](https://doi.org/10.1007/s00330-014-3215-9), indexed in Pubmed: [24859597](https://pubmed.ncbi.nlm.nih.gov/24859597/).
 34. Watson CJE, Harper SJF. Anatomical variation and its management in transplantation. *Am J Transplant.* 2015; 15(6): 1459–1471, doi: [10.1111/ajt.13310](https://doi.org/10.1111/ajt.13310), indexed in Pubmed: [25981150](https://pubmed.ncbi.nlm.nih.gov/25981150/).
 35. Whitley A, Oliverius M, Kocián P, et al. Variations of the celiac trunk investigated by multidetector computed tomography: Systematic review and meta-analysis with clinical correlations. *Clin Anat.* 2020; 33(8): 1249–1262, doi: [10.1002/ca.23576](https://doi.org/10.1002/ca.23576), indexed in Pubmed: [32012339](https://pubmed.ncbi.nlm.nih.gov/32012339/).
 36. Yamagami T, Nakamura T, Iida S, et al. Embolization of the right gastric artery before hepatic arterial infusion chemotherapy to prevent gastric mucosal lesions: approach through the hepatic artery versus the left gastric artery. *Am J Roentgenol.* 2002; 179(6): 1605–1610, doi: [10.2214/ajr.179.6.1791605](https://doi.org/10.2214/ajr.179.6.1791605), indexed in Pubmed: [12438063](https://pubmed.ncbi.nlm.nih.gov/12438063/).
 37. Yi SQ, Li J, Terayama H, et al. A rare case of inferior mesenteric artery arising from the superior mesenteric artery, with a review of the review of the literature. *Surg Radiol Anat.* 2008; 30(2): 159–165, doi: [10.1007/s00276-007-0298-x](https://doi.org/10.1007/s00276-007-0298-x), indexed in Pubmed: [18189117](https://pubmed.ncbi.nlm.nih.gov/18189117/).

Anatomical traps for arteriovenous fistula creation

Z.M. Ziętek^{1, 2}

¹Department of General Surgery and Transplantology, Pomeranian Medical University, Szczecin, Poland

²Department of Normal and Clinical Anatomy, Pomeranian Medical University, Szczecin, Poland

[Received: 7 May 2020; Accepted: 16 June 2020]

Background: The risk of complications in undisclosed vascular variability appears relatively likely. Therefore, it is important to assess the probability of encountering anatomical-topographic variability in the venous system of the upper limb. The catalogue of patterns of the upper limb venous system seems to be unlimited and should therefore be constantly updated. The aim of the study was to explore the venous system of upper extremity and discuss some problems that would be encountered with the formation of an arteriovenous fistula.

Results: In 17 (85%) explored upper limbs, the venous system showed a pattern similar to the reports already described. But in (15%) 3 of them, the venous system showed certain differences in relation to the accepted anatomical textbooks. Especially in one of them the anatomical variant of basilic and cephalic vein contrasted distinctly with the other veins. Based on the revealed anomalies, a statistical analysis of the probability of occurrence of any anatomical variant and the risk of complications associated with fistula creation was conducted. Even on such small group an assessed probability of anatomical variability of the upper limb venous system was statistically significant at $p < 0.0244$ (odds ratio 0.0828; 95% confidence interval 0.0095–0.7252).

Conclusions: The probability of any anatomical-topographic variability in the venous system of the upper limb should be considered as statistically significant. Only intense anatomical dissections would undoubtedly help to avoid some anatomical traps and then minimise some complications in the creation of arteriovenous fistulas. (Folia Morphol 2021; 80, 2: 467–470)

Key words: veins, upper limb, anatomy variant, arteriovenous fistula, complications

INTRODUCTION

Since the development of the first arteriovenous access, many reports have appeared, not always flattering it [5, 9, 10, 13, 15, 18]. Particularly risky is an undisclosed variability of vascular system of the upper limb which could discourage surgeons from using a classic approach [1, 11–13].

In many published reports, rates of arteriovenous fistula complications were assessed [1]. Most of them included aneurysm, infection, terminal ischaemia syndrome, thrombosis or venous hypertension [1, 17]. It seems that all of this could have contributed to the collapse of an interest in the creation of arteriovenous fistulas [11]. So at the end of the 70s, other alternative

Address for correspondence: Prof. Z. Ziętek, Department of General Surgery and Transplantology, Pomeranian Medical University, Al. Powstańców Wielkopolskich 72, 70–111 Szczecin, Poland, tel: +48 91 4661480, mobile: 503502735, e-mail: zzietek@poczta.onet.pl

This article is available in open access under Creative Common Attribution-Non-Commercial-No Derivatives 4.0 International (CC BY-NC-ND 4.0) license, allowing to download articles and share them with others as long as they credit the authors and the publisher, but without permission to change them in any way or use them commercially.

vascular access approaches began to be used [4, 12, 17, 18]. However, longer observations of the results revealed them as more dangerous with even more severe complications [1, 4, 11, 12, 17, 18].

Many authors emphasized that complications associated with fistula formation started with technical problems related to vascular topography [9, 11]. The traditional anatomy textbooks offer little description of the upper limb veins and are particularly silent in regards to their variations. The number of patterns seems to be unlimited and therefore should be constantly updated. Continuous updating and, more importantly, a permanent reminder of those already discovered would be particularly useful in vascular procedures, including arteriovenous fistulas [3, 7, 9]. Arteriovenous fistula is again becoming a popular vascular access procedure [3]. There are many reasons, and one of them is an intensive anatomical work that broadens knowledge about the vascular system of the upper limb [3, 6, 7, 9, 10, 15]. Classic arteriovenous fistula still seems to be a good method associated with a lower rate of complications compared to other methods [1, 4]. All of that has resulted in a slow return to classic arteriovenous fistulas [1, 3].

Despite of our modest anatomical material of the upper limbs, we would like to present some revealed variants of the venous system. In addition, some possible anatomical traps in the creation of an arteriovenous fistula were analysed.

MATERIALS AND METHODS

The material was consisted of 20 preparations of the upper limb taken from 10 deceased (6 men and 4 women). The anatomical explorations were conducted at the Faculty of Normal and Clinical Anatomy of the Pomeranian Medical University in Szczecin. The cadavers were preserved and stored in a solution of formalin, glycerine and ethyl alcohol. Among the cadavers were 6 males and 4 females. The registered age on the day of their death was 67–81 years. The body storage period was 10–20 years. The upper limbs were without visible genetic deformities or previous surgery. Apart from typical sectional instruments such as scalpels, tweezers and raspators, a magnifying camera was also used, which was particularly useful in the exploration of small blood vessels. For clarity of photographic documentation, the dissected blood vessels have been coloured. Then the dissected upper limbs were photographed for the scientific purposes and then allocated for educational programme.



Figure 1. The correct picture of the cephalic vein (1) and the basilic vein (2).

RESULTS

The main intention of this exploration was to educate students. But during the preparation of the upper limbs, some variants of the venous system were discovered, which have not yet been described in anatomy textbooks.

In 17 (85% of all) upper limbs, the venous system showed a pattern similar to the reports already described (Fig. 1). But in 3 (15%) of them, the venous system showed certain dissimilarities in relation to the accepted anatomical textbooks.

Especially in one of them the topography of the basilic and cephalic vein contrasted significantly with the others (Fig. 2). At the beginning the both veins ran along both sides of the forearm, but instead of climbing on the arm, they both approached the cubital fossa, where they connected to the deep venous system. The next unusual thing was the brachial vein. Usually in the cubital fossa can be found two brachial veins, but unexpectedly there was only one. Only this one brachial vein was formed from the

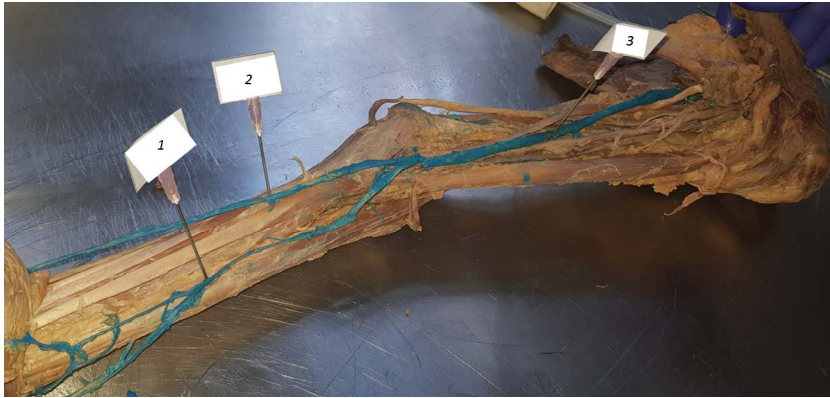


Figure 2. The correct picture of the cephalic vein (1) and the basilic vein (2) and brachial vein (3).

connection of the superficial and deep veins. This was finally confirmed by further exploration of the upper limb. To the surprise, the estimated probability of occurrence of anatomical variability of the venous system of the upper limb was statistically significant at $p < 0.0244$ (odds ratio 0.0828; 95% confidence interval 0.0095–0.7252). In extrapolation analysis it can be stated that about 90% of fistulas would not have encountered any topographic diversity during surgery, but every tenth may already occur. This would mean that there may really be topographic difficulties with the venous system in creating an arteriovenous fistula.

DISCUSSION

The knowledge about anatomical variabilities of upper limb venous system is intensively updated, but in clinical practice still encounters some limits [2, 3, 7–10, 14, 16].

Anatomical exploration of human body is a challenge for both anatomists and, especially, clinicians, because undiscovered variations can cause many problems in their daily medical practice [1, 4, 9, 12, 13].

In addition to updates, it should be reminded about already discovered patterns. It seems to be crucial for the successful treatment [3, 7, 9].

Although anatomy departments all over the world suffer from a body deficiency, intensive anatomical dissections have been conducted and undoubtedly contributed to restored priorities of arteriovenous fistulas [3, 6, 8, 10].

We did not expect that in our very small group of limbs we would encounter some anomalies of deep and superficial veins. Indeed, in 17 preparations of the upper limbs, the topography of venous vessels was consistent with the classic descriptions of textbooks. The basilic and cephalic vein runs up along both side of forearm. The basilic one comes

into arm on the medial side of it, and in half of arm dives more proximally to join one of two brachial veins near the axilla. But cephalic vein runs higher to join the axillar vein in the deltopectoral triangle. It can be supposed that in these anatomical variations the creation of an arteriovenous fistula would not encounter any anatomical or topographic difficulties. But in 3 (15%) limbs the topography of brachial, basilic and cephalic vein did not coincide with the descriptions of textbooks and literary reports. Especially in one limb it was completely different, which is the subject of this case report. Searching the literature data, a similar variant was found, which has already been described and classified as very rare [14]. This prompted us to re-present this variant, but in the aspect of creating arteriovenous fistulas. The accidental ligation of such an unpaired brachial vein would stop the outflow of blood and develop some complications such as oedema or even phlegmasia cerulea dolens. Therefore, we would like to remind of this and anticipate some problems in creating of fistula [1, 14, 17].

Our variant could be described as the second case report. However, in our opinion, more important than report numbering is whether a particular case is really rare, as is supposed. The disclosure of a similar variety on our small anatomical material may indicate that this variant should not be considered very rare. Especially it is important in creation of arteriovenous fistula in the middle arm (middle arm fistula [MAF]). This method (MAF) is rapidly becoming a more common vascular access procedure, especially in so called difficult arteriovenous fistulas [16]. This should remind surgeons about this topography pattern when they plan to form an arteriovenous fistula in the arm with basilic vein transposition [2, 3, 6, 15]. The presented variability seems particularly interesting in the context

of possible complications after the creation of MAF [1, 17]. The clinical report of Kaiser et al. [9] confirms the possibility of occurrence of some complications with MAF creation in atypical junction to the basilic vein with the unpaired brachial vein.

CONCLUSIONS

Because of the likelihood of variability in the venous system of the upper limb, examining it before surgery would contribute to avoiding some difficulties and pitfalls. These preliminary results of the upper limb venous system require further investigations.

REFERENCES

- Al-Jaishi AA, Liu AR, Lok CE, et al. Complications of the arteriovenous fistula: a systematic review. *J Am Soc Nephrol*. 2017; 28(6): 1839–1850, doi: [10.1681/ASN.2016040412](https://doi.org/10.1681/ASN.2016040412), indexed in Pubmed: [28031406](https://pubmed.ncbi.nlm.nih.gov/28031406/).
- Altıparmak B, Korkmaz Toker M, Uysal Aİ, et al. Double axillary vein variation diagnosed with ultrasound guidance during infraclavicular nerve block intervention. *BMJ Case Rep*. 2019; 12(1), doi: [10.1136/bcr-2018-227495](https://doi.org/10.1136/bcr-2018-227495), indexed in Pubmed: [30696646](https://pubmed.ncbi.nlm.nih.gov/30696646/).
- Anaya-Ayala JE, Younes HK, Kaiser CL, et al. Prevalence of variant brachial-basilic vein anatomy and implications for vascular access planning. *J Vasc Surg*. 2011; 53(3): 720–724, doi: [10.1016/j.jvs.2010.09.072](https://doi.org/10.1016/j.jvs.2010.09.072), indexed in Pubmed: [21144691](https://pubmed.ncbi.nlm.nih.gov/21144691/).
- Astor BC, Eustace JA, Powe NR, et al. Type of vascular access and survival among incident hemodialysis patients: the Choices for Healthy Outcomes in Caring for ESRD (CHOICE) Study. *J Am Soc Nephrol*. 2005; 16(5): 1449–1455, doi: [10.1681/ASN.2004090748](https://doi.org/10.1681/ASN.2004090748), indexed in Pubmed: [15788468](https://pubmed.ncbi.nlm.nih.gov/15788468/).
- Brescia MJ, Cimino JE, Appell K, et al. Chronic hemodialysis using venipuncture and a surgically created arteriovenous fistula. *N Engl J Med*. 1966; 275(20): 1089–1092, doi: [10.1056/NEJM196611172752002](https://doi.org/10.1056/NEJM196611172752002), indexed in Pubmed: [5923023](https://pubmed.ncbi.nlm.nih.gov/5923023/).
- Fontaine C. Some help for literature study in anatomical variation reports. *Surg Radiol Anat*. 2001; 23(5): 293–294, doi: [10.1007/s00276-001-0293-6](https://doi.org/10.1007/s00276-001-0293-6), indexed in Pubmed: [11824125](https://pubmed.ncbi.nlm.nih.gov/11824125/).
- Griffioen FMM, Drukker J, Hoogland PVJM, et al. General plan anatomy. Objectives of the teaching of anatomy/embryology in medical curricula in the netherlands. *Eur J Morphol*. 1999; 37(4-5): 288–325, doi: [10.1076/ejom.37.4.288.4721](https://doi.org/10.1076/ejom.37.4.288.4721).
- Jones DG, Dias GJ, Mercer S, et al. Clinical anatomy research in a research-driven anatomy department. *Clin Anat*. 2002; 15(3): 228–232, doi: [10.1002/ca.10017](https://doi.org/10.1002/ca.10017), indexed in Pubmed: [11948960](https://pubmed.ncbi.nlm.nih.gov/11948960/).
- Kaiser CL, Anaya-Ayala JE, Ismail N, et al. Unrecognized basilic vein variation leading to complication during basilic vein transposition arteriovenous fistula creation: case report and implications for access planning. *Eur J Vasc Endovasc Surg*. 2010; 39(5): 627–629, doi: [10.1016/j.ejvs.2010.01.011](https://doi.org/10.1016/j.ejvs.2010.01.011), indexed in Pubmed: [20172752](https://pubmed.ncbi.nlm.nih.gov/20172752/).
- Lee H, Lee SH, Kim SJ, et al. The clinical anatomy of the cephalic vein in the deltopectoral triangle. *Folia Morphol*. 2008; 67: 72–77.
- Lemson MS, Tordoir JH, Daemen MJ, et al. Intimal hyperplasia in vascular grafts. *Eur J Vasc Endovasc Surg*. 2000; 19(4): 336–350, doi: [10.1053/ejvs.1999.1040](https://doi.org/10.1053/ejvs.1999.1040), indexed in Pubmed: [10801366](https://pubmed.ncbi.nlm.nih.gov/10801366/).
- Miller A, Hölzenbein TJ, Gottlieb MN, et al. Strategies to increase the use of autogenous arteriovenous fistula in end-stage renal disease. *Ann Vasc Surg*. 1997; 11(4): 397–405, doi: [10.1007/s100169900068](https://doi.org/10.1007/s100169900068), indexed in Pubmed: [9236998](https://pubmed.ncbi.nlm.nih.gov/9236998/).
- Quinton W, Dillard D, Scribner BH, et al. Cannulation of blood vessels for prolonged hemodialysis. *Trans Am Soc Artif Intern Organs*. 1960; 6(1): 104–113, indexed in Pubmed: [13738750](https://pubmed.ncbi.nlm.nih.gov/13738750/).
- Sadeghi A, Setayesh Mehr M, Esfandiari E, et al. Variation of the cephalic and basilic veins: A case report. *J Cardiovasc Thorac Res*. 2017; 9(4): 232–234, doi: [10.15171/jcvtr.2017.40](https://doi.org/10.15171/jcvtr.2017.40), indexed in Pubmed: [29391938](https://pubmed.ncbi.nlm.nih.gov/29391938/).
- Sandhu NPS, Sidhu DS. Mid-arm approach to basilic and cephalic vein cannulation using ultrasound guidance. *Br J Anaesth*. 2004; 93(2): 292–294, doi: [10.1093/bja/aei179](https://doi.org/10.1093/bja/aei179), indexed in Pubmed: [15194622](https://pubmed.ncbi.nlm.nih.gov/15194622/).
- Sanudo JR, Vazquez R, Puerta J. Meaning and clinical interest of the anatomical variations in the 21st century. *Eur J Anat*. 2003; 7(S1): 1–3.
- Tellis VA, Veith FJ, Soberman RJ, et al. Internal arteriovenous fistula for hemodialysis. *Surg Gynecol Obstet*. 1971; 132(5): 866–870, indexed in Pubmed: [4929209](https://pubmed.ncbi.nlm.nih.gov/4929209/).
- Wijeyaratne SM, Kannangara L. Safety and efficacy of electrospun polycarbonate-urethane vascular graft for early hemodialysis access: first clinical results in man. *J Vasc Access*. 2011; 12(1): 28–35, doi: [10.5301/jva.2011.6278](https://doi.org/10.5301/jva.2011.6278), indexed in Pubmed: [21279948](https://pubmed.ncbi.nlm.nih.gov/21279948/).

Unilateral triple mandibular canal with double mandibular foramen: cone-beam computed tomography findings of an unexpected anatomical variant

A. Borghesi¹, M.P. Bondioni¹

Department of Medical and Surgical Specialties, Radiological Sciences and Public Health, University of Brescia, ASST Spedali Civili of Brescia, Italy

[Received: 7 May 2020; Accepted: 17 May 2020]

The mandibular canal is a bony channel located within the spongiosa of the mandible. The main structure contained in the mandibular canal is the inferior alveolar nerve. The inferior alveolar nerve is a very important structure that requires due consideration during dental or surgical procedures involving the mandible. Therefore, a detailed morphological analysis of the mandibular canal should be carried out before any surgical procedure in the mandibular region in order to avoid complications and to reduce the risk of inadequate local nerve blocking. The human mandible typically has a single mandibular canal on each side; however, accessory mandibular canals have been described previously in the literature. The most common variant of the mandibular canal is the bifid mandibular canal, which has a prevalence ranging from 10% to 66% on cone-beam computed tomography (CBCT) examinations. A rare variant of bifid mandibular canal is the trifid canal, accounting for less than 6% of all bifid canals. In some cases, the bifid and trifid mandibular canals are associated with a double mandibular foramen, which is a rare anatomical variant with a reported incidence of 1.35% on CBCT images. Herein, we present the interesting CBCT images of an unexpected anatomical variant characterised by unilateral triple mandibular canal with double mandibular foramen in a young Caucasian woman. (Folia Morphol 2021; 80, 2: 471–475)

Key words: mandibular canal, anatomic variation, accessory mandibular canal, accessory mandibular foramen, mandible, cone-beam computed tomography

INTRODUCTION

The mandibular canal is a bony channel located within the spongiosa of the mandible, typically close to the apices of the roots of the molars. The mandibular canal starts at the mandibular foramen (located on the lingual aspect of the mandibular ramus) and

ends at the mental foramen (located on the buccal aspect of the mandibular body) [9]. It runs from the top to the bottom of the mandible, and forms an upward-facing curve.

The main structure contained in the mandibular canal is the inferior alveolar nerve (IAN). The IAN is

Address for correspondence: A. Borghesi, MD, Department of Medical and Surgical Specialties, Radiological Sciences and Public Health, University of Brescia, ASST Spedali Civili of Brescia, Piazzale Spedali Civili, 1, I-25123 Brescia, Italy, tel: +39 030395900, fax: +39 0303399897, e-mail: andrea.borghesi@unibs.it

This article is available in open access under Creative Common Attribution-Non-Commercial-No Derivatives 4.0 International (CC BY-NC-ND 4.0) license, allowing to download articles and share them with others as long as they credit the authors and the publisher, but without permission to change them in any way or use them commercially.

the largest branch of the mandibular nerve, which is the third division of the fifth cranial nerve (*the trigeminal nerve*) [13]. Inside the mandibular canal, the IAN appears as a single large nerve bundle; however, it has been previously demonstrated that the IAN includes two distinct branches spirally twisted around each other [8]. Both nerves are wrapped in a layer of connective tissue (*the perineurium*). The larger branch corresponds to the mental nerve, whereas the smaller branch corresponds to the dental nerve [8, 13]. The mental nerve comes out at the level of the mental foramen, while the dental nerve continues its intra-mandibular course beyond the mental foramen within the incisive mandibular canal [13].

The IAN is a very important structure that requires due consideration during dental or surgical procedures involving the mandible, such as dental implant placement, endodontic treatment, mandibular molar extractions (especially of the third molars), and periapical and orthognathic surgeries [8]. Therefore, a detailed morphological analysis of the mandibular canal should be carried out before any surgical procedure in the mandibular region in order to avoid complications, such as neurosensory impairment, traumatic neuroma, or bleeding, and to reduce the risk of inadequate local nerve blocking.

In the interest of contributing a novel finding to the literature, this report presents interesting cone-beam computed tomography (CBCT) images of an unexpected anatomical variant characterised by a triple mandibular canal with double mandibular foramen in the same hemimandible in a young Caucasian woman.

CASE REPORT

During a retrospective search on the department radiology information system/picture archiving and communication system between January 2012 and December 2019, we came across interesting CBCT images of a young Caucasian woman who underwent a CBCT scan of the mandible as part of her routine dental examination. The patient was in good health, and no systemic disease or hereditary syndromes were reported. The examination was carried out with high-quality CBCT scanner (NewTom Cone Beam 3D Imaging, Verona, Italy) using the following parameters: tube voltage 90 kVp, tube current 4 mA, and field of view 10×8 cm. The CBCT acquisition data were reconstructed in the axial plane as thin-section images with a voxel size of $150 \mu\text{m}$.

Unexpectedly, the CBCT images revealed an extremely rare anatomical variant characterised by a triple mandibular canal on the left side of the mandible (Figs. 1, 2). On the same hemimandible, a double mandibular foramen (MF_1 and MF_2) was also observed (Figs. 1, 2). The maximum diameter of the left main mandibular canal (MC_{main}) was 2.6 mm, and the maximum diameters of the two accessory mandibular canals (AMC_1 and AMC_2) were 2 mm and 1.4 mm, respectively.

The intra-mandibular position of AMC_1 and AMC_2 was in close proximity to MC_{main} (Fig. 1). AMC_1 originated from MC_{main} at the level of the second molar (Fig. 1). From its origin, AMC_1 ran forward in contact with the lingual cortex of the mandibular body, lingual to MC_{main} (Fig. 1). AMC_1 joined MC_{main} at the level of the mental foramen, continuing mesially into the incisive mandibular canal (Fig. 1). AMC_2 originated from a small accessory mandibular foramen (MF_2) located inferior to the main mandibular foramen (MF_1) (Fig. 2). From its origin, AMC_2 ran forward and inferior to MC_{main} (Figs. 1, 2). AMC_2 joined MC_{main} at the level of the second premolar (Fig. 1).

With respect to the distomesial course of the triple mandibular canal, while the intra-mandibular course of MC_{main} and AMC_2 formed an upward-facing curve (Fig. 2), the intra-mandibular course of AMC_1 showed a serpiginous shape in the anterior portion (Fig. 2).

DISCUSSION

The human mandible typically has a single mandibular canal on each side; however, accessory mandibular canals have been described previously in the literature [6, 10, 12, 14, 15]. The presence of accessory mandibular canals is likely due to the incomplete fusion of three distinct IANs that merge to form the IAN during the prenatal period [3].

The most common variant of the mandibular canal is the bifid mandibular canal, which has a prevalence ranging from 10% to 66% on CBCT examinations [6, 10, 12, 14, 15]. It is detected in the posterior mandible or mandibular ramus [6, 10, 12, 14, 15]. The most common and clinical important type of bifid mandibular canal is the retromolar canal [6, 10, 12, 14, 15]. A rare variant of bifid mandibular canal is the trifid canal, accounting for less than 6% of all bifid canals [12, 14].

In some cases, the bifid and trifid mandibular canals are associated with a double mandibular foramen [12], which is a rare anatomical variant with a reported incidence of 1.35% on CBCT images [4].

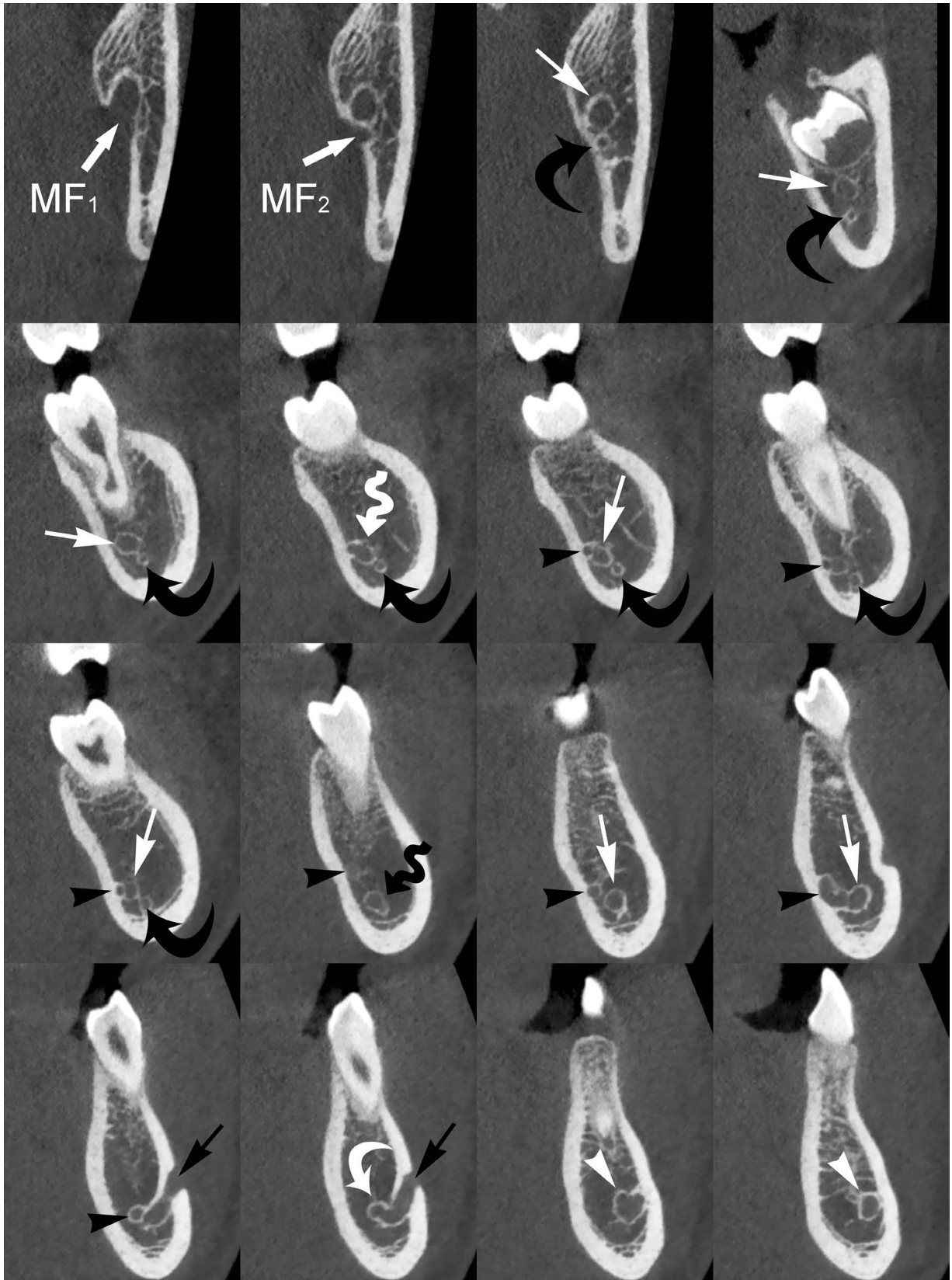


Figure 1. Cross-sectional cone-beam computed tomography images show the buccolingual position of the three mandibular canals (MC_{main} , AMC_1 , AMC_2) on the left hemimandible. AMC_1 (black arrowheads) originates from MC_{main} at the level of the second molar (white wavy arrow). AMC_1 joins MC_{main} at the level of the mental foramen (white curved arrow). AMC_2 (black curved arrows) originates from a small accessory mandibular foramen (MF_2) inferior to the main mandibular foramen (MF_1). AMC_2 joins MC_{main} at the level of the second premolar (black wavy arrow); white arrows — MC_{main} ; white arrowheads — mandibular incisive canal; black arrows — mental foramen.

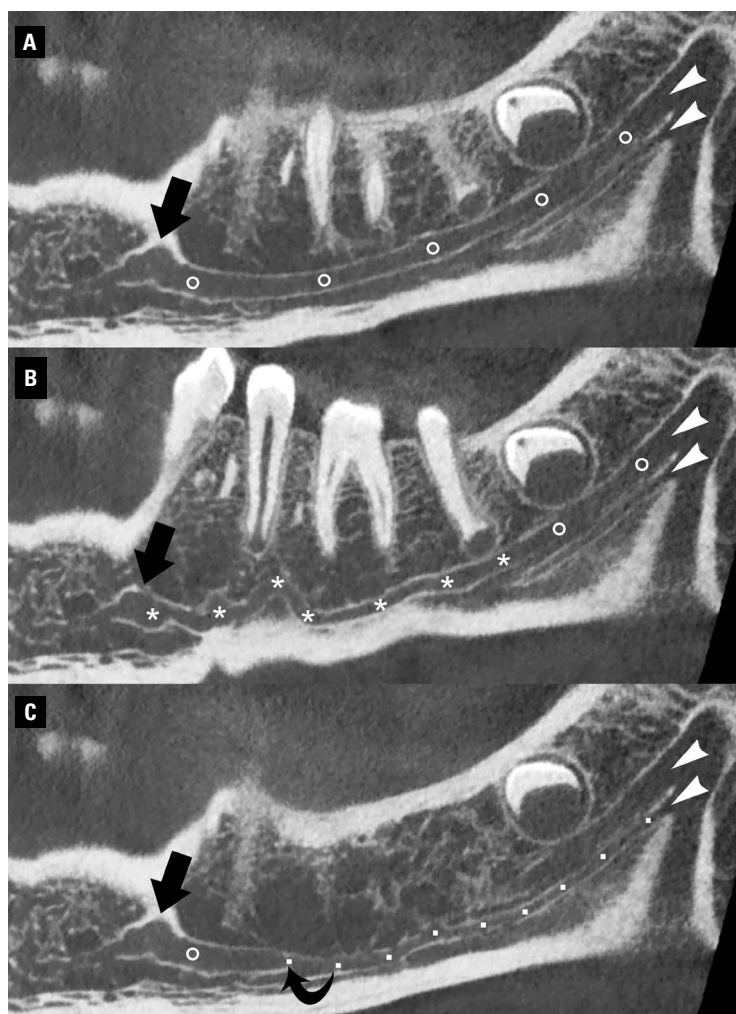


Figure 2. Panoramic cone-beam computed tomography images demonstrate the distomesial course of the three mandibular canals (MC_{main} , AMC_1 , AMC_2) within the left hemimandible; **A, C.** The intra-mandibular course of MC_{main} (circles) and AMC_2 (dots) forms an upward-facing curve. AMC_2 joins MC_{main} at the level of the second premolar (curved arrow); **B.** The intra-mandibular course of AMC_1 (asterisks) shows a serpinginous shape in its anterior portion. AMC_1 originated from MC_{main} at the level of the second molar. Double mandibular foramen is also shown (arrowheads); large black arrows — mental foramen.

To the best of our knowledge, the current report describes the CBCT findings of a novel anatomical variant characterised by the presence of a triple mandibular canal associated with a double mandibular foramen; a variant that is not included in the classification systems of mandibular canal branching [2, 11], and that has not been reported previously.

Differently from bifid and trifid mandibular canals [12, 14] which are confined in the retromolar or molar region, our accessory mandibular canals (AMC_1 and AMC_2) ran forward and continued their intra-mandibular course beyond the posterior mandible by reaching the premolar region (Fig. 2). AMC_1 joined MC_{main} at the level of the mental foramen, whereas AMC_2 joined MC_{main} at the level of the second premolar (Figs. 1, 2).

From a clinical point of view, accessory mandibular canals and foramina have relevant clinical implications because they can increase the risk of neurovascular complications and inadequate local anaesthesia during mandibular surgical procedures. Therefore, preoperative radiological analysis of mandibular anatomical landmarks and their variations is of great importance to determine appropriate clinical management and reduce the occurrence of iatrogenic complications and IAN block failures.

In clinical practice, the presence of one or more accessory mandibular canals and/or foramina may be detected with different radiological techniques such as conventional X-rays, multidetector CT and CBCT. The main limitations of conventional X-rays (periapical and panoramic radiographs) include the two-dimen-

sional nature of these radiographic examinations and the overlap of adjacent anatomical structures due to the lack of any cross-sectional information. Given these limitations, certain anatomical variants within mandible may be difficult to detect. In addition, the presence of these variants could sometimes be misinterpreted as osteolytic lesion on conventional X-rays.

Both multidetector CT and CBCT are usually adequate for radiological assessment of the mandible. However, it is well known that CBCT outperform multidetector CT in displaying fine anatomical details (such as canals and foramina). Therefore, CBCT is currently considered the most accurate radiological imaging technique to study of fine anatomical details of the mandible and its variants.

With the introduction and broad availability of CBCT scanners in clinical practice, an increasing number of anatomical variants are being detected, especially in the mandibular region [7, 9]. The number of reports that describe unusual anatomical variants within the mandible is also steadily increasing [1, 4, 5]. Therefore, radiologists should be aware of the clinical importance of reporting the number, size and course of any accessory mandibular canals and any additional variants that are incidentally observed during CBCT examinations.

CONCLUSIONS

This report describes the novel presentation of a triple mandibular canal associated with double mandibular foramen in a living human subject. Given that the occurrence of critical anatomical variants associated with an increased risk of iatrogenic injury of the IAN is becoming more frequent nowadays, a preoperative CBCT study of the mandible is recommended before any oral and dental procedures are carried out in the mandibular region. In addition, awareness about the presence of these critical anatomical variants can also help prevent future misdiagnosis and unnecessary radiological investigations.

REFERENCES

- Borghesi A, Pezzotti S, Nocivelli G, et al. Five mental foramina in the same mandible: CBCT findings of an unusual anatomical variant. *Surg Radiol Anat.* 2018; 40(6): 635–640, doi: [10.1007/s00276-018-1969-5](https://doi.org/10.1007/s00276-018-1969-5), indexed in Pubmed: [29318364](https://pubmed.ncbi.nlm.nih.gov/29318364/).
- Castro MA, Lagravere-Vich MO, Amaral TM, et al. Classifications of mandibular canal branching: A review of literature. *World J Radiol.* 2015; 7(12): 531–537, doi: [10.4329/wjr.v7.i12.531](https://doi.org/10.4329/wjr.v7.i12.531), indexed in Pubmed: [26753068](https://pubmed.ncbi.nlm.nih.gov/26753068/).
- Chávez-Lomeli ME, Mansilla Lory J, Pompa JA, et al. The human mandibular canal arises from three separate canals innervating different tooth groups. *J Dent Res.* 1996; 75(8): 1540–1544, doi: [10.1177/00220345960750080401](https://doi.org/10.1177/00220345960750080401), indexed in Pubmed: [8906121](https://pubmed.ncbi.nlm.nih.gov/8906121/).
- Choi YY, Han SS. Double mandibular foramen leading to the accessory canal on the mandibular ramus. *Surg Radiol Anat.* 2014; 36(9): 851–855, doi: [10.1007/s00276-014-1310-x](https://doi.org/10.1007/s00276-014-1310-x), indexed in Pubmed: [24817561](https://pubmed.ncbi.nlm.nih.gov/24817561/).
- de Souza Tolentino E, Silva PA, Pagin O, et al. Uncommon trajectory variations of the mandibular canal and of the mandibular incisive canal: case report. *Surg Radiol Anat.* 2013; 35(9): 857–861, doi: [10.1007/s00276-013-1138-9](https://doi.org/10.1007/s00276-013-1138-9), indexed in Pubmed: [23728516](https://pubmed.ncbi.nlm.nih.gov/23728516/).
- Fuentes R, Arias A, Farfán C, et al. Morphological variations of the mandibular canal in digital panoramic radiographs: a retrospective study in a Chilean population. *Folia Morphol.* 2019; 78(1): 163–170, doi: [10.5603/FM.a2018.0058](https://doi.org/10.5603/FM.a2018.0058), indexed in Pubmed: [30009366](https://pubmed.ncbi.nlm.nih.gov/30009366/).
- Kawai T, Sato I, Asaumi R, et al. Cone-beam computed tomography and anatomical observations of normal variants in the mandible: variant dentists should recognize. *Oral Radiol.* 2018; 34(3): 189–198, doi: [10.1007/s11282-017-0307-7](https://doi.org/10.1007/s11282-017-0307-7), indexed in Pubmed: [30484034](https://pubmed.ncbi.nlm.nih.gov/30484034/).
- Kqiku L, Weiglein AH, Pertl C, et al. Histology and intra-mandibular course of the inferior alveolar nerve. *Clin Oral Investig.* 2011; 15(6): 1013–1016, doi: [10.1007/s00784-010-0459-x](https://doi.org/10.1007/s00784-010-0459-x), indexed in Pubmed: [20737177](https://pubmed.ncbi.nlm.nih.gov/20737177/).
- Leite GM, Lana JP, de Carvalho Machado V, et al. Anatomic variations and lesions of the mandibular canal detected by cone beam computed tomography. *Surg Radiol Anat.* 2014; 36(8): 795–804, doi: [10.1007/s00276-013-1247-5](https://doi.org/10.1007/s00276-013-1247-5), indexed in Pubmed: [24337387](https://pubmed.ncbi.nlm.nih.gov/24337387/).
- Muinelo-Lorenzo J, Suárez-Quintanilla JA, Fernández-Alonso A, et al. Descriptive study of the bifid mandibular canals and retromolar foramina: cone beam CT vs panoramic radiography. *Dentomaxillofac Radiol.* 2014; 43(5): 20140090, doi: [10.1259/dmfr.20140090](https://doi.org/10.1259/dmfr.20140090), indexed in Pubmed: [24785820](https://pubmed.ncbi.nlm.nih.gov/24785820/).
- Ngeow WC, Chai WL, Ngeow WC, et al. The clinical anatomy of accessory mandibular canal in dentistry. *Clin Anat.* 2020; 33(8): 1214–1227, doi: [10.1002/ca.23567](https://doi.org/10.1002/ca.23567), indexed in Pubmed: [31943382](https://pubmed.ncbi.nlm.nih.gov/31943382/).
- Rashsuren O, Choi JW, Han WJ, et al. Assessment of bifid and trifid mandibular canals using cone-beam computed tomography. *Imaging Sci Dent.* 2014; 44(3): 229–236, doi: [10.5624/isd.2014.44.3.229](https://doi.org/10.5624/isd.2014.44.3.229), indexed in Pubmed: [25279344](https://pubmed.ncbi.nlm.nih.gov/25279344/).
- Rodella LF, Buffoli B, Labanca M, et al. A review of the mandibular and maxillary nerve supplies and their clinical relevance. *Arch Oral Biol.* 2012; 57(4): 323–334, doi: [10.1016/j.archoralbio.2011.09.007](https://doi.org/10.1016/j.archoralbio.2011.09.007), indexed in Pubmed: [21996489](https://pubmed.ncbi.nlm.nih.gov/21996489/).
- Yang X, Lyu C, Zou D. Bifid mandibular canals incidence and anatomical variations in the population of Shanghai area by cone beam computed tomography. *J Comput Assist Tomogr.* 2017; 41(4): 535–540, doi: [10.1097/RCT.0000000000000561](https://doi.org/10.1097/RCT.0000000000000561), indexed in Pubmed: [28722697](https://pubmed.ncbi.nlm.nih.gov/28722697/).
- Zhang YQ, Zhao YN, Liu DG, et al. Bifid variations of the mandibular canal: cone beam computed tomography evaluation of 1000 Northern Chinese patients. *Oral Surg Oral Med Oral Pathol Oral Radiol.* 2018; 126(5): e271–e278, doi: [10.1016/j.oooo.2018.06.008](https://doi.org/10.1016/j.oooo.2018.06.008), indexed in Pubmed: [30093317](https://pubmed.ncbi.nlm.nih.gov/30093317/).

Determination of anomalous pulmonary venous return with high-pitch low-dose computed tomography in paediatric patients	336
E. Gözgeç, M. Kantarci, F. Guven, H. Ogul, N. Ceviz, S. Eren	
Revisiting the anatomy of the cephalic vein, its origin, course and possible clinical correlations in relation to the anatomical snuffbox among Jordanian	344
M.A. Salameh, A.T. Shatarat, D.H. Badran, M.A. Abu-Abeeleh, T.M. Kanaan, A.M. Bani-Hani, M.Q. Hamdan	
Hypothyroidism: morphological and metabolic changes in the testis of adult albino rat and the amelioration by alpha-lipoic acid	352
A.A. Ibrahim, N.A. Mohammed, K.A. Eid, M.M. Abomughaid, A.M. Abdelazim, A.M. Aboregela	
Protective effect of <i>Coriandrum sativum</i> extract against inflammation and apoptosis in liver ischaemia/reperfusion injury	363
A. Kükner, G. Söyler, P. Toros, G. Dede, F. Meriçli, S. Işık, O. Edebal, C. Özoğul	
Computer-assisted measurements of the histological structure of the tibial nerve and its terminal branches	372
Ł. Warchoł, J.A. Walocha, E. Mizia, H. Liszka, M. Bonczar, I. Zamojska	
Effect of genistein and oestradiol on the adrenal cortex of the ovariectomised adult female albino rats	380
H.D. Yassa, N.M. Safwat, R.M. Ahmed, M.Z. Fathy, H.L. Metry	
Febuxostat ameliorates methotrexate-induced lung damage	392
S.M. Zaki, G.H.A. Hussein, H.M.A. Khalil, W.A. Abd Algaleel	
Normal and five-fingered hand: comparative X-ray morphometry in the post-natal age	403
M.P. Bondioni, L. Casati, A.G. Salvi, A. Minini, E. Zini, U.E. Pazzaglia	
Morphology of sesamoid bones in keyboard musicians	410
K.P. Dąbrowski, H. Stankiewicz-Jóźwicka, A. Kowalczyk, J. Wróblewski, B. Ciszek	
Surface localisation of master knot of Henry, <i>in situ</i> and <i>ex vivo</i> length of flexor hallucis longus tendon: pertinent data for tendon harvesting and transfer	415
P. Wan-ae-loh, P. Danginthawat, T. Huanmanop, S. Agthong, V. Chentanez	
Evaluation of the relationship between the maxillary third molars and pterygomaxillary fissure by cephalometric radiographs	425
S. Sadry, C.G. Koca, I. Kaya	
Evaluation of facial soft tissues by stereophotogrammetry method in patients with obstructive sleep apnoea: a morphological study	432
B. Karadede Ünal, C. Hüseyin	
A structural magnetic resonance imaging study in therapy-naïve transsexual individuals	442
A. Starcevic, M. Dakovic, Z. Radojicic, B. Filipovic	
CASE REPORTS	
Infrequent disposition of the first metacarpal artery related to anastomoses of the superficial and deep systems of the hand	448
H.F. Bianchi, N.E. Ottone	
A tale of two arteries: dual posterior cerebral arteries with vascular bridges. A possible protective pattern?	455
Y. Mansour, R. Kulesza	
Rare combined variations of the coeliac trunk, accessory hepatic and gastric arteries with co-occurrence of double cystic arteries	460
A. Mazurek, A. Juszcak, J.A. Walocha, A. Pasternak	
Anatomical traps for arteriovenous fistula creation	467
Z.M. Ziętek	
Unilateral triple mandibular canal with double mandibular foramen: cone-beam computed tomography findings of an unexpected anatomical variant	471
A. Borghesi, M.P. Bondioni	

CONTENTS

REVIEW ARTICLE

- The distribution of ghrelin cells in the human and animal gastrointestinal tract: a review of the evidence**225
K.M. Mehdar

ORIGINAL ARTICLES

- The contribution of the middle cerebral artery and callosal artery to the vascularisation of the Facies convexa of the brain in horses with reference to the equine-specific cartographic pattern of the neopallium**237
L. Böing, F. Heun, H. Gasse
- The anatomical landmarks effective in the localisation of the median nerve during orthopaedic procedures**248
E. Mizia, P.A. Pekala, B. Skinningsrud, B. Rutowicz, P. Piekos, A. Baginski, K.A. Tomaszewski
- An anatomical investigation of rare upper limb neuropathies due to the Struthers' ligament or arcade: a meta-analysis**255
E. Mizia, M.P. Zarzecki, J.R. Pekala, A. Baginski, L.N. Kaythampillai, M. Golebiowska, P.A. Pekala, J.A. Walocha, K.A. Tomaszewski
- Ultrasound-guided topographic anatomy of the medial calcaneal branches of the tibial nerve**267
L. Warchoń, J.A. Walocha, E. Mizia, M. Bonczar, H. Liszka, M. Koziej
- The dimensions of the sphenoid sinuses: evaluation before the functional endoscopic sinus surgery**275
J. Jaworek-Troć, M. Zarzecki, I. Zamojska, J. Iwanaga, W. Przybycień, M. Mazur, R. Chrzan, J.A. Walocha
- Unusual variations in the branching pattern of the coeliac trunk and their clinical significance** ...283
A. Juszcak, J. Czyżowski, A. Mazurek, J.A. Walocha, A. Pasternak
- Anatomical variants of coeliac trunk in Polish population using multidetector computed tomography angiography**290
A. Juszcak, J. Czyżowski, A. Mazurek, J.A. Walocha, A. Pasternak
- A macroscopic comparison study on main branches of arteria brachialis and arteria subscapularis in southern Karaman and Hasak sheep breeds**297
H. Kara, Z. Özüdogru, H. Balkaya, D. Özdemir
- Case series and a systematic review concerning the level of the aortic bifurcation**302
E. Panagouli, I. Antonopoulos, G. Tsoucalas, D. Chrysikos, A. Samolis, V. Protogerou, D. Venieratos, T. Troupis
- Morphological particularities and morphometry of rats' kidneys under the effect of experimental mild traumatic brain injury**310
R. Prus, P. Pokotylo, M. Logash, T. Zvir
- Types of left brachiocephalic vein aberrations detected during cardiac implantable electronic device implantation procedures**317
R. Steckiewicz, P. Stolarz, E.B. Świętoń
- Variations in the gonadal artery with a single common trunk: embryological hypotheses by observation**324
H. Terayama, Y. Miyaki, N. Qu, S. Katsuki, R. Tanaka, K. Umemoto, N. Kosemura, K. Suyama, O. Tanaka, K. Sakabe
- Origin and main ramifications of coeliac artery in *Cerdocyon thous***331
S. Viana-Peçanha, E.C. Souza, D.M.L. Guerra, F.C.S. Bernardes, R.B.J. Carvalho, P. de Souza Junior, M. Abidu-Figueiredo



INDEXED in: BIOSIS Previews, CAS, CINAHL, CrossRef, Dental Abstracts, EBSCO, Elsevier BIOBASE, EMBIOLOGY, FMJ, Google Scholar, Index Copernicus (154.80), Index Medicus/MEDLINE, Index Scholar, Ministry of Science and Higher Education (70), NCBI/National Center for Biotechnology Information, Polish Medical Bibliography, Scopus, SJR, Thomson Reuters, Thomson Scientific Products — Biological Abstracts, Ulrich's Periodicals Directory, Veterinary Bulletin, WorldCat and Zoological Record.

Cover picture: Fragmented renal glomeruli (arrow) with sclerosis (arrowhead) and blood stasis (asterisk); 21st day after traumatic brain injury; trichrome. For details see: Prus et al., Folia Morphol 2021; 80, 2: 310–316.